UNIVERSIDADE DE LISBOA
FACULDADE DE CIÊNCIAS
DEPARTAMENTO DE GEOLOGIA

Plume-lithosphere interaction at Santiago Island (Cape Verde): Implications for ocean island magma genesis models

Sofia Maria Marques Martins

DOUTORAMENTO EM GEOLOGIA
(GEOQUÍMICA)

2014

UNIVERSIDADE DE LISBOA
FACULDADE DE CIÊNCIAS
DEPARTAMENTO DE GEOLOGIA

Plume-lithosphere interaction at Santiago Island (Cape Verde): Implications for ocean island magma genesis models

Sofia Maria Marques Martins

Tese orientada pelos Profs. Doutores João Mata e José Munhá, especialmente elaborada para a obtenção do grau de doutor em Geologia (especialidade em Geoquímica)

2014

Plume-lithosphere interaction at Santiago Island (Cape Verde): Implications for ocean island magma genesis models

Sofia Maria Marques Martins

Doutoramento em Geologia
(Geoquímica)

In loving memory of my mother,
Maria Manuela Martins

Abstract

Santiago Island is the largest one in the Cape Verde archipelago with a total area of 991 km^2. It belongs to the southern group with Maio, Fogo and Brava Islands. Apart from the substrate (Complexo Antigo) Santiago's volcanostratigraphy is largely composed of subareal and submarine alkaline lavas outcrops, which cover a time span of circa 5 Ma.

Santiago alkaline lavas are testimony of a complex magmatic history, where chemical and lithological heterogeneous mantle sources and the interaction of advecting magmas with thick metasomatized oceanic lithosphere is preponderant in the observed isotopic and trace element signatures.

The distinctive major and trace element characteristics of Santiago lavas stand as a strong indicator of a carbonated mantle source with contributions from peridotitic and silica deficient garnet pyroxenite domains. The correlation of these elemental evidences with radiogenic isotopic data attests the presence of these domains within the plume, as well as their ancient signature.

Young (< 3.3 Ma) primitive Santiago lavas show evidence for the equilibration with modal and cryptically metasomatized oceanic lithospheric mantle. The metasomatism is responsible for the inferred hydrous mineral assemblage (amphibole and phlogopite) as well as specific geochemical tracers. Interestingly this signature is not ubiquitous in Santiago lavas mantle source, since the older formations do not show strong evidences for interaction with metasomatized domains of the lithosphere.

The carbonatitic nature of the metasomatic agent is attested from indirect geochemical signatures in alkaline lavas and direct evidence portrayed by lherzolitic xenoliths. It is important to acknowledge that the metasomatic agent composition is elemental and isotopically distinct from outcropping carbonatites.

In accordance with the overall isotopic characteristics of the Southern Cape Verde Islands, elemental and isotopic signatures of Santiago alkaline lavas suggest the involvement of HIMU and EM1-type mantle end-members, with the contribution a relatively undegassed and unradiogenic reservoir (Lower Mantle). The geochemical characteristics of Santiago allow us

to consider the EM-1 like end-member as resulting from the involvement of subcontinental lithospheric mantle in Santiago's magma genesis.

Tholeiitic outcropping lavas in the Santiago's northern area are considered as formed in a mid oceanic ridge environment. The lavas are highly depleted in LREE and incompatible elements, even when compared with D-MORB values. This depletion seems to be ubiquitous in Central Atlantic MORB erupted between 160 to 118 Ma.

The eruption of highly depleted lavas at the initial stages of the Atlantic opening is here interpreted as the result of high degrees of partial melting induced by sub-lithospheric elevated temperatures brought on by continental thermal insulation.

Santiago gabbroic xenoliths show geochemical similarities with Santiago MORB affinity lavas attesting their cumulate formation from abyssal-type magmas. The enrichment observed in some is most certainly derived from the interaction of ascending alkaline magmas with the pre-existing N-MORB crust.

Keywords: Ocean island magmatism; Cape Verde; Plume-lithosphere interaction; Carbonatite metasomatism; Mantle lithologic heterogeneity; MORB.

Resumo

A ilha de Santiago é a maior no arquipélago de Cabo Verde com uma área total de 991 km2. Pertence ao grupo Sul juntamente com as ilhas de Maio, Fogo e Brava. Não considerando o substrato (Complexo Antigo) a vulcanoestratigrafia de Santiago é constituída essencialmente por afloramentos de lavas alcalinas subaéreas e submarinas, que cobre um intervalo de tempo de cerca 5 Ma.

As lavas alcalinas de Santiago são testemunho de uma história magmática complexa, onde fontes mantélicas heterogéneas litológicamente e quimicamente e a ascensão de magmas através de uma litosfera oceânica espessa e metassomatizada, são preponderantes nas assinaturas isotópicas e em elementos traço observadas.

As características distintivas em elementos maiores e traço das lavas de Santiago são indicativas de uma fonte mantélica carbonatada com contribuições de domínios peridotíticos e piroxenitos granatíferos de baixa sílica. A correlação destas evidências elementares com dados isotópicos radiogénicos confirma a presença desses domínios na pluma, bem como a sua assinatura antiga.

As lavas primitivas recentes de Santiago (<3.3 Ma) mostram evidências para o equilíbrio com o manto litosférico metassomatizado cripticamente e modalmente. O metassomatismo é responsável pela associação mineralógica hidratada (anfíbola e flogopite) bem como traçadores geoquímicos específicos. Notavelmente, esta assinatura não é omnipresente na fonte mantélica das lavas de Santiago, uma vez que as formações mais antigas não mostram evidências para a interação com domínios metassomatizados da litosfera.

A natureza carbonatítica do agente metassomático é comprovada indiretamente, através de assinaturas geoquímicas nas lavas alcalinas e diretamente por evidências presentes em xenólitos peridotíticos. É importante salientar que a composição do agente metassomático é distinta elementar e isotopicamente dos carbonatitos aflorantes.

Em concordância com as características globais do grupo Sul das ilhas de Cabo Verde, as assinaturas elementares e isotópicas das lavas alcalinas de Santiago sugerem o envolvimento dos componentes mantélicos HIMU e EM1, com a contribuição de um reservatório relativamente desgaseificado (manto inferior). As características geoquímicas dos magmas de Santiago

permitem atribuir ao componente EM1 uma origem relacionada com o manto litosférico subcontinental.

As lavas toleíticas que afloram na área Norte de Santiago são consideradas como tendo sido geradas num ambiente de crista médio oceânica. As lavas são altamente empobrecidas em terras raras leves e elementos incompatíveis, mesmo quando comparadas com dados de D-MORB. Este empobrecimento parece ser ubíquo nos MORB do Centro Atlântico no período entre 160 e 118 Ma.

A formação de lavas altamente empobrecidas nas fases iniciais da abertura do Atlântico é aqui interpretada como o resultado de maiores graus de fusão, induzidos pelo aumento de temperatura em zonas sublitosféricas devido a isolamento térmico continental.

Os xenólitos gabroicos de Santiago mostram semelhanças geoquímicas com as lavas de afinidade com os MORB, comprovando a sua formação por acumulação de magmas do tipo abissal. O enriquecimento observado, em alguns, é certamente derivado da interação de magmas alcalinos em ascensão, com a crosta pré-existente.

Palavras-chave: Magmatismo de ilhas oceânicas; Cabo Verde; Interação pluma-litosfera; metassomatismo carbonatítico; heterogeneidade litológica mantélica; MORB

Acknowledgements

There are a number of people who deserve my heartfelt appreciation because, one way or other, helped me reach the end of this journey. I apologise in advance in case that somebody is missing from this list.

First of all I want to thank my supervisors, Professor Dr. João Mata and José Munhá, who proposed the continuation of my work in Santiago Island, initiated with my master's thesis. To Professor José Munhá I'm thankful for all the rewarding discussions and the availability demonstrated, as well as the patience in guiding me in the correct path.

To Professor João Mata I wish to thank not only for his role as my supervisor but also for being a dearest friend. I'm truly thankful not only for all the discussions, corrections, back and forth of the chapters, but also for is guidance towards my growth as an investigator and a teacher. He gave me confidence to believe in myself and my work by supporting me, criticizing my work (sometimes archly, but so necessary for a person to grow and learn), promoting international learning experiences and by the confidence demonstrated when working together. For me, Professor João Mata is a role model to whom I only aspire to be. The PhD process is a long one, more to some than others, and life goes on. I can honestly say that he was there for me during the losses, to support me, and during the happy times to rejoice with me. I'm truly grateful with all my heart for this journey together.

Special thanks for all the people that welcomed me at Université Libre de Bruxeles (ULB). A special word to Professor Nadine Mattielli who made me feel right at home. I learned a lot under her supervision not only at the laboratories but also working with the MC-ICP-MS Nu Plasma. I am also indebted to Claude Maerschalk for all that I learned at the laboratory, his meticulous methods will always be a guide to follow. I cherish our talks early in the morning at the lab. A further thank you to Sophie Verheyden, my office colleague, who was a great friend and helped me adapt to the university and the city. I'm also thankful to Jérôme Petit, Jeroen de Jung and Aurélien Taillez.

I would like to acknowledge Professor Maria do Rosário Azevêdo for access to the Laboratório de Geologia Isotópica da Universidade de Aveiro (Portugal). Where, Sr and Nd isotopic analyses for MORB-type rocks were performed by Dr. Sara Ribeiro.

I would like to express my thanks to FCT (Fundação para a Ciência e Tecnologia) for funding a PhD scholarship (SFRH/BD/17453/2004) during four years and the financial support provided by two projects PLINT (POCTI/CTA/45802/2002) and CV-PLUME (POCTI/CTE-GIN/64330/2006), which were instrumental for the realization of this thesis.

A very special thank you to Professor Línia Martins my mentor as teacher and true friend. It is a pleasure and a privilege to work with her due to her inspiring and rich knowledge not only as a teacher but also as an educator. I love our daily talks about all things, big and small. I also treasure her caring words and advices.

I wish to thank Professor Isabel Costa for her friendship, constant concern and stimulating suggestions. A further thank you to other Professors for their motivational words and constant support: José Madeira, Luís Celestino da Silva, Raúl Jorge, Catarina Silva, Isabel Moitinho, Paulo Fonseca, Fátima Africano, Teresa Palácios and Filipe Rosas.

I am also indebted to the Departamento de Geologia staff for their precious help on bureaucratic issues and their sympathy: Sr. Alberto Verde, D. Cleta Melo, D. Nídia Pereira, Célia Lee, Ana Sousa, Marta Antunes, Dina Gouveia and Marisa Santos. Also, a special word of recognition to Sr. Chaveiro for all the countless hours on the microprobe, that due to his humours character and sympathy, passed swiftly. To Dr. Pedro Rodrigues a sincere thank you for the support in the microprobe, his patience and dedication to his work made the data acquisition a rewarding experience.

One of the most important recognition is to my family, specially my dad, José. If it wasn't for him, this thesis would not have been completed. In a more practical and direct way due to the constant and necessary financial support provided. The vicissitudes of such a prolonged PhD process, part of which with no scholarship associated, requires a financial sustainability not easily achievable in the nowadays economical situation. Also, I owe him the ability to start fresh every day, no matter how hard yesterday was. The importance of knowledge, the

perseverance, strength and resilience necessary to achieve what a person aspires to, are all traits passed on by my parents who I love tenderly.

My sisters, Margarida and Sílvia, who I love so much, were always at my side, encouraging me and taking care of me. Their constant support enabled the conclusion of this journey. To my nephews Joseph, Collin and Miguel and niece Catarina a tender gratitude just for being present in my life…just the sight of them makes all things fall into place.

To my dearest friend and colleague Cyntia Morão I wish to thank her presence in my life. Her big heart, sensibility and friendship has no limits and in this long path she was one of my pillars, supporting me in every situation. As a colleague, our proximity regarding the studied subject, allowed the growth and maturation of many ideas portrayed in this thesis.

To my friend and colleague Inês Cruz a special thanks for her constant support, kind words and truthful companionship.

To a dear friend, Maria José Trindade, I wish to thank for always cheering me up and being there for me. A tender word of recognition to Carla Feiteira for her friendship, support, coaching lessons and for always demonstrating a hugely positive outlook on life.

A special thanks to Pedro Madureira for his constant encouragement, advices and caring words.

Other people that always helped and supported me through this process, being essential to put a smile in my face were: Isabel Martins, Zenaida Diogo, David Martins, João Carvalho, Filipa Marques, Paula Figueiredo, Ana Margarida Bento, Ana Jesus, Anabela Cruces, Rui Miranda, Telmo Santos, Bruno Ribeiro, Ricardo Ramalho and José Borrego.

I am also in debt to my managers at Bertrand, Vanda Verganista, Domingas Nogueira and Pedro Almeida who were always tolerant and helpful regarding my responsibilities in the university, as a PhD student and a teacher. Big thanks to my friends at the bookstore for their support: Ana Pessoa, Ana Filipa Neves, Bruno Oliveira, Bárbara Vasconcelos, Sofia Petisca, Rita Labareda, João Ferreira and Inês Lourenço.

Thanks also to all my students, for their interest and support and above all for helping me get through the more difficult days…teaching a class makes all the hardship worthwhile.

To Lulu, Mimosa, Rafael and Dalila a furry thanks.

Table of contents

Glossary of acronyms and abbreviations

The following acronyms and abbreviations are used throughout this thesis:

APSL	Above Present Sea Level
BSE	Bulk Silicate Earth
CAMP	Central Atlantic Magmatic Province
CCD	Calcite Compensation Depth
CMB	Core Mantle Boundary
DMM	Depleted MORB Mantle
DSDP	Deep Sea Drilling Project
EM	Enriched Mantle
EPMA	Electron Probe Micro-Analysis
Fo	Forsterite
FOZO	Focal Zone
GDH	Global Depth and Heat Flow model
GERM	Geochemical Earth Reference Model
GTR	Geoid-to-topography ratio
HFSE	High Field Strength Elements
HIMU	High "μ", or high $^{238}U/^{204}Pb$
HREE	Heavy Rare Erath Elements
IUGS	International Union of Geological Sciences
LAB	Lithosphere-Asthenosphere Boundary
LA-ICP-MS	Laser Ablation- Inductively Coupled – Mass Spectrometry
LILE	Large Ion Lithophile Elements
LIP	Large Igneous Province
LLSVP	Large Low Shear Wave Velocity Province
LOI	Loss On Ignition

LPA	Lower Pico da Antónia
LREE	Light Rare Earth Elements
LVZ	Low Velocity Zone
MC-ICP-MS	Multiple Collector - Inductively Coupled – Mass Spectrometry
MORB	Mid-Ocean Ridge Basalt
MREE	Middle Rare Earth Elements
NHIS	Northern Hemisphere Ice Sheet
NASA	National Aeronautics and Space Administration
NHRL	Northern Hemisphere Reference Line
OIB	Ocean Island Basalts
PGZ	Plume Generation Zone
PM	Primitive Mantle
PPM	Parts Per Million
PREMA	Prevalent Mantle
REE	Rare Earth Elements
ROC	Recycled Oceanic Crust
SCLM	Sub-Continental Lithospheric Mantle
SEM	Scanning Electron Microscopy
SINCLAS	Standard Igneous Norm and Volcanic Rock Classification System
SMEAN	Shear Wave Velocity Anomaly Map
TAS	Total Alkalis-Silica
Te	Lithosphere elastic thickness
TIMS	Thermal Ionization Mass Spectrometry
ULVZ	Ultra Low Velocity Zone
UPA	Upper Pico da Antónia
WPM	Within Plate Magmatism

CHAPTER 1

INTRODUCTION

Small bay between Monte Vermelho and Ponta Fazenda (Santiago Island – Cape Verde)

In the lower left corner it is visible a carbonatitic plug

1.1. Interest

The geological study of the different islands of the Cape Verde archipelago started 80 years ago with the work of Bebiano (1932). Since then numerous studies regarding field geology, petrography, geochemistry, geochronology, volcanology and geologic hazard assessment have been carried out establishing a strong geological knowledge of the several islands.

The strong roots that Centro de Geologia and Departamento de Geologia da Universidade de Lisboa has in the Cape Verde school of knowledge steams from its long term research association with IICT (Instituto de Investigação Científica e Tropical) an institution that has been studying the African territory since 1883. Its extensive heritage/legacy stands as the base for all the work that is accomplished national and internationally.

The strength of the Universidade de Lisboa in the study of Cape Verde archipelago also results from the fruitful cooperation between its Geosciences departments (Geology and Geophysics) enabling the publication of more multidisciplinary papers and, also, from the joint research with foreigner scientists from highly renowned institutions.

1.1.1. Why study intraplate magmatism?

Intraplate magmatism is thought to sample the Earth's mantle to great depths, not only because part of it is associated with deep rooted mantle plumes, which allows taping of otherwise inaccessible material, but also because such mantle dynamics permits the ascent and mixing of an assortment of materials to shallow regions (Hofmann, 1997). However when the essential aim is the study of the Earth's mantle, oceanic environments distant from continental settings, enables a more straightforward interpretation without potential contamination by low solidus crustal rocks and/or without the effects of the interaction of ascending magmas with the long-lived and highly heterogeneous subcontinental lithospheric mantle (SCLM).

Since the introduction of the concept of deep mantle plumes in 1971 by Morgan, the plume theory is becoming more and more a debatable and controversial subject. Even thought the assumptions associated with hotspots (linear chain of volcanoes, presence of LIP, particular geochemical signatures, amongst other) have been widen and simplified to accommodate

situations that depart from the idealized "Hawaiian" model, there are still magmatic occurrences that seem to be explained by shallower mechanisms. These alternative explanations range from edge driven convection (King and Anderson, 1998; King, 2007) to lithospheric gravitational instability (Elkins-Tanton and Grove, 2003), small scale convection (Haxby and Weissel, 1986; Ballmer et al., 2007) and shear-driven upwelling (Conrad et al., 2010).

However advances in geophysical methods seem to confirm the existence of identifiably structures extending from the lower mantle that can be causing some of the intraplate magmatism observed (van der Hilst and Kárason, 1999; van der Hilst, 2004; McNamara et al., 2010). This evidence is particularly unquestionable beneath Africa where large seismically slow structures, extending upward from the core-mantle boundary, have been identified (Ni et al., 2002; Davaille et al., 2005; Dziewonski et al., 2010; Frost et al., 2013; Lynner and Long, 2014). Also, recent experimental studies have demonstrated that the presence of primitive reservoirs in the deep mantle is dynamically viable as well as the entrainment of heterogeneous material into deep mantle plumes (Deschamps et al., 2011).

It is important to note that nature is not easily placed in boxes and hermetic theories. All hypothesis must start with some assumptions or with, what some people call, corollaries (Anderson, 2006). It seems feasible to assume that the reality will be most certainly the association of several mechanisms, deep and shallow, that contribute to the spectrum of intraplate magmatism worldwide.

1.1.2. Why study the Cape Verde archipelago?

The Cape Verde archipelago is located in the central Atlantic Ocean and consists of 15 islands and islets (Fig. 1.1). An extensive list of article has been published about the archipelago concerning volcanology, geomorphology, geophysics, petrology, geochemistry and geodynamics (see following chapters for respective references within each subject).

The Cape Verde archipelago is especially interesting in mantle studies due to its particular characteristics and geodynamic setting:

1. Islands implanted in old ocean crust (120-140Ma) and atop a slow-moving thick lithosphere;
2. Implanted on the largest oceanic swell on Earth;

3. Non-uniform age progression of the islands as expected for a moving plate across a "fixed" mantle plume;
4. Long magmatic history of the archipelago spanning, at least, 25.6 Ma of emmerged evolution;
5. Intra and inter-island geochemical heterogeneities;
6. Outcropping of extensive extrusive and intrusive carbonatitic rocks in 5 of the 10 islands, being the most outstanding occurrence of oceanic carbonatites in the world.

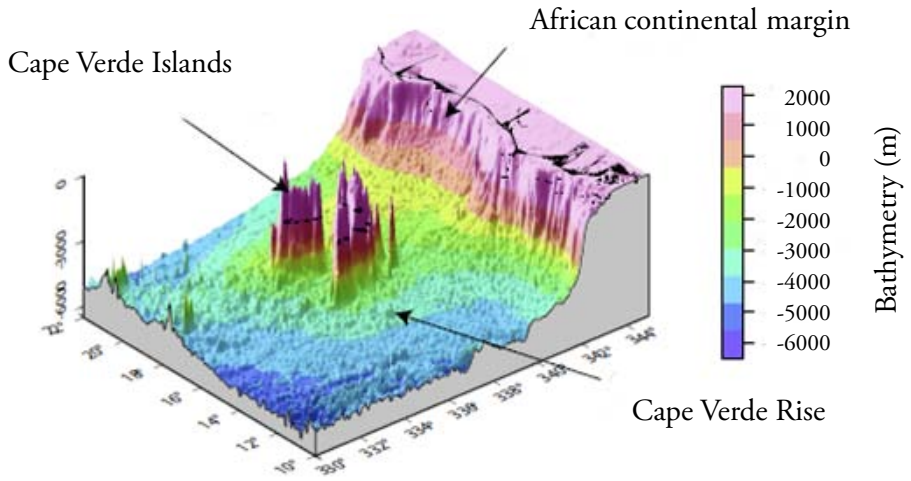

Figure 1.1 - 3D representation of the bathymetry in the Cape Verde archipelago region (adapted from Pim, 2006).

1.1.3. Aims of the study

This thesis stands as a contribution to the clarification of magmatogenesis of Santiago Island, not only within the context of geodynamic evolution of the archipelago but also within the intraplate magmatism present in old Atlantic oceanic crust.

The study is centered in subareal and submarine basaltic lavas collected from all volcanic formations covering the complete volcanostratigraphic island sequence. To accomplish this geochemical study, data comprising major and trace element whole rock analyses, radiogenic isotopes (Sr, Nd, Hf and Pb) and to a lesser degree, punctual mineral analyses of lavas, will be used.

The main subjects that are going to be addressed are:

- Mantle source chemical heterogeneities;

- Mantle source lithological diversity;
- Identification of processes that change the so-called "normal" mantle mineralogy and geochemistry;
- Metasomatism (recent and ancient);
- Identification of the metasomatic agent trough the study of lavas and xenoliths data;
- Plume-lithosphere interaction, i.e., influence of processes occurring within the lithosphere that are susceptible to be, partially, responsible for the heterogeneities observed in the magmas.

This study of Santiago Island also comprises the analyses of submarine lavas of MORB affinity that outcrop on the north of the island as well as gabbroic xenoliths found within the alkaline lavas of the main eruptive event. These two occurrences can be seen as testimonies of the oceanic crust that underlies Santiago Island.

The outcropping pillow lavas, after screening for alteration processes before and after their emersion, will be described geochemically. Their characteristics will be tested to confirm the expected mid-ocean ridge magmatic context and will allow the identification of ancient magmatic characteristics at the mid-Atlantic ridge.

Petrological and geochemical analyses of Santiago's gabbroic xenoliths will supply important information regarding the sub-surface lithologies, allow the inference of their parentage and give information about alterations imposed on the oceanic lithosphere through intraplate volcanism.

1.2. Structure of the thesis

For the purposes stated above, this PhD dissertation has been structured in 6 chapters. After the present introductory part, Chapter 2 comprises the geologic and geodynamic setting of the Cape Verde archipelago. It will be presented general information concerning the geographic, geomorphologic and tectonic context of the archipelago as a whole. Special attention is given to the geophysical particularities of the Cape Verde area such as heat flow, geoid and gravity anomalies as well as lithospheric structure and swell description. The

compelling and numerous evidences supporting the existence of a deep mantle plume will be presented in addition to the more common alternative models described in the literature.

Chapter 3 is entirely dedicated to Santiago Island geology, specifically the detailed description of its stratigraphy, with new data regarding the distinction between two subunits of the main eruptive complex, based on new field evidence associated with geochemical data.

The analyses and interpretation of major, trace and isotopic data of Santiago alkaline lavas is addressed in Chapter 4. The variability of Santiago magmas is discussed considering shallow level processes, source heterogeneities, mantle metasomatism and plume/mantle components.

The process of plume-lithosphere interaction is thoroughly described, analysed and discussed in Chapter 5. This subject is addressed separately due to its importance as a cause of Santiago Island, and Cape Verde, magmas heterogeneity and also due to my conviction of the significant, but variable, role of plume-lithosphere interaction in the composition of ocean island magmatism in general.

Gabbroic xenoliths and the submarine tholeiitic lava suite will be described petrographically and its mineral paragenesis characterized through microprobe data analyses. Major, trace and isotopic data will be analysed enabling a geochemical characterization of the Mesozoic oceanic crust and crustal xenoliths (Chapter 6).

The last Chapter includes the summarized conclusions obtained from each one of the preceding chapters, as all well as suggestions for future research in Cape Verde archipelago and Santiago Island.

1.3. Analytical facilities

This work would not be possible without the use of the following analytical facilities:

- Laboratories of Centro de Geologia (Universidade de Lisboa, Portugal) which enabled the preparation of rock samples and the production of thin sections and polished thin sections;
- Microprobe mineral analyses were obtained in a JEOL SUPERPROBE, model JXA-8200 also at the Centro de Geologia (Universidade de Lisboa, Portugal);

- The chemical preparation of alkaline lava samples for isotopic analyses was made at the Department of Earth and Environmental Sciences of the Université Libre de Bruxelles and Nd-Hf -Pb isotopic data were determined on a Nu plasma multi-collector inductively coupled mass spectrometer (MC-ICP-MS). Sr isotopic data was determined by a Finnigan Triton Thermo-Ionization Mass Spectrometer (TIMS) at the Pacific Centre for Isotopic and Geochemical Research at the University of British Columbia (Canada);
- Nd and Sr isotopic data from the tholeiitic lavas suite was performed at the Laboratório de Geologia Isotópica da Universidade de Aveiro (Portugal).

CHAPTER 2

GEOLOGIC AND GEODYNAMIC SETTING OF THE CAPE VERDE ARCHIPELAGO

Prainha (Santiago – Cape Verde)
Pillow lavas from the main eruptive event, Pico da Antónia Formation

2.1. Introduction

Cape Verde archipelago stands as a privileged location to study intraplate magmatism, not only due to its particular petrological/geochemical traits, such as the presence of intrusive and extrusive carbonatite occurrences (scarce in oceanic environment) and its geochemical diversity, but also for its geodynamic context. Located in the Central Atlantic Ocean associated with a slow spreading setting in old oceanic crust, the islands are thought to have been formed by a thermochemical mantle plume of deep origin.

In this chapter the main physical characteristics of the archipelago, as a whole will be described and discussed, being associated with the available geophysical, tectonic and geodynamic data of the area.

Even thought the existence of deep mantle plumes is still a matter of intense debate, the plume model is the privileged by the author and will be here described and discussed in the perspective of all the numerous indirect evidences supporting its occurrence. Also, the most important alternative non-plume models will be taken in consideration and discussed.

2.2. Geographic setting

The Cape Verde Archipelago belongs to Macaronésia, a wide group of Atlantic islands located between 10ºN and 40ºN of Latitude, which is assigned to a bio-geographic zone made up of islands with a volcanic substrate characterized by the presence of endemic species (Chevalier, 1935). The archipelagos of Azores, Madeira and Canary also belong to this group of "fortunate islands" (from the Greek "Makarón Neseu").

The archipelago consists of 15 islands and islets, encompassing a total emerged area of 4033 km^2. It is located between 17º12'-14º48' N and 22º41'-25º25' W, 460 km away from the Senegalese coast and 2500 km from the Mid-Atlantic Ridge (Assunção, 1968). The islands are arranged in an arc opening West, being divided in two groups: North (or windward) and South (or leeward). The islands of Santo Antão, São Vicente, Santa Luzia, São Nicolau, Sal and Boavista, as well as the Branco and Raso islets belongs to the Northern group and Brava, Fogo, Santiago, Maio and the Secos islets to the Southern group. The largest island in the archipelago

is Santiago, with a total area of 991 km^2. Santa Luzia is the smallest with only 35 km^2 (Bebiano, 1932; Machado, 1967) (Fig. 2.1).

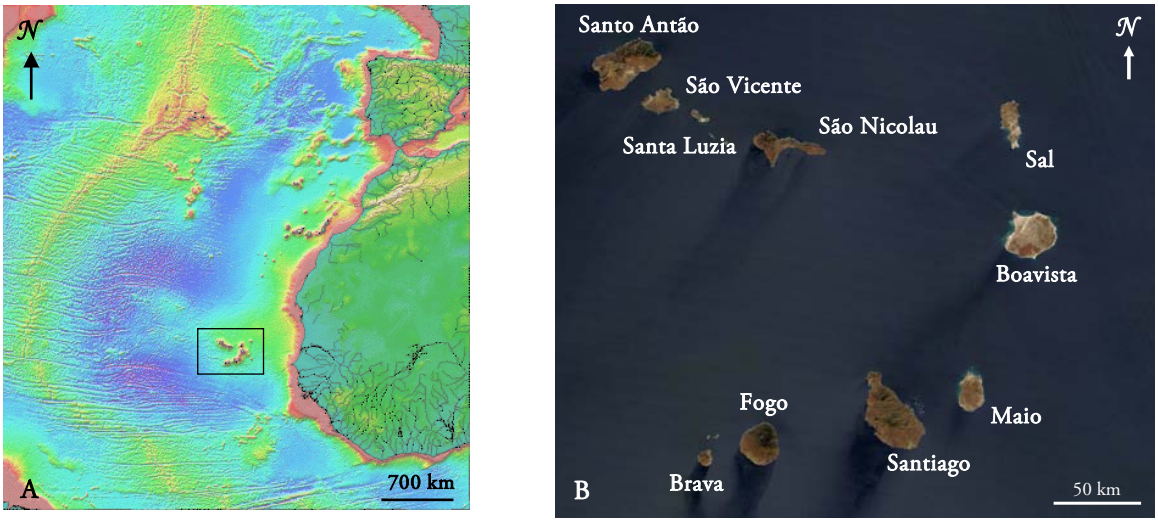

Figure 2.1 – A) Cape Verde Archipelago location in the Atlantic Ocean (image from topex.ucsd.edu); B) Detailed map of the Cape Verde Archipelago and constituting islands (image adapted from eoimages.gsfc.nasa.gov).

2.3. Geomorphologic characteristics

As in all volcanic islands, the morphology of the Cape Verde islands is dependent on the duality between constructive and destructive processes. The constructive events comprise volcanic activity and tectonic uplifting while the destructive processes involve wind, marine and stream erosion as well as mass movements and subsidence.

At the geomorphologic level the islands can be subdivided in two groups, those with a strong relief, where the volcanic edifices are the structures responsible for the main orographic characteristics (Santo Antão, São Nicolau, Santiago, Fogo and Brava), and those with extremely flat areas (São Vicente, Santa Luzia, Sal, Boavista and Maio) (Madeira et al., 2008). The maximum altitudes are observed on the islands of Fogo (2829 m), Santo Antão (1979 m) and Santiago (1392m). Maio, Boavista and Sal, located more to the East, are characterized by a more gentle terrain, testimony of an extensive and ongoing erosive process, the maximum altitudes not going over the 400 m (Assunção, 1968). On these islands the slopes tend to be

lower, being the sedimentary depositional events more evident than the erosive ones (Mitchell-Thomé, 1976) (Fig. 2.2).

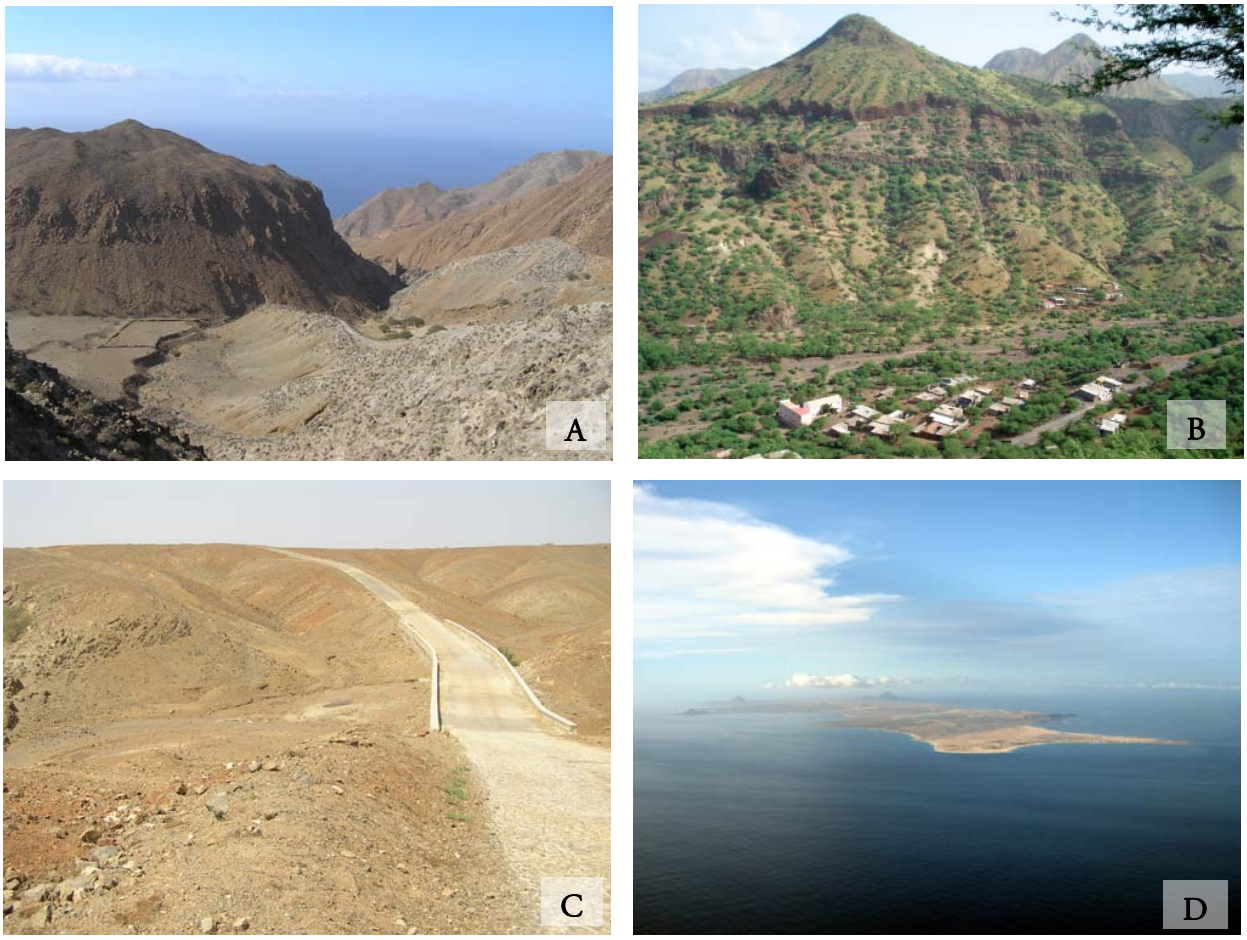

Figure 2.2 – Contrasting geomorphologic characteristics of the Cape Verde islands: A) Brava (photo by João Mata); B) Santiago; C) Maio (photo by João Mata); D) Sal (image from namma.msfc.nasa.gov). The West-East orography change (photo A to D) attesting the relief attenuation, from more recent to older islands with implicit magmatism migration.

The hydrographic network is restricted to short-lived streams, withstanding only two small rivers of permanent character in Santo Antão Island (Mitchell-Thomé, 1976). The absence of significant water lines comes from the low precipitation rate registered on the archipelago (3 to 20 days per year, in a study conducted between 1980-1987 on Santiago; Mannaerts and Gabriels, 2000) although, during storm events the rainfall can be very significant. This climatic situation is typical of sub-arid tropical regions.

These sparse storm events are responsible for abrupt changes in the relief, particularly along cliffs and water courses. The presence of deep narrow gorges, waterfalls, steep longitudinal stream profiles are all indicative of water's potential as an important modelling/erosional agent (Mitchell-Thomé, 1976). This author also points out the differences in the valley's characteristics as a way of corroborating the age difference between the islands. The younger islands, located to the West (Santiago, Santo Antão, Brava) have steep walled gorged streams that flow straight to the sea, whereas the more mature islands to the East (Sal, Boavista, Maio) are characterized by broad streams, with abundant sediments that meander to the sea over longer distances.

Zazo et al. (2007) observed at Sal Island the existence of significant variations in sea level (eustatic) during the Quaternary, testified by the occurrence of numerous marine terraces that may reach 60 m a.p.s.l (above present sea level).

The study of sea level oscillations in the last 20-30 Ma is of extreme importance in deciphering the stratigraphic particularities present on several of the islands, as an example the occurrence of submarine lava flows at 450 m a.p.s.l. in Santiago Island (Serralheiro, 1976).

However, in order to assess the importance of crustal movements we must take into account information regarding sea-level changes. The Oligocene marks a major climatic change from a greenhouse world[1] to an icehouse world[1] that remains until today. Eustatic changes of about 30 to 60 m, are observed during the Oligocene and early Pliocene (~33.8 to 2.5 Ma) being explained by growth and decay of the ice coverage in Antarctica. More extreme sea levels changes (60 to 120 m) are inferred for the late Pliocene to Holocene (~2.5 to 0.0 Ma), being attributed to variations in large Northern Hemisphere Ice Sheets (NHIS) (Miller et al., 2005). The Mid-Pliocene is of particular interest because it stands as the most recent period significantly warmer than today. The explanation for this is still controversial (high CO_2 concentrations, variations in oceanic circulation, increase in heat advection, etc.) but the consequences are recognized worldwide: reduced Arctic sea ice, elevated air temperatures at high altitudes, warmer sea surface temperature at mid-latitude and higher sea-level (Raymo et al., 1996; Haywood and Valdes, 2004; Fedorov et al., 2006).

[1] Greenhouse-icehouse world refers to a super cycle with an approximate period of ≈ 300 Ma, which marks an oscillation between two climatic extremes: the greenhouse world, were the poles were much warmer and temperature gradients were about half of the ones today, and the icehouse world with very cold poles and large temperature difference between poles and the equator (Plimer, 2003; Schlager, 2005).

During the Pliocene the maximum sea-level rise is about 80 m (Fig. 2.3) and so, the oddity of the occurrence of submarine lavas as high as 450 m a.p.s.l in some of the Cape Verde islands, as well as the occurrence of marine deposits at 120 a.p.s.l in the Canary Archipelago (Meco et al., 2007), must be explained by uplift in response to stress imposed in the lithosphere/upper mantle (tectonic-volcanic uprise) at a local and/or regional scale (Hardenbol et al., 1998). Another example of the magnitude of crustal movements in the archipelago is the emplacement of ocean floor fragments (outcropping MORBs) in the island of Maio and Santiago (Stillman et al., 1982, Gerlach et al., 1988).

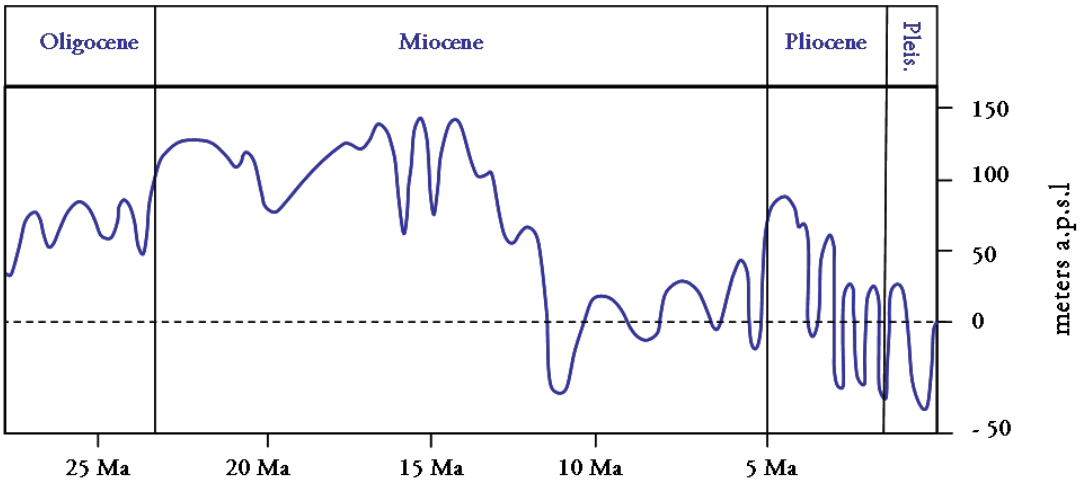

Figure 2.3 - Eustatic sea level curve for the Cenozoic (a.p.s.l stands for above present sea level) (adapted from Hardenbol et al., 1998).

Ramalho et al. (2010a,b,c) made an extensive study concerning the vertical movements of uplift and subsidence in the Cape Verde Archipelago. In order to quantify and understand the significance of those movements specific sea-level palaeo-markers were used: submarine volcanic units, lava deltas, marine sediments and marine abrasion surfaces.

The uplift history of the Cape Verde islands is distinct and there are islands were no significant uplift was detected (Santo Antão, São Vicente, Santa Luzia and Fogo) whereas other experience significant positive vertical displacements reaching 450 m, 350 m and 280 m (Santiago, Brava and São Nicolau, respectively) (Ramalho et al., 2010c). The islands of Boavista and Maio also exhibit episodes of uplift and subsidence but less extreme. Sal Island is characterized by a variable series of old uplift movements (up to 350 m detected in the Ancient

erupted complex) and more recent subtle uplift and subsidence episodes already observed by Zazo et al. (2007) (Fig. 2.4).

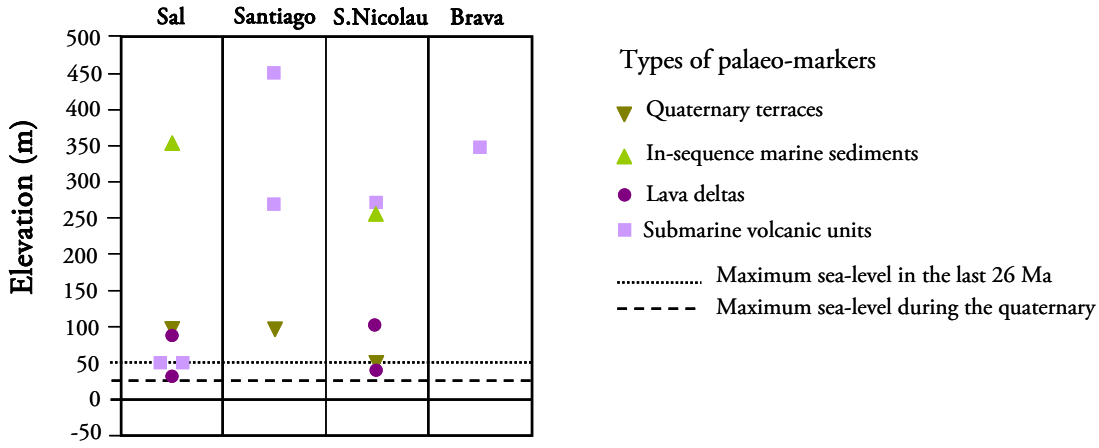

Figure 2.4 – The most significant sea-levels heights inferred from the indicated palaeo-markers in the Cape Verde islands (adapted from Ramalho et al., 2010c).

The islands of Santiago and São Nicolau were studied further by Ramalho and co-authors (2010a, b) due to their significant and almost constant uplift. While São Nicolau experienced two distinct uplifting events one at 5.4 – 4.7 Ma and another at 0.5 – present, Santiago is characterized by a nearly constant uplift in the last 4 Ma at a rate of 100 m/Ma. These vertical movements appear to be synchronous with the volcanic activity responsible for the island growth. This observation along with the already stated disparity of uplift history among the archipelago led Ramalho et al. (2010a,b) to conclude that the most likely mechanism responsible for the observed uplift is regional at the scale of one individual island, most probably due to basal laccolith emplacement at crustal levels.

An uplift at the swell length scale in the period of 0.25 – 1.25 Ma was also identified, related with the building of the Cape Verde Rise but is small (100 m) compared with the above stated vertical movements of some specific islands (Ramalho et al., 2010a).

Main volcanic characteristics

The only volcanically active island in the archipelago is Fogo. On this island the last eruptions occurred in 1995, being the estimated total volume of erupted volcanic material 54 -

$60x10^6$ m^3, during a period of 55 days (from 2nd of April until May 26), however there were some twenty historical volcanic events dated back until 1664 (Torres et al., 1997a,b).

From the interpretation of volcanic products it is possible to infer that the predominant volcanic activity of the islands belongs to Hawaiian and/or strombolian style. The Hawaiian activity is characterized by the emission of fluid lavas that tend to erupt non-explosively due to the low viscosity nature of most of the predominant volcanic products, which correspond to basic-ultrabasic highly SiO_2 undersaturated melts. Magmatism occurs essentially along fissures or simple eruptive centers. Strombolian activity is related with discrete explosive events and is associated with less fluid lavas, ejected along an emission center. Pahoehoe and aa lava flows, as well as spatters and pyroclastic materials are the volcanic products associated with these eruptions types (Wallenstein et al., 1997).

It has been described in some of the islands (Santo Antão and Brava) extensive pumice deposits derived from large subplinian to plinian eruptions of more evolved magmas. In Santo Antão Island the Cão Grande deposit comprises phonolitic pumice lapilli material (up to 8.5 km thick) derived from the dispersion of a 30-34 km high column through a vent located on the westernmost side of the island (Mortensen et al., 2009). In Brava Island several surge deposits of phreato-magmatic and phreato-plinian origin were identified associated with the most recent magmatism (Madeira et al., 2008; 2010).

In some islands (Santiago, Brava, Santo Antão, Boavista) lava domes and plugs of traquitic/phonolitic affinity are also identified. The more viscous magmas tend to erupt pasty lava that has more difficulty in flowing, accumulating above the vent as a dome-shaped mass (Cas and Wright, 1987) (see Fig. 2.2A).

In some islands it can be identified levelled structures as “achadas”, “fajãs” and marine terraces. “Fajã” is a typical geomorphologic term widely used in Macaronésia, describing terrains most commonly present in shorelines, made up of lava flows or detritic sedimentary material. In the Cape Verde Islands, “achadas” are broadly present and correspond to flat areas between hills, particularly plateaus hanging between big central volcanoes.

As in many volcanic islands, calderas are also observed in the archipelago, the "Caldeira da Pedra Lume" (Sal Island), "Caldeira de Fundo Grande" (Brava Island) and the most noteworthy the "Caldeira do Fogo" (Fogo Island). This last one has a maximum diameter of 9 km, in the N-S direction, being characterized by step internal walls, almost vertical ("Bordeira"). The altitude difference between the "bordeira" top and the bottom of the caldera may reach 1000 m (Assunção, 1968) (Fig. 2.5).

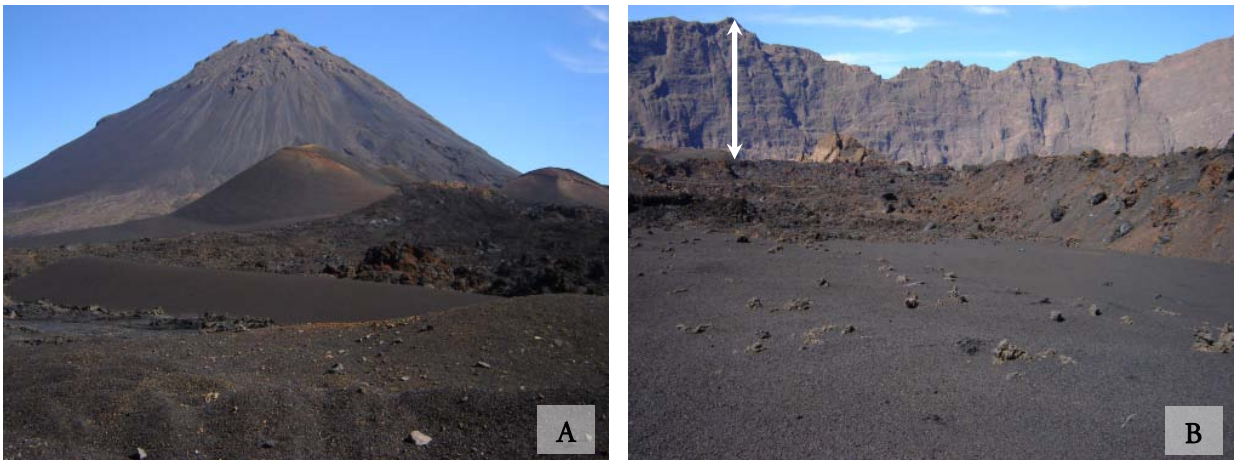

Figure 2.5 – A) The Fogo summit volcano Fogo Island; B) "Caldeira do Fogo" characterized by high steep walls up to 1000 m (photos by Cyntia Mourão).

2.4. Geotectonic setting

As already referred the Cape Verde Islands form two distinct alignments converging eastwards, clearly different from what it would be theoretically expectable from the lithosphere drift over a mantle plume.

Bebiano (1932) and Assunção (1968) were the first to suggest the existence of important fracture zones controlling the positioning of the Cape Verde Islands. For them the alignment of most of the northern islands seems to suggest the presence of a deep WNW-ESE fracture zone, mimicking the West African coast fractures. Another well defined direction is the one marked by the islands grouped more to the East (Sal, Boavista e Maio), being N-S, more precisely NNE-SSW, which is also present on the African continent.

The WNW-ENE fracture is now known as the "Blake Spur Fracture Zone", and passes south of the island of Santo Antão, between the islands of Boavista and Maio, prolonging to

the Senegalese coast where it ends. This fracture zone corresponds to a remnant of a transform fault (Courtney and White, 1986). Williams et al. (1990) identified several fracture zones (about 13), around the Cape Verde Archipelago, based on magnetic lineation offsets. The average spacing is about 70 km and the predominant direction is WNW-ENE. These authors also stated that these features must be original Mesozoic seafloor fracture zones and not the product of the magmatic event responsible for the generation of the Cape Verde Islands.

On a more restricted area, near the islands, Torres (1998) identified the main hypothetical fractures that could be responsible for the peculiar disposition portrayed by the archipelago (Fig. 2.6). Fracture 1, with an N-S orientation was divided in three fragments, being 1b and 1c shifted segments due to the action of fractures 2 (Blake Spur Fracture Zone) and 3. The preferred orientation observed in dikes of Santo Antão and São Vicente, corresponds to the direction of maximum compression (N60ºE; fracture 4), also testified by the presence of two seamount NW of Santo Antão that mimics this direction (Banco do Noroeste). The recent volcanic activity on Sal Island has a NNE-SSW direction (fracture 5).

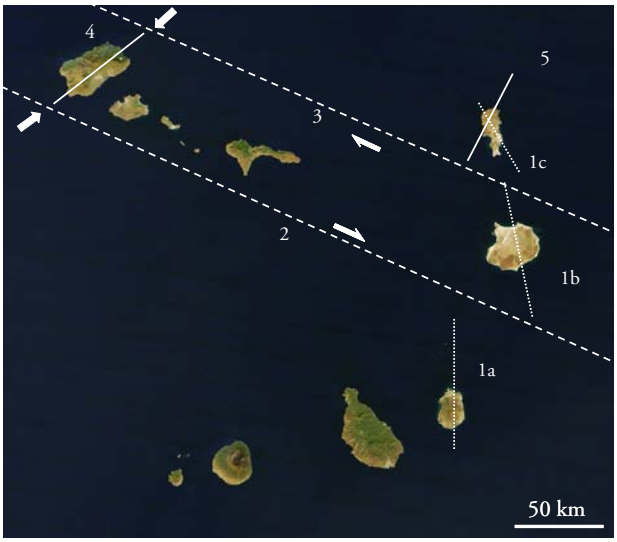

Figure 2.6 - Main fractures in the Cape Verde Archipelago (adapted from Torres, 1998): 1a, 1b,1c – Segments of a N-S fracture; 2- "Blake Spur Fracture Zone"; 3 – Fracture between the islands of Sal and Boavista; 4 – Mean orientation of dikes occurring in Santo Antão and S. Vicente; 5 – Alignment of the more recent volcanism in Sal (image from eoimages.gsfc.nasa.gov).

In a study preformed on the islands of Santo Antão, São Vicente, Sal, Maio, Santiago e Fogo, Scheidegger (2002) reports joint strike directions of NNW-SSE (154º-181º) and ENE-WSW (65º-81º), as the most common in the archipelago, noticing that these are similar to the

direction of the Mid-Atlantic ridge and the lineaments associated with it. Scheidegger (2002) also states that due to the fact that streams, joints and ridges directions agree with each other, this is probably the result of the action of the neotectonic stress field. These directions are in agreement with those reported by Torres (1998) for the alignment of magmatic activity (dikes and volcanic episodes, fractures 4 and 5 respectively).

Even though the Atlantic-type oceans margins are considered to be tectonically passive, recent studies (Skolotnev et al., 2007) around and south of the Cape Verde area (Cape Verde Ridge and Cape Verde Abyssal Plain) show evidence for tectonic movements that started in the Early Pliocene and prolonged in to the Quaternary. This conclusion was drawn due to observations in bottom topography and internal structures of sedimentary sequences as well as the identification of newly formed morphostructures (anticlines, horsts and diaper-like structures) (Skolotnev et al., 2007; 2009).

The seismic activity in the Cape Verde area is not very significant (Fig. 2.7A). Ever since seismic monitoring is available for this region, several earthquakes have been detected with a maximum magnitude of 6 (Matias et al., 1997). In the period between 1977 and 1989 (Fig. 2.7B) the seismic activity in the archipelago was centered to the west, where several alignments of epicenters have been identified which seem to suggest the presence of fracture zones oriented NW-SE and NNW-SSE in a sector comprising the islands of Santo Antão, São Vicente, Fogo and Brava (Brum da Silveira et al., 1997).

More recently Grevemeyer et al. (2010) stated that the Cadamosto seamount, a 3 km high submarine volcanic edifice, is the seismically most active feature in the archipelago (see Fig. 2.8). During the *Meteor* M62/3 cruise (summer 2004) several local volcano-tectonic earthquakes were detected and attributed to rock failure due to dike injection/intrusion. The data recovered in the 2004 cruise, in the Fogo-Brava-Cadamosto area, suggest that the seismic and most probably the volcanic activity is moving away from Fogo and centering in the Cadamosto seamount, which could lead, in the future, to a new island (Grevemeyer et al., 2004; 2010).

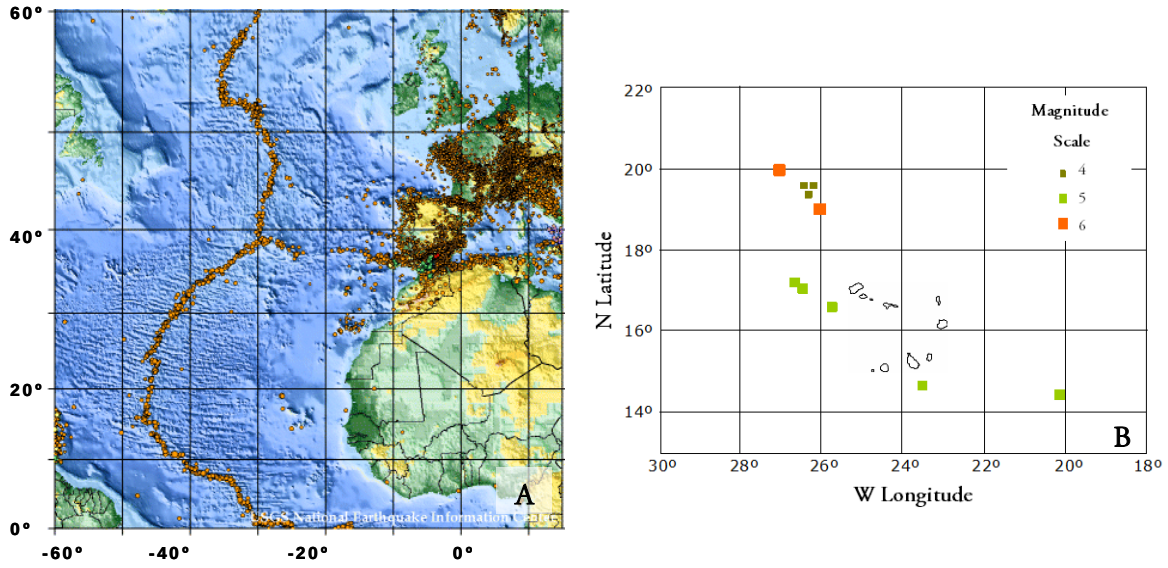

Figure 2.7 - A) Seismicity of the North Atlantic Ocean between 1975 and 1995 (from earthquake.usgs.gov); B) Seismic activity registered between 1977 and 1989 (adapted from Brum da Silveira et al., 1997).

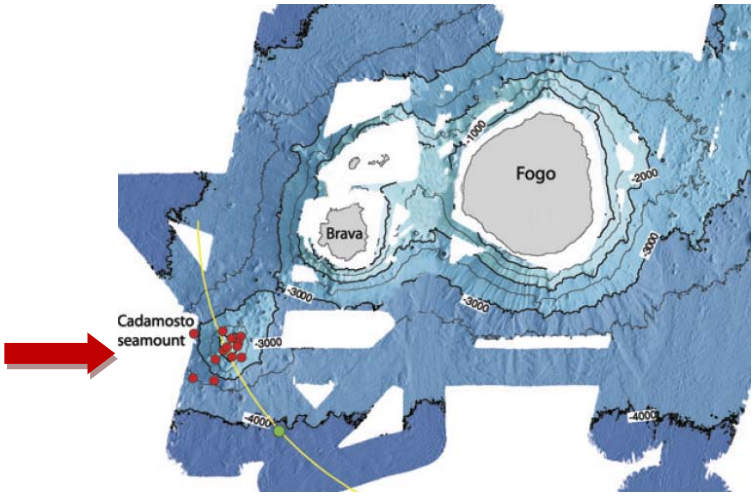

Figure 2.8 – Seismicity detected at the Cadamosto seamount during the cruise M62/3 of the German R/V Meteor (red dots represent local earthquakes) (image adapted from Grevemeyer et al., 2010)

2.5. Geodynamic context

The Cape Verde Archipelago is the result of intraplate magmatism in the West African plate in the central Atlantic Ocean. The geotectonic setting of the African plate imprints

specific characteristics on the islands implanted on it. Even though the most plausible mechanism responsible for the generation of the Cape Verde Archipelago is a mantle plume of deep origin, in accordance with that proposed for other intraplate magmatism in the Atlantic Ocean, there is still some debate around it, which is closely related with the discussion of existence/absence of those structures in the mantle elsewhere and in the Cape Verde region in particular. For Cape Verde this uncertainty is enhanced by the lack of a single linear trend concerning the islands distribution.

The Mid-Atlantic Ridge is characterized by slow spreading rates (20 ± 1 mm/year; O'Connor et al., 1999), compared to the Pacific fast spreading rate (80-180 mm/year; Dick et al., 2003). The absolute plate motion of the African plate, in particular, has changed at 6 Ma (gradually along 8 to 4 Ma), from a situation of counterclockwise rotation around a pole at 33ºN, 35ºW (period of 30 - 6 Ma) to a counterclockwise rotation at a pole situated at 19ºN, 16ºW (6 - 0 Ma) (Pollitz, 1991)(Fig. 2.9).

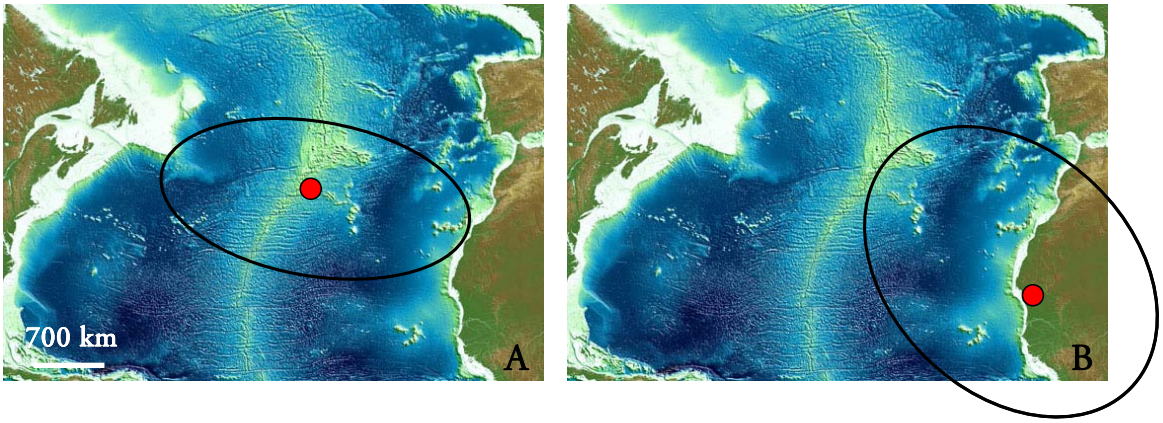

Figure 2.9 – Location of African absolute motion poles in the period of 30-6 Ma (A) and 6-0 Ma (B) (adapted from Pollitz, 1991; image from www.geoware-online.com).

Holm et al. (2008) made a compilation of several data regarding the motion of the African plate at the Cape Verde Archipelago and estimated an average dislocation of the plate to NE at a rate of 9 mm/year during the last 6 Ma.

According to Silver et al. (1998) the cause for deceleration of the African plate, around 30 Ma, is probably due to its collision with the Eurasian plate, which stands as the largest and slowest moving plate. This was counterbalanced by an acceleration of the South Africa plate,

which promoted the increase in cordilleran activity in the west zone of the plate. Also, within this time frame, there was an increase in hotspot magmatism across the African plate, which can be attributed to the almost stationary character of the plate which caused an increase in lithosphere heating due to a prolonged influence of mantle plumes (O'Connor et al., 1999).

The Cape Verde Archipelago is implanted on the largest amplitude oceanic swell on Earth being associated with several geophysical particularities which are going to be described next. The interpretation of these geophysical parameters enables the clarification of the process (or processes) susceptible of causing the observed swell (Fig. 2.10) and give information about the crustal and mantle structure.

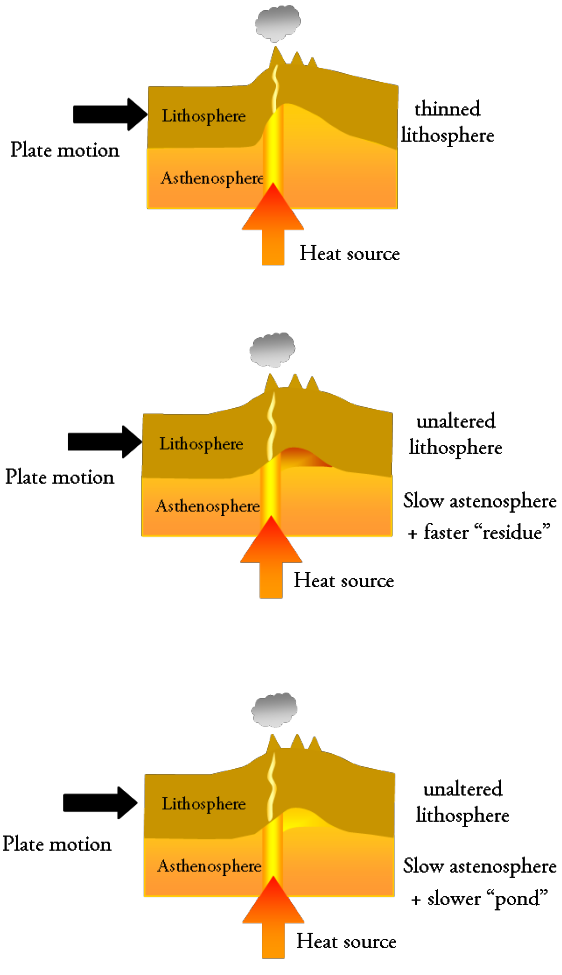

Thermal rejuvenation

The uplift is a consequence of diffuse heating at the base of the lithosphere, which leads to thermal expansion in order to attain equilibrium thermal structure (Cserepes et al., 2000; DeLaughter et al., 2005).

Compositional Buoyancy

Swell formation is explained by the presence of a buoyant low-density mantle residue left behind after the extraction of melt through volcanism (chemical compositional buoyancy, Laske et al., 2007) or due to the original buoyancy of the anomalously hot material (Schubert et al., 2001).

Dynamic support

Dynamic support is associated with hot and less dense material moving within the asthenosphere and lithosphere, which applies a dynamic pressure for enabling the flow of the material supplied by the plume (Sleep, 1990). Most of the reheating is at the base of the lithosphere (Stein amd Von Herzen, 2007).

Figure 2.10 - Possible mechanisms susceptible of causing swell formation (adapted from Laske et al., 2007).

2.5.1. Geophysical particularities of the Cape Verde area

2.5.1.1. Topography

The Cape Verde islands are implanted in old oceanic crust between M21 and M0 magnetic anomalies (120-140 Ma; Hayes and Rabinowitz, 1975), and are associated with the Cape Verde Rise, one of the largest swell on the ocean basins that ascends 2.2 km above what would be expected for ocean floor of Jurassic-Cretaceous age, according to half-space cooling model (seafloor depth increases approximately as the square root of lithosphere age; Davis and Lister, 1974). The Cape Verde Rise has an E-W orientation with a horizontal distance of 600 km, in diameter, which is vertically limited by the 3700 m bathymetric line (Courtney and White, 1986) (Fig. 2.11). If the northwester bulge, centered at 20ºN-30ºW (marked as a star in Fig. 2.11) is considered as part as the Cape Verde Rise (Crough, 1982), then its wide increases until 1200-1600 km, in diameter.

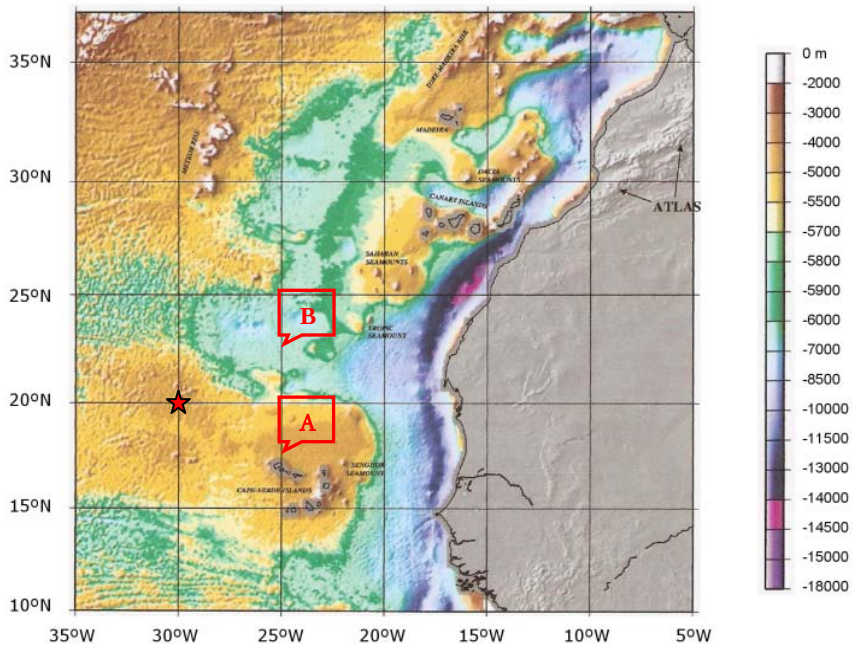

Figure 2.11 – Basement map of the Central Atlantic Ocean (calculated from extracting the sediment thickness from the topography) (Patriat and Labails, 2006). A and B correspond to the location of the highest and lowest heat flow measurement respectively, determined by Courtney and White (1986).

2.5.1.2. Heat flow anomaly

Several models of lithospheric thermal evolution have been presented since the seventies when Davis and Lister (1974) introduced the half space model (e.g., Parson and Sclater, 1977; Stein and Stein, 1992). These are important because they provide a reference model of average variation in depth and heat flow with age of normal lithosphere, thus allowing the identification of uncharacteristic zones that deviate from the standard. The dome where the Cape Verde islands are implanted is characterized by a broad heat flow anomaly, with a maximum excess heat of 17 ± 3.7 mW/m^2 at the centre of the swell that drop to lower values towards the flanks. The highest measured value was 60.5 ± 4.0 mW/m^2 (see A in Fig. 2.11) and the lowest 43.5 ± 3.4 mW/m^2 (see B in Fig. 2.11) (Courtney and White, 1986).

Considering that the normal heat flow in ocean floor with the same age as the Cape Verde Rise (≈ 125 Ma) is 50 mW/m^2, according to the Global Depth and Heat flow model (GDH1) by Stein and Stein (1992), the observed thermal anomaly is approximately 10 mW/m^2 and the corresponding depth anomaly is 285 m (assuming that ≈ 60 mW/m^2 heat flow corresponds to a lithospheric thermal age of 69 Ma) (Stein and Stein, 1993). Considering that the total depth anomaly is 2200 m, the fraction endorsed to thermal rejuvenation is only 13%. The remaining uplift is probably caused by dynamic support due to the impingement of ascending hot asthenospheric material (i.e., mantle plume) in sublithospheric domains (Sleep, 1990; Zhong and Watts, 2002).

It is important to state that the determined thermal anomaly is directly related to the chosen reference model since it establishes the guidelines for what is considered a normal lithosphere.

Another important aspect described by Von Herzen (2004) and Harris and McNutt (2007) is the possibility that the scatter observed in the regional heat flow surveys, including the one done by Courtney and White (1986) in the Cape Verde Rise (Fig. 2.12), is the result of heat loss by advection due to hydrothermal convective circulation. Even though this mechanism is thought to be inexistent beyond the 65 Ma "sealing age" the large variations observed suggest fluid flow in crust of Cretaceous age (Harris and McNutt, 2007 and references therein). The driving mechanism seems to be bathymetric relief of the volcanic

edifices. Considering this alternative there is the possibility that a component of basal heat flow is not being accounted for (Harris and McNutt, 2007).

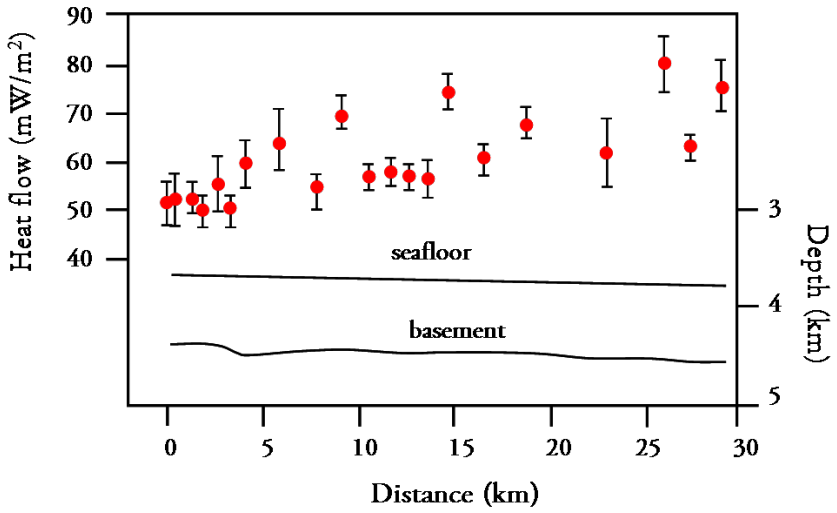

Figure 2.12 – Heat flow data of site A (see Fig 2.11) in the Cape Verde Rise, being evident the scatter of the measurements within one survey station. Error bars represent standard deviation (from Harris and McNutt, 2007).

2.5.1.3. Geoid and gravity anomalies

The geoid is the gravitacional equipotencial surface of the Earth, coinciding with sea-level in oceanic areas. Deviations of the geoid from an idealized hydrostatic ellipsoid are known as geoid anomalies and are the result of the existence of mass heterogeneity distribution inside the Earth (see Fig. 2.13). While geoid anomalies decrease inversely with distance to source mass, gravity anomalies decreases inversely with the square of distance. For this reason gravity anomalies are particularly susceptible to mass changes at crustal levels while geoid anomalies provides a long-range probe in a wide range of depths (Condie, 2001; Li and Götze, 2001; Urchulutegui, 2007).

Crough (1982) reported geoid height anomalies, determined by satellite altimetry, for the Cape Verde Rise and also presented residual geoid anomalies, after the regional field had been subtracted of the original measured values. The value obtained is the difference between the positive geoid anomaly for the excess topography and the negative geoid anomaly from the density deficiency at depth (Sleep, 1990). The Cape Verde Rise is characterized by a residual geoid height with a central high at 16ºN-25ºW (>8.0 m) and a smaller bulge at 20ºN-30ºW (>

5.0 m) (Fig. 2.14). Such anomaly, indicating a low mass domain beneath Cape Verde Archipelago is compatible with an upward flow caused by a mantle plume.

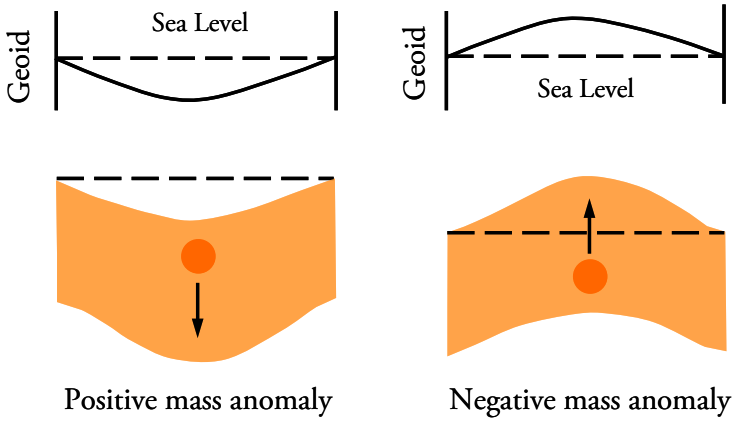

Figure 2.13 - Effects of positive and negative mass anomalies on the geoid. Owing to its ductile behaviour, the mantle can deform. A positive mass anomaly causes a downward flow in the mantle producing a depression on the surface of the planet with the resulting replacement of rock by air or seawater. So the depression can be regarded as a mass deficiency relative to a laterally uniform Earth, which results in a negative geoid anomaly. A negative mass anomaly causes the opposite effect (Condie, 2005) (figures adapted from Condie, 2005).

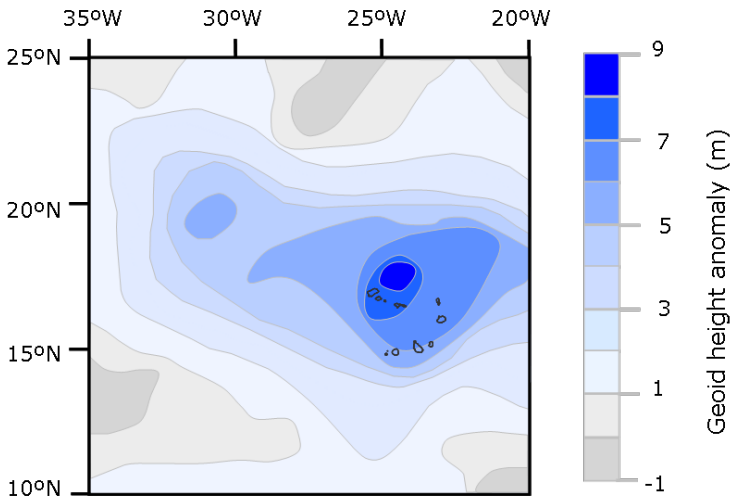

Figure 2.14 - Geoid height anomaly observed at the Cape Verde Rise (adapted from Crough, 1982).

The existence of such negative mass anomaly beneath Cape Verde is also demonstrated by gravity anomalies. The measured residual gravimetric anomalies reflect the gravity balance between the material in, and below, the crust which is intrinsically associated with their density

and structure. The Cape Verde Rise is coincident with a wide negative free-air anomaly from which some gravity anomaly highs emerge in the immediate vicinity of the islands and seamounts (Ali et al., 2003)(Fig. 2.15).

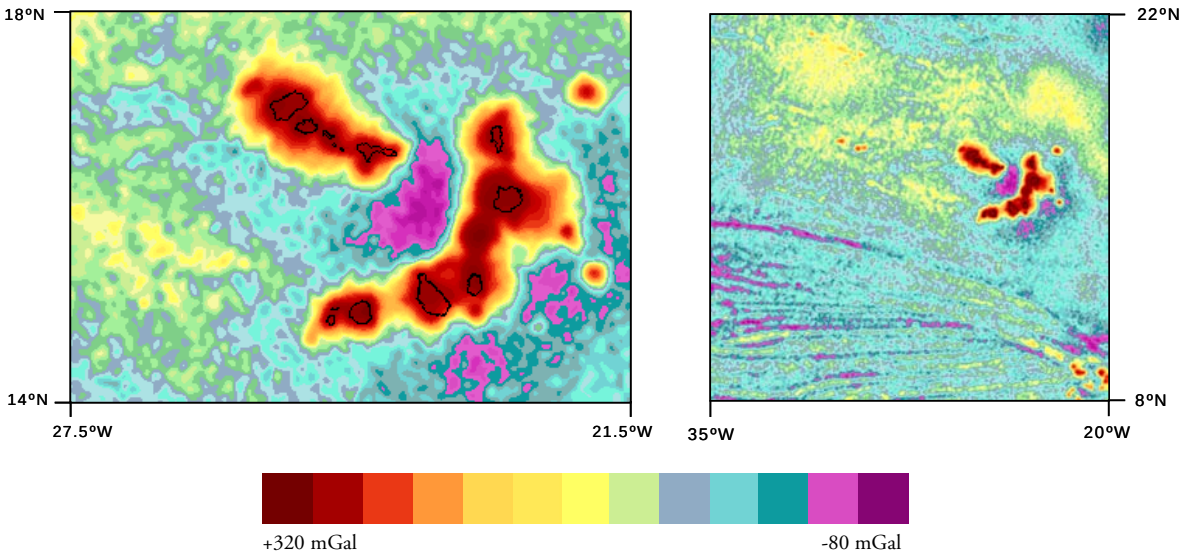

Figure 2.15 - Gravity anomaly map derived from satellite altimetry using the method by Sandwell and Smith (1997), for the Cape Verde islands (A) and surrounding Atlantic region (B) (images and simplified scale colour from www.serg.unicam.it/Gravity.htm).

The large negative anomaly is interpretable as the result of an important mass deficiency in depth, while the more localized positive anomalies beneath the islands are probably the reflex of the core complex of the islands where cumulate rocks are abundant. It should be noticed that an alternative interpretation of the broad negative anomaly emerge from the Lodge and Helffrich (2006) proposition that Cape Verde is underlain by a low density domain corresponding to a depleted root located at 80 km depth formed as a response to magma extraction due to the preferential partitioning of Fe over Mg into the melt (compositional buoyancy; Fig. 2.10).

Since the apparent compensation depth, for oceanic plateaus and swells, is linearly related to the geoid to topography ratio (GTR or admittance) its quantification is of fundamental importance in what concerns the physical aspect of the swell support (Cserepes et al., 2000). GTR values of 4.1 m/km (Cazenave et al., 1988), 4.3 m/km (Sandwell and MacKenzie, 1989)

and 4.8 m/km (Marks and Sandwell, 1991) were obtained for the Cape Verde Rise, by plotting geoid height and topography data and calculating the slope of the best fit line (Fig. 2.16). More recently, Grevemeyer (1999) obtained an intermediate value of 4.4 m/km[2], based on recent Geosat/ERM altimeter measurements of geoid height data and seafloor topography data from ship borne data.

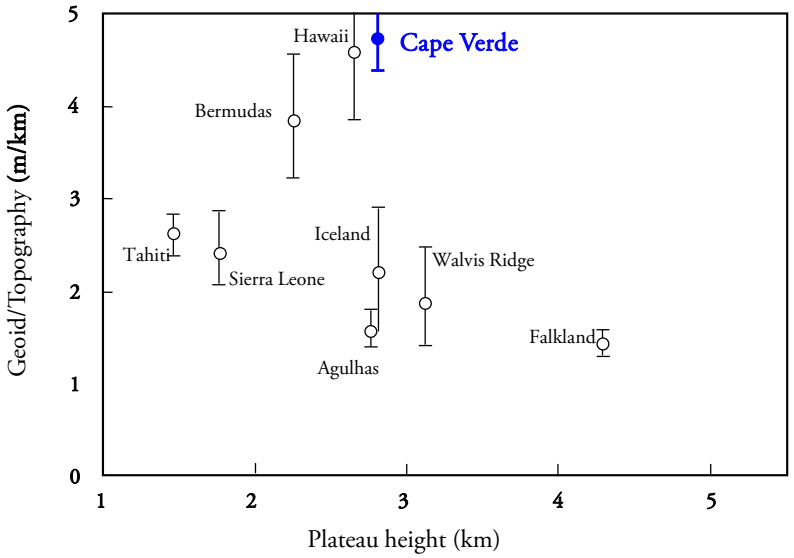

Figure 2.16 - GTR values plotted against topography, for several oceanic islands associated with plateaus (altered from Marks and Sandwell, 1991).

By analyzing the geoid and topography correlation in 53 of the largest oceanic plateaus and swells, Sandwell and MacKenzie (1989) came to the conclusion that low GTR (0-2 m/km) are thought to imply Airy-type compensation by crustal thickening, intermediate ratios (2-6 m/km) are ascribed to average compensation depths of 50 and 80 km, while higher values are considered to reflect lithosphere reheating or dynamical support[2] (Monnereau and Cazenave, 1988; Grevemeyer, 1999; Cserepes et al., 2000).

Since the geoid-to-topography ratios (GTR) determined for the Cape Verde swell are of intermediate values, it is assumed that the compensation depth[3] is located between 50 and 80

[2] In the Airy compensation model the topography is isostatically supported by increasing the crustal thickness by an amount X. The lithospheric thinning model of Detrick and Crough (1978) was used to explain the higher GTR, where the topography is supported by hot, relatively low density material, in the lower half of the lithosphere.

[3] The compensation depth is considered as the depth where the low density material, that compensates the swell, is situated.

km. McNutt (1988) using forward filtering and admittance techniques, obtained a compensation depth of 69±10 km. A similar value was achieved by Monnereau and Cazenave (1988) assuming that the compensation depth is defined by $7t^{1/2}$, and since the Cape Verde islands are implanted in oceanic crust with 120-140 Ma, gives a range between 77 and 83 km, and a average value of 80 km. More recently, Wilson (2011) trough gravity-topography slope and geoid-topography ratios analysis attained values between 77 and 88 km whereas Ali et al. (2003) reached the highest value of 100 km. All these values can be considered as minimum lithosphere thickness values.

2.5.1.4. Crustal structure

Crustal thickness is anomalously high (up to 22 km) beneath the islands, which is attributed to magmatic transfer from the mantle plume source to crustal levels (Lodge and Helffrich, 2006). However, between the islands the crust is only ≈7 km thick or even thinner, which is normal for oceanic settings (Ali et al., 2003; Pim et al., 2008). The crust seems to be flexed downward beneath volcanoes by up to 4 km and over a horizontal distance of 300 km (Ali et al., 2003).

In 1976, Dash et al. proposed the first crustal structure for Cape Verde, based on seismic data, in the segment between the islands of Sal, São Vicente and Santiago: 2–3 km of semi-consolidated sediments, 3–6 km of basalt and 6–8 km of plutonic rocks. The estimated Moho depth was 16-17 km. Recently Ali et al. (2003) were able to better define the sedimentary load, individualizing four main units, through seismic reflection profiles (Fig. 2.17).

Unit I corresponds to the earliest sediments deposited over the oceanic crust, probably Jurassic to early Cretaceous in age and Unit II to silts, clays and shale of Late Cretaceous to Late Oligocene age. These first sedimentary units were interpreted to reflect sedimentary loading of the West Africa continental margin. Units III and IV thicken towards the islands, suggesting that they represent the infilling of the moats produced by volcanic load. Unit III is made up of volcanic material derived from the islands and was deposited in early to late Miocene. Pliocene to recent pelagic sediments of chaotic character represents Unit IV, interpreted as being formed by large scale collapse of the islands, i.e. from mass movements originated at the islands.

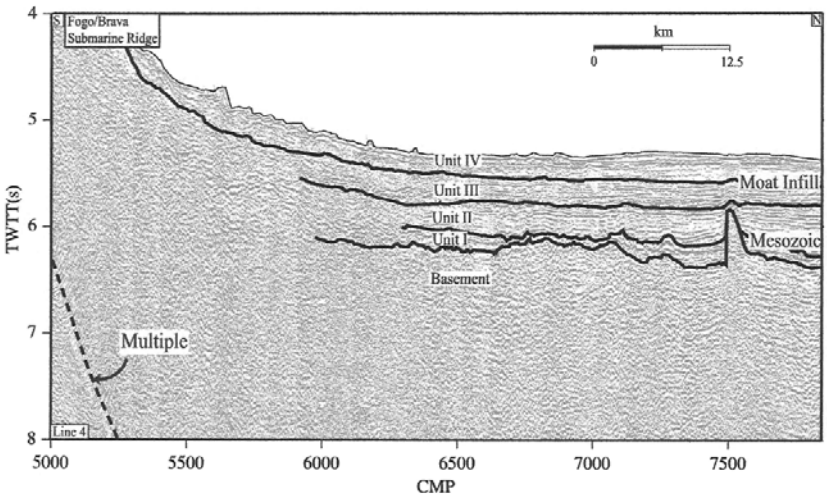

Figure 2.17 – Seismic reflection profile of the north flank of Brava and Fogo, showing the sedimentary units and arching of the sediments towards the island (Line 4 of Ali et al., 2003).

One of the most striking features of the sediments around the islands is that, even though they thicken in the moat infill, they are domed and tilted away from the islands, suggesting that there is an upward movement of the lithosphere counteracting the expected downward curvature of the material due to loading of the volcanic edifice (Ali et al., 2003). This stands as a favourable argument to the dynamic support of the Cape Verde Rise by a mantle plume (Fig. 2.10).

Another model was recently proposed by Pim et al. (2008) for the crust and uppermost mantle structure in the Cape Verde area, by modelling seismic refraction data (Fig. 2.18). Several layers were identified, including a sedimentary column with a mean thickness of 1.71 km, upper oceanic crust (extrusive material) with an average thickness of 1.16 ± 0.37 km, lower oceanic crust (intrusive material) corresponding to a 5.95 ± 0.45 km thickness and the upper mantle that initiates at 12 km (Moho depth).

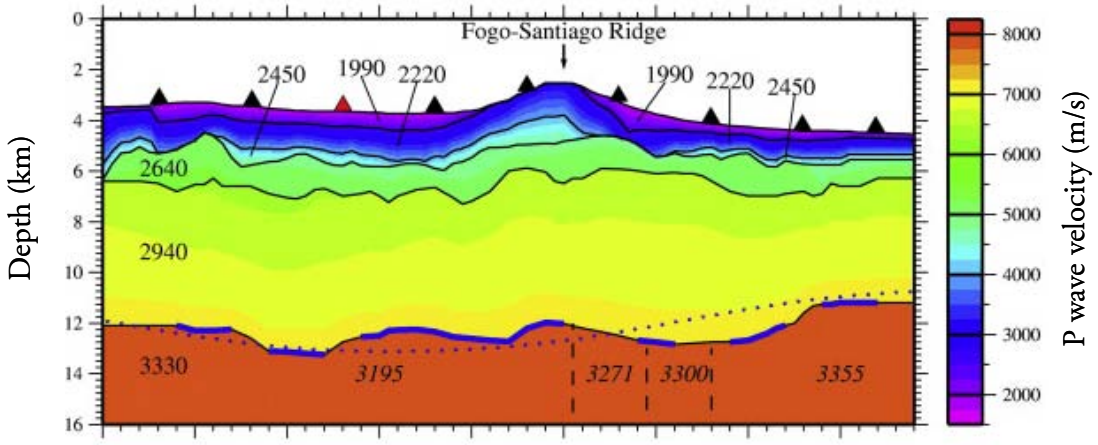

Figure 2.18 –Crust and upper mantle structure modelled by refraction seismic data (image adapted from Pim et al., 2008).

2.5.1.5. Lithosphere structure and its implications

The lithosphere is the rigid outer layer of the Earth comprising the crust and the uppermost part of the mantle. The definition of the lithosphere is dependent on the different geophysical and petrological properties considered: thermal, seismic, elastic/mechanical and chemical.

The thermal lithosphere is the external zone of the Earth that loses heat conductively above an adiabatic interior. As previously mentioned, several models of the thermal lithosphere have been presented, namely the Parson and Sclater (1977) and the Stein and Stein (1992) models. The former estimates a lithospheric thickness of 125±10 km with a bottom potential temperature of 1350±275 ºC and the latter a 95±15 km thick lithosphere with a bottom boundary of 1450±250 ºC. Other estimates of potential temperature where done by McKenzie and Bickle (1988) (1280ºC) and McKenzie et al. (2005) and Kawakatsu et al. (2009) (both with 1315ºC). The seismic lithosphere is delimited according with the travel time of P and S-waves, being considered the zone comprising the upper mantle and crust above the Low Velocity Zone (LVZ) which is characterized by the decrease in P-wave velocity to < 9 km/s.

When a volcanic island is formed, its weight acts as a downward load on the oceanic plate, causing it to flexure and deforms (Sandwell and Smith, 1997). The part of the lithosphere that supports that load is the elastic lithosphere (Pim, 2006). By modelling the shape of the flexure it is possible to estimate the elastic thickness of the lithosphere (Te), which

stands as a measurement of its resistance to deformation. This parameter shows a dependency with the thermal age of the lithosphere at the time of loading (Watts and Zhong, 2000). The elastic thickness of the lithosphere is distinct and smaller from its description according with thermal and mechanical definitions, because only the central part is dominated by elastic behaviour (Stüwe, 2007).

For the Cape Verde area several Te estimates have been obtained, by different authors: 28±4 km (McNutt, 1988), 30±5 km (Calmant et al., 1990) and 15±3 km (Young and Hill, 1993). Ali et al. (2003) obtained a Te of 50 km, deduced from seismic reflection profile data. However these authors acknowledge that the Te value of 50 km is significantly higher than that reported based on the age difference between the islands and the oceanic lithosphere where they are implanted (27-37 km) (Fig. 2.19). This inconsistency was explained as subsurface loads that work against the surface load, acting as a vertical propelling agent that acts at or near the base of the oceanic crust (Ali et al., 2003). The existence of a subsurface load implies that the surface mass must be counterbalanced by a mass deficiency probably associated with magmatic underplating related with density driven convection or compositional buoyancy. After combining these counteracting forces Ali et al. (2003) obtained a best fit model for a Te of 29 km, similar to those reported earlier.

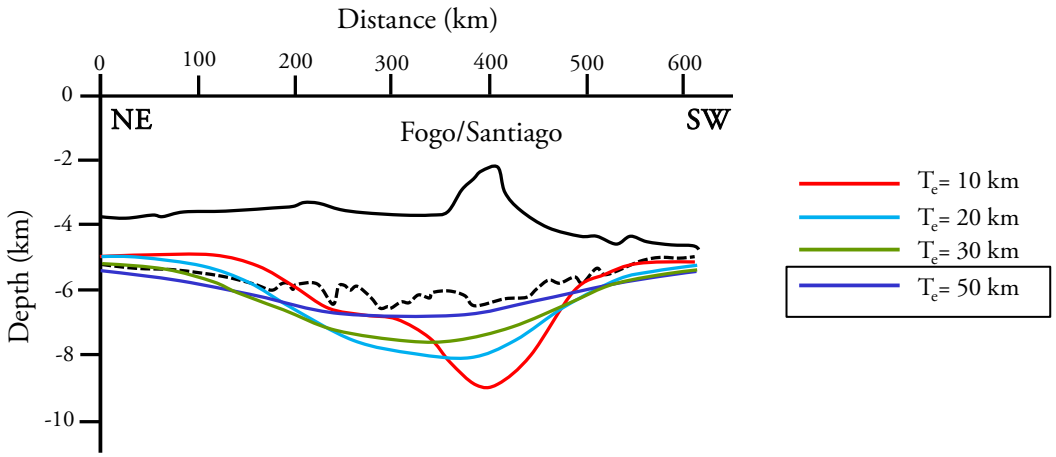

Figure 2.19 –Observed flexure on the top of the crust across a NE – SW section (transecting the Cape Verde Archipelago between Fogo and Santiago) (dotted black line) and several calculated flexures (see legend) (image adapted from Ali and Watts, 2003).

Recently Wilson et al. (2013) also identified a misfit between Te determined by two distinct methods: gravity anomaly fits (Te=30 km) and flexural modelling (Te=60 km) (see Wilson et al., 2013 for further information regarding quantification). These authors suggest that a combination of several mechanisms should explain the observed discrepancy, already detected by Ali et al. (2003): the influence of a column of hot upwelling material impinged at the base of the lithosphere, that would account for the dynamic support and thermal rejuvenation, which leads to the upward-acting buoyancy that result in the unbending of the lithosphere (Wilson et al., 2013).

2.5.2. Swell formation and support

The evidences presented seem to confirm the complex origin and support of the Cape Verde swell:

a) heat flow anomaly detected suggest a thermal rejuvenation of only 13%;
b) positive geoid anomaly at the regional level is indicative of a low mass domain beneath the area;
c) large negative gravity anomaly at the regional scale also indicates a mass deficiency at depth;
d) intermediate geoid-to-topography ratios (≈ 4.5 m/km) implies compensation depths of 50 to 80 km (using diverse data the compensation depth varies from 59 to 100 km);
e) sedimentary units are tilted away from the islands suggesting a upward motion that compensates the loading of the volcanic edifice;
f) inconsistencies between the determined and expected Te suggest the presence of subsurface loads.

As already stated, Lodge and Helffrich (2006) through the analysis of seismograms, suggests that the crust beneath the islands of the Cape Verde Archipelago is thickened to as much as 22 km, being more significant below the older islands to the East. Also, the

determined depth to the low velocity zone (LVZ) is variable: 60±10 km (Fogo Island) to 108±15 km (Sal Island).

The existence of a large low velocity body is precluded by Pim et al. (2008) by seismic refraction data, even though its existence is not ruled out completely due to the type of data collected and the location of the seismic transect (away from the volcanic edifices) as well as limited access of mantelic information. In fact, Lodge and Helffrich (2006) identified a high velocity low density body beneath all the islands, even though the material seems to spreads from different loci beneath the archipelago displaying a non-radial flow pattern from a central point within the swell.

The presence of a deep mantle plume susceptible can also be detected by perturbations along the mantle transition zone[4], located between 410 and 660 km. Being a phase transition it will react to temperature variations either thinning due to heating or thickening in response to cooling (Helffrich, 2000). Indeed the olivine-β spinel transformation has a positive slope while the contrary is the case for the γ spinel to Mg-perovskite (Fig. 2.20A). Taking this into account if there is a vertical deep seated hot upwelling beneath Cape Verde, it is expected that the 410 km discontinuity will get deeper and the 660 km will be shallower, making the transition zone thinner (Fig. 2.20B). However there are divergent results, while Helffrich et al. (2010) do not detect a significant alteration in the transition zone, Vinnik et al. (2012) argues that there is a 30 km reduction, compared to ambient mantle.

From the geophysical arguments stated above it is clear that assigning only one cause for the swell origin is very difficult and also unlikely. The hypothesis described earlier change according with the used data (geoid, topography, gravity, seismic refraction and reflection) as well as the location of the collected data (on or around the island edifices) being difficult to reconcile it all. However the consensus is that the primary driving mechanism is the impingement of a mantle plume at sublithospheric levels being the final topography a combination of several of the processes described (Laske et al., 2007). The role of a deep mantle plume to the origin of the Cape Verde magmatism is supported, from a geochemical point of view by noble gas signatures, as discussed at 4.5.

[4] The mantle transition zone is limited by two seismic discontinuities located at 410 and 660 km corresponding to phase transitions from olivine to β-spinel (wadsleyite) and γ-spinel (ringwoodite) to perovskite, respectively (Anderson, 1967).

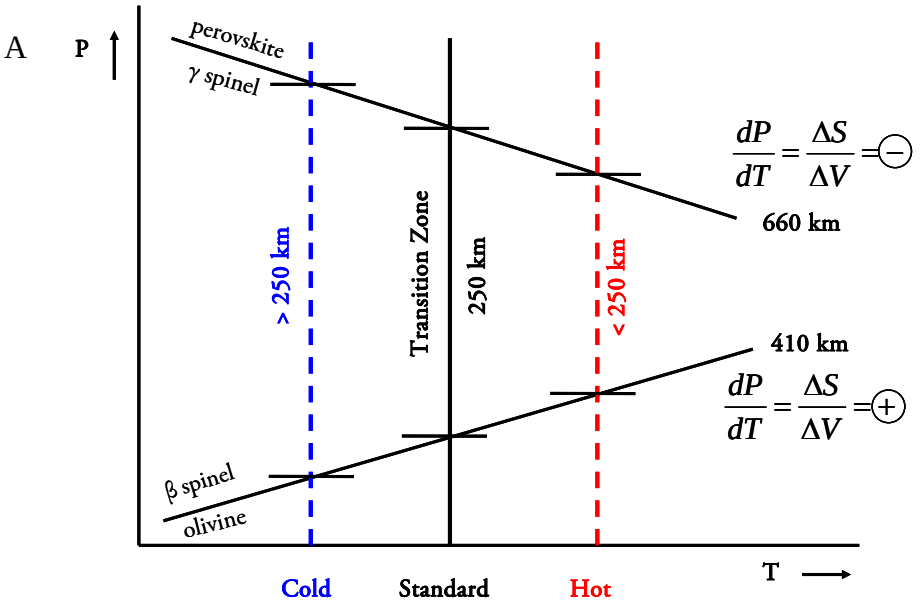

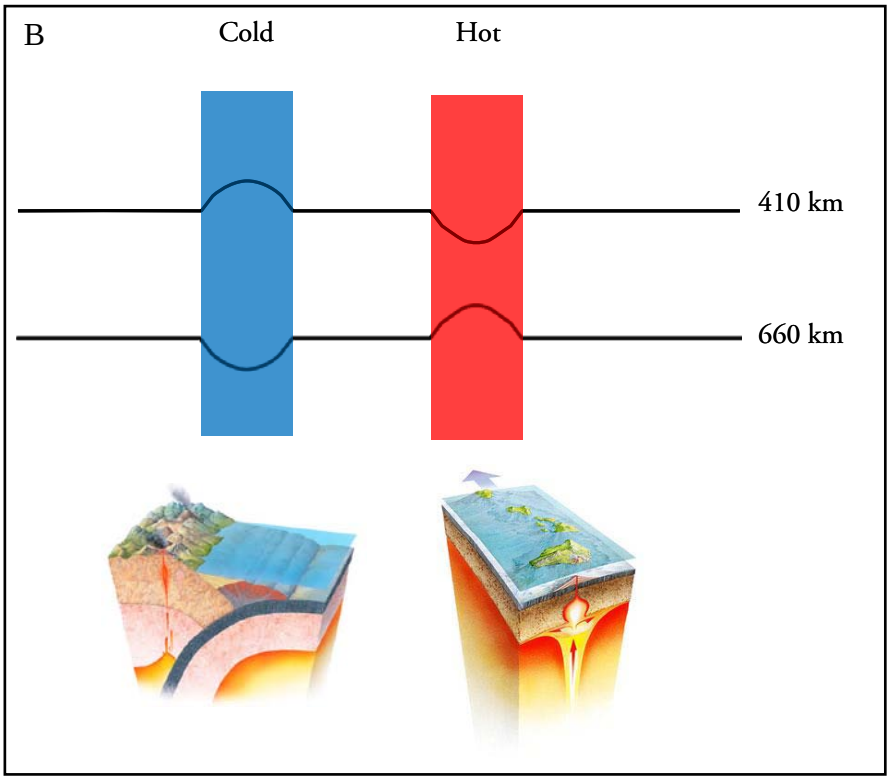

Figure 2.20 – A) Phase diagram of olivine phase transitions (not to scale) showing the opposite Clapeyron slopes signs; B) Graphic representation of the possible phase transition (410 and 660 km) behaviour imposed by thermal perturbations (figures from extremeearth.net).

2.6. Cape Verde islands chronological time-line

The oldest rocks reported from Cape Verde Archipelago belong to Island and possibly to Santiago. In Maio there is a group of magmatic and sedimentary formations that are considered to be remnants of the original Mesozoic oceanic basement and associated sediments (Stillman et al., 1982; Mitchell et al., 1983). The Mesozoic section comprises pillow lavas of N-MORB affinity (Fig. 2.21), pelagic limestones, cherts, black shales and tuffs/conglomerates. This group of sedimentary formations represents a continuous marine sedimentary event, which lasted from Lower Cretaceous. Chronological constrains were made from micropaleontological evidence from siliceous lenses and calcareous beds between pillows giving an age of 138-140 Ma (Fourcade et al., 1990; Azéma, 1990) and recently ages were extrapolated from strontium isotopic ratios[5] giving 133 Ma for pelagic limestones (Holm et al., 2008).

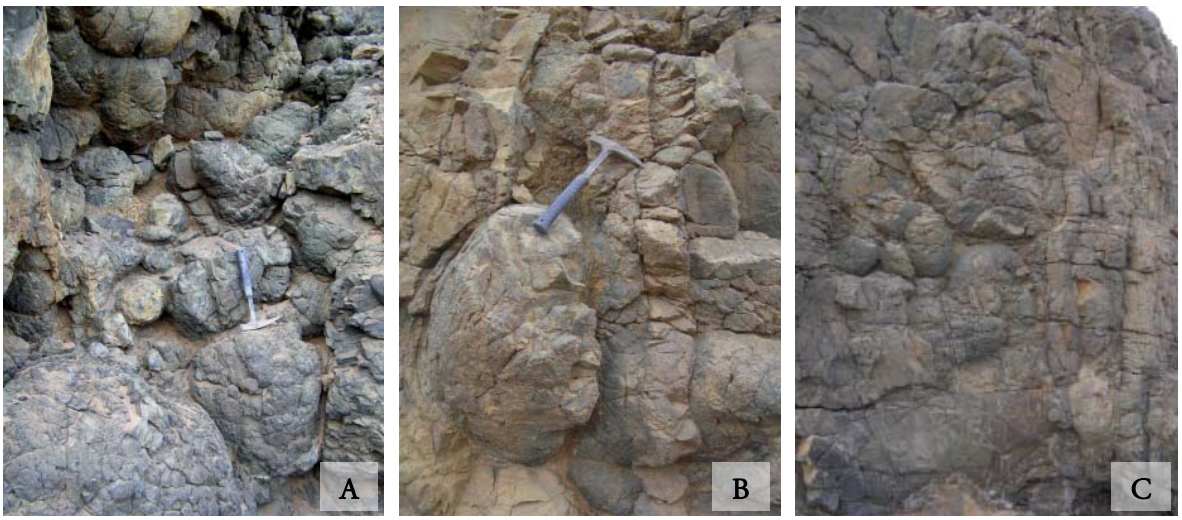

Figure 2.21 – Pillow lavas from the Batalha Formation (photos from João Mata).

Through published ages is possible to envision the beginning of the Cape Verde volcanism around 26-22 Ma, according to the oldest rocks dated in the eastern islands (Mitchell et al., 1983; Torres et al., 2002b; Holm et al. 2008). According to Holm et al. (2008) it seems that

[5] The assumption made from the ages extrapolated from strontium isotopic ratios is that they can reflect seawater composition at the time of carbonate crystallization. Due to easily altered nature of these isotopic ratios particular attention was given to alteration indexes (Holm et al., 2008).

the swell formation started at around Mid-Miocene, by observing the transition between argillaceous Oligocene seafloor sediments through the Calcite Compensation Depth (CCD) to marls, in the DSDP hole 368 (located NE of Senghor seamount, see Fig. 2.1). Figure 2.22 represents a compilation of the available and new geochronological data by Holm et al. (2008), which allows us to see an apparent age-distance relationship within the eastern and southern islands (Sal, Maio, Santiago, Fogo and Brava; represented by the grey arrow) and an almost similar evolution throughout the northern islands of Santo Antão, São Vicente and São Nicolau (black arrow).

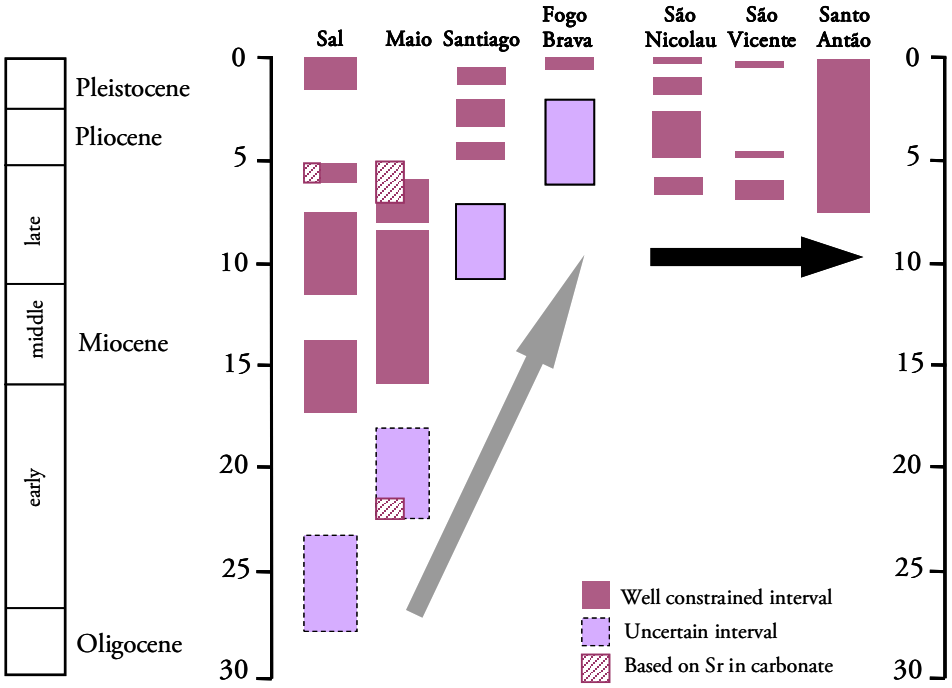

Figure 2.22 – Geochronological data from Cape Verde islands compiled from Holm et al. (2008).

In order to attempt to identify the Cape Verde plume trajectory, the age of the shield building phase (main eruptive phase) of each of the islands were compiled (Fig. 2.23). The main eruptive phase is where the volcanic eruption rate is the highest, being characterized by the occurrence of thick lava piles. High eruption rates are commonly associated with on-axis plume location (center of the upwelling) (Bianco et al., 2008).

By analyzing the dating of the main eruptive phase it is possible to hypothesize that for the eastern and southern islands there is a plume track, being evident a decrease in the age from

Sal to Brava islands (east-west migration). For the northern islands the trend is not evident and seems that the main eruptive phase may be contemporaneous in some of them, in accordance with tectonic constrains as proposed by Torres (1998), which attribute an off-axis position to these islands.

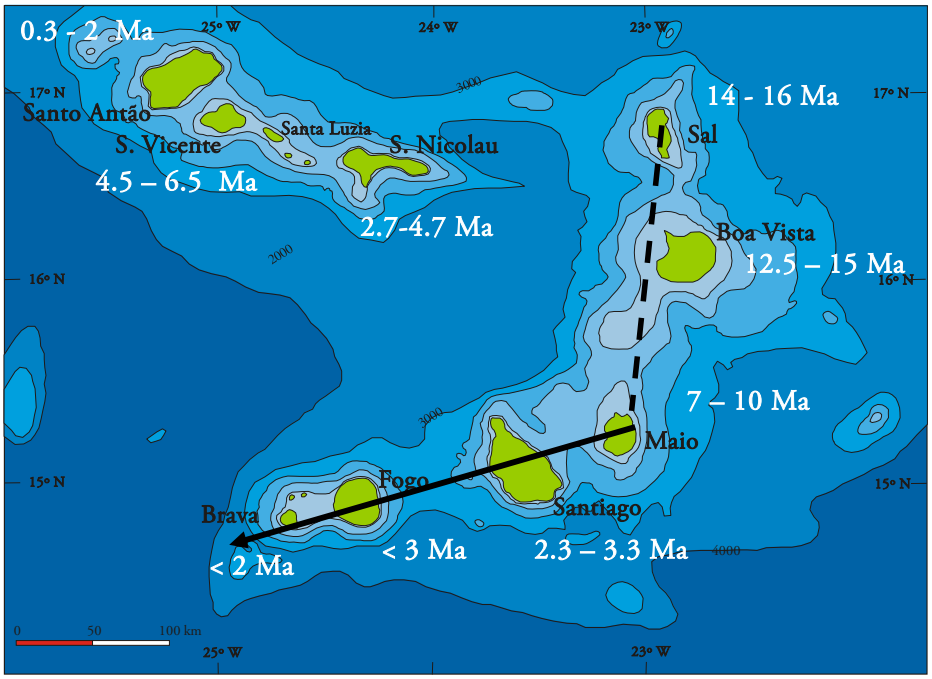

Figure 2.23 – Dating of the main eruptive phase on several islands (data from Mitchell et al., 1983; Gerlach et al., 1988; Torres et al, 2002b; Jørgensen and Holm, 2002; Plesner et al., 2002; Madeira et al., 2005; Holm et al., 2006; Duprat et al., 2007; Holm et al, 2008; Dyhr and Holm, 2010; Madeira et al., 2010)

2.7. Deep mantle plume below Cape Verde Archipelago?

The theory initially proposed by Morgan (1971) to explain the origin of intraplate magmatism has been the subjected on an intense debate, with strong supporters from either side. Due to its significance, not only for the scientific community, a web site has built to discuss and present the latest studies regarding the subject: www.mantleplumes.org. According to Morgan (1971) a mantle plume is a narrow, thermally driven upwelling, not related with plate tectonic processes.

As stated earlier Cape Verde is both a privileged and a problematic location to test the plume theory, due to its geodynamic particularities, and several studies have been done to try

to explain this oceanic intraplate magmatism, in accordance with several distinct theories. The present subchapter aims to scratch only the surface of the problem, because the amount of publications concerning the subject is overwhelming and impossible to describe accurately in a few pages.

When considering the several anomalies associated with the Cape Verde Rise (topography, geoid, gravity and heat flow) it becomes evident that there must be a somewhat deep origin for the magmatism at the archipelago. Courtillot et al. (2003) proposed a set of criteria that supposedly should be observed if a plume originated from deep in the mantle ("primary" plumes): linear chain of volcanoes with observed age progression; flood basalt at the origin of the track; large buoyancy flux; high $^{3}He/^{4}He$ ratios; presence of a significant low shear wave velocity (V_S) in the underlying mantle. According to Courtillot et al. (2003) the Cape Verde Archipelago due to the lack of a track of islands with a clear age-distance relationship, absence of either a flood basalt record or slow V_S at 500 km, is classified as secondary, being related to asthenosphere and passive mechanism of lithosphere breakup.

Anderson (2005), with the intent to improve and expand the hotspot/melting anomalies classification approach done by Courtillot et al. (2003), introduces a larger number of criteria in order to account for the deep and/or thermal processes that could be responsible for those magmatic events. In addition to some already used by Courtillot et al. (2003), the new criteria includes thermal and heat flow data, nature of the volcanic chain, tectonic context, tomographic information at several depths, transition zone thickness and supplementary noble gas parameters. In this classification a total of twelve points can be attributed to either a plume score or a plate score, if the criteria are interpreted as pointing to a primary plume signature or other processes associated with the lithosphere/upper mantle, respectively. According to Anderson (2005), Cape Verde scores one, in the plume hypothesis and eight, in the plate scenario.

It is necessary to point out that Anderson (2005) makes a distinct interpretation of some of the criteria used, as opposed to Courtillot et al. (2003) that applies the interpretations more commonly used in the literature when selecting the five assumptions for the identification of "primary" plumes (Fig. 2.24). As an example, Anderson (2005) questions the validity of the high $^{3}He/^{4}He$ ratio as a deep mantle diagnostic, stating that instead of representing an

"undegassed" mantle it could result from encapsulated low-U domains trapped in the upper mantle, since the degassing event (see Anderson, 2005 for further explanations on all the selected criteria). As confirmed by Anderson (2005) the scoring is subjective, in that the criteria used can be chosen arbitrarily, conflicting data can be selected from the literature and the influence of the criteria can be pondered in different ways.

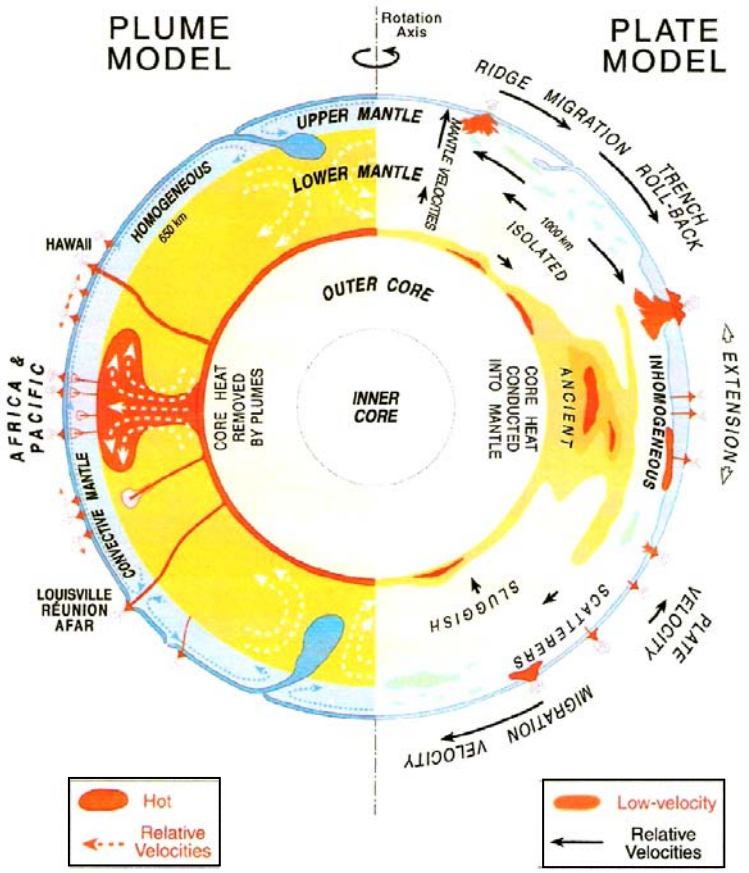

Figure 2.24 – The plume and plate models represented schematically in a cross-section of the Earth (from Anderson, 2005).

It must be emphasized that the points of view of Anderson are also highly debated, particularly in what concerns the interpretation of noble gases signatures. For Cape Verde, relatively unradiogenic $^{3}He/^{4}He$ signatures, excess of ^{129}Xe and very low primary $^{4}He/^{40}Ar^{*}$ has been considered to reflect a contribution of the lower mantle (Christensen et al., 2001; Doucelance et al., 2003; Mata et al., 2010; Mourão et al., 2012).

One of the most important criteria that can help prove, or refute, the existence of plumes is geophysical evidence, due to the expected occurrence of low-velocity anomalies in response to the reduction in seismic wave velocity of hot material (Montelli et al., 2004). Recent studies of seismic tomography (Montelli et al., 2004; 2006) have identified in the Cape Verde area, a deep rooted mantle plume by finite-tomography of P-wave and S-wave velocity images, up to 1900 and 2800 km (core-mantle boundary), respectively (Fig. 2.25). There is a low resolution for the Cape Verde plume in the upper mantle, which imprints the absence of a strong plume signal near the surface. A minimum plume radius of 300 km was estimated by resolution analysis in both cases (Montelli et al., 2004; 2006).

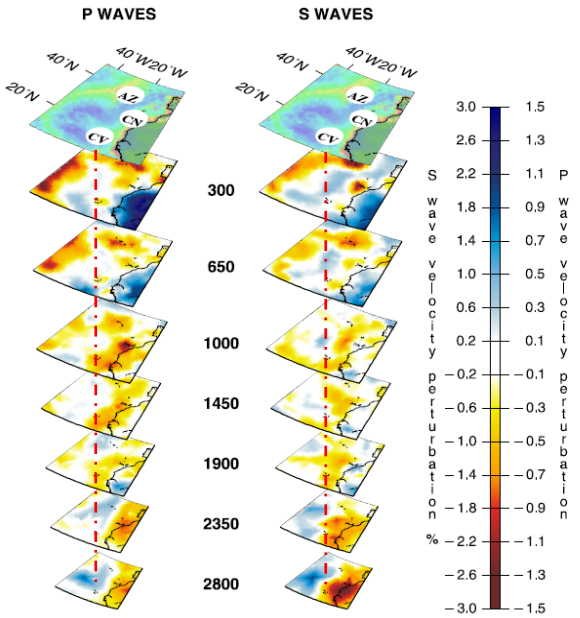

Figure 2.25 – P-wave and S-wave tomography models represented in three dimension view of the structures beneath the Cape Verde (CV), Canary (CN) and Azores (AZ) (from Montelli et al., 2006).

According to Montelli et al. (2006) the plumes responsible for the Cape Verde and Canary archipelagos, as well as the Azores, are strong individualized structures until 1000 km, were they merge into a broader anomaly and bend eastward with depth, towards the base of mantle, approximately at 20-25ºN, beneath the Canary islands (Fig. 2.26).

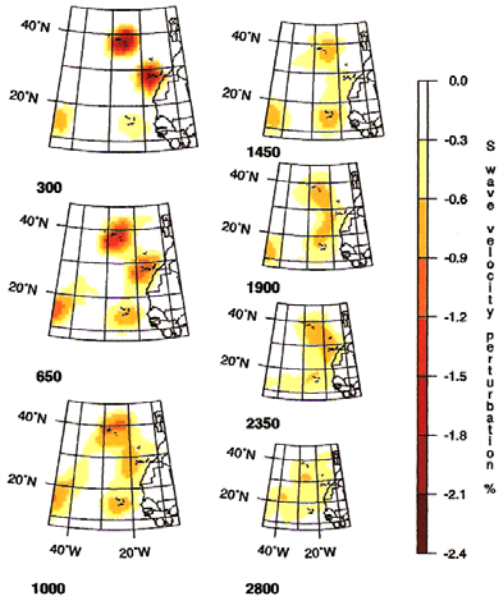

Figures 2.26 – Reconstructed synthetic plumes down to the core-mantle boundary, were is apparent the merging of the three adjacent plumes with depth until 2800 km (from Montelli et al., 2006).

Zhao (2007) using a new global tomography model, identified below the Cape Verde Archipelago, a continuous low velocity anomaly in both upper and lower mantle, which complements and agrees with the results of Montelli et al. (2004, 2006) (Fig. 2.27).

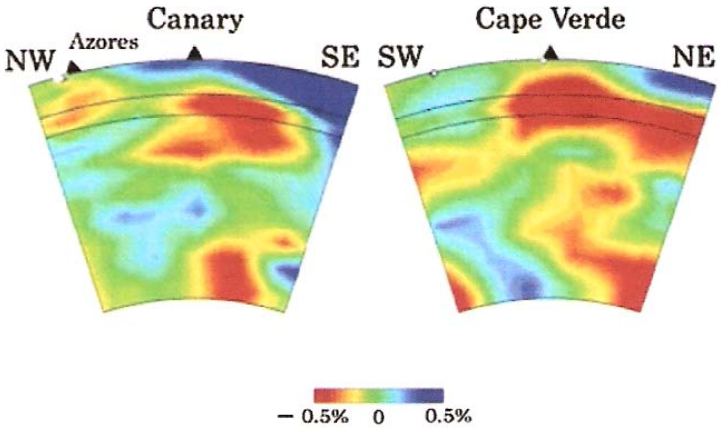

Figures 2.27– Cross sections of P-wave velocity images from the surface to 2800 km, below the Canary and Cape Verde areas ; red and blue zones indicate slow and fast velocity, respectively (from Zhao, 2007).

Using seismic tomographic long-wavelength Vs models, in order to study the morphology and geometry of slow anomalies through the mantle, Davaille et al. (2005) showed that beneath the Cape Verde area there is a 2000-4000 km-wide anomaly above the core-mantle boundary (CMB), rising up to 1000-800 km, that seems to be vertical and cylindrical (Fig. 2.28).

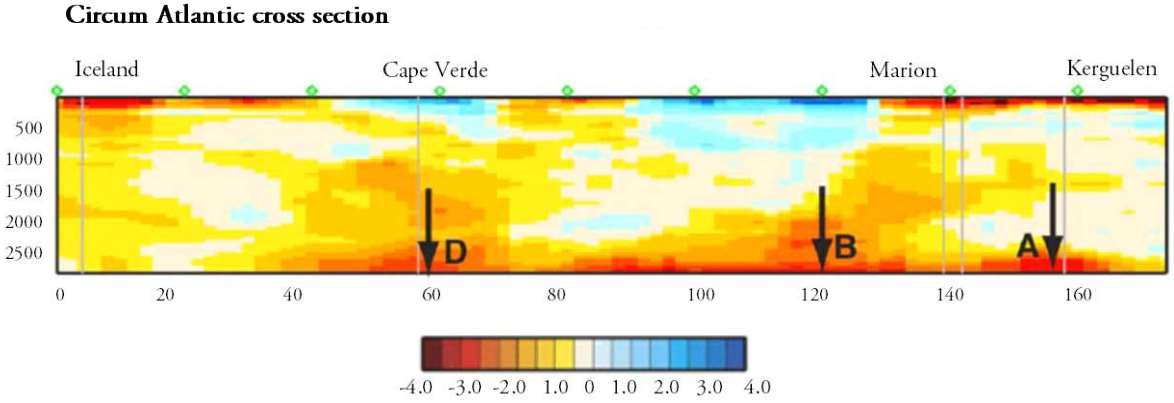

Figures 2.28 – Circum-Atlantic cross-section of long-wavelength Vs model, were is evident the presence of a broad anomaly beneath the Cape Verde area (from Davaille et al., 2005)

Geochemical and seismic observations show that the mantle is heterogeneous in density and composition. Convection studies in heterogeneous fluids made by Davaille et al. (2005), suggest that the interaction between compositional heterogeneities and thermal convection is responsible for the generation of a diversity of plumes with different morphologies. Farnetani and Samuel (2005) also agree that the head-tail of plumes structure should not be considered unique, and that plumes lacking a head can existing, not being diagnostic of shallow origin.

According to Davaille et al. (2005), the accumulation of material in the transition zone (670 km) could lead to the onset of secondary plumes from the stranded hot dome plumes (Fig. 2.29, 2.30). However, there are no reliable images of the mantle between 400 and 1000 km, and so the connection between the large anomalies in the lower mantle and the secondary plumes of the upper mantle remains hypothetical. It is worth noticing that the identification of structures with less than 200 km in diameter is not possible with seismic tomography methods (Davaille et al., 2005).

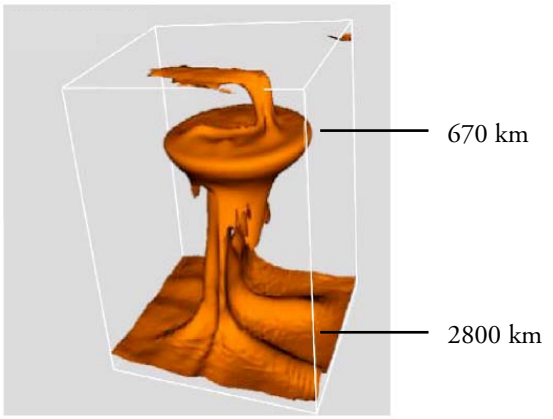

Figures 2.29 – Numerical modelling of a thermo-chemical plume detained at the 670 km discontinuity (from Campbell, 2007).

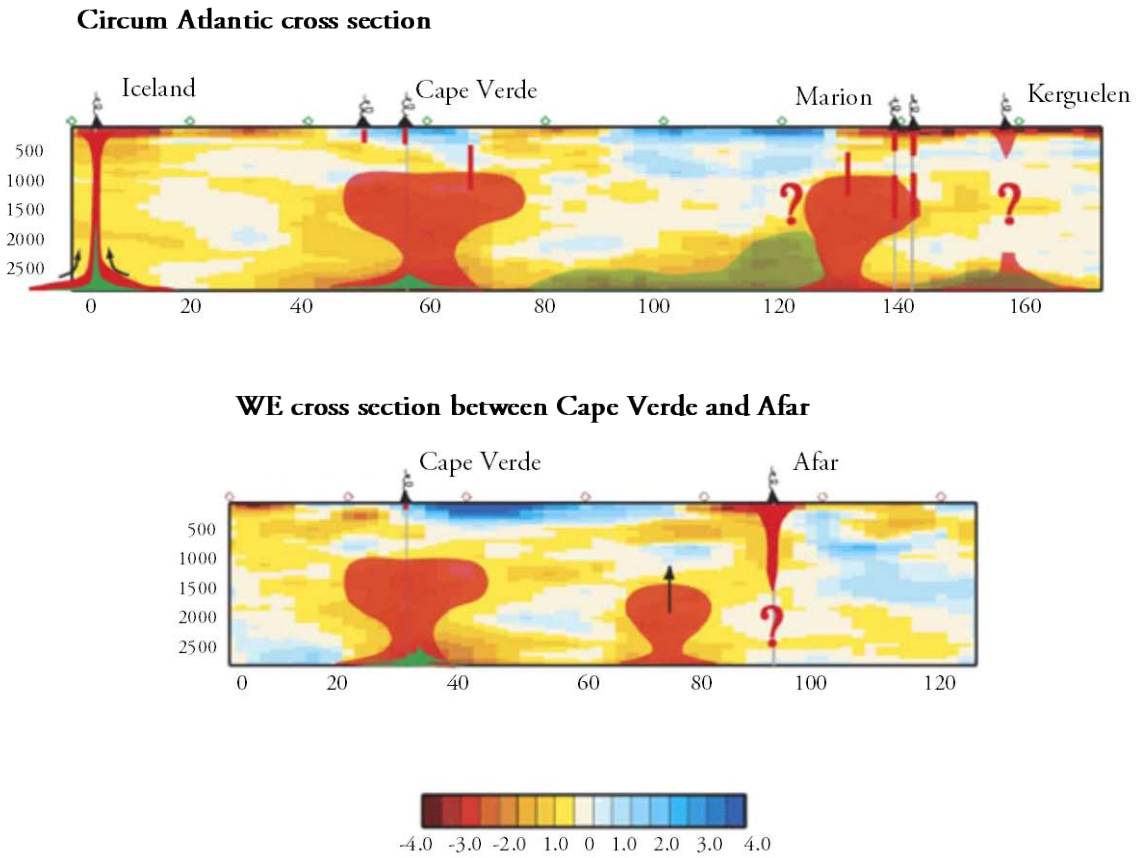

Figures 2.30 – Cross section of long-wavelength Vs model superimposed with the interpretation done with heterogeneous fluid models across the Atlantic (A) and in the Cape Verde-Afar section (B) (from Davaille et al., 2005).

Davaille et al. (2005) made a comparison between the paleomagnetic reconstruction of Pangea and the locations of flood-basalts at the time of eruption with the seismic velocity anomalies at the CMB. The authors concluded that the shape of the seismic low-velocity anomaly in the Atlantic resembles the shape of the Pangea core around 250 Ma and that the original location of Large Igneous Provinces (LIPs) corresponded to the edges or within the anomaly. Torsvik et al. (2006) made a very similar correlation, using a shear wave velocity anomaly map (SMEAN), further stating that at the margins of this large low velocity zone exist very steep velocity gradients pointing to a boundary within the D'' zone[6]. Is within those boundary areas that a great number of LIPs are projected, and if the present location of the low velocity anomaly is coincident with those events, it can be concluded that the anomaly has been present for as long as the formation of the huge magmatic events (≈ 200 Ma) and within the same location (Fig. 2.31).

Torsvik et al. (2006) argues that it is not only the LIPs that are closely related with the margins of the low velocity anomaly in the CMB, but also the deep-seated mantle plumes, a conclusion also supported by Burke et al. (2008) that states that the horizontal gradients in temperature along the steeply inclined margins of the low velocity anomaly are important promoters in the generation of plumes.

Another important piece of evidence for the existence of plume comes from thermal calculations of mantle upwelling. According to geophysical and petrological data, the observed excess temperature in mantle plumes should be around 200 ºC (Sleep, 1990). Putirka (2008) made temperature calculations for 28 hotspots based on olivine/melt thermometers, obtaining values indicating an excess temperature above that of the ambient mantle (Mid Ocean Ridge Basalts, MORB). Temperatures obtained gave an excess in the 175-195ºC range assuming a peridotitic source, implying that ocean islands analyzed are the result of thermally driven mantle plumes.

The calculated excess temperatures correlate positively with buoyancy flux, which seems to suggest that thermal plumes are also responsible for the topographic anomalies, discussed earlier (Putirka, 2005). High $^{3}He/^{4}He$ ratios are also positively related with excess temperature,

[6] D'' is a thick layer (≈200 km) of the lower mantle directly above the core-mantle boundary (Lay et al., 1998).

which according to Putirka (2008) implies that the mantle is layered and that the "undegassed" reservoir is stored in a lower thermal boundary layer, because otherwise, in a non layered mantle the "domains" harbouring the elevated He ratios should only melt at lower temperatures than depleted MORB mantle, and so a negative correlation between excess temperature and high $^{3}He/^{4}He$ should be observed.

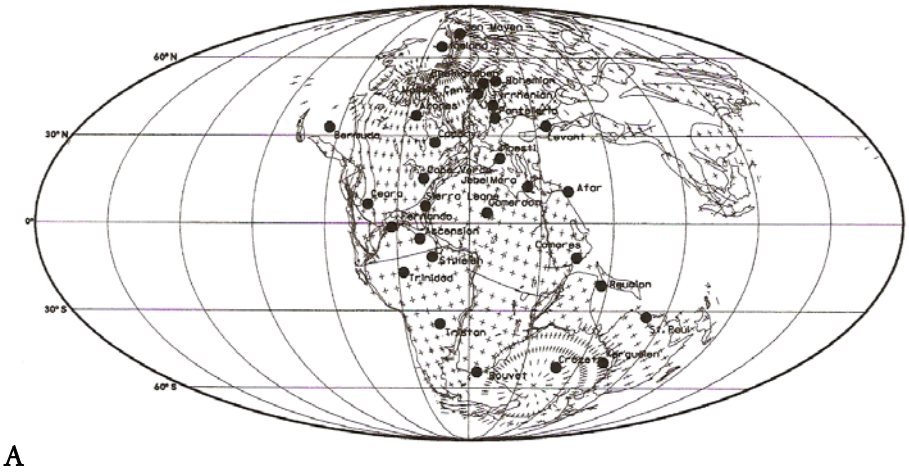

A

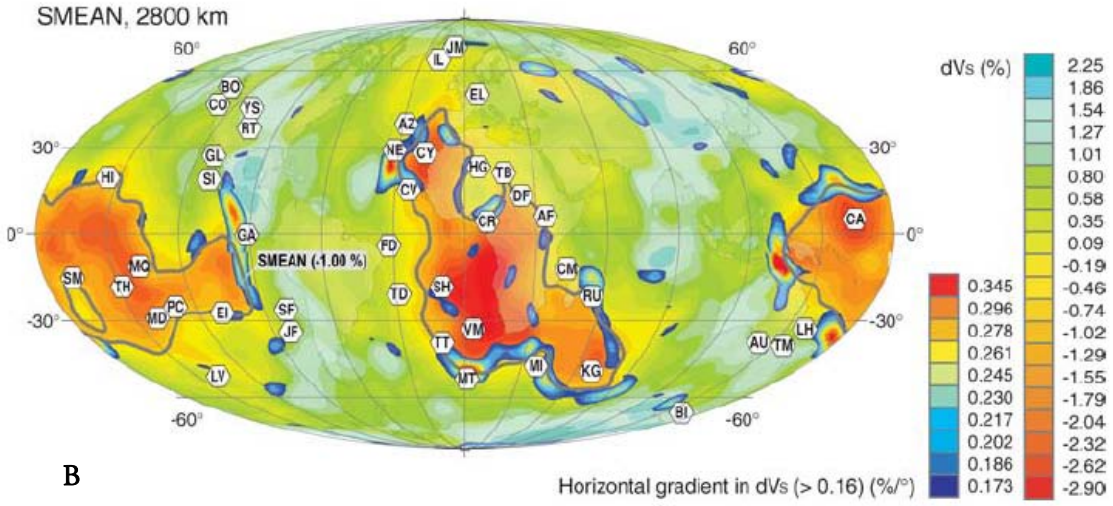

B

Figures 2.31 – A) Paleomagnetic reconstruction of the plates in the Late Triassic with the positions of major Pangean hotspots (from Golonka and Bocharova, 2000); B) SMEAN shear wave velocity anomaly for 2800 km, with hotspot locations indicated (from Torsvik et al., 2006).

2.8. Alternative models for the genesis of the Cape Verde Archipelago

Due to the Cape Verde proximity to the African continent, a mechanism of edge-driven convection was proposed by King and Ritsema (2000) to explain the intra-plate oceanic volcanism. Temperature variations in the upper mantle are expected in a continent-ocean boundary, being the mantle beneath cratons more cold and depleted, with higher viscosity and lower density than the mantle beneath oceanic crust (King, 2007). This discontinuity could lead to the formation of a small scale convection cell, divided in a downwelling portion at the margin of the craton and an upwelling at the ocean lithosphere (Shahnas and Pysklywec, 2004) (Fig. 2.32).

Even though several authors have catalogued the Cape Verde Archipelago as being derived by shallow mantle processes (King and Ritsema, 1998; Courtillot et al., 2003; Anderson, 2005; King, 2007) recent geophysical and geochemical evidence, reported below, seems to preclude this theory. Even if the edge-driven convection may not be the prime cause of magmatism it may still have a local impact in the upper mantle (for instance the deviation of the plume) and should be taken in consideration in that respect.

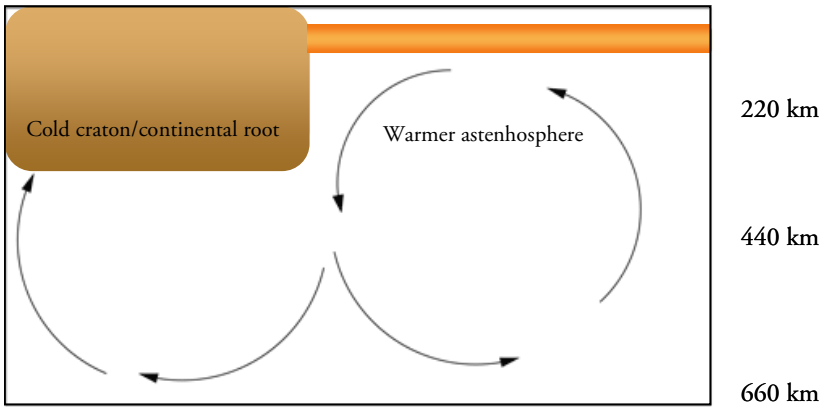

Figure 2.32 – Schematic representation of the generation of the edge-driven convection near a craton margin (King, 2004).

The Cape Verde and Canary archipelagos, as well as Cenozoic volcanic events reported in Senegal and Tarfaya basins have been considered the magmatic rejuvenation, during the Cenozoic, of the event responsible for the opening of the Atlantic Ocean and formation of the CAMP (Central Atlantic Magmatic Province) (Lo et al., 1992). This magmatic event occurs

discontinuously throughout NW Africa from the Oligocene to the Quaternary, with a peak activity in the Miocene (Hansen et al., 2008). It has been suggested that a comparison between Atlantic islands, nearest to the African margin, and the Cenozoic continental magmatism should be made, due to their similar geochemical and geodynamic evolution (Crevola, 1995).

Similarly Oyarzun et al. (1997) ascribe the alkaline magmatism along the eastern Atlantic margin (Late Cretaceous) and Europe (Paleocene-Oligocene) to a tectonomagmatic channelling of the plume responsible for the CAMP event (Triassic-Jurassic) (Fig. 2.33). Plume spreading would be favoured along that specific path due to the already existing thinned corridor corresponding to the southwestern branch of the Variscan belt (Appalachians-Mauritanides belt) and also by the thinned European area (Oyarzun et al., 1997).

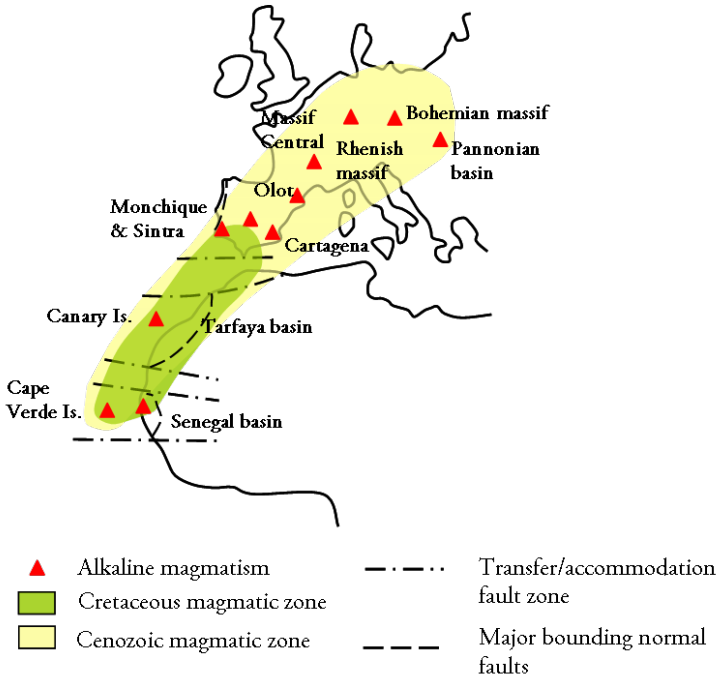

Figure 2.33 – Schematic map showing the model proposed by Oyarzun et al. (1997) of the passive margin alkaline stage since the Late Cretaceous.

Regarding the Cenozoic magmatism that characterizes the NW Africa and the oceanic intraplate events (Cape Verde and Canary archipelagos) there are also alternatives to the most widely and accepted model of mantle plumes (see section 2.7). Patriat and Labais (2006) link the Cape Verde and Canary archipelagos based on an apparent basement morphological continuity as well as similar magmatic and sedimentary evolution. In order to explain this

connection and simultaneous evolution, a model based on the tectonics between African and European plates is suggested. These authors propose that the Canary-Cape Verde ridge could have been an oceanic continuation of the South Atlas, being linked to a transform fault located in the Cape Verde plateau in Late Cretaceous, which was later abandoned. Compressive Cenozoic events that were identified in the Atlas region could also be responsible for the observed basement bulge that characterizes the two archipelagos. Even though the tectonic model still lacks to be tested, for the authors it seems to be the most suitable explanation to explain the similarities between the groups of islands.

Hansen et al. (2008) also suggest that, as Cenozoic magmatism of Senegal, Cape Verde could also be formed due to reactivation of old weakness zones with the magmatic event being the result of extraction owing to the collision between African and European plates within the Mediterranean zone.

CHAPTER 3

SANTIAGO ISLAND GEOLOGY

São Francisco Bay (Santiago – Cape Verde)
Thick lava piles from the main eruptive event (Pico da Antónia Formation)

3.1. Introduction

3.1.1 Previous studies

The first geological reference to Santiago Island was done by Darwin (1844) in the aftermath of the Beagle voyage which started in 1831 at Plymouth, England. The first port visited was, in his own words, Porto Praya in St.Jago (Praia, Santiago) where he made an extensive and detailed description of the outcrops in the area surrounding Praia (Fig. 3.1). It is interesting to note that Darwin, examining lavas overlying limestones, makes an important reference to vertical movements of the crust, even speculating that volcanic activity and uplift were driven by the same forces.

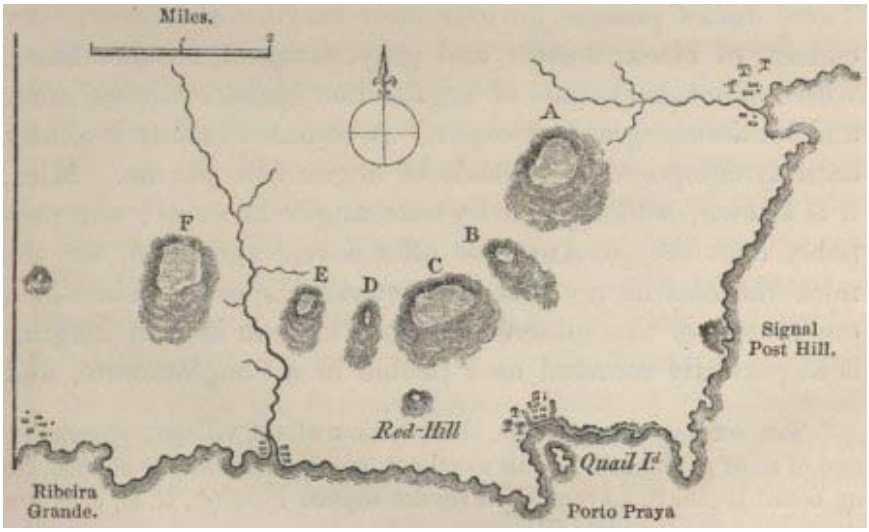

Figure 3.1 –Sketch of the southern region of Santiago Island by Darwin (1844).

The work done by Bebiano (1932) stands as the first extensive geological description of the Cape Verde archipelago (including Santiago Island) in particular in what concerns to igneous petrology. The volcano-stratigraphy of Santiago was established by Serralheiro in 1976 during his PhD thesis, while Alves et al. (1979) performed the first detailed petrologic study of Santiago in a work where the first trace element analyses were published. Such data was presented in conjunction with geological and volcanological observations enabling a reconstruction of magmatic temporal evolution.

By the end of the eighties the first papers, applying isotopic studies, were published with the intent of deciphering the genetic processes of Santiago magmas (Gerlach et al., 1988; Davies et al., 1989). More recently Holm et al. (2008) made a broad ^{40}Ar-^{39}Ar study in Santiago [19 samples covering all the volcanic formations described by Serralheiro (1976)] constraining the volcanic activity from 4.6 to 0.7 Ma (see section 3.2). Barker et al. (2009a, b) performed specific geochemical studies on Flamengos Valley and presented a model for Santiago's mantle source evolution. Martins et al. (2010) discuss specific geochemical characteristics of Santiago's lavas and peridotitic xenoliths attesting the influence of carbonatitic metasomatism in the oceanic lithospheric in a clear example of plume-lithosphere interaction in the Cape Verde archipelago.

Santiago's carbonatitic rocks have also been studied since the seventies, trough petrographic (Alves et al., 1971), field descriptions (Silva et al., 1981) and major, trace and isotopic geochemistry (Kogarko et al., 1992; Kogarko et al., 1993; Hoernle et al., 2002; Mata et al., 2010).

3.1.2. Morphological characteristics

Santiago Island (991 km^2) belongs to the Cape Verde archipelago and is located between the island of Fogo, to the west (≈55 km) and Maio to the east (≈ 25 km). It has an irregular shape being the largest of the archipelago.

The island is orientated northwest to southeast, measuring 55km from "Ponta Moreira" in the north to "Ponta Mulher Branca" in the south, with a maximum width of 29 km in the south region. However there is a notorious narrowing between "Chão Bom do Tarrafal" and "Porto Formoso" with only 6 km width (Bebiano, 1932) (Fig. 3.2).

The geomorphology of the island is mostly conditioned by its volcanic origin and climate. The climate is arid being strongly influenced by the dry and hot air masses that originate in the Sahara region. Precipitation is scarce with an average of 265 mm/y, mainly focused between July and October usually in intense and erratic events (Gonçalves et al., 2006). Temperatures vary slightly between 22 ºC in mean winter and 27 ºC in mean summer seasons (Carreira et al., 2009).

Figure 3.2 – Santiago Island topography. Image courtesy of the Image Science & Analysis Laboratory, NASA Johnson Space Center (ISS006-E-5219; http://eol.jsc.nasa.gov).

Santiago's topography was mostly shaped by seasonal streams that formed deeply incised valleys (see Fig. 3.2) leaving behind narrow ridges or plateaus (achadas). Rock slides, debris slides and slopewash are common erosional processes affecting Santiago hillslopes (Lopes & Meyer, 1993). These landslides can be triggered by earthquakes, volcanic activity, precipitation or gravity instability and are important topography modifiers. Studies on the identification and characterization of subaerial and submarine mass movements, as well as their geohazard potential have been made in several islands of the archipelago (e.g., Fogo, Brava, Santo Antão and São Vicente) (Le Bas et al., 2005; Madeira and Brum da Silveira, 2005; Masson et al., 2008; Madeira et al., 2008).

Santiago has a very complex relief comprising mountain ranges in the interior, with a plateau on its center and extensive lowlands to the south and southeast. Pico da Antónia and Malagueta with a height of 1394 and 1064 m above sea level, respectively, stand as the highest elevations, belonging to the central mountain range which resulted from the erosive destruction of the last big volcanic edifice (Serralheiro, 1976). The eruption style seems to have been mainly Hawaiian, occurring probably along a central vent (shield volcano) and/or along fissures giving rise to sub-horizontal flows or with shallow slopes (up to 10º). The most recent volcanism in Santiago, composed of small pyroclastic cones (e.g., ash, lapilli, bombs) could be due to strombolian eruptions which are characterized by a more explosive character relative to the Hawaiian type. The scarce occurrence of domes and small lava flows of traquitic and phonolitic nature stand as testimonies of episodic pelean volcanic activity/phreato-magmatism which seems to have been very localized and of minor expression compared to the abundant mafic magmatism (Serralheiro, 1976).

Several uplift episodes of the island are testified by raised marine abrasion platforms, marine terraces and outcropping pillow lavas above the present sea level (a.p.s.l.) (Mitchell-Thomé, 1976; Serralheiro, 1976; Holm et al., 2008). Ramalho et al. (2010) made an extensive study on uplift and subsidence tracers in the archipelago and concluded that Santiago has one of the highest vertical displacements observed within the islands. The occurrence of submarine lavas of the Flamengos Formation (± 4.9 Ma; Holm et al., 2008) up to 450 m a.p.s.l. implies a vertical displacement in excess of 420-450m. Indeed the accepted eustatic curves, reveals a mean sea level at the time of extrusion, close to the actual one (maximum of only 21 m) (Fig 3.3). An uplift of 200 m, around 2-3 Ma, is also inferred by the occurrence of submarine lavas from the Pico da Antónia Formation up to 270 m a.p.s.l. (Ramalho et al., 2010b). Quaternary sea-level palaeo-positions are testified by marine abrasion surfaces which were identified and described by Serralheiro (1976) at seven levels: 2-4 m, 5-10 m, 15-25 m, 30-40 m, 50-60 m, 60-80 m and 80-100 m a.p.s.l.

One of Santiago's peculiarities is the occurrence of pillow lavas with characteristic geochemical signatures which allow them to be interpreted as seafloor basalts (MORBs) (Gerlach et al., 1988; Mendes and Silva, 2001). If the portion of uplifted seafloor is considered (see section 3.2) then at least 4000 to 6000 m of upward movement is necessary to explain its

presence of up to 220 m a.p.s.l.. The incorporation of these deep-seated blocks occurred probably in the seamount phase of the island evolution but the mechanism is not yet understood (Ramalho et al. 2010b).

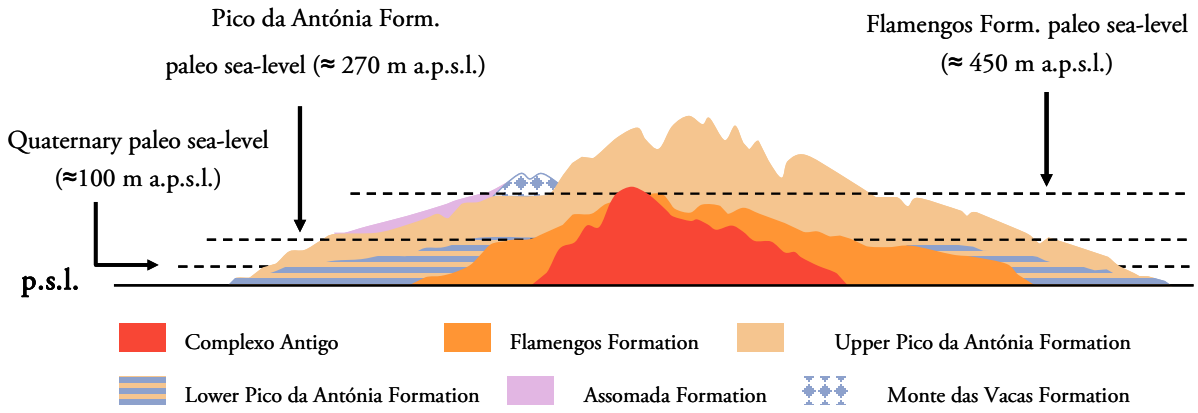

Figure 3.3 – Santiago Island idealized cross-section with information concerning past sea-levels (p.s.l. stands for present sea level) (adapted from Ramalho et al., 2010b).

According to Ramalho et al. (2010a) each one of the Cape Verde islands endured distinct uplift histories, suggesting local constrains such as different amounts of underplating or intrusions at the base of each edifice. However the more homogeneous Quaternary uplift seems to affect the archipelago globally implying a more wide mechanism related to hotspot swell dynamics (see section 2.4).

3.2. Stratigraphy

Santiago's stratigraphy was established by Serralheiro (1976) trough extensive field work supported by aerial photo interpretation, culminating in the elaboration of a 1:25 000 scale geologic map comprising 11 sheets. Alves et al. (1979) presented a simplified geologic map in 1:100 000 scale, based on the work of Serralheiro (1976), along with interpretation of the volcano-stratigraphy supported by petrological and geochemical studies (Fig. 3.4).

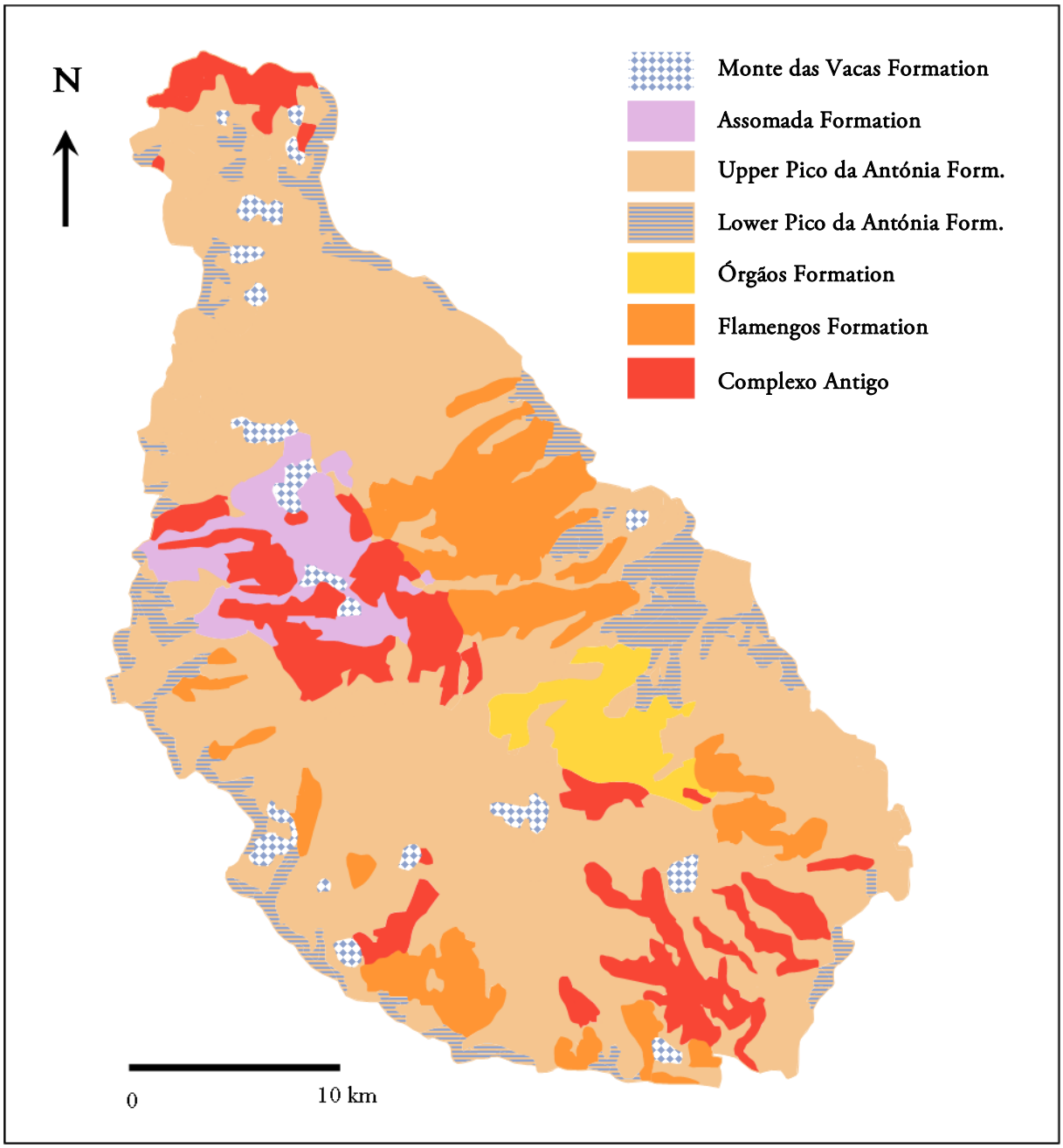

Figure 3.4 – Simplified Santiago stratigraphy (adapted from Serralheiro, 1976; Alves et al., 1979 and Silva et al., 1981). The subdivision of Pico da Antónia Formation was previously proposed (Martins et al., 2003) based on geochemical and field arguments (see also section 3.2.4).

The stratigraphy of Santiago Island defined by Serralheiro (1976) comprises six main units, from the oldest to the youngest: Complexo Antigo and Flamengos, Orgãos, Pico da Antónia, Assomada and Monte das Vacas Formations. This subdivision is still broadly accepted not withstanding some recent refinements that have been proposed (see below).

The oldest unit identified in Santiago comprises Mesozoic oceanic crust and sediments that outcrop in the Angra area (northeastern Santiago) (Gerlach et al., 1988; Davies et al., 1989). This area was mapped by Serralheiro (1976) as belonging to the Complexo Antigo and consequently these Mesozoic oceanic rocks are usually not represented on Santiago's stratigraphic column. The outcrop is composed of uplifted and tilted pillow lavas of N-MORB affinity within an area of 330 m^2 (Fig. 3.5). As in the neighbouring island of Maio, it is believed that this unit corresponds to an oceanic crust fragment incorporated in the island substrate during its growth (De Paepe et al., 1974). Its exposure is probably related to tectonic and isostatic processes and subsequent erosional processes (Wipf et al., 2009). In the Canary Islands similar outcrops have been described in Fuerteventura (Stillman et al., 1975; Steiner et al., 1998), however no other occurrences are known at within plate ocean islands worldwide.

Figure 3.5 – Mesozoic outcrop of pillow lavas in Santiago Island (Angra area).

The Mesozoic occurrence in Maio Island is well described due to its major spatial expression being incorporated in the island's stratigraphy however Santiago's outcrop is small and not thoroughly described, with very little published data (Gerlach et al., 1988; Davies et al., 1989; Mendes and Silva, 2001). According to Gerlach et al. (1988) the pillow lavas yield an imprecise Pb-Pb age of about 130 Ma, similar to the occurrences in Maio Island (138-140 Ma for the Batalha formation; Fourcade et al., 1990). This data is in agreement with the age of the

oceanic crust in the region as deduced from the positioning of magnetic anomalies relatively to the Cape Verde archipelago.

The Angra outcrop consists of intricate altered pillow lavas, displaying yellowish colours making them easily identifiable in the field. The interpillow spaces are filled with alteration material, probably hyaloclastites or sediments, with several occurrences of jasper, limestone and possibly phosphates (Silva, L.C., person. commun.). It is worth mentioning the preservation state of these massive submarine flows where it is still possible to identify perfect ovoid shaped pillows with its chilled margins and radial joints (Fig. 3.6).

Figure 3.6 – A) Well preserved structures in pillow lavas of MORB affinity; B) Pillow lava and associated interpillow space filled by alteration material (Angra area) (photo by João Mata).

3.2.1. Complexo Antigo (CA)

The Complexo Antigo makes up the substrate of Santiago Island and outcrops mainly in the northernmost area, in the western central zone and in several dispersed occurrences in the south (Fig. 3.4). This formation is very heterogeneous. Outcropping lithologies include basic lavas flows and dykes, intrusive nepheline-syenites, phonolites, trachytes, gabbros, ijolites, pyroxenites and carbonatites. The stratigraphic relations between the different lithotypes are very complex, not being easy to make a clear chronological sequence of events (Serralheiro, 1976; Alves et al., 1979; Holm et al., 2008). However it is possible to establish a relative

chronology within several subunits, grouped according to their petrographic affinities: basaltic dyke complex, intrusive granular silicate rocks, volcanic breccias, intrusive and extrusive phonolites/trachytes and carbonatites (Serralheiro, 1976; Alves et al., 1979).

The dyke complex is essentially composed of extremely altered vertical or subvertical dykes, occurring occasional subaerial lava flows intensely weathered. The dykes form an extremely dense and complex network, sometimes being impossible to be individualized. In most cases they are basaltic in nature with a porphyritic core becoming increasingly aphyric towards the rims (Serralheiro, 1976).

There is a diverse and intricate association of intrusive silicate rocks in the Complexo Antigo, comprising gabbros, pyroxenites, nepheline-syenites and rocks of the ijolite-melteigite series (Alves et al., 1979) (Fig. 3.7). These intrusions are often spatially associated with carbonatites, which could lead to the conclusion that they are cogenetic. However the Complexo Antigo is scarcely studied and even though there is the possibility that carbonatites and silicate rocks have a genetic association, several studies in alkaline-carbonatite complexes have shown that Nd and Sr isotope data, between these lithotypes, diverge significantly (Harmer and Gittins, 1998; Harmer, 1999).

The areas occupied by volcanic breccias vary between a few m^2 to over 200 000 m^2, in the Monte Pensamento area (north of Praia). These breccias are characterized for being compact and sometimes showing evidence for more than one breccification event. The most common elements are basaltic however phonolite and granular clasts (gabbros, melteijites, carbonatites, etc.) have also been identified (Fig. 3.7E). The cement that binds the clasts is usually basaltic or carbonatitic (Serralheiro, 1976).

Phonolites and trachytes occur in dykes and pipes outlining small elevations with conical and sharp configurations. They correspond to deep volcanic edifice roots whose structures have been totally dismantled (Alves et al., 1979). Serralheiro (1976) also reports the presence of associated pyroclastic material and breccias.

Carbonatites, due to their worldwide and oceanic rarity and to their geochemical peculiarities, are one of few lithotypes of the Complexo Antigo that have been studied with more detail in Santiago Island (Allègre et al, 1971; Alves et al., 1971; Bernard-Griffiths et al.,

1975; Silva et al., 1981; Kogarko et al., 1992; Kogarko, 1993; Hoernle et al., 2002; Mata et al., 2010).

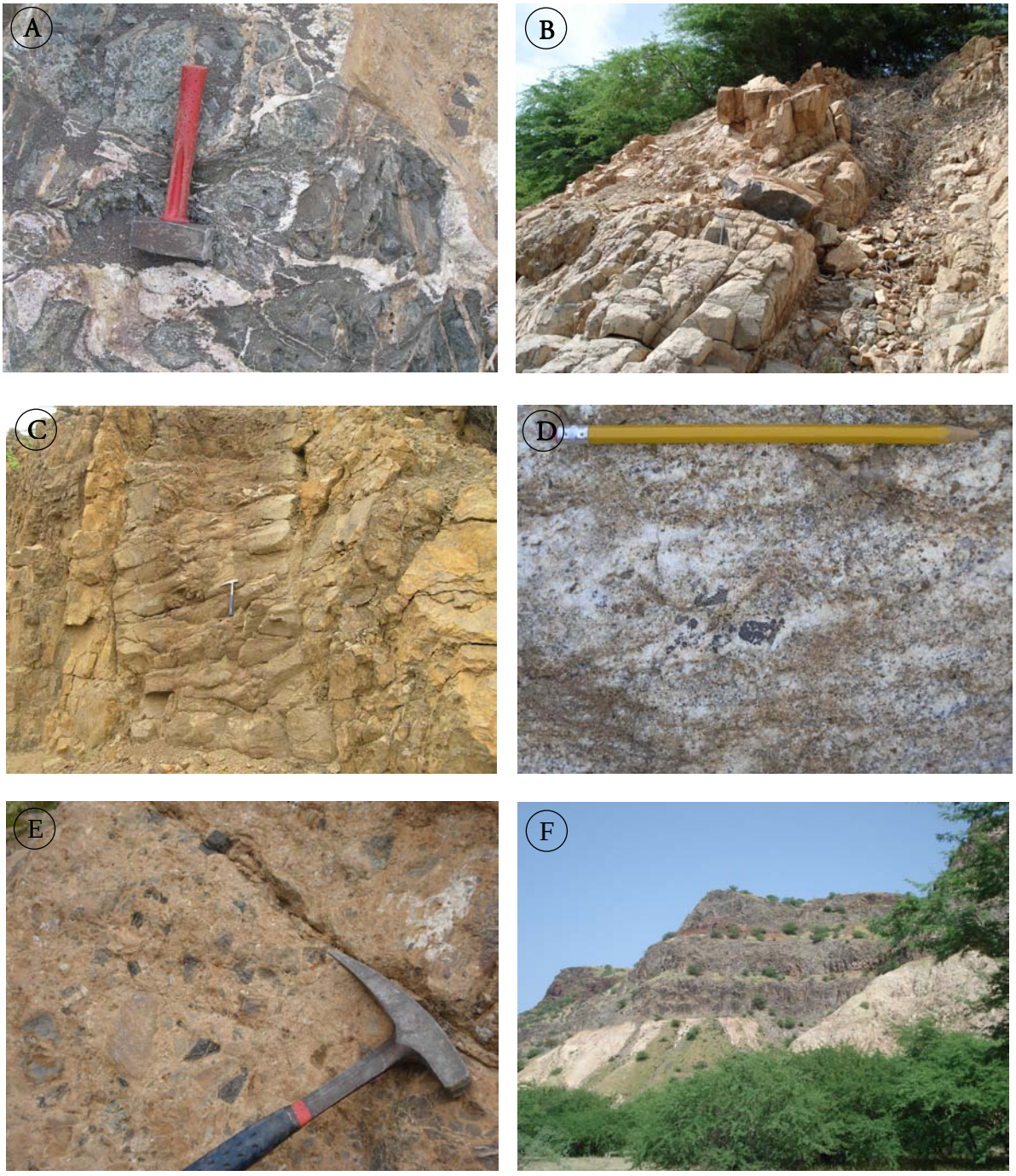

Figure 3.7 – A) Gabbro/Ijolite with veins of carbonatite (Ribeira Barca, João Mata photo); B) Nepheline syenite dyke, Complexo Antigo (Monte Pensamento); C) Carbonatite dyke, Complexo Antigo (Monte Pensamento, João Mata photo); D) Detail of outcropping carbonatite (Ribeira da Barca, João Mata photo); E) Carbonatitic breccia, Complexo Antigo (Angra area); F) Contact between Complexo Antigo and Pico da Antónia Formation (Ribeira do Charco).

In Santiago Island the outcropping carbonatites occur in small areas, the biggest one being located in Ribeira da Barca, with 300-400 m across and 100 m high (Serralheiro, 1976). Other locations where carbonatites occur as plugs and dykes include Monte Pensamento, Monte Gonçalo Afonso, Ribeira Sansão and Ribeira do Charco areas.

Santiago's carbonatites are classified as calciocarbonatites, magnesiocarbonatites and ferrocarbonatites being commonly associated with ijolite-melteijite complexes and showing frequent xenoliths of granular rocks and miccaceous nodules (Alves et al., 1971; 1979; Kogarko et al., 1992).

Of particular interest is the discovery made by Silva et al. (1981) of the first carbonatite volcano described in an oceanic setting in the Arruela area (north of Tarrafal). These authors described the eroded remains of the volcano as comprising carbonatitic and nephelinitic subaerial tuffs cut by carbonatite and nephelinite dykes (Fig. 3.8). The structure and lithologies identified allowed the authors to establish a parallelism with Oldoinyo Lengai, the only active carbonatitic volcano on Earth, even though natrocarbonatites were not found in Arruela area.

A detailed study of the tuffs revealed that they are composed of more than 95% of rounded grains of calcite crystallites with abundant biotite flakes and lithic fragments (calciocarbonatite, ijolite, pyroxenite and nephelinite). Petrographic and field evidences suggest a pyroclastic mechanism of eruption probably with pyroclastic flow events (Silva et al., 1981). Intrusive plugs stand out in the field cutting through the bedded tuffs in Baia do Medronho and Arruela area. Some of these occurrences correspond to diatremes which are composed of breccia with carbonatitic cement (Fig. 3.8). The origin of these structures can be due to phreatomagmatic eruptions or to fluidization by exsolution of volatile phases (Kurszlaukis and Lorenz, 1997), corroborating the explosive character of the volcanism.

The greater part of the volcanic edifice appears to have been destroyed by erosive processes with the consequent re-deposition of the material as shallow marine epiclastic carbonatitic conglomerates, siltstones and calcilutites. Silva et al. (1981) estimated that the total area of the remaining carbonatitic volcano exceeds 10 km^2.

Figure 3.8 – A) Detail of carbonatitic tuffs (Baía do Medronho); B) Outcrop of layered tuffs (Baía do Medronho); C) Diatreme standing out in the field (Chão da Arruela); D) Detail of carbonatitic breccia that compose the diatreme (Chão da Arruela); E) Panoramic view of the carbonatitic volcano remnant, covered with lava flows of more recent formations (Baía do Medronho); F) Syenite plug and greenish nephelinites in the background (Chão da Arruela).

It is very difficult to constrain the time span of the Complexo Antigo due to limited available data. Bernard-Griffiths et al. (1975) present a K-Ar age of 10.3±0.6 Ma for a theralite, the oldest reported age for Santiago's Complexo Antigo. These authors also analyze two carbonatite mica's which gave 9.8±0.3 and 8.5±0.7 Ma and a phonolite dyke with 7.1±0.4 Ma, which most probably belongs to the Complexo Antigo. In 2002 Hoernle et al., present distinct U-Pb age determinations for calcio and magnesiocarbonatites, with a group of samples from Ribeira da Barca indicating 2.1 Ma and other group, with samples from Monte Pensamento and Arruela, with ages around 7.0 – 7.4 Ma. Due to the fact that carbonatites seem to be confined to the Complexo Antigo and subaerial lava flows that overlie these deposits have been ascribed a 2.3-2.6 Ma age (Pico da Antónia Formation, Holm et al., 2008), a 2 Ma age for the Ribeira da Barca carbonatites does not seem very plausible.

Abranches et al. (1990) trough paleomagnetic data reports a Paleogene age for a low temperature recrystallization event affecting some Complexo Antigo samples, suggesting that their emplacement was in the Late Cretaceous. However, this paleomagnetic data should be confirmed by other dating techniques since the present Complexo Antigo age data is very scarce.

3.2.2. Flamengos Formation

The Flamengos Formation is the first well defined extrusive volcanic phase of Santiago Island. It outcrops mainly in the central and east costal area with various occurrences in the south. The majority of the outcrops are located in river valleys, the biggest exposure occurring in the Flamengos valley which extends inland for 14 km, from the coast to altitudes reaching≈ 450 m, in Portal da Furna (Serralheiro, 1976; Ramalho et al., 2010).

This formation is entirely submarine and comprises pillow lavas of basaltic (s.l.) composition, hyaloclastites, pyroclasts and breccias of great thickness, uniformity and length (Fig. 3.9). The thickness of lava flows and associated pyroclastic layers, suggests prolonged magmatic activity with alternating extrusive and more explosive phases (Serralheiro, 1976; Alves et al., 1979).

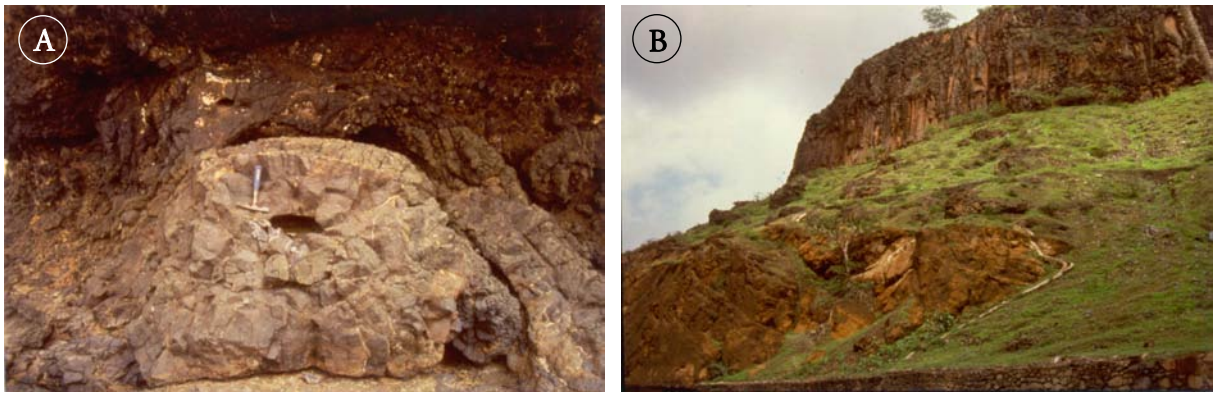

Figure 3.9 – A) Pillow lavas of Flamengos Formation (São Francisco); B) Outcrop of thick pyroclastic layer covered by pillow lavas both of the Flamengos formation, superimposed by extensive subaerial lava flows of Pico da Antónia Formation (Pinga Mel).

The discriminating characteristics that allow the distinction between volcanic submarine occurrences of Flamengos Formation and other similar outcrops belonging to other formations are the intense alteration/weathering degree (e.g. presence of bluish clay material). Interestingly Serralheiro (1976) describe its presence at altitudes commonly reaching 300 m.

Serralheiro (1976) inferred ages above 9 Ma for Flamengos Formation based upon macrofossil data of sedimentary formations/layers which were used to indirectly constrain the age of the associated magmatic occurrences. However Bernard-Griffiths et al. (1975) assign a 4.1±0.4 Ma age for a basaltic pillow lava of the Flamengos Formation through K-Ar dating, which is in accordance with the most recent ^{40}Ar-^{39}Ar dating by Holm et al. (2008) of 4.6 Ma.

3.2.3. Orgãos Formation

In Santiago Island the only individualized and described sedimentary unit is the Orgãos Formation. It is a very complex and heterogeneous unit, including very thick deposits of angular, subangular and rounded basaltic (and more rarely trachyte and phonolite) clasts embedded in a matrix of the same nature (Serralheiro, 1976). Several sandstone layers have been described as well as rare volcanic events, testified by lava flows of small expression (Alves et al., 1979).

In the Orgãos Formation there have been identified deposits of terrestrial, estuarine and marine environments. The terrestrial deposits are the most abundant, being distributed irregularly across the island, the largest outcrop being in the central area of Santiago around São Lourenço dos Orgãos (Fig. 3.4). Estuarine and marine facies occur in peripheral areas relative to the terrestrial ones (Alves et al., 1979).

The occurrence of terrestrial deposits of such length and thickness implies the presence of volcanic edifices with a significant spatial expression but in an advanced state of weathering and dismantling which act as the source of the deposited material. Since the genesis of this unit is thought to be the result of mud flows and/or lahars there is the need for very intense and concentrated rains promoting torrential regimes towards an endorreic basin. The decline of volcanic activity needed for erosion to play a significant role is also confirmed by the rare occurrence of magmatic products within the Orgãos Formation (Serralheiro, 1976).

3.2.4. Pico da Antónia Formation

In Santiago Island the most significant unit concerning spatial coverage, volume of emitted materials and volcanic time span is the Pico da Antónia Formation (see Fig. 3.4). The volcanic activity seems to have been dispersed and not centered in a unique vent, as present in some phases of the development of other islands (e.g., Fogo), suggesting the occurrence of several vents and volcanic fissure vents.

Within this unit it is possible to identify several episodes distinguished by the type of volcanism and associated extruded and/or intruded material. Serralheiro (1976) differentiate five volcanic subunits within the subaerial faceis and two in the submarine facies (see Table 3.1, Fig. 3.10). All along the formation there are sedimentary deposits and erosional surfaces indicating hiatus in the extensive volcanic activity.

3.2.4.1 Pico da Antónia Formation subunits

A - Thick lava flows and interlaid pyroclasts/ Upper and Lower submarine lavas

The oldest unit corresponds to thick piles of subaerial lava flows and submarine lavas, which makes up the most part of the exposed Santiago Island. Associated with the extensive

subaerial lava flows are several pyroclastic deposits which seem to represent the first products expelled with every new extrusive phase/pulse (Serralheiro, 1976). The submarine lavas outcrop all around the coast of the island constituting almost a continuous ring. Serralheiro (1976) subdivided them due to the presence of fossiliferous limestone or subaerial flows between what seemed to be two different submarine volcanic episodes.

Table 3.1 – Pico da Antónia Formation subunits (adapted from Serralheiro, 1976)

Subaerial facies*	Submarine facies
E – Pyroclasts and interlaid lava flows	
D – Lava flows and interlaid pyroclasts	
C – Breccia-tuff	
B – Phonolite and trachyte	
A - Thick lava flows and interlaid pyroclasts	A1 – Upper and Lower submarine lavas

* A as the oldest and E the youngest.

The submarine lava flow deposits are composed of pillows piles/stacks or more rarely sheet lavas. The interpillow spaces are commonly filled with a breccia composed of glassy debris though to be the result of fragmentation of the outermost rim of the pillow. This hyaloclastitic material is frequently cemented by calcite due to subsequent weathering events (Serralheiro, 1976). It is worth mentioning the occurrence of mega-pillows in several locations (Mangue de Sete Ribeiras, Porto Formoso) with dimensions of up to 7x13 m (Serralheiro, 1976) (Fig. 3.10C). These mega-pillow facies have been described in other islands (North Island, New Zealand; Tasmania) their genesis being controlled mainly by high effusive rates and low slope angle of the depositional area (Goto and McPhie, 2004; Bear and Cas, 2007)

The sampling of subaerial and submarine lavas of Pico da Antónia Formation focused mainly on subunit "A" because of its length and extensive outcrop of unaltered samples. However, even thought Serralheiro (1976) considered the submarine events as peripheral manifestations of the subaerial ones, the present and previous studies (see Chapter 4, Martins et al., 2003; 2007) strongly suggests that there are significant geochemical differences between the two implying their non-comagmatic origin and, probably, non coeval character. Field work in 2006 and 2008 (trough PLINT and CV-PLUME projects, see acknowledgements)

confirmed the existence of several features corroborating the existence of two distinct lithostratigraphic units.

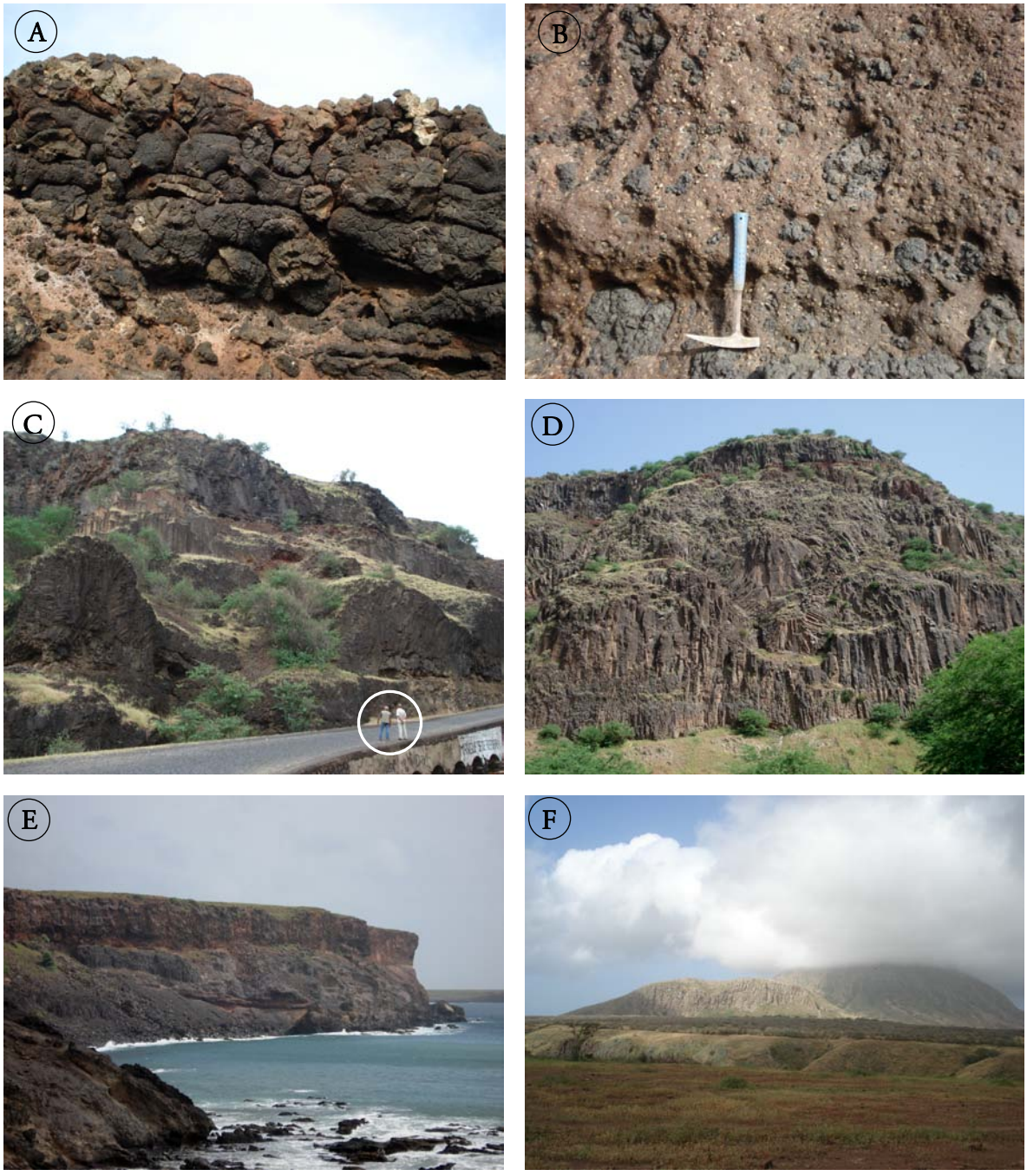

Figure 3.10 – A) Pillow lavas of Pico da Antónia Formation (Prainha); B) Hyaloclastites with pillow lava fragments from Pico da Antónia Formation (Prainha); C) Mega-pillow lava from Pico da Antónia Formation (Porto Formoso); D) Prismatic junction in Pico da Antónia Formation (Ribeira do Charco); E) Thick subaerial lava flow of Pico da Antónia Formation, with a very regular surface (São Francisco); F) Phonolitic domes from Pico da Antónia Formation (Trás os Montes).

3.2.4.1.1 Upper and Lower Pico da Antónia distinction – field evidence

The aim of the field work was to verify the synchronicity or not between the subaerial and submarine lavas integrated in the Pico da Antónia Formation defined by Serralheiro (1976). Several areas were identified and field evidences, corroborating the distinction between these units, will be described briefly.

São Martinho Pequeno

Near the village of S. Martinho Pequeno, on a road cutting, an extensive and fresh outcrop allows the observation of the contact between the Upper and Lower Pico da Antónia (Fig. 3.11). Between the thick pile of subaerial lava flows and the submarine pillow lavas, a reddish paleo-horizon with variable thickness is observed (1.0 - 2.5 m) (Fig. 3.12). This horizon seems to correspond to a paleosoil composed of oxidized material that resulted from the degradation and alteration (physical and chemical) of the underlying level (submarine lavas). In several areas it is possible to distinguish semi-circular structures that might correspond to less altered/preserved pillow cores (Fig. 3.13).

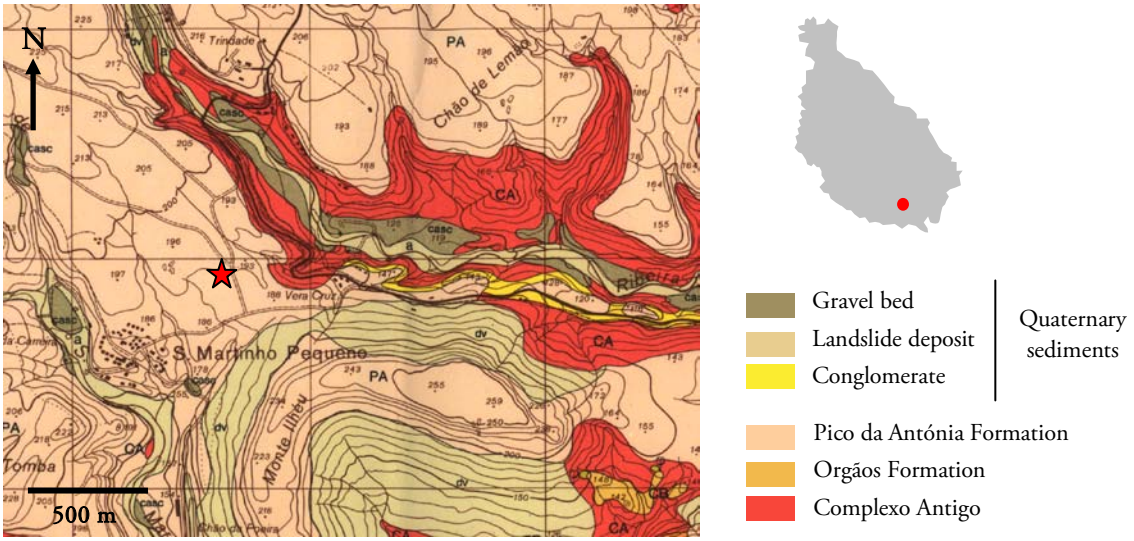

Figure 3.11 – Location of São Martinho Pequeno outcrop (section of sheet 58; Serralheiro, 1976)

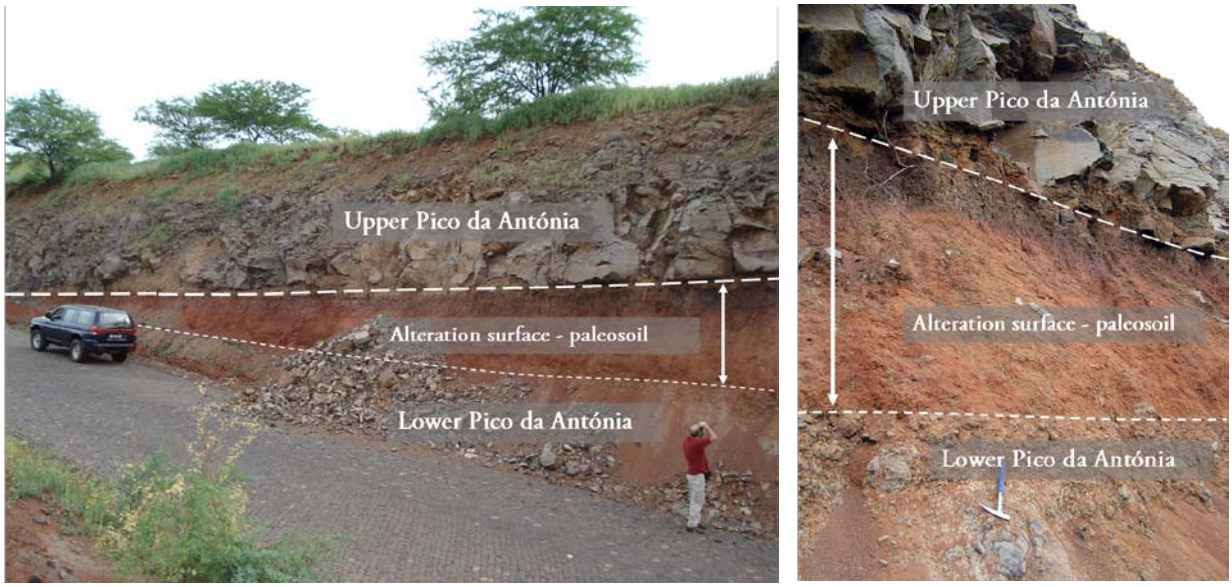

Figure 3.12 – São Martinho Pequeno outcrop where a paleosoil occurs between the Upper and Lower Pico da Antónia Formations.

The presence of a paleosoil implies land exhumation (since the underlying layer was of submarine origin) with subsequent pause in volcanism which allowed the soil to form. All this sequence of events implies a considerable temporal hiatus between the deposition of the Lower and Upper Pico da Antónia Formations.

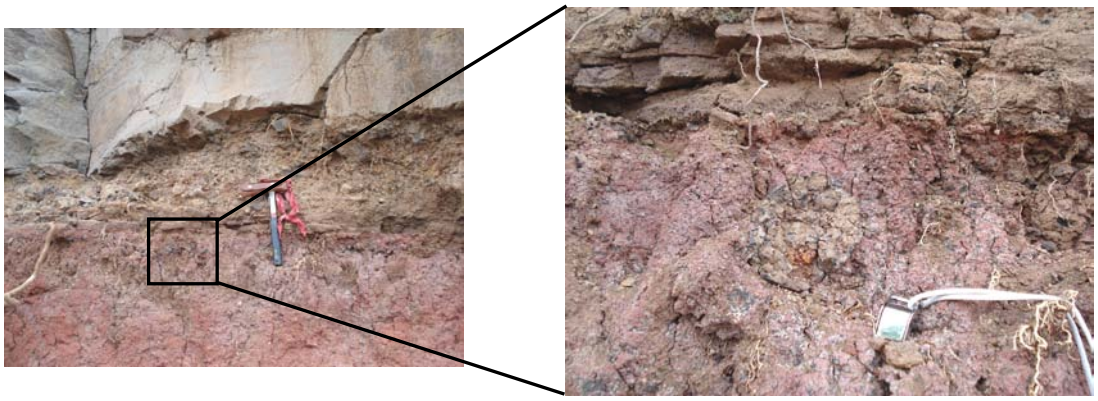

Figure 3.13 – Detail of the contact between Upper and Lower Pico da Antónia Formation with an extremely altered pillow lava within the paleosoil.

Ponta Pinha

On the southeastern Santiago coast, near Ponta Pinha, there is an impressive outcrop where the contact between submarine and subaerial lavas of Pico da Antónia Formation is marked by the presence of a conglomeratic level (Fig. 3.14 and 3.15).

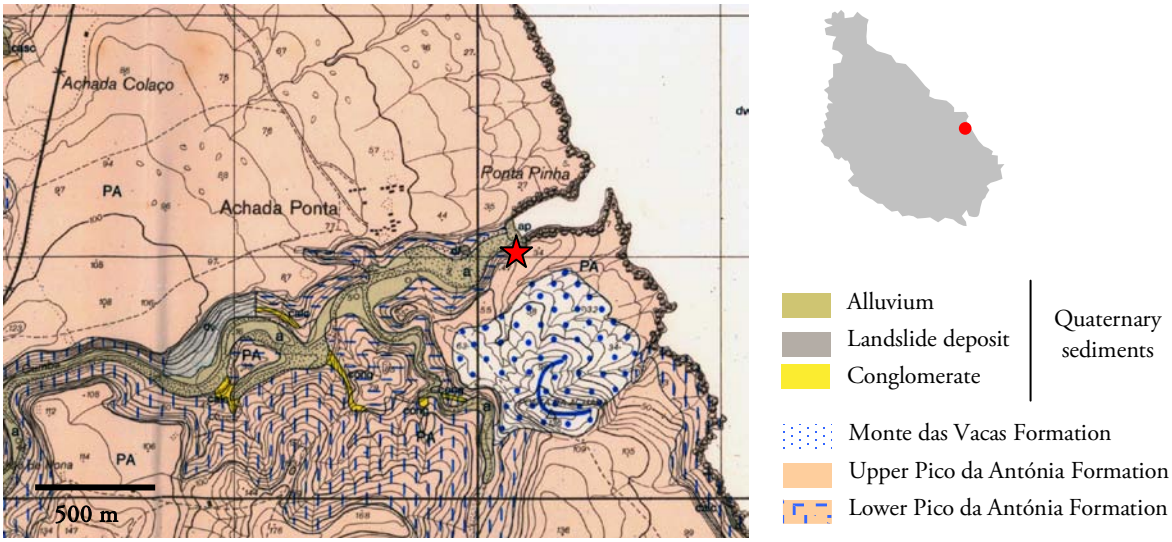

Figure 3.14 – Location of Ponta Pinha outcrop (section of sheet 55; Serralheiro, 1976)

In this area the Lower Pico da Antónia Formation is characterized by the occurrence of thick hyalocastite layers and pillow lavas (Fig 3.15C). The conglomeratic level was deposited above this unit suggesting quiescence in volcanism and change in environmental conditions.

The sedimentary horizon is ≈ 1.5 m thick with several layers of flat rounded pebbles showing normal gradation. This feature might have been caused by fluvial processes with mass flow transport, the bigger clasts being transported when the stream velocity was highest and with decreasing energy the smaller pebbles and coarser sand were deposited (Fig. 3.15B). The presence of various layers within this horizon suggests that these events were episodic and repetitive. Thick, massive subaerial basaltic lava flows belonging to the Upper Pico da Antónia Formation covered the entire sedimentary unit (Fig. 3.15A).

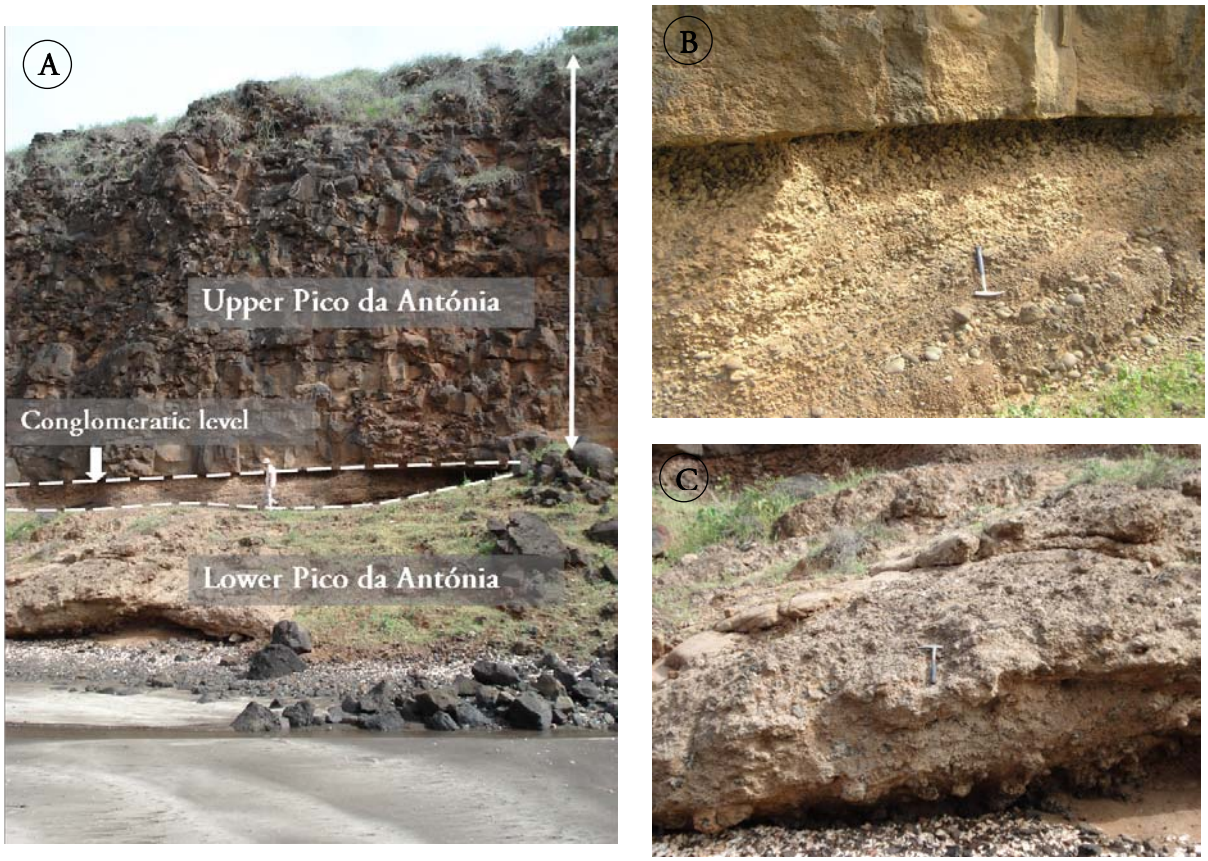

Figure 3.15 – Ponta Pinha outcrop: A) Sequence of submarine and subaerial lavas interlaid by a conglomeratic level; B) Detail of the contact between the conglomeratic level and Upper Pico da Antónia Formation (photo by João Mata); C) Hyaloclastites and pillow lavas of Lower Pico da Antónia Formation.

Cidade Velha – S. João Baptista

Near the village of S. João Baptista an erosional surface cuts the submarine deposits belonging to the Lower Pico da Antónia Formation as well as the dykes that cross them (Fig. 3.16 and 3.17). This unconformity is covered by layers of sedimentary material with variable thickness, testifying once more the existence of a considerable time interval between Lower and Upper Pico da Antónia.

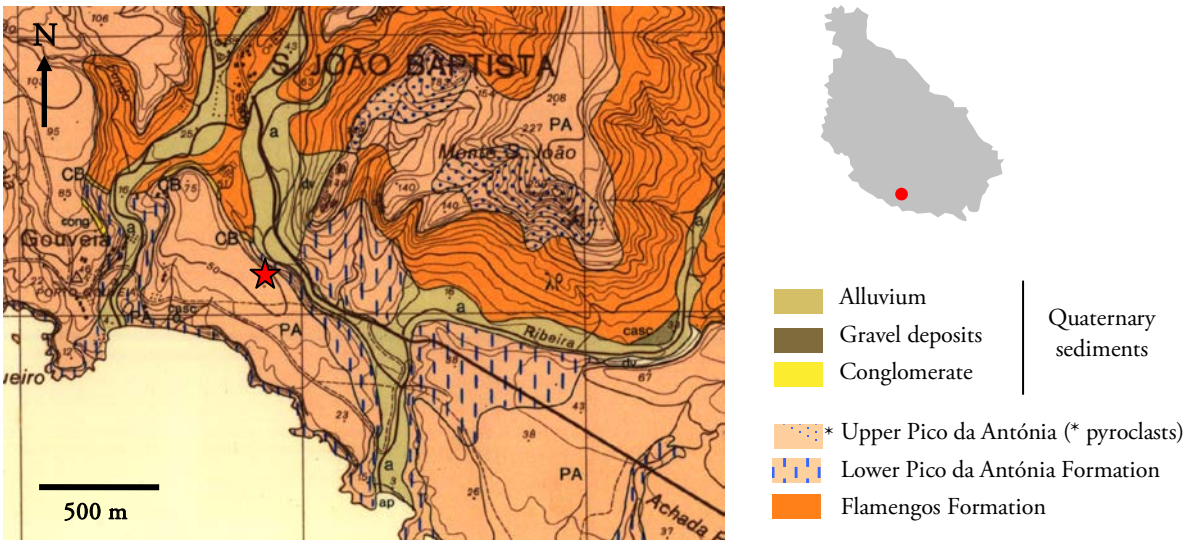

Figure 3.16 – Location of Cidade Velha – João Baptista outcrop (section of sheet 57; Serralheiro, 1976)

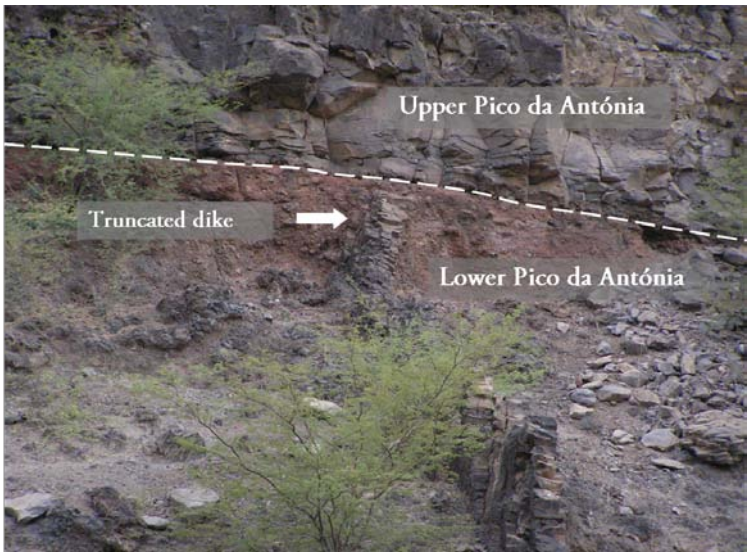

Figure 3.17 – Contact between Upper and Lower Pico da Antónia Formation marked by an erosional surface that cut the dykes belonging to the submarine unit (photo by José Madeira).

Baía de São Francisco

On the northern area of São Francisco bay, a thick layer of hyaloclastites with pillow fragments and submarine lava sequences is covered by a small deposit of calcarenite (≈ 20 cm), which is then covered by subaerial lavas of the Upper Pico da Antónia Formation (Fig. 3.18 and 3.19). Even though the sedimentary level is thin the conclusion of a temporal hiatus is still valid.

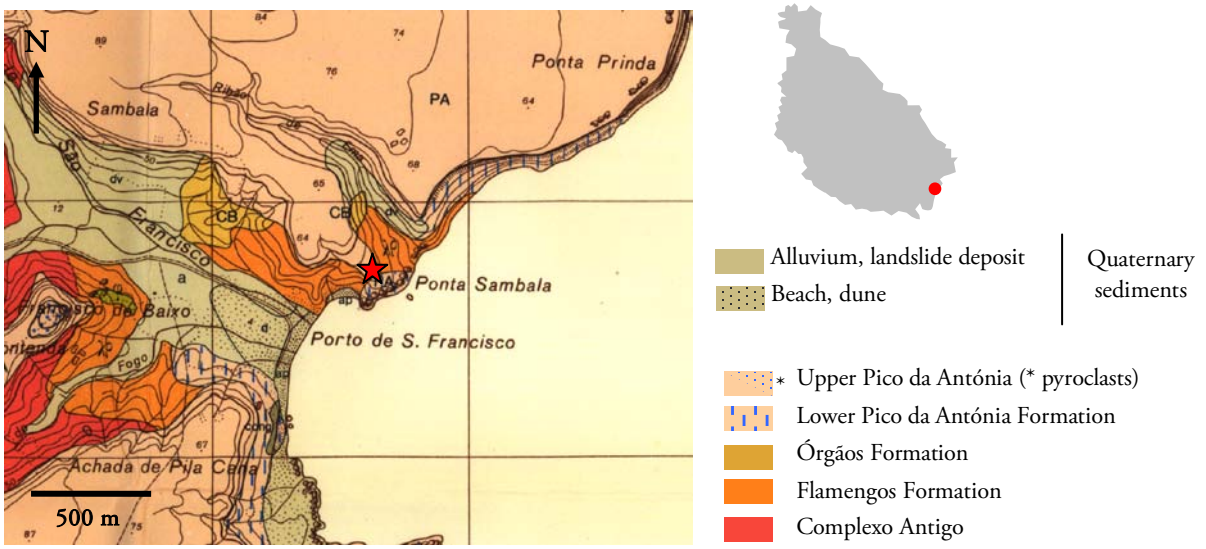

Figure 3.18 – Location of Cidade Velha – João Baptista outcrop (section of sheet 59; Serralheiro, 1976)

Figure 3.19 – A) São Francisco outcrop of the contact between Lower and Upper Pico da Antónia ; B) Detail of the calcarenite level between the subaerial and submarine lavas.

B – Phonolite and trachyte

The most differentiated deposits of the Pico da Antónia Formation correspond to outcrops of phonolite and trachyte in domes, vents, dykes, breccias, pyroclasts and lavas flows (Fig. 3.10F). This subunit is well preserved with the most significant outcrops being located in

the west coast to the north of Ribeira da Barca (Serralheiro, 1976; Alves et al., 1979). Considering that the Pico da Antónia Formation is mainly basaltic (s.l.) these events are considered episodic and restricted in their spatial expression.

C – Breccia-Tuff

On the northeastern and northwestern slopes of the Pico da Antónia mountain there are extremely localized deposits of breccias and interlaid tuff layers of yellowish to reddish colour. Breccia clasts are basaltic and phonolitic being cemented by basaltic tuff and scoria. This subunit is the result of episodic but repetitive explosive volcanic activity (Serralheiro, 1976; Alves et al., 1979).

D/E – Lava flows and interlaid pyroclasts/ Pyroclasts and interlaid lava flows

These subunits correspond to the last volcanic events of the Pico da Antónia Formation. The deposits consist mainly of lavas and pyroclastic material extruded after the phonolite-trachyte and breccia-tuff subunits, and so are more obvious were those units outcrop (Serralheiro, 1976).

Holm et al. (2008) dated thirteen lavas of the Pico da Antónia Formation, twelve of which gave an eruption period between 2.9 and 2.3 Ma. One sample of São Gonçalo area (southwestern Santiago coast) gave an age of 3.3 Ma, however the authors interpreted this as an early and less significant phase of the Pico da Antónia Formation.

The field evidences described earlier, between Lower and Upper Pico da Antónia Formation, are also supported by Holm et al. (2008) dating, which reported older ages, for the submarine lavas (2.9–2.8 Ma) than for the main subaerial event (2.6–2.3 Ma).

On the basis of their chemical characteristics and consistent field relations, the subaerial lavas will be referred from now on as Upper Pico da Antónia Formation (UPA) and the submarine lavas as the Lower Pico da Antónia Formation (LPA).

3.2.5. Assomada Formation

The Assomada Formation outcrops in the central area of Santiago Island displaying a trapeze-like configuration with 10 km across (Fig. 3.4). The volcanic products occur between Ribeira da Barca and Santa Catarina, reaching the west coast. Amaral (1964, in Serralheiro, 1976) suggested that the restricted configuration of this formation can be due to the presence of a fault line on its eastern limit, which could be responsible for the rise of the Serra da Malagueta block.

This unit is composed of subaerial lavas and pyroclastic material, with some interlaid tuff layers, occurring in angular discordance over the Pico da Antónia Formation (Fig. 3.20). The Assomada Formation deposits show a very regular disposition in thickness and length in most of the lava piles (Serralheiro, 1976).

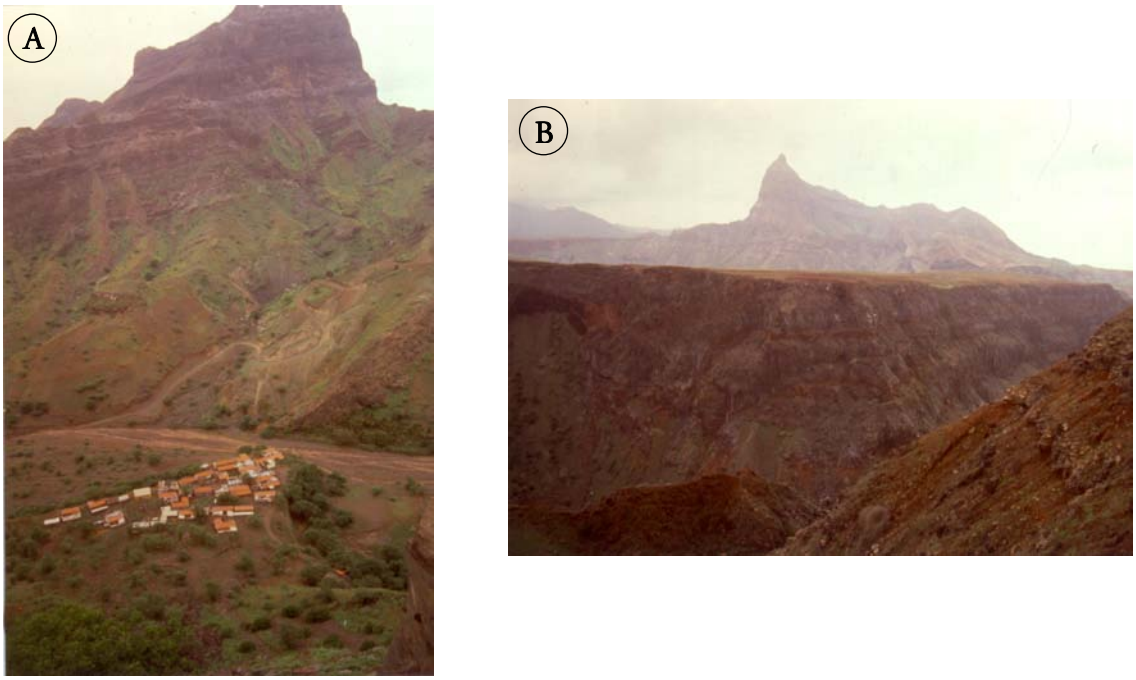

Figure 3.20 – A) Thick piles of lava flows and pyroclasts of Assomada Formation (on the road to Porto Rincão); B) Outcrop of Assomada Formation deposits.

3.2.6. Monte das Vacas Formation

The last volcanic event of Santiago Island is represented by the Monte das Vacas Formation trough 50 scoria cones widely dispersed over the island (Fig. 3.4). These cones are

characterized by slopes between 20º and 25º and heights up to 250 m being composed of pyroclastic products (bombs, blocks, lapilli and ash) and small lava flows (Fig. 3.21)(Alves et al, 1979).

The volcanic edifices are weathered which is attested by their small slope, the destruction of the crater and removal of small size particles, of unconsolidated material, leaving behind only the largest product (bombs and blocks). These products also exhibit a distinctive reddish colour typical of subaerial alteration (Serralheiro, 1976).

Figure 3.21 –A) Monte Braga, scoria cone from Monte das Vacas Formation (Achada Bilim); B) Monte das Vacas, scoria cone from Monte das Vacas Formation (Praia area).

Holm et al. (2008) suggest that even thought the Assomada and Monte das Vacas Formations comprise different volcanic facies they were erupted during one episode. From the three samples collected and analyzed, one does not give a reliable age determination (sample 1144965) and the one collected as belonging to Monte das Vacas Formation gave and older age than the one from Assomada Formation (1.13 and 0.74, respectively), which according to Serralheiro's (1976) stratigraphy is incorrect. Since only two samples were dated, one from each formation, the results obtained by Holm et al. (2008) are useful only to loosely constrain the time interval of the youngest formations. More data is necessary to better characterize each one of these formations and if necessary revise the established stratigraphy.

3.3. Geological evolution of Santiago Island: a synopsis

The growth, emergence and build-up of the Cape Verde Islands in general and of Santiago in particular, are still not completely understood. As for some of the Canary Islands, Santiago growth and evolution seem to be slow and dependent on the construction and destruction of successive large edifices (Ancochea et al., 2008).

The most ancient unit in Santiago corresponds to what was interpreted as a fragment of exposed Mesozoic oceanic crust with 130 Ma (Gerlach et al., 1988; Davies et al., 1989; Mendes and Silva, 2001). The emplacement mechanism of this fragment is still not known as is the time of the emplacement, synchronous or post-Complexo Antigo. However an upward movement of at least 4000 m is necessary to explain its present location at 220 m a.p.sl. (Ramalho et al. 2010a).

The hypothesis presented by Gutiérrez et al. (2006) to explain the presence of Mesozoic oceanic crust in Fuerteventura (Canary Islands) can also be considered as a probable explanation for Santiago's occurrence. These authors suggest a dynamic alternative to the classic model of static seamount growth where a listric fault was reactivated due to uplift /doming caused by the impingement of a mantle plume on the base of the lithosphere with the consequent exposure of Mesozoic oceanic basement. In this model the tectonic evolution of the oceanic floor constrains the growth and emergence of the island.

As mentioned in Chapter 2 several fracture zones have been identified near the Cape Verde Islands (Bebiano, 1932; Assunção, 1968; Williams et al., 1990; Torres, 1998) and in the surrounding area (Skolotnev et al., 2006; 2007, 2009) suggesting a tectonic active setting, not normally associated with Atlantic-type oceans margins. The published structural information of Santiago Island is very scarce making it impossible to extrapolate further on the emplacement of the exposed oceanic fragment.

The Complexo Antigo stands as the basal complex of the island and is represented by a very dense basaltic dyke complex, occasional lava flows, intrusive granular rocks and carbonatites. This unit is thought to represent an early submarine growth stage of the island but also the subvolcanic root (plutons and dykes) of the ensuing subaerial episodes (see

Ancochea et al., 1996 for Canary archipelago examples). For Sal Island Torres et al. (2002) affirmed that some of the intrusive rocks previously attributed to the Complexo Antigo seem to be younger and may correspond to shallow magmatic chambers of posterior volcanic events.

As stated before it is very difficult to establish a stratigraphic relation between the several subunits that compose the Complexo Antigo which associated with the lack of geochronological data unable the reconstruction of the sequence of events that contributed to the growth of the seamount/island. The oldest sample reported from the Complexo Antigo is a theralite with 10 Ma (Bernard-Griffiths et al., 1975). However Abranches et al. (1990) trough paleogmagnetic data speculates about a pre-Paleogene age for some of the rocks of the basal complex.

Holm et al. (2008) based on this putative pre-Paleogene age data suggests that most of the Complexo Antigo as well as the MORB-like volcanic do not belong to the construction phase of the island but instead represent raised seafloor. This hypothesis is somewhat doubtful because even though, Mesozoic units only outcrop in two of the ten islands, the Complexo Antigo seems to be very similar in all of them, which could lead to the conclusion that all of the islands present some raised seafloor on their structure. This suggestion should be corroborated with more stratigraphic and geochronological data analysis as well as petrographic/geochemical studies in order to better constrain the meaning and age of the Complexo Antigo.

A period of intense weathering and volcanic quiescence resulted in the degradation of the Complexo Antigo with the consequent deposition of extensive submarine sedimentary deposits. At about 4.6 Ma there is a volcanic rejuvenation with the extrusion of thick piles of pillow lavas and hyaloclastites of basaltic composition (Flamengos Formation). The occurrence of pillow lavas of the Flamengos Formation at 450 m a.p.s.l. implies a significant uplift after its emplacement in the order of 420-450m (one of the highest reported for the archipelago), since the eustatic curve at 4.0 - 5.0 Ma exhibit a sea level close to the actual one (with a maximum of 21 m) (Ramalho et al., 2010c). These submarine deposits that comprise the first well defined volcanic formation in Santiago Island can be interpreted as belonging to the growth stage of the seamount.

Another extensive erosional event follows and is testified by the deposition of the Orgãos Formation, which comprises terrestrial, estuarine and marine sediments and is thought to have endured for 1.3 Ma (Holm et al., 2008).

Between 3.3 and 2.2 Ma the main building stage of the island (shield stage) and subsequent emergence takes place with the extrusion of the Pico da Antónia Formation. The early Pico da Antónia Formation deposits are exclusively submarine and are almost ubiquitous along Santiago's coast but also inland reaching 270 m a.p.sl. (Ramalho et al., 2010c). In accordance with early Pleistocene sea level oscillations these occurrences indicate an uplift of 100-200 m of Santiago Island after this submarine volcanic phase (Holm et al., 2008; Ramalho et al., 2010c).

As already mentioned this submarine occurrence referred as Lower Pico da Antónia Formation appears to be distinct from the more dominant subaerial lava sequences of the Upper Pico da Antónia Formation, not only from geochemical evidences (see Chapter 4) but also from field evidence (see section 3.2.4). The transition from submarine to subaerial volcanism appears to have occurred between 2.8 - 2.6 Ma, with the submarine deposits probably reflecting intermediate to shallow water depths extrusions.

The Upper Pico da Antónia Formation is mainly characterized by extensive subaerial basaltic lava flows and associated pyroclastic deposits however several occurrences of phonolites and trachytes have also been described representing a less expressive event of this formation. Several sedimentary deposits occur interlaid with volcanic extrusions, reflecting intermittent volcanic activity in time and space.

After another volcanic dormancy period of 1 Ma and associated erosional events, the restricted Assomada Formation is extruded in the central area of Santiago Island followed by or contemporaneous with Monte das Vacas Formation with widely dispersed scoria cones around the island. This last volcanic event occurred between 0.7 and 1.1 Ma.

Subsequent erosional and sedimentary events developed in the Quaternary leading to the formation of alluvium, dunes, beach and land slide deposits amongst others.

CHAPTER 4

GEOCHEMISTRY OF ALKALINE LAVAS

Ponta Pinha (Santiago – Cape Verde)
Thick lava piles from the upper Pico da Antónia formation, which is considered representative of the main eruptive phase in Santiago Island.

4.1. Introduction

Alkaline magmas from oceanic islands can be regarded as preferred candidates for the study of mantle evolution since, due to their isolated position, they carry the smallest risk of being contaminated by continental crust and be unaffected by orogenic, metamorphic and tectonic processes (Greenough et al., 2005).

Geochemical tracers, such as concentration ratios of incompatible elements and isotopic ratios, are the most widely used to identify conditions and processes operating during magma generation and evolution such as: source composition and heterogeneity, metasomatic events, degree and mechanism of melting, degree of magma fractionation, mixing events, and contamination processes amongst many other (Hofmann, 1997; Hofmann et al., 2003). However, even though isotopic signatures and trace element abundances are the main tools used in mantle studies, it is necessary to keep in mind that major elements control the physical properties of the mantle, hence being the most relevant guides for geodynamic and seismic models (Dasgupta et al., 2010). Consequently to study the evolution of the mantle it is necessary to take into account its composition concerning major elements, trace elements and isotopic ratios.

From the 70 alkaline lava samples collected at Santiago Island (see Chapter 3), 56 were selected for major and trace analysis and from this sub-group, 18 for isotopic ratios (Sr-Nd-Hf-Pb) determination. The selection was based on: 1) alteration, seen on hand specimen and thin section, 2) absence of filled vesicles and fractures, 3) the amount of phenocrysts (ideally less than 15%, in order to try to avoid the magmatic liquid modification induced by crystal accumulation) and 4) the necessity to choose the most representative ones from each Formation and station.

4.2. Whole rock major and trace element chemistry

4.2.1. Post-magmatic alteration

In order to ensure that the interpretations based on geochemical data are trustworthy, the presence of significant post-magmatic alteration must be ruled out.

Subaerial and submarine alteration of lavas can lead to considerable mobility of major and trace elements. Even thought attention has been paid in sample selection regarding this subject, it is important to assess the possible weathering effects in the data presented. Elements most susceptible to mobilization seem to be alkali (Na and K) and LILE (Rb, Ba, Cs, Sr - Large Ion Lithophile Elements) which, due to their low ionic potential (charge/radius ratio), are preferentially remobilized in aqueous solution (e.g. White, 2013). Common element ratios used to evaluate the alteration degree are K_2O/P_2O_5, K_2O/Rb and Ba/Rb (West et al., 1992)[1]. However some of these ratios in basic/ultrabasic magmas can also be significantly constrained by residual mantle mineralogy (see 4.4.3.2. for discussion). As a consequence it was decided not to use the criteria defined by West et al. (1992) in this study. As an alternative the most mobile elements were projected as a function of LOI (Loss On Ignition), which stands as a rough alteration index, in order to evaluate alteration effects (Fig. 4.1). The absence of any trends and the concomitant lack of alteration minerals in most of the samples analyzed, allows the interpretation that the data set is not biased by weathering.

4.2.2. Sample classification and characterization

Due to fine granularity and very common glass occurrence, in most samples, mode calculation was not possible and so a chemical classification was chosen for the Santiago lavas, according to IUGS (International Union of Geological Sciences) principles (Le Bas and Streckeisen, 1991). As recommended, major chemical analyses were recalculated anhydrous to 100%, using the SINCLAS (Standard Igneous Norm and Volcanic Rock Classification

[1] The alteration criteria used by West et al. (1992) include the negative correlation between K_2O/P_2O_5 and Ba/Rb at $K_2O/P_2O_5<1$, probably due to alkali loss. Also the positive correlation between K_2O/Rb and Ba/Rb and the negative correlation between Rb/Cs and Ba/Rb seems to suggest that Rb was more mobile than K and Cs.

System) software which was also used to calculate the Fe_2O_3/FeO ratio[2] and CIPW norm (Verma et al., 2002).

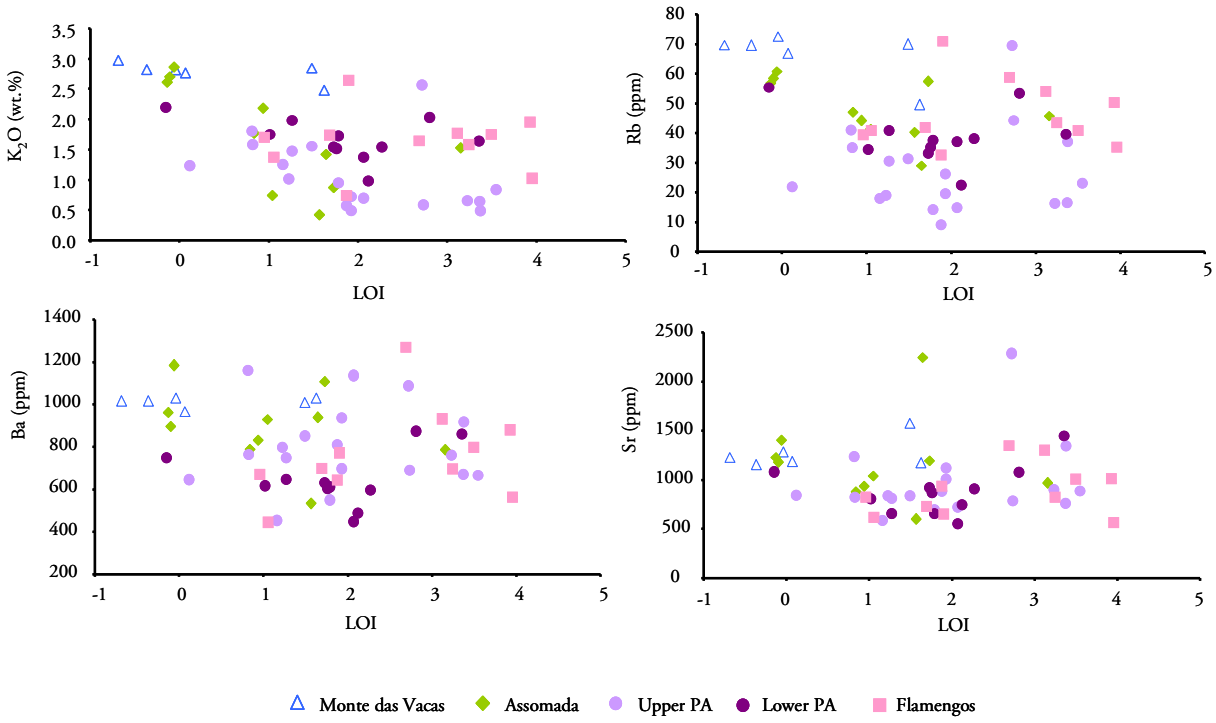

Figure 4.1 – Detecting alteration effects using LOI against mobile elements in Santiago lavas. Upper and Lower PA stands for Upper Pico da Antónia and Lower Pico da Antónia, respectively.

The studied Santiago lavas are classified as ultrabasic to basic ($38 < SiO_2 < 47$ wt. %) alkaline rocks. The samples project in the field of basanite/tephrite (U_1) with some small scatter to foidite (F) and picro-basalt (Pc) in the total-alkalis versus silica diagram (TAS) (Le Maitre et al., 2002) (Fig. 4.2). Due to the objective of the present study the sampling procedure at Santiago Island, was focused on the basaltic domain *s.l.*, and so more evolved rocks like the phonolites described by Alves et al. (1979) as occurring on the NW of the island (see also Chapter 3) were not collected. Consequently it is necessary to considerer that the range of Santiago silicate volcanic rocks is wider, than showed by the TAS diagram of Figure 4.2. Such range extending up to the phonolite field is similar to the observed in other islands of the archipelago (e.g. Santo Antão, Holm et al., 2006; Brava, Mourão et al. 2010; Boavista, Dyrh

[2] From the options available on the SINCLAS software, for Fe_2O_3/FeO ratio calculation, the recommendation of Middlemost (1989) was chosen.

and Holm, 2010; see also Bebiano, 1932). However the volume of outcropping intermediate rocks is clearly less significant than in the mentioned islands.

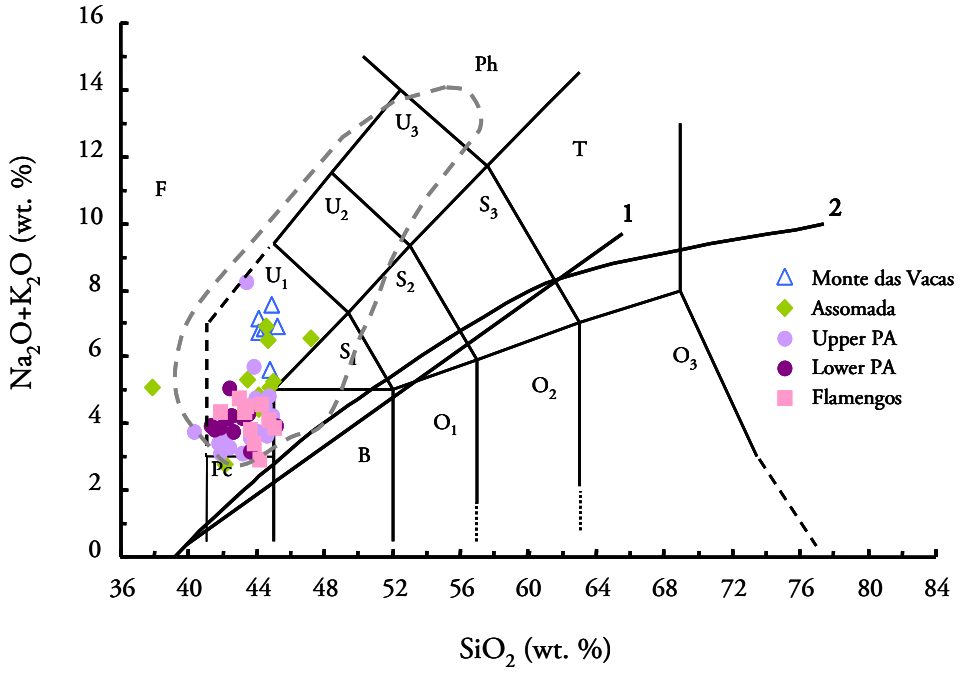

Figure 4.2 – Chemical classification and nomenclature of the studied silicate Santiago lavas using the total alkalis-silica (TAS) diagram. Fields by Le Bas et al. (1986): F- Foidite; U_1- Tephrite/Basanite; U_2- Phono-tephrite; U_3- Tephri-phonolite; Ph- Phonolite; Pc- Picrobasalt; S_1- Trachybasalt; S_2- Basaltic trachy-andesite; S_3- Trachy-andesite; T- Trachyte; B- Basalt; O_1- Basalt andesite; O_2- Andesite; O_3- Dacite. Subdivision of the alkaline and subalkaline field is from 1) MacDonald and Katsura (1964) and 2) Irvine and Baragar (1971). In order to give the reader a better idea of the chemical/lithological variability of the Santiago silicate rocks the field of the rocks studied by Alves et al. (1979) is also shown (closed dotted line).

Projection in the tetrahedron of Yoder and Tilley (1962) confirms the silica undersaturated character for Santiago lavas. Indeed the representation in the Ne-Di-Ol diagram of Thompson (1984), which stands as an expanded version of the Yoder-Tilley tetrahedron, corroborates the abundance of normative olivine and nepheline (Fig. 4.3A). Significant differences in Na_2O/K_2O and CIPW normative olivine/diopside ratios between lavas from different formations suggest time-dependent variations in the major element compositions of Santiago magmas. For example, Flamengos Formation lavas (4.6 Ma; Holm et al., 2008) are characterized by lower average normative olivine/diopside (0.45) and Na_2O/K_2O ratios (2.9 -4.5) than lavas from the younger Assomada Formation (0.7 – 1.1 Ma), of similar degree of magmatic evolution (average olivine/diopside ratio= 0.74; Na_2O/K_2O up to 6.9).

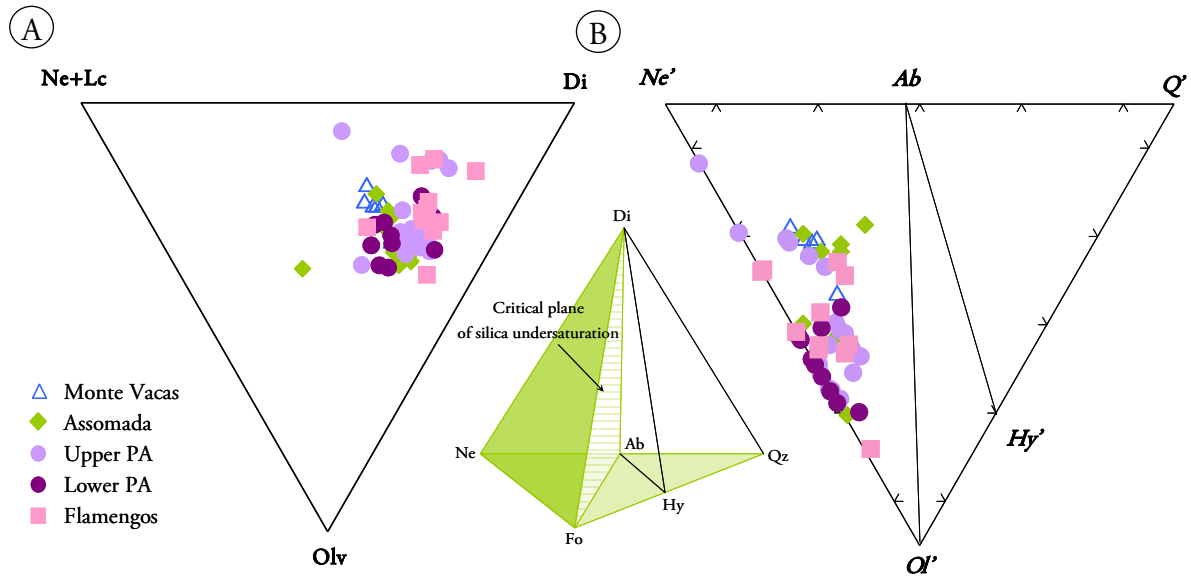

Figure 4.3 – Santiago lavas projected in the Yoder-Tilley diagram (Yoder and Tilley, 1962). A) Expanded version in the triangle Ne-Di-Ol from Thompson (1984); B) Base of the tetrahedron, where samples are projected from Di onto the base Ne'-Q'-Ol' (Olv'= Olv+[0.714 – (Fe/(Fe+Mg)) x 0.067] x Hy, Ne'= Ne + 0.542 x Ab and Q' = Q + 0.4 x Ab + 0.25 x Hy; according to Best and Christiansen, 2001).

The base of the tetrahedron, with the apices represented by adjusted normative minerals, gives a global view of the Santiago lavas within the whole range of the Yoder-Tilley diagram (Fig. 4.3B).

The inability of TAS diagram to discriminate between alkaline low-silica rock types is due to the incapacity of distinguish the presence of plagioclase and nepheline, using only silica and alkalis, and so an overlap between nephelinitic and basanitic rocks might occur in the U_1 field (Le Bas and Streickeisen, 1991). To differentiate between these rocks types, the diagram proposed by Le Bas (1989), based on normative proportion of Ne and Ab is used (Fig. 4.4). Only one sample is identified as nephelinite *s.s.* (rock containing nepheline as a major constituent, both as phenocryts and in the matrix), the rest of the samples being subdivided in melanephelinites (52%) and basanites (46%). Melanephelinites can be further subdivided in olivine or pyroxene melanephelinites, according the most abundant mineral and chemically by the amount of MgO (> and < 10 wt. %, respectively) and alkalis [< 8 wt. % (Na_2O+K_2O)] (Le Bas, 1989).

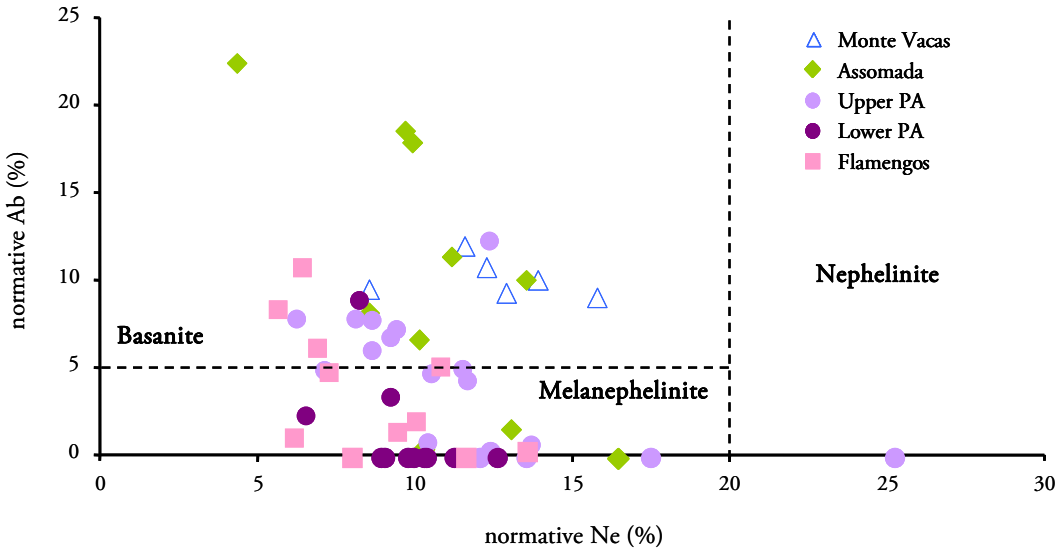

Figure 4.4 – Discriminating diagram for basanitic and nephelinitic rocks using normative minerals (Le Bas, 1989).

A couple of samples stand out due the presence of larnite (dicalcium silicate) as a normative mineral. According to recommendations of the IUGS (Woolley et al., 1996) ST-18 and ST-48 are classified as melilitite and melilite nephelinite, respectively. Both samples project in the foid field of TAS, have $K_2O<Na_2O$ and normative larnite (ST-18 > 10% larnite, classified as melilitite; ST-48 < 10% larnite, classified as melilite nephelinite) (Woolley et al., 1996).

As stated above, Santiago lavas are alkalic with Na_2O+K_2O between 3 and 8 wt. % existing a predominance of sodic lavas (Na_2O/ K_2O up to 7.4) in UPA formation and potassic lavas in Monte das Vacas, LPA and Flamengos formations (Na_2O/K_2O as low as 0.62)(Fig. 4.5). Rocks from the Assomada Formation are equitatively divided by potassic and sodic series fields.

4.2.2.1 Primary and primitive magmas

The main objective of the present study is to characterize the mantle source composition from which Santiago Island originated from. In order to accomplish this purpose it is necessary to use samples which are thought to represent primary magmas, i.e. those presenting the composition generated by partial melting of a mantle source and not affected by any subsequent major modification such as crystal fractionation, accumulation or contamination (Clague and Frey, 1982).

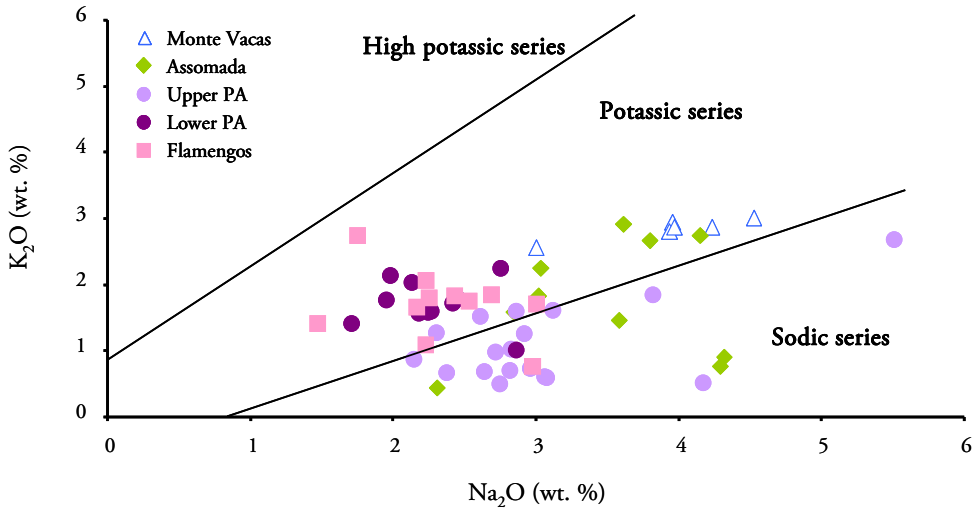

Figure 4.5 – K_2O vs. Na_2O diagram showing the alkalic magmatic series subdivisions (after Middlemost, 1975).

There is not a consensus about the geochemical criteria used for the identification of primary magmas. Assuming that the source is a peridotite dominated by magnesium-rich olivine (Fo_{90}) and that the partition coefficient of Fe^{2+}/Mg, between olivine and the melt in equilibrium, is 0.3±0.03 (Roeder and Emslie, 1970; Beattie, 1993), a Mg number (Mg#)[3] of ≈68.5 is expected for primary magmas (e.g. Frey et al., 1978; Best and Christiansen, 2001).

Considering, in addition, that Mg# in melts is a parameter significantly affected by the fractionation of even small amounts of olivine and pyroxene, it can be concluded that it can be used as a good fingerprint of a primary melt.

Under equilibrium conditions the chemical composition of olivine phenocrysts will also reflect the composition of the magma from which they crystallize. For Santiago lavas the highest Fo content in olivine phenocryts cores is 88 %, which is equivalent to its Mg# ($Mg\#_{olv}$). From this value is possible to extract the (Fe^{2+}/Mg) ratio in olivine (0.136) from Equation (1).

$$\left(Fe^{2+}/Mg\right) = (100 - Mg\#)/Mg\# \qquad (1)$$

[3] Mg# = $[Mg^{2+}/(Fe^{2+} + Mg^{2+})]$ x 100

Assuming the above considered value of $K_D(Fe^{2+}/Mg)$[4] between olivine and melt, as well as equation (2)

$$(Fe^{2+}/Mg)_{melt} = (Fe^{2+}/Mg)_{olv}/0.3 \pm 0.03 \quad (2)$$

the (Fe^{2+}/Mg) in the melt is between 0.41 and 0.50 .

Taking this in consideration and Equation (3)

$$Mg\#_{melt} = 100.\frac{1}{1+(Fe^{2+}/Mg)_{melt}} \quad (3)$$

the Mg# value of the parental melt from which the most forsteritic Santiago olivines crystallized varies between 66 and 71.

By analyzing the Fo content of olivine in Santiago lherzolite xenoliths (Fig. 4.6), which can be considered as a Santiago mantle source proxy, it can be seen that they range between 87 and 92, as expected for off-craton mantle xenoliths (Pearson et al., 2003), suggesting equilibration with melts with Mg# of 67 to 77 at mantle conditions. So the "boundary line" for primary lavas in Santiago is set at Mg# 68.5.

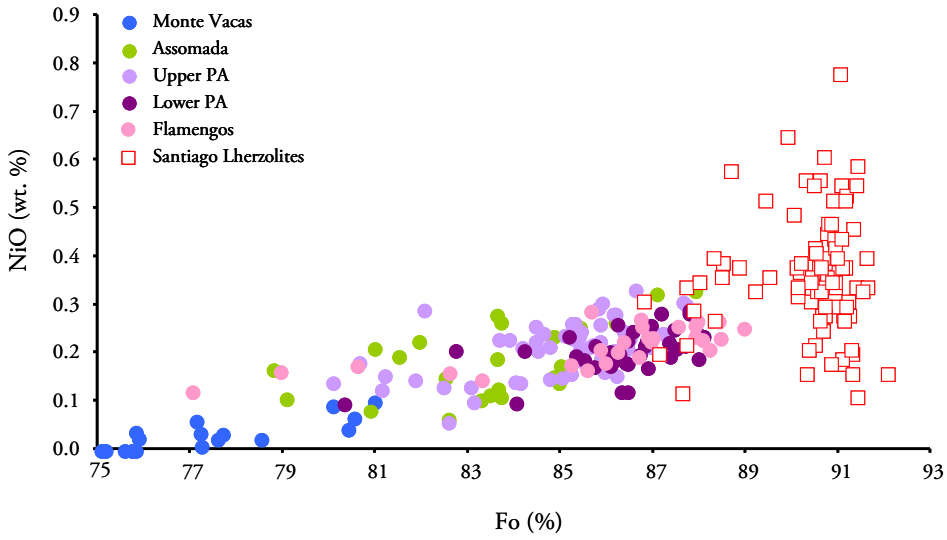

Figure 4.6 – Forsteritic content of olivine from Santiago lavas and included lherzolitic xenoliths (data from Mendes, 1995) against NiO content (lava data represent exclusively olivine core analyses).

[4] $K_D(Fe/Mg) = [(Fe/Mg)_{olv}]/[(Fe/Mg)_{melt}]$

In Santiago these primary magmas are also characterized by MgO >12 wt. %, Ni > 250 ppm and Cr > 480 ppm. These samples are used in normalized REE and incompatible elements diagrams (e.g. Fig. 4.9 and 4.10) constructed in order to describe the pristine characteristics of the magmas generated in the mantle beneath Santiago Island.

However modelling of petrogenetic processes implies the use of a larger set of samples, and when it was necessary, the above mentioned criteria was broaden in order to include all the samples with Mg# down to 59. These samples are also characterized by MgO > 8.5 wt. %, Ni > 130 ppm and Cr > 250 ppm.

Considering that fractional crystallization is described by the Rayleigh equation (Neuman et al., 1954):

$$\left(\frac{Fe}{Mg}\right)_l = \left(\frac{Fe}{Mg}\right)_0 \times F^{(D_{Fe}-D_{Mg})} \qquad (4)$$

where,

$\left(\frac{Fe}{Mg}\right)_l$ = Fe/Mg concentration in residual liquid

$\left(\frac{Fe}{Mg}\right)_0$ = Fe/Mg initial concentration

F= Fraction of residual liquid

$D_{Fe;\,Mg}$=Fe-Mg partition coefficients

and 0.3±0.03 as the value for the partition coefficient between olivine and liquid (e.g. Roeder and Emslie, 1970; Beattie, 1993), the above referred composition for the primitive magmas imply the previous fractionation of only ≈ 7% of the initial liquid.

It is important to note that samples with high MgO, Cr and Ni, like those assigned to primary and primitive magma contents, can also be associated with olivine and pyroxene accumulation, an hypothesis that must be addressed when choosing a data set for the above mentioned purposes. Even though the accumulation of olivine does not significantly modify trace element ratios due to low and similar partition coefficients for most of the elements

(D<0.02, except for some transition elements), clinopyroxene may alter significantly the incompatible element ratios as can be deduced, for example from the following values: $D^{olv}_{La/Sm} = 0.075$ vs. $D^{cpx}_{La/Sm} = 0.184$ (Shaw, 2006).

Most of the samples are aphanitic to slightly porphyritic (typically with less than 10% phenocrysts) being considered as good representatives of magmatic liquids. However in some samples (e.g. ST-12; ST-11) the estimated volume of phenocryts can reach some 30% (Fig. 4.7). These samples will be discarded from major and trace element geochemical analysis because they do not represent magmatic liquids and so are not suited to mantle source geochemistry studies.

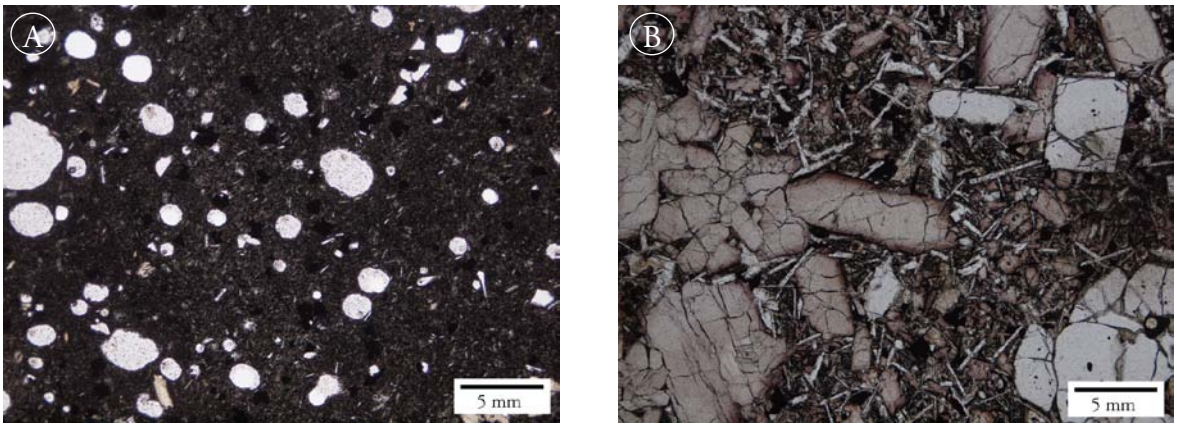

Figure 4.7 – Petrographic comparison between aphanitic (A: ST- 3) and accumulated lava (B: ST-12).

4.2.3. Major elements chemistry

Santiago lavas have MgO contents varying from 3.8 to 16 wt. %, generally showing negative correlation with SiO_2, alkalis and Al_2O_3 (whole rock compositions are given in Appendix III). Although the major element composition of Santiago formations essentially overlaps each other, there are small differences between them. The youngest formation (Monte das Vacas) shows the least variability, with a very restricted range in all major elements. These samples have the highest SiO_2 and the lowest MgO content, and distinctly higher FeO_t, Na_2O and low CaO, suggesting influence of crystal fractionation processes with consequent chemical differentiation (see section 4.4.2) (Fig. 4.8). Some of the Flamengos Formation samples seem to be characterized by a lower Na_2O content for a given MgO, compared with the other formations (Fig. 4.8).

The TiO_2 content of Cape Verde basic/ultrabasic lavas is high compared with many other OIB. The average value for primitive Cape Verde lavas (MgO > 8.5 wt.%) is 3.5 wt.% (primitive Santiago lavas range: 2.5 to 4.4 wt.%) compared with 1.0 wt.% from Iceland, 2.1 wt.% from Reunion Island and 2.5 wt.% from Pitcairn Island (reference TiO_2 value from Prytulak and Elliot, 2007). Prytulak and Elliot (2007) performed a study on an extensive OIB dataset and concluded that the high TiO_2 content reported for some ocean island lavas, like Cape Verde, cannot be derived exclusively form a peridotite source and an additional Ti-enriched component is necessary to account for the observed data (see section 4.4.3.).

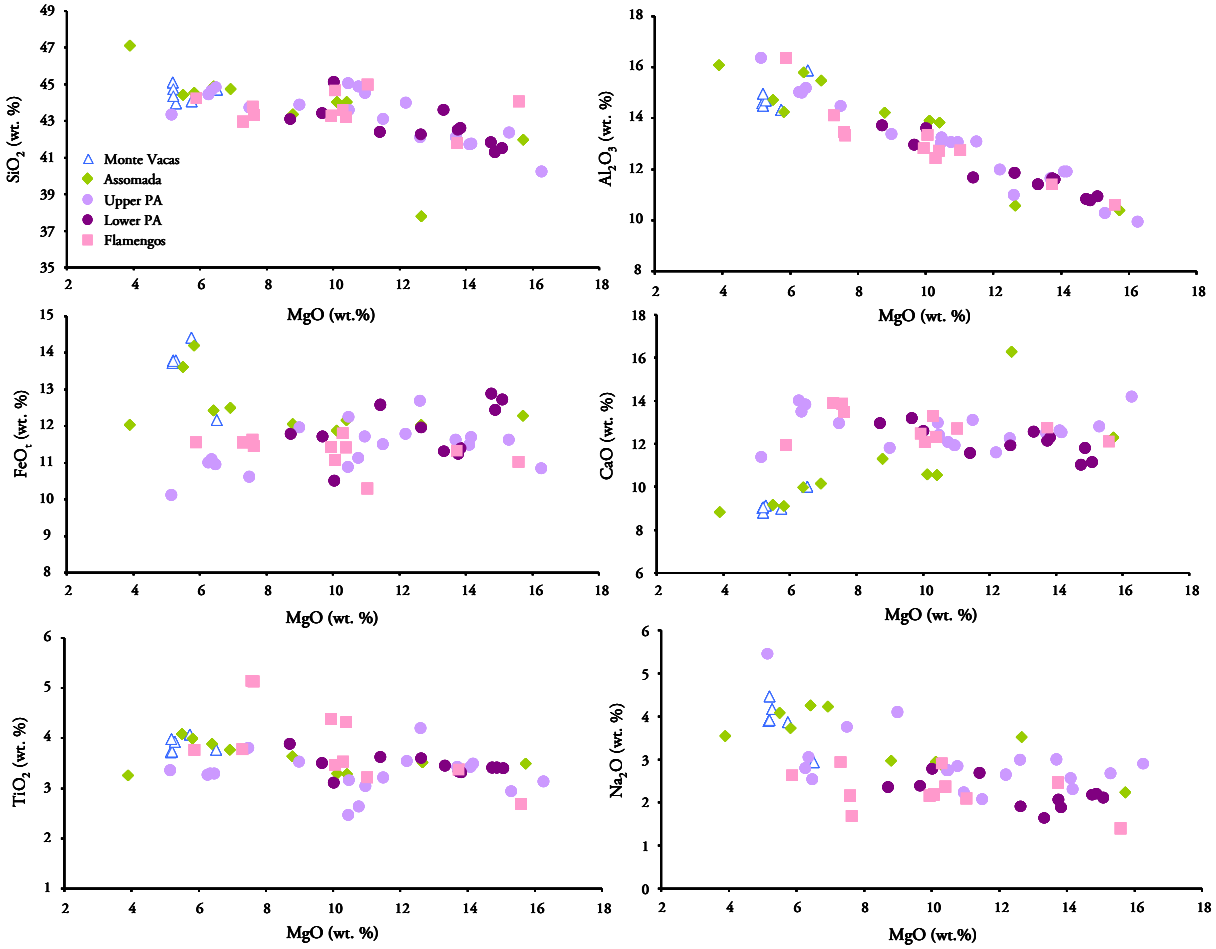

Figure 4.8 – Selected major element variation diagrams for Santiago Island lavas.

4.2.4. Trace element chemistry

Santiago primary lavas have steep trends in chondrite-normalized REE (Rare Earth Elements) patterns [$(La/Yb)_{cn}$=15 - 45] (Fig. 4.9). Abundances of La range from ≈ 145× to

540× chondrites whereas Yb and Lu range from ≈ 6.4 × to 13× chondrites, attesting the strong enrichment in LREE (Light REE) relative to MREE (Middle REE) and HREE (Heavy REE). Moreover, Santiago lavas are depleted in the heaviest REE (Yb and Lu) when compared with N-MORB (1.42 and 0.17 vs. 3.15 and 0.47; mean values of Yb and Lu, for Santiago Island and N-MORB[5] respectively), suggesting that melting events took place within the garnet stability field (see 4.4.3.2 for further development).

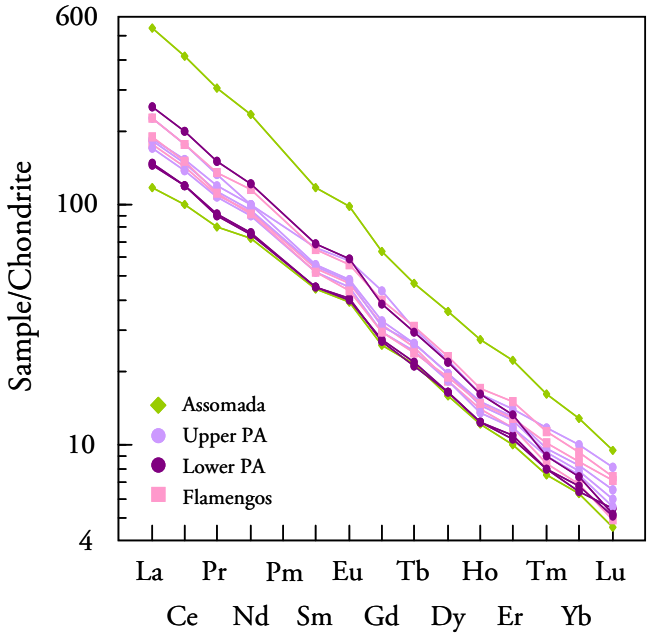

Figure 4.9 – Chondrite normalized (Palme and O´Neill, 2003) REE concentrations of representative Santiago samples.

The patterns of the formations are very similar, being sub-parallel, differing only in the concentration of REE, which may be related to either the amount of partial melting (i.e. magmas derived from small partial melting degrees are more enriched) or source heterogeneities.

The sample that stands-out as the most enriched is a melilitite of Assomada Formation which is interpreted as reflecting very low degree of partial melting at its origin, a percept endorsed by experiments of partial melting of garnet lherzolites (Gudfinnsson and Presnall, 2005).

[5] N-MORB data is from a precompiled database from GERM (Geochemical Earth Reference Model; http://earthref.org/GERM)

It is evident the presence of small positive Eu anomalies (Eu/Eu*=1.07-1.17)[6] in Santiago lavas. Europium is the only REE that can occur in both 3^+ and 2^+ oxidation state, which is oxygen activity dependent. Europium is in its divalent form at low oxygen fugacity and in trivalent state at high oxygen fugacity. A study by Philpotts (1970) show that Eu^{2+} as a similar partition coefficient to Sr, and since the normal mantle paragenesis (clinopyroxene, garnet and orthopyroxene) reject Sr relative to Eu^{3+} and olivine rejects both Eu^{3+} and Sr, the partial melting of mantle under reducing conditions will promote a positive Eu anomaly in the melt (Sun and Hanson, 1975). Another possibility arise from the fact that in reduced conditions Eu (Eu^{2+}) can substitute for Ca^{2+} in plagioclase, giving rise to small positive anomalies in REE patterns, due to potential accumulation processes (Rollinson, 1993). However, since the plotted samples are primary this latter hypothesis does not seem appropriate.

Primitive mantle normalized incompatible element patterns (Fig. 4.10) show Nb and Ta enrichment relative to Rb and K (LILE, Large Ion Lithophile Elements) and REE, which is strongly indicative of the influence of HIMU component in Santiago source (e.g. Weaver, 1991). There is an overall decrease in enrichment trough the heaviest REE and HFSE (High Field Strength Elements) of similar incompatibility similar to other alkaline OIB. A significant positive anomaly in Ba is present in all the formations as well as a small Zr and Hf negative anomalies.

The behaviour of K is noteworthy in that negative anomalies are very significant for almost all Assomada and Upper Pico da Antónia Formations samples and nearly absent in Lower Pico da Antónia and Flamengos Formation samples. The lower concentrations of K in the samples from Assomada and Upper Pico da Antónia Formations foresee the presence of a mantle mineral phase capable of retaining this element (i.e. for which this element is compatible). However the residual presence of potassic minerals is not ubiquitous in Santiago mantle source since the older formations (Lower Pico da Antónia and Flamengos Formation) show less pronounced evidence of K compatibility (Fig. 4.11).

[6] $Eu/Eu^* = Eu_n \Big/ \sqrt{(Sm_n).(Gd_n)}$; X_n stands as element X normalized for the chondritic value of Palme and O'Neill (2003).

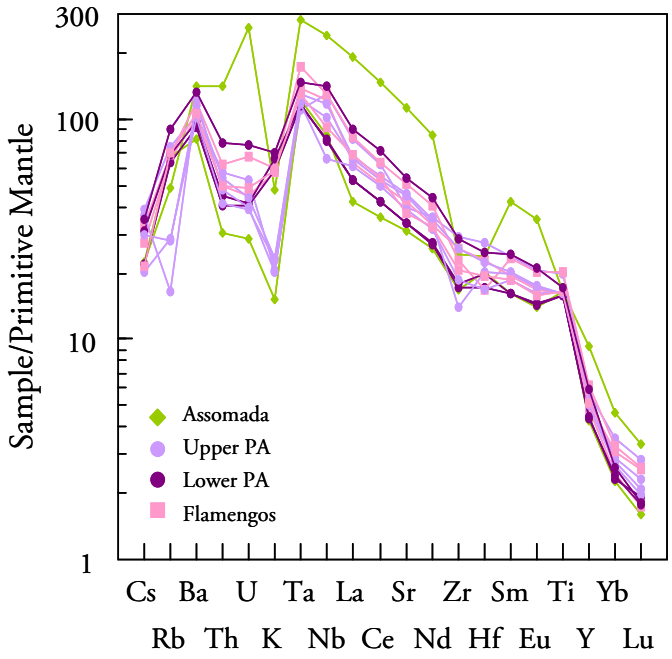

Figure 4.10 – Primitive mantle normalized (Palme and O'Neill, 2003) incompatible element concentrations of representative Santiago samples.

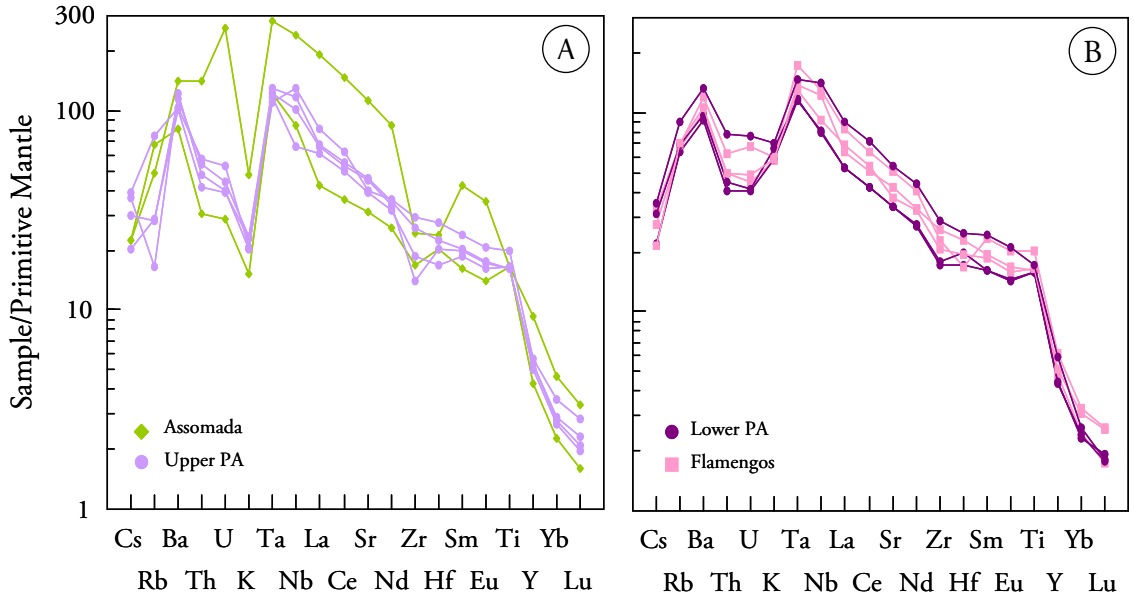

Figure 4.11 –Primitive mantle normalized (Palme and O'Neill, 2003) incompatible element concentrations of Assomada and Upper Pico da Antónia (A) and Lower Pico da Antónia and Flamengos Formations (B).

Woodhead (1996) suggested that the strong K negative anomaly common in OIB trace element diagrams is due to an artefact of the plotting procedure, since K should be placed

between Ba and Rb based on ionic radius/ charge constraints, and also, in the case of magmas with HIMU influence, the high concentration of HFSE. This is not the case in Santiago lavas because K shows a distinct behaviour among the various formations, suggesting source heterogeneities rather than data plotting artifices. The behaviour of K cannot be explained either by fractionation processes (all the plotted lavas are primary) nor by post-magmatic alteration due to K mobility. Santiago primitive lavas also exhibited high Ce/Pb and U/Pb ratios (28-45 and 0.29-0.96, respectively) characteristics of HIMU end-member (see section 4.5).

By comparing the primitive mantle normalized incompatible element patterns of the most recent versus the older formations besides the distinct behaviour of K, the patterns seem to be broadly similar. The concentration of Rb shows a slight dispersion in the Upper Pico da Antónia Formation, probably related with the compatible behaviour portrayed by K (Fig. 4.11A). The more recent formations also tend to be more enriched in HREE, compared with Lower Pico da Antónia Formation (Fig. 4.11B)

Notwithstanding the above mentioned HIMU fingerprints, Ba/Th ratios in Santiago lavas are high [167 ± 44 (SD)] as compared with other HIMU-rich intraplate oceanic islands as Madeira and St. Helena (83 and 43.4, respectively; Mata, 1996; Mata et al., 1998; Willbold, 2005) and even relatively to Gough and Tristan da Cunha that are considered to carry signs of EM-1 mantle component (103 and 149, respectively; Willbold, 2005; Workman et al., 2004).

An attempt to assess the behaviour of trace elements during Santiago Island mantle melting is illustrated by using primitive basaltic samples on binary plots of $\frac{1}{C_y^l}$ vs. $\frac{1}{C_x^l}$ in Figure 4.12. Indeed, the batch melting equation (Shaw, 1970) can also be rewritten in a linear form in the space of $\left(C_y^l\right)^{-1} = f\left(C_x^l\right)^{-1}$:

$$\frac{1}{C_y^l} = m\frac{1}{C_x^l} + b \qquad (5)$$

where,

$$m = \frac{C_x^0\left(1-D_y\right)}{C_y^0\left(1-D_x\right)}$$

and

$$b = \frac{\left(D_y - D_x\right)}{C_y^0\left(1-D_x\right)}$$

m= slope;

b= intercept;

C_L= weight concentration of a trace element in the liquid;

C_0=weight concentration of a trace element in the original unmelted solid;

D_0=Bulk distribution coefficient of the original solids

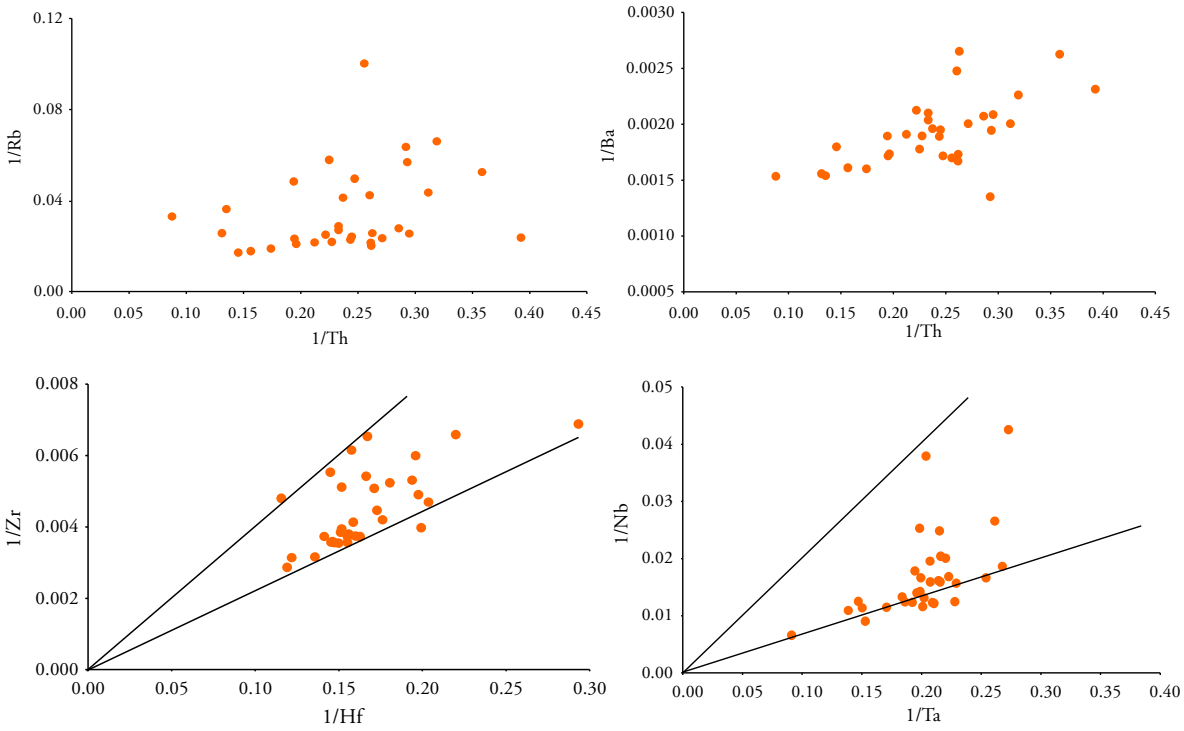

Fig. 4.12 - 1/Rb, 1/Ba vs. 1/Th, 1/Zr vs. 1/Hf and 1/Nb vs. 1/Ta plots for Santiago Island primitive magmas. Increasing compatibility of Ba (and Rb) with decreasing degrees of partial melting (decreasing 1/Th) and the wide range of Rb/Th, Zr/Hf and Nb/Ta element ratios require complex variations on residual assemblages (e.g., garnet lherzolite ± amphibole ± mica) and development of compositional heterogeneities in Santiago mantle source(s).

Representation in the form of equation (5) has the advantages that (a) the data to be fit are statistically independent, (b) the data are dispersed over a wide range and across a similar order of magnitude on both axis being sensitive for evaluating trace element ratio fractionation and, (3) allows simultaneous access to information on both the source ratio (m = slope) and the relative partitioning behaviour of the two elements (b = intercept). Several trace elements (including some of those with similar crystal-chemical properties; e.g., Zr – Hf, Nb – Ta, K – Rb) display considerable scatter on $\frac{1}{C_y^l}$ vs. $\frac{1}{C_x^l}$ plots (Fig. 4.12), indicating significant variability on their respective contents in Santiago mantle sources and/or on their degrees of compatibility relative to residual mantle assemblages.

Notwithstanding the dominant heterogeneity of element fractionation in Santiago magmas, U, Th, Pb and REE display consistent linear distributions in Figure 4.13 suggesting predictable behaviour during partial melting processes. Within the analytical uncertainty, the Santiago data suggests that (1) U, Th, La and Ce should have had similar (very-low) bulk solid-liquid distribution coefficients and, (2) $D_{Ce} < D_{Pb} < D_{Nd}$, which is consistent with recent reviews on Pb relative compatibility during generation of OIB (e.g., Hart and Gaetani, 2006).

Linear regression among the different binaries, $\frac{1}{C_y^l}$ vs. $\frac{1}{C_x^l}$, coupled with experimentally determined mineral/melt distribution coefficients (e.g., Johnson, 1998), allow to estimate a compositional pattern for the source of U, Th, Pb and REE in Santiago Island silicate magmas. Numerical data were normalized relative to their respective Primitive Mantle (PM) values (Palme and O´Neil, 2003) and the results are displayed graphically in Figure 4.14.

The general pattern displays progressive enrichment towards the more incompatible LREE and a relative depletion on Th and U; which is a characteristic feature of metassomatic re-fertilization of (previously depleted) OIB mantle sources elsewhere (Hofmann, 2003). The scarcity of reliable Pb analytical data and relatively poor correlations with REE do not advise a rigorous quantification of lead behaviour during partial melting. Nevertheless, analysis of the data suggests that Pb was depleted relative to LREE (Ce/Pb ≈ 33) in the mantle source of Santiago magmas; which is similar to the distinctive Pb depletions inferred for HIMU dominated (Mangaia, Tubai) OIB mantle sources (Hofmann et al., 1986; Hart and Gaetani, 2006).

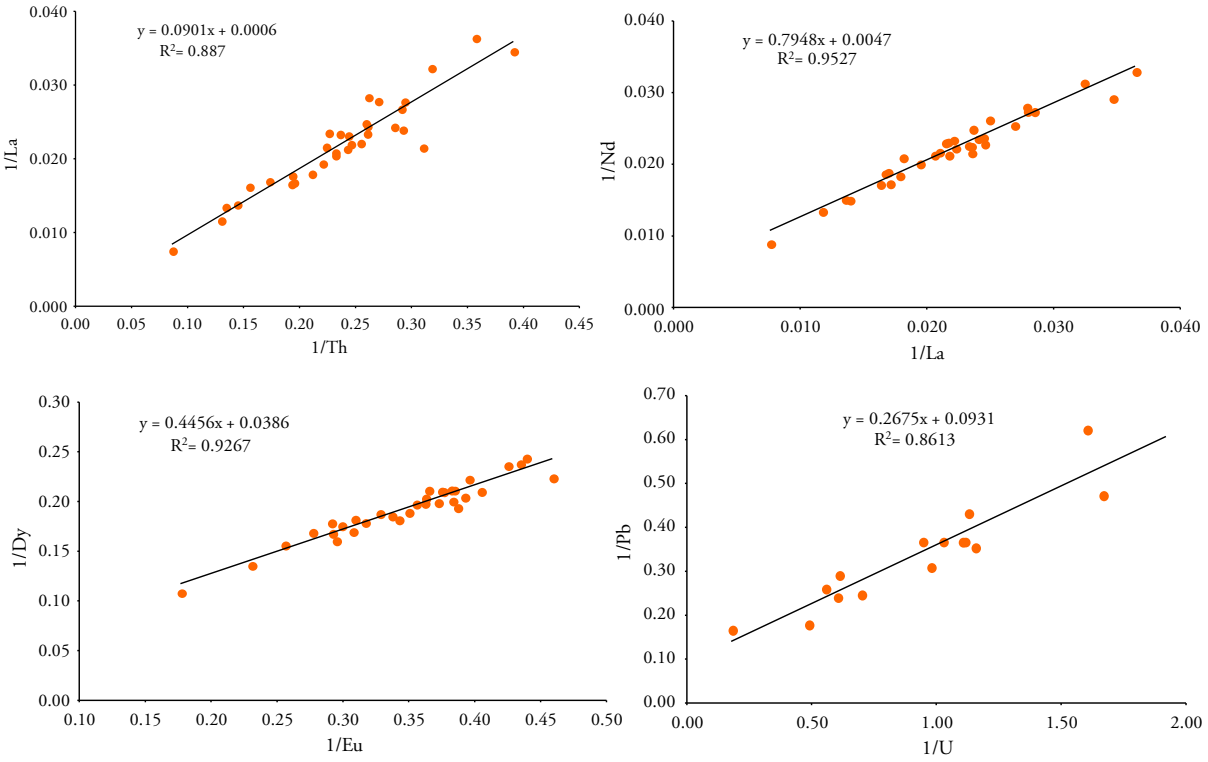

Figure 4.13 - $1/C_y$ vs. $1/C_x$ binary plots for U, Th, La, Nd, Eu, Dy and Pb contents in Santiago Island primitive magmas. Linear regression analysis [y = mx + b; see equation (5)] indicate (1) that $D_U \sim D_{Th} \sim D_{La} \sim D_{Ce} < D_{Pb} < D_{Nd} < D_{Sm} < D_{Eu} < D_{Dy} < D_{Er}$ during partial melting and, (2) that the Santiago mantle source(s) should have been enriched in U, Th and LREE.

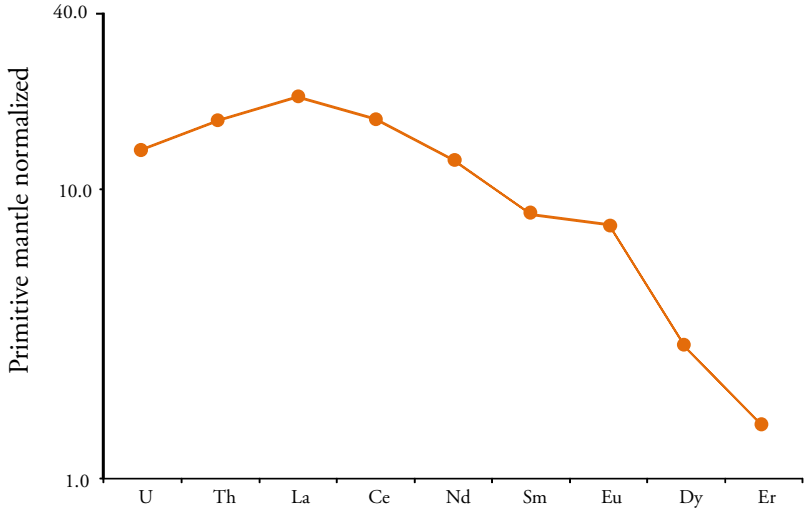

Figure 4.14 - Primitive mantle normalized plot of estimated U, Th and REE concentrations in the mantle source of Santiago Island silicate magmas. Trace element contents (see insert) assume $C_{Er} = 1.5 \times C_{Er(PM)}$ (Palme and O'Neil, 2006) and were obtained from $(1/C_y) = f(1/C_x)$ regressed data (see text) and experimentally determined bulk garnet lherzolite (60% olv + 20% opx + 10% cpx + 10% gt) solid/melt distribution coefficients (Johnson, 1998; McKenzie and O'Nions, 1991).

4.2.4.1. On the variability of Ce/Pb and Nb/U ratios

Hofmann et al. (1986) stated that Ce/Pb and Nb/U ratios are remarkably constant and similar in OIB and MORB (25±5 and 47± 10, respectively) allowing them to be used as tracers of mantle sources, since these element pairs do not fractionate during partial melting. Some questions have been raised concerning the constancy of these values and their significance (Halliday et al., 1995; Sims and DePaolo, 1997) and recent studies Hofmann (1997, 2003) have proven that Nb/U is indeed not constant in OIB. However, this author claimed that Nb/U is the ratio of incompatible elements which shows the least and lowest systematic variations (as opposed to Nb/La and Nb/Th). The Nb/U ratio for non-EM type OIB is set as 52 ± 15 (Hofmann, 2003).

Concerning Ce/Pb Hofmann (2003) recognized that the ratio is variable and that, in accordance with significant issues raised by Sims and DePaolo (1997) (e.g. variability of the data and probable influence of plagioclase fractionation), Nd/Pb could be a more suitable indicator of source chemistry, particularly after screening for continental contamination or continental recycling (Rehkämper and Hofmann, 1997). The mean value of Nd/Pb for OIB is set as approximately 15 however the common mantle end-members have statistically distinct ratios (EM 1=10.2; HIMU =15.9; EM 2=11.9; Hart and Gaetani, 2006).

Sun et al. (2008) have also confirmed, by analyses of MORB glass using LA-ICP-MS, that there is a variation in Nb/U and Ce/Pb by almost a factor of 2 (25-60 and 15-30, respectively) which they attributed to the ongoing process of mixing between subducted oceanic crust into MORB and OIB sources, supporting the absence of total "dilution" of this component in the mantle and the probable presence of megaliths of recycled material in the lower mantle.

Recently White (2007) by analyzing an extensive data set from on-line geochemical databases (GEOROC and PetDB)[7] reinforced that mean values of Nb/U and Ce/Pb are indeed similar in MORB and OIB. However several island chains, including the Cape Verde and Canary archipelagos, were signalled as being different from the overall OIB mean. The data from Santiago and other islands within the archipelago sustain that observation with high Nb/U (25.4 – 74.9, excluding two values considered outliers) (Fig. 4.15) and Ce/Pb values (28-44, higher than the canonical value of 25 for OIB; Hofmann, 2003).

[7] See Reference List for web sources.

The heterogeneity seen in the ratios of these incompatible elements will be further discussed in sections 4.4.4.

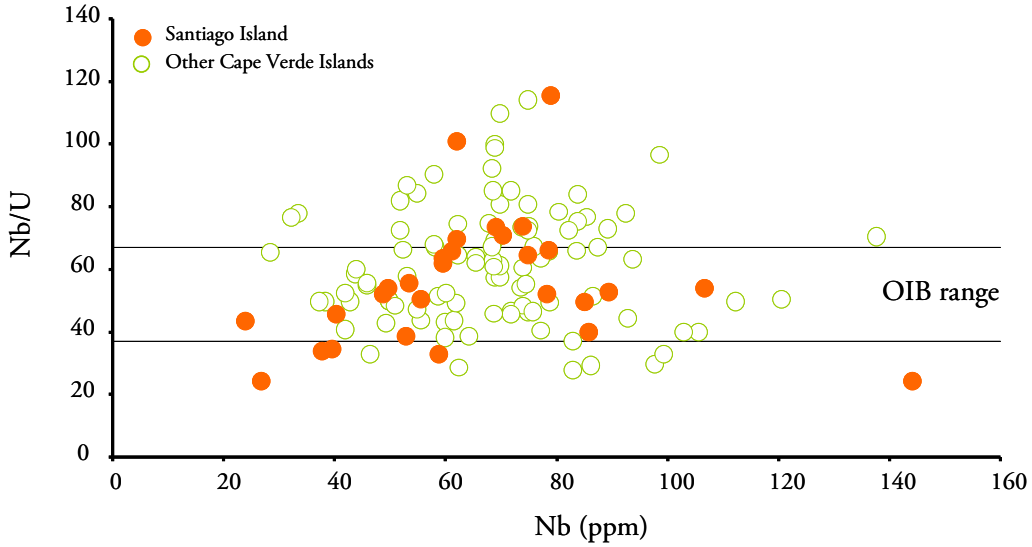

Figure 4.15 – Variability in Nb/U ratios in Santiago and other Cape Verde Islands (compilation of lavas with SiO_2<45 wt. %, and MgO from 7 to 15 wt. %; data from Gerlach et al., 1998; Torres, 1998; Jørgensen and Holm, 2002; Trindade, 2002; Doucelance et al., 2003; Escrig et al., 2005; Millet et al., 2008; Duprat et al., 2007; Holm et al., 2006 and unpublished data from Fogo). OIB range is from Hofmann (2003).

4.2.4.2. Nb/Ta vs. Zr/Hf – HFSE fractionation

Selected High-Field Strength Element pairs as Nb-Ta ($HFSE^{5+}$) and Zr-Hf ($HFSE^{4+}$) due to their almost identical ionic radii and same charge are considered to not fractionate from each other, maintaining a (relatively) constant ratio in oceanic basalts. However, Santiago lavas are characterized by significant variations in those element ratios (Nb/Ta=5.3 – 17.6, Zr/Hf=23.5 – 49.0) which is not common in primitive OIB (Fig. 4.16). It is important to point out that Flamengos Formation samples exhibit the narrowest variation in Nb/Ta and Zr/Hf (10.5-13.3 and 37.8-49.0, respectively) not showing evidence for strong HFSE fractionation, which is in contrast with the observed Nb/Ta and Zr/Hf variations on the other formations.

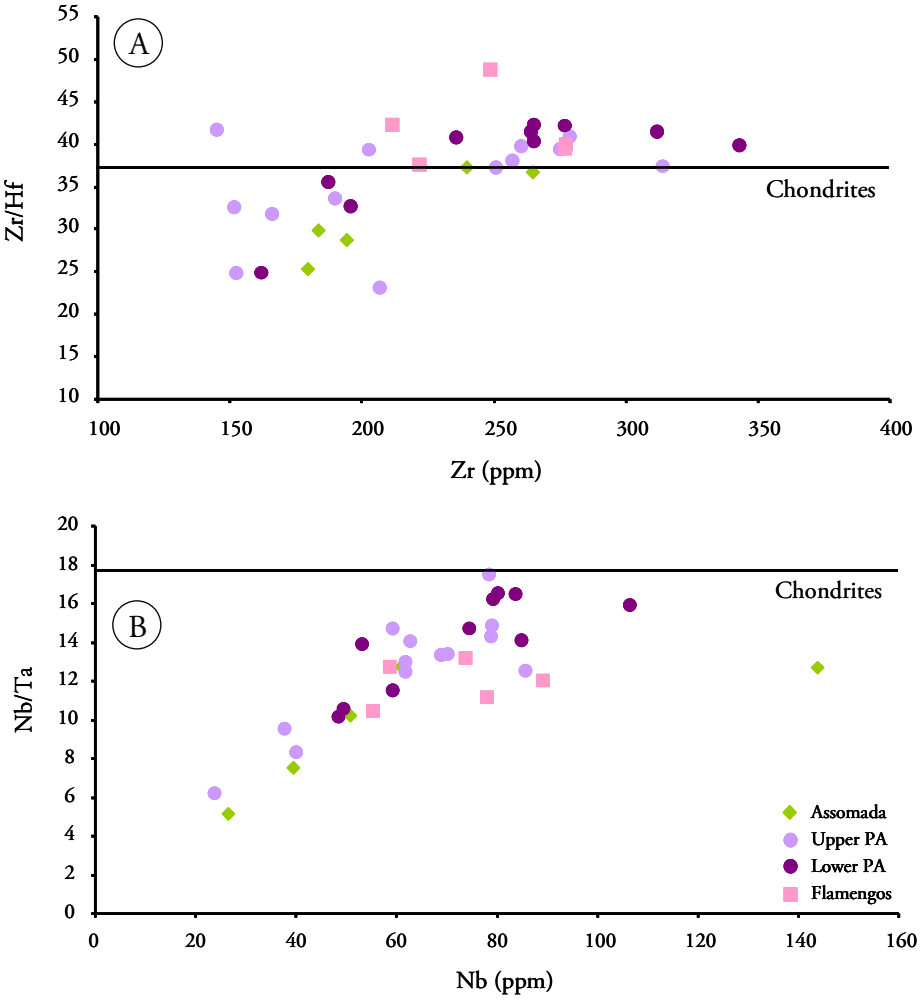

Figure 4.16 – Variation in Zr/Hf (A) and Nb/Ta (B) ratios in Santiago primitive samples. Chondritic values are from McDonough and Sun (1995).

Pfänder et al. (2007) made an OIB data compilation, concerning HFSE ratios, covering the isotopic spectrum portrayed by the most common mantle components (HIMU, EM 1 and EM 2) and observed that all the islands were characterized by superchondritic Zr/Hf ratios (35.5 – 45.5) and subchondritic Nb/Ta (14.6 – 17.6).

Within the Cape Verde archipelago Nb/Ta ratios are almost entirely subchondritic, however the northern islands (São Vicente and Santo Antão) seem to be characterized by higher values relatively to the southern islands (Santiago and Fogo) (Fig. 4.17A). Most of the islands show some evidence of Nb-Ta fractionation, Santiago being the one with lower Nb/Ta ratios.

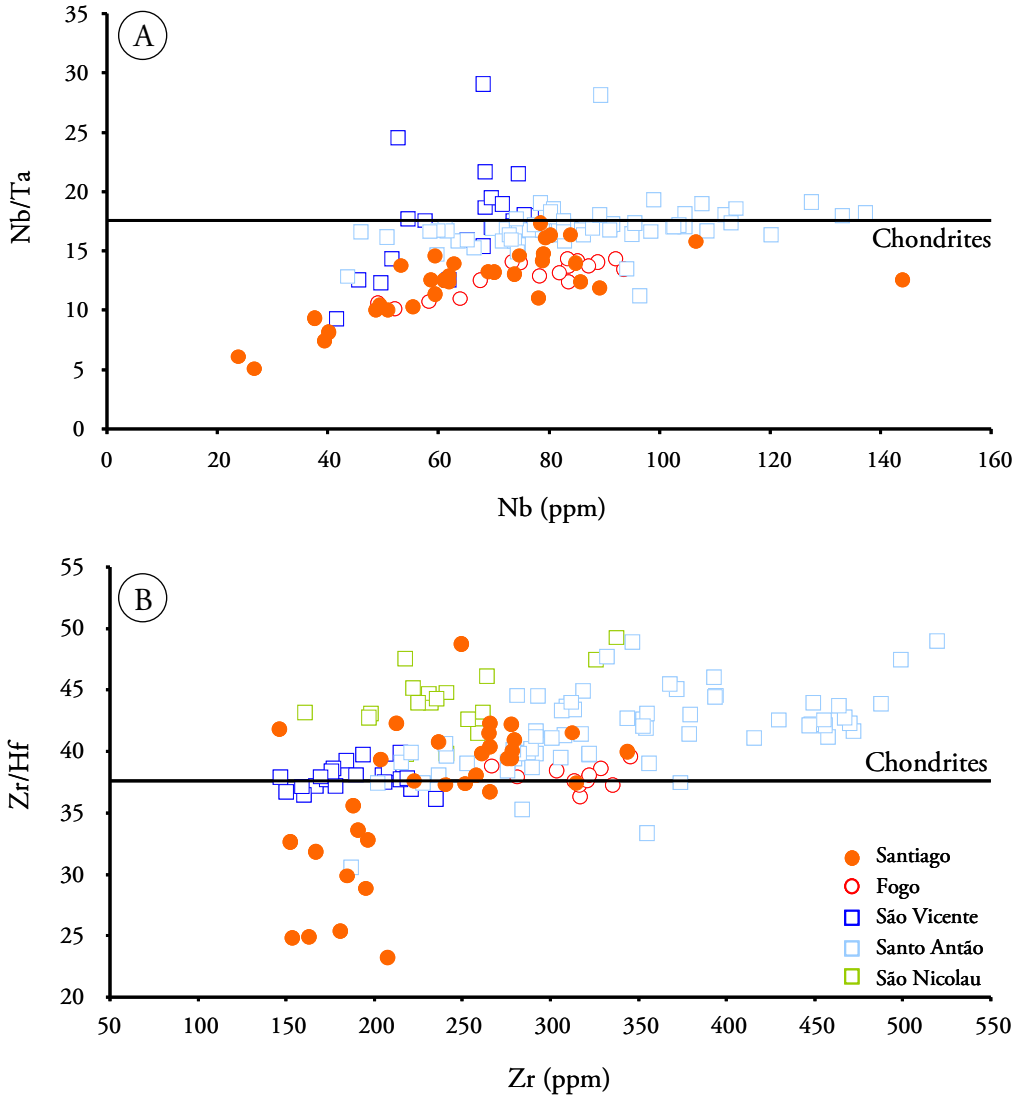

Figure 4.17 – Heterogeneity in Nb/Ta (A) and Zr/Hf (B) ratios in Cape Verde islands. The samples projected represent "primitive" samples with SiO_2< 45 wt.% and MgO from 7 to 15 wt.%. from Jørgensen and Holm, 2002; Trindade, 2002; Doucelance et al., 2003; Escrig et al., 2005; Millet et al., 2008; Duprat et al., 2007; Holm et al., 2006 and unpublished data from Fogo. Chondritic values are from McDonough and Sun (1995).

Concerning Zr/Hf all of the islands show chondritic to superchondritic ratios, however Santiago is characterized by a group of samples with subchondritic values, which is distinct from the other islands of the archipelago (Fig. 4.17B) and from the general tendency observed for OIB by Pfänder et al. (2007).

There are several mechanisms susceptible of causing significant HFSE variation and decoupling: presence of residual Ti minerals such as rutile or ilmenite (Green and Pearson,

1987), occurrence of amphibole and phlogopite as residual minerals or crystallizing phase (Moine et al., 2001; Tiepolo et al. 2000, 2001), sphene crystallization (Green, 1995), fractional crystallization of clinopyroxene (Pfänder et al., 2007), carbonatite metasomatism (Dupuy et al., 1992), influence of eclogite/garnet pyroxenite source material (Pfänder et al., 2007).

Different Nb-Ta and Zr-Hf partition coefficients between major/minor silicate phases (clinopyroxene, amphibole, phlogopite, sphene, ilmenite) and silicate melts, makes them potential causes of HFSE fractionation, as residual or crystallizing phases (Munhá et al., 2006).

Clinopyroxene fractionation is expected to increase Zr/Hf ratios due to higher $D_{Hf}^{cpx/melt}$ relative to $D_{Zr}^{cpx/melt}$ ($D_{Hf}^{cpx/melt}=0.55$, $D_{Zr}^{cpx/melt}=0.27$; $D_{Hf}^{cpx/melt}=0.37$, $D_{Zr}^{cpx/melt}=0.18$; Blundy et al., 1998, McDade et al., 2003, respectively). However Pfänder et al. (2007) showed that even with 30% of Rayleigh fractionation[8] the initial Zr/Hf ratios were only shifted by about 6-7%. Due to lower Nb and Ta partition coefficients in clinopyroxene ($D_{Zr}^{cpx/melt} \approx 13x\, D_{Nb}^{cpx/melt}$, $D_{Hf}^{cpx/melt} \approx 10x\, D_{Ta}^{cpx/melt}$; Blundy et al., 1998, McDade et al., 2003) Nb/Ta ratios are anticipated to vary less than Zr/Hf ratios, with an expected increase of ≈ 1% for the same amount of crystallization (Pfänder et al., 2007). In Santiago lavas Nb/Ta and Zr/Hf show a tendency to decrease as differentiation increases and there is no correlation between Nb/Ta and Zr/Hf with Sc ($D_{Sc}^{cpx/melt}$=3.2; Blundy et al., 1998), reinforcing the absence of HFSE control by clinopyroxene fractionation (David et al., 2000).

Ti-rich minerals (rutile, ilmenite, sphene) can also fractionate Zr/Hf and Nb/Ta ratios due to their high partition coefficients for the HFSE (see Table 4.1). As $D_{Zr/Hf}$ and $D_{Nb/Ta}$ are less than 1 for all these minerals, even a small amount of fractionation would elevate Nb/Ta and Zr/Hf and simultaneously a decrease in TiO_2, which is not observed in Santiago primitive samples.

[8] Rayleigh fractionation is a crystallization mechanism where the crystals are immediately extracted, from the magmatic liquid, after their formation (Neumann et al., 1954; Shaw, 1970).

Table 4.1 - Partition coefficients for HFSE in Ti-rich minerals.

$D^{mineral/silicate-melt}$	Ilmenite	Sphene	Rutile
Nb	1.23 – 2.3	3.5 – 5.7	14.4 – 96.0
Ta	1.7 – 2.7	10.8 – 18.4	24 – 195.0
Zr	0.29 – 0.70	4.0	1.1 – 8.8
Hf	0.38 – 0.96	10.0	1.6 – 12.0
References	Green and Pearson (1987) Klemme et al. (2006) Zack and Brumm (1988)	Green and Pearson (1987) Weaver (1990)	Klemme et al. (2005)

The role of amphibole and phlogopite as crystallizing phases in HFSE fractionation seems also very unlikely given the low partition coefficients and the similarity between them (see Table 4.2).

Table 4.2 - HFSE partition coefficients range between amphibole/phlogopite and silicate melt (compilation from Grégoire et al. 2000).

$D^{mineral/silicate\ melt}$	Amphibole	Phlogopite
Nb	0.02 – 0.19	0.08 – 0.14
Ta	0.07 – 0.21	0.10 – 0.14
Zr	0.12 – 0.33	0.02 – 0.13
Hf	0.33 – 0.83	0.048 – 0.19

In conclusion the almost unfractionated character of most of the samples and partition coefficients reasoning (see above) points to the inability of fractional crystallization as a cause for the observed Zr/Hf and Nb/Ta variability.

Fractionation of HFSE during partial melting events is also a possibility. The most common and abundant mantle minerals (olivine, orthopyroxene and clinopyroxene) are unable to account for the observed variations in Nb/Ta and Zr/Hf ratios due to the high incompatible character of those elements for these residual phases. Metasomatic phases such as amphibole, phlogopite and ilmenite may be important reservoirs of trace elements in the upper mantle since the HFSE are less incompatible relatively to them (Moine et al., 2001). However it

should be emphasized that these accessory phases will only have a large impact at very low extents of melting, because mantle peridotite normally begins to melt around unstable hydrous minerals which will melt out after larger degrees of melting (McBirney, 2007).

At Santiago, the extreme subchondritic Nb/Ta and Zr/Hf ratios are more significant at higher melting degree (Fig. 4.18) which seems to preclude such HFSE fractionation derived exclusively from partial melting in the presence of those accessory residual phases. By modelling non-modal batch melting with different paragenesis and distinct partition coefficient data sets (not shown) (Fig. 4.18) the low Nb/Ta and Zr/Hf values exhibited by Santiago samples are not reproduced, if their source was characterized by primitive values for those ratios. Moreover from the modelling presented in Figure 4.17 emerges the fact that the presence of residual amphibole raises the Zr/Hf and Nb/Ta ratios instead of diminishing it. The same is true for the other minerals listed in Tables 4.1 and 4.2.

Concerning the possible role of amphibole it should be noted that Green (1995) proposed that for basanitic melts at mantle pressures (2 - 3 GPa) the presence of residual pargasite could be responsible for lowering the Nb/Ta of the derivative melts due to high D_{Nb}/D_{Ta} (1 to 1.4). However Tiepolo et al. (2000, 2001) showed that the partition coefficients of Nb and Ta in amphibole are strongly dependent on the structure and composition of the melt and amphibole itself, concluding that $D_{Nb,Ta}^{amph/melt}$ is negatively related with Mg# and Ti content. Due to the high TiO_2 contents of Santiago primitive lavas[9] (2.5 to 4.4 wt. %), and the high Mg# expected due to buffering of silicate minerals present in mantle peridotite (i.e., olivine), $D_{Nb,Ta}^{amph/melt}$ should be low, making amphibole an unlikely cause for the low Nb/Ta ratios observed.

Metasomatism is another process susceptible of introducing variability on the HFSE budget of mantle sources affected by it. Specifically, carbonatitic metasomatism has been described as being the cause of magmas with Zr/Hf ratios significantly higher than the chondritic value (Dupuy et al., 1992). However Martins et al. (2010) called to the attention that carbonatitic metasomatism can instead be responsible for lowering the Zr/Hf ratio due to stability of garnet with a significant grossularitic component (Ca-rich) for which $D_{Zr}>D_{Hf}>1$ (see 4.4.4 for further development on the subject). van Westrenen et al. (2001) reported

[9] Prytulak and Elliott (2007) have identified the Cape Verde archipelago as portraying one of the highest TiO_2 content in OIB worldwide.

$D_{Zr}>D_{Hf}$ for garnets with a grossular component between 25 and 60 mol.% and Klemme et al. (2002) expands that compositional range until 17 mol.%. The influence of garnet composition is less evident in Nb/Ta ratios, due to their higher incompatibility, however grossular-rich garnet has $D_{Nb/Ta}$ between 1.2 and 2 (Pfänder et al., 2007 and references therein).

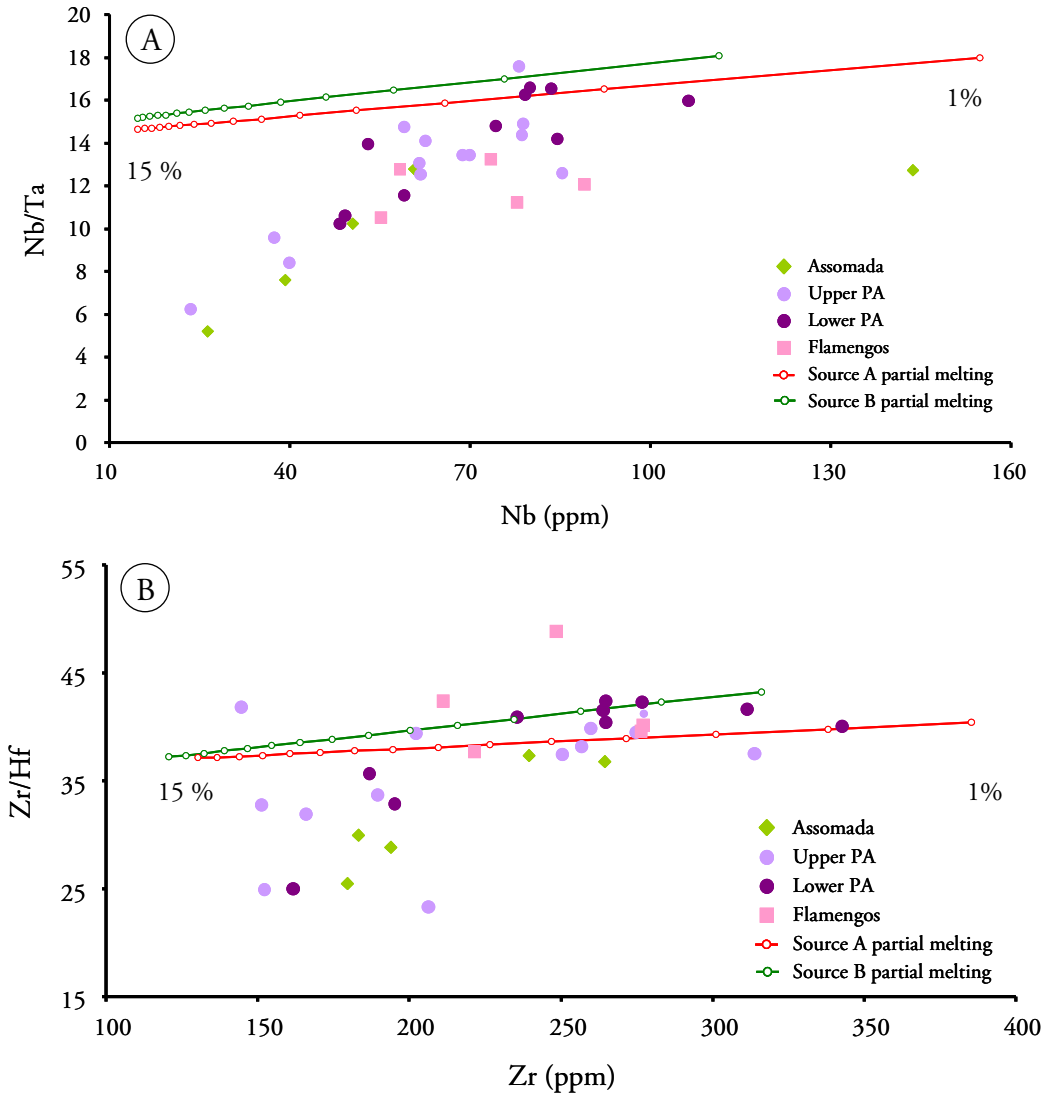

Figure 4.18 –Nb/Ta vs. Nb (A) and Zr/Hf vs. Zr (B) along with non-modal batch partial melting (Shaw, 1970; see Appendix A5.1) modelling of two distinct mantle source paragenesis: (A) 61 olv: 17 opx: 12 cpx: 10 grt and (B) 56 olv: 15 opx: 12 cpx: 10 grt: 7 amph (melt modes are 5:5:40:50 and 5:5:20:30:45, respectively). For Zr and Hf, source composition is assumed to be 2x that of primitive mantle (PM) (Palme and O'Neill, 2003), while the Nb concentration was reduced from 2.4 to 2.24 (4x PM) to fit the required Nb/Ta ratio of 14 in the bulk-silicate Earth after core formation (see Pfänder et al., 2007). Partition coefficients are from Dalpe and Baker (1994), Ionov et al. (1997), Salters et al. (2002) and McDade et al. (2003). Circular marks on curves A and B represent consecutive increments of 1% partial melting degrees.

Notwithstanding, if we assume the presence of grossular-rich garnet, with the intrinsic changes in HFSE compatibility, there will a be "buffering" of Zr and Nb concentrations not in agreement with the very high values (231 ± 52 and 66 ± 23, Zr and Nb mean values ± SD for primitive samples) observed in the lavas from Santiago.

Another possible explanation for the lowest Santiago's HFSE ratios could be a mantle source with lower initial Zr/Hf and Nb/Ta. However the existence of such mantle domains is not very plausible (Nb/Ta as low as 6 and Zr/Hf about 26) given that reservoirs with similar characteristics are very depleted in incompatible trace elements (Pfänder et al., 2007; Fig. 4.19) which is clearly not the case for Santiago Island sources.

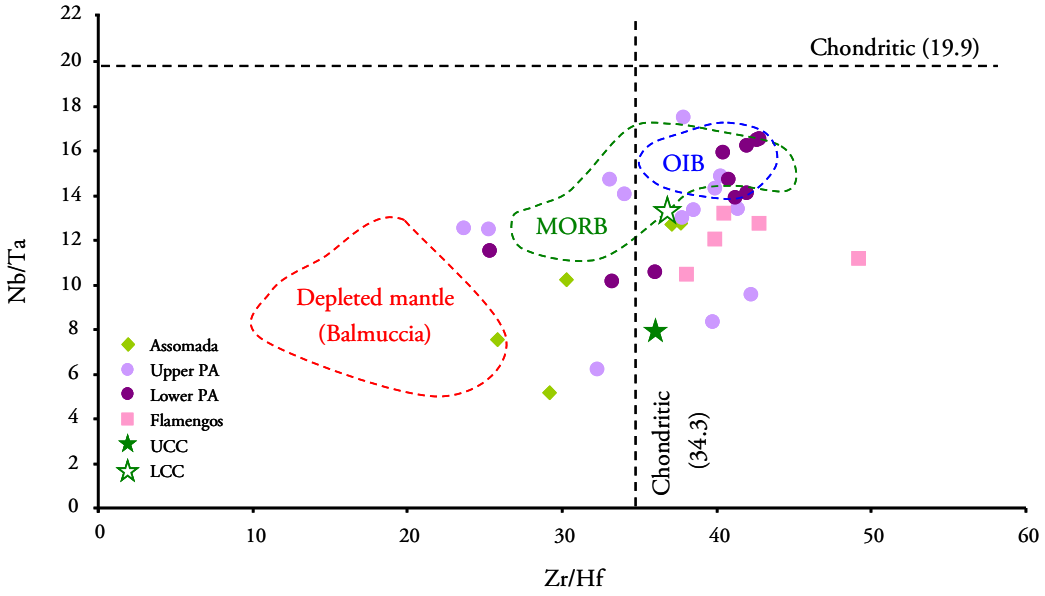

Figure 4.19 – Nb/Ta vs. Zr/Hf values of Santiago formation compared to with major terrestrial silicate reservoirs. Chondritic, MORB, OIB and Balmuccia data are from Münker et al. (2003) and upper and lower continental crust (UCC and LCC, respectively) values are from Rudnick and Gao (2003).

The role of the presence of garnet pyroxenite/pyroxenite in the source have been suggested as important in several OIB (Canary Islands, Day et al., 2009) and for Santiago Island, Barker et al. (2009) suggested its presence in order to explain particular trace element characteristics.

Garnet pyroxenite/pyroxenite/eclogite mantle sources are indeed characterized by low Nb/Ta and Zr/Hf ratios (Pfänder et al., 2007; van Westrenen et al., 2001). However, those domains tend to have lower solidus temperatures when compared to those of

peridotite/carbonated peridotite (Kogiso et al., 2004; Hirschmann and Stolper, 1996; Hirschmann et al., 2003; Yasuda et al., 1994). These features imply that within garnet-rich mantle domains melting will start at higher pressures and with higher melt productivity (Hirschmann and Stolper, 1996; Stracke et al., 1999; Dasgupta et al., 2004). So it is expected that, if those domains are indeed present in the source, the first partial melts will have the strongest evidence and chemical characteristics in accordance. However there is no correlation between the lowest Nb/Ta values and high Th, which can be explained considering that Santiago mantle source is highly enriched which could dilute such particular characteristics.

By modelling the effects of partial melting of mantle sources where garnet pyroxenite is mixed, in different proportions, with peridotites characterized by different degrees of enrichment, the Zr/Hf and Nb/Ta range observed for the majority of primitive Santiago lavas is reasonably accomplished (Fig. 4.20). This evidence seems to suggest that Santiago mantle is not only variable enriched but also lithologic heterogeneous (see section 4.4.3.1) including both peridotites and garnet pyroxenites. However some Nb/Ta values around 12, for Zr/Hf about 25, remain unexplained.

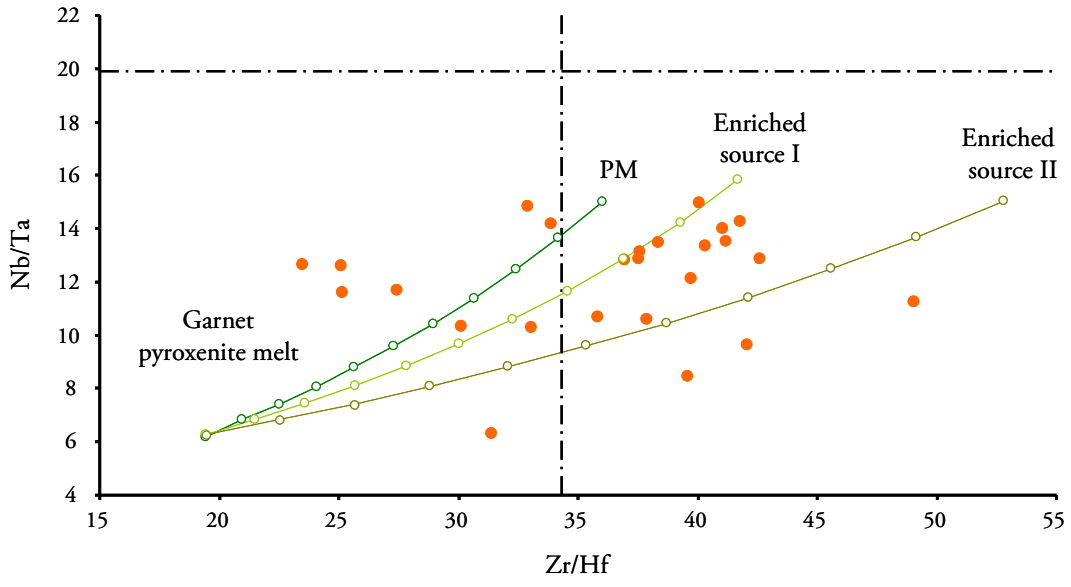

Figure 4.20 – Nb/Ta vs. Zr/Hf mixing modelling between a garnet pyroxenite melt [4% modal partial melting of sample SAE152 (Ishikawa et al., 2007) with mineral proportion 83cpx:17grt, using partition coefficients from Pfänder et al. (2007)] and primitive mantle (PM, Palme and O'Neill, 2003) or enriched sources (I: Nb=1.74, Ta=0.11, Zr=38, Hf=0.91 ; II: Nb=1.8, Ta=0.12, Zr=48, Hf=0.91; in ppm). Chondritic values from Münker et al. (2003). Circular marks represent 10% contaminant.

4.3. Sr-Nd-Hf-Pb isotope chemistry

From the 56 samples analysed for major and trace elements, 18 were further selected for isotopic studies, covering all of Santiago's volcanic formations.

Isotopic data for Santiago lavas are reported in Appendix III.2. New Sr, Nd, Hf and Pb isotopic results are presented (see also Martins et al. 2010). The obtained isotopic data cover the following ranges: $^{87}Sr/^{86}Sr$ = 0.70318-0.70391, $^{143}Nd/^{144}Nd$ = 0.51261-0.51287, $^{176}Hf/^{177}Hf$ = 0.28284-0.28298, $^{206}Pb/^{204}Pb$ = 18.93-19.75, $^{207}Pb/^{204}Pb$ = 15.55 – 15.60, $^{208}Pb/^{204}Pb$ = 38.89 – 39.47 (see Appendix II for detailed analytical procedure and discussion of accuracy and reproducibility).

Since isotopic results from Santiago Island have also been reported by other authors, it is important to make a comparison to check ranges, possible overlaps or deviating values. Even thought Davies et al. (1989) and Doucelance et al. (2003) present isotopic data for Santiago Island, discrimination by formation were not done by these authors. Considering this, the new data is only compared with those from Gerlach et al. (1988) and Barker et al. (2010) (Fig. 4.20).

Comparing our data with those from Gerlach et al. (1988) and Barker et al. (2010) there is a considerable overlap in the Nd isotopic data obtained for each formation by the different authors (Fig. 4.21). The $^{86}Sr/^{87}Sr$ ranges are more scattered, with Assomada and Upper Pico da Antónia formations data from Barker et al. (2010) reaching higher values.

The Hf isotopic data from this study overlap with that of Barker et al. (2010). However the Flamengos formation data from these authors show a much wider range, probably due to the higher number of analysed samples (13 as opposed to 3 from this study). Concerning the Pb isotopic data there is a considerable scatter between the data from this study and Barker et al. (2010) and those from Gerlach et al. (1988). The data from the latter is consistently less radiogenic in all formations. The observed difference could be due to distinct analytical techniques such as leaching procedures, sample digestion, Pb separation and different mass spectrometers used, TIMS in Gerlach et al. (1988) and MC-ICP-MS in Barker et al. (2010) and present work (see Appendix II for detailed analytical procedure).

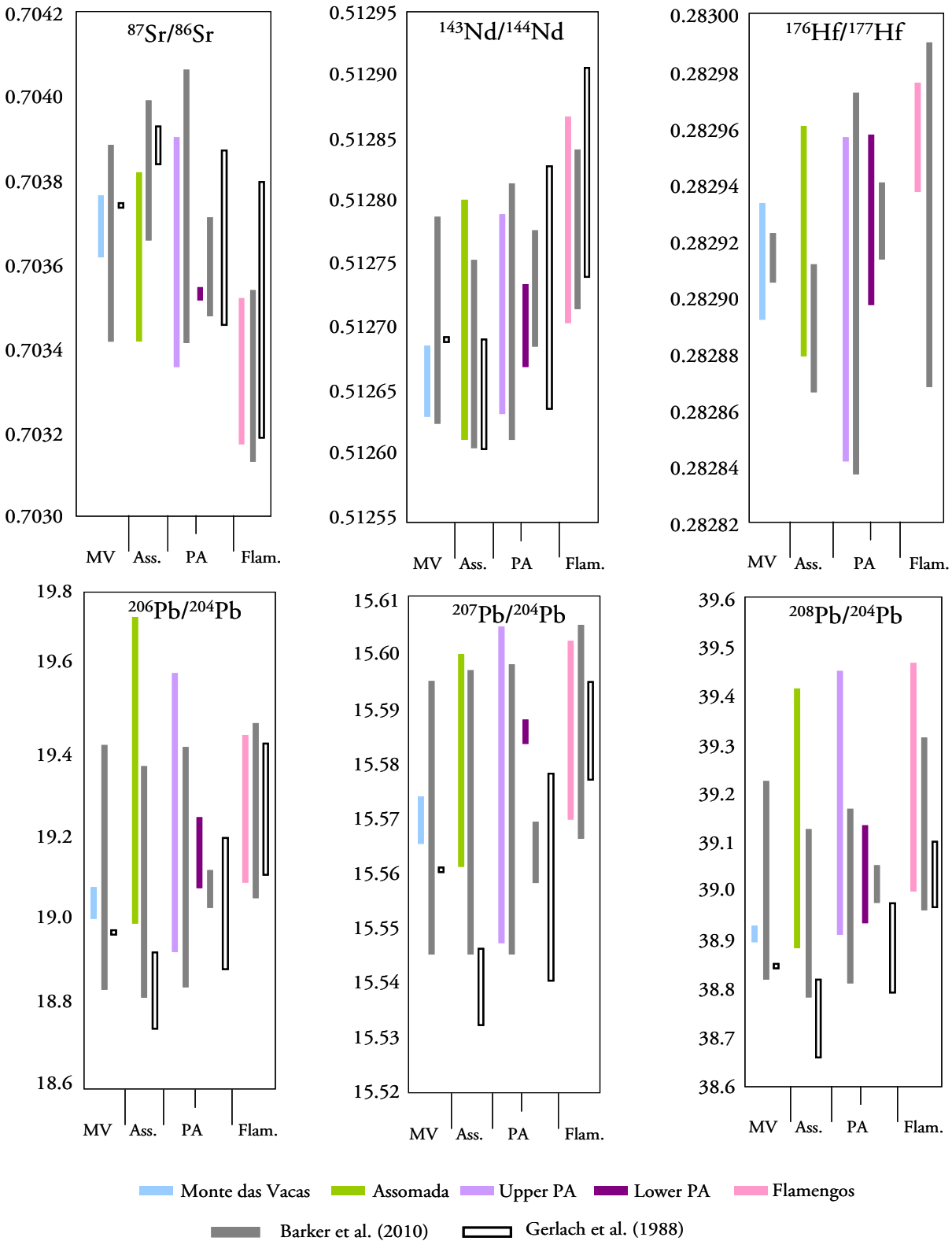

Figure 4.21 – Sr-Nd-Hf-Pb isotopic ranges for Santiago Island volcanic formations. Gerlach et al. (1988) do not distinguish Upper and Lower Pico da Antónia Formations, so the represented range corresponds to the Pico da Antónia Formation as a whole.

The Pb isotopic data presented in this study reaches the highest values reported for Santiago lavas, being more significant in $^{206}Pb/^{204}Pb$ (up is 19.74) and $^{208}Pb/^{204}Pb$ ratios (up to 39.47). These higher values will be discussed in sections 4.3.3.1. and 4.4.4.3.2.

4.3.1. Sr-Nd isotope data

The $^{87}Sr/^{86}Sr$ and $^{143}Nd/^{144}Nd$ ratios are consistent with those previously reported for the southern Cape Verde islands (e.g. Gerlach et al., 1988; Davies et al., 1989; Doucelance et al., 2003; Barker et al., 2010), overlapping 86% of the isotopic range of this group of islands, which represent ≈ 20 Ma of volcanic activity (Holm et al., 2008). The Sr isotope ratios are negatively correlated with $^{143}Nd/^{144}Nd$ and most of the samples plot in the depleted quadrant of the Sr-Nd diagrams (Fig. 4.22).

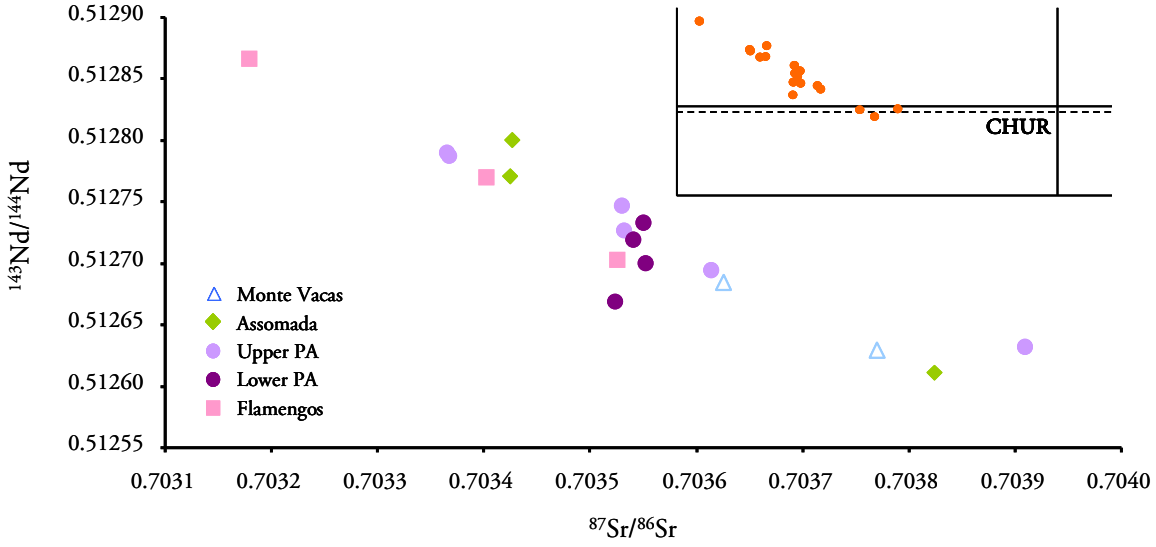

Figure 4.22 –$^{143}Nd/^{144}Nd$ vs.$^{87}Sr/^{86}Sr$ variation displayed by Santiago Island formations. On the inset graph, Santiago samples are projected along with the CHUR values (Chondritic Uniform Reservoir). The solid line for $^{143}Nd/^{144}Nd$ represents the value of DePaolo and Wasserburg (1976) (0.512638) and the dashed line the value from Bouvier et al. (2008) (0.512630). The $^{87}Sr/^{86}Sr$ CHUR value is from Faure and Mensing (2005) (0.7045).

4.3.2. Hf isotope data

In the Hf-Nd isotope diagram, Santiago lavas display a linear array with the expected overall positive correlation and the majority of samples projecting in the depleted quadrant (Fig. 4.23). The samples of Flamengos Formation are characterized by higher values of $^{176}Hf/^{177}Hf$ ratios compared with the ranges from the other formations, indicating that they are originated from source(s) characterized by a time-integrated depletion more marked than the inferred from lavas from the other complexes.

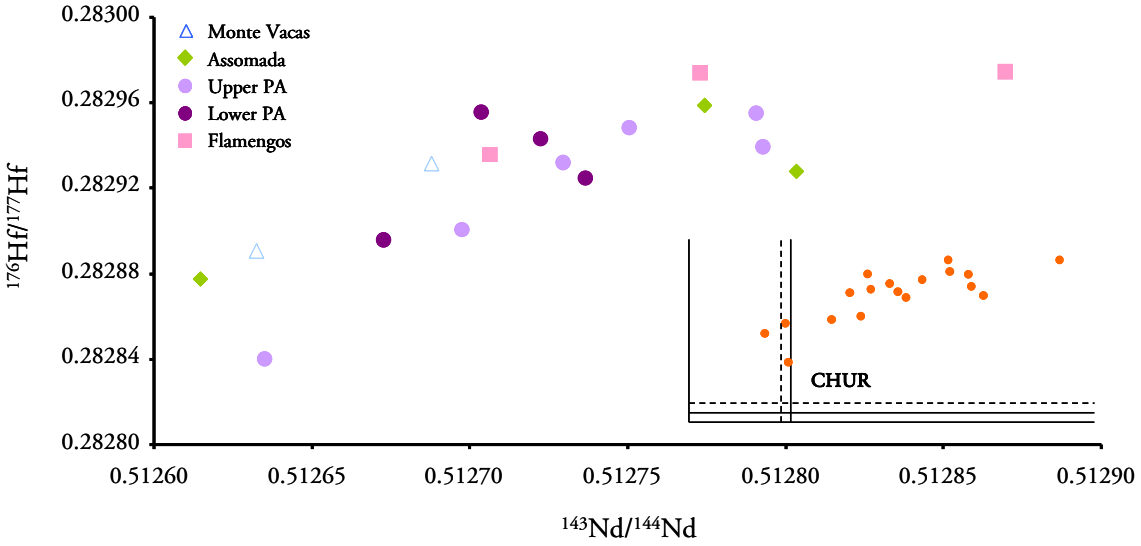

Figure 4.23 – $^{176}Hf/^{177}Hf$ vs. $^{143}Nd/^{144}Nd$ variation displayed by Santiago lavas. On the inset graph, Santiago samples are projected along with the CHUR values. The solid line represents Nd and Hf isotopic CHUR value of DePaolo and Wasserburg (1976) and Blichert-Toft and Albarède (1997) (0.512638 and 0.282772, respectively) and the dashed line, more recent Nd and Hf CHUR values from Bouvier et al. (2008) (0.512630 and 0.282785, respectively).

The variation observed in Santiago Island Hf isotopic data is somewhat limited corresponding to ≈ 5 units of ε_{Hf}[10]. Even thought Hf isotopic data are scarce for North/Central Atlantic Islands, recent data by Geldmacher et al. (2009) reports a lower compositional variation for the Canary archipelago (≈ 4 units of ε_{Hf}) and a slightly broader range for Madeira Island (>6 units of ε_{Hf}). For the Azores Islands, São Miguel exhibit an Hf isotopic variation of

[10] See Appendix V (V.5.1.) for ε_{Hf} calculation procedure.

10 units of ε_{Hf} (Elliot et al., 2007; Beier et al., 2007) while a small group of samples from Pico gives a limited range (≈ 2 units of ε_{Hf}). For comparison the Kerguelen archipelago is characterized by a larger variation corresponding to 14 units of ε_{Hf}, Hawaii Islands has a range of 9 units of ε_{Hf} (Mattielli et al., 2002) and the Galapagos Islands, 7 units of ε_{Hf} (Blichert-Toft and White, 2001).

Santiago is the only island from the Cape Verde archipelago from which $^{176}Hf/^{177}Hf$ data is available for alkaline lavas and one carbonatite (this study, Martins et al. 2010 and Barker et al., 2010). A recent abstract from Bonadiman et al. (2010) also reports Hf isotopic data for clinopyroxene separates of peridotite xenoliths from Sal Island.

Santiago samples plot near to the ε_{Hf}-ε_{Nd} mantle array[11] (Vervoort et al., 1999; Chauvel et al., 2008) but with a distinctly shallower slope (Fig. 4.24). The observed Santiago slope (0.76, n=18) is significantly shallower than the mantle (1.33, Vervoort et al., 1999; 1.59, Chauvel et al., 2008) and OIB arrays (1.42, Vervoort et al., 1999), indicating a time-integrated decoupling of Lu/Hf from Sm/Nd relative to compositions lying on the mantle array (Fig. 4.24). The Santiago data from Barker et al. (2010) gives an even shallower slope (0.62, n=22), however the data is more scattered (r^2=0.29 compared with r^2=0.64 from this study data). It is interesting to note that the dispersion in the Barker et al. (2010) Hf isotopic data is due to Flamengos Formation samples which show lower Hf isotopic ratios for a given Nd isotopic ratio (not shown).

Hf isotopic compositions of Santiago correlate negatively with $^{87}Sr/^{86}Sr$ and positively with Pb isotopic data. However correlation with Sr isotopic data is particularly better (r^2=0.74) than with Pb isotopic ratios (r^2=0.15, r^2=0.34 and r^2=0.11, correlation with $^{206}Pb/^{204}Pb$, $^{207}Pb/^{204}Pb$ and $^{208}Pb/^{204}Pb$, respectively), which is mainly due to three Pb data outliers that distort the correlation. The meaning of these more radiogenic Pb signatures (up to 19.75 in $^{206}Pb/^{204}Pb$ ratio) will be discussed in the next sections.

[11] The "Hf-Nd mantle array" is a line produced by the linear regression through the oceanic basalt dataset (OIB and MORB). It has been defined by the equation $\varepsilon_{Hf} = 1.33 \times \varepsilon_{Nd} + 3.19$ (Vervoort et al., 1999) or, more recently, by $\varepsilon_{Hf} = 1.59 \times \varepsilon_{Nd} + 1.28$ (Chauvel et al., 2008). See Appendix V (V.5.1.) for ε_{Nd} calculation procedure.

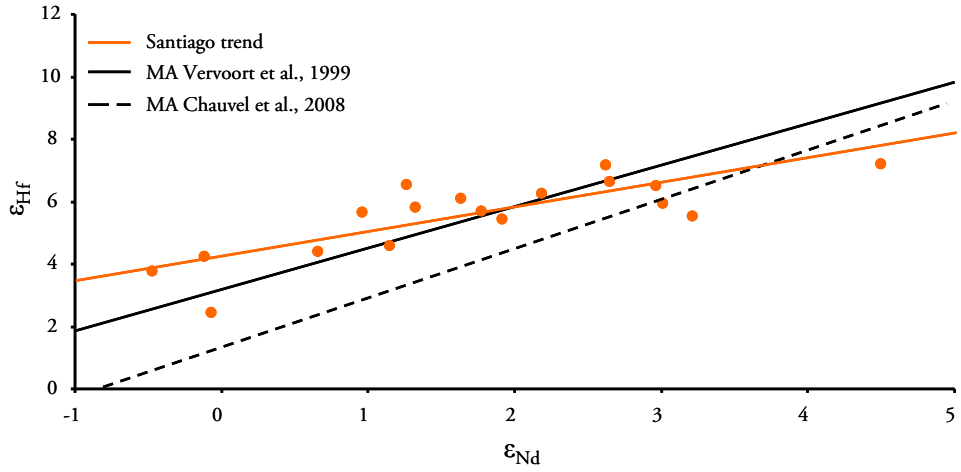

Figure 4.24 –ε_{Hf} vs. ε_{Nd} variation displayed by Santiago lavas, compared with the mantle array (OIB and MORB data) from Vervoort et al. (1999) and Chauvel et al. (2008).

4.3.3. Pb isotope data

Santiago lavas show a broad range in $^{206}Pb/^{204}Pb$ and $^{208}Pb/^{204}Pb$, with a smaller variation in $^{207}Pb/^{204}Pb$ ratios. Three samples stand out of the main Santiago group reaching values as high as 19.75 and 39.47 in $^{206}Pb/^{204}Pb$ and $^{208}Pb/^{204}Pb$ ratios, respectively. The majority of the samples plot above the NHRL[12] in $^{207}Pb/^{204}Pb$ vs. $^{206}Pb/^{204}Pb$ and $^{208}Pb/^{204}Pb$ vs. $^{206}Pb/^{204}Pb$ diagrams as typical for the southern Cape Verde Islands ($\Delta 7/4$= -3 to 3 and $\Delta 8/4$= -8 to 40)[13](Fig. 4.25). The $^{206}Pb/^{204}Pb$ ratios of some samples (up to 19.75) are clearly higher than those assigned to DMM, EM 1 and EM 2 mantle endmembers (Stracke, 2012) and suggest derivation from a mantle source with a high time-integrated U/Pb ratio [high μ ($^{238}U/^{204}Pb$), i.e. HIMU].

[12] NHRL stands for Northern Hemisphere Reference Line which expresses the average trend of oceanic basalts in the Northern Hemisphere (Hart, 1984) (see Appendix V.5 for calculation procedure).

[13] $\Delta 7/4$ and $\Delta 8/4$ stand as the deviation from the NHRL in $^{206}Pb/^{204}Pb$ vs. $^{207}Pb/^{204}Pb$ and $^{206}Pb/^{204}Pb$ vs. $^{208}Pb/^{204}Pb$, respectively (see Appendix V.5 for calculation procedure).

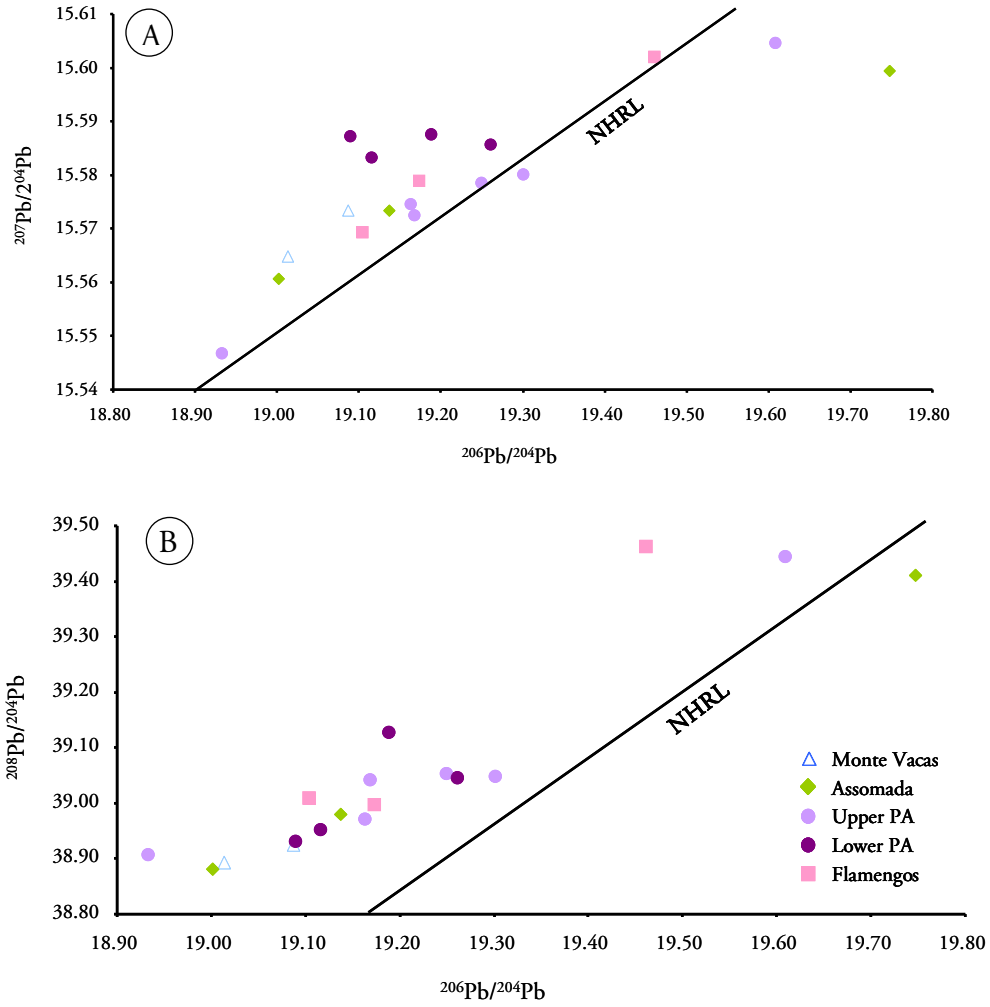

Figure 4.25 –$^{207}Pb/^{204}Pb$ vs. $^{206}Pb/^{204}Pb$ (A) and $^{208}Pb/^{204}Pb$ vs. $^{206}Pb/^{204}Pb$ diagrams (B) for Santiago lavas, where the majority of the samples plot above the NHRL.

Santiago lavas shows an increase in $^{87}Sr/^{86}Sr$ with decreasing $^{206}Pb/^{204}Pb$, consistent with the described for southern Cape Verde islands, the exception being the sub-set of samples already mentioned (Fig. 4.26).

In contrast Nd and Hf isotope ratios are poorly correlated with $^{206}Pb/^{204}Pb$ and $^{207}Pb/^{204}Pb$ (Fig. 4.27). However, when projected against time-integrated Th/U ($^{208}Pb^*/^{206}Pb^*$)[14], the correlations improve implying that Sm-Nd, Lu-Hf and U-Th fractionations in the mantle, must have been related with each other, but not with U-Pb (White, 2013) (Fig. 4.28).

[14] See Appendix V.5 for calculation procedure.

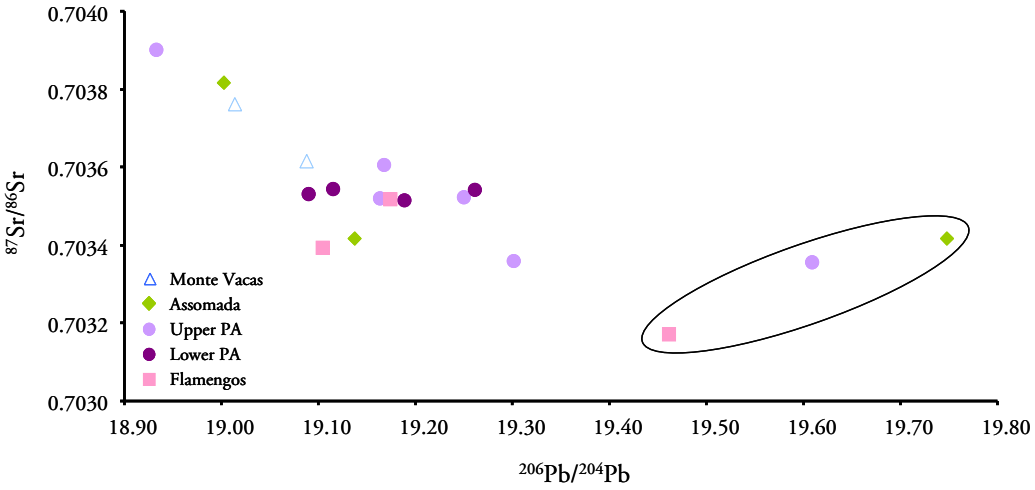

Figure 4.26 – $^{87}Sr/^{86}Sr$ vs. $^{206}Pb/^{204}Pb$ ratios for Santiago lavas. The most Pb radiogenic samples are encircled.

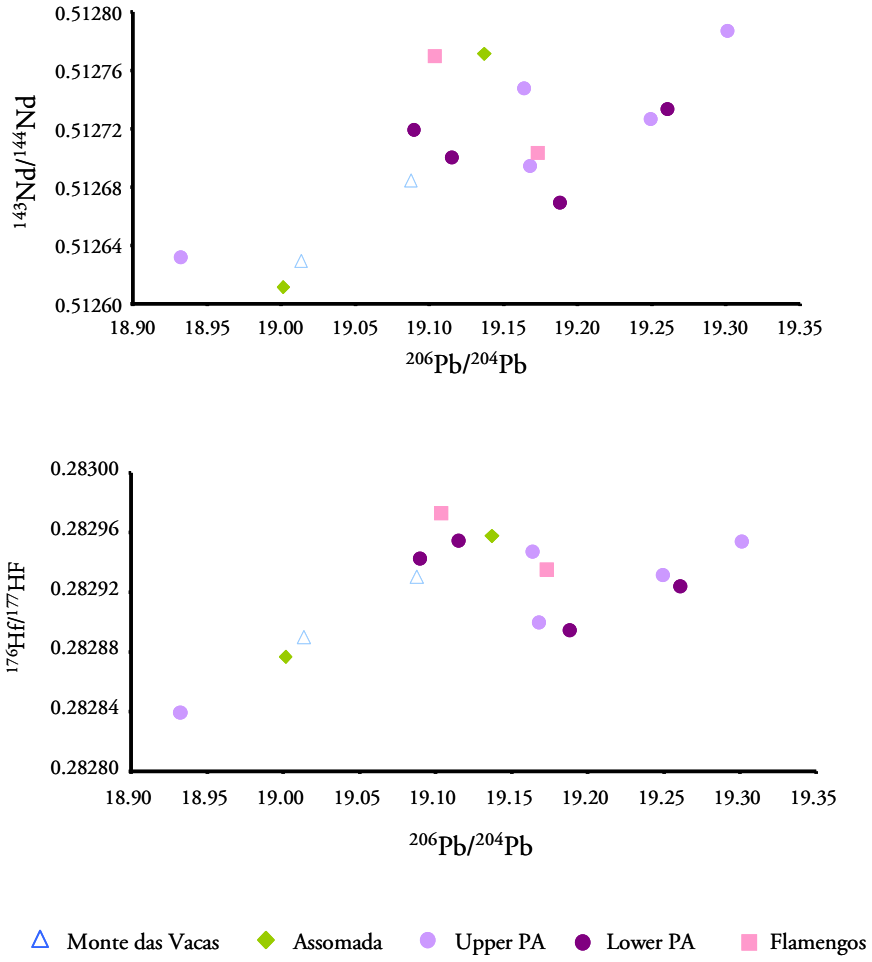

Figure 4.27 – Poor correlation between $^{143}Nd/^{144}Nd$ and $^{176}Hf/^{177}Hf$ with $^{206}Pb/^{204}Pb$ in Santiago lavas. The highly Pb radiogenic samples were removed for better visualization.

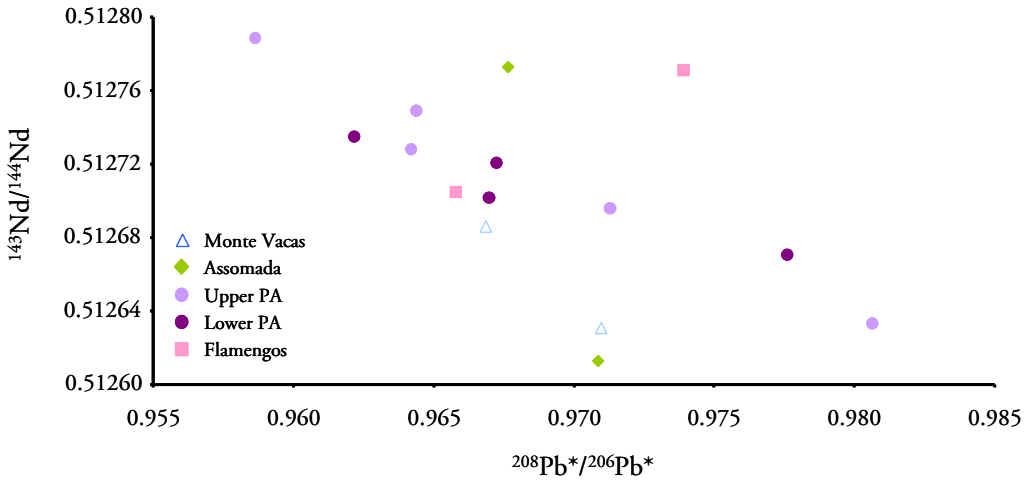

Figure 4.28 – Improved correlation between $^{143}Nd/^{144}Nd$ and $^{208}Pb^*/^{206}Pb^*$ ratios compared with Figure 4.27.

4.3.3.1. Pb isotope signatures: outliers

As stated, three Santiago samples are characterized by distinctly higher $^{206}Pb/^{204}Pb$, $^{207}Pb/^{204}Pb$ and $^{208}Pb/^{204}Pb$ values displaying a different trend from the remaining samples. While the majority of the samples tend to plot almost parallel to the NHRL, the more radiogenic group displays a horizontal trend that crosses the NHRL (Fig. 4.25). The group is composed of a sample from each formation: ST-5 (Flamengos, submarine sample), ST-48 (Upper Pico da Antónia, subaerial sample) and ST-18 (Assomada, subaerial sample).

Considering the variation observed in the Pb isotopic data published for Santiago alkaline lavas (Fig. 4.29), it is evident that the radiogenic group stands out, making them the most radiogenic samples described, so far, for Santiago Island. Due to their distinct Pb isotopic data it is necessary to assess the validity of these results.

Since Pb isotopic composition in Ocean Island basalts are highly susceptible to modification by non-magmatic Pb derived from contamination by seawater and hydrothermal alteration, subaerial weathering, aeolian dust and sample processing techniques, it is necessary to rule out these possibilities before trying to find an explanation in terms of primary geochemical signature. As described in Appendix II, all Santiago lava samples were leached according with the method developed by Weis and Frey (1991, 1996) and considered by Weis et al. (2005) as the most suitable for removing secondary alteration phases. The method consists in the repeated leaching with a 6 N sub-boiled HCl until a clear solution is obtained (Weis et al., 2006). The three samples span a limited range of SiO_2 (38 - 43 wt. %) with

moderate to high LOI value (1.6 – 1.9 wt. % in the subaerial samples and 3.9 wt.% in the submarine sample). It is worth mentioning that other Santiago samples, subaerial and submarine, with similar LOI ranges (2.7 to 3.4) do not display anomalously high Pb isotopic data, nor are the Pb isotopic ratios ($^{206}Pb/^{204}Pb$, $^{207}Pb/^{204}Pb$, $^{208}Pb/^{204}Pb$) correlated with LOI (not shown).

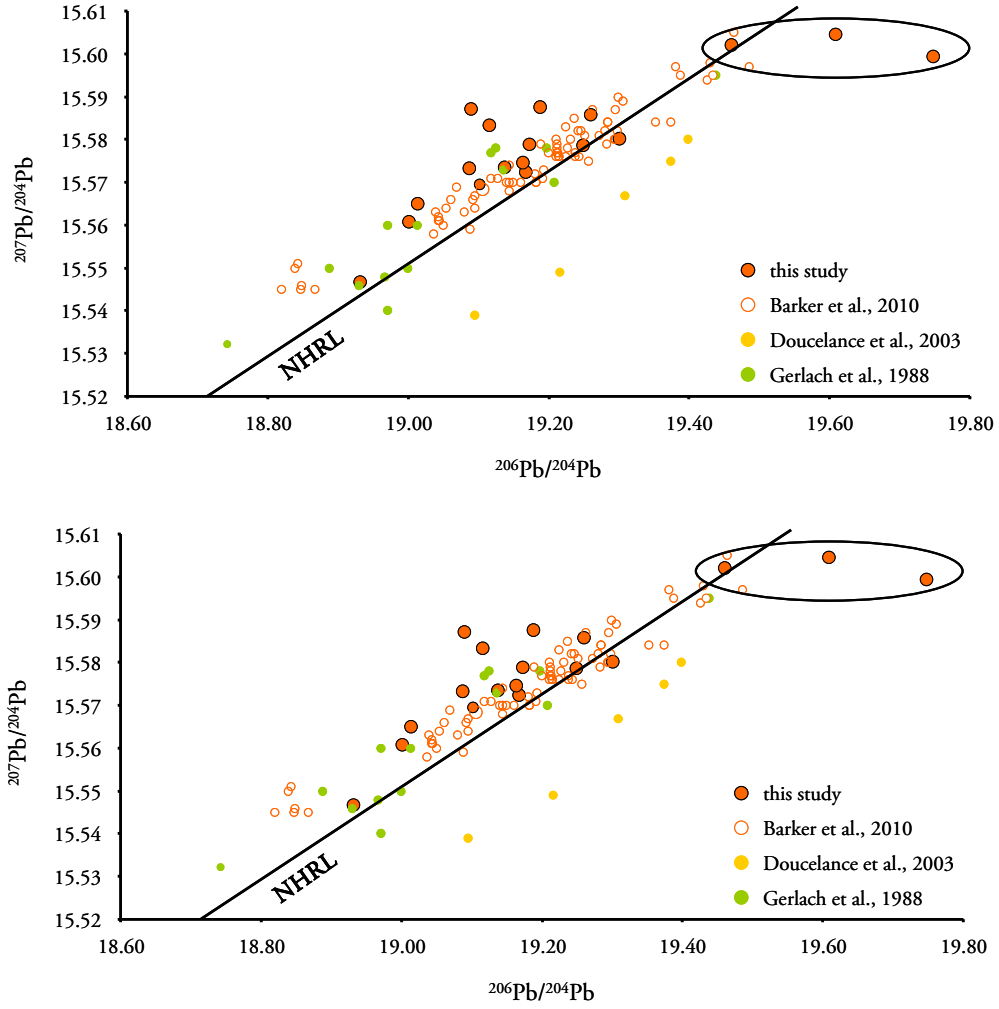

Figure 4.29 – Santiago Island Pb isotopic ratios from this study and published data with the three samples, with unusually radiogenic values, being encircled.

Through the leaching procedure Santiago lavas lost an average of 40% of their initial weight, which is assumed to be composed of secondary minerals related to submarine/subaerial alteration that can host "foreign" Pb. To test if the leaching technique was not entirely successful and could account for the radiogenic group, Santiago samples were plotted against Atlantic Fe-Mn nodule data, a proxy for local contaminant related to seawater (Fig. 4.30)

(Nobre Silva et al., 2009; Hanano, 2008). Even though Fe-Mn nodules are characterized by high values of $^{207}Pb/^{204}Pb$, their comparatively low $^{206}Pb/^{204}Pb$, $^{208}Pb/^{204}Pb$ and extremely high $^{87}Sr/^{86}Sr$ values (0.708-0.711, O'Nions et al., 1998) precludes seawater alteration and ineffective acid-leaching as cause of the deviant Pb data.

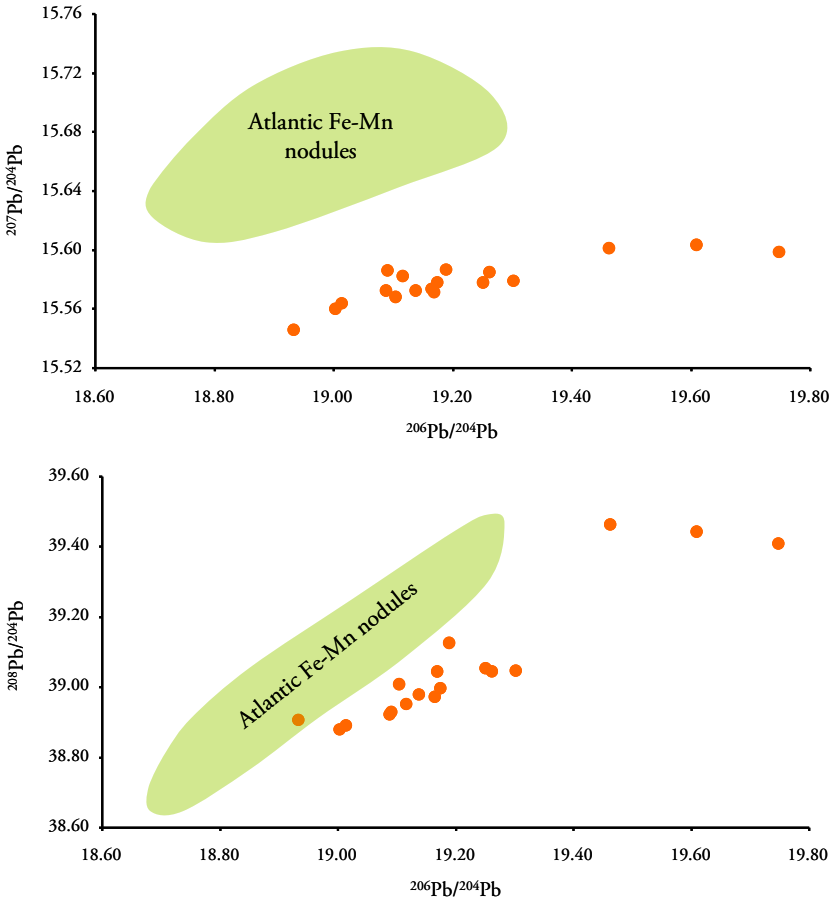

Figure 4.30 – Santiago Pb isotopic data compared with Atlantic Fe-Mn nodule field (von Blanckenburg et al., 1996; O'Nions et al., 1998; Abouchami et al., 1999).

Anthropogenic Pb could also be considered a source of contamination, since 95% of the environmentally available Pb comes from industrial activity, coal burning and vehicle exhaust (Roy and Négrel, 2001). This anthropogenic signature is passed on to the atmosphere and hydrosphere, leading to high Pb contents in rainwater, aerosols, snow and pelagic/lacustrine sediments (Wittig et al., 2009). Due to sample exposure at the Earth's surface this contaminant could be imprinted on lavas causing significant changes on Pb data. Santiago Pb isotopic data were compared with Pb atmospheric data (rainwater, aerosol dust) to attest if any anthropogenic Pb is identifiable (Fig. 4.31). The low $^{206}Pb/^{204}Pb$ and $^{208}Pb/^{204}Pb$ values

characteristic of these materials makes them an unsuitable contaminant for the radiogenic Santiago samples.

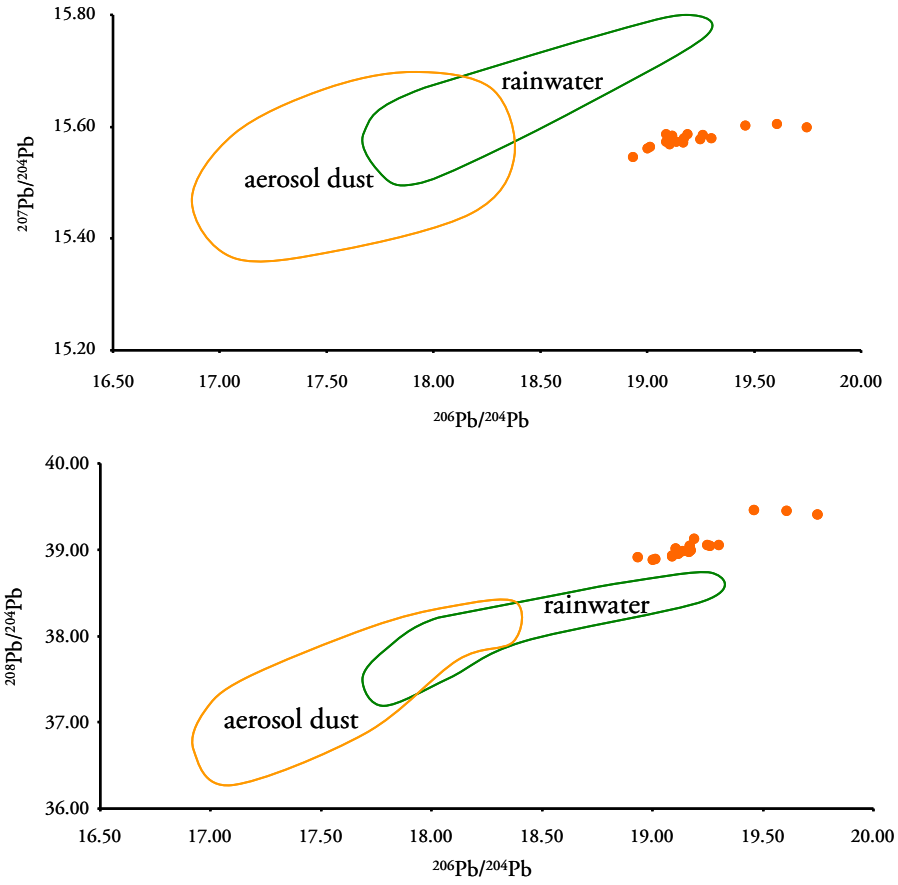

Figure 4.31 – Santiago Pb isotopic data compared with anthropogenic Pb data from western Europe and North Africa (aerosol dust: Grousset et al., 1994; rainwater: Roy and Négrel, 2001).

Since the higher Pb isotopic data of a three sample sub-group cannot be justified by sample alteration or contamination, another "contaminant" with radiogenic Pb isotope signature must be accounted for.

Two complete procedural duplicates (separate powder leaching and dissolution) were also done in samples ST-5 and ST-18, with Pb isotope results almost indistinguishable from one another (see Appendix III.2.1.1.).

It is important to mention that the most Pb radiogenic samples are also amongst those with the lowest $^{87}Sr/^{86}Sr$ (≤ 0.70342) and highest $^{143}Nd/^{144}Nd$ (≥ 0.51279) values. Also, those three samples (ST-5, ST-18 and ST-48) are enriched in incompatible trace elements relative to the remaining primitive Santiago samples (Table 4.3). So, the distinctly higher Pb isotopic

signature of the samples is associated with other geochemical particularities indicating that their characteristics are related with mantle source heterogeneities or other enrichments processes (see section 4.4.4 for further discussion).

Table 4.3 - Incompatible element enrichment portrayed by the most Pb radiogenic samples.

	Primitive sample average (ppm ± SD)	ST-5	ST-18	ST-48
Ba	708 ± 144	893	952	947
La	46 ± 12	59	131	74
Ce	95 ± 23	118	264	149
Th	4.3 ± 1.1	5.8	11.6	7.5

4.3.4. Isotopic heterogeneity

The heterogeneous isotopic signature of the Santiago magmas is especially obvious within the range observed among those characterised by lower degrees of partial melting (i.e., higher Th contents). The initial low melt fractions (higher Th and La concentrations or La/Yb ratios) tend to sample more restricted portions of the mantle, and so are more likely to image several distinct domains. With the gradual increase of partial melting (lower Th and La concentrations) such diversity tends to be dissipated towards a homogeneous composition, better reflecting the mean Santiago mantle signature (Fig. 4.32).

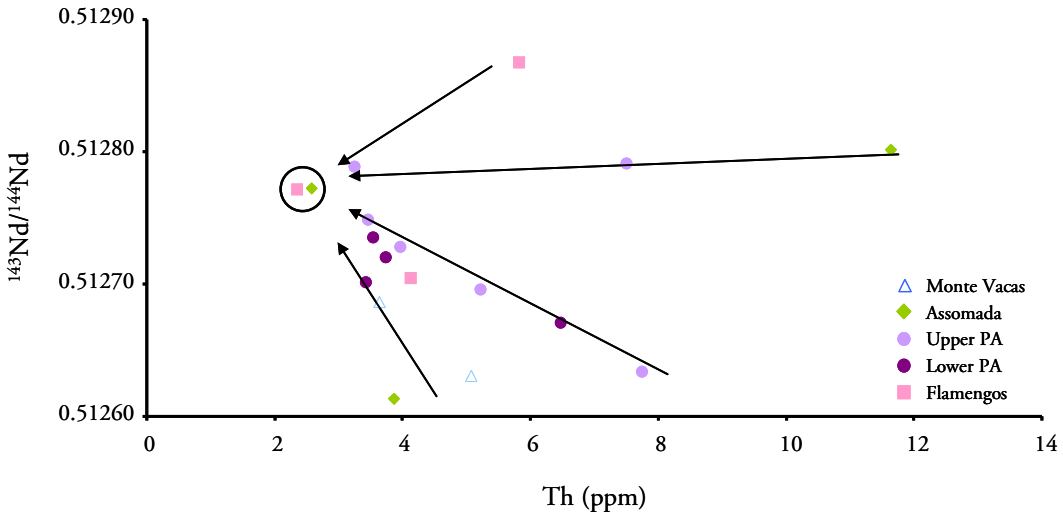

Figure 4.32 - $^{143}Nd/^{144}Nd$ vs. Th relationships for Santiago lavas, attesting the convergence towards a more homogeneous composition with increasing partial melting degree, i.e. with increasing Th concentrations.

As already noticed for major elements (see 4.2.), the isotopic composition of Santiago lavas also changed over time. In general, the $^{143}Nd/^{144}Nd$ ratios decrease while the $^{87}Sr/^{86}Sr$ ratios increase from the oldest to the youngest formation, as previously reported by Gerlach et al. (1988). However it is difficult to actually be certain about this tendency due to the reduced number of samples analysed within each formation. For example the Pico da Antónia formation exhibit an isotopic range that almost covers the entire Santiago lavas array, one Flamengos formation sample being the exception. In light of this temporal variation uncertainty when discussing the isotopic heterogeneities and evolution in Santiago lavas, the set of samples will the studied as a whole.

4.4. Diversification of Santiago magmas

Various processes are susceptible of causing the observed compositional and isotopic diversity of magmatic rocks. The chemical variability of primary magmas can arise from different chemical and mineralogical source compositions as well as of distinct melting conditions (e.g. depth, pressure, temperature, presence/absence of volatiles) constraining their formation (e.g. Best and Christensen, 2001). Magmatic differentiation leads to further modifications of these magmas after leaving their source. Crystal fractionation is one of the dominant process whereby distinct portions are physically separated, inducing different evolutionary paths for the segregated phases (crystals and residual melt) (Winter, 2001). It is, therefore, of crucial importance to identify and discuss each one of these processes in order to understand the variability of the Santiago lavas.

4.4.1. Shallow-level assimilation

Another mechanism capable of altering trace element and isotopic characteristics is shallow-level assimilation. It has been identified the possible contribution of crustal assimilation to the composition of Cape Verde island magmas, specifically in S. Nicolau Island (Doucelance et al. 2003; Millet et al., 2008).

In the Cape Verde archipelago the most probable contaminants are: (1) old oceanic crust (130-140 Ma), where the islands are implanted; (2) young sediments and (3) magmatic products of the volcanic edifice.

In order to check the influence of Cretaceous basement assimilation on Santiago lavas the available isotope data for comparison comes from samples recovered at the DSDP Site 367≈(330 km SSE of the Cape Verde islands) (Janney and Castillo, 2001) and from altered oceanic crust uplifted and outcropping at Santiago (Gerlach et al., 1988; Millet et al., 2008; this study). The data from the DSDP and the altered outcropping oceanic crust (Gerlach et al. 1988) are very similar and exhibit high $^{87}Sr/^{86}Sr$ (0.70348-0.70371), $^{206}Pb/^{204}Pb$ (19.6 – 22.33) and low $^{208}Pb/^{204}Pb$ (38.18 – 39.01) compared with pristine, unaltered N-MORB [0.70229, 18.28 and 37.2, respectively extreme Atlantic N-MORB values, Rollinson (1993)]. Such differences are due to seawater interaction and hydrothermal processes which significantly increases the U/Pb and U/Th leading to uranogenic lead isotopes ratios (Davies et al., 1989). Moreover seawater is highly Sr-radiogenic ($^{87}Sr/^{86}Sr$= 0.709241±32; Veizer et al., 1989), and strongly enriched in Sr and characterized by high Rb/Sr while it $^{143}Nd/^{144}Nd$ ratio (0.512074 to 0.512125, North Atlantic Deep Water; Rickli et al., 2009) is unradiogenic and its concentration in Nd is very low ($4.2x10^{-6}$; Banner, 2004). All these characteristics usually confer to seawater altered rocks high $^{87}Sr/^{86}Sr$ signatures for a given $^{143}Nd/^{144}Nd$.

The analyses performed by Millet et al. (2008) for the cretaceous MORB outcropping at Santiago Island as well as those performed in this study, were preceded by leaching in order to minimize the effects of seawater alteration. So, it is not surprising that their data is different from those presented by Gerlach et al. (1988). Moreover the difference between both data sets allows visualizing the effects of such alteration processes (Fig. 4.33).

If Santiago magmas had assimilated a significant amount of altered oceanic crust it would be expected higher $^{87}Sr/^{86}Sr$ and $^{206}Pb/^{204}Pb$ isotopic ratios and low $^{208}Pb/^{204}Pb$ (38.18 – 39.01, Janney and Castillo, 2001; Gerlach et al., 1988) (Fig. 4.33).

As described in section 4.3.3, due to their distinct and extreme isotopic characteristics, recent sediments, represented by Fe-Mn nodules in the Atlantic ($^{207}Pb/^{204}Pb$ between 15.62 and 15.72 and $^{87}Sr/^{86}Sr\geq0.708$; von Blanckenburg et al., 1996; O'Nions et al., 1998; Abouchami et al., 1999) are dismissed as possible contaminants in Santiago magmas.

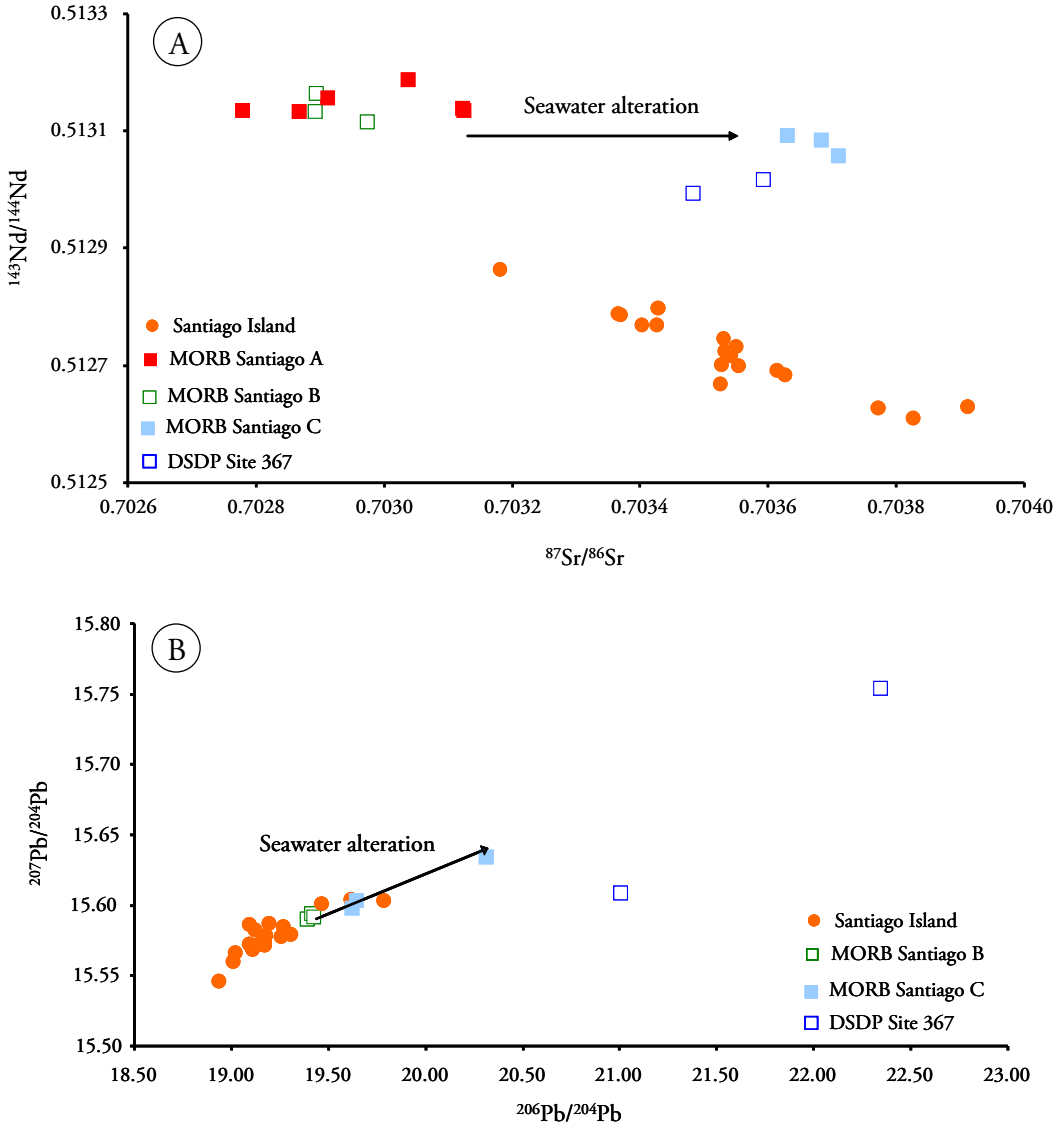

Figure 4.33 - Possible contaminants of Santiago magmas in Nd-Sr (A) and Pb-Pb (B) isotopic space. MORB A data from this study, MORB B is from Millet et al. (2008), MORB C is from Gerlach et al. (1988) and DSDP site 367 is from Janney and Castillo (2001).

The studied Santiago lavas are ultrabasic to basic alkaline rocks most of them with primitive-like characteristics which implies small residence time in magmatic chambers and so the assimilation of pre-existing magmatic material of the volcanic edifice should be minimal. Also, most of the island volcanic building must be very similar in composition, concerning major, trace element and isotopic characteristics. Similar major element compositions imply identical melting temperatures making also difficult the occurrence of contamination, while similar trace element and isotopic signatures make difficult the identification of contamination.

In conclusion from the above arguments it can be concluded that if the occurrence of contamination cannot be completely dismissed, it did not play a major role as a cause from the chemical variability of the studied Santiago Island.

4.4.2. Crystal fractionation processes

Santiago silicate lavas present a compositional/lithological range spanning from foidites (SiO_2=37.9 wt. %) to phonolites (SiO_2 up to 60 wt. %) (see Fig. 4.1 and Alves et al., 1979). Considering the main objectives of the present work, some 60% of the samples studied fall on the established primitive magmas category (see 4.2.2.1.) indicating a relatively minor role of crystal fractionation processes on the observed chemical variability. In the following paragraphs the role of fractional crystallization on the variability of the set of the studied samples will be addressed. For a discussion of the same process extending until phonolitic compositions, see Alves et al. (1979).

From the micropetrographic study and the determination of phases occurring as phenocrysts, inferences can be made on the nature of the fractionating minerals (see Martins, 2003 for full petrographic description). The study of Santiago lavas suggest that the main fractionating phases were olivine and clinopyroxene, the most abundant phenocrysts, and minor amounts of Cr-rich spinels and apatite, occurring as inclusions in those phenocrysts. In some cases plagioclase may also have played a role as constrainer of the liquid line of descent[15].

By analyzing major and trace element behaviour along a liquid line of descent it is possible to confirm the petrographic-based assumptions regarding the crystallizing mineral assemblage. In the following discussion it will be considered that each of the Santiago formations has its own specific magmatic evolution because, as stated, there are differences that imply distinct magma sources and so different crystallization paths.

Considering trace elements ratios, a distinction can sometimes be made between partial melting and crystal fractionation processes, due to the different behaviour of one of the elements which for one the processes is highly incompatible ($D<0.01$) and for the other is less incompatible element ($D\approx0.1$) (Fig. 4.34; White, 2013). An interesting example is that of

[15] Liquid line of descent materializes the chemical evolution of a magma suffering fractional crystallization, i.e. relates a series of liquids derived from a single parental magma (Cox et al., 1979).

La/Yb ratio. While La is highly incompatible in both processes, Yb is clearly less incompatible than La during partial melting events in the presence of residual garnet ($D_{Yb}^{grt/melt}$ = 4.03; McKenzie and O'Nions, 1991), while it is only slightly less incompatible than La during fractional crystallization. Accordingly in the case of partial melting the La/Yb ratio decreases as the degree of partial melting increases, whereas in crystal fractionation the ratio of incompatible elements does not change as much, therefore producing a trend with a less steep slope.

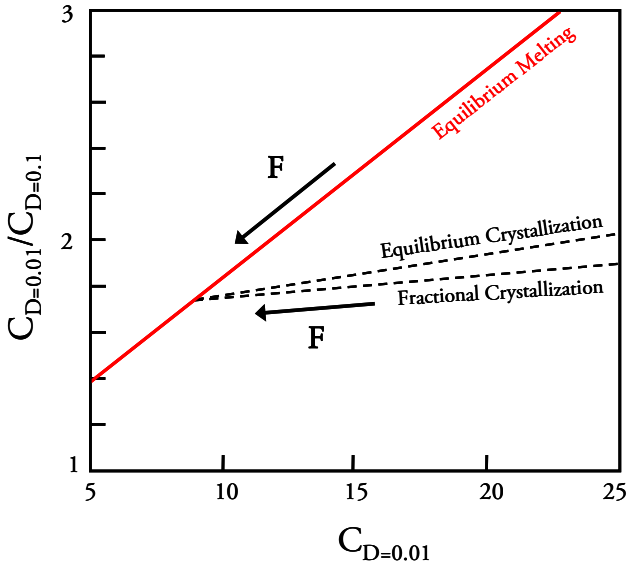

Figure 4.34 - Differential behaviour between partial melting and crystal fractionation, identified by plotting the ratio of a highly incompatible element by a less incompatible one versus the concentrations of the more incompatible (adapted from White, 2013). For all the processes considered, F represents the amount of liquid. So, increasing of F corresponds to an increase of partial melting degree to a decrease of the degree of evolution during crystallization.

Using La/Yb ratio against La (Fig. 4.35), it is possible to visualize that even though the majority of the studied Santiago variability can be explained by partial melting processes there is still some deviation that can be related with crystal fractionation events. However it must be kept in mind that the different La/Yb ratio on this diagram is mainly related with chemically heterogeneous mantle source or with distinct amounts of garnet.

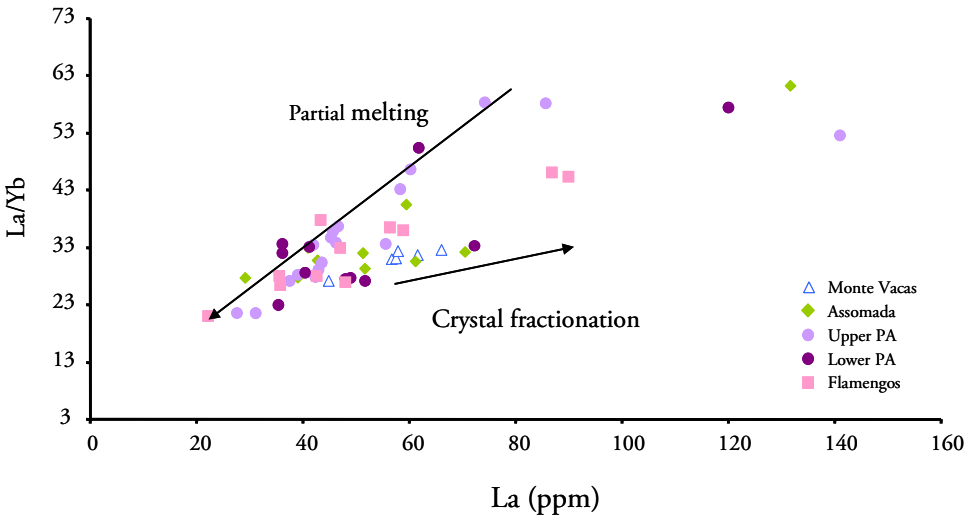

Figure 4.35 - La/Yb vs. La plot illustrating the action played by partial melting and crystal fractionation in the Santiago lavas differentiation process.

The heterogeneous character of Santiago magmas can also be inferred from the Ni vs. La diagram (Fig. 4.36) where it is also represented the contrasting effects of partial melting and fractional crystallization. Indeed in such diagrams crystal fractionation of a single primary magma tend to initially (high Ni content) produce a well defined quasi-vertical evolutionary trend which afterwards becomes asymptotic with the abysses for high evolution degree (low Ni). In this perspective the high dispersion of La concentration for rocks representative of primitive liquids (Ni> 150 ppm) is a clear indication for the existence of a wide variety of primary magmas in Santiago. However such variability is detectable even when considered rocks which, belonging to the same formation, were presumably erupted almost contemporaneously[16].

Such significant variability of the Santiago primary magmas, evident either when considered the entire data bank or a single formation, emphasizes the existence of heterogeneous mantle source, confirmed by the range of isotopic signatures (see 4.3), and/or variations on the partial melting degree. That such heterogeneity is evident for "coeval" rocks indicates that the Santiago magma plumbing system was characterized by small and/or ephemeral magmatic chambers inhibiting the homogenization of the magma compositions (e.g. Mata et al., 1998 and references therein). This percept is reinforced by the frequent

[16] Flamengos formation: 4.6 Ma; Pico da Antónia formation: 3.3 to 2.2 Ma; Assomada and Monte das Vacas formation: 1.1 to 0.7 Ma (Holm et al., 2008).

occurrence of mantle (peridotite) and crustal (gabbroic) xenoliths in Santiago lavas (e.g. Mendes, 1995) and by the relative rarity of rocks representative of evolved magmas (e.g. phonolites; see Alves et al., 1979).

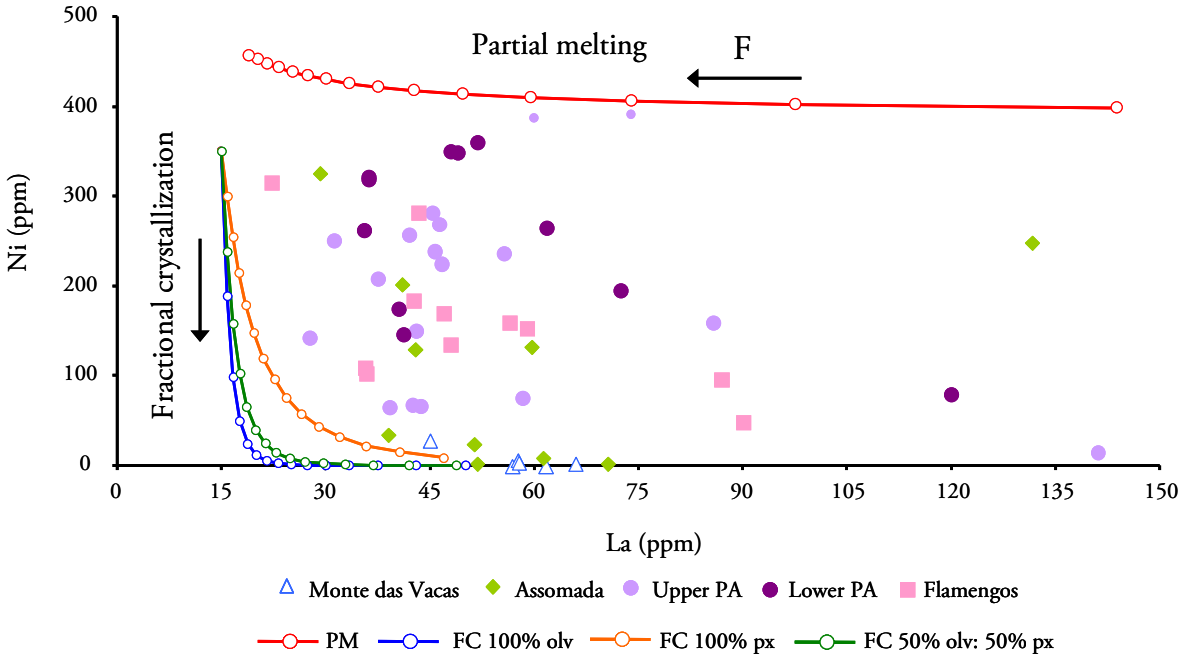

Figure 4.36 – Heterogeneous character of Santiago magmas demonstrated by highly variable La values as well as the contrasting effects of partial melting and fractional crystallization. Partial melting trend was modelled using modal batch melting assuming a source composition with 2x primitive mantle values and a paragenesis of 60 olv:20 opx: 9cpx: 6grt:4 amph. Partition coefficients of La and Ni are from Shaw (2006). Circular ticks represent consecutive increment of 1% degree partial melting. Fractional crystallization was modelled using the Rayleigh equation with an initial composition of 15 ppm for La and 350 ppm for Ni. Partition coefficients are from Shaw (2006). Circular ticks represent consecutive increment of 5% crystallization.

From Figure 4.36 it is evident that for the studied samples, Monte das Vacas and Assomada are the formations where the relatively evolved rocks (Ni< 150 ppm) are more abundant. In order to focus the attention on these formations it was constructed the diagram of Figure 4.37, only considering samples from Assomada and Monte das Vacas formations. This figure emphasizes the heterogeneous character of the Assomada magmas, given that samples ST-18 and ST-19 cannot be explained by fractionation of the least evolved compositions (ST-21: Ni=328 ppm; ST-20: Ni=203 ppm).

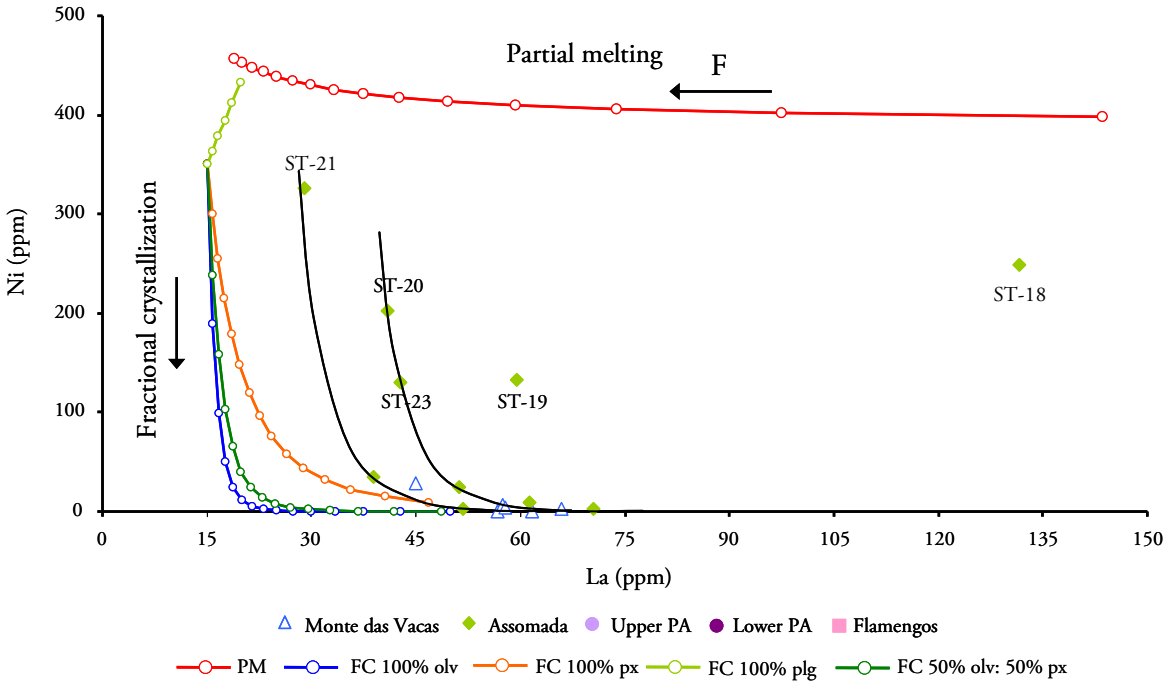

Figure 4.37 – Evolutionary trend of the Assomada and Monte das Vacas formations where samples ST-18 and ST-19 stand out of the trend implying their non-cogenetic character. Partial melting and fractional crystallization trends were modelled as explained in Fig. 4.36.

Even though the two less evolved samples cannot be considered strictly cogenetic all the Assomada samples, with the exception of the above mentioned ST-18 and ST-19, will be handled as a single comagmatic group in order to analyse the process of fractionation.

The analysis of the Ni vs. La diagram (Fig. 4.37) suggest that after an initial stage of olivine and/or olivine plus pyroxene fractionation (supported by petrographic evidence) the evolution process may be marked by the onset of plagioclase crystallization which would constrain the graphical expression of the liquid line of descent to a quasi-horizontal trend. However, it must be noted that this horizontal trend can only reflect the almost complete Ni depletion of residual liquids after the removal of ferro-magnesian phases at the initial stages of fractionation.

In order to check this situation the Sc vs. La diagram was analysed (Fig. 4.38). Here the observed trend seems to be compatible with olivine plus pyroxene removal all along the evolution process. However, if we assume an initial La concentration of 30 ppm and a partition

coefficient approaching zero, for this highly incompatible element, the more evolved sample (La=70 ppm) represent a liquid generated after more than 50% fractionation, a value difficult to reconcile with fractionation of olivine along all the evolution process. In this context the observed trend in the Sc vs. La diagram is interpreted as implying an initial phase dominated by olivine plus pyroxene removal followed by one where plagioclase fractionation counteract the effect of pyroxene crystallization.

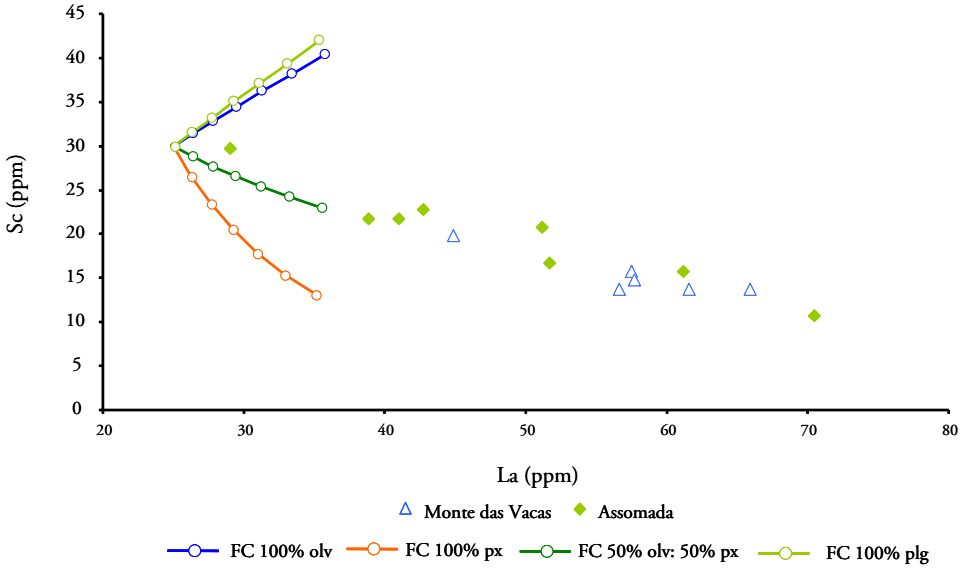

Figure 4.38 – Liquid line of descent for Assomada and Monte das Vacas formations explained by fractional crystallization of olivine and pyroxene in similar proportions. Fractional crystallization trends were modelled as explain in Figure 4.36.

The significant role of clinopyroxene fractionation is also endorsed by the compatible behaviour of V and Sc (Fig. 4.39) both of which have high partition coefficients for clinopyroxene ($D_V^{cpx/melt} = 4.0; D_{Sc}^{cpx/melt} = 2.3$; GERM, Geochemical Earth Reference Model, http://earthref.org/GERM). Vanadium can also be incorporated in oxide minerals ($D_V^{mag/melt} = 26$; Rollinson, 1993) but since there is a positive correlation between V and CaO, it seems more likely that, at least some of it is being fractionated by clinopyroxene.

The importance of pyroxene crystallization is also supported by lower than chondritic CaO/Al_2O_3 ratio for most of the lavas from Monte das Vacas and Assomada formations in opposition to that observed for the more primitive samples (Fig. 4.40) (see Clague and Frey, 1982)

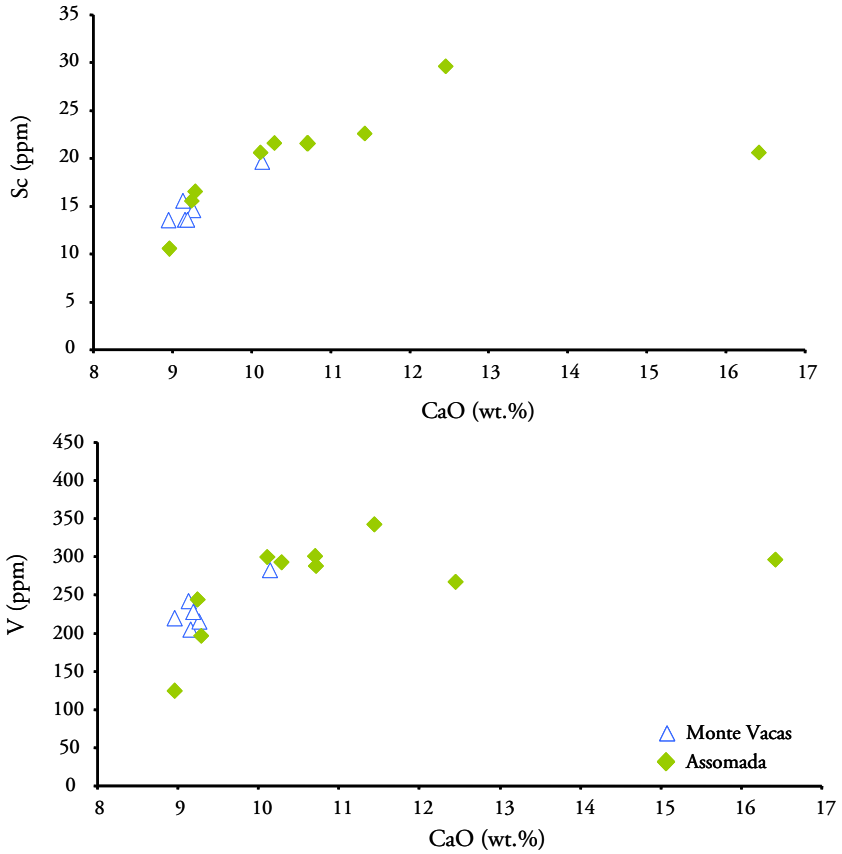

Figure 4.39 – Compatible behaviour of V and Sc in Monte das Vacas and Assomada formations.

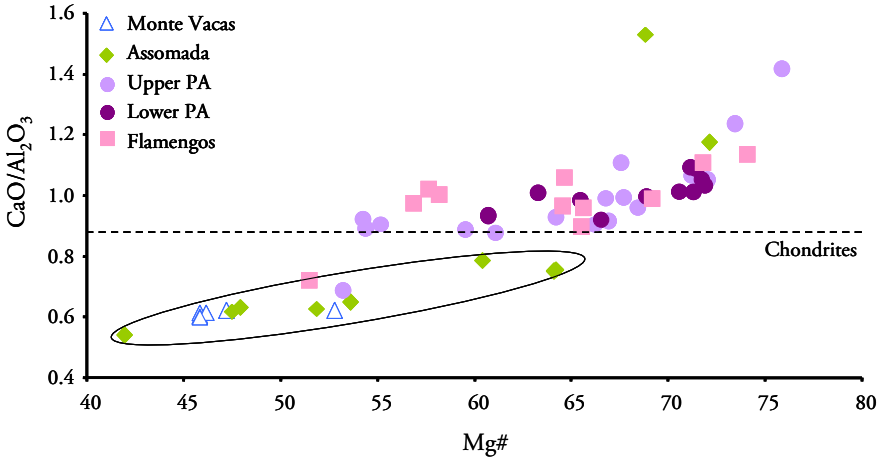

Figure 4.40 – Distinct CaO/Al_2O_3 ratios for Monte das Vacas and some Assomada formation samples.

From Figure 4.40 it can be inferred that the less evolved samples of Santiago are characterized by super-chondritic CaO/Al_2O_3 ratios. The probable cause for this characteristic will be discussed later (see 4.4.4). Even more significant are the super-chondritic TiO_2/Al_2O_3

ratios (Fig. 4.41) indicating a significant Ti-enrichment of Santiago lavas. This fact was recently emphasized by Prytulak and Elliot (2007) which consider the Cape Verde archipelago one of the most Ti-rich ocean islands in the world.

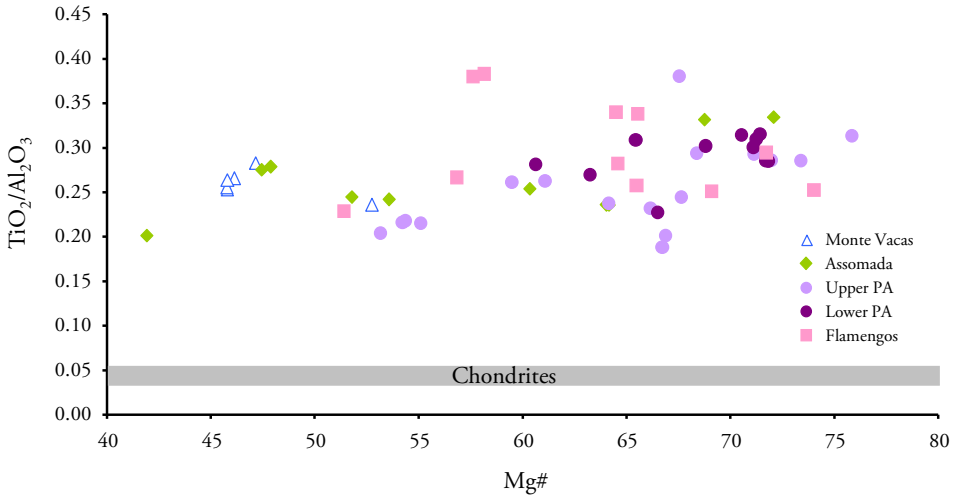

Figure 4.41 – Super-chondritic TiO_2/Al_2O_3 ratios portrayed by Santiago alkaline lavas (chondritic range from Clague and Frey, 1982).

4.4.3. Source heterogeneities

Santiago mantle source heterogeneities are evident from major and trace element variability as well as isotopic ratios observed in the studied lavas (e.g. see section 4.3). The nature, scale and causes of these heterogeneities can be multiple and distinct.

There are a number of causes that can contribute to a heterogeneous geochemical signature in magmas from a given igneous province. These include diverse partial melting percentages, metasomatism, minor mantle residual phases, shallow level processes, lithospheric influence, magma mixing, lithologic variability and contribution from distinct mantle components/end-members. In the next sections these possibilities will be studied and discussed in detail to better constrain Santiago lavas geochemical variability.

4.4.3.1. Lithologic heterogeneity in the mantle

4.4.3.1.1. Carbonated peridotite

The comparison of the compositions from primary/primitive lavas with experimentally obtained magma compositions can help to constrain Santiago mantle source conditions and processes. The distinctive high CaO concentration associated with the undersaturated character of Santiago lavas stands as a strong indicator of a carbonated mantle source. Studies concerning olivine melilitites generated at pressures below 3 GPa in the presence of $CO_2 \pm H_2O$, attests the importance of CO_2 in reducing the silica content of mantle derived melts due to suppression of near-liquidus crystallization of olivine and clinopyroxene against orthopyroxene stabilization (Brey and Green, 1975; 1977).

Dasgupta et al. (2007) performed partial melting experiments on two carbonated-bearing natural lherzolite compositions, PERC (fertile peridotite + 2.5 % CO_2) and PERC3 (fertile peridotite + 1.0 % CO_2). Composition analysis of near-solidus partial melts and associated crystal phases allowed Dasgupta et al. (2007) to conclude that the amount of dissolved CO_2 is a very significant factor resulting in enhanced CaO and diminished SiO_2 in peridotite partial melts. Experiments in volatile-free peridotite at 2-3 GPa leads to partial melts with CaO reaching 10.2 to 10.9 wt. % (Kogiso et al., 1998; Walter, 1998) as opposed to a maximum of 25 wt. % when dissolved CO_2 is at the highest concentration (Dasgupta et al., 2007) (Fig. 4.42).

Santiago primary magmas have a range of 11 to 16 wt. % CaO associated with less than 44 wt. % of SiO_2 plotting similar to those obtained from carbonated peridotite melt experiments and away from partial melts derived from volatile-free peridotite which are characterized by relative SiO_2 enrichment and lower amounts of CaO.

Herzberg and Asimow (2008) considering the importance in distinguishing between a volatile-free and carbonated peridotite mantle sources, suggested an estimated boundary in a SiO_2 vs. CaO diagram (Fig. 4.42) according with equation

$$\text{CaO (wt. \%)} = 2.318 \times \text{SiO}_2 \text{ (wt. \%)} - 93.626 \qquad (6)$$

obtained through the analysis of experimental data. Santiago primary lavas plot to the left side of the line confirming the carbonated peridotite mantle source.

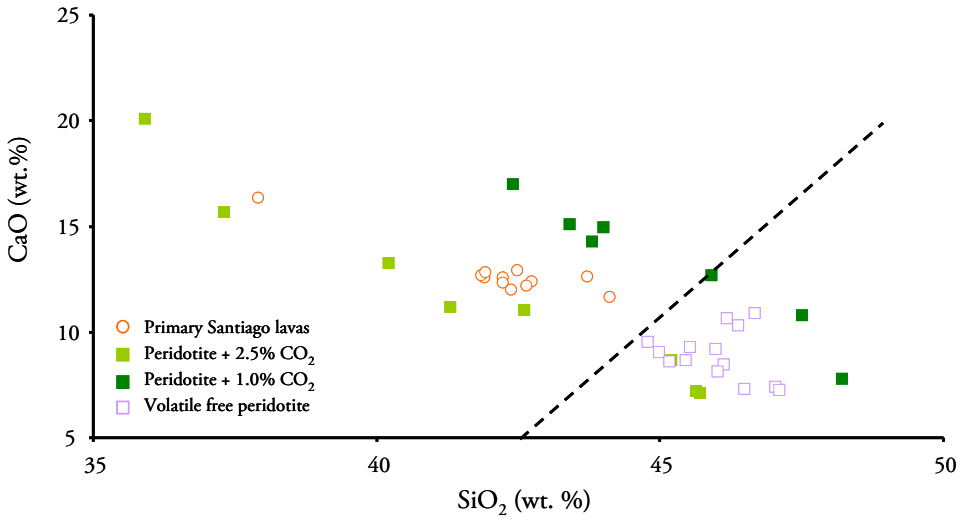

Figure 4.42 – CaO vs. SiO_2 contents of primary Santiago lavas, along with carbonate-bearing silicate partial melts from carbonated peridotite partial melting experiments at 3 GPa (Dasgupta et al., 2007) and experimental partial melts from volatile free peridotite at 3 to 7 GPa (Walter, 1998) (for purpose of comparison all the data was recalculated to 100% on a CO_2-free basis). The black dotted line represents an approximate limit that separates CO_2-enriched and deficient lavas (Herzberg and Asimow, 2008).

OIB which are characterized by an array of lithotypes ranging from melilitites to alkali basalts, as reported for the Cape Verde archipelago, are thought to be derived by small degrees (1-5 %) of partial melting from garnet peridotite with 0.1 – 0.25 wt. % CO_2 (Dasgupta et al., 2007). Experimental work done in the system CaO-MgO-Al_2O_3-SiO_2-CO_2 (CMAS-CO_2) by Gudfinnsson and Presnall (2005) confirms the gradation between kimberlite towards melilitite composition at low pressures and towards basaltic and picritic compositions near the CO_2-free lherzolite solidus at pressures below 4 GPa.

By plotting primary Santiago lavas (melanephelinites and melilitites) in Gudfinnsson and Presnall (2005) discrimination diagram of SiO_2/Al_2O_3 vs. MgO/CaO where three isobars are projected (3, 5, and 8 GPa), it can be shown that samples plot within the field of melts generated in equilibrium with garnet lherzolite in the CMAS-CO_2 system towards pressures of about 3 GPa and below (Fig. 4.43). For comparison carbonated and volatile-free peridotite partial melts are also projected (as in Fig. 4.42) and again there is an overlap of Santiago primary samples with the carbonated peridotites field.

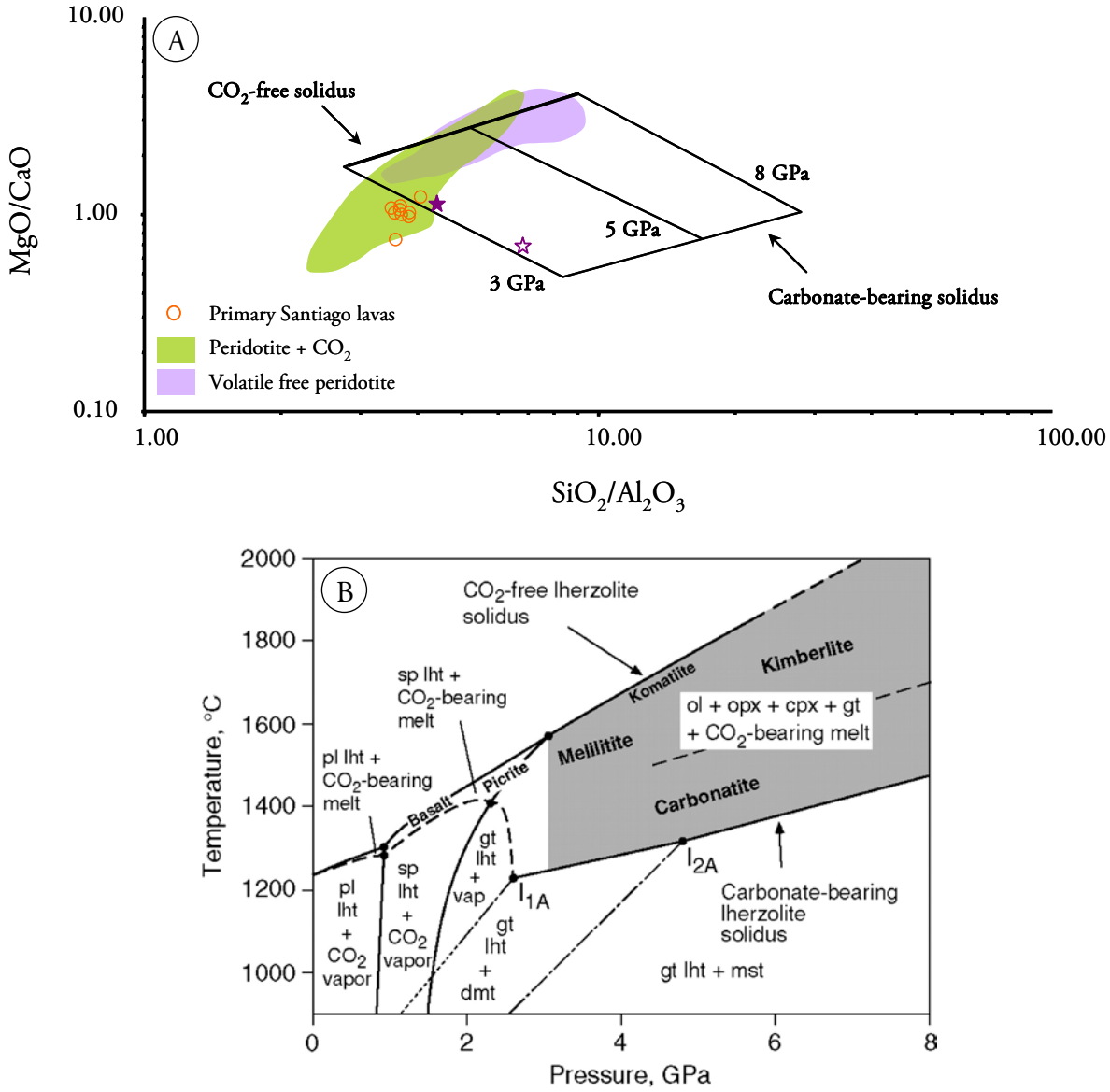

Figure 4.43 – (A) MgO/CaO vs. SiO_2/Al_2O_3 ratios of primary Santiago lavas. Also shown are the field of carbonated peridotite (Dasgupta et al., 2007) and volatile-free peridotite partial melts (Walter, 1998), as well as partial melts from carbonated phlogopite-garnet lherzolite (filled star) and phlogopite-garnet lherzolite (star) (see Thibault et al., 1992). The area between the CO_2-free and carbonated-bearing solidus and corresponding isobars, are from Gudfinnsson and Presnall (2005) and correspond to the marked grey area in (B) which corresponds to figure from Gudfinsson and Presnall (2005).

Thibault et al. (1992) made a rare experimental study concerning near-solidus melts formed from carbonated phlogopite-garnet lherzolite and phlogopite-garnet lherzolite at 3 GPa. In Figure 4.43A partial melts generated in this experiment are plotted and it can be seen that the one generated from phlogopite-garnet lherzolite (filled star) plots in close proximity to

Santiago primary lavas, attesting the probable presence of hydrous phases in mantle source paragenesis.

4.4.3.1.2. Carbonated silica-deficient eclogite/garnet pyroxenite

Santiago primary magmas are characterized by high FeO_t and TiO_2 contents which are higher than those portrayed by magmas formed from a carbonated peridotitic source (see Dasgupta et al., 2007) (Fig. 4.44).

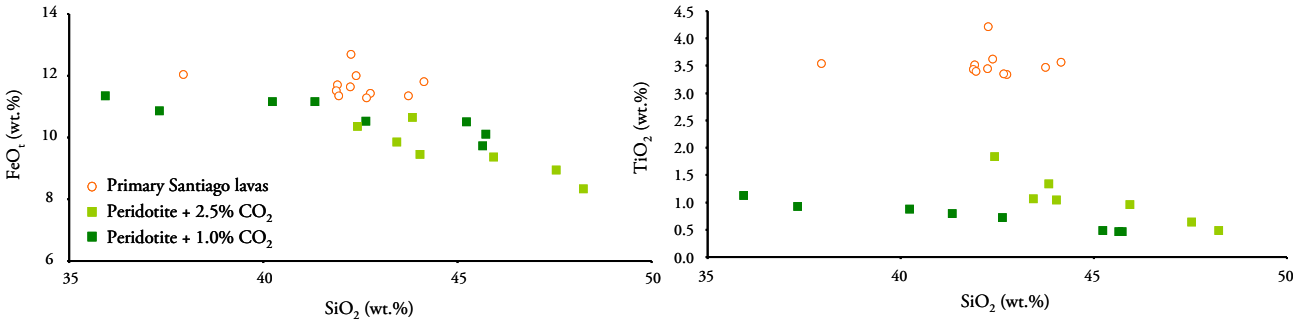

Figure 4.44– FeO_t and TiO_2 content of Santiago primary lavas compared with carbonate-bearing silicate partial melts from carbonated peridotite partial melting experiments at 3 GPa (Dasgupta et al., 2007).

These compositional difference, in major elements, could be ascribed to lithospheric thickness control, since melt concentration in SiO_2 and Al_2O_3 decrease and FeO_t and MgO increases with plate thickness which is consistent with increasing pressure of melting (Humphreys and Niu, 2009; Dasgupta et al., 2010). Also the increase in TiO_2 and P_2O_5 could be tied to decreasing extent of melting (limited due to thick lithosphere) since these elements are incompatible during mantle melting (Humphreys and Niu, 2009). However Dasgupta et al. (2010) points out that there is a significant dispersion and variability in major element data from OIB within thick lithosphere and even though lithospheric thickness can provide some control on magma compositions, there must be an additional source effect, since deep melting of peridotite cannot explain the observed dispersion on the OIB database.

The TiO_2 content of Santiago primitive lavas (2.5 to 4.4 wt. %) is high compared with many other islands (Prytulak and Elliot, 2007). These authors demonstrate that the minimum TiO_2 source content necessary to produce such high TiO_2 content in primitive OIB lavas

would be greater than the primitive mantle value, even if infinitesimally low partial melting degrees are considered, which implies the presence of a Ti-enriched component in the source.

There are several components and processes susceptible of increasing the Ti content of the OIB sources, such as: modally metasomatized mantle (Pilet et al., 2008), the lowering of Ti partition coefficient between residual minerals and melt due to high concentrations of CO_2 and the mixture of peridotite mantle melts with Ti-enriched melts derived from carbonated silica-deficient garnet pyroxenite (Prytulak and Elliot, 2007).

The expression "silica-deficient garnet pyroxenite" appears as an alternative to eclogite (formed by recycling of basaltic protoliths) since partial melting of the latter would lead to silica oversaturated rather than alkaline melts (Pilet at al., 2008). The origin of such silica-deficient pyroxenite is considered the result of deep recycling of oceanic crust previously affected by the extraction, during subduction, of silica-rich melts (Schiano et al., 2000; Hirschmann et al., 2003).

Dasgupta et al. (2010) ascribed the distinct FeOt-SiO_2 trend of OIB as the most convincing argument for major element heterogeneity of the mantle source. The observed shallower slope of the OIB trend (-0.22, including Santiago Island) is distinct from volatile free peridotite partial melts (-1.04), and even though silicate partial melts from carbonated peridotite display a similar slope, both groups do not overlap the OIB range (Fig. 4.45).

Santiago lavas plot between the fields of melts generated from carbonated peridotites and from silica-deficient eclogites in a position which, according to Dasgupta et al. (2010) would be occupied by melts coming from sources where, besides the carbonated peridotites, a silica deficient eclogite/pyroxenite is also present.

The contribution, location and mixing mechanisms of fertile lithologies with peridotite are still a matter of debate and an ongoing study (Sobolev et al., 2005, 2007; Dasgupta et al., 2006). It is important to emphasize that these components are not ubiquitous on OIB and are most commonly detected in islands located on thicker lithosphere (Dasgupta et al., 2010) (see Chapter 5).

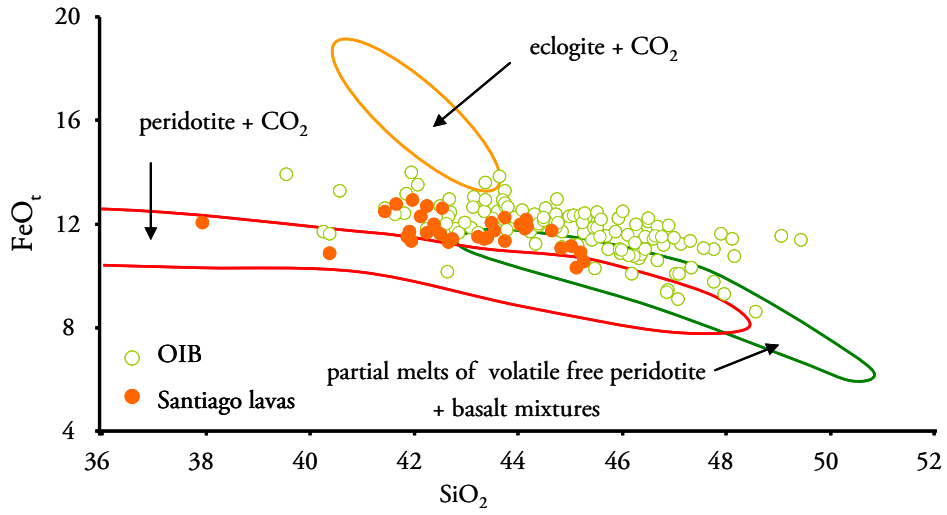

Figure 4.45 – FeOt-SiO_2 trend for Santiago primitive lavas and OIB (Dasgupta et al., 2010), along with carbonate-bearing silicate partial melts from carbonated peridotite partial melting experiments at 3 GPa (Dasgupta et al., 2007), volatile free peridotite–basalt mixture between 1.5 and 2.0 GPa (Kogiso et al., 1998) and carbonated silicate melts from a silica-deficient eclogite at 3 GPa (Dasgupta et al., 2006).

Le Roux et al. (2010) propose the use of Zn/Fe ratios for detecting lithologic components that diverge from normal peridotite, dominated by an olivine and ortopyroxene assemblage. Due to the distinct geochemical behaviour of Fe and Zn, between olivine/ortopyroxene ($K^{Zn/Fe}_{(olv/melt)} \approx K^{Zn/Fe}_{(opx/melt)} \approx 1$) and clinopyroxene/garnet ($K^{Zn/Fe}_{(cpx/melt)}$ and $K^{Zn/Fe}_{(grt/melt)} < 1$), Zn/Fe ratio is expected to be none or only slightly fractionated during partial melting of a peridotite source and strongly fractionated when clinopyroxene and garnet-rich lithologies are involved (Le Roux et al., 2010). Santiago primary lavas have a predicted mean[17] $(Zn/Fe)*10^4$ ratio of 12.23, very similar to the value reported by Le Roux et al. (2010) for the Cape Verde archipelago of 13.91±1.45, but distinct from the average peridotite value of 8.5 (extreme value is 11). Melts derived from sources enriched in clinopyroxene and garnet will yield $(Zn/Fe)x10^4$ ratios as high has 14 (melt derived by a theoretical source with 75% clinopyroxene and 25% of garnet).

It is important to note that the predicted $(Zn/Fe)x10^4$ ratio depends directly on the assumed MgO content of primary melts. In section 4.2.2.1., Santiago primary lavas where ascribed to be characterized by MgO>12 wt. % for example. If we assign an MgO content of

[17] The predicted $(Zn/Fe)x10^4$ ratio of Santiago primary lavas was calculated from the equation of the regression line obtained in the diagram $(Zn/Fe)x10^4$ vs. MgO (wt. %), for MgO = 12 wt. %.

13 wt.% for parental Santiago magmas, the $(Zn/Fe)x10^4$ ratios is reduced to 11.45, approaching the extreme value portrayed by peridotites. Even though the rise in MgO content will reduce the needed amount of an eclogite like component, they do not eliminate it.

Zeng et al. (2010) proposed a plot of total alkalis against TiO_2 to discriminate between all the possible mantle lithologies described and discussed above. Through the observation of Figure 4.46 it is apparent that Santiago lavas (both the larger primitive group and the more restricted primary group) shown a TiO_2 enrichment for a given total alkalis content compared with carbonated peridotite and garnet-pyroxenite (eclogite) melts. Once more, Santiago lavas plot in an intermediate position between melts produced from carbonated peridotites and those originated from carbonated silica deficient garnet pyroxenite (Fig. 4.46).

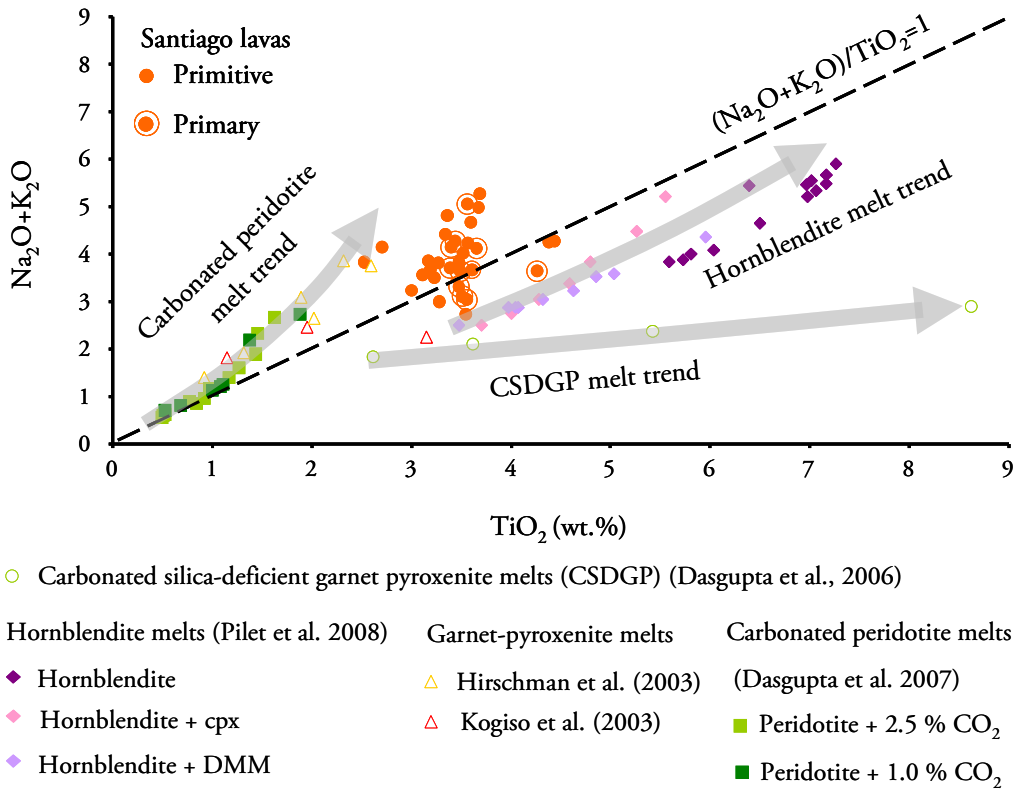

Fig. 4.46 - Total alkalis vs. TiO_2 diagram proposed by Zeng et al. (2010) to distinguish between contributions of different mantle lithologies. Trends developed by high-pressure melting experiments of different lithologies are represented.

The presence of pyroxenite or eclogite domains in the mantle has been widely accepted as well as their major influence in ocean island basalt generation (Hirschmann and Stolper, 1996;

Stracke et al., 1999; Kogiso et al., 2003; Hirschmann et al., 2003; Sobolev et al., 2005; 2007; Prytulak and Elliot, 2007; Dasgupta et al., 2010). According to Dasgupta et al. (2004) eclogitic/garnet pyroxenite domains occurring in the upper mantle (300-400km) can release small volume, highly mobile carbonatitic melts that can act as an important metasomatic agent for the surrounding peridotite. Indeed Keshav et al. (2006) and Gerbode and Dasgupta (2010) also defend that the pyroxenite source component is unlikely to be transported directly to the surface and that processes such as melt-rock reaction and melt-melt mixing may be involved, creating a refertilized lherzolitic source.

If these garnet-pyroxenite domains are considered to be remnants of recycled oceanic crust they must have kept their integrity during incorporation within OIB mantle source. Pyroxenites are expected to have lower Lu/Hf and Sm/Nd and higher Rb/Sr compared to peridotites which, with isotopic ingrowth will lead to enriched isotopic signatures (low $^{143}Nd/^{144}Nd$ and $^{176}Hf/^{177}Hf$ and high $^{87}Sr/^{86}Sr$) (Stracke et al., 1999).

Santiago primitive lavas display a negative correlation between $^{176}Hf/^{177}Hf$ and Gd/Yb ratios (Fig. 4.47), suggesting that the highest content of residual garnet (higher Gd/Yb ratios) is associated with the least radiogenic Hf signature, indicating the influence of ancient garnet-pyroxenite domains in Santiago mantle source more specifically within the plume.

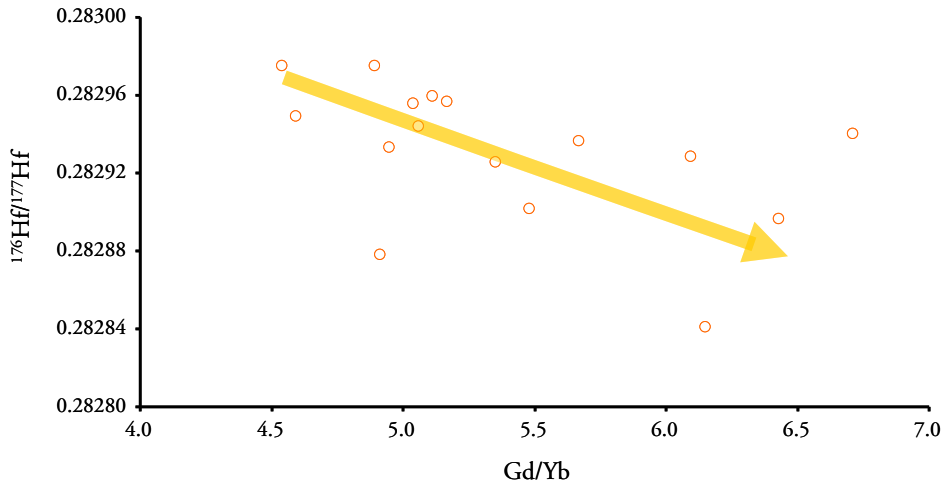

Figure 4.47 - Negative correlation between Hf isotopic ratio and the amount of residual garnet, represented by Gd/Yb ratio, in primitive Santiago lavas.

As already mentioned the high FeOt and TiO_2 content that characterize primary Santiago lavas was ascribed to the presence of carbonated silica deficient garnet pyroxenite, which is further corroborated by their negative correlation with $^{176}Hf/^{177}Hf$ (Fig. 4.48). The samples which exhibit the highest FeOt and TiO_2 contents are also those who are more Hf radiogenic. This poses another evidence for the presence of these veins/fragments within the plume since there is a correlation between major and incompatible trace element ratios (Fig. 4.46) with radiogenic isotopes ascribing an ancient signature.

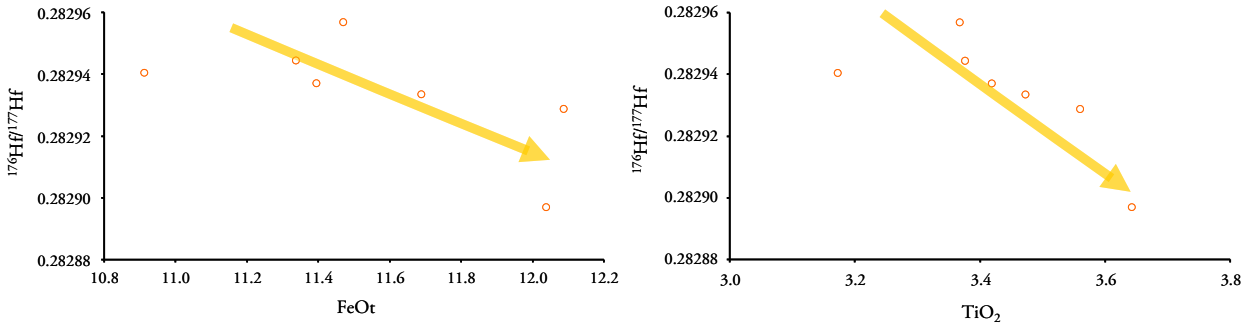

Figure 4.48 - Correlation between the high FeOt and TiO_2 content of primary Santiago lavas and the lowest $^{176}Hf/^{177}Hf$ isotopic ratio, attesting for the presence of carbonated silica deficient garnet pyroxenite in the mantle source.

The contribution/influence of carbonated silica-deficient garnet pyroxenite melts in Santiago magmas mantle source seems unquestionable from the above interpretations. The same was proposed recently by Barker et al. (2010) based in somewhat different arguments. These lithologies can be formed by a variety of processes and in very distinct contexts: subducted/recycled eclogitic crust, delaminated lower crust, metasomatic veins in the mantle, melt-rock reaction products (Sobolev et al., 2005) and fractionated cumulate assemblages of metasomatic agents (Pilet et al., 2008) amongst others. So it becomes necessary to try to identify the origin of this signature imprinted on primitive Santiago magma's geochemistry (see 4.6 for further discussion).

The role of olivine-free source components on the chemistry of magmas has also been addressed based on Ni contents of olivines occurring in primary/primitive magmas (e.g. Sobolev et al. 2005, 2007). This is based on Ni and Mn (Ca) distinct compatibilities between mantle minerals, Ni being highly compatible in olivine, while Mn and Ca have higher partition

coefficients for ortopyroxene and clinopyroxene. Some of Santiago high magnesium olivines (> 84 mol% Fo) present Ni contents as high as those reported for the Hawaiian shield-phase olivines interpreted (Sobolev et al., 2005; 2007) as reflecting the equilibration of this host magma with pyroxenitic (s.l.) residues (Fig. 4.49 see also Gurenko et al., 2009). This similarity could be used to confirm above indications for some olivine-free component at the Santiago source.

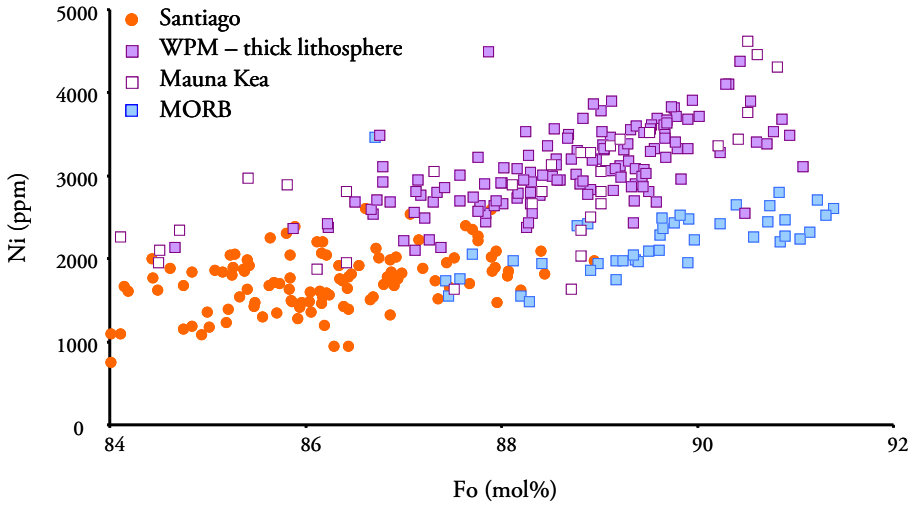

Figure 4.49 – Olivine data from Santiago primitive lavas, within plate magmatism (WPM) in thick lithosphere (70 km; Sobolev et al., 2007), Mauna Kea lavas (shield-phase Hawaiian magmatism; Garcia, 1996) and MORB (Sobolev et al., 2007).

However Sobolev et al. (2005, 2007)'s model has been strongly contested based on several types of arguments:

- the large amount of eclogite required (>60%) for the generation of OIB (Wang and Gaetani, 2007; 2008);
- the occurrence of Ni-rich lherzolite olivine samples by the Hawaii Scientific Drilling Project (Putirka and Ryerson, 2008);
- errors on the equation proposed by Sobolev et al. (2007)[18], for quantifying the pyroxenitic component, since it fails to include element concentration in magmas,

[18] X_{px}=3.48 - 2.071 x (100 x Mn/Fe), where X_{px} stands for the amount of pyroxenitic component in the source and Mn/Fe ratio to that present in olivines.

using only element ratios of olivines, which leads to a meaningless value since element concentration in magmas is essential in mixing calculations (Li and Ripley, 2010).

However olivines occurring in lavas erupted from regions with thick lithosphere are also characterized by high Ni contents (see Figure 4.49). Niu (2009) argued that the difference observed in olivine Ni content of basalts erupted in thick and thin lithosphere can be explained by the "lid effect", i.e., the melting pressure/temperature on the mantle increases with increasing lithospheric thickness, whereas $D_{Ni}^{olv/melt}$ decreases, implying that mantle melts derived from greater depths will be characterized by higher Ni content, leading to subsequent crystallization of Ni-rich olivines.

4.4.3.2. Mantle source mineralogy: a qualitative approach

The previous discussion already suggests that Santiago mantle source is probably an association of carbonated garnet-peridotite and silica deficient eclogite that could include hydrous minerals. Through further major and trace element analysis the residual mineralogy will be identified and discussed.

The strong HREE depletion relative to LREE and relatively high $(La/Yb)_{cn}$ values observed in samples with primitive characteristics, can be explained by the preferred incorporation of HREE in one of the mantle minerals. Among the most common and quantitatively significant mantle mineral, garnet has the highest partition coefficient for HREE ($2.0 < D_{HREE}^{grt/melt} < 5.5$; Shaw, 2006) suggesting that it can be the responsible for the fractionation from LREE making it a plausible residual phase in Santiago mantle source.

Variable MREE/HREE ratios allows the confirmation of HREE retention by residual garnet (Fig. 4.50) moreover this figure enables, as a first approximation, the assessment of the amount of residual garnet as well as of degree of partial melting involved in the genesis of Santiago magmas. Using Gd/Yb ratio against La (a proxy of the amount of partial melting due to its highly incompatible character) and a grid calculated for partial melting of lherzolite with different mineral paragenesis, but with an homogeneous composition (3x primitive mantle, Palme and O'Neill, 2003), it is perceptible that Santiago chemical range requires sources characterized by amounts of garnet varying more than 100%. Indeed assuming that the source

was characterized by the above mentioned composition the amount of residual garnet ranges from 6 to 14% (George and Rogers, 2002; Yokoyma et al., 2007)(Fig. 4.50).

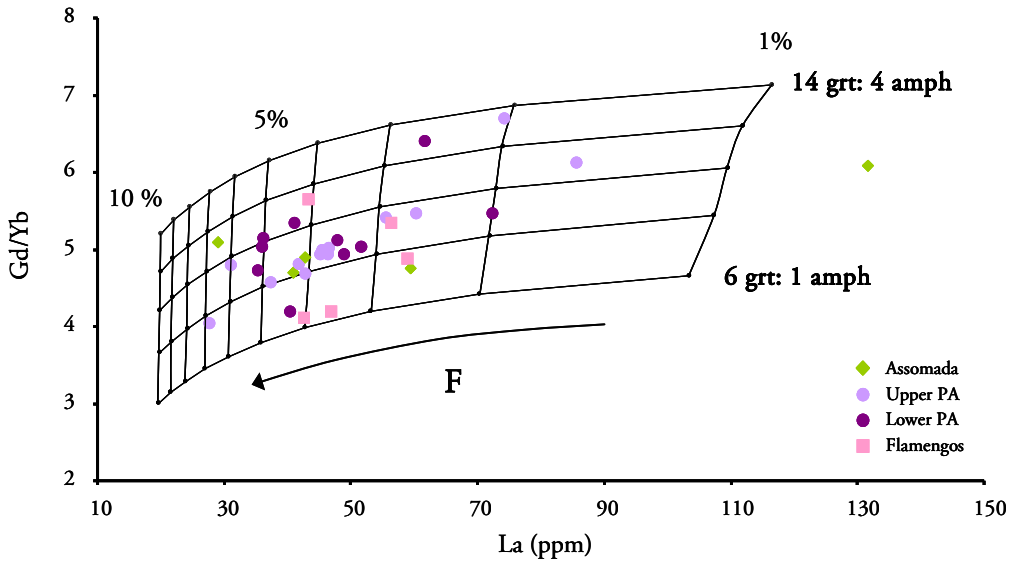

Figure 4.50 – Gd/Yb vs. La diagram for primitive Santiago lavas showing evidence for variable degrees of partial melting along with variable amount of residual garnet in the source. The grid represent modelling of non-modal batch partial melting of a source composition with 3x that of primitive mantle (Palme and O'Neill, 2003) and variable paragenesis (from olv:opx:cpx:grt:amph ratios of 58:18:6:14:4 to 58:18:17:6:1 and 10:10:20:20:40 for the rock and melt, respectively). Partition coefficients of La and Gd are from Shaw (2006) and Yb from Rollison (1993).

Even though the amount of garnet might seem high for a garnet lherzolite, it should be kept in mind that it has been established that Santiago mantle source is unquestionably heterogeneous at the lithologic level and high Gd/Yb ratios have already been assigned to the presence of garnet-pyroxenite domains in Santiago mantle source.

The presence of residual hydrous potassic minerals in Santiago mantle source have already been suggested due to the presence of strong K negative anomalies for some Santiago formations in primitive mantle normalized incompatible element patterns (see Figure 4.9). The distinct behaviour of K is evident when plotted against a strong incompatible element (Figure 4.51). It can be seen that Flamengos and Lower Pico da Antónia Formations display a positive La-K correlation (indicating that K behaves incompatibly) whereas K values in Upper Pico da Antónia Formation remain almost invariant regardless of the degree of partial melting

(represented by La concentrations) thus indicating a compatible behaviour, i.e. that the K concentration in such magmas are buffered by a K-rich residual mineral.

Assomada Formation shows a more variable K content suggesting that the presence of a residual mineral capable of retaining K was not ubiquitous along the magmatogenesis of this formation.

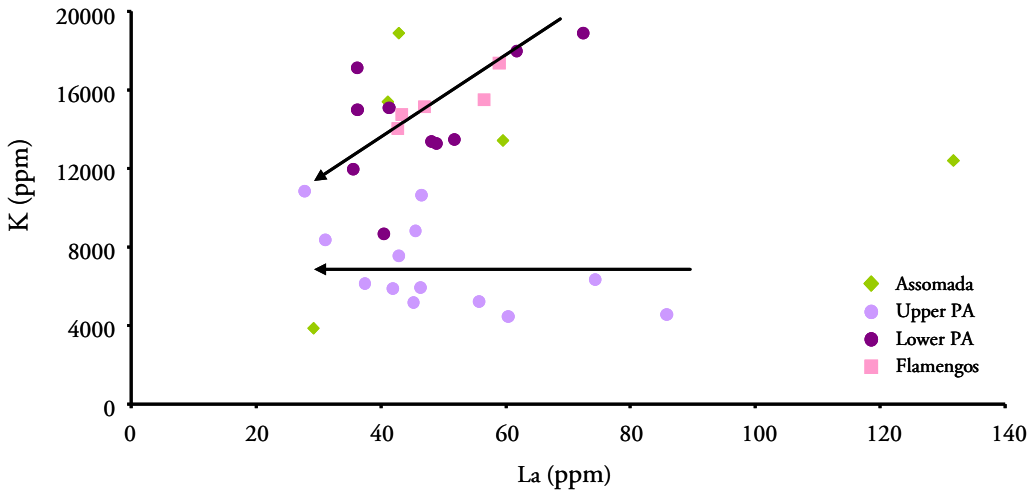

Figure 4.51 – Distinct potassium behaviour portrayed by Santiago formations.

The different slopes displayed by Santiago samples in La vs. La/K diagram (Figure 4.52) supports the distinct bulk partition coefficient for K. Through a simple modal batch partial melting modelling (Shaw, 1970) it becomes evident that samples from Flamengos and Lower Pico da Antónia (and some of Assomada) Formations were derived from a mantle source with none or only minor potassic residual mineralogy (source A). However the tendency depicted by the Upper Pico da Antónia data clearly follows a trend indicating that during melting $D_K \gg D_{La}$ thus pointing to the existence of a K-rich phase as a residue.

In order to distinguish between the two most probable residual potassic minerals, amphibole and phlogopite, Rb/K ratio was used for those formations previously identified as having a K-bearing phase (Fig. 4.53) (Francis and Ludden, 1995). The increase of Rb/K ratio with Rb requires that the bulk partition coefficient of K exceeds that of Rb, endorsing amphibole as the most probable candidate to K retention in the source according to distinct partition coefficients of these elements in both minerals

($D_K^{amph/melt} = 1.36$, $D_{Rb}^{amph/melt} = 0.22$ and $D_K^{ph\log/melt} = 3.6$, $D_{Rb}^{ph\log/melt} = 6.2$ Dalpe and Baker, 1994; LaTourette et al., 1995; Adam and Green, 2006).

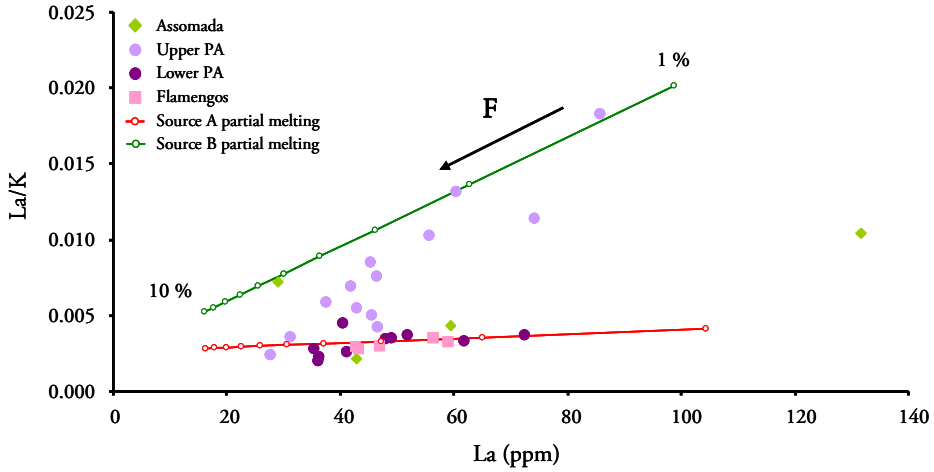

Figure 4.52 – Variable La/K ratios in Santiago primitive lavas. Also shown is modal batch partial melting (Shaw, 1970) of two distinct mantle source paragenesis (A) 58 olv: 18 opx: 11 cpx: 12 grt: 1 amph and (B) 58 olv: 18 opx: 7 cpx: 8 grt: 9 amph. Source composition is assumed to be 3 x that of primitive mantle (Palme and O'Neill, 2003). Partition coefficients are from Shaw (2006) and from the compilation made by Williams et al. 2004 (see also Appendix A5.1). Circular ticks on curves A and B represent consecutive increments of 1% degree partial melting.

To reinforce this hypothesis data from amphibole and phlogopite from xenoliths carried by alkaline lavas were also plotted in Fig. 4.53, confirming the strong influence of amphibole due to similar slope and collinear behaviour between their data and Assomada and Upper Pico da Antónia samples (Greenough, 1988; Jung and Hoernes, 2000).

However due to the apparent compatible behaviour of Ba in some samples (Fig. 4.54) and considering the partition coefficients of the pertinent K-bearing phases ($D_{Ba}^{amph/melt} \approx 0.22$ and $D_{Ba}^{ph\log/melt} \approx 3.6$; Adam and Green, 2006) the additional presence of residual phlogopite cannot be excluded completely. It should be emphasized that Ba is only compatible in samples characterized by very high concentrations of incompatible elements indicating that phlogopite only subsisted as residual during very low degree partial melting events. This percept is also endorsed by the high SiO_2-undersaturated character of these samples (melilitites and olivine melanephelinites).

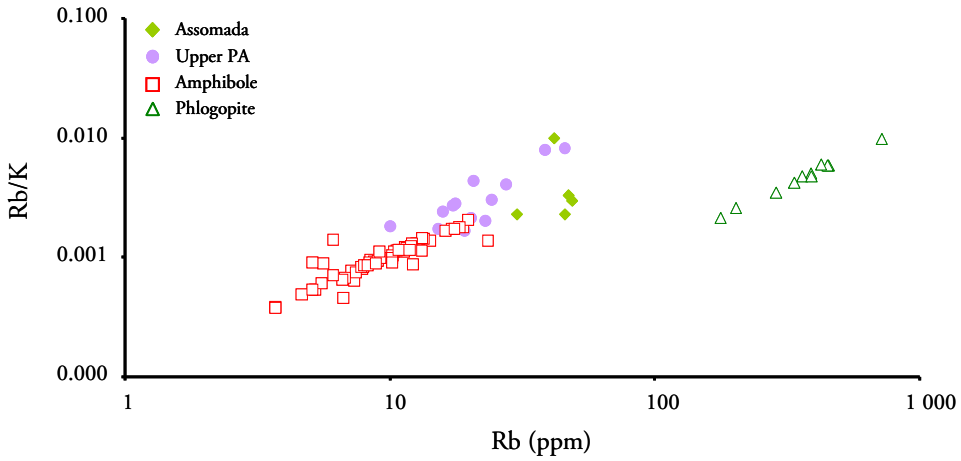

Figure 4.53 – Collinear behaviour between Upper Pico da Antónia and most of Assomada Formation samples and amphiboles occurring in mantle xenoliths in a log-log diagram. Phlogopite data is plotted for comparison purposes. Amphibole and phlogopite data are from O'Reilly et al. (1991), Yaxley and Kamenetsky (1999), Grégoire et al. (2000) and Moine et al. (2001).

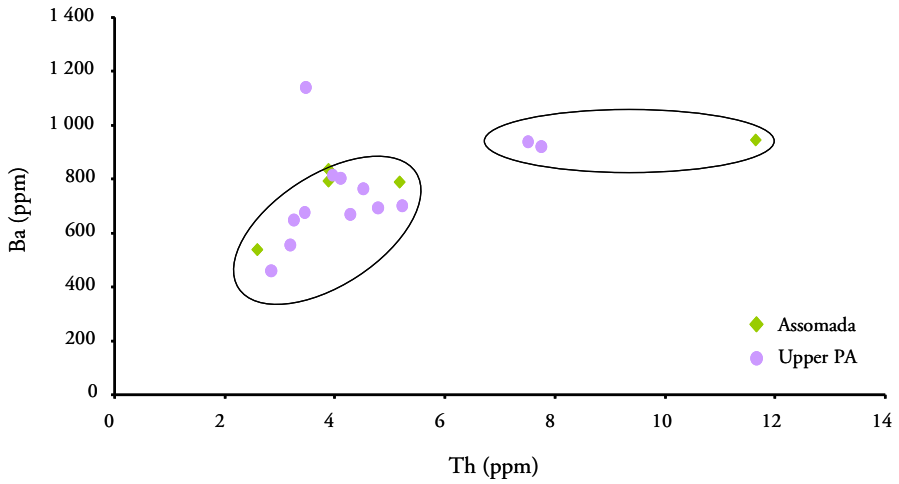

Figure 4.54 – Ba compatibility along high Th concentrations, corresponding to low degree partial melting events, in opposition to the majority of the samples for which Ba is incompatible.

4.4.3.3. Trace element inverse modelling constraints on residual mineralogy and degree of partial melting

From geochemical arguments exposed above (see 4.2.3, 4.4.3.1 and 4.4.3.2) first approximations were made to the complexity of the residual paragenesis with which magmas from Santiago equilibrated. However the discussion was made only on a qualitative base. In order to confirm/infirm the suggestions made above relatively to residual minerals and to

determine their relative proportions, the inverse modelling approach proposed by Class and Goldstein (1994) will be used.

The bulk partitioning ($D_a^{solid/melt}$) of a trace element a, between a melt and a residual paragenesis depends on the proportion of the mineral phases present. Considering incompatible elements the D for each paragenesis can be accessed from the variation on the degree of enrichment as function of variation on the degree of partial melting. This enables an indirect approximation to the relative proportion of residual minerals.

4.4.3.3.1 - Enrichment factors

In the Class and Goldstein's method the concentration of a highly incompatible element is chosen as an index of the degree of partial melting. The lowest (FL) and highest degree (FH) of partial melting is thought to be represented by the highest (C_{FL}) and lowest concentration (C_{FH}) of the selected element within each magmatic suite. According with the objective stated a set of incompatible elements were chosen and projected against the index element (see Fig. 4.55 for example).

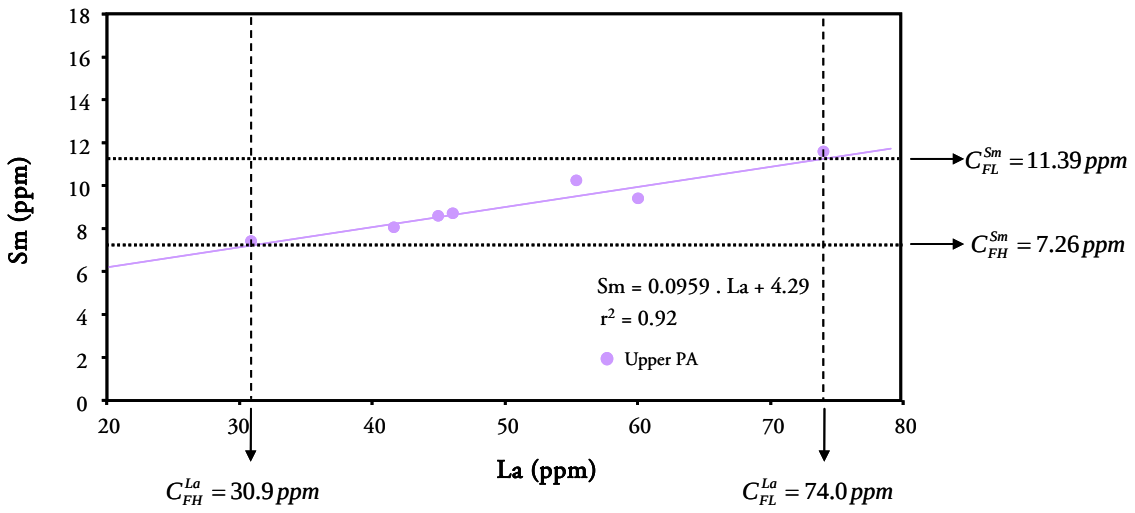

$$C_{FL}^{Sm} = 0.0959 \cdot C_{FL}^{La} + 4.29 = 11.39\,ppm \quad \text{(lowest F)}$$

$$C_{FH}^{Sm} = 0.0959 \cdot C_{FH}^{La} + 4.29 = 7.26\,ppm \quad \text{(highest F)}$$

Figure 4.55 – Schematic representation of the regression method to determine C_{FL} and C_{FH} (Williams et al., 2004). As an example it is showed the calculation of the concentrations of Sm, corresponding to the lowest and highest melting degree, for the Upper Pico da Antónia formation.

Through linear regression the concentrations, corresponding to the highest and lowest degree of melting, of all the elements were estimated (Class and Goldstein, 1994). An enrichment factor (E) is then calculated by dividing the two extreme concentrations of all the elements (C_{FL}/C_{FH}), which stands as the enrichment during the melting interval, reflecting the bulk distribution coefficient of the mantle source. So, when comparing two enrichment factors of elements X and Y, if $E_X>E_Y$ then $D_X<D_Y$ (Class and Goldstein, 1997; Williams et al., 2004).

One of the biggest advantages of this method is the absence of assumptions regarding the initial source composition, which is accomplished by combining the partial melting equations of an element in the highest and lowest degrees of melting (Class and Goldstein, 1994). If it is considered the occurrence of non-modal batch melting the use of Shaw's (1970) equation:

$$C_L = \frac{C_0}{D_0 + F \cdot (1-P)} \tag{7}$$

enables the formulation:

$$E = \frac{C_{FL}^x}{C_{FH}^x} = \frac{D^x + FH \cdot (1-P^x)}{D^x + FL \cdot (1-P^x)} \tag{8}$$

E: enrichment factor

C_{FL}^x : Concentration of the element x at the lowest degree of melting

C_{FH}^x : Concentration of the element x at the highest degree of melting

D^x: Bulk distribution coefficient of element x ($D^x = x_1 \cdot Kd_1 + x_2 \cdot Kd_2 + x_3 \cdot Kd_3 + ...$)

P^x: Bulk distribution coefficient of the minerals that make up the melt ($P^x = p_1 \cdot Kd_1 + p_2 \cdot Kd_2 + p_3 \cdot Kd_3 + ...$)

This method can only be applied to a set of samples with near primary compositions presumably derived from a chemically uniform source by partial melting (Class and Goldstein, 1997; Williams et al., 2004). For Santiago Island, and in accordance with the evidence

presented earlier from significant differences between sources of the various formations, each one is treated as a separate suite. This option is endorsed by isotopic data which reveals a tendency for intra-formation homogeneity.

The Assomada and Flamengos formations have only two samples that match the primary magma criteria. A new set of samples were added, widening the primary spectrum in order to better examine the trends that would be biased if the calculations were based only on two samples. The new set of samples, designated semi-primary, have Mg#>64, Ni>135 ppm, Cr> 350 ppm and MgO above 9.5 wt. %. The element chosen as the most incompatible is La and Monte das Vacas formation is not modelled due to its fractionated character.

In Table V.1 (Appendix V) the slopes, intercepts and r^2 values for the regressions against La, (that allows the calculation of the concentration for all the element in the highest and lowest degree of melting) as well as the enrichment ratios, are presented for the Assomada, Upper and Lower Pico da Antónia and Flamengos formations, being graphically represented in Figure 4.56.

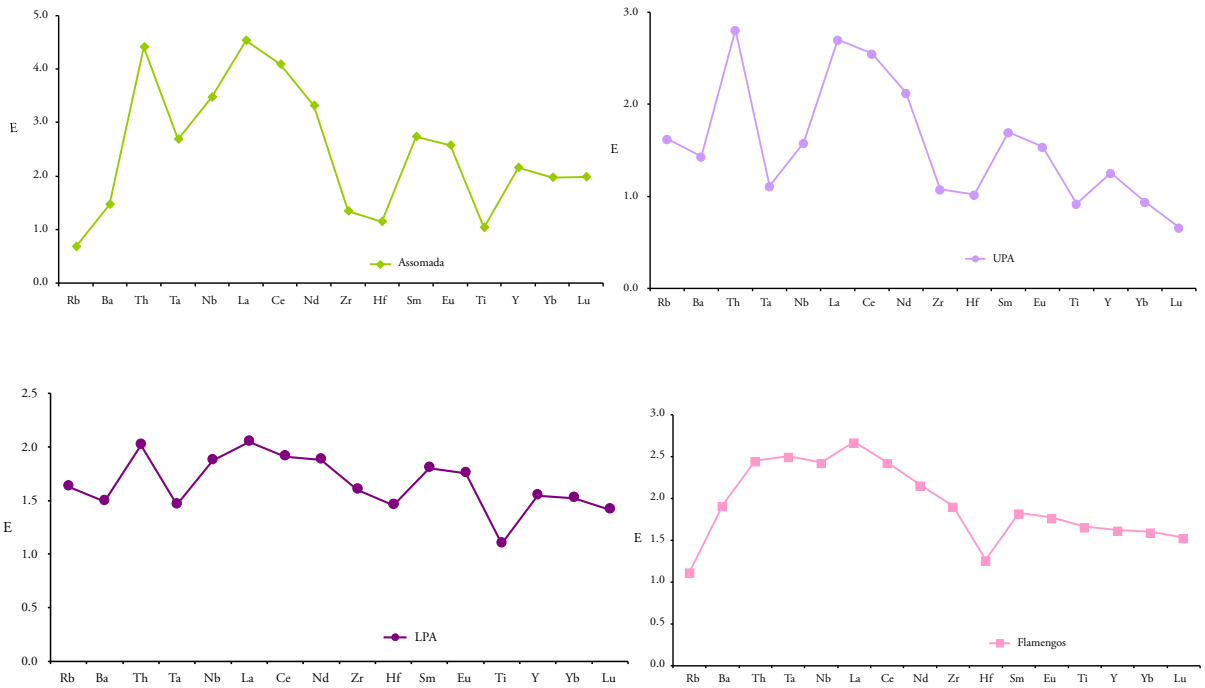

Figure 4.56 – Enrichment ratios for the Santiago formations plotted on a multi-element diagram

By the analysis of the enrichment patterns of Santiago formations (Fig. 4.56) it is evident the difference between them. The Assomada and UPA formations are characterized by negative anomalies in Ta, Nb, Zr, Hf and Ti, but show distinct behaviours of Rb and the HREE which allow the distinction between them. The LPA formation shows negative anomalies in Ba, Ta, Hf and Ti with enrichments in LREE and MREE. The Flamengos formation, as opposed to the more recent ones, lacks the negative Nb and/or Ta anomalies, but is characterized by negative anomalies in Rb and Hf.

It should be emphasized that this type of diagrams must not be regarded as primitive mantle normalized trace elements. In the enrichment ratio diagrams the E value depends only on the melting regime, mineral-melt partition coefficients and mantle source mineralogy, being independent of the initial composition of the mantle source (see equation 6; Class and Goldstein, 1994; Williams et al., 2004). In this perspective this methodology is a more robust approach to the determination of the residual mineralogy than the usual method using primitive mantle/chondritic normalized diagrams given that in this case the obtained pattern also depends on the source chemical compositions.

4.4.3.3.2 - Estimates of partial melting degree and modal composition of the source

In order to model the mantle source mineralogy using equation (6), the highest and lowest degrees of melting have to be known. Using an incompatible element, like La for which D approaches zero it can be seen, from equation (6), that for such element the ratios of concentrations obtained by the lowest and highest degree of melting (C_{FL}/C_{FH}) tend toward FH/FL, allowing the FH determination by assuming a FL (Williams et al., 2004).

Using a set of mineral-melt partition coefficients, melt modes, selecting a melting regime and knowing the melting interval, it is possible to replicate the modal mineralogy of the mantle source. This was done independently for each of the formations modelled, due to their intrinsic differences.

For the success of this kind of modelling is crucial the use of an appropriate data set of partition coefficients. Two sets of mineral-melt partition coefficients were used due to the difficulty encountered in modelling all the formations using the same set (Table V.2 and V.3, Appendix V). The difficulties may arise from the fact that Santiago mantle source was variably

affected by carbonate-rich metasomatism (see 4.4.4). Indeed, it is well known that partition coefficients are strongly dependent on melt composition (Adam and Green, 2003; Girnis et al., 2006). This could explain why the modelling for Assomada and Upper Pico da Antónia formations, those with the strongest evidences for carbonatitic metasomatism, was not successful when using partition coefficients determined in the presence of silicate melts.

According to experimental work done by Gudfinnsson and Presnall (2005) a continuous gradation from carbonatitic to silicate (kimberlitic/melilitic/melanephelinitc/basanitic) melts can be generated from CO_2 enriched mantle sources by progressive increase of partial melting degree. In accordance, this gradation is also expectable in metasomatic effects (Grégoire et al., 2000) implying the variation in element compatibility between the carbonatite and basanite melts range. Dasgupta et al. (2009) present trace element partition coefficients experimentally determined between natural fertile lherzolite and near solidus carbonatitic liquid for olivine, orthopyroxene, clinopyroxene and garnet. A major conclusion from the study of Dasgupta et al. (2009) is that the composition of the carbonated melt in equilibrium with garnet peridotite is distinct from erupted carbonatites, and so, models of carbonatite metasomatism should use melt compositions derived by high pressure partition coefficients instead of those of erupted carbonatites. Such statement is reinforced by recent studies (see Martins et al., 2010; see also 4.4.4) showing that carbonatitic-like metasomatic agent affecting Santiago mantle source is characterized by elemental signatures distinct from the outcropping carbonatites at Cape Verde archipelago.

Because the melt regime chosen to model was non-modal equilibrium partial melting, another variable inferred was the melt mode (P), which is the proportion of each of the source minerals contributing to the melt. The generation of the first melt (eutectic point) and the course of the melting path depend on a variety of variables as initial source composition, temperature, pressure and volatile concentration (White, 2013). Assuming the partial melting of a common lherzolite, it should be expected that the solid residue progressively loses amphibole/phlogopite, garnet and/or spinel, clinopyroxene and then orthopyroxene (Best and Christiansen, 2001). The values of the melt mode chosen for each modelled mantle source paragenesis took this in consideration.

The mantle source for the Assomada formation was modelled as a garnet lherzolite with significant amounts of a hydrous K phase (9% of amphibole/phlogopite), that can account for the behaviour of Rb and Ba (Fig. 4.57). The enrichment pattern of Assomada formation was mimicked using a melting interval of 2 to 9 % of the source.

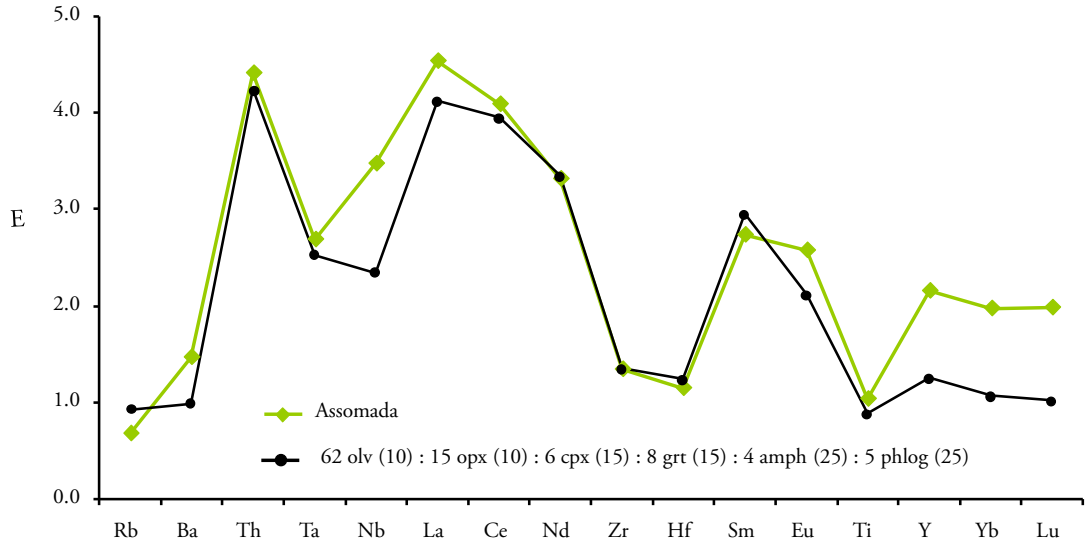

Figure 4.57– Enrichment ratios for the Assomada formation and the peridotite melting model. The mineral assemblage of the peridotite is indicated in the diagram, as well as the melt modes in parentheses. Partition coefficients are given in Table V.3 (Appendix V).

The Upper Pico da Antónia is less enriched, relatively to the Assomada formation, with the modelling implying the generation from a garnet-amphibole lherzolite with a partial melting interval of 3 to 7% (Fig. 4.58).

For this formation two enrichment patterns are presented, the difference being the clinopyroxene/amphibole ratio and also the melt modes. In lherzolite A, the enrichment is higher than in lherzolite B, due to the greater amount of clinopyroxene and, even though the melt mode of the amphibole was raised, it was not enough to account for the observed enrichment in Rb and depletion in Ba. Lherzolite B has a higher amount of amphibole however it does not meet the enrichment seen in the Upper Pico da Antónia pattern.

Ilmenite is often considered a frequent metasomatic phase along with amphibole and phlogopite, accommodating HFSE and LILE (Moine et al., 2001). In order to better fit the

modelled mantle source, a small amount of ilmenite was added improving the enrichment pattern.

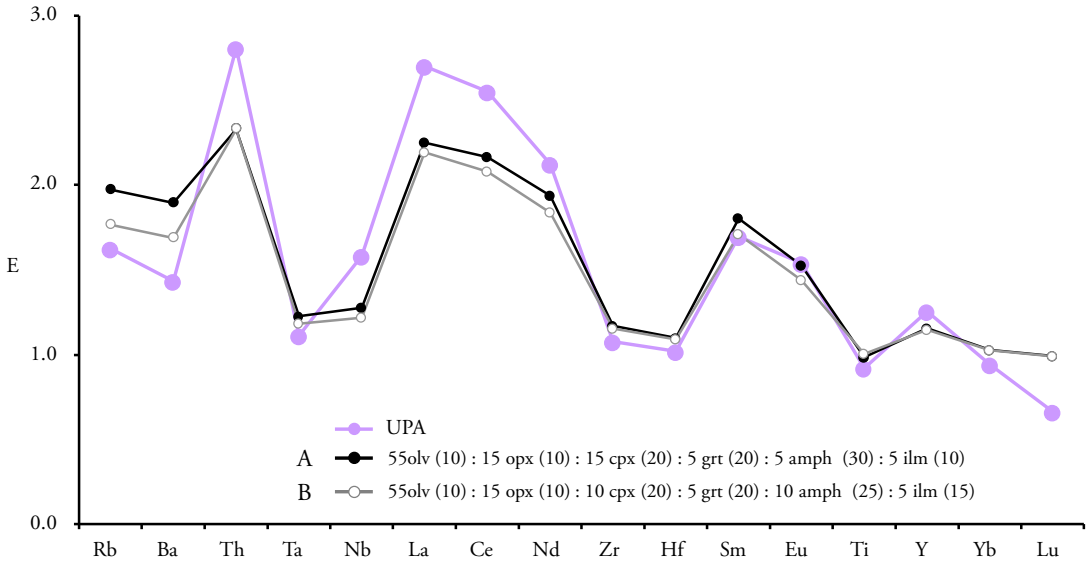

Figure 4.58– Enrichment pattern for the Upper Pico da Antónia (UPA) formation and the peridotite melting models. The mineral assemblages of the peridotites are indicated in the diagram, as well as the melt modes in parentheses. Partition coefficients are given in Table V.3 (Appendix V).

Since the Lower Pico da Antónia and Flamengos formations show less evident signs of carbonatitic metasomatism, the set of partition coefficients used in the Assomada and Upper Pico da Antónia formations (Table V.2, Appendix V), do not allow the satisfactory modelling of their source mantle enrichment patterns. For the oldest formations a set of partition coefficients for mineral-silicate melt, compiled by Williams et al. (2004), is then used (Table V.3, Appendix V).

The mantle source model that gave a better fit to the Lower Pico da Antónia pattern, was 4 to 7% partial melting of a lherzolite (Fig. 4.59). Even thought the negative anomalies in K, are less evident in the primitive mantle normalized diagram, according with the trace element inverse modelling, the need for the presence of a hydrous K phase is obvious, to account for the behaviour of Rb and Ba. The addition of a very small amount of amphibole (2%) is necessary to adjust the Ba and Rb value.

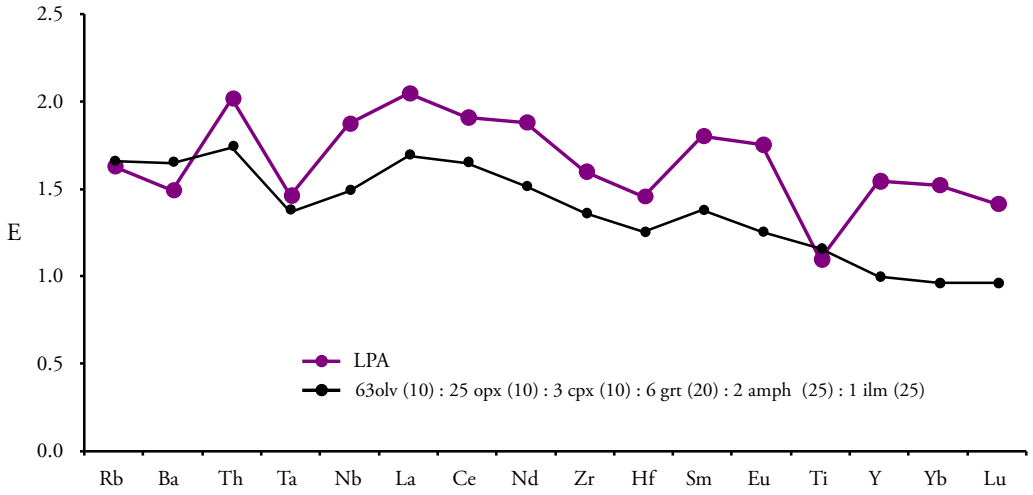

Figure 4.59– Modelled enrichment pattern for the source of Lower Pico da Antónia (LPA) formation and respective lavas. The mineral assemblages of the peridotites are indicated in the diagram, as well as the melt modes in parentheses. Partition coefficients are given in Table V.2 (Appendix V).

As for the Lower Pico da Antónia formation, the mantle source modelled for Flamengos formation is a garnet-lherzolite with small amounts (2%) of a hydrous K phase (amphibole and phlogopite) (Fig. 4.60). The difference between the two is the higher degree of partial melting modelled for the latter, twice as much (8 to 16%). In the enrichment pattern of Flamengos formation it is evident a very low value for Hf, due to the very extreme values reported by the selected samples. Since it seems very unlikely that this could be explained by the presence of a residual mineral, it is considered not representative of the source mineralogy but associated with heterogeneities in the source.

From inverse modelling it is clear that Santiago mantle source is heterogeneous in respect to residual mineralogy and also on the effects of carbonatitic metasomatism, with magma being always generated by small degree partial melting events (Table 4.4). This analysis corroborates the earlier qualitative approach to the residual paragenesis made by Martins et al. (2003) allowing, in addition, the quantification of each mineral phase involved, as well as the discovery of probable subordinate minerals, not identified so far (e.g. ilmenite).

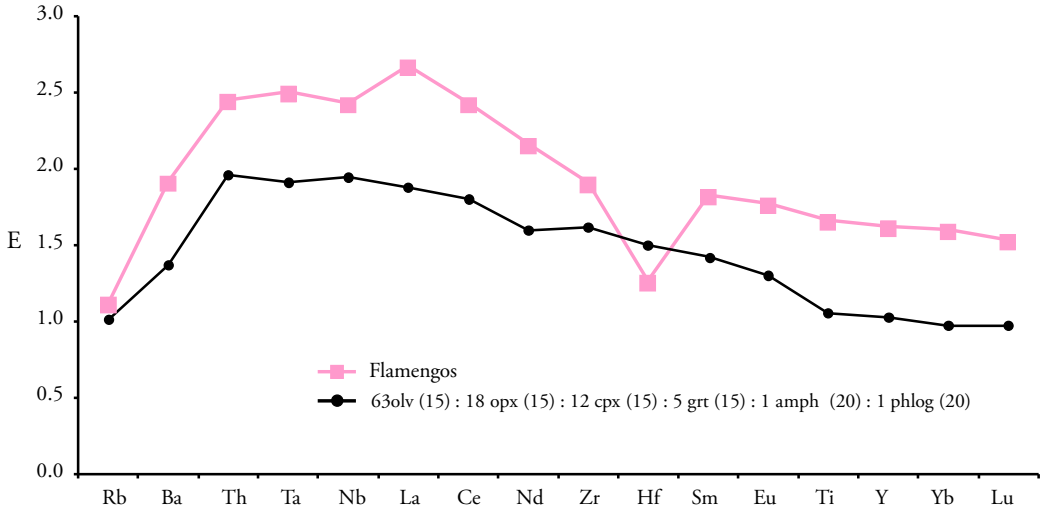

Figure 4.60– Enrichment pattern for the Flamengos formation and respective mantle source modelling. The mineral assemblages of the peridotites are indicated in the diagram, as well as the melt modes in parentheses. Partition coefficients are given in Table V.2 (Appendix V).-

Table 4.4 – Mantle residual paragenesis and degree of melting inferred for Santiago magmas

Formation	Residual mineral proportion	Degree of melting
Assomada	62 olv: 15 opx: 6 cpx: 8 grt: 4 amph: 5 phlog	2 – 9 %
Upper Pico da Antónia	55 olv: 15 opx: 15 cpx: 5 grt: 5 amph: 5 ilm	3 – 7 %
	55 olv: 15 opx: 10 cpx: 5 grt: 10 amph: 5 ilm	3 – 7 %
Lower Pico da Antónia	64 olv: 25 opx: 3 cpx: 5 grt: 2 amph: 1 ilm	4 – 7 %
Flamengos	63 olv: 18 opx: 12 cpx: 5 grt: 1 amph: 1 phlog	8 -16 %

4.4.4. Mantle metasomatism

The highly variable major, trace and isotopic geochemical compositions that characterize intraplate OIB are generally considered to reflect deep seated mantle components that are entrainment in mantle plumes (Zindler and Hart, 1986; Hart, 1988; Weaver, 1991; Stracke et al., 2005), including recycled veined/metasomatized oceanic or continental lithosphere (e.g. Pilet et al., 2005, 2008).

Metasomatism is a subsolidus modification of the chemical composition of a rock through the action of an invasive percolating agent, which is in disequilibrium with the host material (Best and Christiansen, 2001). There is still much debate about the physical and chemical nature of metasomatic agents, however low degree silicate-carbonated melts or fluids

dominated by C-O-H components are the most commonly described and discussed (Odling, 1994).

Metasomatic events can be subdivided in cryptic and modal/patent (Dawson, 1984). Modal metasomatism is identifiable given that hydrous or other secondary mineral phases, in addition to the normal mantle mineralogy, are developed. When the modifications are restricted to geochemical enrichment or depletion processes without mineralogical changes it is designated as cryptic.

Ultramafic xenoliths constitute an important source of knowledge on the nature and evolution of the lithospheric mantle since they are testimonies of mantle mineral paragenesis and subsequent process, such as metasomatic events, prior to or during entrainment in the host lavas that carry them to the surface. Lavas generated by low degree partial melting events are also valuable tools in deciphering the occurrence of metasomatized domains that often characterizes the sources of oceanic intraplate magmatism.

The geodynamic setting of the Cape Verde archipelago, implanted on old and thick oceanic lithosphere, makes it an ideal location for the study of magma-lithosphere interaction and other shallow level processes that can alter the magma during its ascent and how these events contribute to OIB variability.

4.4.4.1. Petrological and geochemical evidences from Santiago peridotitic/lherzolite xenoliths

Lithospheric xenoliths carried by Santiago lavas show evidence of modal metasomatism. Noticeable mineralogical features include the occurrence of late kaersutite, phlogopite and calcite associated with alkali-rich (up to 14.4 wt% Na_2O+K_2O) glasses and the development of secondary olivine + clinopyroxene + spinel assemblages (Mendes, 1995) (Fig. 4.61). Replacement of orthopyroxene by newly formed clinopyroxene + olivine suggests the interaction of a lherzolite/harzburgite host rock and a metasomatic agent with a_{SiO2}^{melt} too low to be in equilibrium with orthopyroxene under lithospheric P-T-conditions (e.g. Kogarko et al. 2001). According to Yaxley et al. (1991) the metasomatic agent is probably carbonate-rich as can be inferred by the following reactions:

$$CaMg(CO_3)_2 + 2MgSiO_3 = CaMgSi_2O_6 + 2\,MgCO_3 \quad (9)$$
(melt) (opx) (cpx) (magnesite)

$$4MgSiO_3 + CaMg(CO_3)_2 = CaMgSi_2O_6 + 2Mg_2SiO_4 + 2CO_2 \quad (10)$$
(opx) (melt) (cpx) (ol)

$$4MgCrAlSiO_6 + [Na_2CO_3+SiO_2] = 2NaCrSi_2O_6 + 2Mg(Al,Cr)_2O_4 + Mg_2SiO_4 + CO_2 \quad (11)$$
(opx) (melt) (cpx) (sp) (ol)

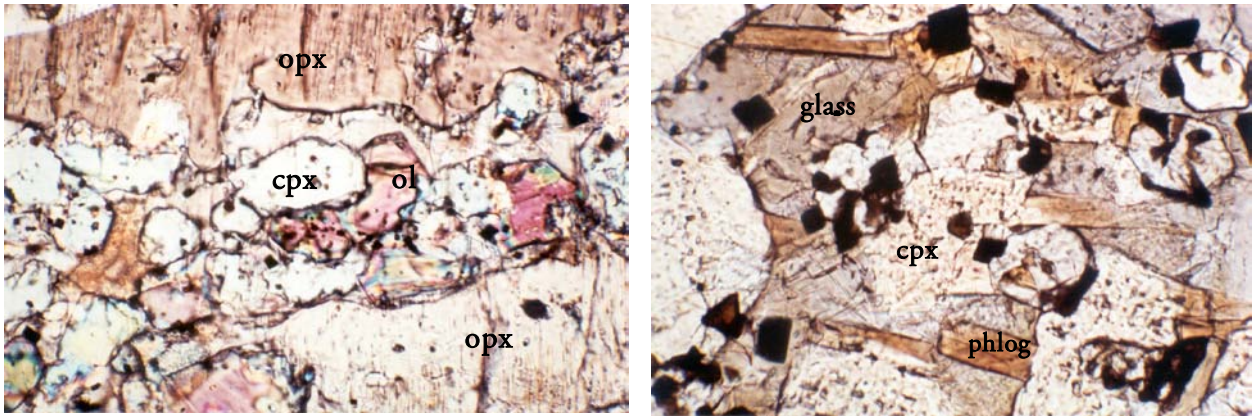

Figure 4.61 - Photomicrographs of thin sections showing mineralogical characteristic of modally metasomatized lherzolites.

Furthermore, the high Cr# of spinels may indicate mantle–melt interactions as well, producing the dissolution of clinopyroxene + orthopyroxene + low Cr/Al spinel and the formation of Cr-enriched spinels. Kelemen and Dick (1995) found that variations in Cr-numbers relative to Ti contents in spinels constitute reliable indicators to distinguish metasomatic products (characterised by enrichments in both Cr# and Ti) from residual melting products (characterised by decreasing Ti and increasing Cr#). Without an unequivocal Cr# - Ti trend, spinels from modal metasomatized Santiago lherzolites indicate a simultaneous increase in both Cr# and Ti (see Mendes, 1995).

The presence of glass associated with reaction zones within lherzolite-harzburgite xenoliths have been explained by several mechanisms, such as: incipient melts of garnet-pyroxenites

domains (Schiano and Clocchiati 1994; Klemme et al. 2002), partial melting product of low solidus phases (amphibole, apatite, phlogopite and carbonate) (Yaxley and Kamenetsky, 1999; Ban et al., 2005; Shaw, 2009), low degree partial melting of the mantle (Perinelli et al., 2008), interaction with magma during transport (Shaw, 1999; Shaw et al., 2006) and metasomatic processes in the mantle (Bonadiman et al., 2005).

Glass compositions reported by Mendes (1995) for Santiago lherzolites are very similar to those presented by Bonadiman et al. (2005) and within the range described by Ryabchikov et al. (1995) for spinel lherzolites/harzburgites from Sal Island (Table 4.5). It is worth mentioning that the Sal xenoliths described by Ryabchikov et al. (1995) do not include hydrous phases, unlike those from Santiago that are characterized by the presence of phlogopite, amphibole and carbonate.

Table 4.5 - Glass compositions of Santiago and Sal lherzolite/harzburgites.

	Santiago (S-180)	Santiago (S-194/3)	Sal	Sal
wt. (%)	Mendes (1995)	Mendes (1995)	Bonadiman et al. (2005)	Ryabchikov et al. (1995)*
SiO_2	62 -64	59 - 61	59 – 64	58 – 67
TiO_2	0.2 – 0.3	0.1 – 0.3	0.4 – 1.7	0.3 – 1.6
Al_2O_3	20 - 23	19 – 20	17 – 20	16 - 23
FeOt	0.04 – 0.14	0.64 – 0.77	0.7 – 1.2	0.3 – 1.7
MgO	0.00 -0.15	0.4 – 0.8	0.3 – 1.6	0.1 – 8.7
CaO	1.0 – 4.1	0.0 – 0.7	0.2 – 2.5	1.0 – 4.2
Na_2O	4.3 – 8.4	4.1 – 8.1	3.9 – 6.1	0.3 – 6.7
K_2O	1.3 – 4.7	6.2 – 9.5	6.6 – 8.7	1.8 – 8.1

* The range does not consider all the analyses by Ryabchikov et al. (1995) since some of the analyses reported as glass show extremely high concentrations of MgO, resembling quenched orthopyroxene.

The analyses reported in Table 4.5 for Santiago's lherzolite glasses show chemical differences between them, specifically higher concentrations of SiO_2, CaO and lower K_2O in sample S-180 in comparison to S-194/3. This may be partially attributed to the composition of metasomatic agent given that, at the reaction zone, in addition to secondary clinopyroxene, olivine and spinel, sample S-180 shows phlogopite and K-feldspar, while sample S-194/3 has carbonate.

Shaw et al. (2006) defend that reaction zones and associated glass observed in lherzolites/harzburgites in Sal Island are due to reaction between the host lava (or similar) and orthopyroxene, from xenoliths refuting the results from Bonadiman et al. (2005) that ascribe the alkali-rich glasses to remnants of a kimberlitic metasomatic melt. However, glass compositions reported by Shaw (1999) for dissolution of orthopyroxene in basanitic magma, which are used in the conclusions drawn by Shaw et al. (2006), are more enriched in FeOt (4.5 – 10.7 wt.%), CaO (1.9 – 15.5 wt.%) and MgO (1.6 – 14.7 wt.%), than to those occurring naturally in the Cape Verde xenoliths. Also, in the experiments by Shaw (1999) no hydrous minerals were formed, suggesting that the glasses present in Santiago xenoliths can be the result of distinct processes.

The glass composition reported by Perinelli et al., (2008) in experimental studies performed to simulate metasomatic events induced by alkaline melts (melanephelinite) in the lithosphere, also allow to discard this hypothesis for Santiago lherzolite glasses due to their depletion in SiO_2 (42-55 wt. %) and enrichment in TiO_2 (2 – 4 wt. %) and MgO (1.2 – 9.4 wt. %) as compared with the reported for Santiago xenoliths (see Table 4.5).

The transport-related breakdown of a metasomatic assemblage present in the xenoliths as the source for the glass can also be ruled out since the melting of these phases will produce melts that are enriched in CaO (3 - 9 wt. %), FeO_t (3 – 5 wt. %) and MgO (2 – 8 wt. %) as opposed to what is identified in Santiago (c.f. Yaxley and Kamenetsky, 1999; Ban et al., 2005; Shaw, 2009). Mendes (1995) had also discarded this hypothesis based on the absence of relics of pre-existing minerals as well as the low CaO content that characterize Santiago's glass.

4.4.4.2. The nature of the metasomatic agent: petrological and geochemical evidence from xenoliths

The presence of carbonates in lherzolite reaction zones stand as a powerful indicator of the carbonate-rich nature of the metasomatic agent (Fig. 4.61). The presence of carbonates is rare in xenoliths essentially due to decarbonation reactions during exhumation (Rosatelli et al, 2007). However their occurrence in xenoliths has been described in oceanic and continental lithospheric mantle associated with LIP's, subduction zones and mantle plumes (Yaxley et al., 1998; Delpech et al., 2004; Rosatelli et al., 2007 and references there in; Su et al., 2010),

suggesting that metasomatism by carbonate-rich fluids/melts can be more common than it could be inferred from the rarity of carbonates in xenoliths.

Indeed several models have been proposed to explain the carbonate presence in mantle xenoliths all of them with some connection with carbonate rich melts which can result from silicate/carbonatite immiscibility affecting a carbonated silicate melt, extreme fractionation or from very low degree of partial melting (Rosatelli et al., 2007 and references there in). The lack of more extensive geochemical data concerning these carbonate does not allow any conclusions to be drawn concerning the carbonate genesis, however the association with a carbonate rich melt seems undeniable.

The role of carbonate-rich melts is also compatible with the evidence for ortopyroxene transformation in clinopyroxene and olivine as can be inferred from the reactions reported by Yaxley et al. (1991) (see 4.4.4.1.).

Indeed the transformation of refractory harzburgite/lherzolite into secondary clinopyroxene-rich lherzolite assemblages observed in Santiago metasomatized lherzolites is consistent with experimental data on carbonatite melt-peridotite equilibrium within the mantle (e.g. Dalton and Wood, 1993). From those experiments it is known that carbonatite melt stability (in equilibrium with mantle lherzolites) is restricted to high pressures; upon decompression, decarbonation reactions (enstatite + dolomite = diopside + forsterite +CO_2) between components in the carbonatite and peridotite wall-rocks induce the consumption of primary orthopyroxene with the loss of CO_2-rich fluids (e.g. Yaxley and Green, 1996) that were partially retained as carbonic fluid inclusions in the newly formed olivine + clinopyroxene of the Santiago lherzolites (see Mendes, 1995).

Carbonatite melts are ephemeral (Yaxley and Green, 1996). Thus, when leaving their stability field (by decompression and/or by infiltrating depleted mantle domains), carbonatite melts react with lithospheric orthopyroxene, producing sodic Cr-diopsidic clinopyroxene and forsteritic olivine and releasing a CO_2-rich fluid, temporarily imposing a low-$a_{SiO_2}^{melt}$ environment at the reaction/melting front (Matveev et al., 2001). According to Ballhaus (1993), carbonatitic melts may also inherit large amounts of "excess" oxygen when they segregate from their sources; upon infiltration into the shallower upper mantle these melts are

capable of causing both the metasomatism and related oxidation that apparently accompanied lithospheric enrichment processes at the Santiago Island magma sources.

All these features, coupled with the development of metasomatic carbonate-bearing plus hydrous phases (calcite, kaersutite, phlogopite) and low Al_2O_3 and TiO_2 contents in orthopyroxene and clinopyroxene, strongly suggest that the metasomatic agent in the Santiago lherzolites was rich in carbonate and H_2O (Yaxley et al., 1998). Moreover, incompatible element enrichment with strong fractionation of elements (usually) not affected by silicate magma differentiation provides further support for the involvement of carbonatites in the metasomatic process. Indeed, the very low whole-rock Ti/Eu values exhibited by the Santiago (modally metasomatized) lherzolites (Ti/Eu= 892 to 1874 compared with 7914 of primitive mantle; Palme and O´Neill, 2003) are inconsistent with silicate metasomatism (e.g. McPherson et al., 1996).

4.4.4.3. The nature of the metasomatic agent: geochemical evidences from Santiago lavas

From the above discussion it can be concluded that lithospheric xenoliths present in Santiago lavas show evidence for metasomatic processes, such as the occurrence of hydrated or carbonated phases. Modal metasomatic events create low solidus and highly enriched lithospheric domains, particularly prone to melting in conditions of continued re-heating (e.g. Mata et al., 1998; Späth et al., 2001). It is well known that under the low degrees of melting required to generate the silica-undersaturated magmas such as those from Santiago, residual phases other than the major upper-mantle mineral components may be present (see 4.4.3.2). It was demonstrated (see 4.4.3.3) that Santiago lavas where generated by low percent of partial melting (< 8%). This allowed the anticipation that their composition presents evidence from equilibration with such minor, low-solidus phases.

For Santiago it can thus be envisaged a model involving the contamination of plume magmas by melts generated in low-solidus metasomatized lithosphere domains and leaving those hydrous minerals as melting residues.

4.4.4.3.1. Nature of the metasomatic agent

The physico-chemical properties of fluids and melts led to the conclusion that melts (carbonatites or alkali silicates) are more likely to be mantle metasomatic agents than CO_2-H_2O rich-fluids (e.g. Coltorti et al., 2000).

The variability associated with metasomatic melts can be strongly influenced by even small variations in the degree of melting as well as modifications imposed by chromatographic processes during mantle migration (Coltorti et al., 2000). The use of lava compositions in order to discriminate between different metasomatic agents must take into account the experimental knowledge of trace element partition coefficients and their dependence on temperature, melt composition and other thermodynamic variables (P, fO_2, a_{SiO2}^{melt}) (Girnis et al., 2006, Dasgupta et al., 2009) as well as experimental data concerning the nature of the metasomatic agents (Coltorti et al., 2000).

Since the parameters mentioned above (composition of the metasomatic agent and partition coefficients) are inferred experimentally a variety of results and interpretations are expected, making the unambiguous identification of the metasomatic agent's nature a difficult task.

According to experimental work (Gudfinnsson and Presnall, 2005), a continuous gradation from carbonatitic to silicate (kimberlitic/melilitic/melanephelinitic/basanitic) melts can be generated from CO_2-enriched mantle sources by a progressive increase in the degree of partial melting. All these melts are characterised by low viscosity having a strong capability to percolate in mantle rocks, reaching a maximum for carbonatites (0.01 to 0.1 Pa at temperatures above 500ºC; Dobson et al., 1996) (e.g. Hammouda and Laporte, 2000). Carbonate-rich melts are physically and chemically distinct from their silicate counterpart, particularly with respect to their low viscosity and density (Gasparik and Litvin, 2002). Because the dihedral angles between carbonate melts and silicate minerals are very low, carbonatites are characterised by high infiltration diffusibility ($1.8x10^{-9}$ $m^2.s^{-1}$; Hammouda and Laporte, 2000), being particularly prone to penetrative infiltration/reactions (see also Yaxley et al., 1998) (Fig. 4.62).

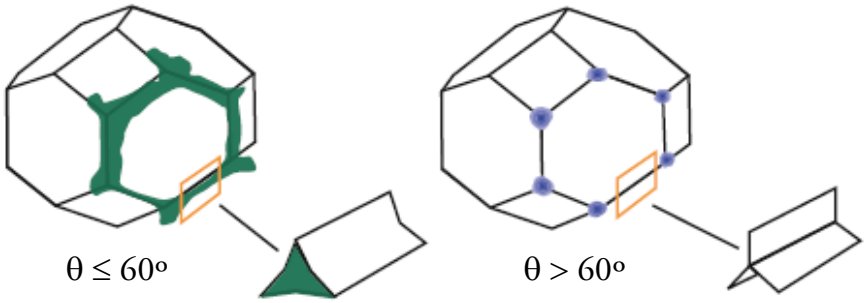

Figure 4.62 - The rate of grain-boundary infiltration, a process essential for metasomatic events, depends on the interfacial energy which is intrinsically linked with the composition of the fluid. Carbonate and silicate melts have low wetting angles, enabling the formation of a continuous interconnection of melt (figure from O'Reilly and Griffin, 2012).

Its consumption by reactions and its dissemination through the mantle inhibits magma pooling and segregation, which together with low CO_2 mantle content could explain the scarcity of carbonatites (Hammouda and Laporte, 2000) and probably also the lack of outcropping carbonatites with geochemical signatures similar to those inferred for the Santiago metasomatic agent.

Considering the batch melting equation of Shaw (1970) (equation 5), it can be concluded that melt enrichment relative to its source progressively approaches 1/F as F tends to zero. Such carbonatitic melts, produced by very low degrees of partial melting (<< 1%; e.g. Rabinowicz et al., 2002), are thus highly enriched in incompatible trace elements, leaving a strong chemical imprint on the metasomatized mantle domains; upon melting, these will transfer such enrichment characteristics to the magmas.

Significant differences in partition coefficient values experimentally determined in the presence of carbonatite or silicate melts result from distinct melt structures occurring with the change from O^{2-} to CO_3^{2-} as the principal coordinating or complexing anion (Klemme et al., 1995; Blundy and Dalton, 2000). This enables the determination of the nature of the metasomatic agent. Provided that a continuous series exists from carbonatite to silicate melts generated from CO_2 enriched sources, a gradation would be expected for the metasomatic effects (Grégoire et al., 2000). In this context, we will consider as carbonatitic melts those with

enough CO_2 to have a behaviour mimicking that experimentally determined for carbonatitic magmas.

Experimental studies indicate that carbonatite melts will have marked depletions in Al, Ga, HREE, Ti and Zr relative to Nb, LREE and alkali/alkali earth elements. Klemme et al. (1995) suggested that low Ti/Eu is the most powerful tool to recognize carbonatite metasomatism. Rudnick et al. (1993) proposed that high Ca/Sc and low Al/Ca can be used to evaluate the occurrence of carbonatite metasomatism in the upper mantle, whereas Ionov et al. (1993) argued that high Sr/Sm can be a signature of carbonate-related metasomatism.

All these geochemical features are characteristic of some of the Santiago magmas. Indeed, primitive lavas characterized by more pronounced negative K anomalies display Ti/Eu ratios substantially below primitive mantle values (down to 3300) which correlates negatively with Ca/Sc. Ti/Eu also correlates negatively with the degree of melting, as measured by Th contents, reflecting the melting of a carbonatitic metasomatized source, which (owing to their lower solidus) was preferentially sampled during lower degrees of melting (Fig. 4.63) (see Mata, 1996; Mata et al., 1999).

Recently, White (2007) reported that among the OIBs there are trace element ratios that are remarkably uniform (e.g. Pb/Ce= 0.036, Nb/U= 48.8) (see also Hofmann et al., 1986). However there are specific islands that show statistically significant differences. The Cape Verde archipelago was identified as one of these cases, being characterised by higher Nb/U (56.8 ± 16.8, in Santiago) and lower Pb/Ce (0.030 ± 0.003, in Santiago) relative to other OIB being ascribed to the action of carbonatitic metasomatism in the mantle due to enrichment in Nb and depletion in Pb as expected for carbonatitic melts. However Nb/U and Pb/Ce do not correlate with Ti/Eu and Ca/Sc, suggesting that at odds with White (2007) proposal the "abnormal" values, these ratios in Cape Verde is not due to carbonate rich-metasomatic events.

Notwithstanding all that has been said, it is important to acknowledge that several studies suggest that near-solidus melts from a carbonated peridotite mantle may not be identical to erupted carbonatites (Rudnick et al., 1993, Girnis et al., 2006, Foley et al., 2009, Dasgupta et al., 2009). Consequently several geochemical features considered to be sensitive indicators of carbonatite metasomatism may be inappropriate.

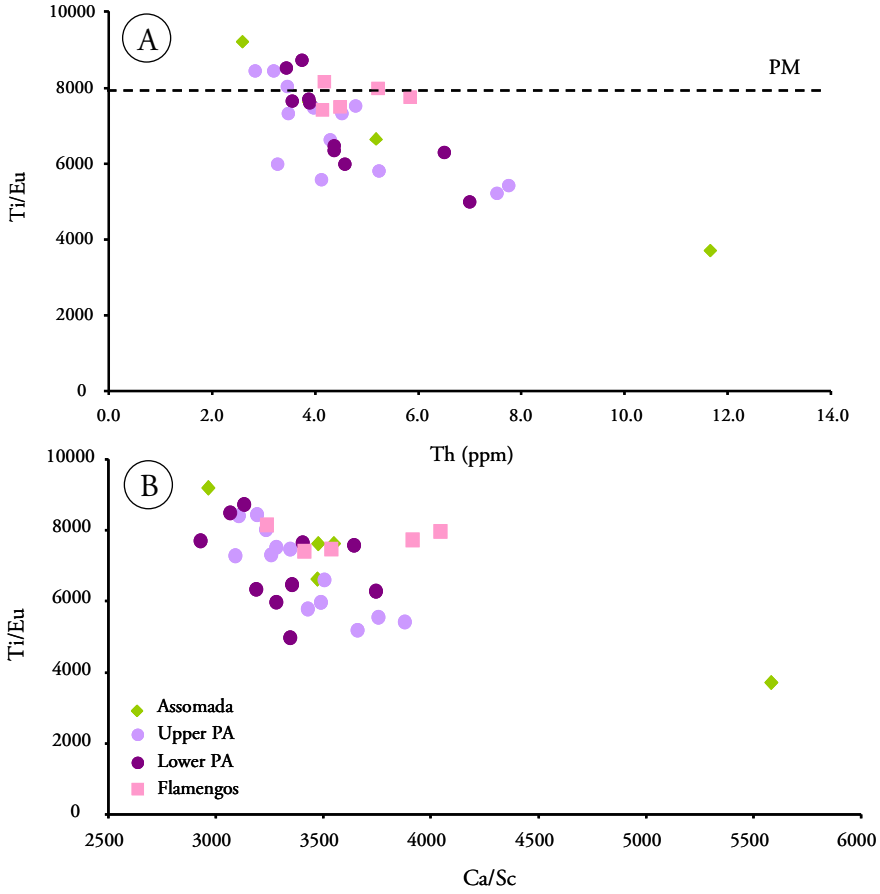

Figure 4.63 - Ti/Eu correlation with Th content (A), a proxy of partial melting degree, and Ca/Sc (B) supporting the evidence of carbonated metasomatic events. Primitive mantle values from Palme and O'Neill (2003).

Dasgupta et al. (2009) trough experimental studies confirmed that near solidus carbonatite melts derived from garnet lherzolite at high pressures (6 – 8 GPa) are significantly different from worldwide outcropping carbonatites. These authors suggest that the discrepancy in incompatible element enrichment (100 – 1000x chondrites as opposed to 1000 – 10 000x chondrites in carbonatites at the earth's surface) and key element ratios (high Nb/Ta and Zr/Hf) could be due to late stage crystal fractionation and liquid immiscibility or the involvement of an enriched source. Consequently these author suggest that when modelling carbonatite metasomatism the carbonated melt composition should be calculated using high pressure partition coefficients (as those determined in their experiments) instead of the composition of outcropping carbonatites.

It is worth mentioning that when determining Santiago's lavas mantle source paragenesis, Assomada and Upper Pico da Antónia Formation (those with more compelling evidence for

carbonate-rich metasomatism) could only be satisfactorily modelled using the partition coefficients determined by Dasgupta et al. (2009) (see 4.4.3.3).

4.4.4.3.2. High radiogenic Pb isotopic signatures as evidence for metasomatism

As described in section 4.3.3 there is a sub-group of Santiago samples that exhibit high $^{206}Pb/^{204}Pb$, $^{207}Pb/^{204}Pb$ and $^{208}Pb/^{204}Pb$ ratios, being distinct from all the other Santiago samples. This marked difference in Pb isotopic signature is concomitant with lower $^{87}Sr/^{86}Sr$, higher $^{143}Nd/^{144}Nd$ ratios and higher enrichment in incompatible elements.

These samples also exhibit higher values of U/Pb and Th/Pb than the main Santiago group, implying a significant enrichment in U and Th relative to Pb. Also, trace element ratios that are considered indicators of carbonatitic metasomatic processes, such as high CaO/Al_2O_3, Ce/Pb and low Ti/Eu are correlated with those enriched Pb signatures (Fig. 4.64).

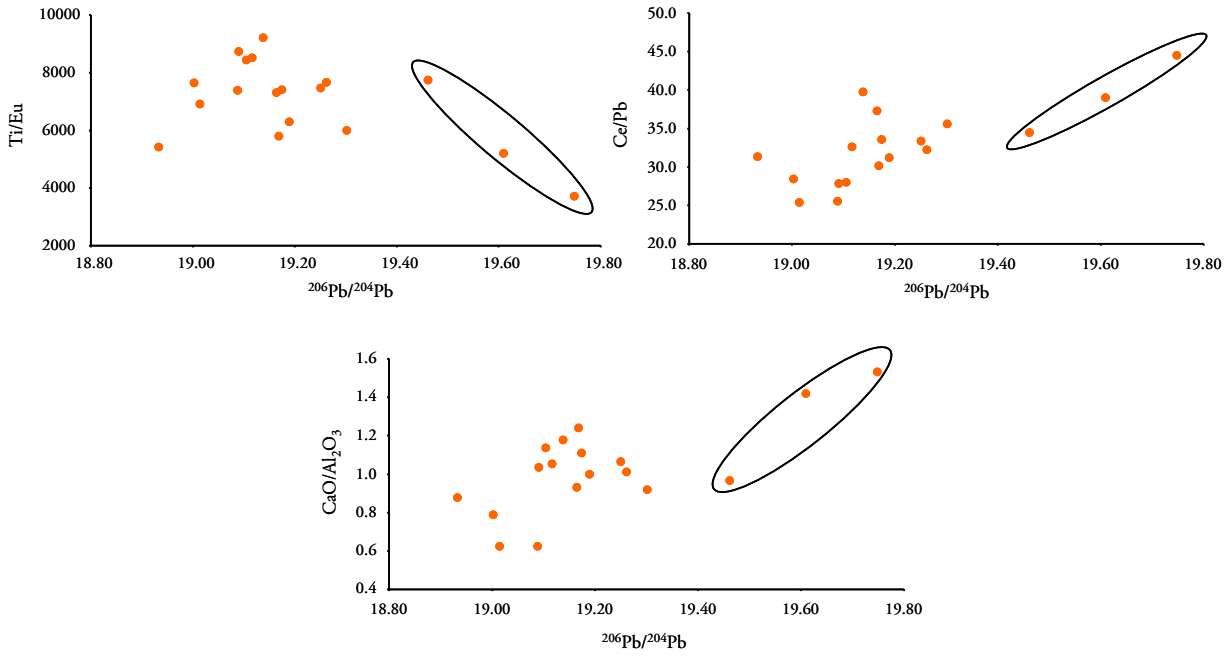

Figure 4.64 - High $^{206}Pb/^{204}Pb$ samples showing correlation with specific elemental ratios indicative of carbonatitic metasomatism.

As stated earlier Santiago lavas and xenoliths have strong evidences for the interaction of lithospheric mantle with carbonatitic melts characterized by with elemental and isotopic characteristics not necessarily akin to the outcropping Cape Verde carbonatites.

Considering the available Cape Verde carbonatite Pb isotope data (Fig. 4.65) it is possible to rule out a carbonatitic metasomatic agent with the same Pb isotopic signature as the outcropping carbonatites in the Cape Verde islands, since the $^{208}Pb/^{204}Pb$ ratios are not sufficiently high to account for the highest values in Santiago lavas (up to 34.46).

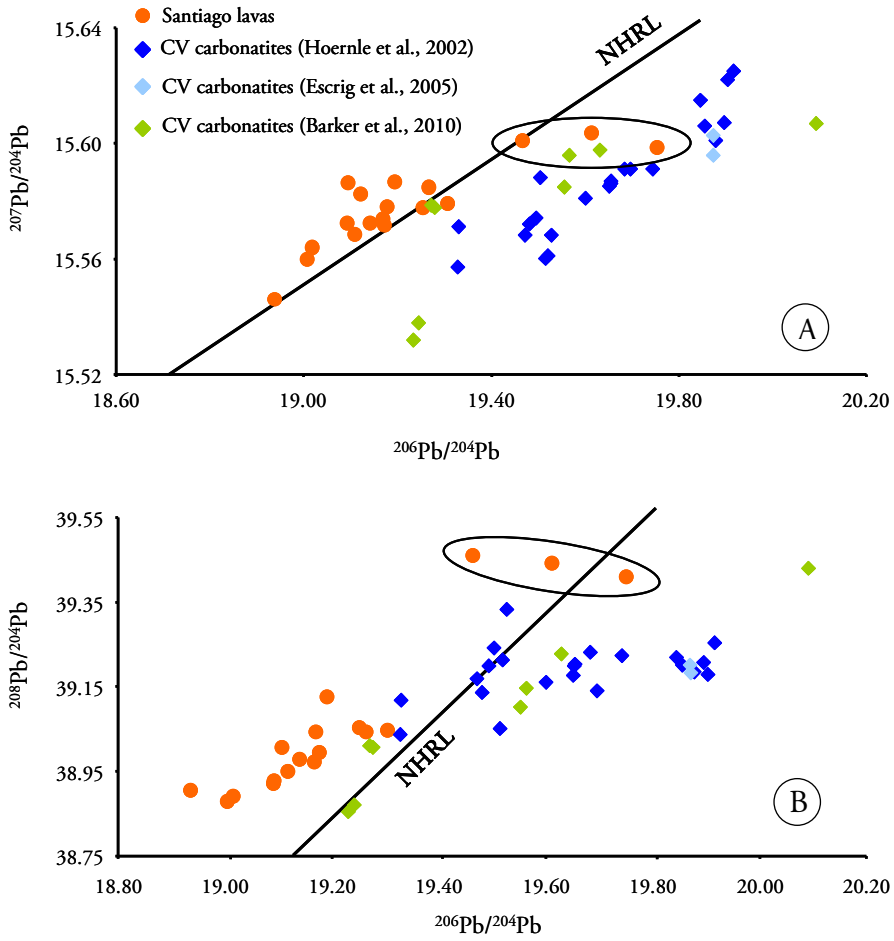

Figure 4.65 - Pb isotopic range of Cape Verde (CV) carbonatites compared with Santiago lavas.

Several studies in mantle xenoliths sampled from Cenozoic intraplate volcanism in Morocco, Algeria, Libya and central Spain, report evidence for mantle metasomatism by melts with HIMU affinity (Beccaluva et al., 2007; 2008; Wittig et al., 2010; Bianchini et al., 2010). These peridotitic xenoliths are characterized by the overprinting of primary texture and composition by metasomatic textures and characteristics, such as alteration of ortopyroxene into secondary olivine and clinopyroxene, occurrence of phlogopite, amphibole, glass patches and significant enrichment in LREE and fractionated REE patterns. Very similar textural and

geochemical characteristics have been described for Santiago xenoliths (Mendes, 1995; see 4.4.3.3).

Those studies focusing on clinopyroxene separates show enriched compositions and particular isotopic characteristics, specifically high Pb isotope ratios (i.e., HIMU affinity). The clinopyroxenes are interpreted as the result of re-equilibration with a percolating metasomatic agent or the product of direct crystallization from it. Even though a consensus about the type of metasomatic agent and its origin is not reached, the metasomatic agent is thought to originate from sublithospheric domains subsequently infiltrating and modifying the shallow lithospheric mantle (Beccalluva et al., 2007; 2008; Wittig et al., 2010; Bianchini et al., 2010). By comparing the data from these clinopyroxene separates and Santiago samples, it is plausible to assume that the Pb radiogenic signature of the Santiago sub-group be due to a metasomatic event with similar geochemical characteristics and comparable genesis mechanism (Fig. 4.66).

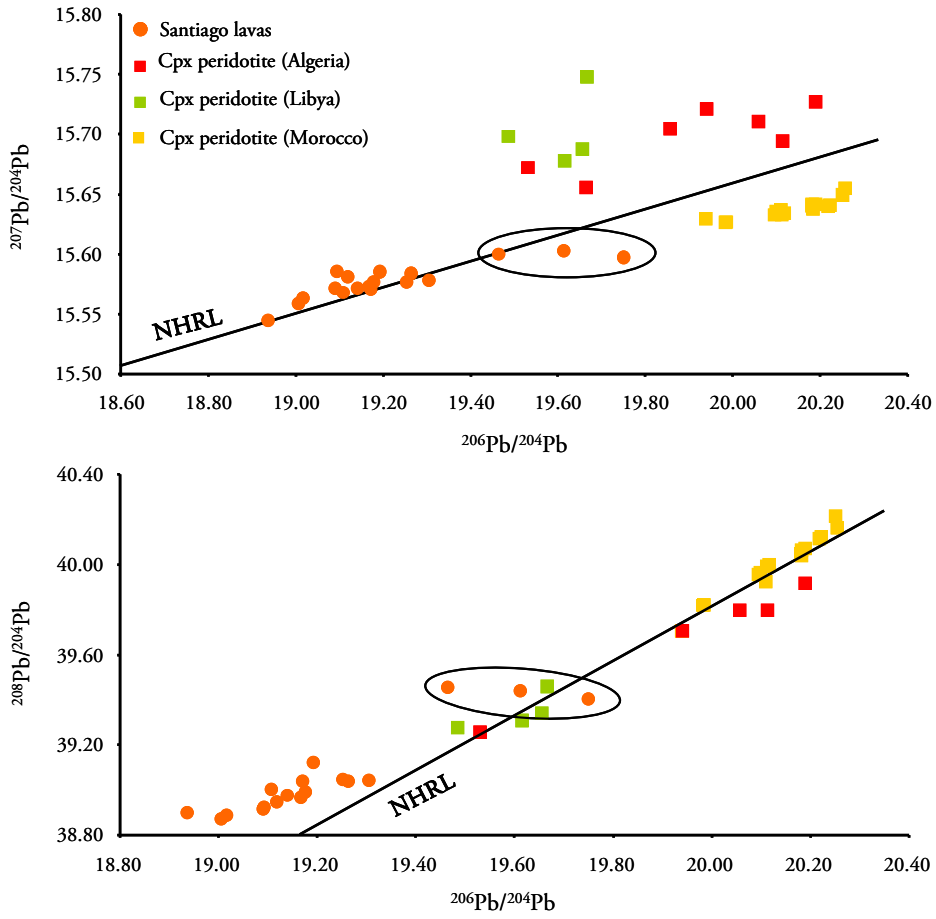

Figure 4.66 – Pb isotopic data of clinopyroxene separates from metasomatized peridotitic xenoliths compared with Santiago Island lavas. Data from Algeria (Beccaluva et al., 2007), Libya (Beccaluva et al., 2008) and Morocco (Wittig et al., 2010).

Recent Hf and Nd isotope data from clinopyroxene separates from metasomatized peridotitic xenoliths of Sal Island (Cape Verde) (Bonadiman et al., 2010) show very similar values to the ones characterizing clinopyroxenes from Calatrava (central Spain) and Middle Atlas (Morocco) xenoliths (Bianchini et al., 2010 and Wittig et al., 2010, respectively), which are also characterized by high Pb isotopic ratios ($^{206}Pb/^{204}Pb$ up to 20.2 in Morocco samples) (Fig. 4.67). This evidence also seems to suggest that there is a similarity in the nature/genesis of the metasomatic agent affecting the lithospheric mantle of these distinct areas.

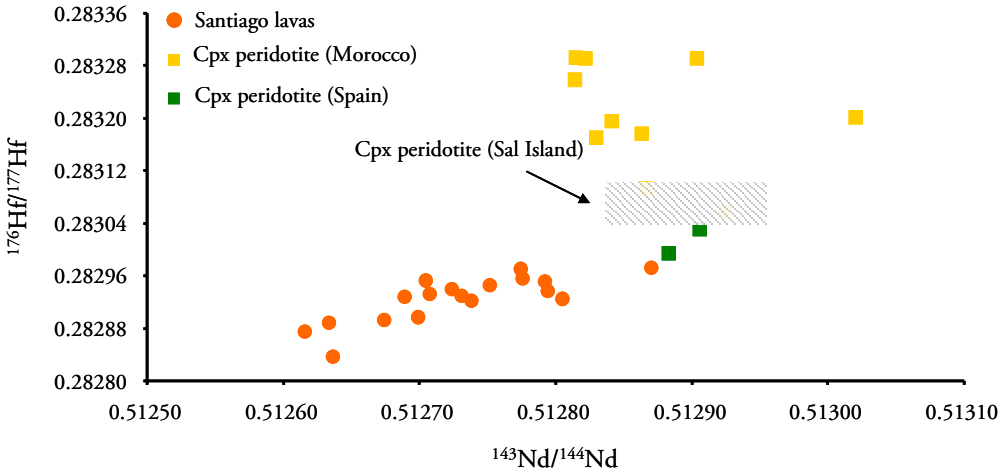

Figure 4.67 - $^{176}Hf/^{177}Hf$ vs. $^{143}Nd/^{144}Nd$ isotopic data of clinopyroxene separates from metasomatized peridotitic xenoliths from Morocco and Spain compared with clinopyroxenes from Sal Island and Santiago lavas. Data from Morocco (Wittig et al., 2010), Spain (Bianchini et al., 2010) and Sal Island (Bonadiman et al., 2010).

The shorter half-lives of U (^{235}U $t_{1/2}$≈0.7 Ga; ^{238}U $t_{1/2}$≈4.5 Ga) and Th (^{232}Th $t_{1/2}$≈14 Ga), relative to other radiogenic elements such as Sr (^{87}Rb $t_{1/2}$≈47.5 Ga), Nd (^{147}Sm $t_{1/2}$≈106 Ga) and Hf (^{176}Lu $t_{1/2}$≈37.2 Ga), may result in rapid in-growth of Pb isotopes during mantle enrichment events over short periods of time (tens of Ma) (Faure, 2005; Wittig et al., 2010). Santiago magmas are originally characterized by high U/Pb and Th/Pb since, as demonstrated before, were generated from a source where the HIMU component plays an important role (Gerlach et al., 1988; Doucelance et al., 2003; Barker et al., 2010).

U and Th have similar partition coefficients during mantle melting, and are more incompatible than Pb, which can lead to melts with high U/Pb and Th/Pb, relative to the residual mantle (Halliday et al., 1995; Ballentine et al., 1997). If the mantle was

metasomatized by an agent enriched in U and Th, such as carbonate rich silicate melts or carbonatitic melts, then the fractionation is even more significant given the very low degree of melting. Also, the mantle was modally metasomatized and hydrous minerals such as phlogopite were residual (see section 4.4.3.2), which can act as a potentially important reservoir of Pb, promoting yet again the intensification of the fractionation between U/Pb and Th/Pb (Rosenbaum, 1993).

4.4.4.4. On the origin of the carbonatitic metasomatic agent

The existence of a mantle plume at Cape Verde seems indisputable, both from tomographic studies (Montelli et al. 2006) and from He isotopic signatures in silicate (Christensen et al. 2001; Doucelance et al. 2003; Mourao et al., 2007) and carbonatite magmas (Mata et al., 2010). These authors identified an unradiogenic He component in Cape Verde magmas, which they assigned to lower mantle material entrained by the plume, thus showing that the contribution of the mantle plume was not restricted to a heat source.

As discussed earlier the influence of a carbonated source in the genesis of Santiago silicate magmas and associated metasomatic agent is unquestionable. Even though the metasomatic agent is identified as being carbonatitic, geochemical evidences attests to the distinction between outcropping carbonatites and the enriched melt responsible for the modal and cryptic modifications imposed on the mantle (see 4.4.3.2 and 4.4.3.3).

However the association of outcropping carbonatites and carbonate-rich/carbonatitic metasomatism does not seem random. The enriched melts from which the carbonatites and associated metasomatic agents (fluid/melts) were ultimately derived probably share a common source. In this perspective the observed final differences are considered as mainly due to carbonatite wall-rock reaction (Dalton and Wood, 2003) or shallow level processes such as crystal fractionation, melt mixing, immiscibility and cumulative processes (Church and Jones, 1995; Lee and Wyllie, 1994, 1998; Panina and Motorina, 2008; Foley et al., 2009). As an example, extrusive carbonatites from Brava Island (Cape Verde) were recently interpreted as resulting from immiscibility processes that also produced conjugate melts of nephelinitic composition (Mourão et al. 2010).

In order to assess the origin of the carbonate-rich metasomatic agent (which is interpreted as being closely related with the source of carbonatitic magmas) is seems important to question the source of carbon. Mantle carbon is envisaged as being originated either from crustal recycling via subduction (carbonated eclogite) or from a primitive reservoir stored deep within the mantle (Bell and Simonetti, 2010).

The rare oceanic carbonatite occurrences (restricted to Cape Verde and Canary archipelagos) have been interpreted as reflecting melting of secondary calcitic carbonate in recycled oceanic crust (≈ 1.6 Ga, Hoernle et al., 2002; ≈ 400 Ma, Doucelance et al., 2010) or derived from a deep seated mantle reservoir (de Ignacio et al., 2006; Mata et al., 2010).

Considering that $^{4}He/^{3}He$ ratios more unradiogenic than those usually reported for MORB and interpreted as the upper mantle signature (R/Ra=8±1[19]), Mata et al. (2010) considered the R/Ra values of Cape Verde carbonatite (up to 15.5) as an indication of a lower mantle contribution to the carbonatites. Taking into account that, according to experimental work, crustal carbonates carried to the mantle by subducting are unlikely to be transported to depth levels below the transition zone, Mata et al. (2010) eliminate crustal carbonate recycling as an origin to the carbon in the Cape Verde carbonatites.

Mata et al. (2010) measured ^{129}Xe excesses relatively to the air ($^{129}Xe/^{130}Xe$ ratios up to 6.84; air=6.50), which also cannot be explained by crustal recycling. Indeed recycling of Te and/or Ba enriched crustal carbonates would decrease, rather than increase the $^{129}Xe/^{130}Xe$ ratios[20]. These authors considered the ^{129}Xe anomalies as resulting from a very long term isolated mantle domain preserving ^{129}Xe resulting from the decay of the now extinct ^{129}I. Also the $\delta^{13}C$ carbonatitic value from - 8.0 to - 4.2‰ clearly favours a mantle rather than a recycling origin for carbon, since carbon isotopic signatures of diamonds, mantle xenoliths and some magmatic rocks display $\delta^{13}C$ values of -5‰, ascribing them to a primordial signature (primitive meteorites) (Hashizume et al., 2004).

According to Mata et al. (2010) this deep reservoir could be either an early-isolated (3.9 Ga) basaltic/komatiitic protocrust, with a chondrite-like regolith containing solar-wind-

[19] R stands for the measured He isotopic ratio; Ra is the $^{3}He/^{4}He$ ratio of the air, $1.384x10^{-6}$.

[20] The successive decay from ^{128}Te to ^{129}Te (by neutron capture), ^{129}I and ^{129}Xe would be accompanied by double beta decay of ^{130}Te to ^{130}Xe and would result in a decrease of the $^{129}Xe/^{130}Xe$ ratio rather than an increase. In addition the elevated Ba contents of carbonates integrated in oceanic crust would also increase the ^{130}Xe by double beta decay of ^{130}Ba.

implanted gases (Tolstikhin and Hofmann, 2005; Tolstikhin et al., 2006) or a stable layer of dense melt formed at the base of the mantle early in Earth's history (Labrosse et al., 2007). In both cases, the D" layer, at the base of the lower mantle, would be a reservoir enriched in rare gases and, eventually, also in C (see Hirschmann and Dasgupta, 2009).

The mobilization of this deep seated carbon to shallower depths and incorporation in melts susceptible of generating carbonatites and inducing carbonatitic metasomatism is complex and still largely debated (Bell and Simonetti, 2010). Carbon can be stored in several forms such as mineral carbonate, diamond, metal carbide or dissolved in metals depending on oxygen fugacity and the oxidizing power of carbon and iron species (Dasgupta and Hirschmann, 2010 and references therein).

The stability of Ca- and Mg-carbonates in the lower mantle have been demonstrated trough high-pressure experimental studies and Isshiki et al. (2004) proposed that the breakdown of magnesite II leads to MgO formation and CO_2 release. This CO_2 would be entrained in the rising thermochemical plume also acting as a facilitator of partial melting in the lower mantle, due to liquidus temperature reduction (Isshiki et al., 2004). These evidences led Collerson et al. (2010) to suggest that the extraction of buoyant CO_2-rich melts from the deepest lower mantle can be considered a mechanism susceptible of transferring lower mantle heterogeneous signature to OIB and carbonatite sources (upper lower mantle/transition zone), playing a crucial role in the initiation and development of thermochemical plumes, also explaining rare gas isotope data from plume derived magmas, as those presented by Mata et al. (2010) for the Cape Verde carbonatites.

The volatile-rich, low viscosity nature of the lower mantle partial melts makes them buoyant with a significant upward migration capacity (Hammouda and Laporte, 2000). The ascent of these melts can have two different evolution paths, if there is thermal equilibrium with the surrounding mantle a re-solidification of the liquid is possible, however if reactive transport occur during melt migration, then it may preserve its percolative properties during mantle transecting (Collerson et al., 2010). If decompression freezing occurs in the mid-lower mantle it will re-melt as the thermochemical upwelling reaches the transition zone (Fig. 4.68) (Collerson et al., 2010).

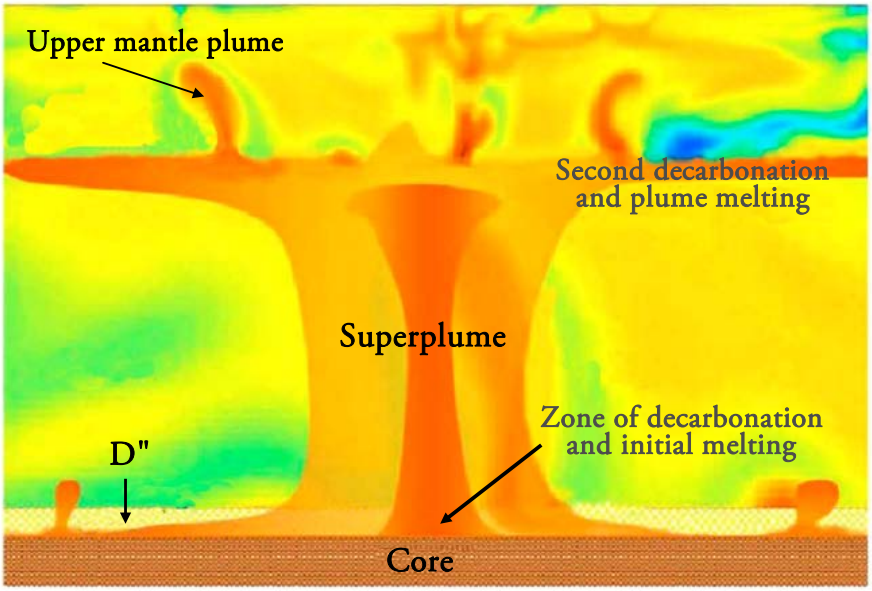

Figure 4.68 - Sketch showing the multiscale nature of mantle plumes from Matyska and Yuen (2008) superimposed with the model of Collerson et al. (2010) for the generation of carbonated melts in the lower mantle and in the transition zone. The red colour represents the maximum temperature while the dark blue colour denotes the minimum temperature.

However it should be emphasized that the isotopic difference between the inferred signature for the metasomatic agent and those determined for the outcropping carbonatites allows for an alternative. Bonadiman et al. (2005) studied spinel-peridotite xenoliths from Sal Island (Cape Verde) and found evidence for the occurrence of kimberlite-like metasomatism, which was interpreted as caused by the melting of a SCLM (subcontinental lithospheric mantle) domain. Taking into account that a continuous gradation from carbonatitic to silicate (kimberlitic/melilitic/melanephelinitc/basanitic) melts is generated from CO_2-enriched mantle sources (Gudfinnsson and Presnall 2005), several different types of mantle metasomatic agents can be envisaged as the result of different degrees of melting of such source. In accordance with Bonadiman et al. (2005), the variety of metasomatic agents in Cape Verde (carbonatitic: Jørgensen and Holm 2002; kimberlitic: Ryabchikov et al. 1995; Bonadiman et al. 2005) could stem from sub-continental lithospheric domains preserved beneath Cape Verde as a result of the thermal influence of a mantle plume.

Coltorti et al. (2009) trough $^{187}Os/^{188}Os$ isotopic data on sulphide grains occurring in lherzolite xenoliths, adds one more convincing proof for the existence of an ancient (Archean-Proterozoic) fragment of ancient subcontinental lithospheric mantle preserved at relatively shallow depths (spinel stability field) (see section 4.5 for further discussion).

As stated earlier the metasomatic agent that affects the Cape Verde lithospheric mantle seems to show affinities with those reported for mantle xenoliths sampled from Cenozoic intraplate volcanism in Morocco, Algeria, Libya and central Spain which are probably also under the influence of subcontinental lithospheric domains (Beccalluva et al., 2007; 2008; Wittig et al., 2010; Bianchini et al., 2010).

4.5. Mantle components

The "mantle component" concept was first introduced by Zindler et al. (1982), White (1985) and Allègre and Turcotte (1986) in an attempt to explain the observed isotopic heterogeneity (Sr, Nd and Pb) in MORB and OIB worldwide.

Zindler and Hart (1986) went a step further and differentiated six mantle components based on their distinct Sr, Nd and Pb isotopic signatures: HIMU [high μ ($^{238}U/^{204}Pb$)], EMI and EMII (enriched mantle I and II), DMM (depleted MORB mantle), PREMA (prevalent mantle) and BSE (bulk silicate earth). The isotopic characteristics of these magmas imply long time scale chemical isolation of the sources in order to account for the observed differences in the abundances of daughter isotopes (Workman et al., 2004) and led these authors to make some assumptions regarding the origin of these components:

- HIMU would probably have evolved from ancient altered ocean crust in accordance with the pioneer work by Chase (1981) and Hofmann and White (1982);
- EM could testify the injection of continental derived sediments, crust, seamounts in subduction zones, delamination of subcontinental lithosphere or mantle metasomatism;
- DMM as the name implies, would have resulted from the extraction of the continental crust from the mantle, leaving it depleted;

- PREMA was interpreted as a distinct mantle component with intermediate isotopic characteristics compared with the other more extreme components, but with high $^{3}He/^{4}He$ ratios, suggesting an undegassed source;
- BSE would represent a primitive undifferentiated mantle that has survived as a closed system after core and atmosphere formation, with primordial abundance ratios.

In the 90's Hart et al. (1992) demonstrated that the majority of OIB plot within a tetrahedron, where the four corners were defined as DMM, HIMU, EMI and EMII. These authors also proposed an additional end-member named FOZO (Focal Zone), where OIB and MORB data seemed to converge (Fig. 4.69). This component has radiogenic Pb isotopic ratios, moderately depleted Sr and Nd signatures and elevated $^{3}He/^{4}He$ ratios, which is most probably located in the lower mantle. Since then the isotopic characteristics of FOZO have varied substantially according with different criteria and interpretation from several authors (Hauri et al, 1994; Stracke et al, 2005; Jackson et al., 2007) although its identification as a ubiquitous mantle component in the source of MORB and OIB is still considered valid.

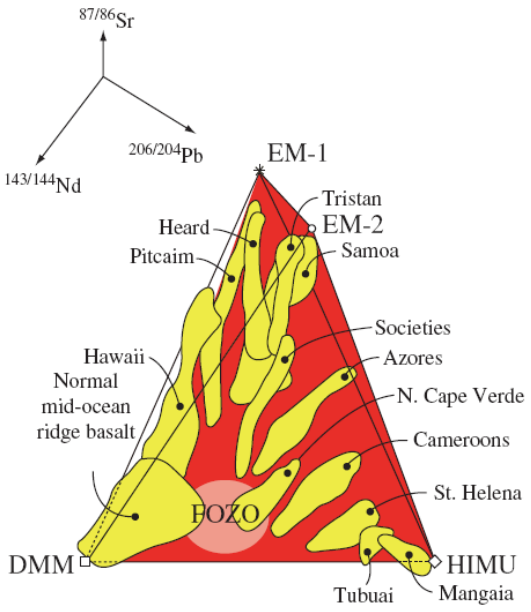

Figure 4.69 - Three-dimensional mantle tetrahedron thought to represent the mixing relationships between four mantle components that could account for OIB variability (Hart et al., 1992; Hofmann, 2003).

Other proposed common components in the source of OIB and MORB are, the "C" (Common) component introduced by Hanan and Graham (1996) with isotopic characteristics

very similar to FOZO, and PHEM (Primitive Helium Mantle) proposed by Farley et al. (1992) with Sr and Nd isotopic ratios near the BSE values, moderate Pb isotope ratios and high $^{3}He/^{4}He$ ratios (>24). These components are less used in international publications, being FOZO the most referred common component.

Since the implementation of the "mantle component" concept a lot has been written towards its reinforcement but also for its discredit. It should be kept in mind that since its early formulation the imperfection and oversimplification of this hypothesis was already acknowledged by Zindler et al. (1982). It is undoubtedly difficult to explain and reconcile not only the isotopic characteristics but also all the major and trace element data into one global theory capable of justifying the heterogeneity that characterizes both OIB and MORB.

One of the most significant and discussed topic is whether or not there is the necessity to invoke the presence of distinct and individualized portions of the mantle to justify the observed geochemical heterogeneity. For this discussion it is crucial a chemical geodynamic approach to the mantle structure, where mantle geochemistry is closely associated with geophysical studies (Allègre, 1982; Zindler and Hart, 1986). Since the introduction of plate tectonics in the 1960's, a continuous and still lively debate exists over whether the mantle is layered or if it's characterized by whole-mantle convection (layered cake vs. plum pudding).

The existence of a layered mantle has been invoked due to the inability to reconstruct the bulk silicate earth (BSE), from the compositions of continental crust and depleted mantle (McDonough and Sun, 1995; Palme and O'Neill, 2003). This hypothesis is supported by mass-balance calculations on heat production by radioactive decay[21] (O'Nions and Oxburgh, 1983) and isotopic budget of incompatible elements[22] (Hofmann, 1997). The layering (upper-lower mantle) was assumed to coincide with the 660-km seismic discontinuity, which is commonly attributed to a change in mantle chemical composition (Wasserburg and DePaolo, 1979).

[21] The current heat flux at the Earth's surface is 44.2 TW (44.2×10^{12} W) which is mostly attributed to the radioactive decay of K, U and Th. Since the upper mantle is assumed to be depleted in those elements, being responsible for only 2-6 TW, the remaining heat flow must be produced in a separate and enriched mantle reservoir and/or core (O'Nions and Oxburgh, 1983; Allègre et al., 1996; Kellogg et al., 1999).

[22] Distinct isotopic ratios (Sr, Nd and Pb) between MORB and OIB imply sampling of different portions in the mantle. Also the ^{40}Ar and ^{4}He atmospheric budget expected from surface heat flow (K decays to ^{40}Ar; U, Th decays to ^{4}He) is not attained (being very low) which implies that the mantle has portions not entirely degassed (O'Nions and Oxburgh, 1983; Hofmann, 1997; Kellogg et al., 1999).

However several arguments/evidences have been presented that seems to support the whole mantle convection scenario: (1) seismic tomography data suggest that some subducted slabs penetrate into the lower mantle, attesting the "permeability" of this frontier (van der Hilst et al., 1997; Fukao et al., 2001, 2009); (2) the seismic discontinuities at 410 and 660 km depth are more likely to be phase transformations under isochemical conditions instead of compositional layering, supporting the existence of a chemically unstratified mantle (Helffrich and Wood, 2001); (3) Lyubetskaya and Korenaga (2007a,b) propose a new composition model of the primitive mantle with about 20% lower abundance of Ca, Al, Ti, REE and heat producing elements which can be enough to resolve the heat-source paradoxes and incompatible elements imbalance.

Cserepes et al. (2000) and Tackley (2008) proposed an intermediate solution between the layered and whole mantle convection hypothesis. According with the emerging model, some slabs of oceanic plate are deflected at the 660 km discontinuity whereas other penetrates into the lower mantle, this being an intermittent event in space and time. On the other hand the deep mantle is probably characterized by the presence of primitive or subducted material that has settled trough gravity. So the entire mantle could be regarded as a mixture of compositionally distinct components, heterogeneous in space and time (Tackley, 2008).

The importance of a deep-mantle/hidden reservoir contribution to OIB geochemistry has been gaining supporters in recent years (Korenaga, 2009; Collerson et al., 2010; Lee et al., 2010). The theories are very diverse and sometimes extreme, from the existence of an early enriched reservoir that was mostly lost by impact erosion early in Earth evolution (Korenaga, 2009) to the existence of dense Fe-rich crystallized Hadean magma oceans at the core-mantle boundary, that provide a source enriched in incompatible element and noble gases, akin to the common component FOZO (Lee et al., 2010).

Collerson et al. (2010) suggests an even more innovative mechanism for generating chemical heterogeneities in the lower mantle which accounts several unanswered questions brought upon by the mantle component theory, such as the overly simplistic recycling model (Collerson and Kamber, 1999; Kamber and Collerson, 2000; Niu and O'Hara, 2004; Niu, 2009), the close association of HIMU and EM sources and the origin and variability of

kimberlite and carbonatite magmas. Through quantitative modelling of partial melting these authors demonstrate that the parent/daughter isotope ratios (U/Pb, Rb/Sr, Sm/Nd, Lu/Hf and Re/Os) of EM and HIMU end-members are related with a single melting process, the EM representing the product of partial melting of a lower mantle carbon-rich while the HIMU would be the resulting melting residue. According with this model the presence of carbon in the deep mantle is essential to the migration of melts originated from "pristine" mantle domains, isolated from whole mantle convection (≥ 1700 km), making them able to migrate to plume magmatogenesis locations[23]. The more extreme isotopic compositions exhibited by HIMU sources could be the result of prolonged residence time due to its refractory nature (Collerson et al., 2010).

Although the existence and/or genetic models for mantle components, reservoirs and end-members has been recently challenged by several authors (Meibom and Anderson, 2003; Willbold and Stracke, 2006; Armienti and Gasperini, 2007; Niu, 2009) with new and alternative hypothesis being presented (Pilet et al., 2005; Niu, 2009; Collerson et al., 2010) their use to explain mantle variability is still considered acceptable and valid if based mainly on isotopic data or if highly incompatible elements ratios are considered (Hofmann, 2003; Stracke et al., 2005).

The persistence of meter scale geochemical heterogeneities seems undeniable for long time scales in solid state (0.5 to 2 Ga; Gurnis and Davies, 1986), even when considering whole mantle convection and subsequent mixing and stirring (Kellogg et al., 2002; van Keken et al., 2002; Farnetani and Samuel, 2003; Stracke, 2010).

To sum up, the following discussion about mantle components/end-members in Santiago Island is going to be directed towards the most commonly discussed approach, however taking into account several considerations: (1) the necessity of evaluating the contribution made by shallow level processes (partial melting, crystal fractionation, magma mixing, metasomatic events among others) and the heterogeneities derived from it, in order to distinguish what is the source composition from what is imprinted afterwards; (2) the geochemical signature observed in lavas is probably the reflection of a multitude of events such as subduction zone processes, core-mantle interaction, aging and mixing of different melts and not a simple

[23] The role of very ancient primitive carbon-rich reservoir located in the deepest levels of the mantle to the genesis of the Cape Verde carbonatites was already acknowledge by Mata et al. (2010).

binary/ternary mixture among distinct homogeneous mantle components (Hauri, 2000); (3) the term "component/end-member" is going to be used according with Stracke et al. (2005) approach, as a portion of the mantle that is geochemically different from other parts of the mantle without any implications concerning size, properties and mineral composition.

4.5.1. Cape Verde archipelago isotopic dichotomy and diversity

Gerlach et al. (1988) were the first to study the Cape Verde archipelago (Fogo, Santiago, Maio, São Vicente and Santo Antão Islands) concerning their trace element and isotopic ratios characteristics. From this study a distinction between northern and southern islands emerged, based on different isotopic signatures (Fig. 4.70). The isotopic variability was explained by mixing of three end-members: depleted mantle (DMM), high-μ (HIMU) and enriched mantle (EM).

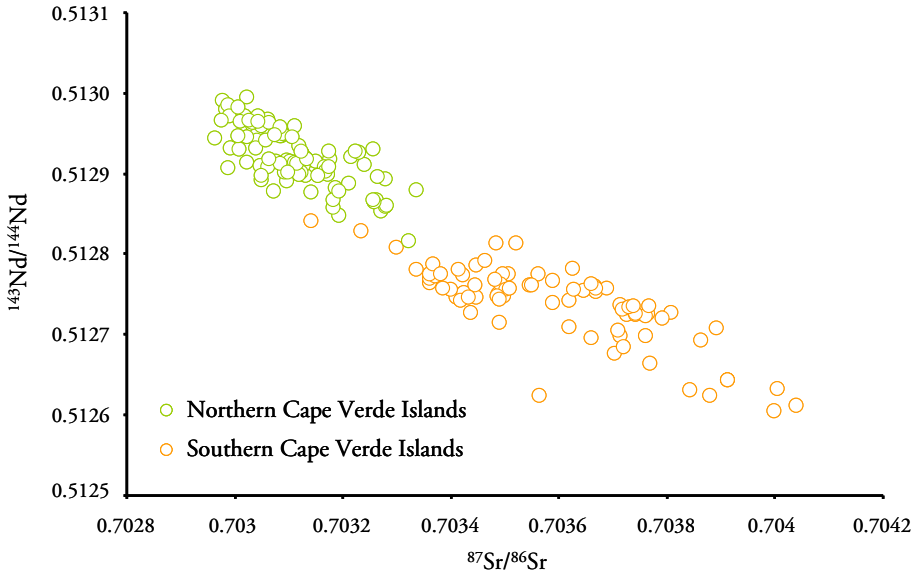

Figure 4.70 – Dichotomy between the northern and southern Cape Verde Islands in Nd-Sr isotopic space. Data from Christensen et al. (2001), Jørgensen and Holm (2002), Doucelance et al. (2003), Escrig et al. (2005), Holm et al. (2006), Millet et al. (2008) and Barker et al. (2010).

In the northern islands only DMM and HIMU signatures were detected while in the southern islands an enriched mantle (EM) was identified as well as the HIMU end-member.

The identification of this dichotomy was possible due to clearly distinct unique isotopic characteristics such as samples systematically plotting below and above the NHRL (northern and southern islands respectively) (Gerlach et al., 1988; Davies et al., 1989) (Fig. 4.71).

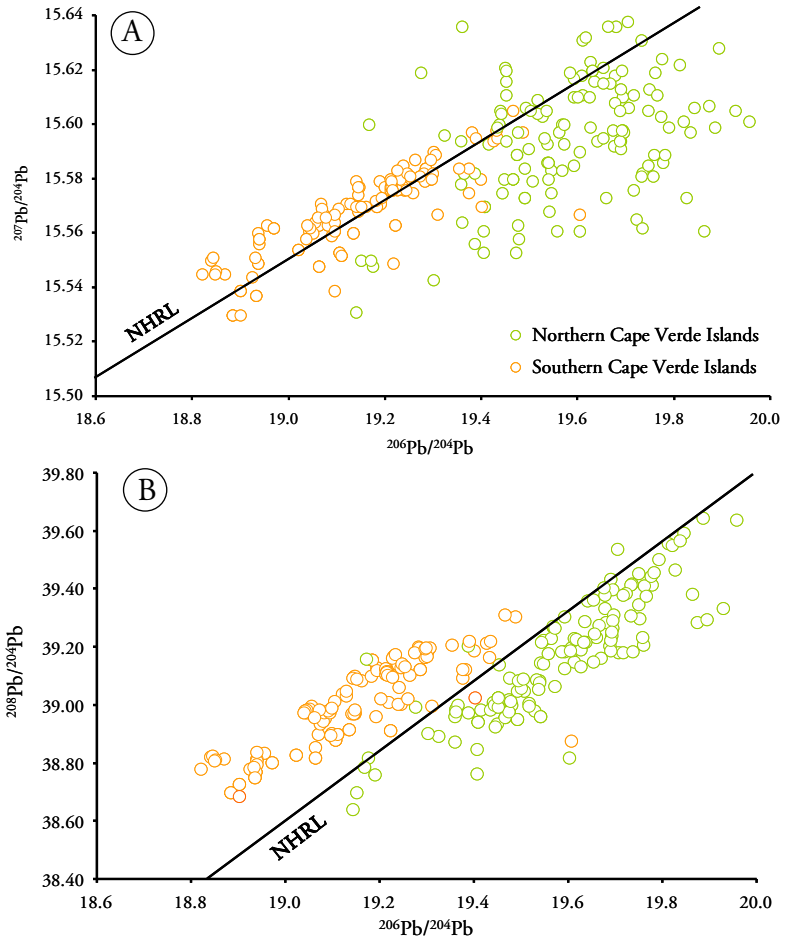

Figure 4.71 – Distinction in Pb isotopic data between the northern and southern Cape Verde Islands. In $^{207}Pb/^{204}Pb$ vs. $^{206}Pb/^{204}Pb$ diagram (A) there is a significant dispersion of northern Islands data, however the majority of the data plots below the NHRL, as in $^{208}Pb/^{204}Pb$ vs. $^{206}Pb/^{204}Pb$ plot (B). Source data are the same of Fig. 4.70.

In addition, some authors (Christensen et al.,2001; Doucelance et al., 2003; Mourão et al., 2007; Mata et al., 2010; Mourão et al., 2012a; b) suggested the involvement of a deep mantle component (lower mantle) in order to justify the rare gas signatures, particularly the moderately unradiogenic He signatures (R/Ra up to 15.5) that characterize both carbonatite and silicate rocks, and the ^{129}Xe excess ($^{129}Xe/^{130}Xe$ up to 6.84) of some of the carbonatites thus

endorsing the models pointing to a deep origin of the plume and their chemical contribution to the magmatism.

In order to explain the occurrence of the HIMU and EM components, Gerlach et al. (1988) proposed two alternative models: (1) the HIMU end-member is supplied by the plume, being associated with entrained depleted upper mantle, while the enriched component is present at the base of the lithosphere; (2) the plume has an enriched character (EM), being the HIMU and depleted end-members located in the upper mantle in a marble-cake structure as proposed by Allègre and Turcotte (1986). In 1998, Kokfelt et al. proposed a distinct model were the plume had only a thermal contribution ascribing both the end-members (HIMU and EM) to a lithospheric origin. The HIMU-like end-member resulted from carbonatitic metasomatism of oceanic crust and associated mantle degassing during the opening of the Atlantic Ocean, while the enriched component was interpreted as being derived from delaminated subcontinental lithosphere.

All the subsequent authors have considered the HIMU-type signatures as reflecting the contribution of ancient recycled altered oceanic crust which after a long period of residence in the mantle are carried to the surface by the mantle plume.

The enriched end-member was assigned to EM1 by Davies et al. (1989) and by most of subsequent papers (e.g. Doucelance et al., 2003; Escrig et al., 2005; Martins et al., 2010). Such EM1-type character for the enriched end-member at Santiago is also clearly evident by the 3D plot presented on Fig. 4.72.

More debatable has been the origin of the EM1-like component which has been assigned to ancient recycled sediments (Gerlach et al., 1988), subcontinental lithospheric mantle stranded in the oceanic lithosphere (Millet et al., 2008) and lower continental crust material (Escrig et al., 2005), the last two hypothesis implying the continental lithosphere delamination during the Atlantic Ocean opening. This hypothesis points to the existence of plume-lithosphere interaction in Cape Verde and will be in Chapter 5.

More recently some of the elemental and isotopic characteristics of lavas from Santiago have been considered to reflect the presence of FOZO (Barker et al., 2010), while even shallower crustal processes, such as contamination by carbonatite material (Jørgensen and

Holm, 2002) and assimilation of oceanic crust (i.e., Jurassic MORB basement) (Doucelance et al., 2003; Millet et al., 2008) have also been invoked.

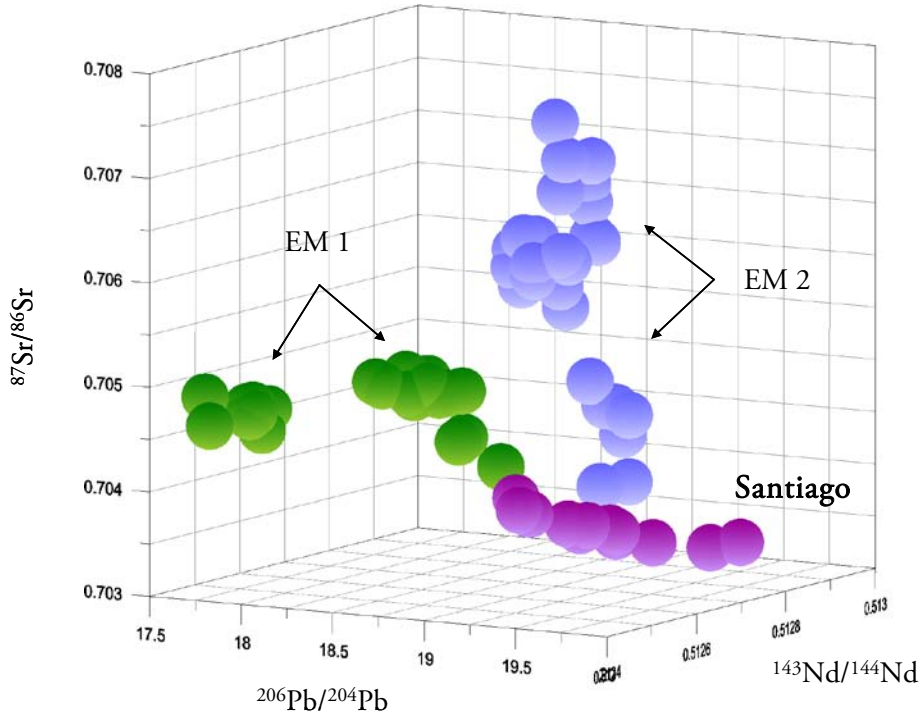

Figure 4.72 – 3D plot showing the influence of EM-1 influence in Santiago alkaline lavas. Source data from Willbold and Stracke (2010). EM1component is represented by Tristan da Cunha and Pitcairn Islands and EM2 component by Samoa and Society Islands.

4.5.2. Santiago Island: mixing between young HIMU, EM and LM

4.5.2.1. On the putative role of FOZO as a contributor to Santiago magmas

As mentioned before, Barker et al. (2009; 2010) considered FOZO as one of the main components constraining the composition of Santiago magmas. Although FOZO composition is still a matter of discussion it has an approximate range for $^{87}Sr/^{86}Sr$ (0.7028-0.7034), $^{143}Nd/^{144}Nd$ (0.51287-0.51303), $^{206}Pb/^{204}Pb$ (19.5-20.5), $^{207}Pb/^{204}Pb$ (15.56-15.71) and $^{208}Pb/^{204}Pb$ (39.1-40.0) (Stracke et al., 2005) which allows the consideration of such a hypothesis (see Appendix III, section III.2.1). Although other Sr, Nd, and Pb isotope compositions can be inferred for FOZO (see Hart et al., 1992; Hauri et al., 1994), this component is usually characterized by high $^{3}He/^{4}He$ (R/Ra > 30, Hart et al., 1992; Ballentine

et al., 2002; Jackson et al., 2009). These values are at odds with the observed values for Santiago silicate rocks and carbonatites (R/Ra < 8.4; Doucelance et al., 2003; Mata et al., 2010) thus clearly eliminating such hypothesis.

It must be emphasized that Jackson et al. (2007) interpreted the Cape Verde Islands as being associated with what they called the FOZO-B (boreal FOZO) component, one of the two hemispherical isolated high $^{3}He/^{4}He$ reservoirs (FOZO-A and FOZO-B). However, this terminology was lately abandoned by the authors (Jackson et al., 2009) by restraining the FOZO denomination to R/Ra >30.

4.5.2.2. Evidences for the occurrence of the HIMU component

The use of the term "HIMU" was defined to refer magmas with very radiogenic Pb isotopic signatures ($^{206}Pb/^{204}Pb>20.5$) associated with relatively low $^{87}Sr/^{86}Sr$ (<0.703), as those characterizing the Islands of St. Helena, Mangaia, Rurutu (old volcanics) and some of the Cook-Austral archipelago (e.g. Chaffey et al., 1989; Chauvel et al., 1992; Hofmann, 2003, Hanyu et al., 2011). Considering the relatively unradiogenic signatures of the Cape Verde magmas ($^{206}Pb/^{204}Pb$ <19.74 for Santiago; Appendix III, section III.2.1) Christensen et al. (2001) and Barker et al. (2010) proposed the presence of an young-HIMU[24] referring to an HIMU-like end-member with ≤ 1 Ga of recycling age as opposed to ≈ 1.8 Ga determined for French Polynesian (Chauvel et al., 1992). However this denomination, introduced by Vidal (1992) and Thirlwall (1995, 1997), is attributed to an end-member characterized by low $^{207}Pb/^{204}Pb$ for a given $^{206}Pb/^{204}Pb$, best expressed by negative Δ 7/4 Pb[25] values, which are not common in Santiago lavas. Indeed as depicted by Figure 4.73 the large majority of the Santiago samples plot on the NHRL or slightly above.

Since at least Zindler and Hart (1986) the HIMU-like end-member has been attributed to recycling of altered oceanic crust trough subduction process. Due to its high U/Pb and Th/Pb ratios it evolves to high $^{206}Pb/^{204}Pb$ and $^{208}Pb/^{206}Pb$ values (Zindler and Hart, 1986).

[24] The term young- HIMU should not be mistaken with the alternative model proposed by Kokfelt et al. (1998) where the high-μ characteristics were attributed to the metasomatic action of carbonatitic fluids on the oceanic crust.

[25] Δ 7/4Pb is a parameter defined by Hart (1984) that expresses the percentage vertical deviation from the NHRL (see Appendix V).

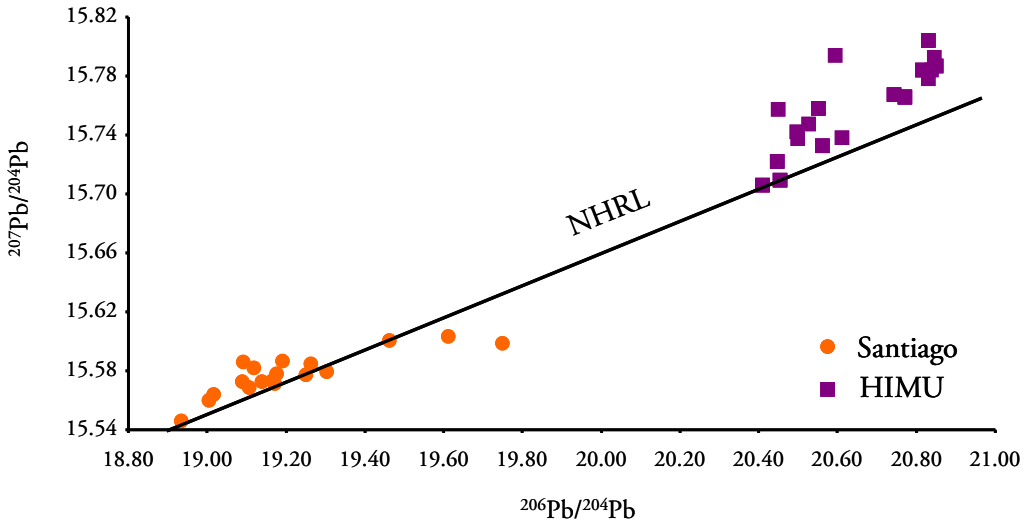

Figure 4.73 – Distinct behaviour between Santiago alkaline lavas and the HIMU component regarding the Pb isotope signature. HIMU data from

Despite the heterogeneous character of the Santiago mantle sources, the HIMU contribution is evident from trace element characteristics such as Nb and Ta enrichment relative to LILE and LREE with Rb/Nb, K/Nb and La/Nb ratios (0.55±0.25, 198±100 and 0.79±0.25, mean values for primary lavas ± SD, respectively) significantly below primitive mantle values (Rb/Nb = 1.0, K/Nb = 433 and La/Nb = 1.14; Palme and O'Neill, 2003) (see Weaver, 1991; Willbold and Stracke, 2006). In a primitive mantle normalized incompatible element diagram (Fig. 4.74) it is evident the parallelism between Santiago magmas and the HIMU-like end-member, except in LILE (Cs, Rb and Ba) which are relatively enriched in Santiago.

The predominance of the HIMU-like end-member relative to the EM 1 is supported by the projection of the lavas in the depleted quadrant of the Sr-Nd and Nd-Hf spaces (Fig. 4.75). This indicates that they were derived from source(s) with time-integrated depletion in the more incompatible trace elements. However, such depletion is less pronounced than that observed for the Northern Cape Verde islands, which are characterised by more unradiogenic Sr and radiogenic Nd signatures (Gerlach et al., 1988; Jørgensen and Holm, 2002; Doucelance et al., 2003; Holm et al., 2006).

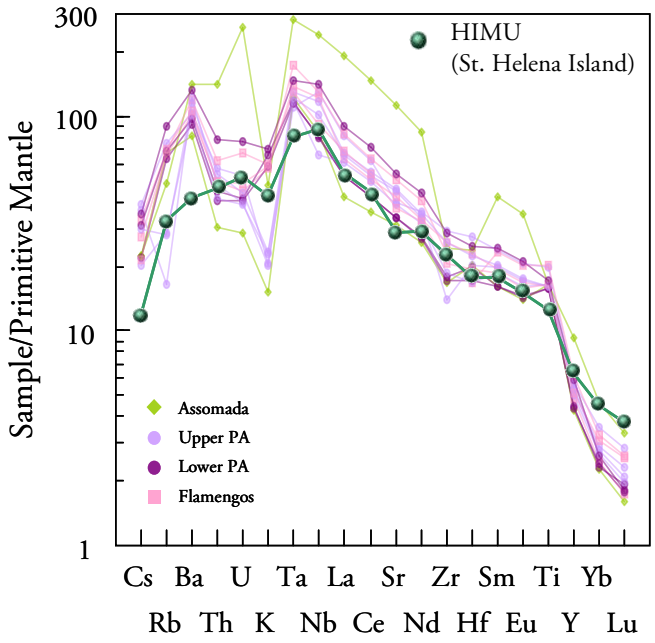

Figure 4.74 – Primitive mantle normalized (Palme and O'Neill, 2003) incompatible element concentrations of representative Santiago samples against an average HIMU composition from St. Helena Island (Willbold, 2005).

Even though the highest and most extreme Pb isotopic data recorded in this study has been assigned to a carbonate-rich metasomatic event (see section 4.4.4), the relatively radiogenic lead isotopic signatures of the remaining samples continues to support the strong influence of an HIMU-like end-member ($^{206}Pb/^{204}Pb$ up to 19.3; see also Gerlach et al., 1988, Doucelance et al., 2003, Barker et al., 2009; 2010).

Barker et al. (2010) ascribes the variations observed in Santiago's lavas $^{208}Pb/^{204}Pb$ ratios at almost constant Δ7/4 Pb values to the recycling of ocean crust at 1 Ga with subtle variations in μ and κ with time. Due to the amount of data, these authors were able to model small differences in μ (11.8 – 14.5) and κ (3.1 – 3.7) for each formation, attributing the variation to lateral changes in the recycled ocean rust.

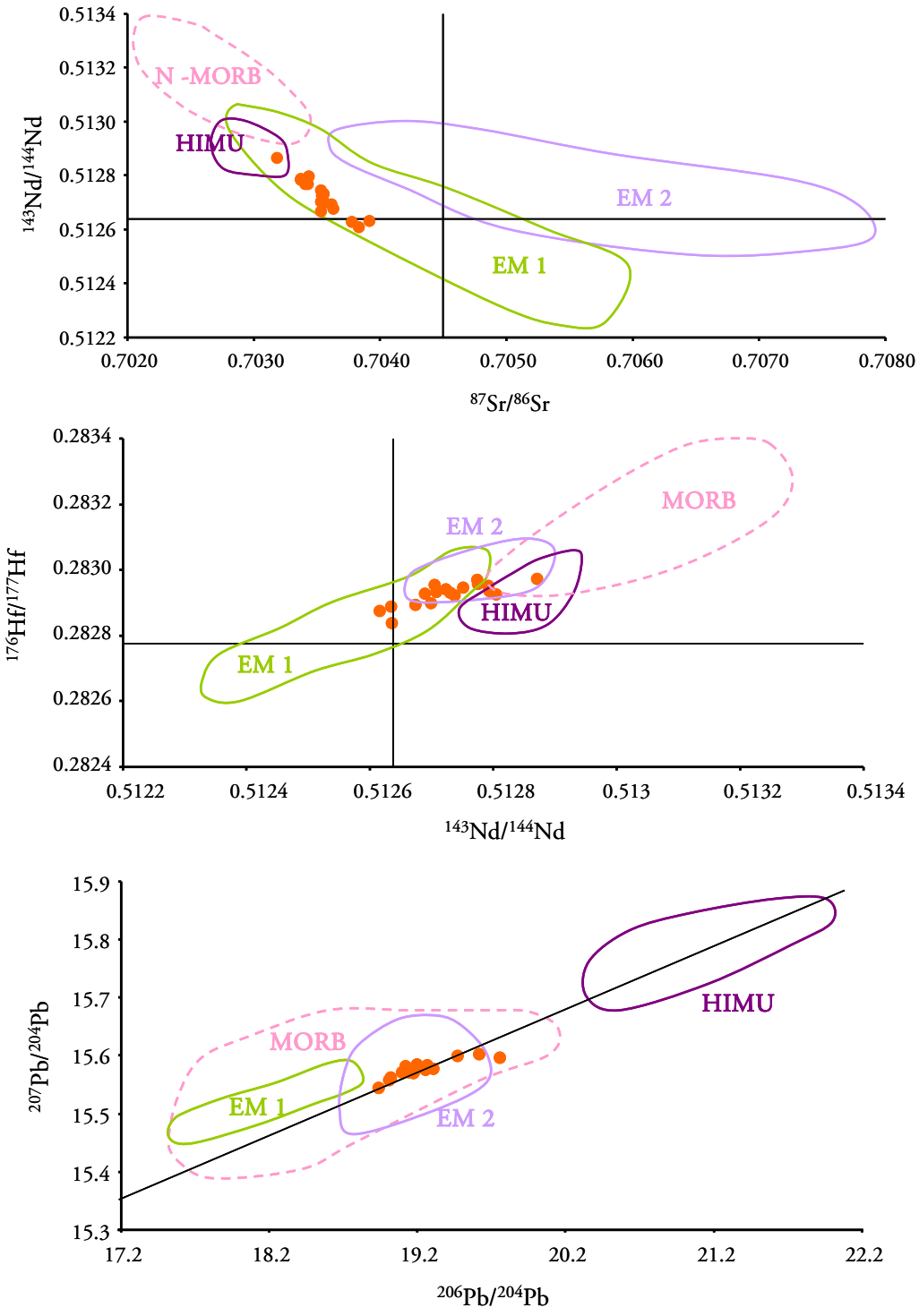

Figure 4.75 – Mantle end-members fields projected with Santiago lavas. Data from: MORB (Dosso et al., 1991; PETDB database with focus on the Mid-Atlantic Ridge); HIMU (Mangaia, Tubuai, Rurutu and St. Helena Islands data from GEOROC database; Salter and White, 1998; Willbold and Stracke, 2010); EM 1 (Pitcairn-Gambier chain, Tristão da Cunha archipelago and Gough Island from the GEOROC database, Walvis Ridge from Salter and Hart, 1991; Salters and Sachi-Kocher, 2010) and EM 2 (Samoa, Society and Marquesas Islands from GEOROC database , Workman et al., 2004 and Jackson et al., 2007). Also represented are the CHUR and NHRL (see section 4.3)

4.5.2.3. Origin of the EM1 component

The high $^{176}Hf/^{177}Hf$ for a given $^{143}Nd/^{144}Nd$, the somewhat high $^{87}Sr/^{86}Sr$ and low $^{143}Nd/^{144}Nd$ and $^{176}Hf/^{177}Hf$ ratios, as well as the occurrence of some (unaltered) samples with Ba/Nb > 10 (Appendix III.2.) also confirms the contribution from an enriched end-member, which has been ascribed to the EM 1 in previous studies on the southern Cape Verde islands (see Gerlach et al., 1988; Doucelance et al., 2003; Escrig et al., 2005; see also Fig.4.72).

Plotting lavas from key islands, assigned to represent the EM 1 end-member (Tristão da Cunha and Gough Islands), with Santiago's lavas it becomes apparent that the LILE, Ba, Rb and Cs deviates negatively from HIMU characteristics which may be explained by the contribution of an EM1-type end-member (Fig. 4.76).

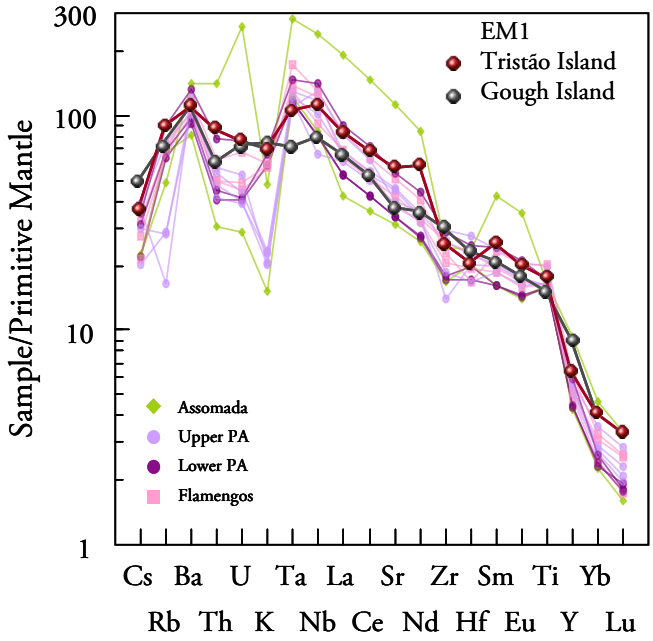

Figure 4.76 – Primitive mantle normalized (Palme and O'Neill, 2003) incompatible element concentrations of representative Santiago samples against an average EM 1 composition from Tristão da Cunha and Gough Islands (Willbold, 2005).

The nature of the enriched mantle component (EM 1) has been the subject of a intense debate and several hypothesis have been suggested such as recycled, ancient pelagic and/or metalliferous sediments (Weaver, 1991), recycled oceanic plateaux (Gasperini et al., 2000), ancient subcontinental lithospheric mantle (SCLM) (Hofmann, 1997), ancient delaminated lower continental crust (Willbold and Stracke, 2006), interaction with deep metasomatized

recycled oceanic lithosphere (Niu and O'Hara, 2003) and involvement of pyroxenitic restites (Tatsumi, 2000). For the southern Cape Verde islands, ancient recycled pelagic sediments, subcontinental lithospheric mantle (SCLM) and ancient delaminated lower continental crust have been considered as possible origins for the EM 1-like end-member (Gerlach et al., 1988; Doucelance et al., 2003; Escrig et al., 2005).

Sediments

Santiago samples plot close to the εNd-εHf mantle array (Vervoort et al., 1999; Chauvel et al., 2008) but with a distinctly shallower slope. The observed Santiago slope (0.76, r^2 =0.64) is significantly shallower than OIB (1.42) (Vervoort et al., 1999) and mantle arrays (1.33 and 1.59, Vervoort et al., 1999 and Chauvel et al., 2008, respectively), indicating a higher time-integrated Lu/Hf for a given Sm/Nd (see Fig. 4.24 from section 4.3).

Chauvel et al. (2008) concluded that the mantle array in Hf-Nd space cannot be explained exclusively by the mixture of recycled oceanic crust and depleted mantle and that a small amount of oceanic sediments is necessary to account for the OIB and MORB data trend. Due to the even shallower slope displayed for Santiago lavas, the presence of a sedimentary mantle component has to be assessed.

Indeed, similar "shallow" trends in εNd vs. εHf isotopic space have also been reported for Pitcairn lavas (1.0; Eisele et al., 2002) as well as for specific Hawaiian volcanoes (0.8; Koolau and Haleakala) and are considered to be indicative of recycled pelagic sediments in the source (see also, Blichert-Toft et al., 1999). In addition to the Hf isotopic evidence, some Santiago primitive lavas also show significant Ba enrichment (up to 1150 ppm), as well as high La/Nb (0.8±0.2) and Ba/Nb (12.5±3.2), in agreement with the putative influence of sediments in the mantle source (Kahoolawe: La/Nb=1.0±0.1, Ba/Nb=8.6±2.5, Huang et al., 2005; Koolau: La/Nb =1.3±0.1, Ba/Nb=9.2 ±1.5, Huang and Frey, 2005). However, Santiago lavas are clearly less radiogenic in Sr ($^{87}Sr/^{86}Sr \leq 0.70390$) than Pitcairn ($^{87}Sr/^{86}Sr \leq 0.7052$; Eisele et al., 2002) and Gough lavas ($^{87}Sr/^{86}Sr \leq 0.7053$, Class and le Roex, 2008), and they lack Nb and Ce

negative anomalies (Nb/Nb* up to 2; Ce/Ce*≥1.0)[26], which have been identified as reflecting the contribution of ancient recycled sediments (Pitcairn: Nb/Nb*=0.9-1.2, Eisele et al. 2002; Gough: Ce/Ce*≈0.92, Class and le Roex, 2008). Therefore, it is concluded that, if the presence of sediments as a cause for the EM 1 signature cannot be ruled out completely, its role was probably subordinate.

Lower and upper continental crust

Willbold and Stracke (2010) recently defended the hypothesis that the EM end-members are due to a unique and common source: the compositionally heterogeneous continental crust. Their study is based on isotopic (Sr-Nd-Pb) and trace element (Ba/Nb) modelling as well as Eu/Eu* values. In Santiago's case, even though primitive lavas are indeed characterized by small positive Eu anomalies (1.04-1.18), low $(Ba/Nb)_n$ values and somewhat high $(Ba/Th)_n$ (1.09±0.46 and up to 4, respectively[27]), as opposed to those characterizing average lower continental crust values (4.6 and 2.7, respectively; Rudnick and Gao, 2003) makes the lower continental crust an unsuitable explanation for the EM 1-type signatures.

Indeed, considering Santiago lavas compositions and the fact that the dominant HIMU-type end-member is presumably characterised by $(Ba/Th)_n \leq 1$ (Chauvel et al., 1992; Willbold and Stracke, 2006), the Santiago EM 1-type end-member would be characterised by much higher $(Ba/Th)_n$ values than those typical of lower continental crustal compositions. Such a characteristic is better matched by the Leucite Hills lamproites [$(Ba/Th)_n \leq 5.6$], considered to be proxies for SCLM (Mirnejad and Bell, 2006). Low mean $(Th/Nb)_n$, $(La/Nb)_n$ and $(Th/U)_n$ ratios (0.53 ± 0.11, 0.79 ± 0.18 and 1.05 ± 0.2 average values, respectively) of Santiago lavas support the notion that, even if present the role of the lower continental crust [$(Th/Nb)_n$ =1.73, $(La/Nb)_n$=1.48 and $(Th/U)_n$=1.57; Rudnick and Gao, 2003)] must have been minor in Santiago magma mantle source.

Low $^{143}Nd/^{144}Nd$ for a given $^{87}Sr/^{86}Sr$ displayed by Santiago lavas could eventually be due to the influence of lower crustal garnet-bearing mafic granulites, which can have evolved

[26] Nb/Nb* is defined as $Nb_n / \sqrt{(Th_n \cdot La_n)}$ and Ce/Ce* as $Ce_n / \sqrt{(La_n \cdot \mathrm{Pr}_n)}$. N subscript representing values normalized to chondritic values from Palme and O'Neill (2003).

[27] Values normalized to primitive mantle of Palme and O'Neill (2003).

towards high $^{176}Hf/^{177}Hf$, given the high compatibility of Lu in garnet (Janney et al., 2005) (Fig. 4.77).

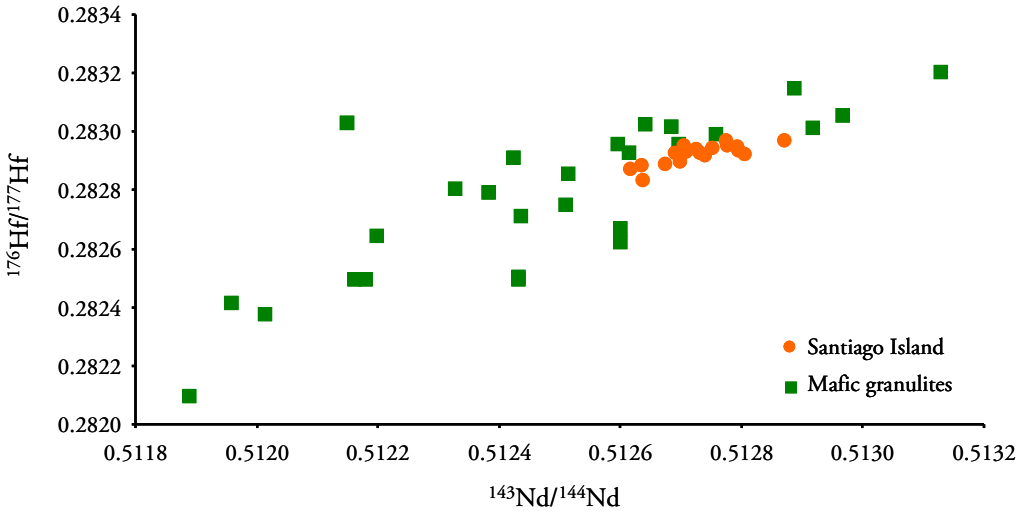

Figure 4.77 – Mafic granulites data projected against Santiago lavas. Data from Vervoort et al. (2000)

As an alternative hypothesis, the high ε_{Hf} relative to ε_{Nd} of the Santiago magma sources can reflect ancient melt extraction from a lithology characterized by high garnet/clinopyroxene ratio, producing a residue with a higher than usual (Lu/Hf)/(Sm/Nd) ratio (Blichert-Toft and White, 2001).

Lamproites and subcontinental lithospheric mantle (SCLM)

In Sr-Nd isotope space, Santiago samples display a trend that deviates from those of Pitcairn, Gough, Tristan da Cunha and, also, from the recently described Godzilla seamounts (Geldmacher et al., 2008), which are all considered the best representatives of the EM 1 end-member (Willbold and Stracke, 2006) (Fig. 4.78). The deviation towards lower values of $^{143}Nd/^{144}Nd$ supports a contribution from an enriched end-member with isotopic affinities such as those displayed by the Leucite Hills lamproites[28]. These lamproites are thought to be the result of preferential melting of a metasomatic vein assemblage (phlogopite ± richterite ± clinopyroxene ± apatite ± titanite) within the continental lithospheric mantle (Mirnejad and Bell, 2006). Interestingly, some of Lages silicate rocks (Eastern Brazil), which belong to the continental alkaline-carbonatitic complex of the Late Cretaceous Paraná-Angola-Etendeka

[28] Lamproite is a general term for mafic volcanic or hypabyssal ultrapotassic rocks (Le Maitre et al., 2002).

Province (Comin-Chiaramonti et al., 2002), are also characterised by similar relatively unradiogenic Nd isotope signatures plotting in the same trend between the Santiago samples and the Leucite Hills lamproites, thus indirectly supporting the contribution of SCLM for magma composition in the southern Cape Verde islands and, in particular, to Santiago Island. This is also endorsed by Figure 4.79 where Santiago lavas are compared with lamproites from other provinces.

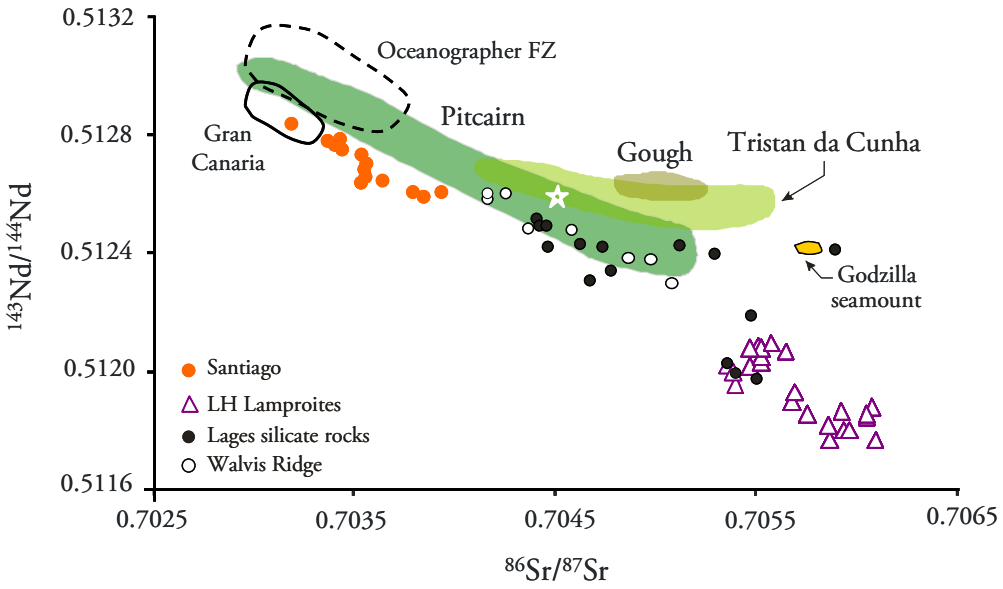

Figure 4.78 – Nd-Sr isotopic range of Santiago lavas. The trend defined by Santiago samples contrasts with those of ocean islands commonly ascribed to represent the presence of the EM 1 end-member (Pitcairn, Gough and Tristan da Cunha), but similar to those reported for Gran Canaria, Walvis Ridge, Lages silicate rocks and Leucite Hills (LH) lamproites (data from GEOROC database: http://georoc.mpch-mainz.gwdg.de). The Bulk Silicate Earth (BSE) value is indicated by a star.

The contribution of SCLM to the Cape Verde magmas had already been proposed for the silicate lavas from the southern Cape Verde islands as one of the possible explanations for the enriched component (Gerlach et al., 1988; Davies et al., 1989; Kokfelt et al., 1998; Doucelance et al., 2003), for the generation of Cape Verde magnesio-carbonatites (Hoernle et al., 2002) and as local of origin of kimberlitic-like metasomatic agents responsible for transformation processes depicted by Sal xenoliths (Bonadiman et al., 2005). However, Escrig et al. (2005) proposed, on the basis of the radiogenic Os isotope signatures of the neighbouring Fogo Island lavas that the EM 1-like signatures testify to the contribution of lower continental

crust to such magmas and extended this explanation to the other southern Cape Verde islands. As stated above, our data favours an SCLM origin for this component in Santiago, suggesting that the contribution of continental lithosphere to the Cape Verde magmatism was variable, including its crustal (e.g. Fogo, Escrig et al., 2005) and mantle portions (e.g. Santiago; Martins et al., 2010; this work).

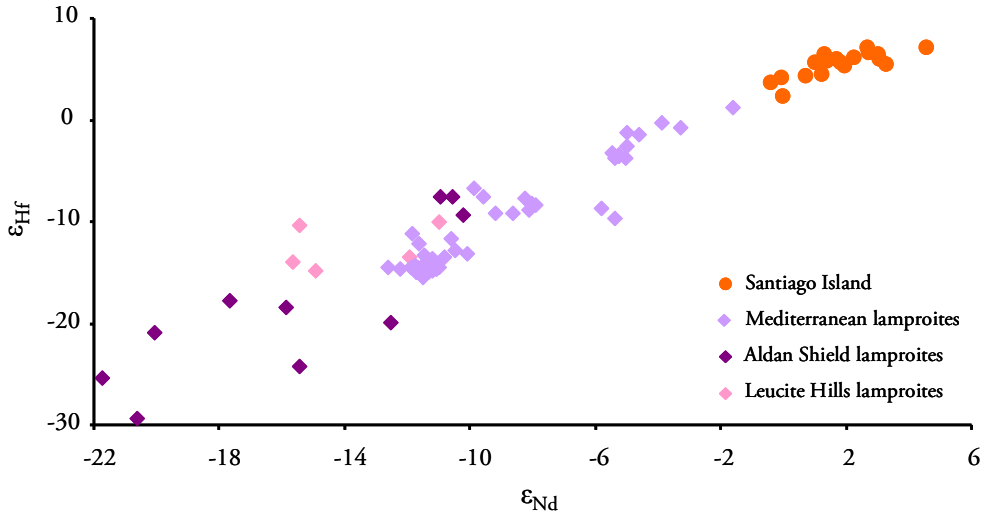

Figure 4.79 – Plotted lamproites are from Mediterranean (Prelević et al., 2010), Aldan shield, Russia (Davies et al., 2006) and Leucite Hills, USA (Salters and Hart, 1991).

In the nearby North Atlantic basin, the only ocean island developing a trend towards an EM 1-type component is Gran Canaria (Hoernle et al., 1991). EM 1-type signatures were also described for samples dredged at the Oceanographer fracture zone (Shirey et al., 1987; Dosso et al., 1999) and for the 34°27 N - 15°32 W Godzilla Seamount (Geldmacher et al., 2008). However, it should be noted that the Sr-Nd isotope trend developed by the Santiago and Gran Canaria lavas is distinct from those defined by the Oceanographer fracture zone and Godzilla Seamount (Fig. 4.78; Fig. 4.80). Indeed, the Santiago-Gran Canaria trend is characterised by a lower $^{143}Nd/^{144}Nd$ for a given $^{87}Sr/^{86}Sr$, being more similar to that reported for the Walvis Ridge in the southern Atlantic and to the Paraná magmatic province in Brazil (Comin-Chiaramonti et al., 2002).

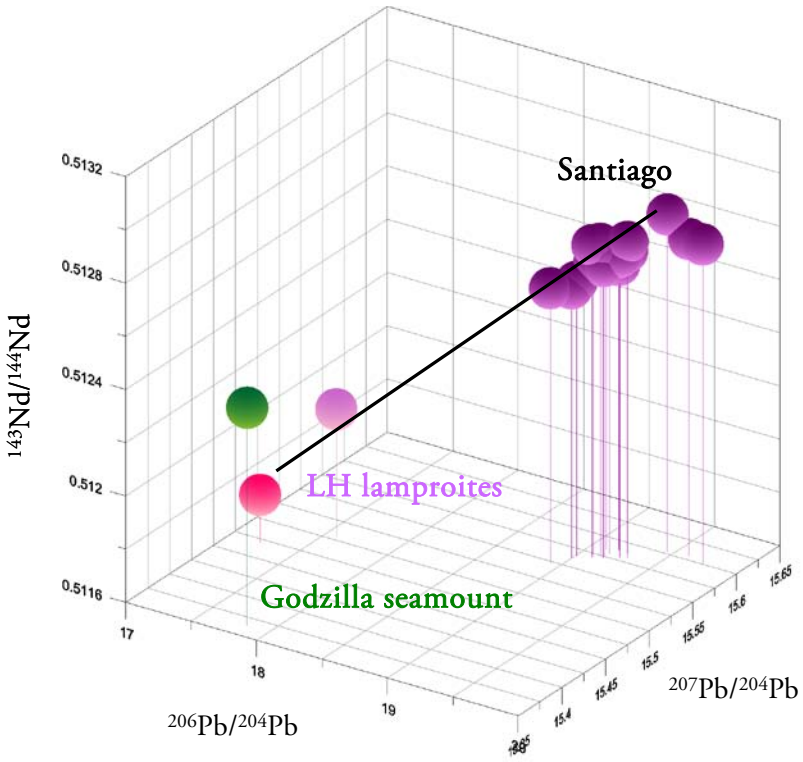

Figure 4.80 – The distinct trend of the Santiago lavas towards the Leucite Hills lamproites as opposed to the Godzilla seamount. Data of Leucite Hills lamproites and Godzilla seamount from Mirnejad and Bell (2006) and Geldmacher et al. (2008) respectively.

For the Godzilla Seamount, Geldmacher et al. (2008) proposed a peculiar EM1-type end-member which, at odds with the common EM1 component, is characterized by low $^{207}Pb/^{204}Pb$ for a given $^{206}Pb/^{204}Pb$, plotting below the NHRL (Δ 7/4 < 0). The authors explained such dichotomy on the lead isotope signatures of the EM1 end-members taking into account the model initially proposed by Mata (1998) for the secular evolution of the Earth's mantle (see also Mata and Kerrich, 2003; Mata et al., 2007). This model is based on the significant change on processes occurring during subduction of oceanic crust, due to the decrease of geothermal gradients throughout the Earth's history, and on its consequences on the U-Pb and Th-U fractionation over time.

During the early history of the Earth, subcontinental lithosphere was metasomatized by melts from subducted slabs along convergent margins generating high μ ($^{238}U/^{204}Pb$) and Th/Pb SCLM domains[29]. As the Earth cooled, hydrous fluids replaced melts as the main slab

[29] During melting $D_{Th}<D_U<D_{Pb}$ (e.g. Pertermann et al., 2004).

component metasomatizing the SCLM producing domains characterized by low μ and Th/Pb. Accordingly, Geldmacher et al. (2008) proposed that the relatively high $^{206}Pb/^{204}Pb$ and $^{208}Pb/^{204}Pb$ of the Godzilla-type EM1 could result from sampling a SCLM domain affected by a more ancient (Archean) metasomatic event than the typical EM1.

The acceptance of such a model and the fact that the Santiago trend is clearly not directed to the Godzilla composition (Fig. 4.78), could, eventually, constrain to the post-Archean the age of the metasomatic event triggering the genesis of the EM1 signatures now depicted by Santiago lavas. However, the Geldmacher's model must be regarded with caution, given that the development in the Archean of the SCLM metasomatized domain responsible by Godzilla signatures would lead to (Δ 7/4 < 0) at odds with the observed. Indeed the significant difference on the ^{235}U and ^{238}U half-life has as consequence the quick decrease of $^{235}U/^{238}U$, which is nowadays at 1/137.88.

4.5.2.4. The contribution of the lower mantle

Recent alternative theories which assign the lower mantle as a significant contributor to OIB magmatism (Lee et al., 2010) or even that mantle end-members are produced entirely by CO_2-fluxed melting in the lower mantle (Collerson et al., 2010) attest the possibility and the importance that a deep mantle contribution might have.

The difficulty of identifying and quantifying the amount of deep mantle contribution to OIB magmatism comes from its uncertain composition. The approaches to this problem are very diverse as well as the obtained results: (1) modelled melting of a deep mineral assemblage with specific partition coefficients (Collerson et al., 2010), (2) time-integrated composition of Fe-rich lithologies generated by ancient sinking liquids (Lee et al., 2010), (3) geochemical modelling of the earth composition since accretion and subsequent formation and evolution of the principal terrestrial reservoirs (Tolstikhin et al., 2006), (4) mixing between BSE material and depleted mantle (Doucelance et al., 2003) amongst others.

The influence of deep lower mantle material in the source of Cape Verde magmas was first defended by Christensen et al. (2001) based on noble gases determinations, namely on relatively unradiogenic He isotope determinations (R/Ra up to 13.8). Two years later Doucelance et al. (2003) based on low $^{4}He/^{3}He$ values (R/Ra up to 15.73) on silicate rocks

reinforced the idea, while Mata et al. (2010) also claims for a deep lower mantle contribution, harbouring primordial carbon, to Cape Verde carbonatite magmas based on He (R/(Ra up to 15.5), Xe ($^{129}Xe/^{130}Xe$ up to 6.84) and $\delta^{13}C$ isotopic evidence. More recently Mourão et al. (2012a) also reported relatively unradiogenic signatures for Brava silicate rocks (R/Ra up to 12.85) and carbonatites (R/Ra up to 11.80). Interestingly these authors demonstrated that Brava carbonatites are characterized by primary $^{4}He/^{40}Ar^{*}$[30] ≤ 0.3 which is clearly below the typical value of 1.5 for the upper mantle (see Moreira et al., 1998) and 1.8 for the lower mantle (Allègre et al., 1986). Such low values imply their origin from a reservoir (the "missing Ar reservoir" of Allègre et al. (1996)) which evolved under very low (U+ Th)/K ratios. Considering that such reservoir has to be isolated from the convective mantle, Mourão et al. (2012a) placed it into the deepest levels of the mantle.

Also, as described in Chapter 2, the presence of a large low velocity zone in the Atlantic area, identified by geophysical methods to be rooted in the D'' zone (Torsvik et al., 2006) and Montelli et al. (2006) data that ascribes the Cape Verde plume down to depths of 2800 km (see also Forte et al., 2010), makes the presence and entrainment of lower mantle material in the plume an almost certainty.

4.5.3. Contributors to the Santiago magmatism: Where does it come from?

From the above discussion is clear that to explain the chemical variability of the Santiago magmatism is necessary to invoke the contribution of the lower mantle and of HIMU- and EM1-type end-members.

The lower mantle extends from depths of 670 km to about 2900 km at the core-mantle boundary. However, combining geochemical, geophysical and numerical data is possible to better constrain the depth of the lower mantle domain involved in the Cape Verde magmatism.

As already mentioned (2.6) Cape Verde magmatism is considered to be related to a mantle plume. Mantle plumes are characterized by an excess of temperature relatively to the ambient

[30] $^{4}He/^{40}Ar^{*}$ stands for the $^{4}He/^{40}Ar$ ratio corrected for the effects of atmospheric contamination (for further calculation details see Mourão et al., 2012a).

mantle, prompting the density instability responsible by the generation/ascension of material. For Cape Verde an excess temperature[31] of 114ºC was calculated by Putirka (2008).

Such excess of temperature imply that the plume is rooted at a temperature discontinuity. Considering this, the tomographic data imaging the plume down to 2800 km (Montelli et al., 2006), the existence in Cape Verde of carbonatites characterized by $^{4}He/^{40}Ar^{*} \leq 0.3$ (Mourão et al., 2012a; see above) and the fact that the entrainment by a plume occurs essentially at the thermal boundary layer from which they rise (Farnetani et al., 2002; Farnetani and Hofmann, 2009) it is suggest that the lower mantle contribution to the Cape Verde magmatism is made through the incorporation of material at the deepest levels of the mantle, probably at the D" layer.

In the benchmark paper by Hofmann and White (1982) it was first proposed that recycled oceanic crust travel deep into the mantle and tend to accumulate at the D" layer, posteriorly being involved in the generation of mantle plumes, when it became gravitationally unstable due to internal heat generation and heat transfer from core. The involvement of recycled oceanic materials in plumes from the lower mantle is endorsed either by seismic tomographic, which has imaged remnants of slabs below the transition zone, some of them located near the core-mantle boundary (e.g. Fukao et al., 2001; Hall and Spakman, 2002; Jarvis and Lowman, 2007), either from density constraints (Hirose et al., 2005).

The HIMU component has been assigned to ancient recycled oceanic crust (Chauvel et al., 1992; Woodhead, 1996; Stracke et al., 2005; Hanyu et al., 2011) and, for Santiago it is proposed that the recycling process occurred at ≈ 1.5 Ga (see below, 4.5.3). This lead to the supposition that the residing place, where the recycled oceanic crust age, was the bottom of the mantle. A question may arise from how an HIMU dominated plume can produce He isotope signatures characterized by R/Ra up to 8.31 (Doucelance et al., 2003) when the enriched U character of recycled ocean crust should drive the R/Ra values to zero. This has been explained by assuming that the noble gas budget of the deep mantle reservoir is "unaffected" by the addition of crustal materials, which were almost completely stripped of He and Ne by degassing at mid-ocean ridges and, later, at subduction zones. In opposition, their lithophile,

[31] The excess temperature is calculated relative to the ambiente mantle, which in Putirka (2008) is the potential mantle temperature of the mid-ocean ridge at Siqueiros (1396 ºC). The potential temperature is calculated from olivine-liquid equilibria (see Putirka, 2008).

Os and Pb isotope signatures are strongly constrained by the recycled crustal material (e.g., Brandon et al., 2007; Jackson et al., 2009; Mata et al., 2010).

Numerical simulations have shown that heterogeneities in mantle plumes tend to be preserved during ascent (e.g. Farnetani et al., 2002; Farnetani and Hofmann, 2009). This could suggest that the EM1 fingerprints in the Santiago magmas were also intrinsic to the mantle plume as already proposed by Gerlach et al. (1988) and Barker et al. (2010). Lodge and Helffrich (2006) described distinct mantle flow patterns beneath the northern and southern Cape Verde islands, suggesting that magmas spread from separate melting loci. According to Barker et al. (2010), this could explain the apparent restriction of EM1 signatures to the southern Cape Verde islands reflecting the mantle plume azimuthal heterogeneity, with the EM1 component constituting sheared plume heterogeneity. Alternatively other authors suggest that this component is not present in the plume but resides in the upper mantle as a passive heterogeneity (Doucelance et al., 2003; Escrig et al., 2005; Millet et al., 2008).

Coltorti et al. (2009) identified mantle derived xenoliths similar to those derived from cratonic lithospheric mantle in Sal Island, from which Re-Os analyses of sulphide grains yield Neoproterozoic to Archean model ages similar to those found in the African and South America cratons. This evidence attests the existence of ancient SCLM domains in the mantle beneath the archipelago, which is also evidenced by the preservation of a K-rich metasomatic signature on clinopyroxenes on such xenoliths (Bonadiman et al., 2005). This is in agreement with seismic data from Begg et al. (2009) who described the occurrence of a high velocity zone in the mantle below the Cape Verde islands. This may represent delaminated fragments of the African continental lithospheric mantle left behind during the opening of the Central Atlantic Ocean (see also Bonadiman et al. 2005; Martins et al., 2010). Interestingly, Sal is one of the Northern Islands of the archipelago. Also Torres et al. (2010) proposed that some of the Sal lavas present characteristics suggesting the incorporation of an EM 1-type component. These demonstrate that the geochemical variability of the Cape Verde can no longer be correlated with a Northern vs. Southern dichotomy a percept also endorsed by recent data on the basal complex of Brava Island (Mourão et al., 2012b) and on the neighbouring Cadamosto Seamount (Barker et al., 2012) for which northern-type signatures were assigned, despite they are located on the southwestern tip of the archipelago.

The local of residence of such SCLM megaliths is still debatable. A shallow residence trapped inside the oceanic lithosphere was previously proposed on the basis of temporal isotopic variations described for Fogo (Escrig et al., 2005) and the correlation between isotopic signatures and differentiation indices (Hoernle et al., 1991; Millet et al., 2008). In opposition Coltorti et al. (2010) considered it as residing in the asthenosphere "surfing" the convecting mantle.

This hypothesis received recent support from Mourão et al. (2012b) through the study of temporal geochemical evolution of the Brava Island. Indeed considering the interaction of ascending plume or magmas with a SCLM megalith a temporal evolution would be expected where the continental lithosphere role diminishes/vanishes with progressive exhaustion of the less refractory/more fertile (i.e., metasomatized) domains. However, the opposite is observed for Brava where the most ancient rocks (Basal Complex) do not provide evidence for significant continental lithosphere contribution, in contrast to the volcanics from the Upper Unit. Considering the observed temporal evolution of Brava, Mourão et al. (2012b) proposed that in the Cape Verde region at least some of the continental megaliths are not attached to the oceanic lithosphere but instead float and move within the asthenosphere at a level that is likely determined by density constraints.

4.5.4. Assessing the age of the oceanic crust recycling

The presence of an HIMU-type component has long been invoked as one of the most important contributors to the Cape Verde mantle source(s) and, in particular to the Santiago one(s) (Gerlach et al., 1988; Barker et al., 2009; 2010; see also 4.5.2). This component has been considered elsewhere the result of ancient recycling of altered oceanic crust (e.g. Hofmann and White, 1982; Chauvel et al., 1992; Woodhead, 1996; Hofmann, 1997; 2003; Stracke et al., 2005; Hanyu et al., 2011).

The Pb isotopic system as long been used in quantitative models to constrain the age of the Earth and its reservoirs (e.g. Gerling, 1942; Holmes, 1976; Houtermans, 1946). The Holmes-Houtermans model is considered the first general model for determining the age of the Earth from the evolution of Pb. The model assumes that 1) the Earth was originally fluid and homogeneous, 2) there was a uniform distribution of U, Th and Pb, 3) the primeval Pb

isotopic composition was the same overall and 4) Earth evolution lead to differentiation of several subsystems with different U/Pb ratios that changed as a result of radioactive decay of U and Pb.

Taking into account that the equations describing the evolution of $^{206}Pb/^{204}Pb$ and $^{207}Pb/^{204}Pb$ ratios

$$\frac{^{206}Pb}{^{204}Pb} = \left(\frac{^{206}Pb}{^{204}Pb}\right)_i + \frac{^{238}U}{^{204}Pb}\left(e^{\lambda t} - 1\right) \tag{12}$$

$$\frac{^{207}Pb}{^{204}Pb} = \left(\frac{^{207}Pb}{^{204}Pb}\right)_i + \frac{^{235}U}{^{204}Pb}\left(e^{\lambda t} - 1\right) \tag{13}$$

can be combined producing:

$$\frac{\frac{^{207}\mathrm{Pb}}{^{204}\mathrm{Pb}} - \left(\frac{^{207}\mathrm{Pb}}{^{204}\mathrm{Pb}}\right)_i}{\frac{^{206}\mathrm{Pb}}{^{204}\mathrm{Pb}} - \left(\frac{^{206}\mathrm{Pb}}{^{204}\mathrm{Pb}}\right)_i} = \frac{^{235}\mathrm{U}}{^{238}\mathrm{U}}\left[\frac{e^{\lambda_{235}t} - 1}{e^{\lambda_{238}t} - 1}\right] \tag{14}$$

which is known as the Holmes-Houterman equation for lead single-stage dating. Bearing in mind that $^{235}U/^{238}U$ takes nowadays the value of 1/137.88, it can be said that equation (13) is the equation of a straight line in the $^{207}Pb/^{204}Pb$ vs. $^{206}Pb/^{204}Pb$ space, where the slope m is function of *t*, being defined by

$$m = \frac{1}{137.88}\left[\frac{e^{\lambda_{235}t} - 1}{e^{\lambda_{238}t} - 1}\right] \tag{15}$$

In order to use the Holmes-Houterman equation for determining the age of the Earth the primeval Pb isotope ratios of the Earth had to be known. This was accomplished by determining those ratios in iron-meteorites, in particular the Canyon Diablo meteorite[32].

By using equations (12) and (13) it is possible to build a Pb-Pb isochron diagram in $^{206}Pb/^{204}Pb$ -$^{207}Pb/^{204}Pb$ space, the graphic representation of the Holmes-Houtermans model (Figure 4.81) (Holmes, 1946, Houtermans, 1946).

The evolution of minerals and rocks start at a precise point (initial $^{206}Pb/^{204}Pb$ and $^{207}Pb/^{204}Pb$ ratios) and follow an arc with a specific radius depending on the U/Pb of the samples (hence different $^{238}U/^{204}Pb$ values, μ)(Armstrong, 1968; Stacey and Kramers, 1975). Even tough, samples with distinct U/Pb ratios portray different paths, they will fall on a line whose slope can yield age information (isochron). Patterson (1956) determined a very important Pb-Pb isochron using iron meteorite data to infer Earth's age, the geochron, with a date of 4.55±0.07 Ga.

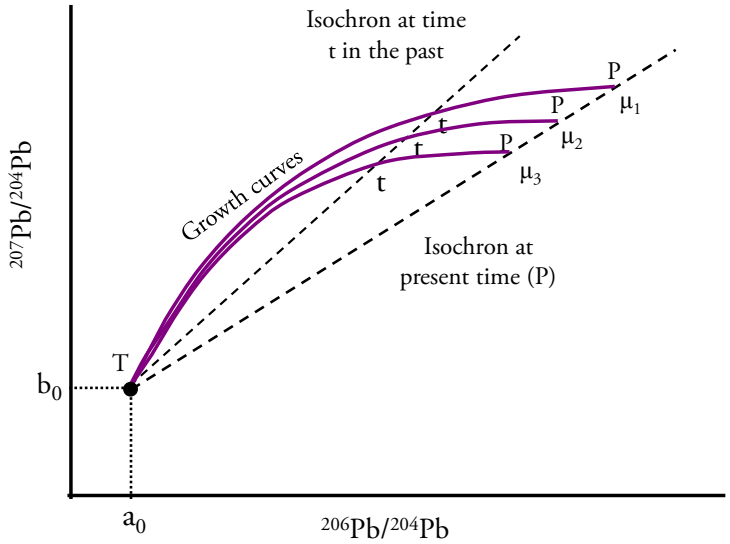

Figure 4.81 – Graphical representation of the Holmes-Houtermans model for the Earth lead isotope evolution. Figure adapted from http://hyperphysics.phy-astr.gsu.edu/.

The majority of magmatic provinces plot to the right-hand side of the geochron, which according with the Holmes-Houterman model would imply negative ages for the corresponding mantle sources (the *future paradox* of Allègre et al., 1968). This characteristic

[32] Pb primeval isotopic ratios of Earth determined in Canyon Diablo troilite (FeS): $^{206}Pb/^{204}Pb$=9.037, $^{207}Pb/^{204}Pb$=10.293 and $^{208}Pb/^{204}Pb$=29.475 (Chen and Wasserburg, 1983).

associated with their shallower slope (compared with that portrayed by the geochron), can be attributed to several processes in the mantle such as mixing, but also can implies a two-stage model.

The fundamental assumption of the two-stage model is that there is a initial period of time when Pb evolves from primordial isotope ratios, at the onset of Earth's history (t=0), and after a period of time the U/Pb ratio of the reservoir changes by geochemical differentiation and remains constant to the present (Stacey and Kramers, 1975).

Santiago samples plot in the right-hand side of the geochron and so, as described above, a set of analytical data defining a straight line with a given slope on the $^{207}Pb/^{204}Pb$ vs. $^{206}Pb/^{204}Pb$ diagram can have an age significance, which allows the calculation of the event which triggered the U/Pb increase responsible by the positioning relative to the geochron. One of the peculiarities of the HIMU component is its positioning, on the $^{207}Pb/^{204}Pb$ vs. $^{206}Pb/^{204}Pb$ diagram, clearly to the right of the geochron being the mantle component characterized by higher $^{206}Pb/^{204}Pb$ (e.g. Zindler and Hart, 1986; Hart, 1988). These indicate that it represents a mantle domain which suffered a significant increase of μ ($^{238}U/^{204}Pb$) during its evolution (e.g. Allègre, 1969). Such interpretation, implying a long term evolution under high μ, justifies the designation of this mantle component.

In the case of the HIMU-type signatures such U/Pb increasing event is considered the recycling of altered oceanic crust (e.g, Chauvel et al., 1992; Hanyu et al., 2011) and its age may be inferred using equation 12. It is worth to note that that this equation is transcendental do not having an algebraic solution. However, t can be obtained by linear interpolation in tables constructed by numerical approach for specific t (e.g. Table 10.3 in Faure and Mensing, 2005).

The application of this methodology to Santiago data set would produce a value of about 1.3 Ga corresponding to a slope of 0.0825 (Fig. 4.82A). However this value must not be considered as a reliable estimate. Indeed, besides the demanding *a priori* intrinsic conditions necessary to ensure the applicability of the method[33], it must be taken into account that 1) the obtained correlation coefficient is very low (r^2 = 0.57) indicating a high dispersion of data relatively to the calculated best fit and suggesting a MSWD >>1; 2) it was demonstrated the

[33] - The studied samples must be considered representative of an initial homogeneous portion of the mantle that at time t suffered a fractionation episode that variable raised the U/Pb ratio, that afterwards and until the actual time, evolved in a closed system relative to U and Pb (relative to μ_i) and without having any homogenization of the until then formed sub-domains).

existence of a temporal variation of the chemical characteristics of Santiago magmatism (see 4.4) indicating that magmas cannot be considered cogenetic all along the volcanostratigraphic pile.

The application of this methodology to the Upper Pico da Antónia formation, for which 5 samples were analysed for lead isotopes, produces a straight line with slope of 0.0943 with r^2=0.95 which, if interpreted as a secondary isochron, would correspond to an age of about 1.52 Ga for the fractionation event[34] (Fig. 4.82B). This age is similar to the ones which have been estimated for the fractionation event at the origin of the HIMU-type end-member sampled by the Cape Verde magmatism (1.4 to 1.6 Ga; Doucelance et al., 2003; Escrig. et al., 20005; Holm et al., 2006; Millet et al., 2008; Mourão et al., 2012b).

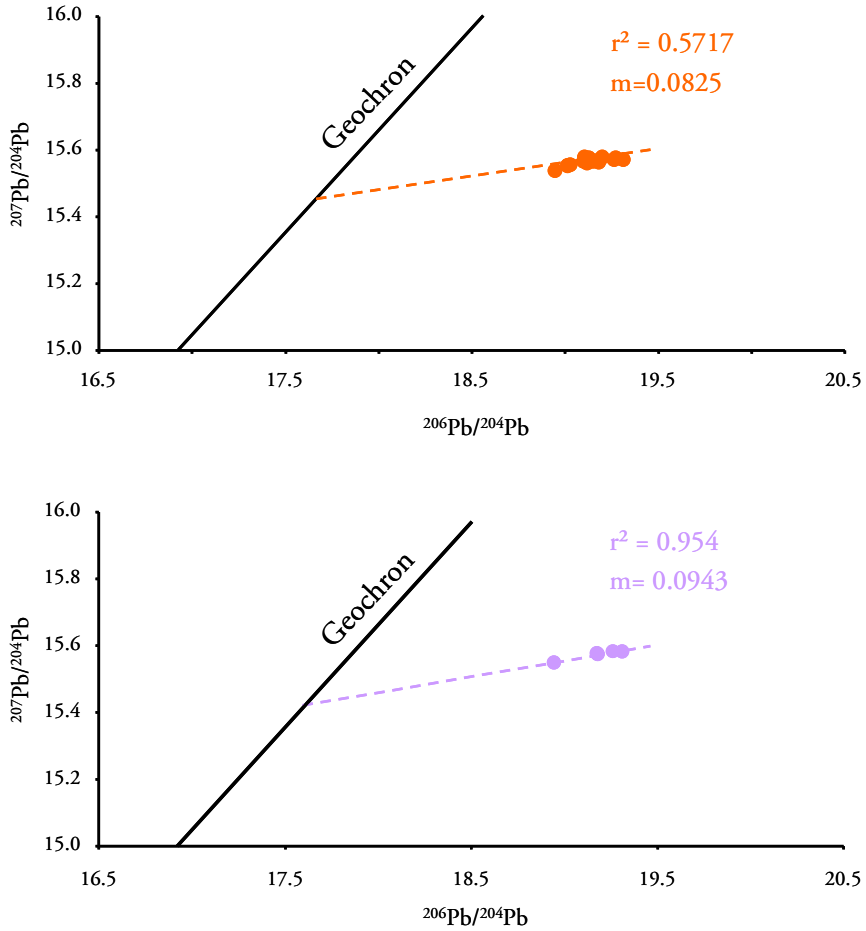

Figure 4.82 – Possible age significance of the trends portrayed by Santiago samples (A) and Upper Pico da Antónia formation samples (B) in $^{207}Pb/^{204}Pb$ vs. $^{206}Pb/^{204}Pb$ space.

[34] For the other formations the low number of lead isotope analyses (Monte das Vacas, two samples; Assomada: three samples; Lower Pico da Antónia: four samples; Flamengos: three samples) were considered inadequate for this type of modeling.

However, mixing processes also produce straight lines in diagrams where, like in Figure 4.82, are considered ratios with the same denominator. Taking into account evidences for mixing involving distinct mantle components at the Santiago mantle source, it is unlikely that the linear trend can be considered a secondary isochron.

In order to assess the validity of this percept the approach used by Abouchami et al. (2000) was used, taking into account Th/U ratios (κ).

According to Abouchami et al. (2000) a comparison can be made between the κ source values (inferred from elemental ratios, atomic $^{232}Th/^{204}Pb$) and the κ values inferred from the Pb isotopic ratios (Th/U ratio integrated in time, κ_{Pb}) (see also Galer and O'Nions, 1985; Allègre et al., 1986). Since

$$\frac{^{208}Pb^{*}}{^{206}Pb^{*}} = \left[\frac{(^{208}Pb/^{204}Pb)_{measured} - (^{208}Pb/^{204}Pb)_{CD}}{(^{206}Pb/^{204}Pb)_{measured} - (^{206}Pb/^{204}Pb)_{CD}} \right] \quad (16)$$

and

$$\kappa_{Pb} = \left(\frac{^{208}Pb^{*}}{^{206}Pb^{*}} \right) \cdot \frac{(e^{\lambda_{238} \cdot t} - 1)}{(e^{\lambda_{232} \cdot t} - 1)} \quad (17)$$

where

λ_{238} : constant decay of ^{238}U;

λ_{232} : constant decay of ^{232}Th;

t: age of the Earth, 4.55 Ga;

CD : Canyon Diablo values (primordial Pb)

Santiago $^{208}Pb^{*}/^{206}Pb^{*}$ ratios, κ_{Pb} and κ values were determined (Table 4.6).

Experimental data reveals that in the presence of garnet $D_{Th}<D_{U}$ (e.g. Beattie, 1993). Considering that it was concluded (see 4.4.3.1.) that Santiago primitive magmas were generated from a lithologic heterogeneous mantle source with a high content of residual garnet

(garnet peridotite/garnet pyroxenite), it is expected that these magmas will the characterized by Th/U ratios higher than those of the source.

Table 4.6 - $^{208}Pb^*/^{206}Pb^*$ ratio, κ_{Pb} and κ determined for Santiago samples[35].

Sample	Formation	$^{208}Pb^*/^{206}Pb^*$	κ_{Pb}	κ
ST-16	Monte das Vacas	0.967	3.915	2.921
ST-24	Monte das Vacas	0.971	3.932	3.577
ST-21	Assomada	0.968	3.918	4.230
ST-23	Assomada	0.971	3.931	3.876
ST-27	Upper Pico da Antónia	0.971	3.933	3.739
ST-40	Upper Pico da Antónia	0.964	3.905	5.919
ST-44	Upper Pico da Antónia	0.964	3.904	4.688
ST-50	Upper Pico da Antónia	0.959	3.882	3.138
ST-59	Upper Pico da Antónia	0.981	3.971	3.864
ST-37	Lower Pico da Antónia	0.967	3.915	3.962
ST-42	Lower Pico da Antónia	0.967	3.917	4.254
ST-30	Lower Pico da Antónia	0.962	3.896	3.999
ST-74	Lower Pico da Antónia	0.977	3.958	4.005
ST-12	Flamengos	0.974	3.944	4.261
ST-34	Flamengos	0.966	3.911	4.348

Table 4.6 indicates that some Santiago samples exhibit κ values lower than κ_{Pb}, in opposition to what would be expected, arguing against the secondary isochron meaning of the Santiago linear trends and reinforcing the mixing hypothesis.

Another method used to infer the age of the oceanic crust recycling is a simplistic two stage-model of Stacey and Kramers (1975), in a similar approached to that of Chase (1981), Chauvel et al. (1992), Doucelance et al. (2003) and many others. A first stage, beginning at 4.55 Ga can be considered as characterized by μ_1=8.1 and the initial Pb isotopic composition identical to Canyon Diablo troilite values (Chen and Wasserburg, 1983). For the second stage, several μ values can be assumed (μ_2=15, 18 and 22) taking in to account the significant higher U/Pb ratio of the deep recycled oceanic crust, consequent from alteration by seawater (U increase) and/or from dehydration during subduction (Pb depletion) (Fig. 4.83).

Considering the linear trend portrayed by Santiago samples as a mixing line, its slope must be constrained by the composition of the end-members. As one of the source end-members for lavas of all the Santiago volcanic complexes is of HIMU-type (see 4.5.2.2.), it can be assumed that the high $^{206}Pb/^{204}Pb$ termination would represent the higher HIMU

[35] κ values are inferred from Pb isotopic ratios, see Appendix V.5 for calculation procedure.

proportion in the source and that its prolongation would pass through the HIMU-type end-member composition. Taking this into account, an attempt can be made to assess the characteristics of the fractionation event responsible by the U/Pb increase, i.e. the characteristics of the second stage. The modelling illustrated in Fig. 4.83 allows the interpretation that the fractionation (oceanic crust recycling) event occurred between 1.5 and 1.6 Ga, being the deep mantle recycled oceanic crust characterized by a μ of about 15, which is consistent with values obtained by Barker et al. (2010) for Santiago Island.

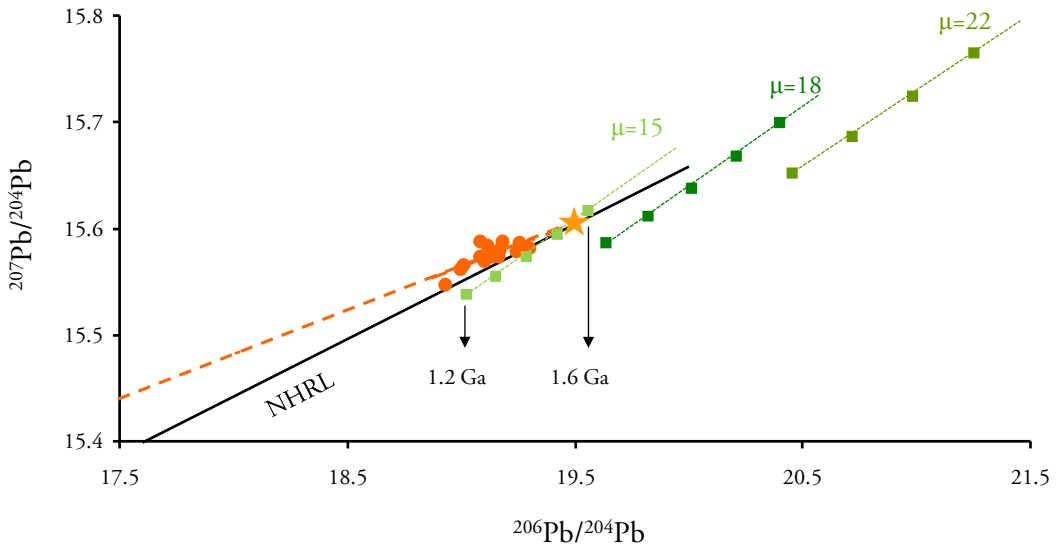

Figure 4.83 –Recycled oceanic crust modelled using a two-stage model with μ_1=8.1 and variable μ_2 (15, 18 and 22) and an age ranging from 1.2 to 1.6 Ga. The intercept of the modelled data with Santiago values assigns the recycling episode between 1.5 and 1.6 Ga, the recycled material being characterized by a μ value of about 15.

4.5.5. Isotopic constraints to the relative proportions of the contributors to the Santiago magmas

According with the above interpretation of trace element and isotopic signatures Santiago mantle source can be envisaged as a mixture of three distinct end-members: recycled oceanic crust (ROC; HIMU-like), subcontinental lithospheric mantle (SCLM; EM 1- like) and lower mantle (LM), in accordance with previous studies (Gerlach et al., 1988; Davies et al., 1989; Doucelance et al., 2003; Barker et al., 2010; Mourão et al., 2012b) and this work (see 4.5.2) In the next paragraphs the relative proportions of those end-members will be assessed. As stated

earlier the enriched end-member is most likely subcontinental lithospheric mantle from which the Leucite Hills lamproites have been considered a proxy, making them a viable end-member to use in quantitative approach to the proportions between the three main end-members in Santiago magmas mantle source.

It is important to acknowledge that the Cape Verde plume material has been considered a mixture of ancient recycled oceanic crust (ROC/HIMU) and lower mantle material (e.g. Doucelance et al., 2003; Mata et al., 2010; Mourão et al., 2012a; see 4.5.2). Considering that, at Santiago, advecting plume magmas interacted with material with SCLM affinities before eruption, it is very difficult to use the chemistry of their magmas to infer about the proportion of ROC and LM in the plume. For Cape Verde some attempts have been made based on islands/complexes not presenting evidences for a SCLM. Doucelance et al. (2003) calculated that in the Cape Verde plume ROC and LM are present in the proportion 42:58, while Mourão et al. (2012) proposed a 90:10 proportion. Considering constrains on numerical and analogical simulations of entrainment (e.g. Davaille, 1999; Farnetani et al., 2002) which severely limit the amount of entrainment of ambient mantle at the locus of plume inception, the proportion calculated by Mourão et al. (2012b) seems to be more reasonable.

In Fig. 4.84 it is represented the modelled mixture of recycled oceanic crust (ROC) with distinct recycling ages (see 4.5.4) with lower mantle material (LM). It can be seen that the variability of Santiago samples can be described by a mixture of distinct proportions between ROC of different recycling ages and lower mantle material. This evidence is not surprising since testimonies of recycling events of different ages may be preserved (maintaining their individual isotopic fingerprint) in the mantle even after incorporation in a rising plume (e.g. Farnetani et al., 2012). Moreover, tomographic (e.g. Montelli et al., 2004; 2006) and noble gas studies (e.g. Mourão et al., 2012a) point to the D'' layer as the root of the Cape Verde plume, which has been considered to be formed by accumulation of ancient recycled materials (e.g. Brandenburg and van Keken, 2007; Tackley, 2011), thus allowing the suggestion that is highly heterogeneous.

However it must be emphasized that part of this variability is probably the result of the interaction of ROC/LM plume material with shallow mantle residing SCLM megaliths as can be seen at Fig. 4.85.

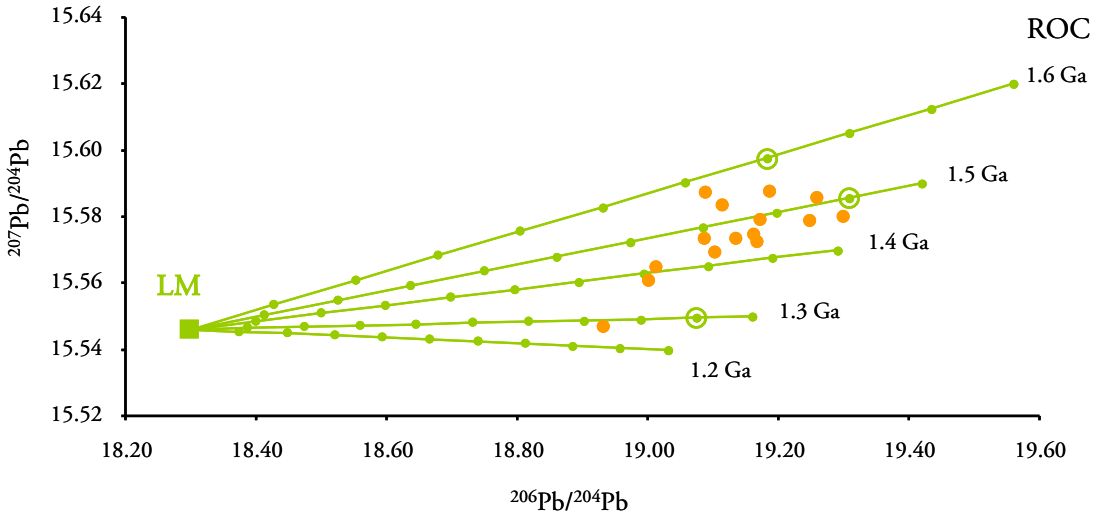

Figure 4.84 - Modelled mixture between recycled oceanic crust of different ages (μ_2=15, see section 4.5.4 for further details) and lower mantle material. The variability of Santiago samples can be explained by a mixture of up to 30LM:70ROC (1.6 Ga recycling age), 10LM:90ROC (1.5 recycling age) and 10LM:90ROC (1.3 recycling age) (points highlighted in the lines of mixture). The data for ROC is from section 4.5.4. and lower mantle from Doucelance et al. (2003). Circular marks represent 10% increments.

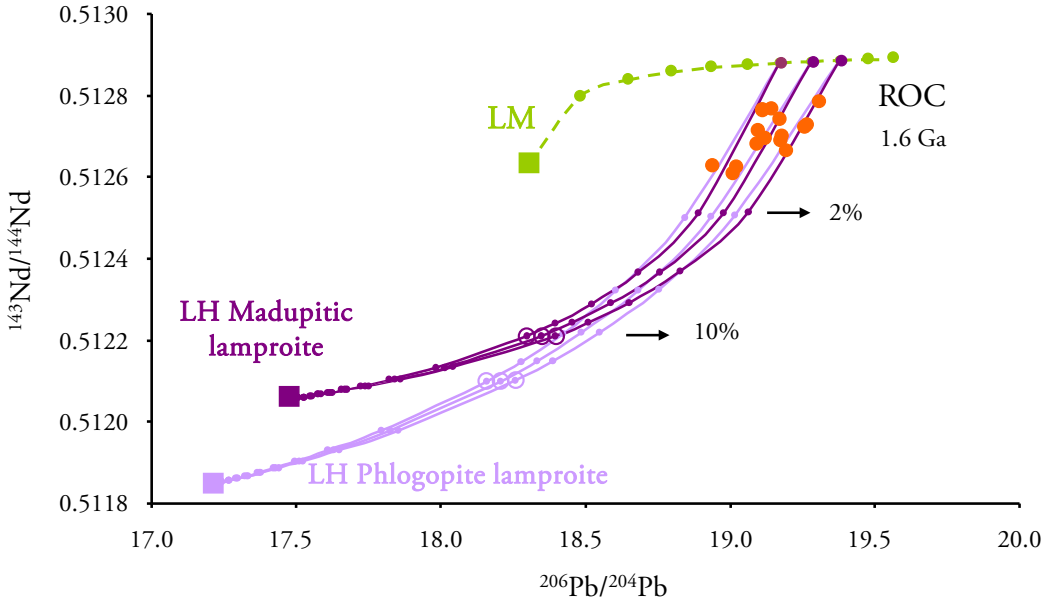

Figure 4.85 – Mixing model between plume material (recycled oceanic crust plus lower mantle material in 80:20, 70:30 and 60:40 proportions, as the starting points) and subcontinental lithospheric mantle proxies. Values are from Doucelance et al. (2003) (lower mantle) and Mirnejad and Bell (2006) (Leucite Hills madupitic lamproites: $^{206}Pb/^{204}Pb$=17.507; $^{143}Nd/^{144}Nd$= 0.512058; phlogopite lamproites: $^{206}Pb/^{204}Pb$=17.245; $^{143}Nd/^{144}Nd$= 0.51185). Circular marks represent 10% increments, except in the mixing trend between plume material and SCLM, before the 10% mark, were circular marks represent 2% increments.

The isotopic and elemental heterogeneity, that certainly characterizes the SCLM, owing their long but variable age and non-convective character, is represented in Figure 4.81 through the selection of two lamproites groups found at Leucite Hills: madupitic and phlogopite varieties[36]. Madupitic lamproites are considered to be derived from lower degrees of partial melting at greater depths relatively to phlogopite lamproites, which allow considering these two types of lamproites as representatives of different depths of the SCLM (Mirnejad and Bell, 2006). It can be seen that Santiago variability can be achieved by mixing different proportion of ROC and lower mantle with up to 2% of the enriched component.

Sr and Nd Santiago isotopic variability was also modelled with a mixture between ancient recycled oceanic crust (1.6 Ga) plus lower mantle (Doucelance et al., 2003) and a subcontinental lithospheric mantle proxy. In Nd vs. Sr space, Santiago data variability was obtain with up to 4% addition of enriched end-member, characterized by heterogeneities at the trace element level, specifically in Nd. For each lamproite (phlogopitc vs. madupitic) Nd variability was modelled with Nd values ranging from 280 to 400 ppm for madupitic lamproites and 118 to 200 ppm for phlogopite lamproites in accordance to that observed in samples from Leucite Hills (Mirnejad and Bell, 2006) (Fig. 4.86). Significantly the obtained value is similar to the one obtained when modelling was performed using Nd and Pb isotopes (cf. Fig. 4.85). From these figures can also be concluded that either type of the above mentioned lamproites, or even mixtures between them, can be considered representatives of the composition of the SCLM domain with which the Santiago interacted during their advection from plume to the surface.

The genesis of subcontinental lithospheric mantle involves multiple depletion and enrichment events at different time scales, conferring to this reservoir very heterogeneous signatures, which given their non-convective character tend to be maintained or even increased, in the case of isotope signatures, through the time. These heterogeneities at the isotopic and trace element level are transmitted to the magmas they came in contact with (Mirnejad and Bell, 2006). For this reason it is important to acknowledge that the assumed values as well as using the Leucite Hills lamproites as proxies to the subcontinental lithospheric mantle is an

[36] Leucite Hills lamproites are characterized by the occurrence of phlogopite, diopside, leucite, sanidine, apatite and perovskite. The term madupitic indicates that phlogopite occurs in the groundmass in poikilitic arrangements, opposed to phlogopite lamproites were phlogopite occurs as phenocryts.

approximation and as so, the calculations made should be considered semi-quantitative due to the associated uncertainties.

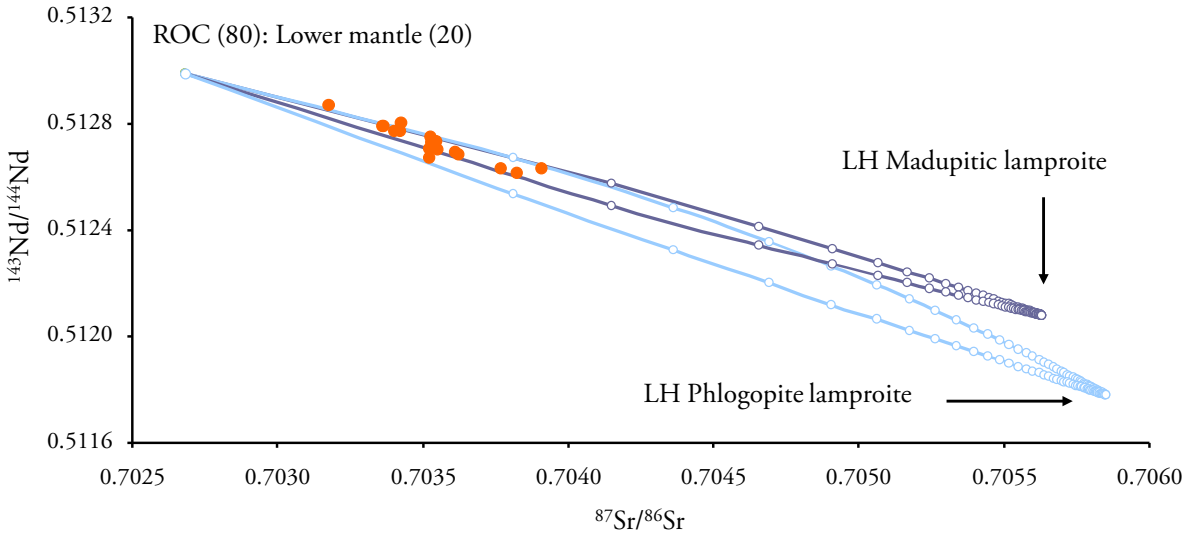

Figure 4.86 – Mixing model between plume material ancient (80:20 proportions of recycled oceanic crust + lower mantle material) (1.6 Ga, $^{87}Sr/^{86}Sr$= 0.702547; $^{143}Nd/^{144}Nd$= 0.512992; Sr=80.5 ppm; Nd=7.449 ppm; Stracke et al., 2003) and subcontinental lithospheric mantle represented by Leucite Hills lamproites (madupitic: $^{87}Sr/^{86}Sr$= 0.70553; $^{143}Nd/^{144}Nd$= 0.51208; phlogopite: $^{87}Sr/^{86}Sr$= 0.70553; $^{143}Nd/^{144}Nd$= 0.51178; Mirnejad and Bell, 2006). Circular marks represent 2% increments.

Doucelance et al. (2003) and Millet et al. (2008) explained part of the Cape Verde magmas variability as the result of the entrainment of depleted upper mantle. For Santiago, however the influence of depleted upper mantle is clearly denied by the mixing trend represented in Fig. 4.87. In Nd vs. Pb isotopic space it is obvious that the trend exhibited by Santiago samples is opposite to the predicted influence of a depleted end-member.

Recently Mourão et al. (2012b) also denied the significant role of the depleted mantle as a constrainer of the Brava magmas chemistry.

For this work Hf isotope signatures were obtained, which could also be used to constrain the proportion of the different contributors to the Santiago magmas. Unhelpfully the use of this isotope system is much less common than the verified for the systems Sr-Nd-Pb. As a consequence the number of incognita concerning the composition of the different Earth reservoirs/materials is still very considerable, reason why Hf isotopes were not used here in attempting to quantify the contributors to the Santiago magmas.

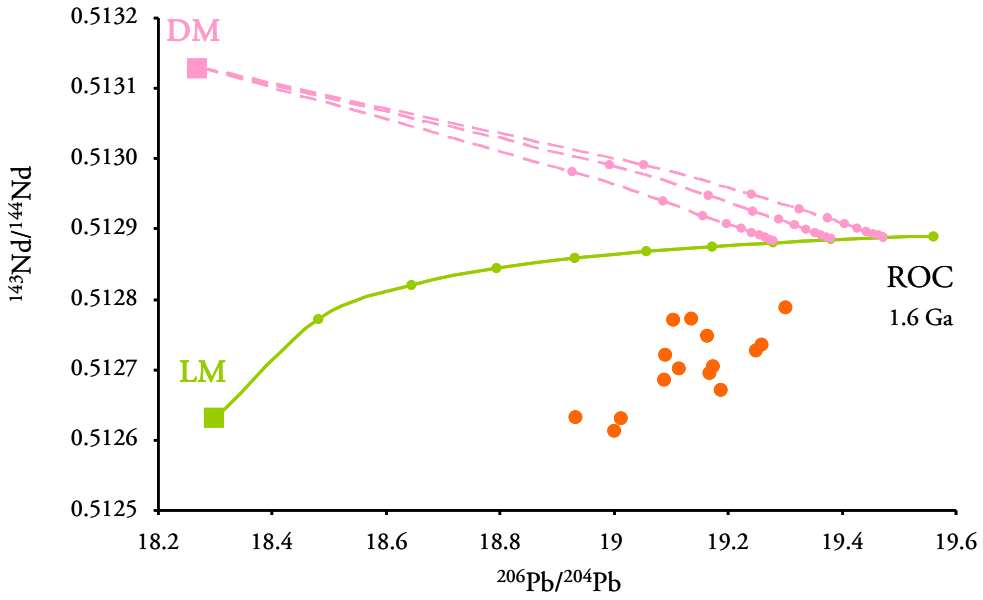

Figure 4.87 –Mixing model between plume material (recycled oceanic crust plus lower mantle material in 90:10, 80:20 and 70:30 proportions, as the starting points) and depleted upper mantle. Values are from Doucelance et al. (2003) (lower mantle) and Workman et al. (2005). Circular marks represent 10% increments.

CHAPTER 5

PLUME-LITHOSPHERE INTERACTION

Ponta Bicuda (Santiago – Cape Verde)
Thick lava piles of Pico da Antónia Formation over Complexo Antigo

5.1. Introduction

Oceanic magmatism erupted away from the influence of "recent" subduction events has been considered as windows to the mantle and, particularly, to their sublithospheric domains (e.g. Hofmann, 1986; 2003 and references therein). This is understandable in the light of the high solidus temperature of the crust (dominated by basalts) and of the relatively young age and refractory composition of the subjacent lithosphere when compared with their continental counterparts. Indeed the low solidus continental crust and the very complex and variable chemistry of continental lithosphere make magmas erupted in continental areas highly prone to lithosphere (s.l.) contamination in opposition to the considered for magmas erupted in oceanic environments for which such processes are generally assumed as negligible.

For Cape Verde the situation was similar until 1988 when Gerlach et al. proposed, as one of the alternatives to explain the EM–type signatures of the Southern Cape Verde islands, the interaction of the ascending plume with SCLM domains attached to the oceanic lithosphere. Later, Kokfelt et al. (1998) attributed to the carbonatitically metasomatized oceanic lithosphere the origin of HIMU and EM-1 type components detected in lava compositions. At least for the HIMU component this idea did not receive the support of any of the subsequent studies, which considered such component as carried by a deep rooted plume to the shallow mantle (e.g. Barker et al., 2010; Doucelance et al., 2003; Escrig et al., 2005; Holm et al., 2006; Martins et al., 2010, Mourão et al., 2012a). Later, the role of lithosphere as a contributor to the Cape Verde magmas was re-addressed by Martins et al. (2003, 2010), this work and Millet et al. (2008) who showed that ascending Cape Verde plume magmas chemically interact with the lithosphere during their ascent to the surface, acquiring fingerprints of such process (es). Recently Doucelance et al. (2010) considered the metasomatized lithosphere as the source of Cape Verde carbonatites, in opposition to the defended by Mata et al. (2010) and Mourão et al. (2012b).

The contribution of the lithosphere to the composition of oceanic magmas has been also invoked in other volcanic provinces (Class et al., 1998; Gaffney et al., 2004; Humphreys and Niu, 2009; Mata et al., 1998; Millet et al., 2009; Niu et al., 2012; Pilet et al., 2005, 2008) clearly

showing that consequences of plume impingement at the base of the lithosphere are not limited to geological and geophysical aspects such as large-scale dynamic topography, thermal, tomographic and gravity anomalies (Burov et al., 2005; Courtney and White, 1986).

All these show that the use of oceanic basalts to assess the composition of sub-lithospheric mantle must be done with care and after filtering the effects of lithospheric contributions to the erupted magmas. However, as emphasized by Millet et al. (2009), this is not usually the case.

Convinced of the importance of this subject, in this chapter it will be presented a compilation of evidences dispersed on former chapters that attests the significance of the plume-lithosphere interaction and its relevance, not only for the specific case of Cape Verde, but also for worldwide studies in similar geodynamic settings. Indeed the Cape Verde area shows specificities that make it an extraordinary site for studying the interaction between lithosphere and a mantle plume. These physical and geochemical particularities are due, not only to regional lithospheric constraints but also to the nature of the mantle under the Cape Verde region and the deep mantle plume associated with it. The presence of ancient lithospheric components in the deep-rooted mantle plume will be also remembered, reinforcing the role of lithosphere to the oceanic within-plate magmas.

5.2. Specificities of the Cape Verde area

5.2.1. Lithosphere constraints

The specificity of the Cape Verde area is partially due to its singular geodynamic context. The archipelago is distant from any plate boundary and is located in the African lithospheric plate, which is associated with a slow spreading rate at the mid-Atlantic ridge. Also the pole of rotation of the African plate is situated in the vicinity of the Cape Verde archipelago (Pollitz, 1991; see Chapter 2) leading to a context of quasi-stationary plate environment relative to the melting source which promotes the non-typical configuration of the islands, as to be expected for a linear age progression, as well as the prolonged action of the plume (e.g. Holm et al., 2008; Ramalho, 2012).

The spatial distribution of the Cape Verde islands is also likely associated with the presumable existence of first order tectonic accidents, which may have controlled the positioning of the Northern islands (Torres et al., 1998; 2010; see also Madeira et al., 2008), thus pointing to a lithospheric control of the magmatism location.

Cape Verde islands are implanted on old oceanic lithosphere which, due to thermal contraction and/or conductive heat loss (as the plate ages and moves away from the ridge) (Parsons and Sclater, 1977; Stein and Stein, 1992), is characterized by considerable thickness. Since the archipelago lies on oceanic crust with ages raging from 140 to 120 Ma (Williams et al., 1990) and that the strongest increase in oceanic lithosphere thickness is observed for ages less than 60 Ma (e.g., Stein and Stein, 1992), the lithosphere thickness under the Cape Verde area is assumed to be ≈ 90 km (Wilson, 2011).

In accordance with the most conventional approach the lithosphere can be defined thermally as a location were the thermal energy is mainly transferred by heat conduction as opposed to transference by convection within the asthenosphere (Stüwe, 2007), and so its base, a thermal boundary layer, is defined by an isotherm (equal surface of constant temperature; potential temperature between 1280 and 1350ºC, see Chapter 2, section 2.4.1 for further explanation).

Another approach to define the lithosphere-asthenosphere boundary (LAB) can be envisaged as the petrological transition between subsolidus amphibole-bearing lherzolites (lithosphere) and a lherzolitic asthenosphere characterized by the presence of small melt fractions enriched in volatiles (≈ 1%; Green et al., 2010; Niu et al., 2011). Indeed, the abrupt drop in shear-wave velocity at the LAB in oceanic environment attests the necessity for the presence of a melt fraction atop the asthenosphere (the LVZ: Low Velocity Zone; e.g. Kawakatsu et al., 2009). Under the Cape Verde area a LVZ has been identified at 90 km by Lodge and Helffrich (2006) thus constraining to that depth the thickness of the lithosphere.

Upon melting, to generate the oceanic crust at ridges, a relatively high Mg# and low density residue is formed which is the main contributor to the oceanic lithosphere. However, the growth of the oceanic lithosphere is accomplished by the basal accretion of LVZ material due to their buoyancy. These low degree melts are probably enriched in volatiles and incompatible elements,

making them the ideal agents for the metasomatism of the overlying lithosphere (Humphreys and Niu, 2009; Niu et al., 2011). The lithosphere growth will therefore record the continuous metasomatism imposed by the incorporation of melts either from LVZ or plumes and subsequent modal and cryptic geochemical signatures (Niu et al., 2012). Considering the old lithosphere where Cape Verde islands are implanted on, the expected influence of metasomatized (low solidus) lithospheric domains in the magmas that pass through it, must be taken into account.

5.2.2. Plume constraints

The location of the Cape Verde Archipelago close (≈ 500km) to the West African craton led some authors to hypothesize about the role of edge driven convection to its origin (King and Ritsema, 1998; King, 2007; see Chapter 2, section 2.7). However, the existence of a deep mantle plume in the Cape Verde area seems undeniable from geophysical (see Chapter 2) and geochemical evidences (see Chapter 4). Considering it differs from the surrounding mantle in chemical (e.g. Gerlach et al., 1989; Martins et al., 2010; Mourão et al., 2012) and temperature (Putirka, 2008) characteristics, it should, more correctly, be referred to as a thermochemical plume (Olson and Yuen, 1982).

The most impressive feature which has been attributed to the presence of a mantle plume is the topographic swell known as the Cape Verde Rise, where the islands stand on. Indeed, this swell with 2 km high and 1200 km across (Crough, 1982), is considered the most prominent oceanic within-plate topographic anomaly (Lodge and Helfrich, 2006)and has been considered to be dynamically supported by a mantle plume (Davaille et al., 2005; Montelli et al., 2006; Zhao, 2007; see Chapter 2).

According with estimated mantle potential temperatures, ambient mantle should be in the 1280-1350 ºC range while plumes are variably hotter (Herzberg et al, 2007; Putirka et al., 2007; Putirka, 2008). For Cape Verde the estimated temperature excess is of about 114ºC (Putirka,

2008). Notwithstanding this small excess of temperature, the plume buoyancy flux (B)[1] value of 1600 kg/s calculated for the Cape Verde is higher than the reported for other Atlantic islands also considered to be formed by mantle plumes (Azores: 1100 kg/s, Canary: 1000 kg/s and even Iceland: 1400 kg/s; Sleep, 1990), even though clearly smaller compared with 8700 kg/s for Hawaii (Sleep, 1990).

Another parameter to describe the plume characteristics is the hotspot swell shape parameter (I)[2] introduced by Schubert et al. (2001). It is a dimensionless number that describe the swell contour and allows making assumptions about plume characteristics. The value of 21.4 obtained for the Cape Verde archipelago[3] implies the presence of a large conduit discharge in a slow moving plate where buoyant spreading dominates leading to a topographic rise nearly circular in shape (Turcotte et al., 2001).

5.2.3. ULVZ/LLSVP

In Chapter 2 it was mentioned that the plume located in the Cape Verde area is of deep origin, this fact being supported by several geophysical and geochemical evidences. For example Montelli et al. (2004, 2006) demonstrated the existence beneath the archipelago of a low velocity zone extending down to depths of about 2800 km (see also Zhao, 2007) strongly suggesting that the Cape Verde plume is rooted at the D'' region[4] close to the core-mantle boundary (CMB)[5]. Interestingly, Davaille et al. (2005) and Torsvik et al. (2006) report a large low velocity zone at the deepest levels of the mantle beneath this area, most probably at the D'' region. That low

---

[1] $B = (\rho_m - \rho_w).A_s.u_p$, where ρ_m and ρ_W are mantle and water densities, A_s is the cross sectional area of the swell in a vertical section perpendicular to the plume track and u_p is the plate velocity (Turcotte and Schubert, 2002).

[2] $I = Q / (96\pi.\mu_p.H_T.u_p^2)$, where Q is the heat transport, μ_p is the viscosity of the plume, H_T is the adiabatic temperature scale height and u_p is the plate velocity (Schubert et al. 2001).

[3] Value obtained assuming a 5 mm/year plate velocity and a dynamic viscosity of the plume of 10^{20} Pa s.

[4] The D'' zone can be foreseen as a location where slabs can accumulate. Thermal/compositional plumes can rise from this location and Large Low Shear-wave Velocity Provinces (LLSVP) can be created (Lay et al., 2008; Kendall and Silver, 1998)

[5] The core-mantle boundary (CMB) is the most significant interface within the earth regarding the disparities observed in temperature, type of material and physical properties (Tr ønnes, 2010).

velocity zone corresponds to one of two large antipodal Large Low Shear-wave Velocity Province (LLSVP) identified by Dziewonski et al. (2010) beneath Africa and the Pacific (Fig. 5.1). These zones are characterized by lower than average wave speeds (Vs and Vp), being this velocity perturbation attributed to thermal as well as chemical effects.

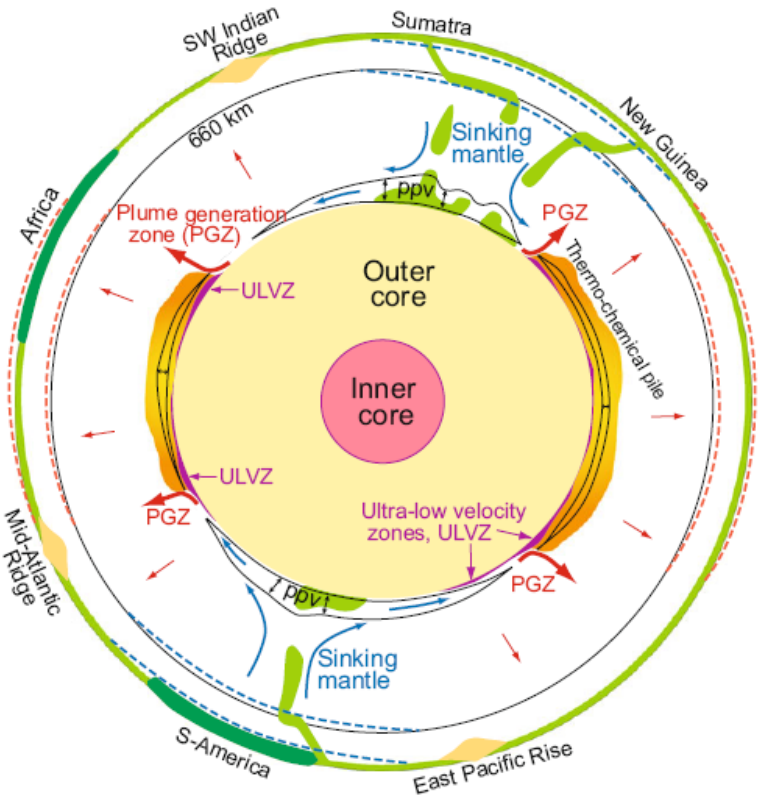

Figure 5.1 – Diagram of the Equatorial Earth section, proposed by Tønnes (2010). The orange areas represent de LLSVP (thermo-chemical pile), the signalled purple zones are the ULZV near the margins were the plume preferentially originate from (PGZ). For detailed information concerning this figure see Tr ønnes (2010).

Without further lengthening the explanation of the configuration of the Earth's lower mantle, since this is not the main concern of this thesis, is however noteworthy the importance of the LLSVP beneath Africa and the Cape Verde region. The magmatism here studied is no doubt influenced by its presence, being certainly one of the factors that give the Cape Verde magmatism its distinctiveness. It is worthwhile mentioning that the role of a long-term isolated reservoir has been considered to explain the noble gas isotopic signatures of Cape Verde (Doucelance et al.,

2003; Mata et al., 2010; Mourão et al., 2012b) which can be tentatively assigned to the above referred LLSVP.

5.3. Geochemical consequences of plume-lithosphere interaction

5.3.1. Lithosphere

Lid effect

Oceanic lithosphere thickness variation exerts a significant control on OIB geochemistry since it limits the extent and depths of melting, this phenomena is known as the lid effect (Niu and Hékinian, 1997; Niu and O'Hara, 2007, 2008). Considering that magma generation in oceanic within-plate settings, like the Cape Verde one, is due to adiabatic decompression melting at asthenospheric depths, the presence of a thick lithosphere will constrain the depth of the melting column top, leading to magmas generated at greater depths (higher pressure) and lower degree melts (Watson & McKenzie, 1991; Ellam, 1992; Brodie et al., 1994; Haase, 1996; Humphreys and Niu, 2009).

For Cape Verde this percept is supported by:

- the occurrence of highly SiO_2-undersaturated rocks such as nephelinites, melanephelinites, melilitites and carbonatites, which according to experimental data (e.g. Brey and Green, 1975; Wilson et al., 1995) are generated by very low degrees of partial melting;
- primitive magmas trace element ratios (e.g. Gd/Yb; Chapter 4) supporting magma genesis in equilibrium with residual garnet, which based on experimental data (Green and Ringwood, 1970; O'Hara et al., 1971) ascribes magma generation at depths above 80 km;
- modelling made in previous sections (Chapter 4, section 4.4.3.3) indicating that Santiago magmas were generated by 2 to 9% degrees of partial melting.

Hydrous residual mineralogy

As described earlier the presence of residual garnet during mantle melting was identified in primitive Santiago lavas which allowed inferring that melting started at least at 70 - 100 km deep. Also the identification of hydrous residual minerals (amphibole and phlogopite) imposes some constraints regarding depths and temperature. The presence of phlogopite in the asthenosphere is not precluded by experimental work (e.g. Harlow and Davies 2004), but it has been shown (e.g. Wallace and Green 1991) that amphibole is not stable at temperatures above 1150°C, i.e., at temperatures prevailing in the asthenosphere or in mantle plumes, thus pointing to the equilibration of some of the Santiago magmas with amphibole present within the lithospheric mantle (see Class and Goldstein 1997).

The presence of these hydrous minerals in the depleted oceanic lithosphere is considered to be the result of their crystallization from infiltrating fluids and/or melts generated by plume influence[6]. Modal metasomatic events create low solidus and highly enriched lithospheric domains, particularly prone to melting in conditions of continued reheating (e.g. Mata et al. 1998; Späth et al. 2001). For Santiago it can thus be envisaged a model involving the contamination of ascending plume magmas by melts generated in low-solidus metasomatized lithosphere domains and leaving those hydrous minerals as melting residues.

As previously mentioned (4.2.4.1) some of the Santiago lavas are characterized by Nb/U higher (up to 74.9, excluding two values considered outliers) than the typical value (52±15) reported for OIB by Hofmann (2003). According to Lundstrom et al. (2003) and Millet et al. (2008), the high Nb/U of silicate lavas can be derived by melting of amphibole present in lithosphere domains previously metasomatized, given the very high Nb/U ratios characterizing this mineral. However Tiepolo et al. (2000, 2001) showed that the partition coefficients for Nb in amphibole is strongly dependent on the structure and composition of the melt and amphibole itself, concluding that D_{Nb} is negatively related with magma Mg# and Ti content. Due to high

[6] There are several possible mechanisms susceptible of generating metasomatic veins in the lithosphere. While some authors consider the veins as representing the direct crystallization of the metasomatic agent (Harte et al., 1993; Pilet et al., 2002), others considered them as the result of percolative fractional crystallization from such melts as they cool and ascent trough the lithosphere, giving rise to a variable mineral assemblage (modal metasomatism) and associated chemical alteration of the surrounding lithosphere (cryptic metasomatism)(Pilet et al., 2008)

TiO_2 that characterize the Cape Verde silicate lavas in general (e.g. Prytulak and Elliot, 2007) and Santiago in particular (see Appendix III), as well as the high Mg# expected due to buffering effect of magnesium-rich silicate minerals present in mantle, it is expectable that amphiboles are not so enriched in Nb, and consequently is not linear, for Cape Verde, that the melting of amphibole-rich domains could imprint such high Nb/U ratios to silicate magmas.

Recently Madureira et al. (2011) noticed that for Terceira Island Nb/U (up to 60) correlated negatively with $^{206}Pb/^{204}Pb$, clearly showing that, for Terceira, such high Nb/U cannot reflect recent metasomatic events, being a long-term characteristic of the source. However in Santiago lavas there is no visible trend between Nb/U and $^{206}Pb/^{204}Pb$.

The deviations observed in Santiago Island regarding Nb/U, trace incompatible elements ratios though as being nearly constant in OIB and MORB, cannot be explained by weathering and alteration effects since U does not correlate positively with LOI. Also Nb/U and Pb/Ce ratios seem to be related with some geochemical particularity within the Cape Verde source (mantle/lithosphere) since the higher values of Nb/U and lower Pb/Ce are also observed in other islands of the archipelago.

However it should be kept in mind that there are other processes able to explain the distinct partition coefficients of these elements as those reported by Hofmann (2003), where under very low degree partial melting, Nb seems to be significantly more compatible than U. This could explain the lowest Nb/U value in Santiago primitive samples (25.4) reported for the melilitite of Assomada Formation.

Further evidence for oceanic lithosphere metasomatism

In the above discussion the occurrence of lithospheric metasomatism is suggested from evidence for equilibration of ascending magmas with residual hydrous minerals, in what can be considered indirect evidence.

However it must be emphasized that direct evidence exists for metasomatic processes. Lithospheric peridotite xenoliths collected on alkaline Santiago lavas exhibit strong evidences for the occurrence of metasomatism in the lithospheric mantle, namely the occurrence of kaersutite,

phlogopite and calcite, in association with alkaline-rich glasses (see Chapter 4, section 4.4.4.1). The replacement of orthopyroxene by the clinopyroxene and olivine association is compatible with a carbonate-rich nature of the metasomatic agent. This fact is supported by whole-rock geochemistry of the modally metasomatized lherzolite xenoliths (see section 4.4.4.2 for more extensive justification).

Additionally, the already mentioned geochemical evidences that support the presence of hydrous residual mantle paragenesis correlate with key trace element ratios, such as low Ti/Eu and Al/Ca and high Ca/Sc giving further evidence for the carbonatitic nature of the metasomatism, which affects lavas and xenoliths (see section 4.4.4.3 for more extensive justification).

5.3.2. The Role of SCLM

The contribution of an EM1-type component to the southern Cape Verde islands is recognized since Gerlach et al. (1989). Recently Barker et al. (2010) considered the EM-1 as a plume component. Following these authors, the restriction of the enriched component to the southern islands reflects its heterogeneous distribution into the plume and the melting from separate melting loci beneath the Cape Verdes (see also Lodge and Helffrich, 2006). However the more complex distribution of the EM-1 signatures in Cape Verde, as shown by its probable presence at Sal (Torres et al., 2010), the occurrence of high s-wave velocity domains beneath Cape Verde (Begg et al., 2009) and the Proterozoic model ages obtained by Coltorti et al. (2010) for Sal xenoliths strongly suggest an alternative origin.

In section 4.5.2.3 the enriched mantle component (EM), identified in the southern Cape Verde islands was ascribed to subcontinental lithospheric mantle (SCLM) due to the strong isotopic affinities reported by Santiago lavas with Leucite Hills lamproites. Indeed, this particular lithology is thought to derive from melting of an enriched metasomatic paragenesis within the continental lithospheric mantle. Several geochemical and geophysical evidences attest the existence of ancient SCLM domains in the mantle under the Cape Verde area (see section 4.5.3) and the

EM-type signatures of the southern Cape Verde lavas is here considered to reflect the interaction of plume magmas with SCLM domains.

These domains should correspond to delaminated fragments left behind during the opening of the Atlantic Ocean (O'Reilly et al., 2009) (Fig. 5.2). However it is not entirely known the location of these megaliths, even though it should be a shallow feature and not associated with the plume. The SCLM can be located within the oceanic lithosphere, which was accreted to it during its thickening, as it moves away from the ridge or, alternatively, it can be located as a buoyant fragment in the asthenosphere has proposed by Mourão et al. (2012) to explain the temporal variation of the Brava Island geochemistry.

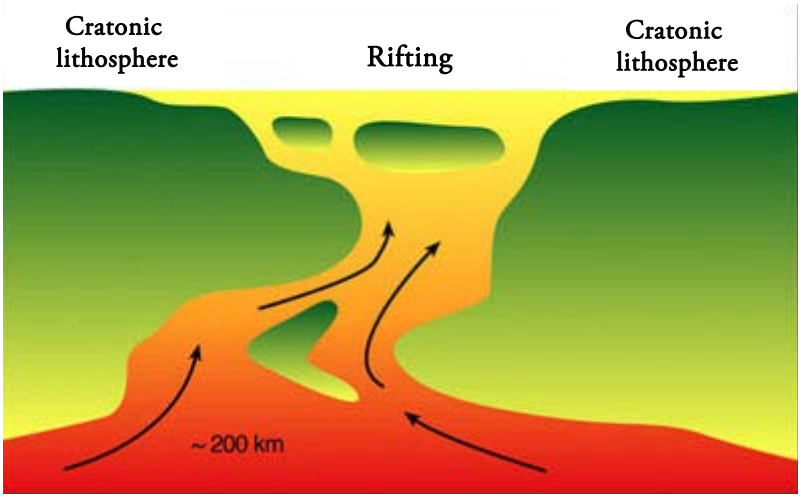

Figure 5.2 – Schematic representation of the possible mechanism responsible for the stranding of buoyant sub-continental lithosphere remnants in the oceanic domain (image from O'Reilly et al., 2009).

5.3.3. Carbonatites in oceanic environment

Carbonatites are primarily located within stable intra-plate continental settings (Carmody, 2012). In a recent compilation of the carbonatite occurrences of the entire world, Woolley and Kjarsgaard (2008) observed that from the 527 occurrences, only 8 where associated with oceanic

islands (two at the Canary Islands, five at Cape Verde archipelago and one in the Kerguelen Islands[7]), making it 1% of the global carbonatite budget (Fig. 5.3).

What these scarce oceanic occurrences have in common, besides their geodynamic within-plate environment, is that all are associated with regions characterized by old oceanic metasomatized lithosphere, as well as the most likely presence of SCLM fragments, either within the lithosphere or as dispersed fragments in the asthenospheric mantle (Mattielli et al., 1999; Hassler, 1999; Martins et al., 2010; Mourão et al., 2012). These facts could lead to the hypothesis that oceanic carbonatites are the melting product of SCLM domains or of the metasomatized oceanic lithosphere.

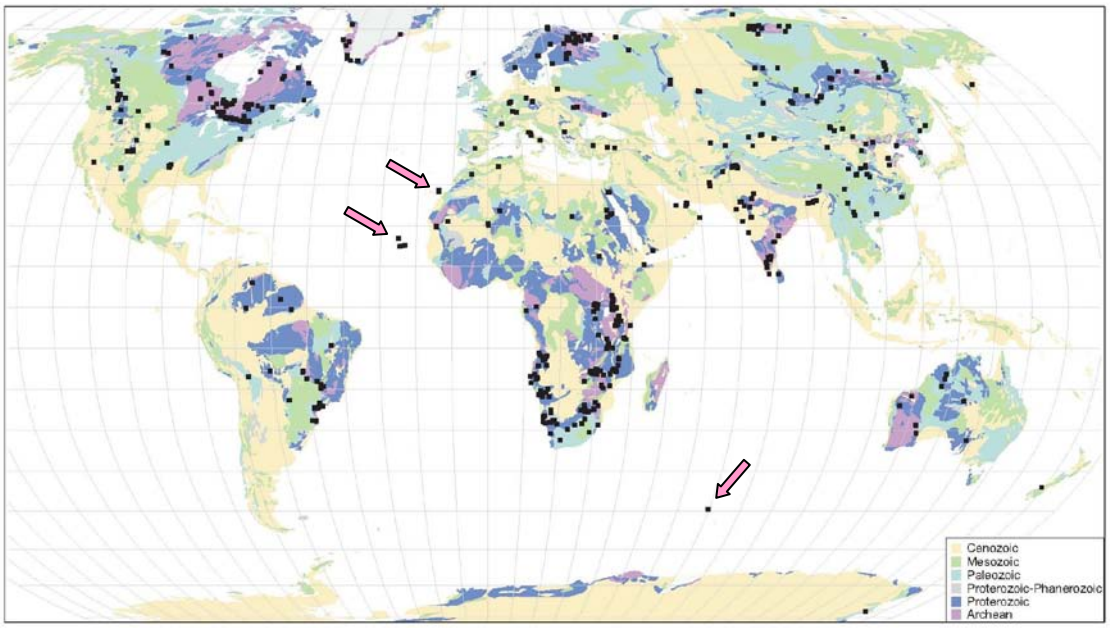

Figure 5.3 – Worldwide carbonatite occurrences map from Woolley and Kjarsgaard (2008) (colours specify the age of the continental areas). Oceanic carbonatite occurrences are highlighted.

[7] The Kerguelen occurrence, even though it is not of an outcropping carbonatite occurrence, it is considered due to the presence of carbonatite interstitial melt pockets in dunitic xenoliths (Carmody, 2012; Moine, 2004). Mattielli et al. in 1999 had already identified a carbonatitic metasomatic agent within Kerguelen, associating it to mantle derived carbonate-rich material with geochemical signatures characteristic of carbonatite rocks (strong enrichment of LREE over HREE and strong depletion in Zr, Hf and Ti). These authors ascribed a strong influence of a continental lithospheric component to the Kerguelen magmatism based on xenolith isotopic data. These authors ascribed a strong influence of a continental lithospheric component to the Kerguelen magmatism based on xenolith isotopic data.

However, it must be emphasized that the outcropping Santiago carbonatitic rocks are characterised by strongly depleted Sr and Nd isotopic signatures (εNd=2.93 to 5.77; $^{87}Sr/^{86}Sr$=0.703101 to 0.70363; Doucelance et al., 2010) which precludes such an SCLM origin. Also, the high $^{206}Pb/^{204}Pb$ values reported for Brava and São Vicente Islands carbonatites (19.76-20.15 and 20.21-20.23, respectively) (Hoernle et al., 2002; Mourão et al., 2012) corroborates the impossibility of SCLM as a precursor of carbonatite magmas.

The petrogenesis of carbonatites is still a very controversial subject regarding not only the role played by the lithosphere and/or plume/asthenosphere (cf. Nelson et al., 1988; Bailey, 1993; Kalt et al., 1997; Bell and Simonetti, 1996, 2009; Tilton et al., 1998), but also in what concerns the source of mantle C involved, either recycled or of primitive/primordial origin (Hoernle et al., 2002; Mata et al., 2010; Doucelance et al., 2010; Mourão et al., 2012).

Mata et al. (2010) based on He isotopes (R/Ra values up to 15) and ^{129}Xe excess on carbonatite samples from several Cape Verde islands argues that the carbonatite melts cannot be derived from recycled crustal carbonate and must be derived from a long term isolated mantle domain most certainly related to the D'' layer that was brought to surface by a mantle plume (see section 4.4.4.3 for further explanation). A similar conclusion was obtained by Mourão et al. (2011) through the demonstration that Brava Island carbonatites are characterized by very low $^{4}He/^{40}Ar^{*}$ which are not explainable by a contribution of recycled carbon. Interestingly an analysis of the Mata et al. (2010) data reveals that such low $^{4}He/^{40}Ar^{*}$ ratios are also present in at least some of the other Cape Verde carbonatite occurrences.

In this perspective the role of thick Cape Verde oceanic lithosphere may be limited to the favouring of the concentration of volatiles at the upper levels of the ascending Cape Verde mantle plume (see Bell and Tilton, 2001; Bell and Simonetti, 2009; Mata et al., 2010). This is in line with Woolley and Kjarsgaard (2008) which attribute the scarcity of large carbonatite occurrences within the ocean to the inability of a thin crust (as opposed to a continental crust) to absorb and concentrate large amounts of CO_2 necessary to produce significant carbonatitic complexes.

This fact associated with the existence of the LLSVP and related deep mantle plumes, as well as the influence of SCLM fragments could make the Cape Verde area an unusual and rare location

were oceanic carbonatites may occur. It is probably the addition of various chemical, geological, structural and geodynamic factors (described previously) that allows the existence of carbonatites in an oceanic environment.

5.3.4. Plume components

The lithosphere to the Cape Verde magmatism is also depicted by the composition attributed to the mantle plume. Indeed, for Santiago magmas the main plume contributors were identified as being HIMU and the lower mantle. The HIMU component was assigned to ancient recycled altered oceanic crust (≈ 1.5 Ga, ROC) (see section 4.5.2 for further explanation and section 4.5.4 for isotopic modelling of the contributors of the Santiago magmatism).

5.4. Cape Verde magmatism: a time constrained model for the lithosphere contributions

All the previously published data and the conclusions emerged from the present work allowed the elaboration of a model here synthesized in graphic form as a cartoon (Fig. 5.4). The magmatogenesis of the Santiago Island is described as resulting from a deep seated thermochemical mantle plume, probably rooted into the deepest levels of the mantle at some 2900 km deep. Considering a temperature-dependent Newtonian viscosity model, plume ascent rates of approximately 1–2 m yr^{-1} are obtained[8] (Burov and Guillou-Frottier, 2005) which leads to the hypothesis that the depart of plume from its source may have occurred less than 3 Ma before it reach the lithosphere, i.e. approximately 43 to 53 Ma ago if we accept the age resetting of MORB's at 40-50 Ma described by (Mitchell et al., 1983), as the age of the arrival of the mantle plume to the shallowest levels of the mantle.

[8] If a non-Newtonian behaviour is assumed, 1000 times higher ascent rates can occur (Burov and Guillou-Frottier, 2005) which would make the plume ascension a quasi-instantaneous process at a geological time-scale.

As mentioned before Cape Verde magmatism is significantly heterogeneous in terms of elemental radiogenic isotope signatures (noble gases included). Southern Islands, where Santiago is included, are less Nd- and Pb-radiogenic and more Sr radiogenic than the Northern Islands, which are also characterised by more unradiogenic He signatures. For Northern islands, $^{206}Pb/^{204}Pb$ ratios up to 19.927 have been determined in silicate rocks which, in conjunction with the Sr and Nd isotopic depleted character and the Nb and Ta enrichment relatively to LREE and LILE, is interpreted as resulting from the contribution of ancient (*circa* 1.5 Ga) recycled altered oceanic crust. The basic character of ancient recycled oceanic crust leads to the hypothesis that the HIMU-type signatures are "retained" in pyroxenitic domains of the ascending plume which in agreement with the evidences for the contribution of such lithologies to the Cape Verde magmas (see 4.4.3.1).

In contrast, Southern islands are more Sr radiogenic and Nd and Hf unradiogenic (down to 0.512607 and 0.282837 respectively, in Santiago Island) implying the involvement of subcontinental lithosphere (SCL). The apparent restriction of SCL signatures to the Southern Cape Verde islands is better understood if the component is not present in the plume but resides in the upper mantle as a passive heterogeneity, which would have resulted from a delaminated megalith left behind during the opening of the Central Atlantic Ocean some 200 Ma ago.

Some of the Cape Verde primitive lavas present pronounced negative K anomalies and other trace element characteristic requiring that, during partial melting, $D_K > D_{Ce}$. These features suggest equilibration of ascending plume magmas with an oceanic lithospheric mantle containing K-rich hydrous mineral assemblages, consistent with the occurrence of amphibole/phlogopite in metasomatized lherzolite xenoliths. Judging by the fact that in Santiago Island the effects of metasomatism are more evident on the more recent volcanic complexes, metasomatism is considered to have occurred mainly during the initial stages of plume magmatic activity leading to the construction of the island.

In conclusion, besides the physical constraint on the degree of partial melting, the lithosphere (s.l.) exerted influence on the chemistry of Cape Verde magmas in periods predating the magmatism by 10^9 years (recycling of altered oceanic crust), 10^8 years (delamination of sub-

continental lithosphere), 10^6 years (metasomatism of the oceanic lithosphere) and $<10^2$ years (interaction of ascending plume magmas with metasomatized oceanic lithosphere) (see also Mata et al., 2010) (Fig. 5.4).

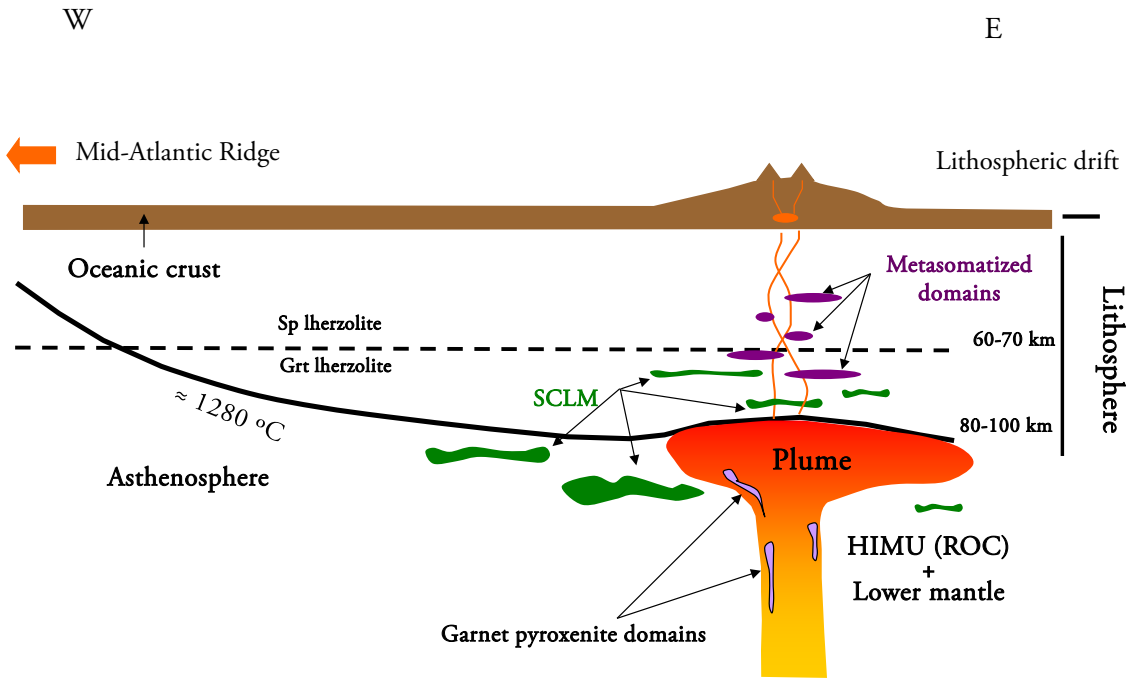

Figure 5.4 - Schematic model for the generation of Santiago magmas with the location of the various contributors for the magmatism (1208 ºC isotherm is considered as the base of the lithosphere).

CHAPTER 6

GABBROIC XENOLITHS AND OUTCROPPING MORB: TESTIMONIES FROM THE OCEANIC CRUST BENEATH SANTIAGO ISLAND

Baía de Angra (Santiago – Cape Verde)
Outcrop of pillow lavas of MORB affinity

6.1. Introduction

In Santiago's northeastern tip (Angra Bay area) outcrops the oldest unit of the island. It corresponds to Mesozoic oceanic crust and sediments with an exposure of up to 180 m (Gerlach et al., 1988; Davies et al., 1989). This unit is partially covered by subaerial and submarine lavas belonging to the main eruptive event (Upper and Lower Pico da Antónia Formation, respectively) (see Chapter 3).

Those MORB-types pillow lavas (Gerlach et al., 1988; Davies et al., 1989; Millet et al., 2008) are intruded by an intra-volcanic breccia, belonging to the Ancient Complex, composed of basaltic and nephelinitic dikes that are cut by dolomitic carbonatite digitations and dikes, belonging to the partially eroded alkaline-carbonatite complex (Silva et al., 1981; Silva, personal communication) (Fig. 6.1). The contact between the old pillow lavas and the volcanic breccia is characterized by intense fracturing and the crystallization of a specific mineralogy composed of fluorite, barite and Mn-oxyhydroxide minerals (Silva, personal communication).

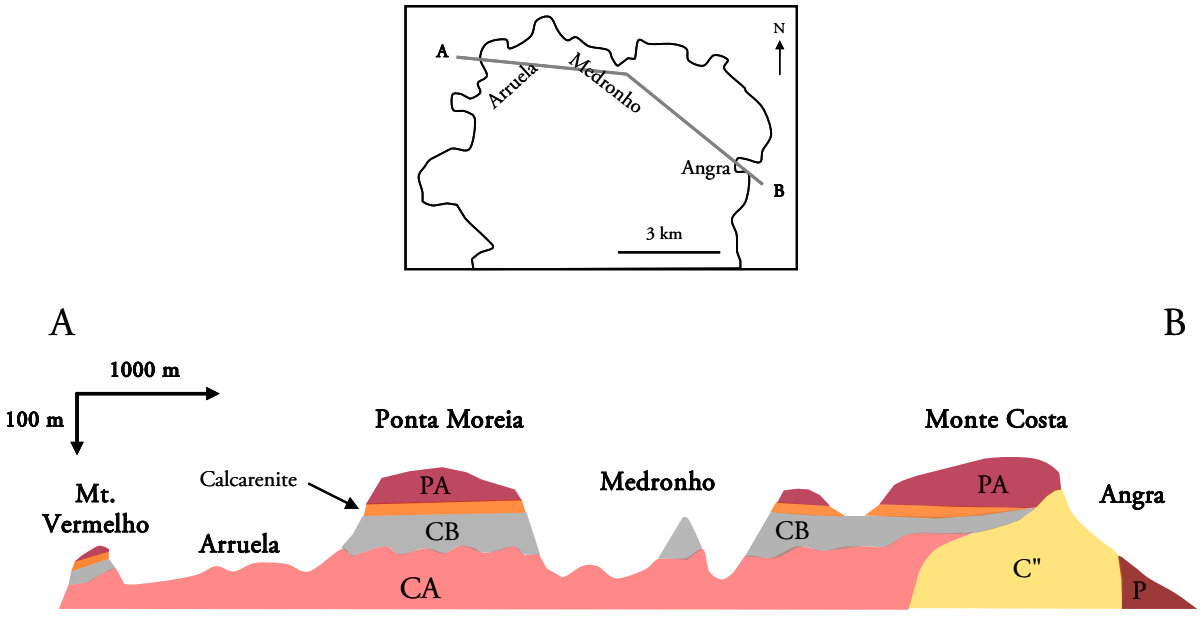

Figure 6.1 – Cross section of the northern Santiago area, along line A-B (see enclosed map for location) where is evident the carbonatite-ijolite-syenite-brecia plug (C") intruding pillow lavas of MORB affinity (P) at Angra Bay area. The area between Monte Vermelho and Monte Costa is characterized by the remains of a carbonatitic volcanic cone (CA), covered by carbonatitic epiclastic beds (CB) and calcarenite. Covering all of this carbonatitic sequence are subareal lavas of Pico da Antónia Formation (PA). Vertical exaggeration is 5x. Images adapted from Silva et al. (1981).

Also in the Angra Bay area, subangular to subrounded gabbroic xenoliths occur within the Lower Pico da Antónia pillow lavas (2.9–2.8 Ma; Holm et al., 2008) associated with numerous peridotite xenoliths (Mendes, 1995; Mendes et Silva, 2001). The gabbroic xenoliths are centimetric with medium to coarse granularity and, even though they are evidently scarcer than the peridotitic ones, they are easily found and identified in the field (Fig. 6.2). As already described by Mendes and Silva (2001) these gabbroic xenoliths are genetically related with the MORB-type lavas.

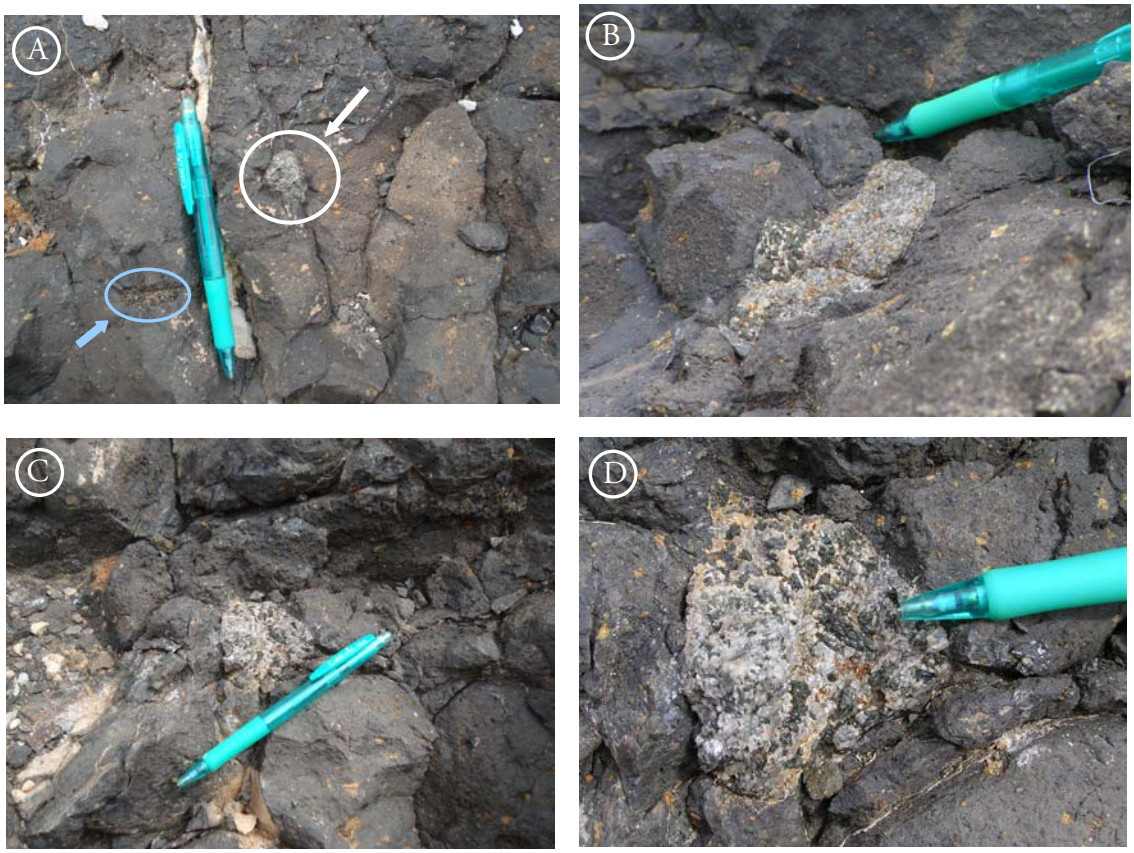

Figure 6.2 – Gabbroic xenoliths within Lower Pico da Antónia pillow lavas. A) Subrounded gabbroic xenolith near a peridotitic xenoliths also highlighted (in blue); B) Two gabbroic xenoliths with distinct granularities and shapes, the one to the left being more cumulated; C) Subrounded gabbroic xenolith; D) Close-up of xenolith in (C) where pyroxene crystals are well developed.

The abundance of ultramafic and mafic xenoliths in the LPA pillow lavas in the Angra area suggests rapid rates of magma ascension that enabled the transportation of dense nodules to the surface in such high numbers (Guest et al., 1995; Kauahikaua et al., 2002).

The presence of pillow lavas of MORB affinity and gabbroic xenoliths at Santiago Island can be considered testimonies of fragments of different sections of the oceanic crust. Trough

seismic data and direct studies on ocean crust fragments thrusted onto continent (ophiolites) and along fracture zones it is possible to infer the structure and layering of the oceanic crust at depth (Hamblin and Christiansen, 1998; Best and Christiansen, 2001).

According to seismic velocity and reflection studies the typical oceanic crust has an approximately constant thickness of 6 - 7 km and can be divided into four major layers, which from top to bottom increase in seismic velocity (V_p) (Hill, 1957; Raitt, 1963; Houtz and Ewing, 1976; White et al., 1992). The layers are thought to represent primary magmatic layering and correspond to pillow basalts, sheeted basaltic and diabase dikes and gabbros (Fig. 6.3).

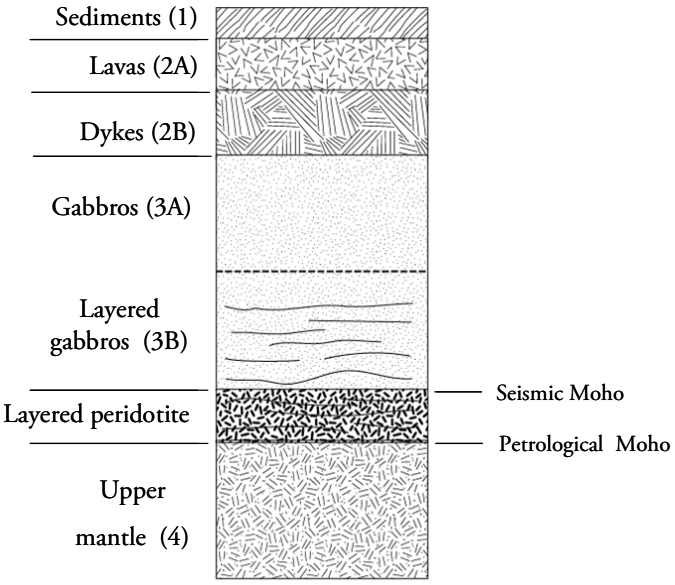

Figure 6.3 – Schematic cross section of oceanic crust (adapted from Kennett, 1982).

By analogy with similar pillow-MORB occurrences in the neighbouring Maio Island, to which De Paepe et al., (1974) attributed a late Jurassic age, Gerlach et al. (1988) considered the imprecise Pb-Pb age of 130 Ma obtained for Santiago occurrences as reflecting alteration processes.

In the neighbouring island of Maio the outcropping section of oceanic crust is considerably more complete (200-400 m of exposed pillow lavas and up to 450 m of sedimentary material) and noticeable than the Santiago occurrence. The Mesozoic section comprises the Batalha Formation, the oldest unit composed of pillow lavas of MORB affinity,

and the Monte Branco Group that accounts for the Lower to Upper Cretaceous marine sedimentation including the Morro, Carqueijo and Coruja Formations (from the oldest to the most recent) (Stillman et al, 1982). The sedimentary sequence varies from marls and pelagic limestones, slowly deposited on deep waters (Morro formation) to calciturbidites and black shales rapidly deposited (Carqueijo Formation) and coarse tuffs and arenite characteristic of high-energy shallower deposition (Coruja Formation) (Stillman et al., 1982) (Fig. 6.4).

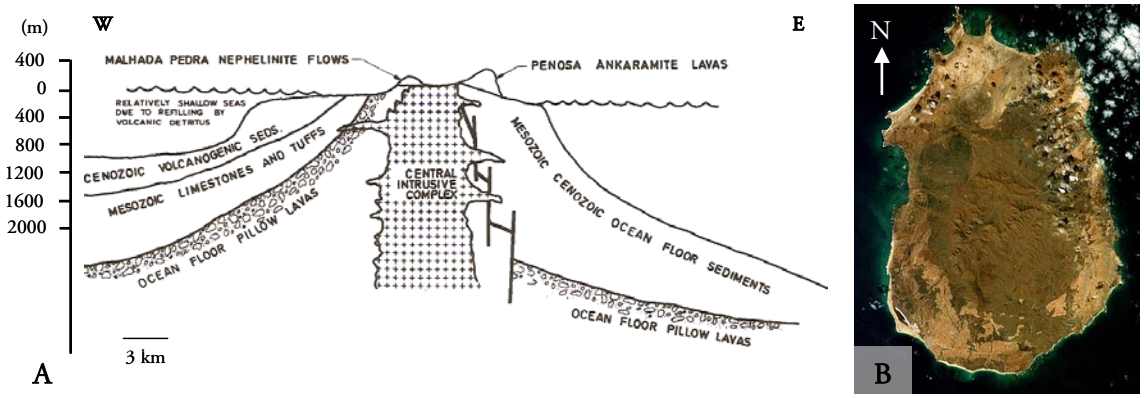

Figure 6.4 – A) Schematic E-W cross section from the Island of Maio (adapted from Stillman et al., 1982); B) Satellite image of the island of Maio, were it can be seen the Central Intrusive Complex (image from www.oceandots.com).

The exposure of Maio's Mesozoic sequence seems to have been caused by a high-level diapiric plutonic event (Central Intrusive Complex, see Fig. 6.4) that was powerful enough to tilt and dome the overlying layers by 3 km above an already depth anomaly of 2 km, during the Paleocene/Paleogene (Stillman et al., 1982).

The identification of Calpionellids (*Calpionellites darderi* and *Tintinnopsella longa*) in a thin calcareous bed within the upper section of the Batalha Formation provides a Lower Valanginian age (≈134-140 Ma) for the Maio Island pillow lavas (Azéma et al., 1990; Fourcade et al., 1990). A similar age was also obtained by Pb-Pb dating (≈130 Ma) for Santiago's MORB pillow lavas (Gerlach et al., 1988). This age is supported by $^{87}Sr/^{86}Sr$ age determined on carbonate rocks from Morro Formation which yields a mean age of 133 Ma (Holm et al., 2008). Taking this in to account the Maio MORB pillow lavas are probably

Lower Cretaceous in age, the same applying most likely to the Santiago occurrence. In this perspective the Pb-Pb age (≈130 Ma) obtained for Santiago by Gerlach et al. (1988) is probably closer to the magmatic age than supposed by the author.

Twelve samples of the MORB pillow lavas in Santiago Island were collected in the Angra Bay area as well as eleven gabbroic xenoliths included in alkaline pillow lavas of the Lower Pico da Antónia Formation (see Appendix I).

The basaltic pillow lavas are visibly altered with light brown to yellowish brown colours and are intensely cut by carbonatitic veins, irregular in orientation and millimetric in thickness (Fig. 6.5). In order to attain the least possible altered rock and representative whole-rock analyses, only the sample cores were recovered and all visible carbonated veins were removed.

The gabbroic xenoliths are fresh with no signs of weathering. From eleven collected samples only four were selected for whole rock analysis due to the small size that characterizes these samples.

Figure 6.5 – Altered pillow lavas of MORB affinity cross cut by numerous carbonatitic veins (photo by João Mata).

The study of the outcropping pillow lavas up today considered of MORB affinity will allow: (1) its geochemical characterization; (2) test the conformity/agreement with mid-ocean ridge magmatism context; (3) detect possible alteration processes before and after implantation in Santiago Island and (4) infer ancient magmatic characteristics at mid-Atlantic ridges.

Occasionally comparisons will be made with Maio Island's pillow MORBs to better understand the regional context in which these outcrops occur and also to detect differences and similarities (Fig. 6.6). This comparison will be made using data of DePaepe et al. (1974), as well using with new data obtained for three samples collected in 2008 during a field campaign realized for the CV-Plume project.

Figure 6.6 – Outcrop of pillow lavas of MORB affinity in Maio Island (A) Detail of the pillow structures (B) (photos by João Mata).

Petrological and geochemical analyses of Santiago's gabbroic xenoliths allow the inference of their parentage (oceanic gabbro cumulates of N-MORB affinity or intrusion/cumulates from mafic alkaline magmas) and the detection of possible changes in oceanic lithosphere imposed by alkaline magmas in their ascent to the surface (Neumann et al., 2000; 2005)

Through petrographic studies, electron microprobe analyses of the most important and representative minerals and whole rock geochemistry, the objectives proposed above are going to be addressed in the following sections.

6.2. Petrography and mineral chemistry

6.2.1. MORB Lavas

The studied pillow lavas are hemicrystalline to holocrystalline with intergranular/intersertal groundmass. The dominant and ubiquitous mineral phase is plagioclase occurring either as phenocrysts or microphenocrysts. Mesostasis is made of plagioclase microlites, clinopyroxene crystals, Fe-Ti oxides, sulphide grains, devitrified glass and alteration material (clays, carbonates).

The Ni content (92 to 101 ppm) and Mg# (57 to 65) are indicative that these rocks are not representative of primary magmas. In this perspective the absence of olivine as a rock forming mineral of the lavas does not exclude its removal prior to the emplacement of the magmas.

On the other hand the above mentioned modes of occurrence of the rock forming minerals are clearly indicative that the crystallization of plagioclase precedes clinopyroxene. Taking in to account the influence of silica activity on the stability of pyroxene and plagioclase (Carmichael et al., 1970):

$$\underset{\text{Ca-Tschermak}}{CaAl_2SiO_6} + \underset{\text{melt}}{SiO_2} = \underset{\text{Anortite}}{CaAl_2Si_2O_8} \qquad (1)$$

Such crystallization order is indicative of a silica activity higher than those characterizing alkaline magma, where clinopyroxene crystallization precedes plagioclase fractionation.

6.2.1.1. Plagioclase

The phenocrysts are exclusively of plagioclase occurring frequently as clusters (glomeroporphiritic tendency). Almost all of the phenocrysts are tabular, euhedral to subeuhedral, with 2-3 mm (length wide) and exhibit some sort of alteration (Fig. 6.7):

- partially or entirely converted in argilitic/sericitic minerals;
- corroded cores;

- carbonate or clay filled veinlets displayed as an irregular network;
- partially or entirely converted in oxide minerals (irregular mass).

Plagioclase can be broadly classified as bytownites to labradorites. In most phenocrysts the core has the highest An content (up to An_{89}), attesting the dominant normal zoning, whereas phenocryts margins, microphenocryts and groundmass crystals have lower Ca contents (as low as An_{54}). However there is some overlap in composition (Fig. 6.8). Oscillatory and reverse zoning are observed, sometimes in the same sample, indicating a complex and variable crystallization history with rapid changes in liquid composition from which the plagioclase crystallized. Results of linear compositional profiles are presented in Figure 6.9.

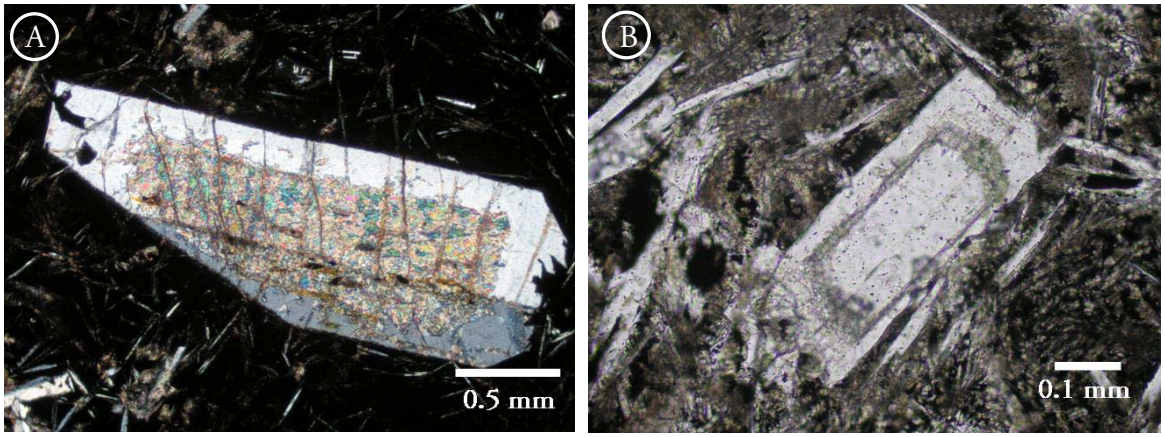

Figure 6.7 – Plagioclase phenocrysts with sericite-altered core (A) and altered intermediate zone (B).

The groundmass is glassy to microlithic containing crystallites of plagioclase which show evidence of very rapid cooling portrayed by their particular shapes: skeletal (hopper like), hollow microlites, rosettes of small crystals and swallow/forked tails (Fig. 6.10). Spinifex-type aggregates are also observed as arrays of neddle-like crystals (Jafri and Charan, 1992).

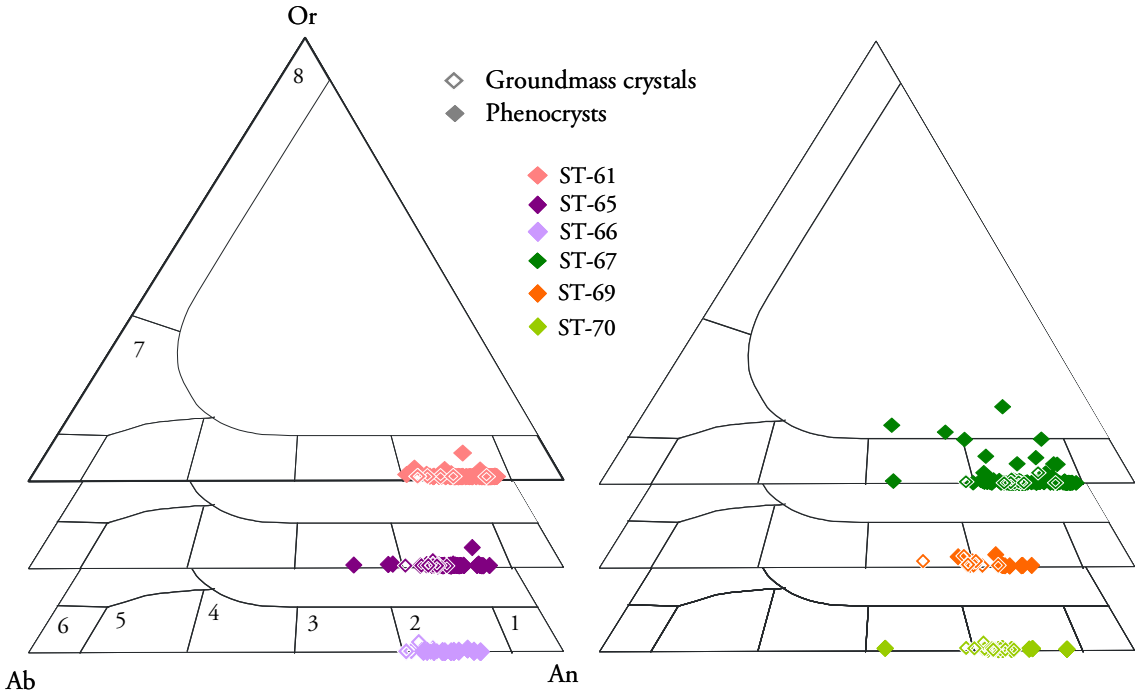

Figure 6.8 – Plagioclase composition of phenocrysts and groundmass crystals (1 – Anorthite; 2 - Bytownite; 3 - Labradorite; 4 - Andesine; 5 - Oligoclase; 6 - Albite; 7 - Anorthoclase; 8 - Sanidine). The dispersion observed in sample ST-67 analyses can be due to crystal alteration and sericite replacement leading to the observed K gain.

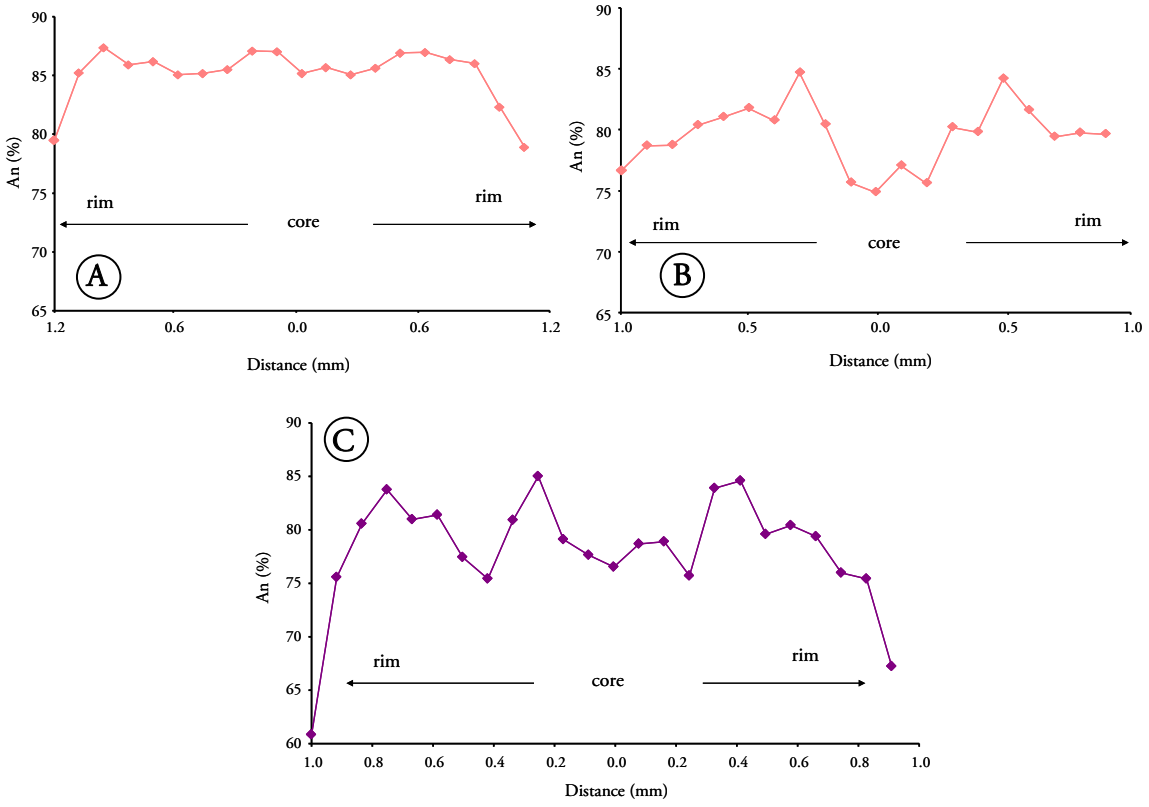

Figure 6.9 – Representative linear compositional profiles of plagioclase phenocrysts with normal (A), reverse (B) and oscillatory (C) zoning. Horizontal scales indicate the distance to the crystal core.

6.2.1.2. Pyroxene

Pyroxene occurrence is limited to the groundmass as acicular and small (< 1mm), subhedral to anhedral crystals usually showing a branching pattern (elongated crystals forming parallel, radial or fan like aggregates) and other quenching shapes such as skeletal, sheaf-like and feather-like dendritic crystals (Yeats et al., 1973; Jafri and Charan, 1992) (Fig. 6.10).

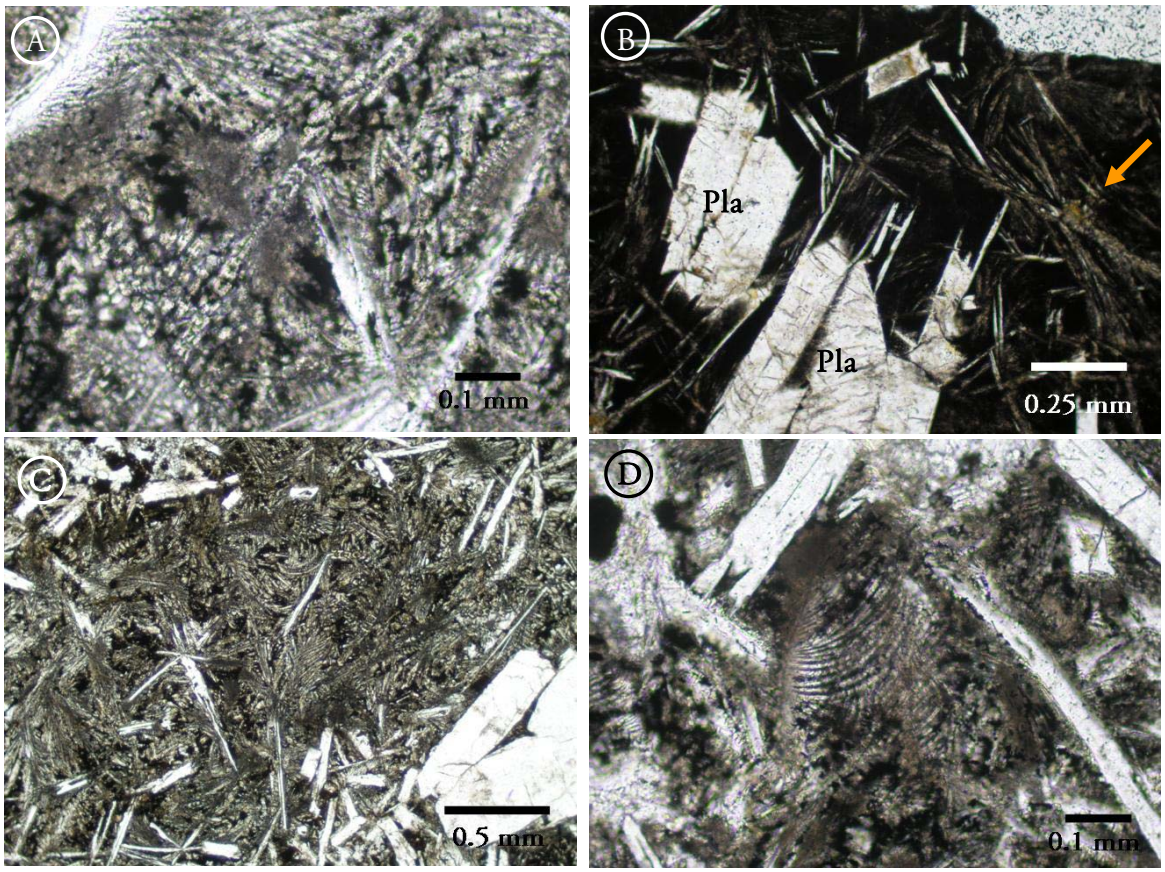

Figure 6.10 – (A) Elongated parallel chains of pyroxene crystals in the groundmass; (B) fine grained basalt with plagioclase phenocrysts with acicular terminations and spherulite pyroxene crystallites radiating from a central point, resembling a bow-tie (sheaf-like pattern indicated by arrow); (C) Rosettes of acicular plagioclase crystals radiating from a common nucleation site and feather like pyroxene crystals within the groundmass; (D) curled feather-like dendritic pyroxene crystals.

The pyroxenes show a small range in composition and according to Morimoto (1989), are classified as quadrilaterals (Quad, Ca-Fe-Mg pyroxenes) trough the projection in the Q-J diagram (Fig. 6.11). These pyroxenes, using the Ca-Mg-Fe "quadrilateral" (Wo-En-Fs

diagram), are further classified as augites with a narrow compositional range of Wo_{39-42} En_{38-46} Fs_{13-22} (Fig. 6.12).

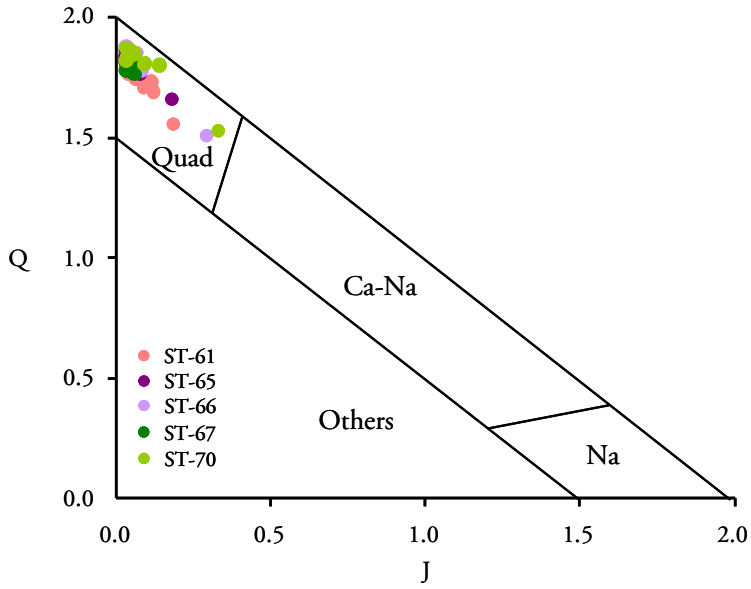

Figure 6.11 – Q-J diagrams for Santiago MORB pyroxenes (Q= Ca+ Mg+Fe^{2+} and J=2 x Na; Morimoto, 1989).

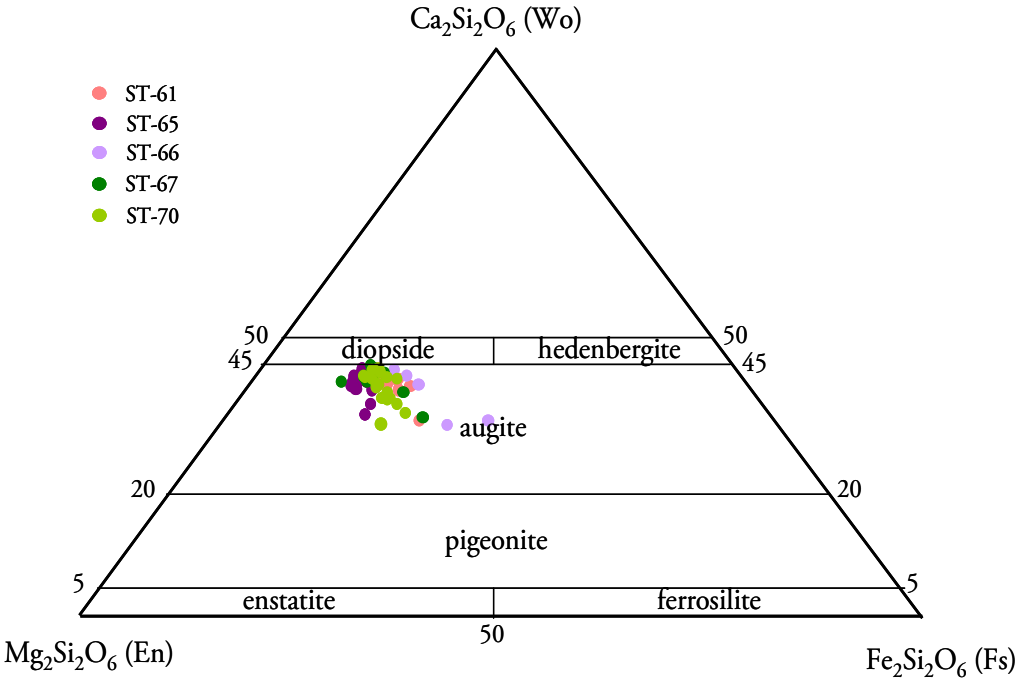

Figure 6.12 – MORB pyroxene compositions plotted on in terms of $Ca_2Si_2O_6$, $Mg_2Si_2O_6$ and $Fe_2Si_2O_6$ proportions.

Pyroxene substitutions

Regarding the chemistry of the tetrahedral site in the clinopyroxene, if a value of 2 Si a.f.u is attained it meant that the tetrahedral site is completely filled by silicon, which is not case in Santiago's alkaline and tholeiitic augites, imposing the entrance of ^{IV}Al to balance the charge deficiency (Fig. 6.13) (Schweitzer et al., 1979). This imbalance is most striking in alkali basalts, since tholeiites have higher Si content which can diminish the substitution of Al for Si. Indeed the Al_2O_3 is higher in Santiago's alkaline lavas augites as opposed to the ones that occur in the MORB affinity lavas (Fig. 6.14) as is usually described elsewhere for tholeiitic and alkaline rocks (Le Bas, 1962; Greenough et al., 2005).

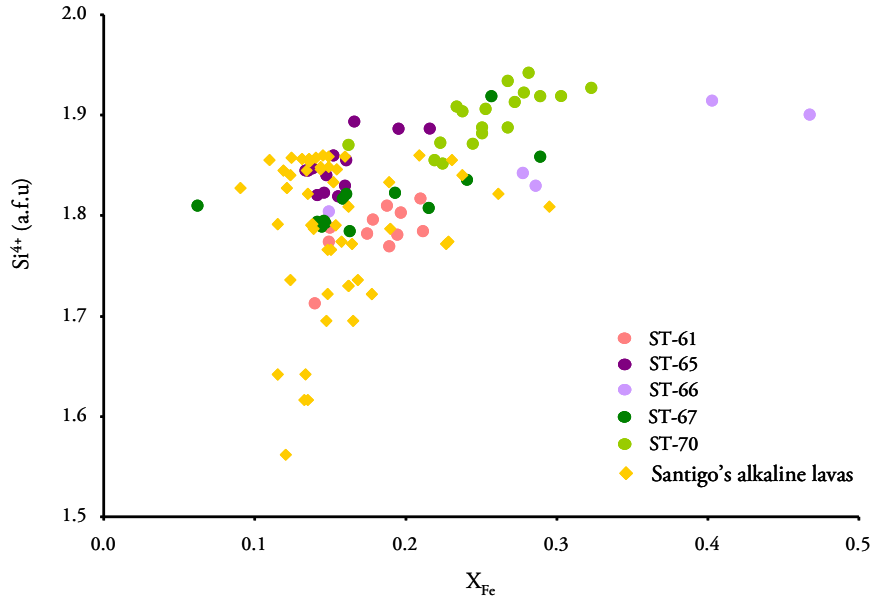

Figure 6.13 – Si vs. X_{Fe} for Santiago's alkaline and tholeiitic augites. X_{Fe} is used to represent fractionation/crystallization [X_{Fe}=Fe/(Fe+Mg)$_{atomic}$]; a.f.u stands for atoms per formula unit.

In pyroxenes charge deficiency caused by the substitutions Si-Al at the tetrahedral site and Ca-Na at the M2 octahedral site is usually compensated by the incorporation of Al^{3+} and Ti^{4+} instead of the usual divalent cations (Mg, Fe, Mn) at the M1 octahedral site. Plotting cations that cause charge deficiencies (Na+Al^{IV}) against those causing charge excess (Al^{VI}+Ti+Cr)[1] it is

[1] The entrance of ^{IV}Al, Fe^{3+} or Cr^{3+} in the M1 site results in a charge excess of +1 relative the quadrilateral component (Mg, Fe^{2+}). When Al substitutes Si in the tetrahedral site a charge deficiency of -1 arises, as well as the substitution of Na in the M2 site for (Ca, Fe^{2+}, Mg) (Schweitzer et al., 1979).

possible to infer that non-quadrilateral substitutions were more important in pyroxene from alkaline rocks than in the ones occurring in tholeiitic rocks (Fig. 6.15).

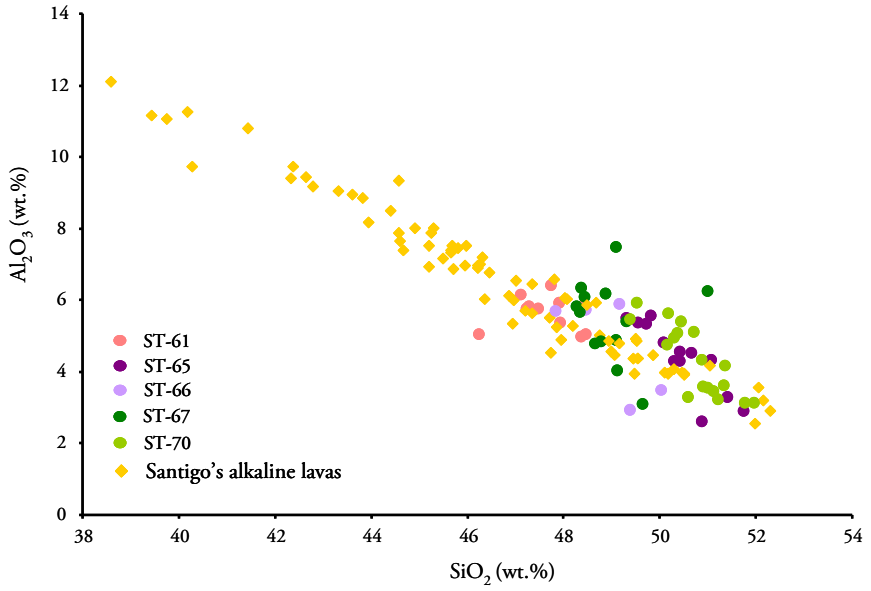

Figure 6.14 –Distinct higher concentration of Al_2O_3 and lower SiO_2 in alkaline lavas augites, compared to those in tholeiitic lavas.

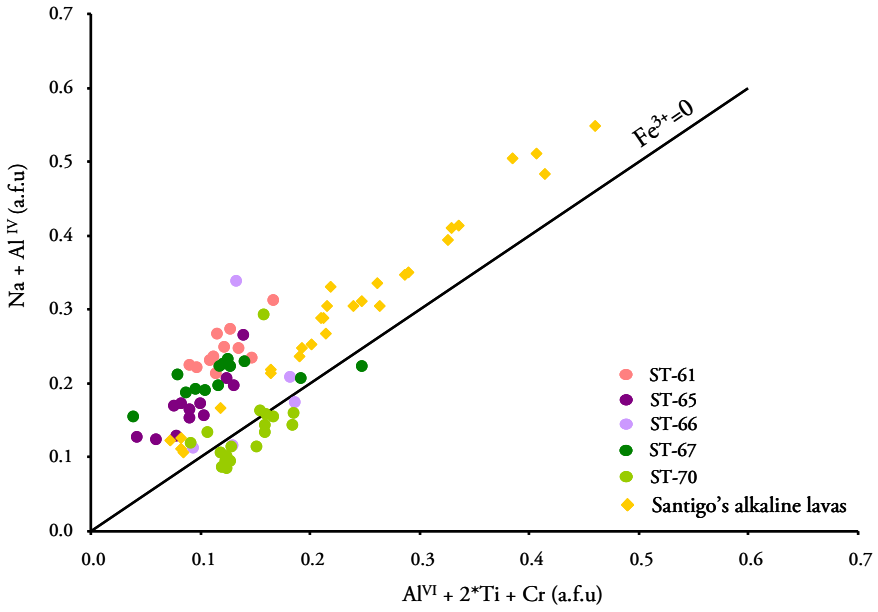

Figure 6.15 – Charge deficiencies (Na+^{IV}Al) against charge excess (^{VI}Al+2Ti+Cr) demonstrating that alkaline lavas augites have more non-quadrilateral substitutions then tholeiitic augites.

The diagram in Figure 6.15 also allows some inferences to be made about the ferric iron content of the pyroxenes and therefore about the oxidation conditions of the magmas. The

projection of the majority of the samples above the Fe^{3+}=0 line, implies the presence of Fe^{3+} in the M1 site in addition to Al, Ti and Cr so that charge balance is maintained. However, augites from sample ST-70 plot near or slightly below the Fe^{3+}=0 line, implying the absence of ferric iron.

6.2.1.3. Opaque minerals

The opaque minerals in the groundmass are iron-titanium oxides and sulphides. The oxides s.l. occurs as skeletal/dendritic crystals dispersed in the groundmass and, less frequently, as inclusions in plagioclase phenocrysts. The analyses totals for the oxides are low and can be due to hydration and alteration, as to be expected from ancient submarine lavas. Even though the analyses can not be considered quantitatively it is evident a compositional difference between the oxides. The majority would be titanomagnetites, however the amount of Cr^{3+}, Al^{3+} and Mg^{2+} are variable, demonstrating heterogeneity among the melt composition or different crystallization conditions (temperature and pressure) (Fig. 6.16).

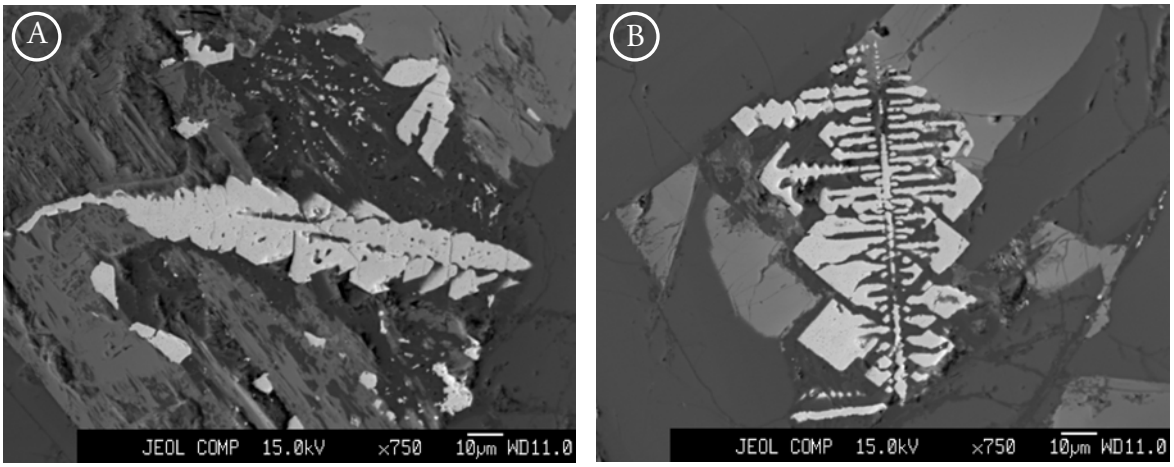

Figure 6.16 – Scanning electron microscopy images of oxide minerals in the groundmass.

For the sulphides, from the 41 performed analyses only 8 are quantitatively significant allowing their classification as pyrites (Table 6.1). Pyrite composition is almost stoichiometric with only minor amounts of cobalt, gold and more rarely arsenic and nickel. The crystals are euhedral to subeuhedral, sometimes with skeletal forms, and they occur as dispersed grains within the groundmass and along veinlets (Fig. 6.17). Since the main mode of occurrence is along veins and veinlets, it seems likely that their crystallization is a late event probably related with some sort of hydrothermal alteration where fluids circulated under reducing conditions

(Humphris, 1972). It is probable that such hydrothermal alteration resulted from oceanic metamorphism triggered by basalt-seawater interaction upon submarine extrusion.

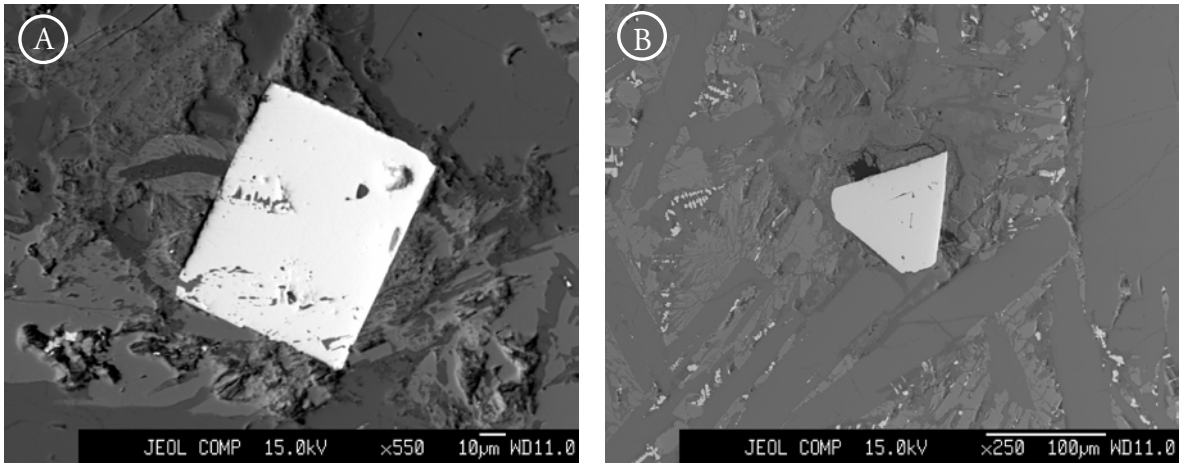

Figure 6.17 – Scanning electron microscopy images of euhedral sulphides in the groundmass.

Table 6.1 – Electron microprobe analyses of sulphides.

	ST-61 G	ST-61 G	ST-67 G	ST-67 G	ST-67 G	ST-67 G	ST-67 G	ST-70 PI
S	52.93	52.94	53.18	53.26	53.06	52.81	52.80	52.56
Fe	45.62	45.39	46.00	45.62	46.04	45.09	44.72	45.16
Cu	0.00	0.00	0.00	0.00	0.00	0.00	0.00	0.00
As	0.03	0.04	0.03	0.01	0.09	0.04	0.04	0.03
Ni	0.06	0.03	0.03	0.01	0.02	0.02	0.37	0.00
Sb	0.00	0.00	0.00	0.00	0.02	0.00	0.00	0.00
Co	0.30	0.11	0.13	0.42	0.12	0.30	0.86	0.06
Zn	0.04	0.04	0.01	0.00	0.00	0.05	0.03	0.03
Pb	0.00	0.05	0.00	0.04	0.07	0.00	0.00	0.05
Sn	0.00	0.02	0.00	0.02	0.00	0.03	0.07	0.03
Ag	0.01	0.00	0.03	0.01	0.00	0.00	0.04	0.00
Au	0.29	0.00	0.10	0.76	0.10	0.78	0.00	0.96
Total	99.28	98.60	99.51	100.16	99.51	99.12	98.92	98.88
Atomic proportion								
S	1.65	1.65	1.66	1.66	1.65	1.65	1.65	1.64
Fe	0.82	0.81	0.82	0.82	0.82	0.81	0.80	0.81
Cu	0.00	0.00	0.00	0.00	0.00	0.00	0.00	0.00
As	0.00	0.00	0.00	0.00	0.00	0.00	0.00	0.00
Ni	0.00	0.00	0.00	0.00	0.00	0.00	0.01	0.00
Sb	0.00	0.00	0.00	0.00	0.00	0.00	0.00	0.00
Co	0.01	0.00	0.00	0.01	0.00	0.01	0.01	0.00
Zn	0.00	0.00	0.00	0.00	0.00	0.00	0.00	0.00
Pb	0.00	0.00	0.00	0.00	0.00	0.00	0.00	0.00
Sn	0.00	0.00	0.00	0.00	0.00	0.00	0.00	0.00
Ag	0.00	0.00	0.00	0.00	0.00	0.00	0.00	0.00
Au	0.00	0.00	0.00	0.00	0.00	0.00	0.00	0.00
Total	2.48	2.47	2.49	2.49	2.48	2.47	2.47	2.45

G: Groundmass crystal; PI: Crystal in plagioclase interior

6.2.1.4. Secondary mineralogy

The basalt outcrop in the Angra Bay area (Santiago Island) is representative of pillow lavas erupted at the Mesozoic ocean floor (see next sections) and so, evidences of alteration due to interaction with seawater or low grade metamorphism (prehnite-pumpellite to greenschist facies) would be expected. Since the outcrop is nowadays exposed subaerially it is also expected that some of the alteration is due to subaerial phenomena. However discerning between the two situations can be difficult.

Hydrothermal alteration is evident in the neighbouring island of Maio, where the outcrop of similar pillow basalts of tholeiitic affinity show extensive weathering with some being metamorphosed in the greenschist facies, and thus exhibiting the characteristic mineral paragenesis of epidote, albite, biotite, chlorite and actinolite (DePaepe et al., 1974). Hydrothermal metamorphism of basalts leads to recrystallization in the greenschists facies where mafic minerals are altered, sometimes to chlorite (≈320 ºC), calcic plagioclase becomes more sodic (albitization) and a new mineralogy appears comprising epidote (≈260 ºC) and actinolite (Humphris, 1972; Nakamura et al., 2007) (Fig. 6.18).

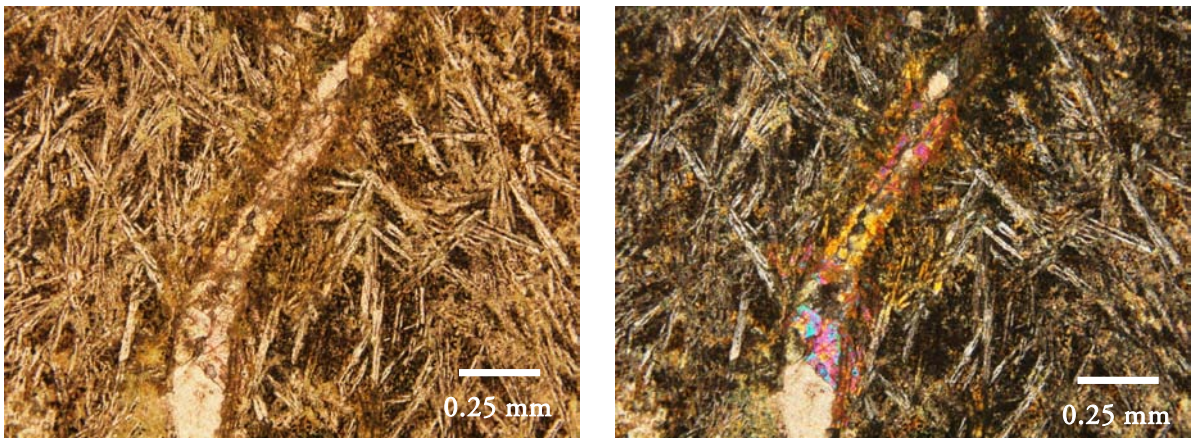

Figure 6.18 – Carbonate vein associated with epidote crystals crosscutting aphanitic basalt (Maio Island).

Maio pillow lavas are also characterized by the abundant occurrence of secondary minerals, mostly phyllosilicates replacing primary minerals (phenocryts, groundmass and glass) and also filling vesicles and veins. The occurrence of clay minerals (possible palagonite, smectites and celadonite) and carbonates suggests an intense deuteric alteration (low-temperature water-rock interaction; < 100ºC) (Fig. 6.19).

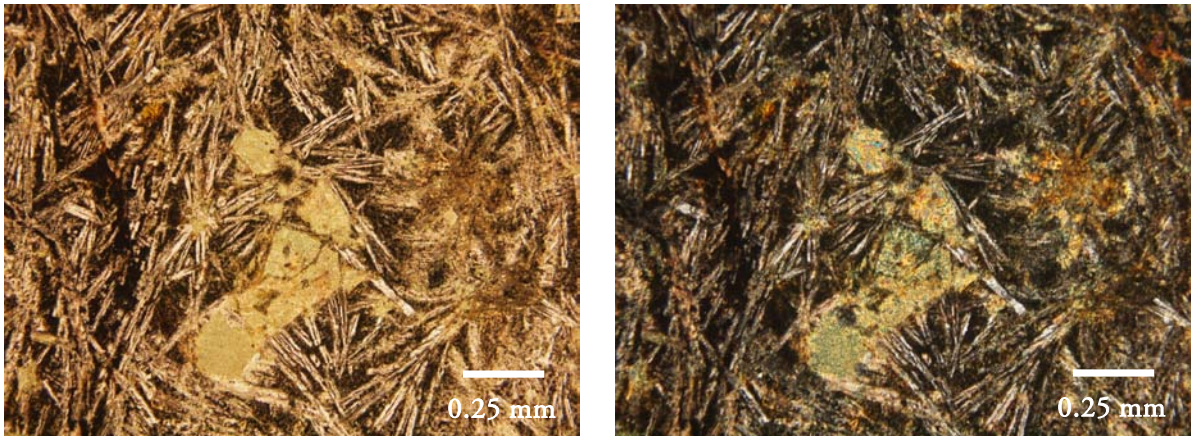

Figure 6.19 – Greenish clay minerals completely substituting primary igneous minerals (Maio Island).

Santiago pillow lavas preserve all the primary igneous minerals with very little evidence of alteration, apart from the occurrence of carbonated veins associated with epidote, sulphides and plagioclase sericitization (Fig. 6.20).

The difference between the degree of alteration depicted by Maio and Santiago ancient pillow lavas is also corroborated by geochemical evidences (see section 6.3.1.5.). This difference could be due to:

- distinct physical properties associated with different extrusion types (pillow size and morphology);
- longer exposition of Maio rocks to subaerial/submarine agents;
- exhumation mechanism (even thought there is no information regarding the specific mechanism responsible for the outcrop of these ancient pillow lavas).

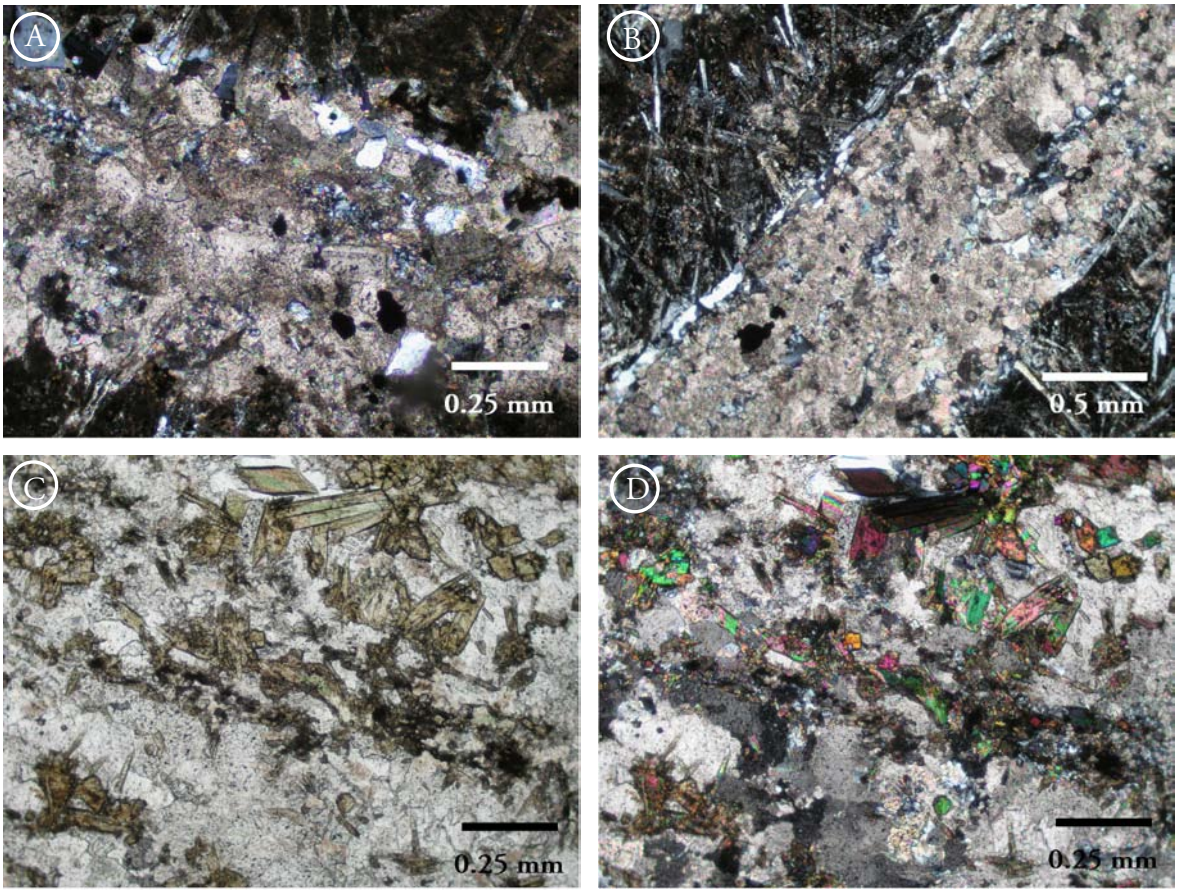

Figure 6.20 – Milimetric vein filled with carbonates, quartz, sulphides (A and B) which in some area exhibit aggregates of epidote crystals with the characteristic greenish yellow pleocroism and moderate birefringence interference colours (C and D, respectively).

6.2.1.5. Fenitic carbonated pockets/vesicules and veins

Santiago pillow lavas are however characterized by the occurrence of a specific mineral paragenesis, not observed or described in Maio pillow lavas. In pseudomorphosed crystals (Fig. 6.21) as well as in veins and more rarely dispersed in the groundmass (Fig. 6.22) a pale bluish green acicular mineral occurs always associated with carbonates. This mineral was chemically identified as a magnesio-arfvedsonite, a Na-amphibole (Fig. 6.23).

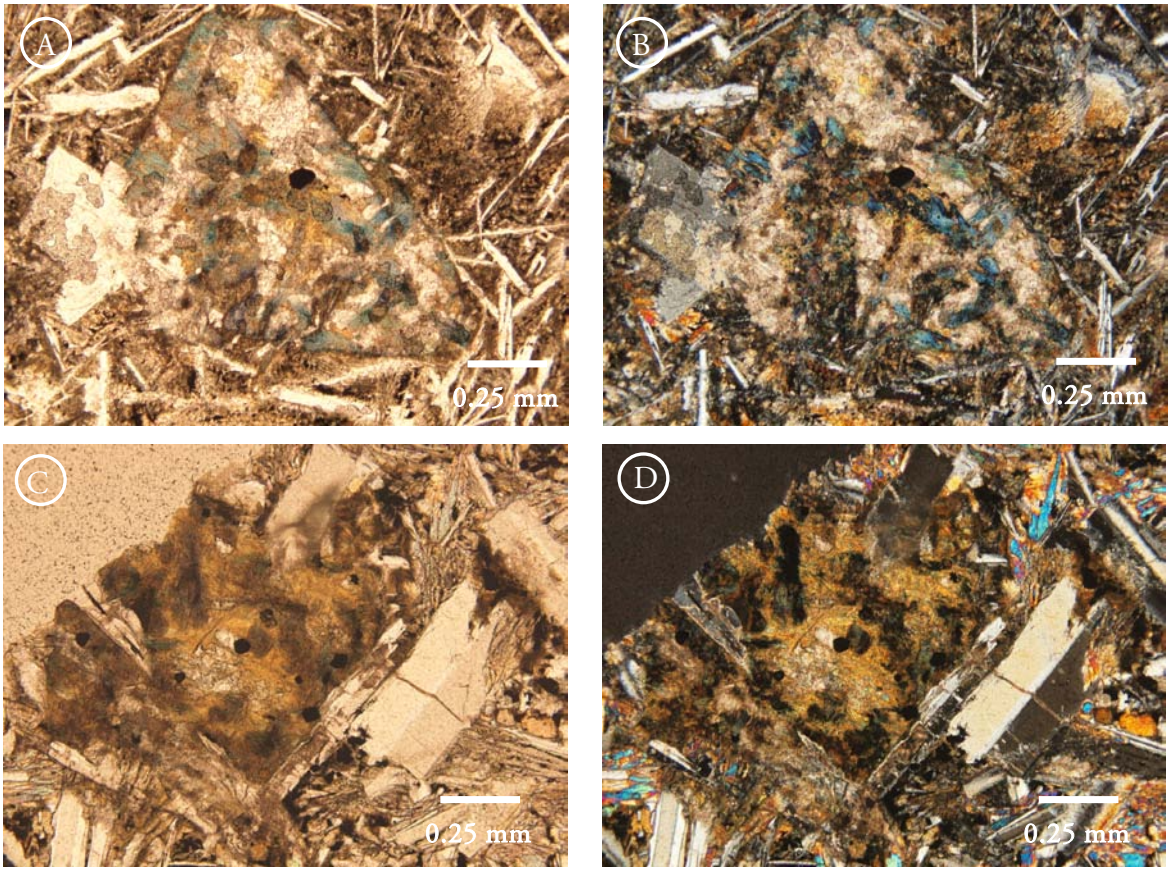

Figure 6.21 –Primary igneous mineral totally pseudomorphosed to an aggregate of carbonates, mossy patches of Na-amphibole and sulphides (A and C plane polarized light, B and C crossed polarized light).

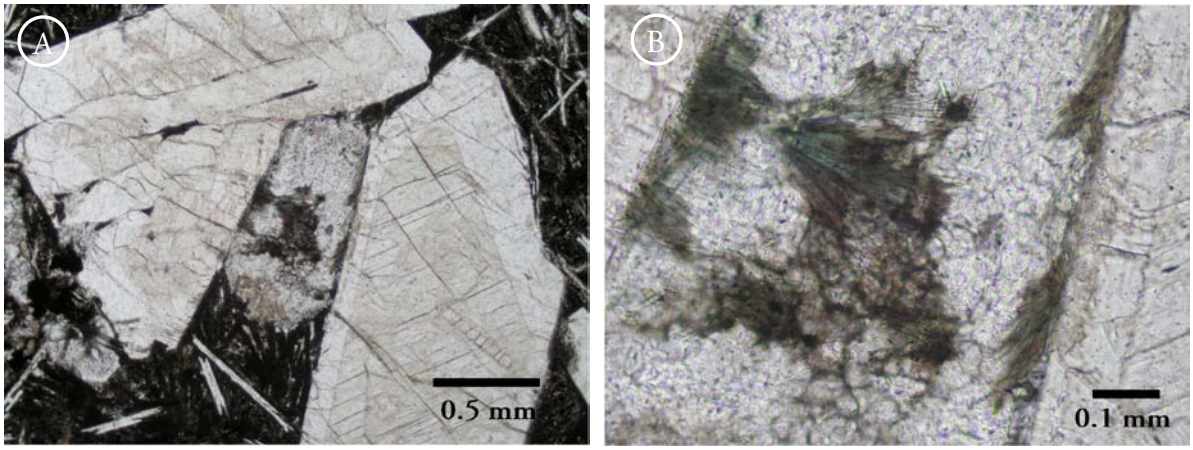

Figure 6.22 – Carbonated filled rounded vesicle with acicular crystals of bluish-green amphibole (A). Acicular blue amphibole detail (B).

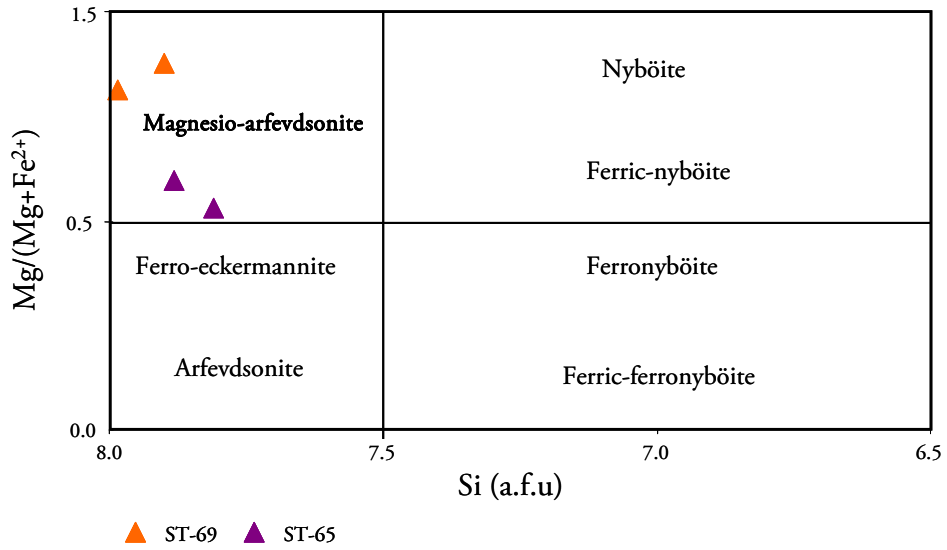

Figure 6.23 –Sodic amphibole classification according to Leake et al. (1997). The diagram chosen meets the required criteria: $(Mg+Fe^{2+}+Mn^{2+})>2.5$ a.f.u; $Na_B \geq 1.5$ and (Mg or Fe^{2+})$>Mn^{2+}$. The analyzed amphiboles plot in the left up quadrant, the distinction between eckermannite and magnesio-arfevdsonite is made since $^{IV}Al<Fe^{3+}$.

Other particular minerals such as aegirine, phlogopite and albite were also optically and chemically identified (see Fig. 6.24; 6.25).

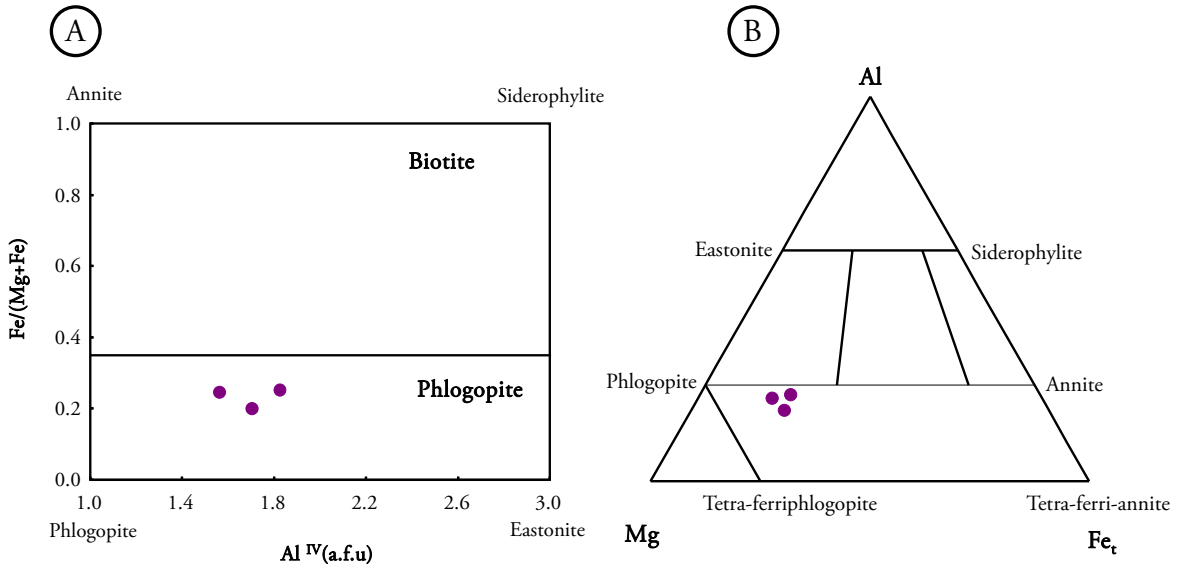

Figure 6.24 – Micas classified as phlogopites (sample ST-65) according to Rieder et al. (1988) (A) and specific composition in terms of Al, Mg and Fe_t (Fe_t, total iron calculated as Fe^{2+}) (adapted from Brod et al., 2001) (B).

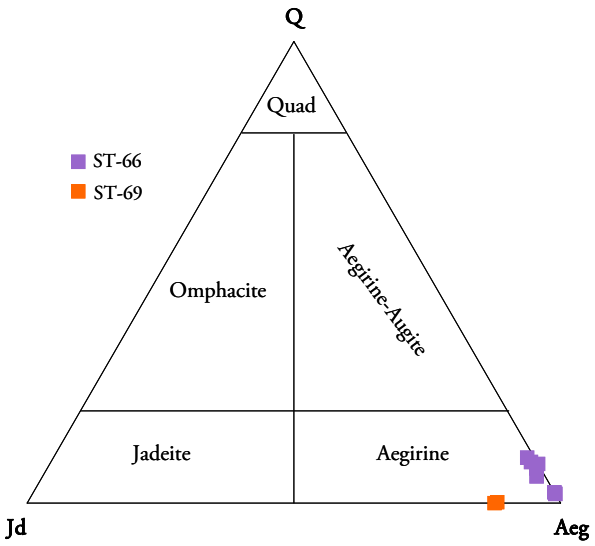

Figure 6.25 – The Na-pyroxenes in samples ST-66 and ST-69 were classified as aegirines (Quad, represent the Ca-Mg-Fe pyroxene area, Jd as jadeite, Aeg as aegirine).

The occurrence of this particular mineral paragenesis calls for an enrichment in alkalis, a process that is most probably related with the intrusion of dolomitic carbonatites within the pillow lavas outcrop. This process is known as fenitization[2] and can be defined as an alkali metasomatism associated with alkaline/carbonatitic igneous activity, leading to the pervasive alteration of the rock both mineralogical and chemically (Le Bas, 2008; Carmody, 2012).

Primary mantle-derived carbonatite melts are rich in alkalis (Na and K) and associated with volatile-rich (C-O-H-S-N) liquids (aqueous or carbonatitic) susceptible of migrating and impart their geochemical fingerprint to the adjacent rocks. Heinrich, in 1985 (in Le Bas, 2008) classified three principal types of fenites around carbonatites: potassic, sodic-potassic and sodic. Since in Santiago the observed mineralogy is dominantly enrich in sodium, as expressed by the occurrence of albite, Na-pyroxene (aegirine) and Na-amphibole (arfevdsonite) the fenitization can be classified as sodic. The appearance of phlogopite associated with the specific Na-paragenesis suggested that this mineral is also associated with the fenitization process and sodium was not the only alkalis present in the metasomatic agent.

The presence of fenites in the Cape Verde islands was already described by Silva (1979) (fenitized grabroic rocks in Santiago Island), Le Bas (1981, 2008) (Brava and São Vicente Islands) and Mourão (2012) (Brava Island).

[2] The terms fenitization and fenite were introduced in 1921 by Brögger (Le Bas, 2008) to describe a group of metasomatically altered rocks adjacent to the alkaline complex of Fen in Norway.

The geochemical fingerprint of this process will be fully addressed in section 6.3.1.6.

6.2.2. Gabbroic xenoliths

The eleven gabbroic xenoliths collected at Santiago Island are relatively homogeneous in mineralogy and texture. The great majority is holocrystalline, coarse-grained with average grain size between 2.5 and 5.0 mm, granular and with cumulate texture (Fig. 6.26). Samples ST-163 and ST-169 are medium-grained with grain size ranging from <0.5 mm to 1.5 mm (Fig. 6.27).

Based on the modal proportions of the rock forming minerals Santiago xenoliths can be classified as gabbros *s.s.* (essential minerals are plagioclase and clinopyroxene) and orthopyroxene gabbros (essential minerals are plagioclase and clinopyroxene with minor amounts of orthopyroxene) (see Streckeisen, 1976).

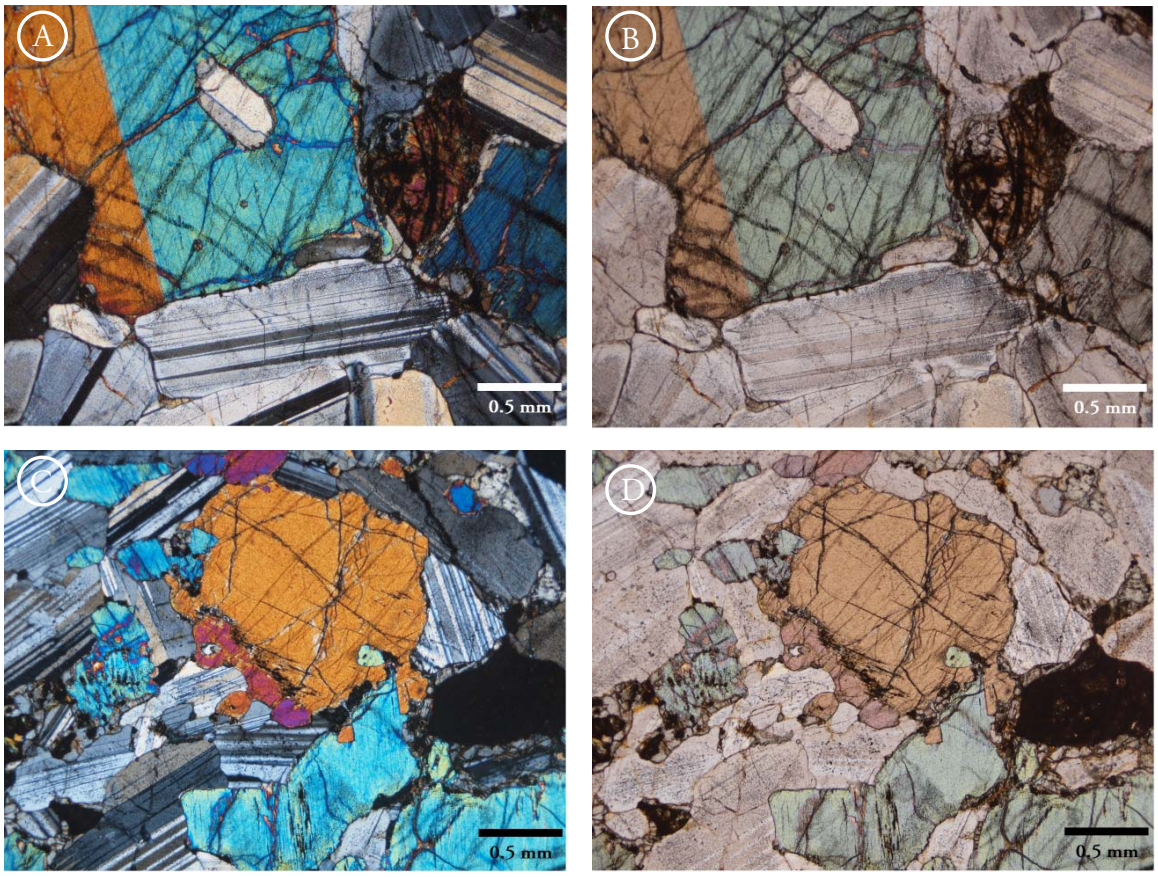

Figure 6.26 – Coarse-grained gabbroic xenoliths. In A and B, a poikilitic clinopyroxene encloses a plagioclase rounded crystal. C and D, subeuedric plagioclase, clinopyroxene and altered olivine. A and C crossed polars, B and D plane polarized light.

The mineral assemblage is dominated by plagioclase (25 to 60% modal) and clinopyroxene (10 to 40% modal) with variable amounts of orthopyroxene (not detected to 20% modal) and olivine (not detected to 20% modal). Oxide grains are occasionally present as anhedral crystals. Clinopyroxene frequently display narrow and parallel exsolution lamellae of orthopyroxene indicative of slow cooling. Evidence of deformation is absent.

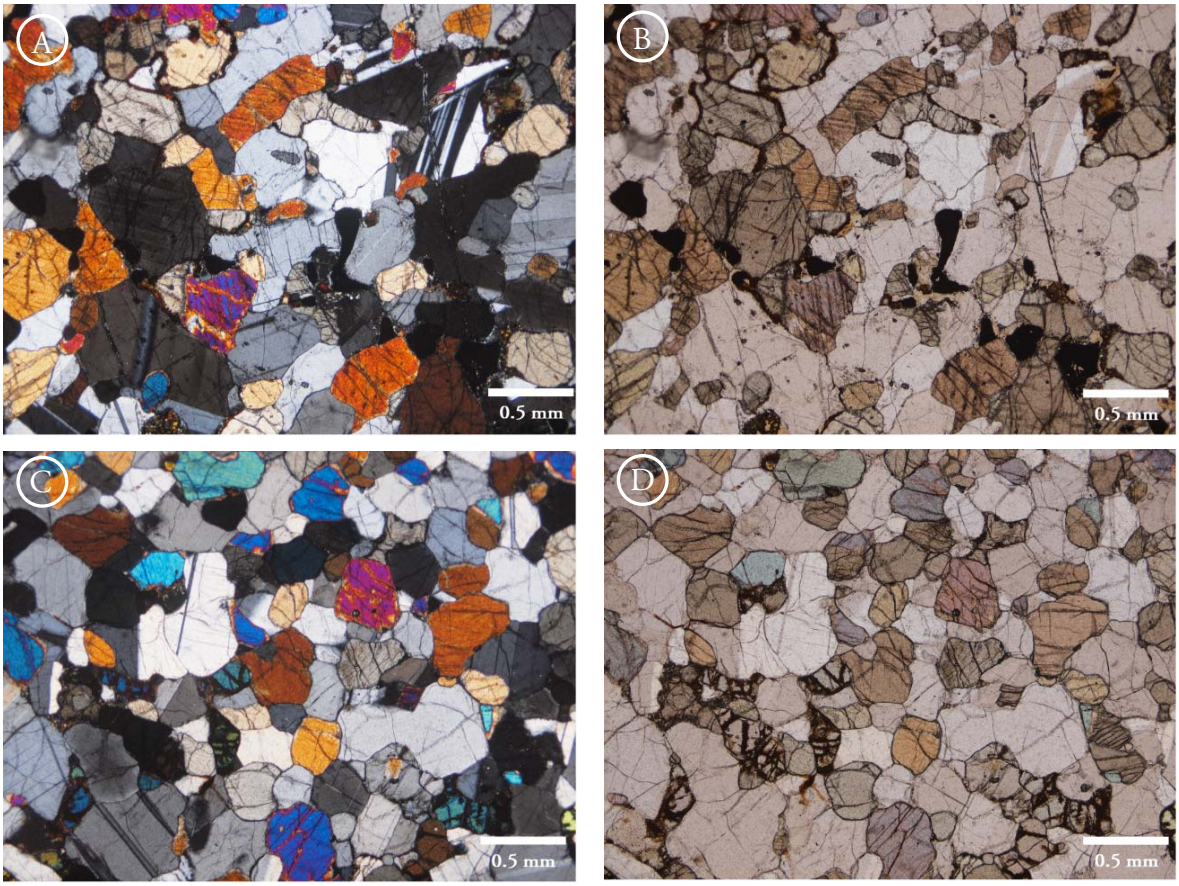

Figure 6.27 – Medium-grained gabbroic xenoliths. In A and B plagioclase, clinopyroxene and oxides. Clinopyroxene crystals are larger than plagioclase ones. In C and D the crystals of plagioclase, clinopyroxene and olivine are almost equigranular and rounded. A and C crossed polars, B and D plane polarized light.

6.2.2.1. Olivine

Olivine present in Santiago gabbroic xenoliths is almost always strongly altered to iddinsgite and oxide minerals (Fig. 6.28). Even though several microprobe analyses were done in the various gabbroic xenoliths samples none was satisfactory and so it is not possible to characterize this mineral of the gabbroic mineral assemblage.

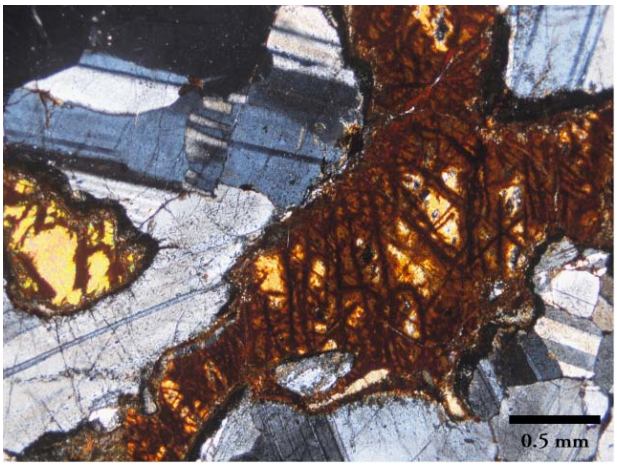

Figure 6.28 – Coarse grained olivine anhedral crystal almost integrally altered to iddingsite.

6.2.2.2. Plagioclase

Plagioclase compositions fall in the range $An_{62.1}Ab_{10.8}Or_{0.0}$ to $An_{89.2}Ab_{37.7}Or_{0.7}$ (see Fig. 6.29 and Appendix III.3.2.) and so the majority can be classified as bytownites. Sample ST-163 is the only that exhibit a slight change in composition towards labradoritic compositions ($An_{62.1}Ab_{293}.Or_{0.1}$ to $An_{70.6}Ab_{37.7}Or_{0.3}$). Plagioclases An-rich and Or-poor are typical of N-MORB rocks (Neumann et al., 2005).

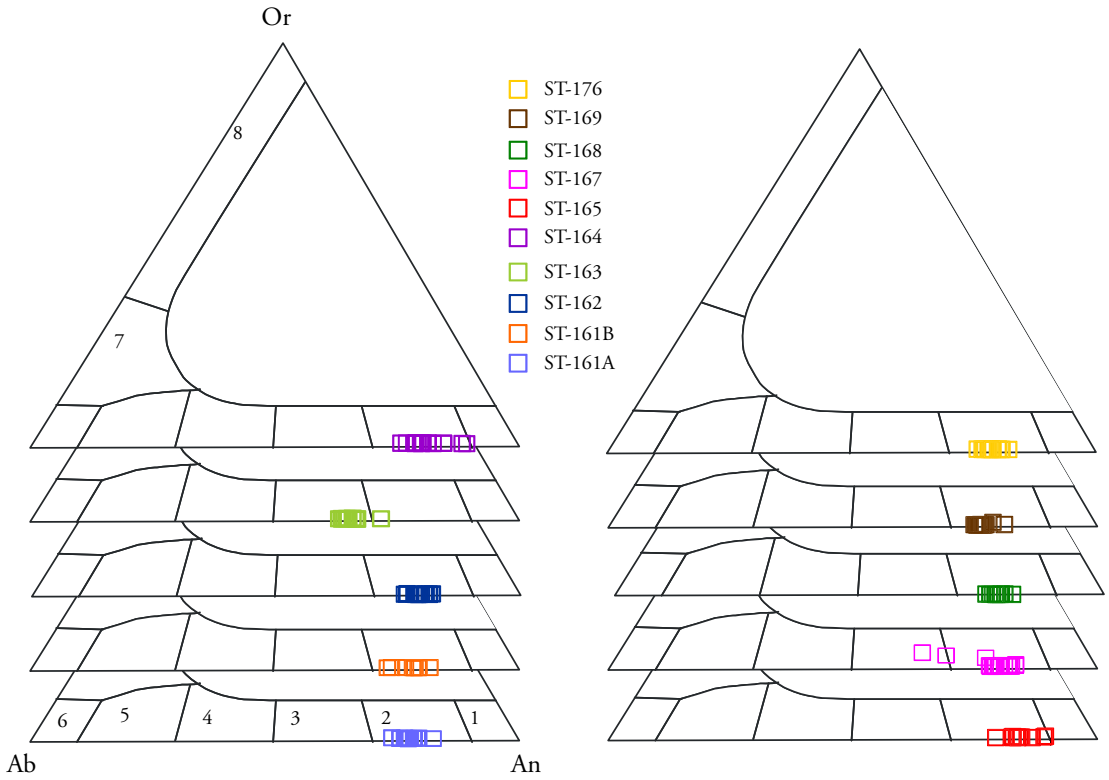

Figure 6.29 – Plagioclase composition of Santiago gabbroic xenoliths (1 – Anorthite; 2 - Bytownite; 3 - Labradorite; 4 - Andesine; 5 - Oligoclase; 6 - Albite; 7 - Anorthoclase; 8 - Sanidine).

6.2.2.3. Pyroxenes

From the 290 analyses of pyroxene done in the gabbroic xenoliths of Santiago about half were classified as augites within the range $Wo_{25}En_{39}Fs_{8}$ to $Wo_{47}En_{60}Fs_{24}$. Diopside corresponds to about 35% of the analyzed pyroxenes, with a compositional range from $Wo_{45}En_{27}Fs_{7}$ to $Wo_{50}En_{47}Fs_{26}$. Only 2% of the entire analyzed pyroxenes plot above the line defining 50% of wollastonite end-member (mean average composition is $Wo_{51}En_{36}Fs_{13}$). Ortopyroxenes, which are not present in all samples, represent 7% of the analyzed pyroxenes being classified as enstatites ($Wo_{0}En_{60}Fs_{18}$ to $Wo_{3}En_{80}Fs_{38}$) (Fig. 6.30).

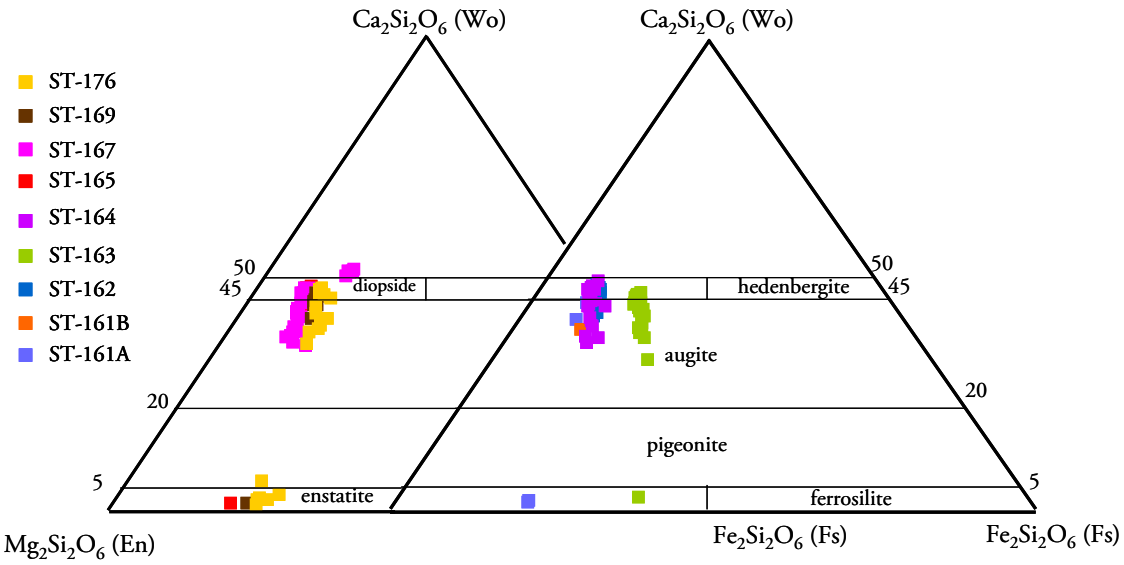

Figure 6.30 –Gabbroic xenolith pyroxene compositions plotted on pyroxene quadrilateral.

On samples ST-168 and ST-173 compositional profiles were made across adjacent pyroxene crystals. It was shown that orthopyroxene is usually present as rims of the clinopyroxene crystals. In Fig. 6.31 and 6.32 the pyroxene compositional variability among adjoining crystals in the same sample are shown.

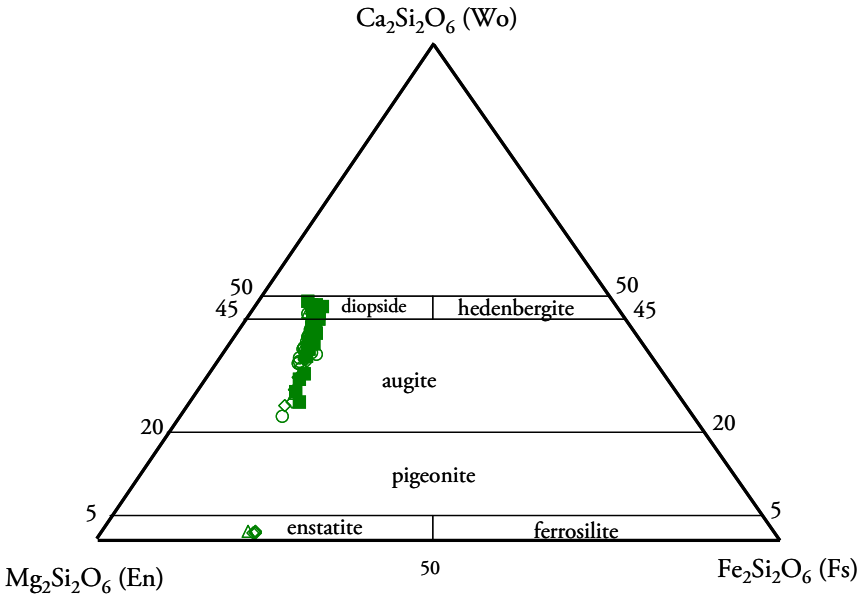

Figure 6.31 – Sample ST-168 pyroxene variable compositions plotted on pyroxene quadrilateral. The different symbols represent two compositional profiles in distinct crystals.

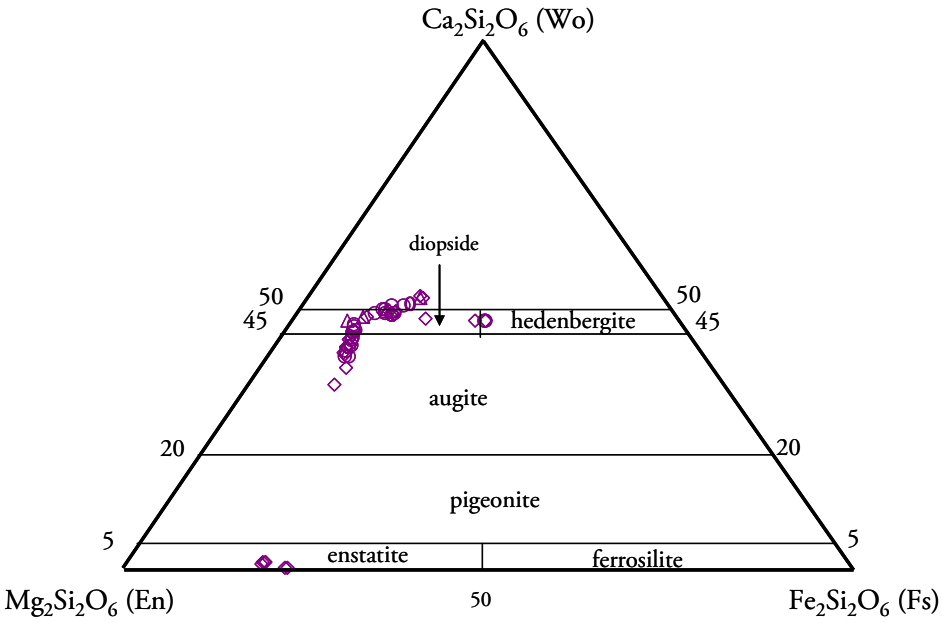

Figure 6.32 – Sample ST-173 pyroxene variable compositions (wollastonite, diopside, augite and enstatite) plotted on pyroxene quadrilateral.

The pyroxene compositions of Santiago gabbroic xenoliths fall within the range of gabbroic rocks from the Mid-Atlantic Ridge (see Fig. 6.33). Compared with pyroxenes from Santiago MORB suite and Santiago alkaline lavas, the pyroxenes from the gabbroic xenoliths

are more depleted in TiO_2 and Al_2O_3. It is worth mentioning that one of the samples exhibit pyroxene compositions similar to those of the alkaline lavas (ST-167) (see section 6.3.2.1.).

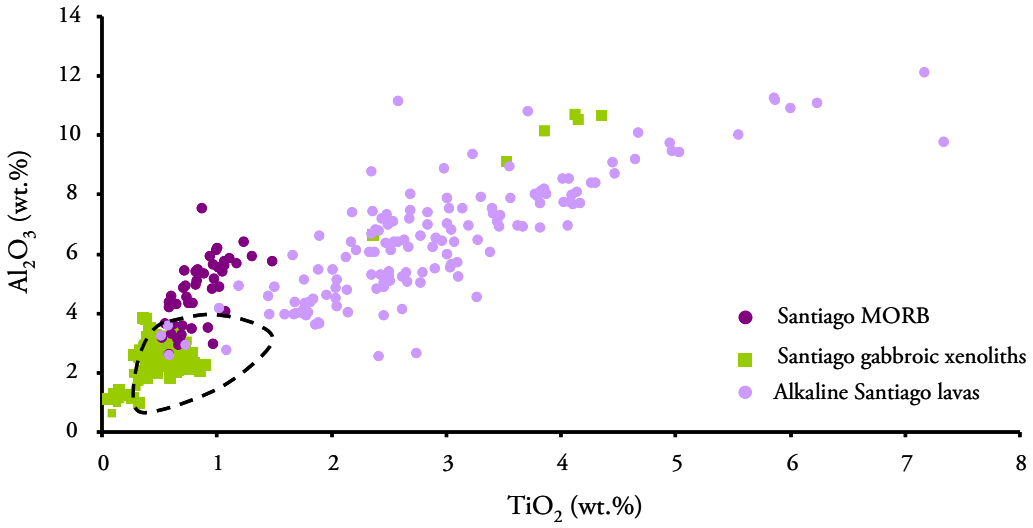

Figure 6.33 – Al_2O_3-TiO_2 relations in pyroxenes from Santiago gabbroic xenoliths compared with Santiago MORB and alkaline lavas. The field of gabbroic rocks from Mid-Atlantic Ridge is marked by a dashed line (data from Cannat et al, 1997). The pyroxene data from Santiago alkaline lavas are from Martins (2003).

6.3. Whole rock major and trace element chemistry

6.3.1. MORB Lavas

6.3.1.1. Classification and magmatic affinity

The volcanic rocks that outcrop in the Angra area are fine grained and frequently glassy, which makes mineral identification and quantification difficult. According with IUGS (International Union of Geological Sciences) recommendations a chemical classification based on whole-rock major element analysis was attempted (Le Bas and Streckeisen, 1991).

The SiO_2 content of the samples range from 47 to 50 wt. %, enabling their classification as basic. If the total alkalis-silica diagram (TAS) (Le Maitre et al., 1989) is used they can be further classified as subalkaline-alkaline basalts. Even thought the analyses were recalculated to 100% in a H_2O-CO_2 free basis, the TAS diagram is not ideal when considering weathered or altered volcanic rocks (Fig. 6.34).

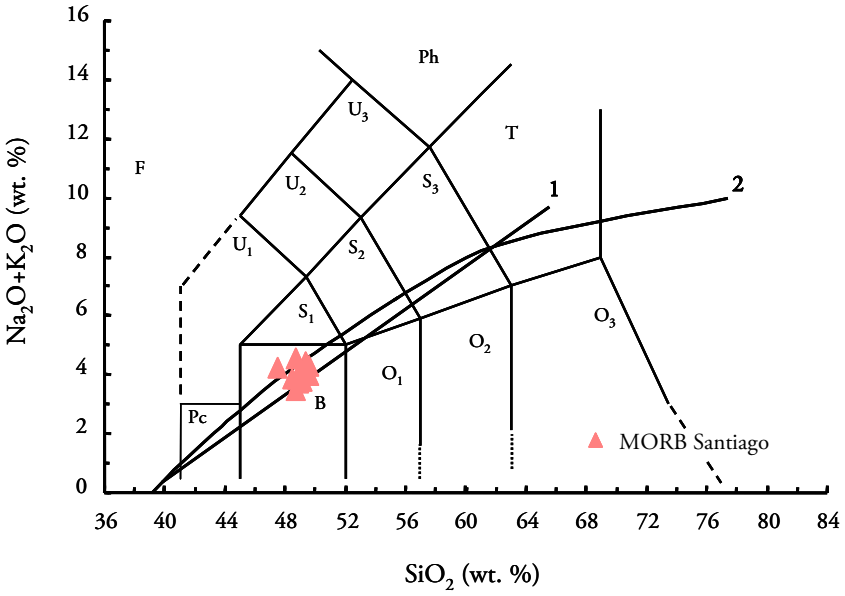

Figure 6.34 – Chemical classification and nomenclature of Santiago pillow lavas using the total alkalis-silica (TAS) diagram. Fields by Le Bas (1986): F- Foidite; U_1- Tephrite/Basanite; U_2- Phono-tephrite; U_3- Tephri-phonolite; Ph- Phonolite; Pc- Picrobasalt; S_1- Trachybasalt; S_2- Basaltic trachy-andesite; S_3- Trachy-andesite; T- Trachyte; B- Basalt; O_1- Basalt andesite; O_2- Andesite; O_3- Dacite. Subdivision of the alkaline and subalkaline field is from 1) MacDonald and Katsura (1964) and 2) Irvine and Baragar (1971).

According to Le Maitre et al. (2002) ideally fresh igneous samples should not contain more than 2 wt. % of H_2O^+ and 0.5 wt.% of CO_2. Santiago tholeiitic lavas are characterized by LOI (Loss On Ignition) ranging from 3.3 to 7.7 wt. %, which is taken as an alteration index associated with modal abundance of secondary minerals (degree of vesicle fillings and glass alteration). The main pitfall about the application of the TAS diagram to the studied rocks is the evidence for fenitization exhibited by some samples (see 6.2.1.2) associated with the carbonatitic breccia intrusion, which will lead to a significant alkali mobilization, compromising the discrimination between the alkaline and subalkaline rock series.

Even thought the TAS classification may not be ideal for Santiago ancient pillow lavas, they can be definitely be classified as basalts, due to their distinct mineralogy. However when their normative composition[3] is projected onto the basalt tetrahedron of Yoder-Tilley (1962), from the diopside apices (Ne-Q-Ol plane), the samples plot in the alkaline field, at odds with

[3] Normative composition was calculated using SINCLAS software (Standard Igneous Norm and Volcanic Rock Classification System) which also determines the Fe_2O_3/FeO ratio (Verma et al., 2002). The Fe_2O_3/FeO ratio calculation was based on the recommendation of Middlemost (1989).

the tholeiitic classification already reported by other authors (Gerlach et al., 1988: Millet et al., 2008) (Fig. 6.35).

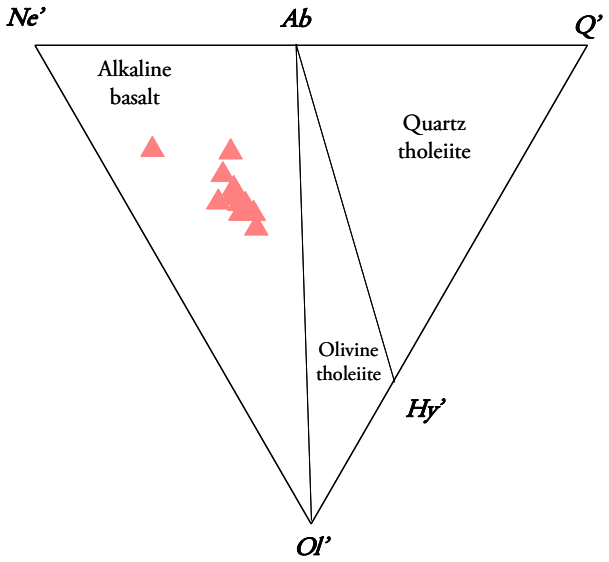

Figure 6.35 – Santiago pillow lavas projected in the Yoder-Tilley diagram (Yoder and Tilley, 1962).

Tholeiitic basalts should be characterized by the occurrence of modal or normative hypersthene, and hence be projected in the Ol-Ab-Hy or Q-Ab-Hy triangles of Thompson (1984) [expansion of Yoder-Tilley (1962) tetrahedron]. Once again the high alkali content of the samples stemming from fenitization processes will be transformed in normative nepheline and orthoclase instead of hypersthene, leading to an erroneous classification based on major elements that are specifically modified by the described metasomatic event.

The occurrence of a suite of basaltic pillow lavas with a distinct chemical signature from the most common and dominant alkaline lavas in Santiago Island as well as the type of emplacement on the field leads to the necessity of fingerprinting the type of oceanic basalt and its former tectonic environment. The use of discrimination diagrams based on elements less susceptible to remobilization/alteration such as Zr, Nb, Y, P_2O_5, Ti and V enables just that.

The diagram from Winchester and Floyd (1976) (Fig. 6.36), based on immobile HFSE allows the discrimination between tholeiitic and alkaline basalts, with Santiago pillow lavas being characterized by low TiO_2 and high Zr/P_2O_5. Also the horizontal trend depicted by the studied samples is typical of sub-alkaline magmas suites, as opposed to the vertical trends usually displayed by alkali basalts.

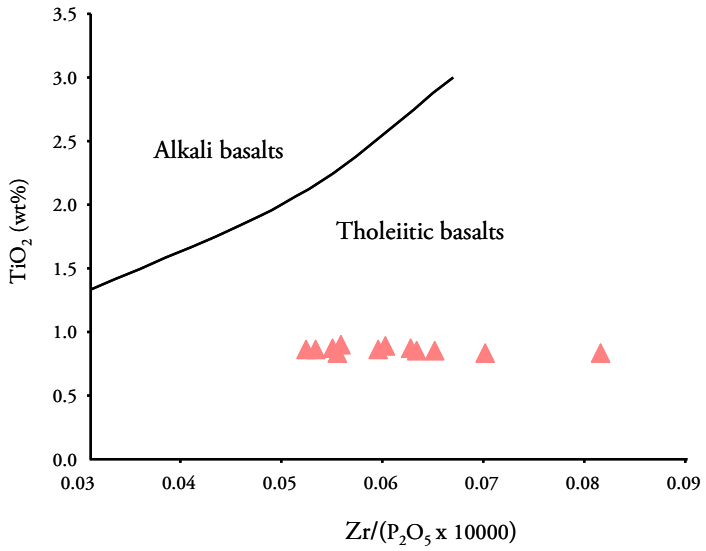

Figure 6.36 – Santiago pillow lavas classified as tholeiitic based on Winchester and Floyd (1976) diagram.

Winchester and Floyd (1977) proposed a similar diagram for the identification of volcanic rocks based on immobile elements (Fig. 6.37), which is widely used as a TAS proxy for altered samples, with Nb/Y ratios used as an alkalinity index and Zr/TiO_2 ratios as a measurement of the evolution degree (proxy to silica saturation). According to this discrimination diagram of Santiago pillow are clearly subalkaline basalts.

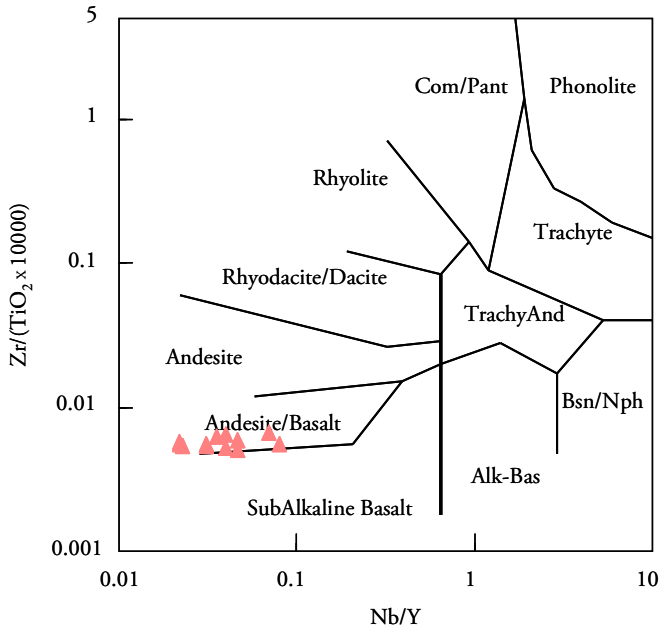

Figure 6.37 - Zr/TiO_2 versus Nb/Y diagram (after Winchester and Floyd, 1977)

Due to possible post-emplacement alteration of whole rock composition, clinopyroxenes can be used as an alternative to constrain the magmatic affinity of magmas, since their composition varies according with the host magma geochemistry (Leterrier et al., 1982). According with the discrimination diagrams proposed by Leterrier et al. (1982), the magmas outcropping in the Angra area can be classified as tholeiitic of non-orogenic origin (spreading zones) (Fig. 6.38).

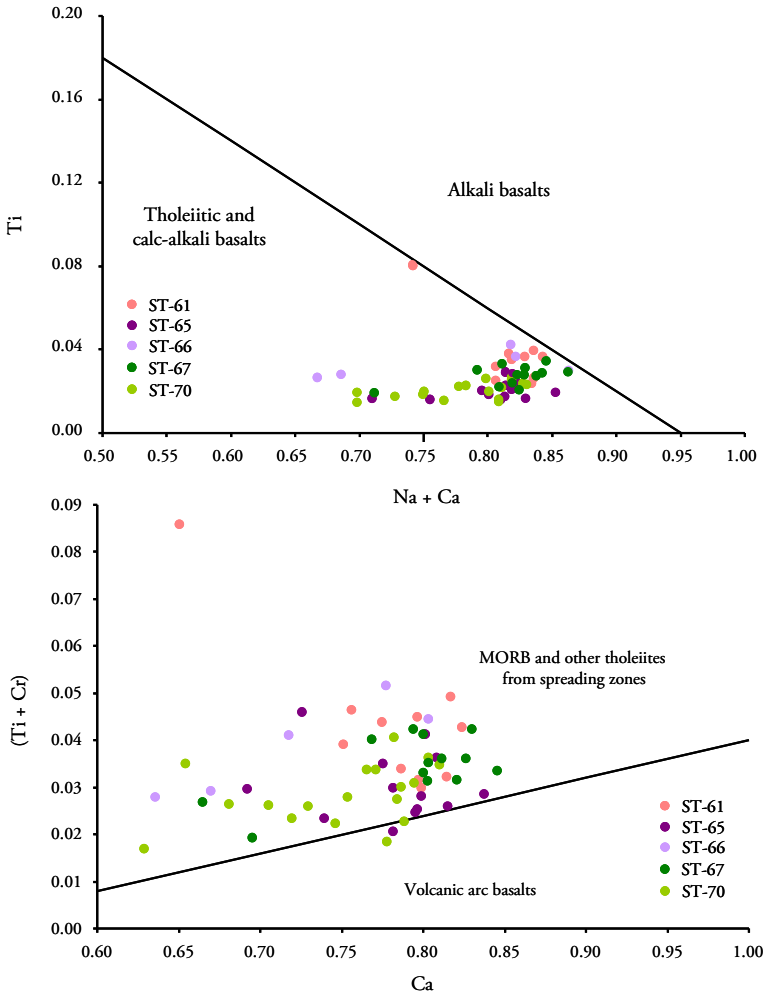

Figure 6.38 – Santiago Jurassic pillow lavas pyroxene composition projected on the discriminating diagram of Leterrier et al. (1982), attesting their non-orogenic origin of the magmas.

The non-orogenic character of the rocks in discussion is further reinforced by the use of Zr-Nb-Y associations as initially proposed by Meschede (1986) (Fig. 6.39A and B).

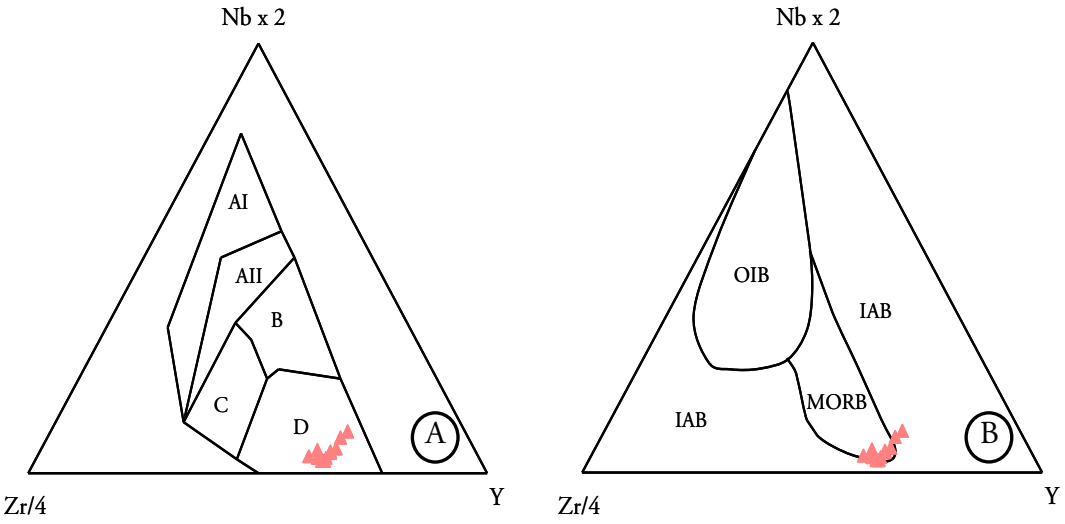

Figure 6.39 – A) Zr-Nb-Y discrimination diagram for basalts after Meschede (1986) (fields as follows: AI - within-plate alkali basalt; AII - within-plate alkali basalt and within-plate tholeiites; B – E-type MORB; C - within-plate tholeiites and volcanic-arc basalts; D – N-type MORB and volcanic-arc basalts; B) Zr-Nb-Y discrimination diagram with new proposed fields by Vermeesch (2006).

The samples are projected on the D field, assigning them to N-type MORB or to volcanic-arc magmatism. Vermeesch (2006) revised some of the most common tectonic discrimination diagrams using more robust statistical methods such as linear discriminant analysis (LDA) and quadratic discriminant analysis (QDA). Since the former boundaries in the classic discrimination diagrams were drawn by eye, the more rigorous statistical approach seems to perform at least as well as the former ones, as it can be seen in Figure 6.39B, were the new boundaries allows to distinguish between MORB and IAB (Island Arc Basalts).

Vermeesch (2006) also proposed new discrimination diagrams, and concluded that one of the most statistically reliable, using only immobile elements is the Ti-V-Sm ternary diagram, which supports the effectiveness of the use of Ti and V in discriminating tectonic environments, already identified by Shervais (1982) (Fig. 6.40). This author chose the combined used of Ti and V, due to the variable partition coefficient of V as a function of oxygen fugacity which can be used as a tectonic discriminate since MORB tends to exhibit reducing conditions as opposed to the more oxidizing environment in convergent margin settings (Shervais, 1982).

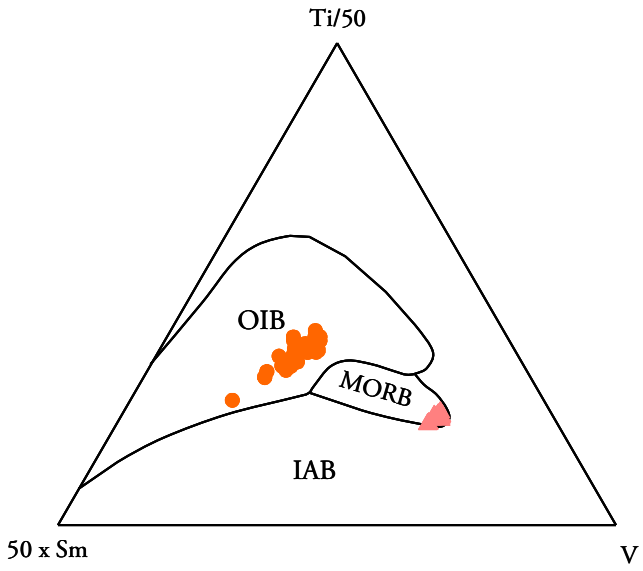

Figure 6.40 – Ti-V-Sm discrimination diagram proposed fields by Vermeesch (2006). Santiago alkaline lavas are plotted for comparison (orange circles).

6.3.1.2. Major and trace elements

Santiago pillow lavas display a very restricted SiO_2 variability (47.5 to 49.5 wt. %, values readjusted to a volatile free basis) and somewhat low MgO contents (5.5 to 7.8 wt. %). This in turn will result in low Mg# (57 to 65) indicating a slight to moderate degree of fractionation of these magmas.

As reported earlier, the metavolcanics are enriched in CaO (12.8 to 15.6 wt. %) and alkalis (3.52 to 4.55, corresponding to the sum of Na_2O and K_2O). These values are high compared with the average values of 11.4 and 2.95 (CaO and alkalis, respectively) reported by Gale et al. (2013) for ALL MORB (see below, 6.3.1.3). Also, TiO_2 content varies from 0.85 to 0.92 wt%, lower than that excepted for a regular MORB (1.68, value from Gale et al., 2013).

Even thought the pillow lavas show evidence of processes susceptible of changing major and trace element concentrations (subaerial/submarine alteration and fenitization processes) some magmatic characteristic/correlation are still evident in major element binary diagrams (Fig. 6.41).

Titanium, sodium and phosphorus behave incompatibly as would be expected while aluminium shows a more random behaviour. The dispersion of the data in MgO-Al_2O_3 space could suggest some degree of plagioclase accumulation (Meurer et al., 2001).

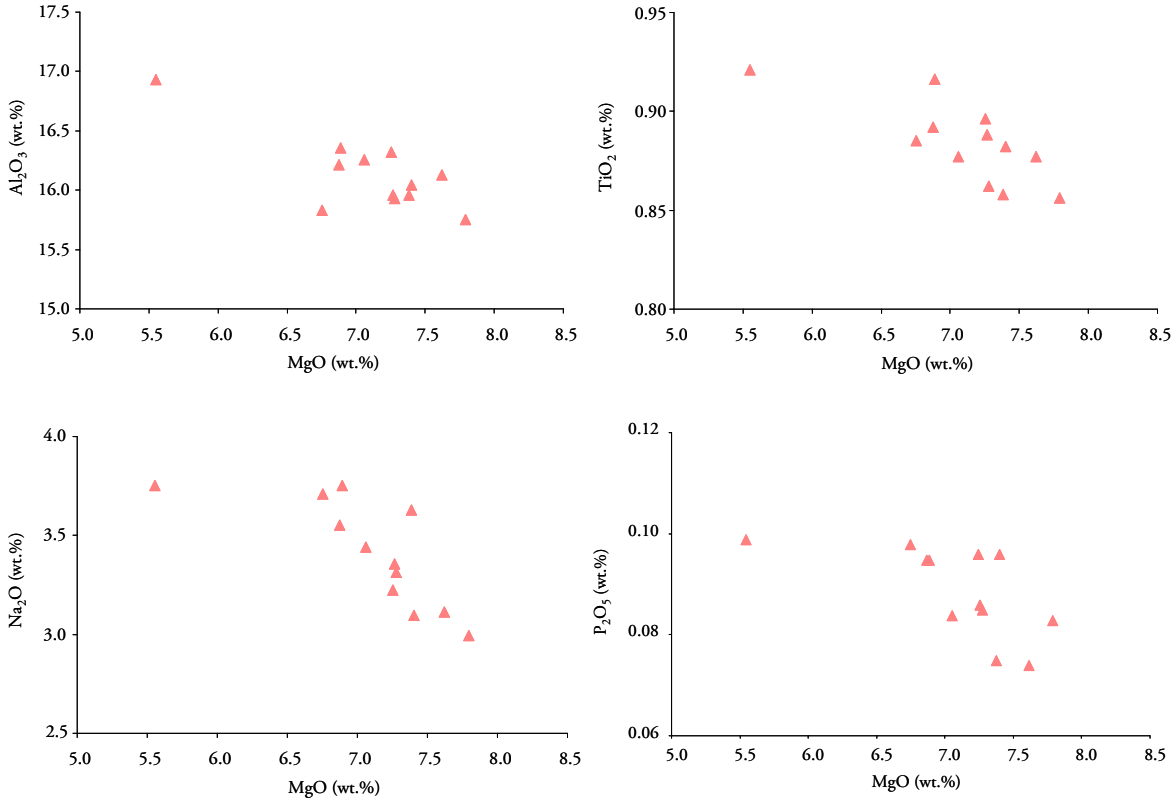

Figure 6.41 – Major element MgO-variation diagrams for Santiago tholeiitic pillow lavas.

CaO, K_2O and FeO values do not co-vary with MgO attesting the influence of post-magmatic processes that will be further discussed in the next sections. Concerning trace elements, Ni and Sc behave compatibly attesting the importance of their incorporation in olivine and pyroxene, respectively (see Fig. 6.42).

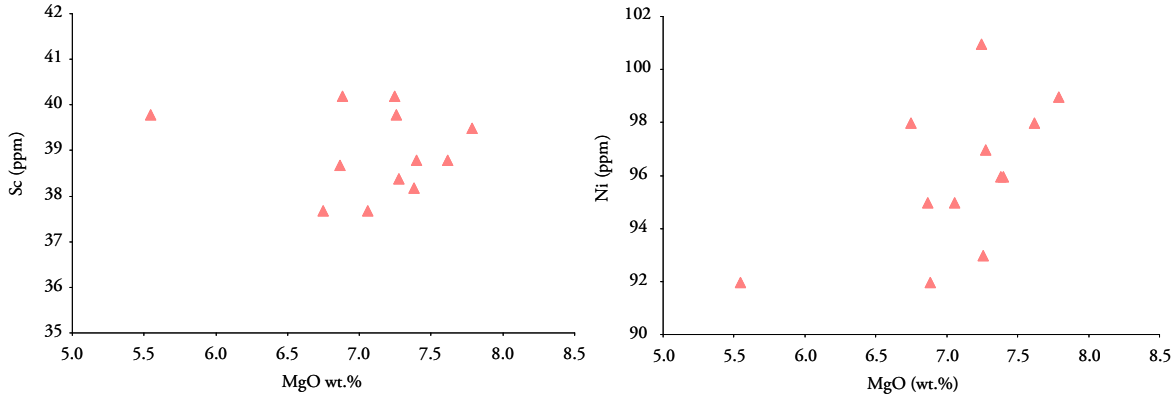

Figure 6.42 – Compatible behaviour of Sc and Ni attesting the fractional crystallization of pyroxene and olivine respectively.

6.3.1.3. Rare earth elements

In chondrite-normalized REE patterns (Fig. 6.43) it is evident the LREE depletion portrayed by Santiago pillow lavas. In fact Santiago tholeiitic suit show evidence for an unusual depletion of the mantle source testified by low $(La/Sm)_n$ and $(La/Yb)_n$ (0.25 to 0.33 and 0.19 to 0.28, respectively; normalized to primitive mantle by Palme and O'Neill, 2003).

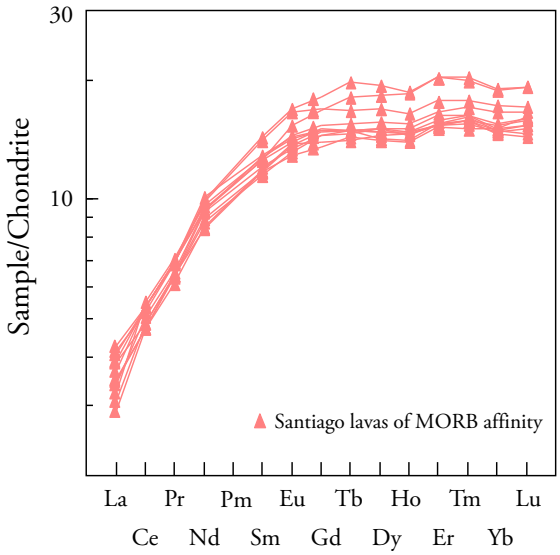

Figure 6.43 – Chondrite normalized REE patterns for Santiago pillow lavas. Normalization values are from Palme and O'Neill (2003).

Gale et al. (2013) propose a new mean composition of mid-ocean ridge basalts (MORB) based on a catalog of 771 ridge segments data. These authors propose a revised nomenclature for MORB:

- ALL MORB are envisaged as representing the composition of the crust apart from back-arc basins;
- N-MORB (normal MORB) is the dominant basalt composition associated with ridges, located 500 km away from hot-spot influence;
- D-MORB (depleted MORB) is the most depleted MORB [$(La/Sm)_n<0.8$];
- E-MORB (enriched MORB) is enriched MORB, not necessarily related with mantelic plume influence [$(La/Sm)_n>1.5$].

According with this classification, Santiago pillow lavas are included in D-MORB suite. In Figure 6.44 Santiago tholeiitic basalts are projected with both N and E-MORB data from Sun and McDonough (1989) and the new MORB data from Gale et al. (2013).

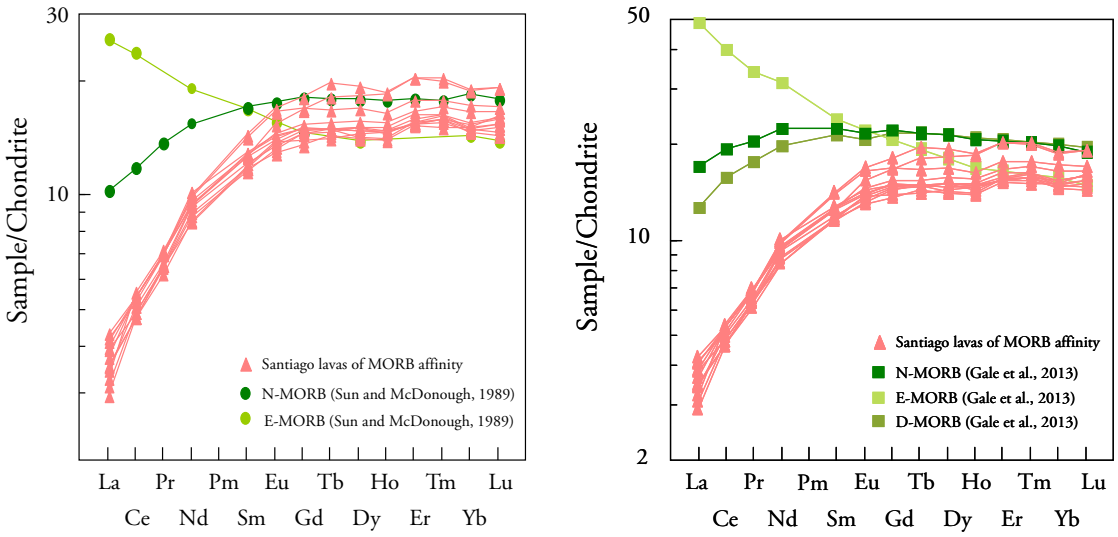

Figure 6.44 – Chondrite normalized REE patterns for Santiago pillow lavas compared with reference values for N-MORB and E-MORB from Sun and McDonough (1989) (A) and the new MORB classification of Gale et al. (2013).

It can be seen that the N-MORB values from of Sun and McDonough (1989) are more depleted then those reported for D-MORB in Gale et al. (2013). As interpreted by Gale et al. (2013) the values commonly thought to represent N-MORB are too depleted to represent the most widespread MORB, however D-MORB values are considered not to be representative of the ocean crust or upper mantle composition. Even so, Santiago pillow lavas are still more depleted in REE that those of the D-MORB of Gale et al. (2013), specifically in LREE.

The possible causes for this extreme depletion in LREE will be discussed in section 6.3.1.9.

The REE content of the Maio MORB-type lavas were first presented by DePapae et al. (1974). Their concentrations are similar to those of the N-MORB presented by Gale et al. (2013) and, thus, not so depleted as those from Santiago (Fig. 6.44). Considering that DePapae et al. (1974) analyses were performed more than 30 years ago and some inter-laboratorial bias may occur, it was decided to make elemental analyses of 3 Maio samples in order to allow a strongly based comparison with the Santiago data. This comparison is made in

Figure 6.45 confirming the much more depleted character of Santiago MORBs as compared with Maio's.

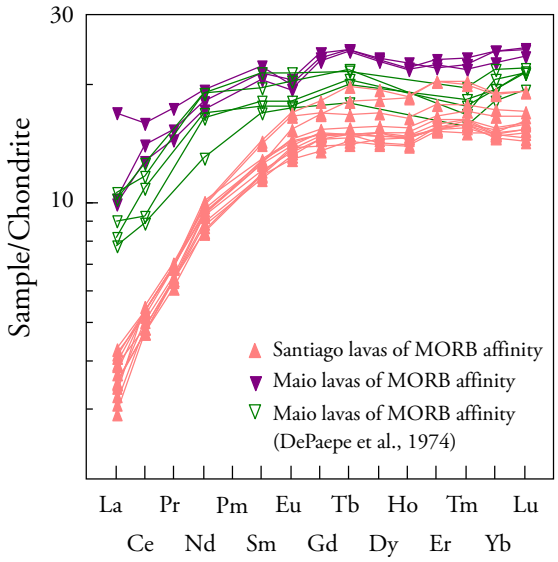

Figure 6.45 – Chondrite normalized REE patterns for Santiago pillow lavas compared with Maio pillow lavas.

6.3.1.4. Other incompatible elements

Santiago MORB samples are characterized by low concentrations of La (0.72 to 1.05 ppm), Nb (up to 2.5 ppm) and Hf (1.3 to 1.5 ppm). Also incompatible trace element ratios normally assumed to be invariant during process of crystal fractionation such as Zr/Nb, La/Sm and Nb/Hf are indicative of a depleted mantle source. Zr/Nb (22 - 80± 20, SD), La/Sm (0.41 - 0.53 ± 0.05, SD) and Nb/Hf (0.47 - 1.67± 0.46, SD) ratios are at their upper limit in accordance with the values of ALL MORB, but their lower values are below the ones attributed to the D-MORB of Gale et al. (2013) (38.5, 0.99 and 1.04, respectively). These values are assumed to represent parent magma signatures and so a geochemical characteristic of the mantle source.

Plotting Santiago tholeiitic pillow basalts incompatible trace elements against the D-MORB values from Gale et al. (2013) it becomes more evident the difference between the two (Fig. 6.46). It is evident an excess of LILE (Rb, Ba, K, Sr), a depletion in the majority of incompatible elements (La, Ce, Nd, Zr, Hf, Ti) a similarity among Y and the HREE, Lu and Yb and a remarkable enrichment in Th.

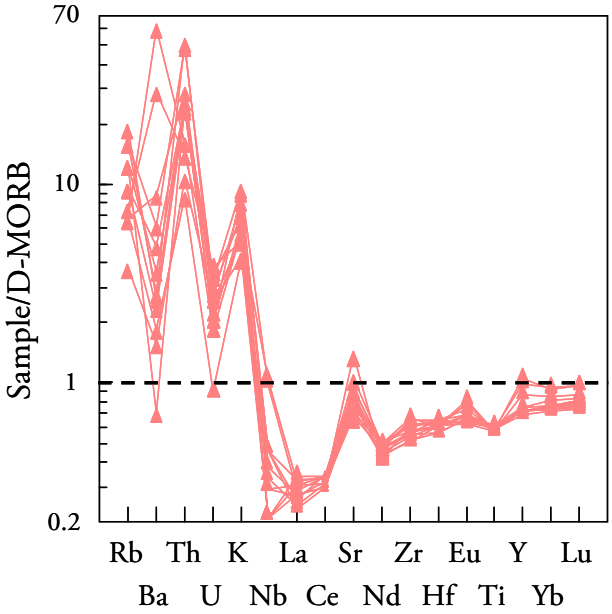

Figure 6.46 – D-MORB normalized incompatible diagram for Santiago pillow lavas (D-MORB values from Gale et al., 2013).

The high values of Th observed (1.3 to 7.9 ppm) are at odds with the low value reported for D-MORB (0.156 ppm; Gale et al., 2013) and the MORB suite in general (up to 1.37 ppm in E-MORB; Gale et al. 2013). The high Th values are corroborated by similar values obtained by Millet et al. (2008) for samples of the same location (Angra Bay area) (see section 6.3.1.5 for further explanation).

Maio tholeiitic suite displays similar incompatible elements patterns generally similar to those of Santiago MORB but with the significant difference in what concerns the significantly more depleted character of Santiago. As mentioned above another difference worth mentioning is Th concentration: Santiago MORBs are characterized by positive Th anomalies while Maio displays negative Th anomalies.

Maio tholeiitic suite displays a similar incompatible elements pattern to Santiago pillow lavas, however some differences are still recognized (see Fig. 6.47). Maio ancient pillow lavas are more enriched in LILE (Rb, Ba, K and Sr) attesting the extensive alteration portrayed by these lavas where some are even metamorphosed in the greenschist facies, as reported on section 6.2.1.4. The majority of the other incompatible elements are in the range of D-MORB (Gale et al., 2013).

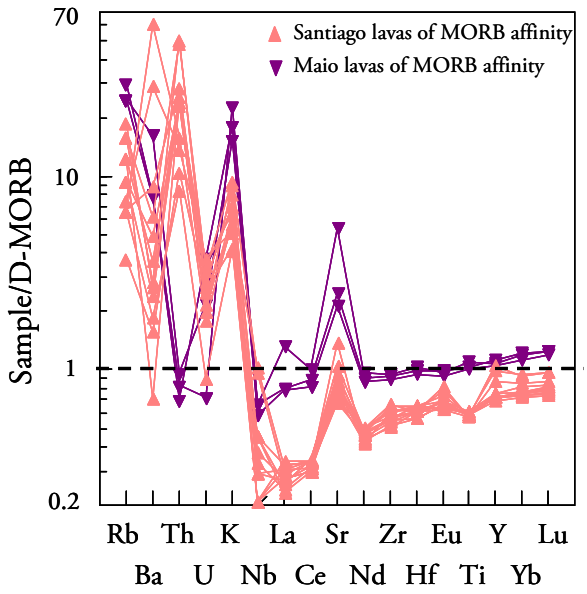

Figure 6.47 – D-MORB normalized incompatible diagram for Santiago and Maio pillow lavas (D-MORB values from Gale et al., 2013).

6.3.1.5. Chemical alteration - effects on major and trace elements mobility

As described in the petrography section, Santiago pillow lava suite does not show evidence for extensive post-magmatic hydrothermal alteration. Instead it is ubiquitous the occurrence of secondary phases such as argilitic material (most probably palagonite and smectite group clays) and carbonates.

As evidenced by the incompatible element diagram, the enrichment of LILE (K, Rb, Ba and Sr) can all be explained by the extreme mobility of these elements in a fluid rich environment. Rb and K show the strongest enrichment while Sr exhibit a more subtle rise compared with D-MORB values (Fig. 6.46). Sr is the element that best correlates with LOI, almost linearly, attesting the influence of alteration processes in the remobilization of this element (Fig. 6.48).

Rb and to a less extent Ba, show a good correlation with K_2O, suggesting a control of both these elements by a K-bearing secondary mineral assemblage formed during alteration events (Fig. 6.49). In the diagram of K_2O vs. Ba, two samples with extreme high Ba values (332 and 693 ppm) were omitted. Since those high values do not correlate with any other element it is assumed that is probably due to a specific mineral, rich in Ba, only present in those two samples (ST-62 and ST-63) even thought it was not identified in thin section.

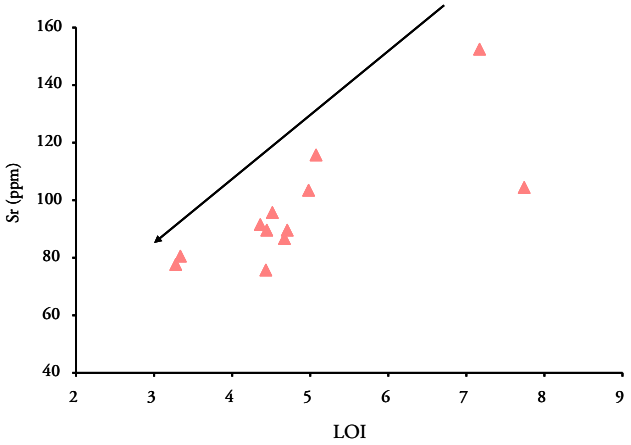

Figure 6.48 – Correlation of LOI with Sr, indicating the influence of alteration processes in Sr variability.

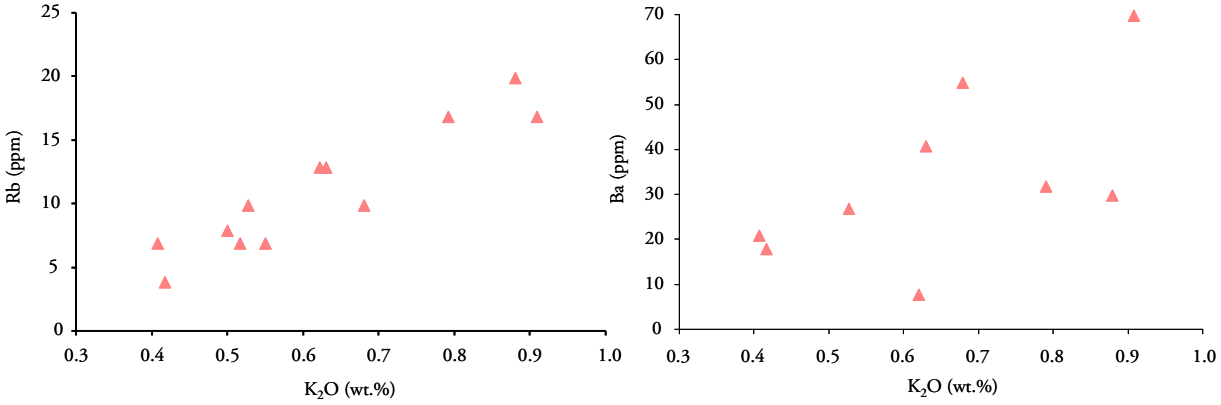

Figure 6.49 – Good correlation of Rb and Ba with K_2O, attesting the occurrence of secondary mineral assemblage that incorporates these elements.

Pb, Th and U are also enriched in the Santiago pillow suite. Pb and U are highly mobile during sweater-dominated hydrothermal alteration due to their chemical characteristic.

The U content shows a good correlation with Sr, and to a less extent with LOI (Fig. 6.50), demonstrating that its enrichment in most probably related with hydrous secondary mineralogy. Fe-oxyhydroxides and sheet silicate minerals, such as micas and clays have been described as having a significant adsorption capability for U (Ames et al., 1983; Nakamura et al., 2007). Also, carbonate minerals can also host U in low-temperature altered rocks (Staudigel et al., 1996).

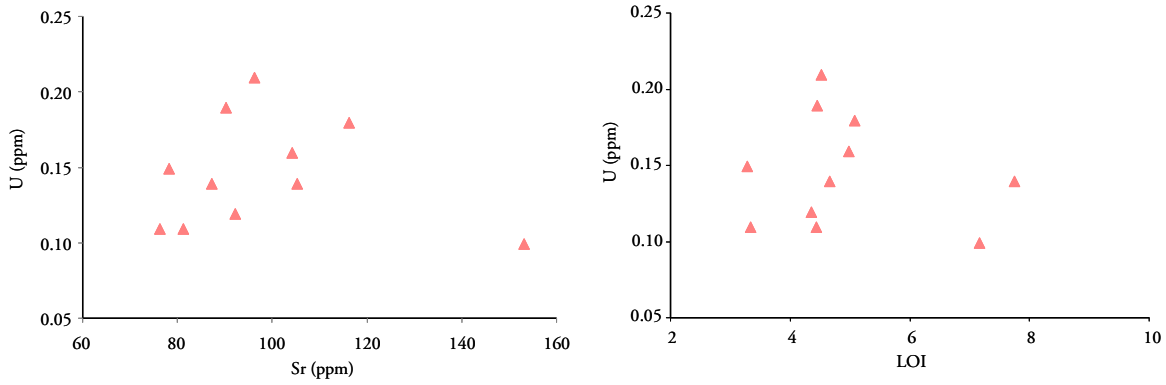

Figure 6.50 – U correlation with LOI and Sr for Santiago MORB lavas.

Th values portrayed by Santiago tholeiitic suite are extremely high (1.3 to 7.9 ppm) compared with the values attributed to either MORB or OIB. These values were confirmed by analyses done by Millet et al. (2008), on similar Santiago samples, suggesting that these values are not due to contamination processes in the laboratory or to analytic error. In fact, Th content correlates with K and to a lesser extent with Rb, suggesting its incorporation in K-bearing alteration minerals (Fig. 6.51).

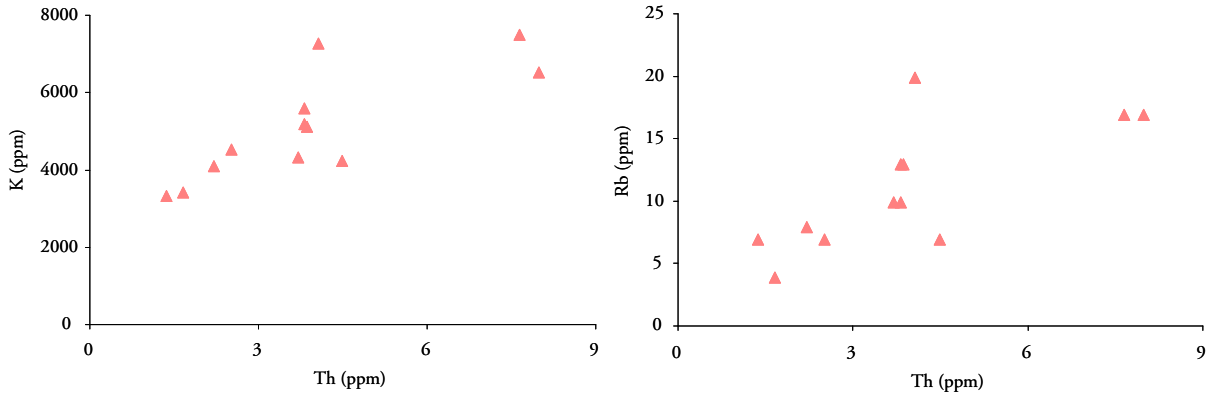

Figure 6.51 – Good correlation of Th with K and Rb suggest an incorporation of this element in post-deuteric mineral paragenesis.

Thorium as a very low mobility under all environmental conditions, due to the stability of the insoluble oxide ThO_2, and is usually not strongly affected by weathering and alteration processes (Salminen et al., 2005). However, if released into solution it can be adsorbed by clay

minerals (Hem, 1992). Since Th values do not correlate with any other element, it is suggested that the high values observed in Santiago pillow lavas are associated with alteration K-minerals.

In Figure 6.52 Santiago pillow lavas suite is normalized to the geochemical reference material for altered oceanic crust, ODP Site 801. Site 801 is located in old fast spreading oceanic crust (170 Ma) east of the Mariana Islands in the subducting Pacific plate (Kelly et al., 2003). Other alteration studies were performed in the Atlantic Ocean, which would be a preferred comparison with the Santigo data however Hart and Staudigel (1989) study of the DSDP/ODP Sites 417/418 in 118 Ma slow spreading Atlantic crust comprise a reduced element data set.

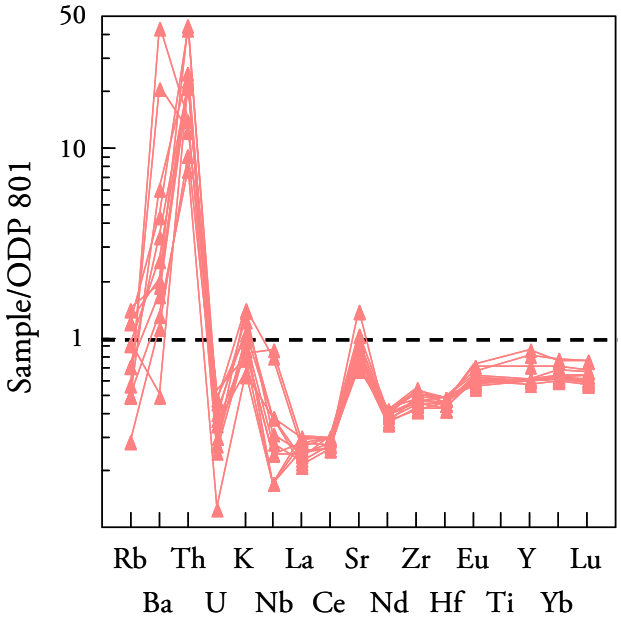

Figure 6.52 – Incompatible trace element diagram of Santiago pillow lavas normalized to the value of the basalts from ODP Site 801 (Kelley et al., 2003).

Compared with the altered oceanic crust reference material (ODP Site 801), Santiago pillow lavas show:

- similar values of Rb, K and Sr;
- higher values for Ba and Th;
- U displays a significant depletion.

6.3.1.6. Fenitization - effects on major and trace elements

The effects of fenitization on Santiago pillow lava suite is most readily identified by the occurrence of a specific mineral paragenesis that is rich in alkalis and not common in MORB (Na–pyroxene, Na-amphibole and phlogopite) as well albite and carbonates. At the geochemical level it is evident the enrichment in Na_2O (3.0 to 3.8 wt. %), K_2O (0.41 to 0.91 wt. %) and CaO (12.8 to 15.6 wt. %) as compared to MORB values (2.8, 0.16 and 11.4 wt. %, respectively; values from Gale et al. 2013 for ALL MORB).

According to Le Bas (2008) the elements most common added during fenitization, besides alkalis, is Ba. Indeed Ba content reaches extreme values (8 to 693 ppm) at odds in the MORB value of 29.2 ppm (value from Gale et al., 2013, ALL MORB). Rubidium is another element that exhibits an extreme enrichment (4 to 20 ppm) compared with MORB values (2.88 ppm, Gale et al., 2013).

The chemical fingerprint imposed by fenitization is determined by several variables including temperature, pressure, CO_2 content, pH conditions and K/Na ratio of the fluid (Carmody, 2012). The intensity of the fenitization process is also dependent on the interaction of the fluid phase, in this case derived from the carbonatitic breccia, and the contact rock (pillow lava suite), so samples collected closer to the contact will show stronger evidences of the fenitization process.

6.3.1.7. Sr-Nd isotope analyses of MORB lavas

From the twelve samples analyzed for whole rock, six were selected for isotopic analyses, which were performed at Laboratório de Geologia Isotópica da Universidade de Aveiro, Portugal (see Appendix III.2.). In an attempt to remove the influence of sweater alteration on the Sr isotopic data (e.g., Sinton et al., 1991), the leaching method adopted by Millet et al. (2008) for Santiago MORB was also applied in this study (see Appendix II for further description). The $^{87}Sr/^{86}Sr$ and $^{143}Nd/^{144}Nd$ isotopic ratios measured for Santiago ancient pillow lavas vary from 0.702776 to 0.703121 and 0.513136 to 0.513191, respectively (Fig. 6.53). The Nd isotopic ratios are homogeneous with all the values being enclosed by a range of 0.000055. These signatures clearly show the prevalence of magmas from a source characterized by long term depletion.

For the same $^{143}Nd/^{144}Nd$, $^{87}Sr/^{86}Sr$ values exhibit a significantly higher dispersion with a range of 0.000345, despite the acid leaching. In Figure 6.53 data from Santiago MORB lavas from other authors are plotted for comparison. Millet et al. (2008) determinations are very similar and are within the range defined by samples analyzed for this study. However the data from Gerlach et al. (1988) is characterized by very high $^{87}Sr/^{86}Sr$ (up to 0.703707) which can be attributed to the lack of leaching procedure for these rocks. Indeed seawater is highly depleted in Nd but enriched in Sr (e.g., Shields and Viezer, 2000) conferring it the ability to alter significantly the Sr isotopic composition of rocks with which it interacts, without any discernible effects on $^{143}Nd/^{144}Nd$ ratios (see also Rickl et al., 2009).

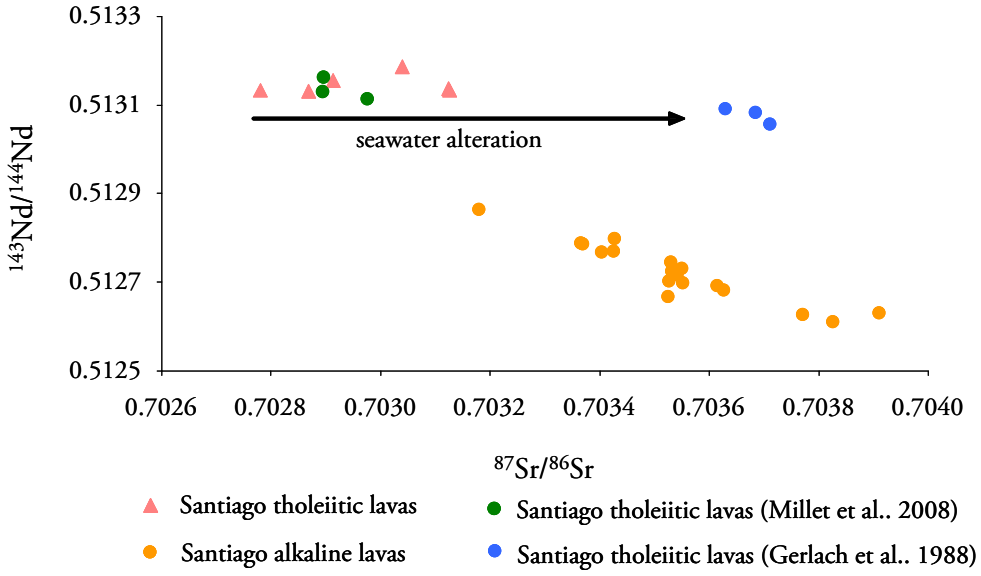

Figure 6.53 - $^{143}Nd/^{144}Nd$ (measured) vs. $^{87}Sr/^{86}Sr$ (measured) isotope correlation diagram for Santiago tholeiitic lava suite. Santiago alkaline lavas are plotted for comparison.

Interestingly, the removal of post-magmatic additions was clearly less efficient in Maio MORB samples even though the same leaching process was applied. This is clearly demonstrated by Fig. 6.54 where Maio MORB compositions are compared with those determined in this study for Santiago MORB and alkaline lavas of Santiago.

It should be remembered that the post-magmatic mineralogical assemblage of Maio MORB is distinct from that described for Santiago (see 6.2.1.4.) which render space to

consider that the leaching process used is not efficient to remove the Maio higher temperature secondary minerals.

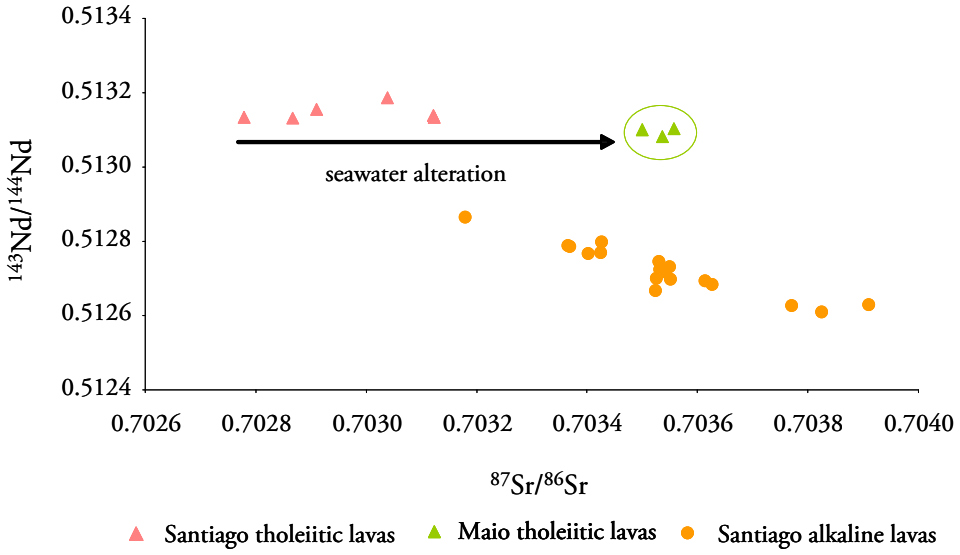

Figure 6.54 – Santiago and Maio tholeiitic suite compared in Sr-Nd isotopic space. Santiago alkaline lavas are plotted for comparison.

In order to compare the Santiago and Maio isotopic compositions, initial $^{143}Nd/^{144}Nd$ ratios assuming an age of 130 Ma, were calculated reinforcing the idea that Santiago mantle source (also the Maio one) is similar to that producing nowadays MORB. The mean values for the initial $^{143}Nd/^{144}Nd$ Santiago MORB is 0.512924 and for Maio 0.512904 are identical to those reported for MORB elsewhere (Gale et al., 2013). Calculations were not performed for $^{87}Sr/^{86}Sr$ given it is considered that the alteration processes significantly affect the LILE, Rb and Sr.

6.3.1.8. MORB comparison around the Atlantic

Santiago pillow lavas have been identified as tholeiitic MORB and, as stated earlier, the age of 130 Ma reported by Gerlach et al. (1988), is assumed to be correct (or near the correct value). Labails et al. (2010) defends that at 170 Ma it was already established the development of normal ocean crust at the Central Atlantic and so the extrusion of the pillow lavas, nowadays outcropping at Santiago Island, occurred at a stable mid ocean ridge (Gaina et al., 2013) (Fig. 6.55).

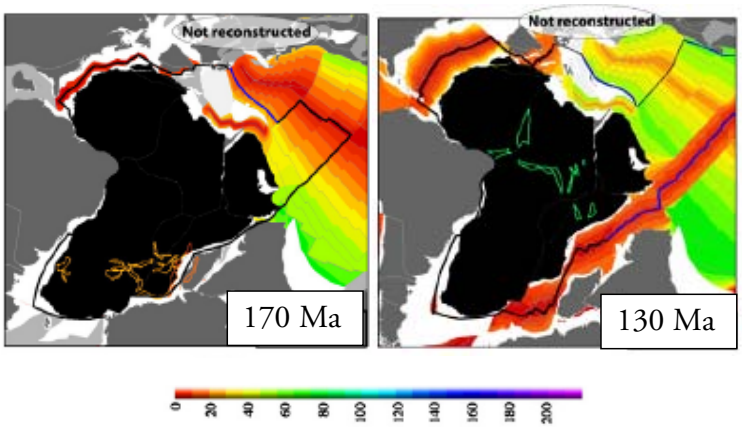

Figure 6.55 – Circum-African ocean paleo-age grids at 170 and 130 Ma, illustrating the onset of rifting at the Central Atlantic Ocean (image modified from Gaina et al., 2013).

Despite the isotopic similarity between Santiago MORB suite and N-MORB (see above) Santiago tholeiitic lavas are highly depleted in incompatible elements like the LREE, at a clearly more significant degree than the mean composition of MORB and even the mean composition of D-MORB, as defined by Gale et al. (2013) (see 6.3.1.3.). To check if this depletion is a regional and temporal event, magmas extruded around 130 Ma at the mid-Atlantic ridge were compared with the tholeiitic Santiago suite using a similar approach as Janney and Castillo (2001) (Fig. 6.56).

Due to age uncertainty of Santiago MORB a selection of six central Atlantic locations with ocean crust comprising an extrusion time span of 118 to 160 Ma, were chosen (see Fig. 6.57 for exact location in the Atlantic region):

- Leg 41-Hole 367 (157 Ma) located at the base of the continental rise in the Cape Verde Basin (Lancelot et al., 1978; Janney and Castillo, 2001);
- Leg 51/52/53 – Hole 417/418 (118 Ma) located in southwest edge of the Bermuda rise (Jahn et al.,1980; Rice et al., 1980);
- Leg 11 – Hole 100 (155 Ma) located at the Cat Gap area, east of the Bahamas (Bryan et al., 1977);

- Leg 11 – Hole 105 (158 Ma) located at the base of the continental rise, east of Cape Hatteras (Bryan et al., 1977);
- Leg 76 – Hole 534 (160 Ma) located in the Blake-Bahamas Basin (Janney and Castillo, 2001).

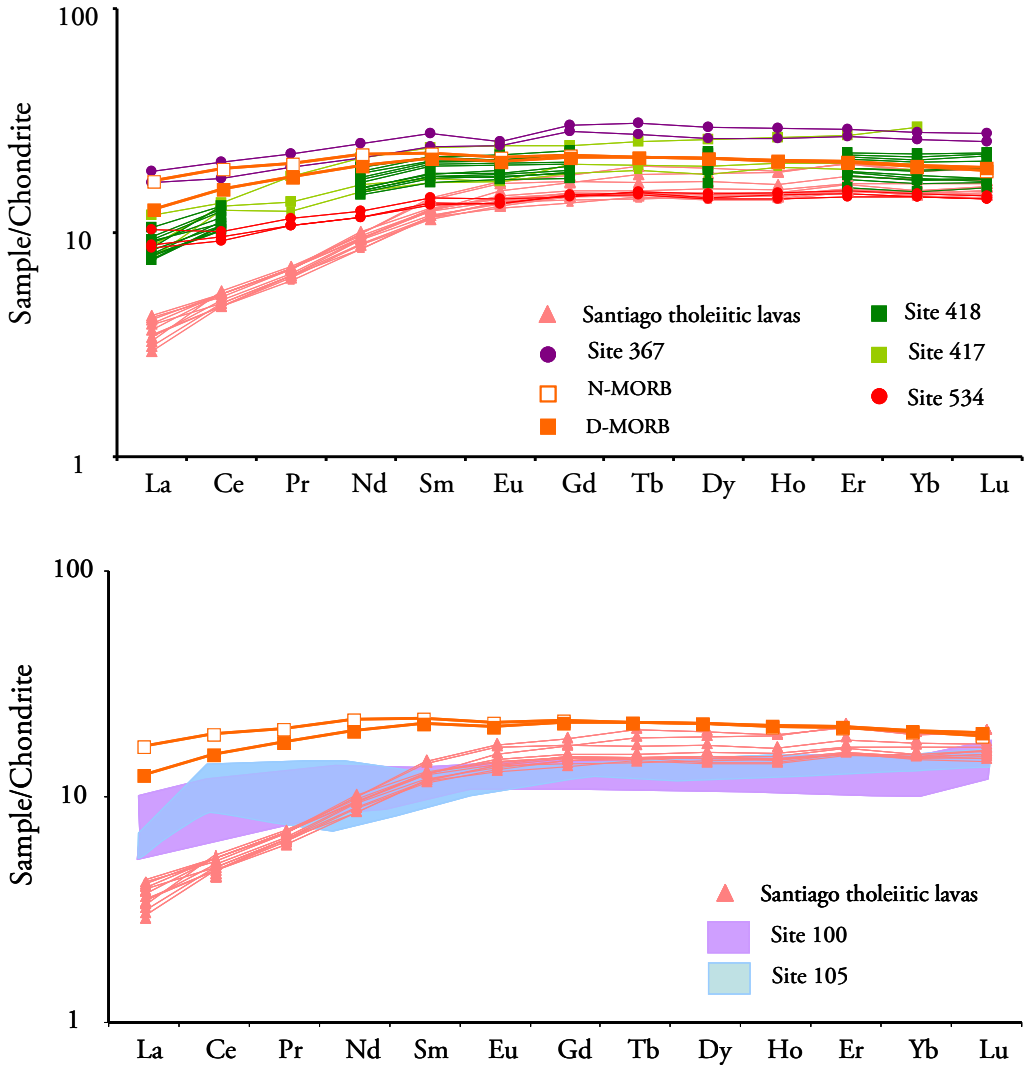

Figure 6.56 – Chondrite normalized REE patterns of Santiago pillow lavas compared with ancient Atlantic Ocean MORB data. Source data as indicated in the text. N-MORB and D-MORB values are from Gale et al. (2013).

The observation of Fig. 6.56 and 6.57 allows the conclusion that at the Central Atlantic highly depleted MORB were erupted between 160 and 118 Ma.

The eruption of highly depleted MORB at the initial stages of the Atlantic opening has been referred by Humler et al. (1999) and Brandl et al. (2013) and being considered by those

authors as a result of continental insulation which, having caused a sub-lithospheric high temperature, induced high degrees of partial melting. However, it must be noticed that among the circum Central Atlantic MORB mentioned above, the Santiago occurrences are the most depleted ones. This is true even when Santiago compositions (130 Ma) are compared with the older (157 Ma) neighbouring floor basalts erupted at the site 367. Interestingly a similar situation is also evident at the North American conjugate margin (cf sites 534 vs. 417/418; Fig. 6.56; Table 6.2).

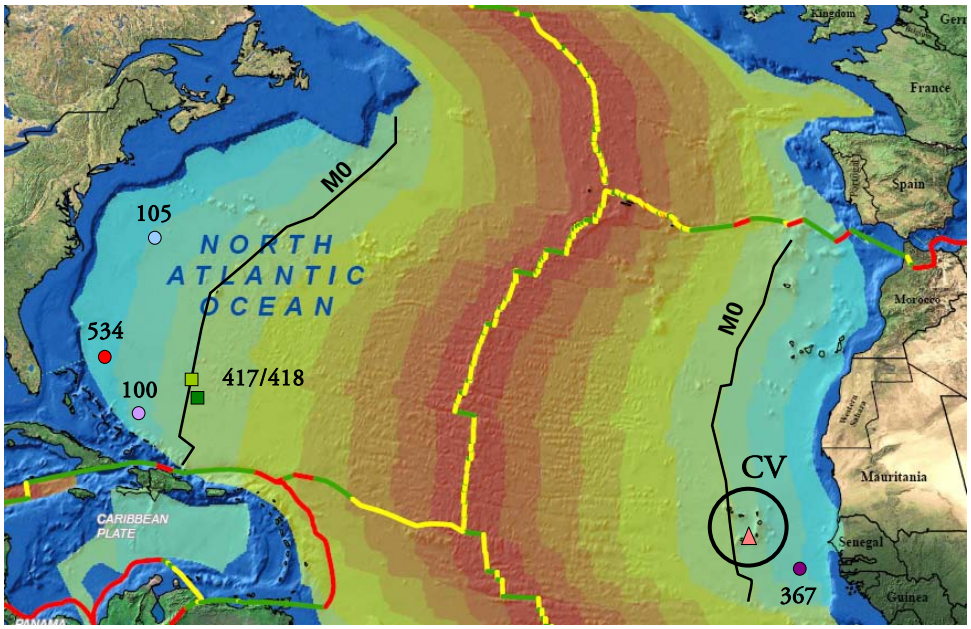

Figure 6.57 - Map of the Central Atlantic Ocean with the location of the samples projected in Figure 6.49, with the corresponding symbols (image from Müller et al., 2008).

Table 6.2 – Incompatible trace element ratios for Santiago tholeiitic suite and sites from Figure 6.50.

	Santiago MORB	Site 367	Site 417	Site 534	D-MORB (Gale et al. 2013)
Nb/Zr	0.023±0.011	0.06±0.0005	0.024±0.02	0.06±0.03	0.026
Nb/Hf	0.87±0.46	2.08±0.09	0.84±0.05	2.19±0.05	1.039

Such apparent tendency for the referred time-dependent increasing depletion could be eventually explained as originating from buoyant refractory mantle domains generated during the high degree melting events occurred at the initial stages of the Atlantic opening. However

we emphasize that the coeval MORB lavas cropping out at Maio (25 km East of Santiago) are clearly less depleted than those from Santiago pointing out for the existence at this region, some 130 ma ago, of a heterogeneous upper mantle.

6.3.1.9. High degree fractional melting event as cause for Santiago MORB singularity

As described in the previous sections, Santiago pillow lavas are characterized by a strong depletion in LREE and other incompatible elements which confer them a distinct place among MORB (see Figure 6.44 for comparison with new MORB classification data from Gale et al., 2013).

The observed distinction can be caused by intrinsic difference in the source (deep source heterogeneities) or by shallow level processes such as mantle source paragenesis/depth of segregation , crystal fractionation events, degree of partial melting and locally depleted upper mantle source.

Ni content as long been considered a criterion to use when evaluating the primordial character of magmas given that Ni is a highly compatible element for olivine, one of the first minerals to crystallize from basaltic magmas. The Ni content of Santiago MORB varies from 92 to 101 ppm very similar to the mean value ascribed by Gale et al. (2013) for ALL-MORB (92 ppm), suggesting that both experienced the same degree of evolution, even tough they exhibit distinct concentration in LREE.

In order to evaluate if Santiago tholeiitic suite has a distinct source from the common MORB, $^{143}Nd/^{144}Nd$ data is used, since isotopic ratios are not fractionated during partial melting or fractional crystallization processes. Given that the studied samples are ancient oceanic crust lavas, $^{87}Sr/^{86}Sr$ data show some variation as observed in Figure 6.48, attributed to seawater alteration.

When comparing the data from Santiago MORB and other ancient Atlantic Ocean MORB with the ALL MORB value and an average of Atlantic MORB data, it is evident that there is a similarity between the values (Figure 6.58). The $^{134}Nd/^{144}Nd$ ratio varies from 0.512995 to 0.51319 within the ancient Atlantic MORB's whereas the ALL MORB and the Atlantic MORB compilation values are 0.513074 and 0.513077, respectively (values from Gale et al., 2013 and Class and Lehnert, 2012, respectively). According with this data it is licit to

assume that these magmas were extracted from a very similar source and so the observed difference in trace element data cannot be assigned to source time-integrated heterogeneities.

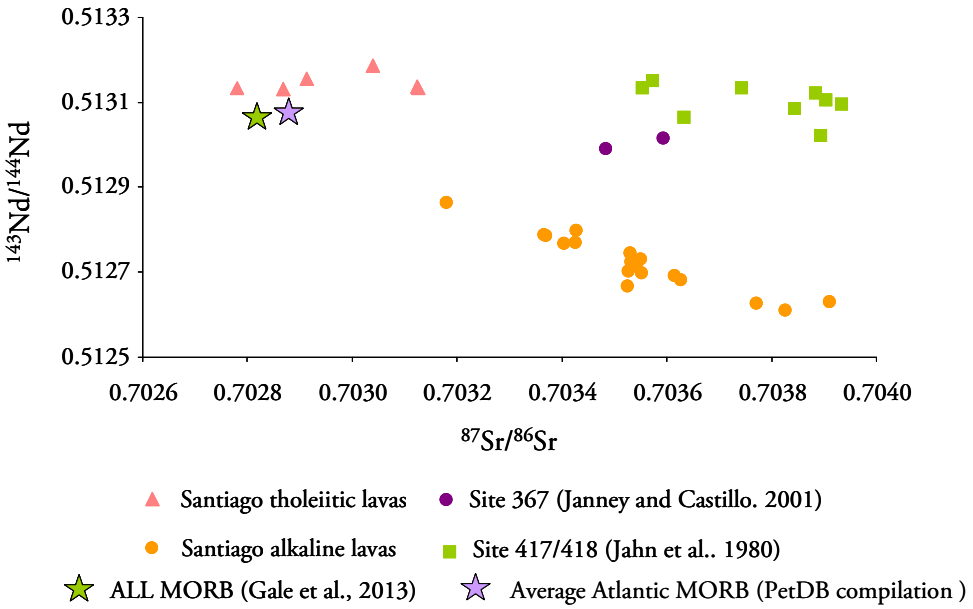

Figure 6.58 – Comparison between Santiago MORB and ancient Atlantic Ocean MORB data with average Atlantic MORB and ALL MORB isotopic data. PetDB compilation is from Class and Lehnert (2012).

Johnson et al. (1990) suggests that fractional melting is the most likely melting model to occur at ocean ridges and so be responsible for the severe depletion in highly incompatible elements. In contrast with equilibrium batch melting the melt leaves the system as soon as it is formed, so the bulk composition of the residual solid changes constantly as opposed as remaining constant (Rollinson, 2003).

However as pointed out by Niu (1997), since there is the necessity of a minimum level of melt porosity in the melting mantle and the assumed high viscosity of very low degree melts, the segregation of the melt may not be effective, so perfect fractional melting seems improbable, thus favouring the operation of an aggregated fractional melting model, in which fractional melts accumulate and mix before extrusion. Their results are similar to the batch melting process. Modelling the melting event as aggregated fractional melting the LREE depleted pattern of Santiago pillow lavas was obtained by 10 to 12% melting of a source with DMM composition (Figure 6.59).

Workman and Hart (2005) suggest values of 6% for average MORB formation. Similar values are also reported by (6-8%) for the generation of young oceanic crust in a continental rifting setting (Red Sea formation) (Ligi et al., 2012).

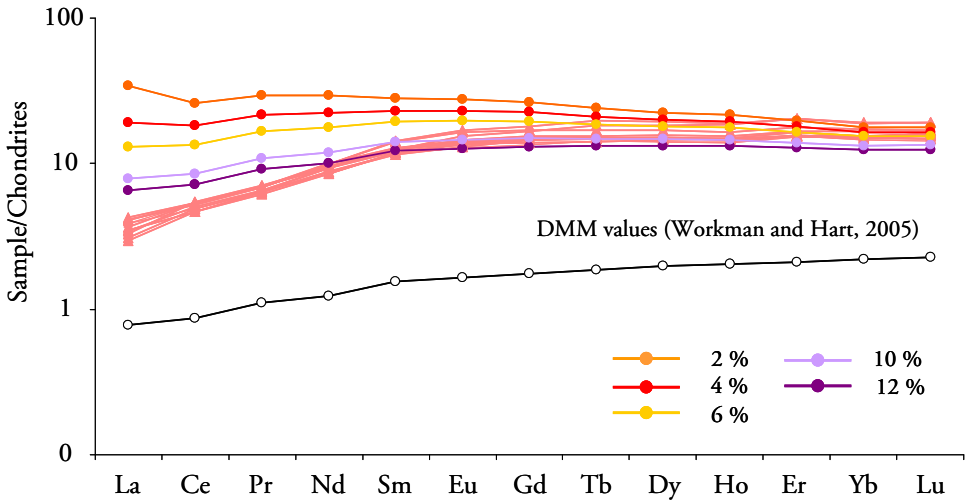

Figure 6.59 – Chondrite normalized REE patterns of Santiago pillow lavas superimposed with patterns for several degrees of aggregated fractional melting. Initial DMM composition and bulk partition coefficients are from Workman and Hart (2005).

.

The higher degree of melting obtained for Santiago MORB is probably linked with the thermal anomaly generated by continental insulation proposed by Humler et al. (1999) and Brandl et al. (2013). This anomaly translated in an upper mantle temperature of up to 150ºC higher than the present day value, which persisted for 60-90 Ma.

6.3.2. Gabbroic xenoliths

As reported earlier only four samples were analyzed for whole-rock major and trace element compositions (see Appendix III.1.4.). From this set of samples, two are silica-undersaturated (ST-164 and ST-167; normative nepheline and leucite) and the other two are silica-saturated (ST-168 and ST-169; normative hypersthene). In accordance SiO_2 and K_2O concentrations are lower in the silica-undersaturated samples in comparison with the silica-saturated. The Al_2O_3 content and LOI are also higher in these samples. The MgO content range from 3.7 to 9.7 wt. % and Mg# varies from 59 to 80.

The gabbroic xenoliths are characterized by low abundance of incompatible elements such as P_2O_5 (<0.17 wt. %), TiO_2 (<0.2 wt. %), Zr (<45 ppm) and Nb (<10.1 ppm). TiO_2/Al_2O_3 ratios are very low (<0.01 wt. %), lower than MORB values but in accordance with the values reported for abyssal gabbros (Figure 6.60).

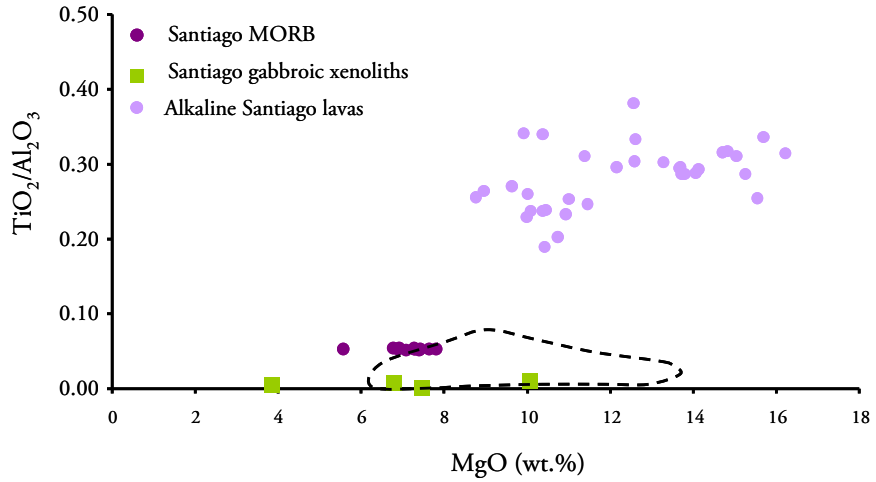

Figure 6.60 – Whole rock TiO_2/Al_2O_3-MgO relations in gabbroic Santiago xenoliths compared with Santiago MORB and abyssal gabbros (data from Seifert et al., 1997). Santiago alkaline lavas are also projected for comparison.

Santiago xenoliths show similarities with Santiago MORB-like pillow lavas regarding chondrite-normalized REE-patterns (Fig. 6.61), even though their concentration in REE is significantly lower. Positive Eu-anomalies are present in all the analyzed gabbroic xenoliths, indicating the accumulation of plagioclase. However, a distinction emerges when comparing the LREE concentration. Samples ST-167 and ST-168 are characterized by enrichment in LREE compared to the other samples (ST-164 and ST-169). The enrichment in La even exceeds the concentration observed in Santiago MORB lavas.

When plotted separately this difference is even more evident, with the enriched group (Group A, samples ST-168 and ST-169) exhibiting a mildly convex-upward REE pattern, while the depleted group (Group B, samples ST-164 and ST-169) is characterized by a mildly concave-upward to linear patterns (see section 6.3.2.1 for interpretation) (Fig. 6.62). So Group A shows enrichment in LREE relative to HREE, being the opposite in Group B.

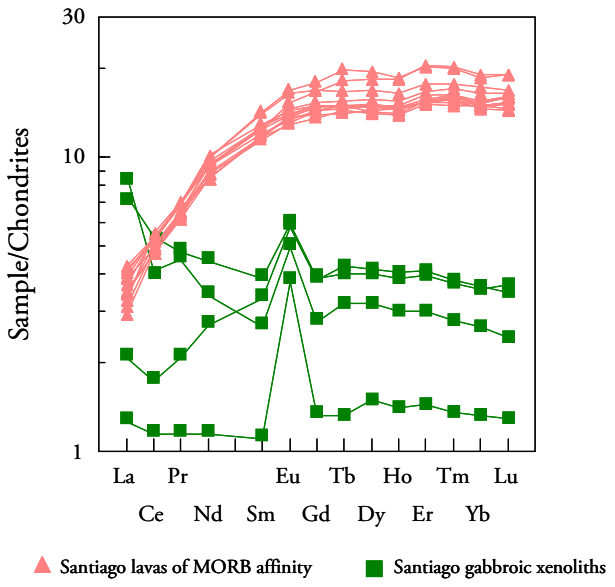

Figure 6.61 – Chondrite normalized REE patterns for Santiago lavas of MORB affinity and gabbroic xenoliths (Chondritic value from Palme and O'Neill, 2003).

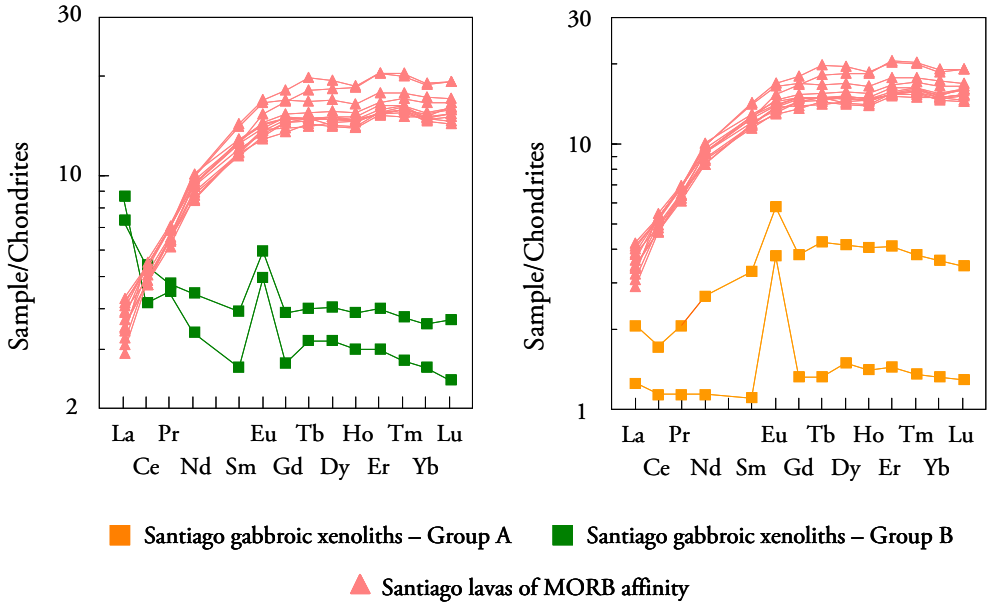

Figure 6.62 – Chondrite normalized REE patterns for Santiago gabbroic xenoliths Group A and B. Normalized values from Palme and O'Neill (2003).

D-MORB normalized incompatible trace element patterns of Santiago gabbroic xenoliths show positive Sr and Ba anomalies and negative Th anomalies. Ba and Sr peaks can be attributed to the accumulation of plagioclase. Compared with Santiago tholeiitic lava suite the gabbroic xenoliths are more depleted, except in Nb and La (Fig. 6.63).

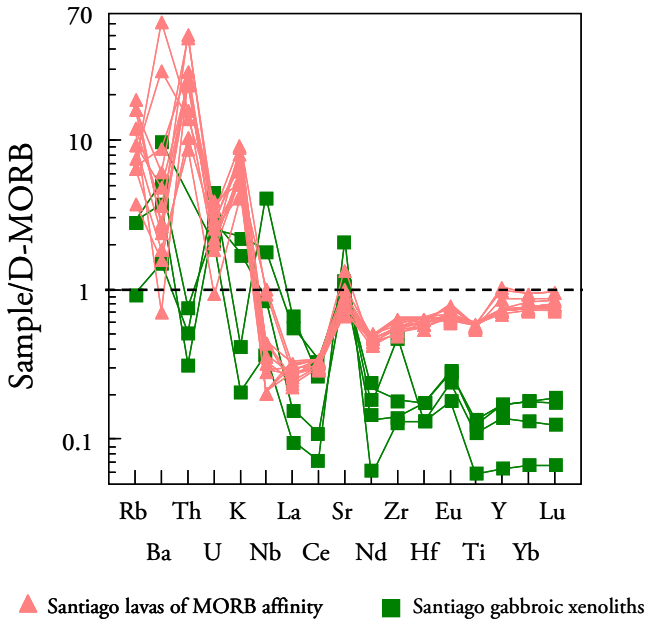

Figure 6.63 – D-MORB normalized incompatible element patterns for Santiago gabbroic xenoliths (D-MORB value from Gale et al., 2013). Santiago lavas of MORB affinity are plotted for comparison.

Group A and B are still clearly individualized in the incompatible trace element diagram (Figure 6.64). Group A shows enrichments in Nb, La, Ce, Nd and Zr compared to Group B.

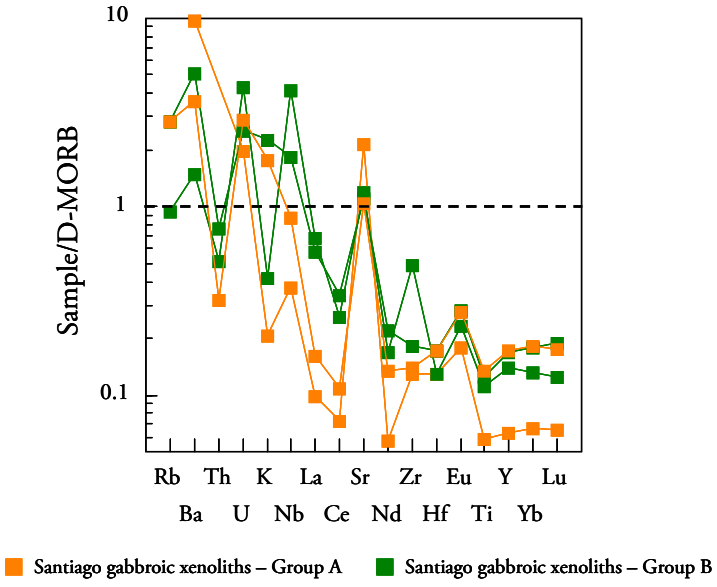

Figure 6.64 – D-MORB normalized incompatible element patterns for Santiago gabbroic xenoliths Group A and B. Normalization values are from Gale et al. (2013)

6.3.2.1. Interaction between alkaline lavas and gabbroic xenoliths

Gabbroic xenoliths of Santiago Island are rather homogenous in textures and mineralogy. Their low concentration in incompatible trace elements and associated Sr and Eu-positive anomalies indicates that they represent cumulates dominated by plagioclase (e.g., Neumann et al., 2000).

Their geochemical characteristics suggest that the gabbroic xenoliths of Santiago originated as plagioclase-rich MORB cumulates. However, the two groups identified based on differences in specific incompatible elements, suggesting that an enrichment process has occurred after their initial formation. When plotted against gabbroic xenoliths of the Canary Islands with identical characteristics (Lanzarote metagabbros and La Palma gabbros) it is evident a similarity with the two group identified (Fig. 6.65).

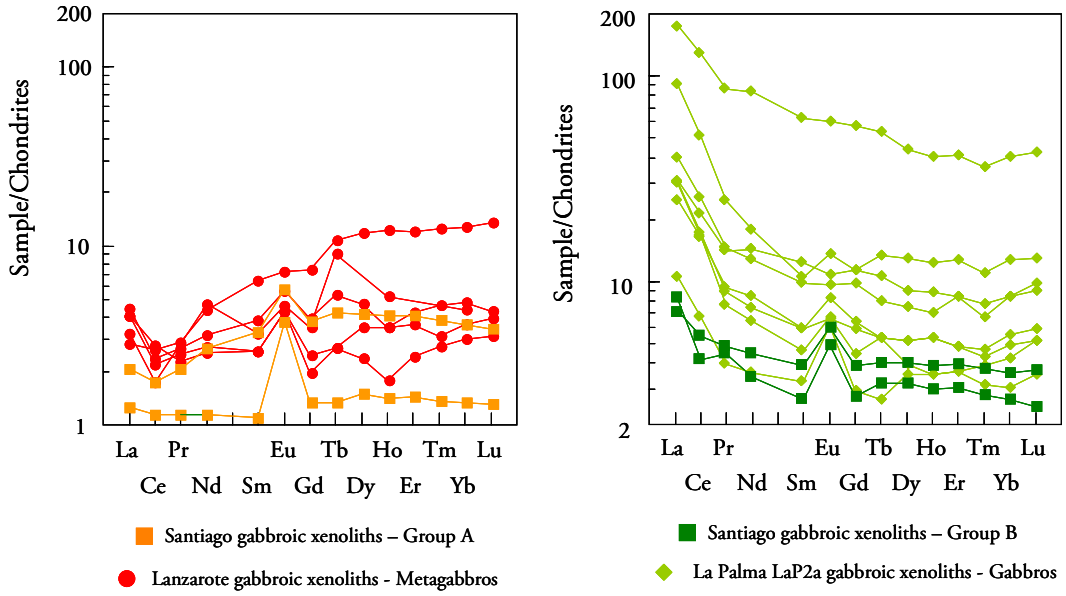

Figure 6.65 – Chondrite normalized REE patterns for Santiago gabbroic xenoliths Group A and Group B compared with Canary Island gabbroic xenoliths (Lanzarote and La Palma; data from Neumann et al., 2000). Normalization values from Palme and O'Neill (2003).

Lanzarote metagabbros also exhibit convex-upward REE patterns and affinities with N-MORB lavas while La Palma gabbros are more enriched in REE with a concave-upward pattern and show a strong enrichment in incompatible elements. La Palma gabbros are also characterized by the occurrence of hornblende and kaersutite rimming clinopyroxene crystals as well as fine-grained aggregates of recrystallized clinopyroxene, orthopyroxene and olivine. This

mineralogic and petrographic evidence suggest the action of metasomatic processes (Neumann et al., 2000).

It seems reasonable to make the analogy between the Lanzarote metagabbros with Group A Santiago gabbroic xenoliths and La Palma gabbros with Group B Santiago gabbroic xenoliths due to geochemical similarity. Even though a hydrous mineralogy and recrystallization evidence were not observed in the collected xenoliths, Mendes and Silva (2001) described similar features in gabbroic xenoliths from Santiago and Sal Islands. However in one sample (ST-167), of the enriched group, several clinopyroxenes, similar to those present in alkaline Santiago lavas, were identified and analyzed (see Figure 6.33). These analyses are mostly of crystals rims and recrystallized grains.

The enrichment observed in Group B gabbroic xenoliths could be due to metasomatic events resulting from ascending alkaline magmas that interact with the pre-existing N-MORB crust (Neumann et al., 2000; Neumann et al., 2005). The infiltration process would involve chemical exchanges between the infiltrating melt and wall-rock minerals, causing not only cryptic (enrichment in some incompatible elements) but also modal metasomatism (occurrence of diopsidic pyroxenes).

CHAPTER 7

CONCLUSIONS AND FUTURE RESEARCH

Ribeira do Charco (Northwestern Santiago Island – Cape Verde)
Contact between Complexo Antigo and Pico da Antónia Formation lavas

7.1. Introduction

In the following section, the main conclusions of this dissertation will be summarized. However, the full comprehension of the ideas here resumed must not exclude the reading of the previous chapters. Indeed in these, and more precisely into the indicated subchapters, the fundaments and argumentation supporting the conclusions are presented, as well as the pertinent bibliographic references.

7.1.1. Santiago Island Geology

- In Santiago Island the most significant unit concerning spatial coverage, volume of emitted materials and volcanic time span is the Pico da Antónia Formation. Within this unit it is possible to identify several episodes distinguished by the type of volcanism and associated extruded and/or intruded material. The oldest unit corresponds to thick piles of subareal lava flows and submarine lavas, which makes up the most part of the exposed Santiago Island. Former studies on Santiago's stratigraphy considered the submarine events as coeval peripheral manifestations of the subareal ones in the Pico da Antónia Formation. However the present study demonstrated that there are significant geochemical differences between the two units implying their non-comagmatic origin and, probably, non coeval character. Field work carried out in several areas corroborated the distinction between those two units by the demonstration of the existence of paleosoils, conglomeratic and calcarenite levels and erosional surfaces, all attesting the existence of significant temporal hiatus between them (see 3.2.4.).

7.1.2. Geochemistry of alkaline lavas

7.1.2.1 – Major and trace element geochemistry

- The studied Santiago lavas are classified as ultrabasic to basic ($38 < SiO_2 < 47$ wt. %) alkaline rocks. Using normative minerals it is possible to further discriminate between

melanephelinites (52%) and basanites (46%). The remaining 2% correspond to less common lithotypes: melilitites, melilite nephelinites and nephelinites (see 4.2.2.)

- CIPW norm data corroborates the abundance of normative olivine and nepheline in the lava samples. Significant differences in Na_2O/K_2O and CIPW normative olivine/diopside ratios between lavas from different formations suggest time-dependent variations in the major element compositions of Santiago magmas (see 4.2.2).

- The Mg# value of the parental melt from which the most forsteritic Santiago olivines crystallized varies between 66 and 71. Also, by analyzing the Fo content of olivine in Santiago lherzolite xenoliths, which can be considered as a Santiago mantle source proxy, it can be seen that they range between 87 and 92, suggesting equilibration with melts with Mg# of 67 to 77 at mantle conditions. So the "boundary line" for primary lavas in Santiago lavas is set at Mg# 68.5. In Santiago these primary magmas are also characterized by MgO >12 wt. %, Ni > 250 ppm and Cr > 480 ppm (see 4.2.2.1.).

- The modelling of petrogenetic processes implies the use of a larger set of samples, and when it was necessary, the primary criteria was broaden in order to include all the samples with Mg# down to 59. These primitive samples are also characterized by MgO > 8.5 wt. %, Ni > 130 ppm and Cr > 250 ppm. This implies the fractionation of only ≈ 7% of the initial liquid considering the fractional crystallization model and 0.3 as the partition coefficient between melt and olivine (see 4.2.2.1.).

- Santiago lavas have MgO contents varying from 3.8 to 16 wt. %, generally showing negative correlation with SiO_2, alkalis and Al_2O_3. Although the major element composition of Santiago formations essentially overlaps each other, there are small differences between them. The youngest formation (Monte das Vacas) shows the least variability, being characterized by the highest SiO_2 and the lowest MgO content, and distinctly higher FeO_t, Na_2O and low CaO, suggesting influence of crystal fractionation processes with consequent chemical differentiation (see 4.2.3.).

o The TiO_2 content of Cape Verde basic/ultrabasic lavas is high compared with many other OIB. The high TiO_2 can be related to the non exclusively peridotite mantle source from which an additional Ti-enriched component is necessary (see 4.2.3.).

o Santiago primary lavas have steep trends in chondrite-normalized REE, attesting the strong enrichment in LREE relative to MREE and HREE. The depletion in the heaviest REE (Yb and Lu) suggesting that melting events took place within the garnet stability field (see 4.2.4.).

o Primitive mantle normalized incompatible element patterns show Nb and Ta enrichment relative to Rb and K and REE, suggesting the influence of HIMU component in Santiago source. A significant positive anomaly in Ba is present in all the formations as well as a small Zr and Hf negative anomalies (see 4.2.4.).

o The behaviour of K is noteworthy in that negative anomalies are very significant for almost all Assomada and Upper Pico da Antónia Formations samples and nearly absent in Lower Pico da Antónia and Flamengos Formation samples. This signature foresee the presence of a mantle mineral phase capable of retaining this element on the more recent formations, making the residual presence of potassic minerals a non-ubiquitous characteristic in Santiago mantle source (see 4.2.4.).

o Even though there is a general consensus that the mean values of Nb/U and Ce/Pb are similar in MORB and OIB, the Cape Verde islands seem to stand out at of those standards. Indeed, Santiago magmas are characterized by high Nb/U and Ce/Pb ratios, relative to the most common MORB and OIB data (see 4.2.4.1.).

o HFSE pairs Nb-Ta and Zr-Hf are considered to not fractionate from each other, due to specific element chemical features, maintaining a constant ratio in oceanic basalts. Santiago lavas show significant variations in those element ratios. Setting aside fractional crystallization, partial melting in the presence of specific accessory residual phases and

metasomatic events as the cause of HFSE fractionation, the data seems to suggest the presence of a mantle lithology susceptible of lowering those ratios (i.e., garnet pyroxenite/pyroxenite/eclogite) (see 4.2.4.2.).

7.1.2.2 – Sr-Nd-Hf-Pb isotope chemistry

- The $^{87}Sr/^{86}Sr$ and $^{143}Nd/^{144}Nd$ ratios of Santiago magmas are consistent with those previously reported for the southern Cape Verde islands. The Sr isotope ratios are negatively correlated with $^{143}Nd/^{144}Nd$ and most of the samples plot in the depleted quadrant of the Sr-Nd diagrams (see 4.3.1.).

- In an Hf-Nd isotope diagram, Santiago lavas display a linear array with a positive correlation and the majority of samples projecting in the depleted quadrant. The variation observed in Santiago Island Hf isotopic data is rather limited corresponding to $\approx$ 5 units of ε_{Hf} (see 4.3.2.).

- Santiago samples plot near the ε_{Hf}-ε_{Nd} mantle array but with a distinctly shallower slope, indicating a time-integrated decoupling of Lu/Hf from Sm/Nd relative to the compositions lying on the mantle array (see 4.3.2.).

- Santiago lavas show a broad range in $^{206}Pb/^{204}Pb$ and $^{208}Pb/^{204}Pb$, with a smaller variation in $^{207}Pb/^{204}Pb$ ratios. The majority of the samples plot above the NHRL diagrams as typical for the southern Cape Verde Islands. The $^{206}Pb/^{204}Pb$ ratios are clearly higher than those assigned to DMM, EM 1 and EM 2 mantle endmembers and suggest derivation from a mantle source with a high time-integrated U/Pb ratio (see 4.3.3.).

- Three Santiago samples are characterized by distinctly higher $^{206}Pb/^{204}Pb$, $^{207}Pb/^{204}Pb$ and $^{208}Pb/^{204}Pb$ values displaying a horizontal trend that crosses the NHRL. The radiogenic group stands out, making them the most radiogenic samples described, so far, for Santiago Island. The higher Pb isotopic data of this sub-group is not justified by

sample alteration or contamination, and is also associated with other geochemical particularities indicating that their characteristics are related with mantle source heterogeneities or other enrichments processes (4.3.3.1.).

7.1.2.3 – Diversification of Santiago magmas

Shallow-level assimilation

- Even though the evidence for possible shallow-level assimilation as been identified in other islands of the Cape Verde archipelago, the incorporation of old oceanic crust and young sediments have been ruled out in Santiago lavas, taking into consideration Sr and Pb isotopic data. The assimilation of magmatic material of the volcanic edifice cannot be excluded due to the similarity in composition, concerning major, trace element and isotopic characteristics, however if in fact occurred it did not play a major role as a cause from the chemical variability observed in Santiago Island (see 4.4.1.).

Crystal fractionation processes

- Even though the majority of the studied Santiago lavas variability can be explained by partial melting processes there is still some deviation that can be related with crystal fractionation events (see 4.4.2.).

- From the studied samples, Monte das Vacas and Assomada are the formations where the relatively evolved rocks (Ni< 150 ppm) are more abundant. For these formations the analysis of trace elements show that evolution process was characterized by initial phase dominated by olivine plus pyroxene removal followed by one where plagioclase fractionation counteract the effect of pyroxene crystallization (see 4.4.2.).

- The significant role of clinopyroxene fractionation is also endorsed by lower than chondritic CaO/Al_2O_3 ratio for most of the lavas from Monte das Vacas and Assomada formations as well as the compatible behaviour portrayed by V and Sc both of which have high partition coefficients for this mineral (see 4.4.2.).

Source heterogeneities

Lithologic heterogeneity in the mantle

- The distinctive high CaO concentration associated with the undersaturated character of Santiago lavas stands as a strong indicator of a carbonated mantle source. Santiago primary magmas have a range of 11 to 16 wt. % CaO associated with less than 44 wt. % of SiO_2 plotting similar to those obtained from carbonated peridotite melt experiments and away from partial melts derived from volatile-free peridotite which are characterized by relative SiO_2 enrichment and lower amounts of CaO (see 4.4.3.1.1.).

- Santiago primary magmas are characterized by high FeO_t and TiO_2 contents which are higher than those portrayed by magmas formed from a carbonated peridotitic source. One of the processes susceptible of increasing the Ti content of the Santiago magma source is the mixture of peridotite mantle melts with Ti-enriched melts derived from carbonated silica-deficient garnet pyroxenite (see 4.4.3.1.2.).

- Zn/Fe ratios are strongly fractionated when clinopyroxene and garnet-rich lithologies are involved, allowing its use to detect lithologic components that diverge from normal peridotite (dominated by an olivine and ortopyroxene assemblage). Santiago magmas have a Zn/Fe ratio of 12.23 what seems to suggest melts derived from sources enriched in clinopyroxene and garnet (see 4.4.3.1.2.).

- Santiago primitive lavas display a negative correlation between $^{176}Hf/^{177}Hf$ and Gd/Yb ratios, suggesting that the highest content of residual garnet (higher Gd/Yb ratios) is associated with the least radiogenic Hf signature, indicating the influence of ancient garnet-pyroxenite domains in Santiago mantle source more specifically within the plume (see 4.4.3.1.2.).

- The high FeOt and TiO_2 content that characterize primary Santiago lavas was ascribed to the presence of carbonated silica deficient garnet pyroxenite, which is further corroborated by their negative correlation with $^{176}Hf/^{177}Hf$. This poses another evidence

for the presence of these veins/fragments within the plume since there is a correlation between major and incompatible trace element ratios with radiogenic isotopes ascribing an ancient signature (see 4.4.3.1.2.).

Mantle source mineralogy: a qualitative approach

- The strong HREE depletion relative to LREE and relatively high $(La/Yb)_{cn}$ values observed in Santiago samples with primitive characteristics, can be explained by the preferred incorporation of HREE in garnet, making it a plausible residual phase in Santiago mantle source. By modelling non-modal batch partial melting of an enriched source and variable mantle paragenesis, using Gd/Yb ratio against La, it is inferred that the amount of residual garnet can ranges from 6 to 14% (see 4.4.3.2.).

- Through a simple modal batch partial melting modelling (in La vs. La/K diagram) it becomes evident that samples from Flamengos and Lower Pico da Antónia (and some of Assomada) Formations were derived from a mantle source with none or only minor potassic residual mineralogy, while the trend depicted by the Upper Pico da Antónia data clearly indicates that during melting $D_K \gg D_{La}$ thus pointing to the existence of a K-rich phase as a residue (see 4.4.3.2.).

- To distinguish between the two most probable residual potassic minerals, amphibole and phlogopite, Rb/K ratios were used for those formations previously identified as having a K-bearing phase, endorsing amphibole as the most probable candidate to K retention in the source. However due to the apparent compatible behaviour of Ba in some samples the additional presence of residual phlogopite cannot be excluded completely (see 4.4.3.2.).

Trace element inverse modelling: a quantitative approach

- By using the inverse modelling approach proposed by Class and Goldstein (1994), a specific D for each paragenesis can be assessed from the variation on the degree of

enrichment as function of variation on the degree of partial melting enabling an indirect approximation to the relative proportion of residual minerals (see 4.3.3.3.).

o For the success of trace element inverse modelling is crucial the use of an appropriate data set of partition coefficients. Two sets of mineral-melt partition coefficients were used due to the difficulty encountered in modelling all the formations using the same set. The difficulties may arise from the fact that Santiago mantle source was variably affected by carbonate-rich metasomatism. The modelling for Assomada and Upper Pico da Antónia formations, those with the strongest evidences for carbonatitic metasomatism, was not successful when using partition coefficients determined in the presence of silicate melts (see 4.3.3.3.).

o The analysis of the enrichment patterns of Santiago formations shows an evident difference between them and accordingly, variable mantle source paragenesis from which they formed. However the modelled mantle source is always a garnet lherzolite, with variable proportion of olivine and clinopyroxene, with strong evidences for hydrous potassic mineralogy for the most recent formations. The methodology used also allowed the identification of probable subordinate minerals, not identified so far (e.g. ilmenite) (see 4.3.3.3.).

Mantle metasomatism

Evidences from Santiago peridotitic xenoliths and alkaline lavas

o Lithospheric xenoliths carried by Santiago lavas show evidence of modal metasomatism. Noticeable mineralogical features include the occurrence of late kaersutite, phlogopite and calcite associated with alkali-rich glasses and the development of secondary olivine + clinopyroxene + spinel assemblages. By comparing glass compositions reported by Mendes (1995) for Santiago lherzolites, with other occurrences of glass within peridotite xenoliths allow to discard hypothesis such as reaction between the host lava and orthopyroxene, metasomatic events induced by alkaline melts (melanephelinite) in the lithosphere and transport-related breakdown of a metasomatic

assemblage. This conclusion seems to suggest that the evidences portrayed by Santiago lherzolite xenoliths are associated with carbonate-rich metasomatic events (see 4.4.4.1.).

- For Santiago lavas it can envisaged a model involving the contamination of plume magmas by melts generated in low-solidus metasomatized lithosphere domains and leaving those, already identified, hydrous minerals as melting residues (see 4.4.4.3.).

- Significant differences in partition coefficient values experimentally determined in the presence of carbonatite or silicate melts, allows the determination of the nature of the metasomatic agent through the analysis of the chemical signal imprint on the metasomatized mantle domains (see 4.4.4.3.).

- Experimental studies indicate that carbonatite melts will have marked depletions in Al, Ga, HREE, Ti and Zr relative to Nb, LREE and alkali/alkali earth elements. The primitive Santiago lavas, characterized by the more pronounced negative K anomalies, display Ti/Eu ratios substantially below primitive mantle values (down to 3300), correlating negatively with Ca/Sc. The lavas are also characterized by high Ca/Sc and low Al/Ca ratios. All these evidences reflect the melting of a carbonatitic metasomatized source (see 4.4.4.3.).

- Notwithstanding all the above mention evidences, it is important to acknowledge that several studies suggest that near-solidus melts from a carbonated peridotite mantle may not be identical to erupted carbonatites and so several geochemical features considered to be sensitive indicators of carbonatite metasomatism may be inappropriate (see 4.4.4.3.).

High radiogenic Pb isotopic signatures as evidence for metasomatism

- There is a sub-group of Santiago samples that exhibit high $^{206}Pb/^{204}Pb$, $^{207}Pb/^{204}Pb$ and $^{208}Pb/^{204}Pb$ ratios, being distinct from all the other Santiago samples. This marked difference in Pb isotopic signature is concomitant with lower $^{87}Sr/^{86}Sr$, higher

$^{143}Nd/^{144}Nd$ ratios and higher enrichment in incompatible elements. Also, trace element ratios that are considered indicators of carbonatitic metasomatic processes, such as high CaO/Al_2O_3, Ce/Pb and low Ti/Eu are correlated with those enriched Pb signatures (see 4.4.4.3.2.).

- Considering the available Cape Verde carbonatite Pb isotope data it is possible to rule out a carbonatitic metasomatic agent with the same Pb isotopic signature as the outcropping carbonatites in the Cape Verde islands, since the $^{208}Pb/^{204}Pb$ ratios are not sufficiently high to account for the highest values in Santiago lavas (see 4.4.4.3.2.).

- A comparison of clinopyroxene separates data from mantle xenoliths sampled from Cenozoic intraplate volcanism from Spain and Northern Africa, with Santiago samples was made due to their enriched compositions and particular isotopic characteristics, specifically high Pb isotope ratios. Santiago xenoliths portray similar textural and geochemical characteristics. The geochemical characteristics of those xenoliths were interpreted as the result of re-equilibration with a percolating metasomatic agent with HIMU affinity. Even though a consensus about the type of metasomatic agent and its origin is not reached, the metasomatic agent is thought to originate from sublithospheric domains subsequently infiltrating and modifying the shallow lithospheric mantle (see 4.4.4.3.2.).

- Recent Hf and Nd isotope data from clinopyroxene separates from metasomatized peridotitic xenoliths of Sal Island show very similar values to the ones characterizing clinopyroxenes from Spain and Morocco xenoliths which are also characterized by high Pb isotopic ratios. This evidence also seems to suggest that there is a similarity in the nature/genesis of the metasomatic agent affecting the lithospheric mantle of these distinct areas (see 4.4.4.3.2.).

On the origin of the carbonatitic metasomatic agent

- The influence of a carbonated source in the genesis of Santiago silicate magmas and associated metasomatic agent is unquestionable. Even though the metasomatic agent is identified as being carbonatitic, geochemical evidences attests to the distinction between outcropping carbonatites and the enriched melt responsible for the modal and cryptic modifications imposed on the mantle (see 4.4.4.4.).

- The association of outcropping carbonatites and carbonate-rich/carbonatitic metasomatism does not seem random. The enriched melts from which the carbonatites and associated metasomatic agents (fluid/melts) were ultimately derived probably share a common source. In this perspective the observed final differences are considered as mainly due to carbonatite wall-rock reaction or shallow level processes such as crystal fractionation, melt mixing, immiscibility and cumulative processes (see 4.4.4.4.).

7.1.2.4. – Mantle components

Cape Verde archipelago isotopic dichotomy and diversity

- The earliest geochemical isotopic studies on Cape Verde showed a distinction between northern and southern islands, based on different isotopic signatures. The isotopic variability was explained by mixing of three end-members: depleted mantle (DMM), high-μ (HIMU) and enriched mantle (EM). The northern group does not show evidence for the participation of the enriched component while in the southern group it is present in all of the islands, as testified by Santiago data (see 4.5.1.).

Santiago Island: mixing between young HIMU, EM and LM

- The use of the term "HIMU" was defined to refer magmas with very radiogenic Pb isotopic signatures ($^{206}Pb/^{204}Pb>20.5$) associated with relatively low $^{87}Sr/^{86}Sr$ (<0.703), as those characterizing the Islands of St. Helena, Mangaia, Rurutu and some of the Cook-Austral archipelago. Even though Santiago lavas isotopic signature is not so extreme as those portrayed by the archetypical HIMU component, its contribution is evident from trace element characteristics such as Nb and Ta enrichment relative to LILE and LREE

with Rb/Nb, K/Nb and La/Nb ratios significantly below primitive mantle values (see 4.5.2.2.).

- The high $^{176}Hf/^{177}Hf$ for a given $^{143}Nd/^{144}Nd$, the somewhat high $^{87}Sr/^{86}Sr$ and low $^{143}Nd/^{144}Nd$ and $^{176}Hf/^{177}Hf$ ratios of Santiago magmas, as well as the occurrence of some (unaltered) samples with Ba/Nb > 10 also confirms the contribution from an enriched end-member, which has been ascribed to the EM-1 in previous studies on the southern Cape Verde islands (see 4.5.2.3).

- Even though Santiago samples plot close to the εNd-εHf mantle array they show a distinctly shallower slope, even when compared with the OIB array indicating a higher time-integrated Lu/Hf for to a given Sm/Nd, with could be due to the presence of a sedimentary mantle component. However Santiago magmas lack Nb and Ce negative anomalies and are clearly less radiogenic in Sr, in comparison to magmas influence by the presence of sediments. Therefore, it is concluded that, if the presence of sediments as a cause for the EM 1 signature cannot be ruled out completely, its role was probably subordinate (see 4.5.2.3.).

- Even though primitive Santiago lavas are indeed characterized by small positive Eu anomalies the lower continental crust seems an unsuitable explanation for the EM 1-type signatures of Santiago mantle source, given the somewhat low $(Ba/Nb)_n$ and high $(Ba/Th)_n$ values as opposed to those characterizing average lower continental crust values (see 4.5.2.3.).

- In Sr-Nd isotope space, Santiago samples display a trend that deviates from those of Pitcairn, Gough, Tristan da Cunha and, also, from the recently described Godzilla seamounts which are all considered the best representatives of the EM 1 end-member. The deviation towards lower values of $^{143}Nd/^{144}Nd$ supports a contribution from an enriched end-member with isotopic affinities such as those displayed by the Leucite Hills lamproites (see 4.5.2.3.).

- The lamproites are thought to be the result of preferential melting of a metasomatic vein assemblage (phlogopite ± richterite ± clinopyroxene ± apatite ± titanite) within the continental lithospheric mantle. Interestingly, some of Lages silicate rocks (Eastern Brazil), which belong to the continental alkaline-carbonatitic complex of the Late Cretaceous Paraná-Angola-Etendeka Province are also characterised by similar relatively unradiogenic Nd isotope signatures plotting in the same trend between the Santiago samples and the Leucite Hills lamproites, thus indirectly supporting the contribution of SCLM for magma composition in the southern Cape Verde islands and, in particular, to Santiago Island (see 4.5.2.3.).

- Santiago data favours an SCLM origin for this component in Santiago, suggesting that the contribution of continental lithosphere to the Cape Verde magmatism was variable, including its crustal and mantle portions (see 4.5.2.3.).

- During the early history of the Earth, subcontinental lithosphere was metasomatized by melts from subducted slabs along convergent margins generating high μ ($^{238}U/^{204}Pb$) and Th/Pb SCLM domains. The acceptance of such a model, constrain to the post-Archean the age of the metasomatic event triggering the genesis of the EM1 signatures now depicted by Santiago lavas (see 4.5.2.3.).

Assessing the age of the oceanic crust recycling

- Santiago samples plot in the right-hand side of the geochron with the data defining a straight line, which allows the calculation of the event which triggered the U/Pb increase responsible by the positioning relative to the geochron. The application of this methodology to Santiago data set would produce a value of about 1.3 Ga, however magmas cannot be considered cogenetic all along the volcanostratigraphic pile. The application of this methodology to the Upper Pico da Antónia formation, which represents the main eruptive event, would yield an age of about 1.52 Ga for the fractionation event (see 4.5.4.).

- It should be kept in mind that mixing processes also produce straight lines in diagrams where ratios with the same denominator are considered. Taking into account evidences for mixing involving distinct mantle components at the Santiago mantle source, it is unlikely that the linear trend can be considered a secondary isochron (see 4.5.4.).

- Another method used to infer the age of the oceanic crust recycling is the simplistic two stage-model of Stacey and Kramers. This method allows the interpretation that the fractionation (oceanic crust recycling) event occurred between 1.5 and 1.6 Ga, being the deep mantle recycled oceanic crust characterized by a μ of about 15 (see 4.5.4.).

Isotopic constraints to the relative proportions of the contributors to the Santiago magmas

- According with the interpretation of trace element and isotopic signatures Santiago mantle source can be envisaged as a mixture of three distinct end-members: recycled oceanic crust (ROC; HIMU-like), subcontinental lithospheric mantle (SCLM; EM 1-like) and lower mantle (LM) (see 4.5.5.).

- By modelling the mixture of recycled oceanic crust (ROC) with distinct recycling ages with lower mantle material (LM), it can be seen that the variability of Santiago samples can be described by a mixture of 30LM:70ROC (1.6 Ga recycling age), 10LM:90ROC (1.5 recycling age) and 10LM:90ROC (1.3 recycling age). This evidence is not surprising since testimonies of recycling events of different ages may be preserved (maintaining their individual isotopic fingerprint) in the mantle even after incorporation in a rising plume (see 4.5.5.).

- However part of this variability is probably the result of the interaction of ROC/LM plume material with shallow mantle residing SCLM megaliths. The isotopic and elemental heterogeneity that characterizes the SCLM is modelled using two lamproites groups found at Leucite Hills: madupitic and phlogopite varieties. It was modelled that

the Santiago variability can be achieved by mixing different proportion of ROC and lower mantle with up to 2% of the enriched component (see 4.5.5.).

- The genesis of subcontinental lithospheric mantle involves multiple depletion and enrichment events at different time scales, conferring to this reservoir very heterogeneous signatures, which given their non-convective character tend to be maintained or even increased, in the case of isotope signatures, through the time. For this reason it is important to acknowledge that the assumed values as well as using the Leucite Hills lamproites as proxies to the subcontinental lithospheric mantle is an approximation and as so, the calculations made should be considered semi-quantitative due to the associated uncertainties (see 4.5.5.).

7.1.3. Plume-lithosphere interaction

Specificities of the Cape Verde area

- The specificity of the Cape Verde area is partially due to its singular geodynamic context: location in the African lithospheric plate, which is associated with a slow spreading rate at the mid-Atlantic ridge, implanted in old oceanic lithosphere characterized by considerable thickness (≈ 90 km) and localized near the plate's rotation pole (see 5.2.1.).

Plume constraints

- The existence of a deep mantle plume in the Cape Verde area seems undeniable from geophysical and geochemical evidences. The plume buoyancy flux calculated for the Cape Verde is higher than the reported for other Atlantic islands.
- In Cape Verde. the hotspot swell shape parameter, implies the presence of a large conduit discharge in a slow moving plate where buoyant spreading dominates leading to a topographic rise nearly circular in shape (see 5.2.2.).

Geochemical consequences of plume-lithosphere interaction

Lithosphere

- Oceanic lithosphere thickness variation exerts a significant control on OIB geochemistry since it limits the extent and depths of melting, this phenomena is known as the lid effect. In Santiago Island this is demonstrated by the occurrence of highly SiO_2-undersaturated rocks according to experimental data are generated by very low degrees of partial melting; primitive magmas trace element ratios supporting magma genesis in equilibrium with residual garnet which ascribes magma generation at depths above 80 km; Santiago magmas were modelled by 2 to 9% degrees of partial melting.
- The identification of hydrous residual minerals (amphibole and phlogopite) imposes constraints regarding depths and temperature. Amphibole is not stable at temperatures above 1150°C, i.e., at temperatures prevailing in the asthenosphere or in mantle plumes, thus pointing to the equilibration of some of the Santiago magmas within the lithospheric mantle.
- In Santiago Island there is direct evidence for metasomatic processes. Lithospheric peridotite xenoliths collected on alkaline lavas exhibit strong evidences for the occurrence of metasomatism in the lithospheric mantle, namely the occurrence of kaersutite, phlogopite and calcite, in association with alkaline-rich glasses. The replacement of orthopyroxene by the clinopyroxene and olivine association is compatible with a carbonate-rich nature of the metasomatic agent (see 5.3.1.).

Plume

- For Santiago magmas the main plume contributors were identified as being HIMU and the lower mantle. The HIMU component was assigned to ancient recycled altered oceanic crust (≈ 1.5 Ga, ROC) (see 5.3.4).

Cape Verde magmatism: a time constrained model for the lithosphere contributions

- The magmatogenesis of the Santiago Island is described as resulting from a deep seated thermochemical mantle plume, probably rooted into the deepest levels of the mantle at some 2900 km deep. It's hypothesized that the depart of plume from its source may have occurred less than 3 Ma before it reach the lithosphere, i.e. approximately 43

to 53 Ma ago if we accept the age resetting of MORB's at 40-50 Ma as the age of the arrival of the mantle plume to the shallowest levels of the mantle (see 5.4.).

- The basic character of ancient recycled oceanic crust leads to the hypothesis that the HIMU-type signatures are "retained" in pyroxenitic domains of the ascending plume which in agreement with the evidences for the contribution of such lithologies to the Cape Verde magmas (see 5.4.).

- The more Sr radiogenic and Nd and Hf unradiogenic imply the involvement of subcontinental lithosphere (SCL). This component is not present in the plume but resides in the upper mantle as a passive heterogeneity, which would have resulted from a delaminated megalith left behind during the opening of the Central Atlantic Ocean some 200 Ma ago (see 5.4.).

- Santiago lavas have trace element characteristic requiring that ascending plume magmas equilibrated with an oceanic lithospheric mantle containing K-rich hydrous mineral assemblages. Judging by the fact that in Santiago Island the effects of metasomatism are more evident on the more recent volcanic complexes, metasomatism is considered to have occurred mainly during the initial stages of plume magmatic activity leading to the construction of the island (see 5.4.).

7.1.4. Gabbroic xenoliths and outcropping MORB

- In Santiago's northeastern tip (Angra Bay area) outcrops the oldest unit of the island. It corresponds to Mesozoic oceanic crust and sediments with an exposure of up to 180 m. Those MORB-types pillow lavas are intruded by an intra-volcanic breccia, belonging to the Ancient Complex, composed of basaltic and nephelinitic dikes that are cut by dolomitic carbonatite digitations and dikes, belonging to the partially eroded alkaline-carbonatite complex (see 6.1.).

- Also in the Angra Bay area, subangular to subrounded gabbroic xenoliths occur within the Lower Pico da Antónia pillow lavas associated with numerous peridotite xenoliths). The gabbroic xenoliths are centimetric with medium to coarse granularity (see 6.1.).

- Twelve samples of the MORB pillow lavas in Santiago Island were collected in the Angra Bay area as well as eleven gabbroic xenoliths included in alkaline pillow lavas of the Lower Pico da Antónia Formation (see 6.1.).

7.1.4.1. Petrography and mineral chemistry

MORB Lavas

- The pillow lavas are hemicrystalline to holocrystalline with intergranular/intersertal groundmass. The dominant and ubiquitous mineral phase is plagioclase occurring either as phenocrysts or microphenocrysts. Mesostasis is made of plagioclase microlites, clinopyroxene crystals, Fe-Ti oxides, sulphide grains, devitrified glass and alteration material (see 6.2.1.).

- The absence of olivine as a rock forming mineral of the lavas does not exclude its removal prior to the emplacement of the magmas. Textural evidences of the rock forming minerals are clearly indicative that the crystallization of plagioclase precedes clinopyroxene (see 6.2.1.).

- The phenocrysts are exclusively of plagioclase occurring frequently as clusters (glomeroporphiritic tendency). Almost all of the phenocrysts exhibit some sort of alteration. Plagioclase can be broadly classified as bytownites to labradorites. In most phenocrysts the core has the highest An content (up to An_{89}), attesting the dominant normal zoning, whereas phenocryts margins, microphenocryts and groundmass crystals have lower Ca contents. Oscillatory and reverse zoning are also observed (see 6.2.1.1.).

o The groundmass is glassy to microlithic containing crystallites of plagioclase which show evidence of very rapid cooling portrayed by their particular shapes: skeletal (hopper like), hollow microlites, rosettes of small crystals and swallow/forked tails (see 6.2.1.1.).

o Pyroxene occurrence is limited to the groundmass as acicular and small (< 1mm), subhedral to anhedral crystals usually showing a branching pattern (elongated crystals forming parallel, radial or fan like aggregates) and other quenching shapes such as skeletal, sheaf-like and feather-like dendritic crystals. The pyroxenes show a small range in composition and are classified as quadrilaterals, specifically augites, with a narrow compositional range of Wo_{39-42} En_{38-46} Fs_{13-22} (see 6.2.1.2.).

o The opaque minerals in the groundmass are iron-titanium oxides and sulphides. The oxides s.l. occurs as skeletal/dendritic crystals dispersed in the groundmass and, less frequently, as inclusions in plagioclase phenocrysts. Even though the oxides analyses where not quantitatively reliable due to hydration and alteration processes, the majority would have been titanomagnetites (see 6.2.1.3.).

o The sulphides where classified as pyrites. The crystals are euhedral to subeuhedral, sometimes with skeletal forms, and they occur as dispersed grains within the groundmass and along veinlets. According with the mode of occurrence, along veins and veinlets, it seems likely that their crystallization is a late event probably related with some sort of hydrothermal alteration (see 6.2.1.3.).

o As opposed to Maio pillow basalts of tholeiitic affinity, which show extensive weathering with some being metamorphosed in the greenschist facies as well as evidence for intense deuteric alteration, Santiago pillow lavas preserve all the primary igneous minerals with very little evidence of alteration, apart from the occurrence of carbonated veins associated with epidote, sulphides and plagioclase sericitization (see 6.2.1.4.).

o Santiago pillow lavas are however characterized by the occurrence of a specific mineral paragenesis, not observed or described in Maio pillow lavas. In pseudomorphosed crystals as well as in veins and more rarely dispersed in the groundmass occurs a pale

bluish green acicular mineral, magnesio-arfvedsonite (Na-amphibole). Other particular minerals such as aegirine, phlogopite and albite were also optically and chemically identified (see 6.2.1.5.).

- The occurrence of this particular mineral paragenesis calls for an enrichment in alkalis, a process that is most probably related with the intrusion of dolomitic carbonatites within the pillow lavas outcrop. This process is known as fenitization. in Santiago the observed mineralogy is dominantly enrich in sodium, as expressed by the occurrence of albite, Na-pyroxene (aegirine) and Na-amphibole (arfevdsonite) and so the fenitization can be classified as sodic (see 6.2.1.5.).

Gabbroic xenoliths

- The gabbroic xenoliths collected at Santiago Island are relatively homogeneous in mineralogy and texture. The great majority is holocrystalline, coarse-grained with average grain size between 2.5 and 5.0 mm, granular and with cumulate texture (see 6.2.2.).

- Based on the modal proportions of the rock forming minerals Santiago xenoliths can be classified as gabbros *s.s.* (essential minerals are plagioclase and clinopyroxene) and orthopyroxene gabbros (essential minerals are plagioclase and clinopyroxene with minor amounts of orthopyroxene) (see 6.2.2.).

- The mineral assemblage is dominated by plagioclase (25 to 60% modal) and clinopyroxene (10 to 40% modal) with variable amounts of orthopyroxene (not detected to 20% modal) and olivine (not detected to 20% modal). Oxide grains are occasionally present as anhedral crystals. Clinopyroxene frequently display narrow and parallel exsolution lamellae of orthopyroxene indicative of slow cooling (see 6.2.2.).

- Olivine present in Santiago gabbroic xenoliths is almost always strongly altered to iddinsgite and oxide minerals (see 6.2.2.1.).

o Plagioclase composition falls in the range $An_{62.1}Ab_{10.8}Or_{0.0}$ to $An_{89.2}Ab_{37.7}Or_{0.7}$ and so the majority can be classified as bytownites (see 6.2.2.2.).

o About 50% of pyroxenes are classified as augites within the range $Wo_{25}En_{39}Fs_{8}$ to $Wo_{47}En_{60}Fs_{24}$. Diopside corresponds to about 35% of the analyzed pyroxenes, with a compositional range from $Wo_{45}En_{27}Fs_{7}$ to $Wo_{50}En_{47}Fs_{26}$. Only 2% of the entire analyzed pyroxenes plot above the line defining 50% of wollastonite end-member. Ortopyroxenes, which are not present in all samples, represent 7% of the analyzed pyroxenes being classified as enstatites ($Wo_{0}En_{60}Fs_{18}$ to $Wo_{3}En_{80}Fs_{38}$) (see 6.2.2.3.).

7.1.4.2. Whole rock major and trace element chemistry

MORB Lavas

o The SiO_2 content of the samples range from 47 to 50 wt.%, enabling their classification as basic (basalts). Even thought the analyses were recalculated to 100% in a H_2O-CO_2 free basis, the TAS diagram is not ideal when considering weathered or altered volcanic rocks. The main pitfall about the application of the TAS diagram to the studied rocks is the evidence for fenitization which will lead to a significant alkali mobilization, compromising the discrimination between the alkaline and subalkaline rock series (see 6.3.1.1.).

o Tholeiitic basalts should be characterized by the occurrence of modal or normative hypersthene, and hence be projected in the Ol-Ab-Hy or Q-Ab-Hy triangles of Thompson. Once again the high alkali content of the samples stemming from fenitization processes will be transformed in normative nepheline and orthoclase instead of hypersthene, leading to an erroneous classification based on major elements that are specifically modified by the described metasomatic event (see 6.3.1.1.).

o Santiago pillow lavas are characterized by low TiO_2 and high Zr/P_2O_5, which allows the fingerprinting of the type of oceanic basalt and its former tectonic environment, being

typical of sub-alkaline magmas suites. The non-orogenic character of these samples is further reinforced by the use of Zr-Nb-Y associations (see 6.3.1.1.).

- Santiago pillow lavas display a very restricted SiO_2 variability and low MgO contents. This in turn will result in low Mg# (57 to 65) indicating a slight to moderate degree of fractionation of these magmas (see 6.3.1.2.).

- Titanium, sodium and phosphorus behave incompatibly in the Angra lavas, as would be expected while aluminium shows a more random behaviour. The dispersion of the data in MgO-Al_2O_3 space could suggest some degree of plagioclase accumulation. Concerning trace elements, Ni and Sc behave compatibly attesting the importance of their incorporation in olivine and pyroxene, respectively (see 6.3.1.2.).

- In chondrite-normalized REE patterns it is evident the LREE depletion portrayed by Santiago pillow lavas. In fact Santiago tholeiitic suit show evidence for an unusual depletion of the mantle source testified by low $(La/Sm)_n$ and $(La/Yb)_n$. Also, when compared to Maio MORB lavas, it is notorious the much more depleted character of Santiago MORBs (see 6.3.1.3.).

- Santiago MORB samples are characterized by low concentrations of incompatible elements (La, Nb and Hf) (see 6.3.1.3.).

- Plotting Santiago tholeiitic pillow basalts incompatible trace elements against D-MORB values it becomes more evident the difference between the two. It is evident an excess of LILE (Rb, Ba, K, Sr), a depletion in the majority of incompatible elements (La, Ce, Nd, Zr, Hf, Ti) a similarity among Y and the HREE, Lu and Yb and a remarkable enrichment in Th (see 6.3.1.3.).

- The enrichment of LILE (K, Rb, Ba and Sr) can all be explained by the extreme mobility of these elements in a fluid rich environment. Sr is the element that best correlates with LOI, almost linearly, attesting the influence of alteration processes in the remobilization of this element. Rb and to a less extent Ba, show a good correlation with

K_2O, suggesting a control of both these elements by a K-bearing secondary mineral assemblage formed during low-temperature alteration events (see 6.3.1.4.).

- The effects of fenitization on Santiago pillow lava suite is most readily identified by the occurrence of a specific mineral paragenesis that is rich in alkalis and not common in MORB. At the geochemical level it is evident the enrichment in Na_2O, K_2O and CaO as compared to MORB values. The element most common added during fenitization, besides alkalis, is Ba. Rubidium is another element that exhibits an extreme enrichment (see 6.3.1.5.).

- To check if magmas, extruded around 130 Ma at the mid-Atlantic ridge, portray the same depletion, a comparison of REE contents of six sites in ancient Atlantic oceanic crust with Santiago MORB data has been made. It was concluded that at the Central Atlantic, highly depleted MORB were erupted between 160 and 118 Ma (see 6.3.1.6.).

- The eruption of highly depleted MORB at the initial stages of the Atlantic opening has been defended by several authors as a result of continental insulation which, having caused a sub-lithospheric high temperature, induced high degrees of partial melting (see 6.3.1.6.).

- It must be noticed that among the circum Central Atlantic MORB, the Santiago occurrences are the most depleted ones. This is true even when Santiago (130 Ma) compositions are compared with the older (157 Ma) neighbouring floor basalts erupted at the site 367. Such apparent tendency for the referred time-dependent increasing depletion could be eventually explained as originating from buoyant refractory mantle domains generated during the high degree melting events occurred at the initial stages of the Atlantic opening (see 6.3.1.6.).

- The melting event that formed the LREE depleted Santiago MORB lavas was modelled as 10 to 12% aggregated fractional melting of a source with DMM composition. Several studies indicate 6 to 8% as the average melting for MORB

formation even in a similar situation of generation of young oceanic crust in a continental rifting setting (Red Sea) (see 6.3.1.8.).

- The higher degree of melting obtained for Santiago MORB is probably linked with the thermal anomaly generated by continental insulation, up to 150ºC higher than the present day mantle value, that could have persisted for 60-90 Ma (see 6.3.1.8.).

- From the twelve samples analyzed for whole rock, six were selected for Sr-Nd isotopic analyses. The $^{87}Sr/^{86}Sr$ and $^{143}Nd/^{144}Nd$ isotopic ratios measured for Santiago ancient pillow lavas vary from 0.702776 to 0.703121 and 0.513136 to 0.513191, respectively (see 6.3.1.8.).

- For the same $^{143}Nd/^{144}Nd$, $^{87}Sr/^{86}Sr$ values exhibit a significantly higher dispersion with a range of 0.000345, despite the acid leaching. Seawater is highly depleted in Nd but enriched in Sr conferring it the ability to alter significantly the Sr isotopic composition of rocks with which it interacts, without any discernible effects on $^{143}Nd/^{144}Nd$ ratios (see 6.3.1.8.).

Gabbroic xenoliths

- Four samples were analyzed for whole-rock major and trace element compositions. From this four set of samples, two are silica-undersaturated and the other two are silica-saturated. The MgO content range from 3.7 to 9.7 wt.% and Mg# varies from 59 to 80 (see 6.3.2.).

- Santiago xenoliths show similarities with Santiago MORB affinity pillow lavas regarding chondrite-normalized REE-patterns even though their concentration in REE is significantly lower. Positive Eu-anomalies are present in all the analyzed gabbroic xenoliths, indicating the accumulation of plagioclase (see 6.3.2.).

- A distinction emerges when comparing the LREE concentration of the four gabbroic xenoliths. Two samples are characterized by enrichment in LREE compared to the other

samples. The enrichment in La even exceeds the concentration observed in Santiago MORB lavas. The enriched group also exhibits a mildly convex-upward REE pattern, while the depleted group is characterized by a mildly concave-upward to linear patterns (see 6.3.2.).

- D-MORB normalized incompatible trace element patterns of Santiago gabbroic xenoliths show positive Sr and Ba anomalies and negative Th anomalies. Ba and Sr peaks can be attributed to the accumulation of plagioclase. Compared with Santiago tholeiitic lava suite the gabbroic xenoliths are more depleted, except in Nb and La (see 6.3.2.).

- The enrichment observed in some gabbroic xenoliths could be due to metasomatic events resulting from ascending alkaline magmas that interact with the pre-existing N-MORB crust (see 6.3.2.1.).

7.2. Suggestions for future research

The data obtained from this study and the proposed hypothesis based on them led to the perception that more work could be done to complete and complement what has been done, not only is this thesis but also by all the researchers having worked in Santiago or other Cape Verde islands (e.g. Serralheiro, 1976; Alves et al., 1979; Gerlach et al., 1988; Davies et al., 1989; Mendes, 1995; Mendes et al., 2001; Hoernle et al., 2002; Doucelance et al., 2003, 2012; Martins et al., 2003, 2010; Holm et al., 2006, 2008; Mata et al.2010; Mourão et al., 2010, 2012a,b; Barker et al., 2009, 2010, 2012).

In this perspective some suggestions for future work are presented:

A- The Cape Verde spatial distribution of the SCLM component

The influence of the SCLM in the geochemistry of, at least, some of the Cape Verde alkaline magmas has been defended by several authors (Gerlach et al., 1988; Davies et. al., 1989; Kokfelt et al., 1998; Doucelance et al., 2003; Escrig et al., 2005; Martins et al., 2009; Mourão et al., 2012b; this work) and demonstrated by specific studies in lherzolite xenoliths of Sal Island (Bonadiman et al., 2005; Coltorti et al., 2010) and seismic data

(Begg et al., 2009; O'Reilly et al., 2009). In those mantle-derived xenoliths, sulphide Re-Os model ages were obtained ranging from Neoproterozoic to Archean. Their age distribution mirrors the tectonic history of the western margin of the West African Craton and the corresponding continental margin of Brazil. It would be of great interest to try to replicate this study in all of the Cape Verde Islands and in doing so, try to understand if a correlation exists between the xenolith data and the whole rock geochemistry evidence for a biased SCLM contribution. These would allow a better understanding of the SCLM remnants distribution all over the Cape Verde archipelago. Indeed the contribution of the SCLM to the magma geochemistry has been considered restricted to the Southern Islands, while Coltorti's data were obtained for xenoliths carried to the surface by magmas erupted at Sal Island, one of the Northern Islands[1].

B- The role of lower mantle and the mantle plume depth of origin

Further olivine helium isotopic analyses are needed in Santiago alkaline lavas in order to further consolidate the presence of lower mantle material (high ^{3}He) which supports the assumption of the presence of a mantle plume deeply anchored in the lower mantle. The only noble gas analyses performed on Santiago Island are restricted to four alkaline silicate rock samples analysed for He by Doucelance et al. (2003) and four carbonatites analysed for He, Ne, Ar, Kr and Xe by Mata et al. (2010).

In opposition to the reported for some Northern Islands, Santiago noble gas signatures do not yield relatively unradiogenic He signatures (i.e. R/Ra > 9), a fact explained by Doucelance et al. (2003) by the presumably high radiogenic character of the SCLM component, which would have masked the lower mantle signatures. However, Santiago calcio-carbonatitic magmas, which do not present evidences for the contribution of SCLM (e.g. Hoernle et al., 2002), do not present either unradiogenic signatures in opposition to the described for S. Vicente (Mata et al., 2010). In order to better understand the cause(s) for the lack of relatively unradiogenic He isotopic signatures more analyses are required, including both silicate and carbonatitic magmas.

[1] Torres et al. (2010) based on the geochemical study of Sal Island lavas also suggest the influence of the SCLM for this Northern Island.

C- The origin of carbonatitic magmas

In the recent past, several papers dealing with the origin of Cape Verde carbonatites have included samples from Santiago (Hoernle et al., 2002; Mata et al., 2010; Doucelance et al., 2010). Problems like the recycled or "primordial" origin of the carbon have been addressed. However, the genetic links with the associated silicate rocks has not been deeply explored. Are the Santiago carbonatites the result of magma immiscibility processes, as has been proposed for Brava Island by Mourão et al. (2010; 2012a), or, alternatively, are they the result of the initial stages of partial melting of the Santigo mantle source, or, even like in the proposal of Doucelance et al. (2010), they result from melting of lithosphere? The complete study of this question depends on the sampling/analyses of a significant number of carbonatite and on their comparison with the existent data for silicate rocks.

Recently Mourão et al. (2012b) proposed that Brava carbonatites ultimately originated from a reservoir characterized by very low $^{4}He/^{40}Ar^{*}$, tentatively assigned to the "missing Ar reservoir" first postulated by Allègre et al. (1996). Independently of their provenance, or not, from such "missing Ar reservoir", very low $^{4}He/^{40}Ar^{*}$ sources are not usually sampled by Earth magmatism, thus allowing the inference of their residence into the deep mantle, isolated from convection leading to the mantle homogenization. The presence of such signatures in the Santiago carbonatites was not investigated before. Its detection would be important for the discussion either of the carbon origin, or to infer the depth of mantle plume roots.

D- Mantle metasomatism

This thesis clearly demonstrated the occurrence of recent metasomatic events affecting the Santiago mantle source (see also Martins et al., 2003; 2010). However, I'm convinced that the study of xenoliths could help to the improvement of our knowledge about such process.

Detailed study of melt pockets within peridotite xenoliths, hosted in Santiago alkaline lavas, should be performed given that the small number of analyses reported from Mendes (1995) already yields a significant variability. Moreover, detailed geochemical study

(elemental and isotopic) in the glasses present in mantle xenoliths (laser-ablation) would help to constrain more effectively the nature of the metasomatic agent.

SEM studies on single grain minerals as well as thin section from peridotite xenoliths would promote the identification or not of, the very likely existence, of a pervasive grain boundary component (PGBC, Bedini and Bodinier, 1999) commonly described in metasomatized peridotite xenoliths, which can be related or derived from the metasomatic agent, not commonly detected by optical methods.

Pb-Sr-Nd-Hf isotopic study of peridotite xenoliths as a whole and in clinopyroxene/metasomatic mineral separates would also aid in the interpretation of the metasomatic event(s) and plume-lithosphere testimonies. It would also be important to determine analytically $^{238}U/^{204}Pb$, $^{232}Th/^{204}Pb$, $^{232}Th/^{238}U$ ratios to try to implement the method described by Wittig et al. (2009, 2010) concerning the timing of the metasomatic event as well as the confirmation of high μ, ω and γ signature of the metasomatic agent.

E - Gabbroic xenoliths

The study of Santiago Island gabbroic xenoliths was not the main objective of this thesis, and so the mineral chemical data obtained was only briefly used to characterize the occurring minerals. However further use of the data is foreseen for mineral geothermobarometric studies/modelling to infer depths of origin in a paper being prepared concerning the outcropping MORB-type lavas in association with gabbroic xenoliths, since they both represent testimonies of the oceanic crust where Santiago Island is implanted.

References

Abouchami, W., Galer, S.J., Koschinsky, A. (1999) Pb and Nd isotopes in NE Atlantic Fe–Mn crusts: Proxies for trace metal paleosources and paleocean circulation. *Geochim. Cosmochim. Acta*, 63, 1489–1505.

Abouchami, W., Galer, S.J., Hofmann, A.W. (2000) High precision lead isotope systematics of lavas from the Hawaiian Scientific Drilling Project. *Chem. Geol.*, 169, 187- 209.

Abranches, M.C., Storetvedte, K.M., Serralheiro, A, Løvlie, R. (1990) The paleomagnetic record of the Santiago volcanics (Republic of Capo Verde); multiphase magnetization and age consideration. *Phys. Earth Planet. Int.*, 64, 290-302.

Adam, J., Green, T. (2003) The influence of pressure, mineral composition and water on trace element partitioning between clinopyroxene, amphibole and basanitic melts. *Eur. J. Mineral.*, 15, 831-841.

Adam, J., Green, T. (2006) Trace element partitioning between mica- and amphibole-bearing garnet lherzolite and hydrous basanitic melt: 1. Experimental results and the investigation of controls on partitioning behavior. *Contrib. Mineral. Petrol.*, 152, 1-17.

Ali, M.Y., Watts, A.B., Hill, I. (2003) A seismic reflection profile study of lithospheric flexure in the vicinity of the Cape Verde Islands. *J. Geophys. Res.*, 108, 2239.

Allègre, C.J. (1969) Comportament des systems U-Th-Pb dans le manteau supérieur et modèle d'évolution de ce dernieur au cours des temps geologiques. *Earth Planet. Sci. Lett.*, 5, 261-269.

Allègre, C.J. (1982) Chemical geodynamics. *Tectonophysics*, 81, 109–132.

Allègre, C.J., Turcotte, D.L. (1986) Implications of a two-component marble-cake mantle. *Nature*, 323, 123-127.

Allègre, C.J., Pineau, F., Bernat, M., Javoy, M. (1971) Evidence for the occurrence of carbonatites on the Cape Verde and Canary Islands. *Nature*, 233, 103-104.

Allègre, C.J., Dupré, B., Lewin, E. (1986) Thorium/Uranium ratio of the Earth. *Chem. Geol.*, 56, 219-227.

Allègre, C.J., Staudacher, T., Sarda, P. (1986) Rare gas systematics: formation of the atmosphere, evolution and structure of the earth's mantle. *Earth Planet. Sci. Lett.*, 81, 127–150.

Allègre, C.J., Hofmann, A.W., O'Nions, R.K. (1996) The argon constraints on mantle structure. *Geophys. Res. Lett.*, 23, 3555-3557.

Alves, C.M.A., Serralheiro, A., Macedo, J., Cramez, P., Sousa, A.A., Mendes, F., David Gomes, R.A. (1971) Carbonatitos de Santiago, Cabo Verde. *I Congresso Hispano Luso-Americano de Geologia Económica*, Madrid, 568-576.

Alves, C.A.M., Macedo, J.R., Silva, L.C., Serralheiro, A., Faria, A.F.P. (1979) Estudo geológico, petrológico e vulcanológico da ilha de Santiago (Cabo Verde). *Garcia da Orta, Série de Geologia*, 3, 47-74.

Ames, L.L., McGarrah, J.E., Walker, B. A. (1983) Sorption of trace constituents from aqueous solution onto secondary minerals. I. Uranium. *Clays Clay Min.*, 31, 321-334.

Ancochea, E., Brändle, J.L., Cubas, C. R., Hernan, F., Huertas M. J. (1996) Volcanic complexes in the eastern ridge of the Canary Islands: the Miocene activity of the island of Fuerteventura. *J. Volcanol. Geotherm. Res.*, 70, 183-204.

Ancochea, E., Brändle, J.L., Huertas, M.J.; Hernán, F., Herrera, R. (2008) Dike-swarms, key to the reconstruction of major volcanic edifices: The basic dikes of La Gomera (Canary Islands). *J. Volcanol. Geotherm. Res.*, 173, 207-216.

Anderson, D.L. (1967) Phase changes in the upper mantle. *Science*, 157, 1165-1173.

Anderson, D.L. (2005) Scoring hotspots: The plume and plate paradigms. In: Foulger, G.R., Natland, J.H., Presnall, D.C., Anderson, D.L. (Eds.). Plates, plumes, and paradigms. *Geol. Soc. Am. Special Paper*, 388, 31–54.

Anderson, D. (2006) Plate Tectonics; The general theory: the complex Earth is simpler than you think. *Geol. Soc. Am. Special Paper*, 413, 29-38.

Armienti, P., Gasperini, D. (2007) Do we really need mantle components to define mantle composition? *J. Petrol.*, 48, 693-709.

Armstrong, R.L. (1968) A model for the evolution of strontium and lead isotopes in a dynamic Earth. *Rev. Geophys.*, 6, 175–199.

Assunção, C. (1968) Geologia da Província de Cabo Verde. *Curso de Geologia do Ultramar, Volume I*, Lisboa, 1-52.

Azéma, J., Fourcade, E., De Wever, P. (1990) Découverte de Valanginien inférieur à Calpionelles à Maio (République du Cap Vert): discussion del'âge des sédiments associés aux laves de type MORB de ce secteur del'Atlantique Central. C.R. *Acad. Sci. Paris*, 310, 277–283.

Bailey, D.K. (1993) Carbonate magmas. *J. Geol. Soc. London*, 150, 637–651.

Ballentine, C.J., Lee, D.-C., Halliday, A.N. (1997) Hafnium isotopic studies of the Cameroon line and new HIMU paradoxes. *Chem. Geol.*, 139, 111-124.

Ballentine, C.J., van Keken, P., Porcelli, D., Hauri, E.H. (2002) Numerical models, geochemistry, and the zero-paradox noble-gas mantle. *Philos. Trans. R. Soc. London A*, 360, 2611–2631.

Ballhaus, C. (1993) Redox states of the lithospheric and asthenospheric upper mantle. *Contrib. Mineral. Petrol.*, 114, 331–348.

Ballmer, M., van Hunen, J., Ito, G., Tackley, P., Bianco, T. (2007) Non-hotspot volcano chains originating from small-scale sublithospheric convection. *Geophys. Res. Lett.*, 34, doi:10.1029/2007GL031636.

Ban, M., Witt-Eickschen, G., Klein, M., Seck, H.A. (2005) The origin of glasses in hydrous mantle xenoliths from the West Eifel, Germany: incongruent break down of amphibole. *Contrib. Mineral. Petrol.*, 148, 511-523.

Banner, J. (2004) Radiogenic isotopes: systematics and applications to earth surface processes and chemical stratigraphy. *Earth-Sci. Rev.*, 65, 141–194.

Barker, A.K., Holm, P.M., Peate, D.W., Baker, J.A. (2009) Geochemical stratigraphy of submarine lavas (3–5 Ma) from the Flamengos Valley, Santiago, southern Cape Verde islands. *J. Petrol.*, 50, 169–193.

Barker, A.K., Holm, P.M., Peate, D.W., Baker, J.A. (2010) A 5 million year record of compositional variations in mantle sources to magmatism on Santiago, southern Cape Verde archipelago. *Contrib. Mineral. Petrol.*, 160, 133-154.

Barker, A.K., Troll, V.R., Ellam, R.M., Hansteen, T.H., Harris, C., Stillman, C.J., Andersson, A. (2012) Magmatic evolution of the Cadamosto Seamount, Cape Verde: beyond the spatial extent of EM1. *Contrib. Mineral. Petrol.*, 163, 949 – 965.

Bear, A.N., Cas, R.A.F. (2007) The complex facies architecture and emplacement sequence of a Miocene submarine mega-pillow lava flow system, Muriwai, North Island, New Zealand. *J. Volcanol. Geotherm. Res.*, 160, 1-22.

Beattie, P. (1993) Uranium-Thorium disequilibrium and partitioning on melting of garnet peridotite. *Nature*, 363, 63-65.

Bebiano, J.B. (1932) A Geologia do Arquipélago de Cabo Verde. *Com. Serv. Geol. Portugal*, XVIII, 275 p.

Beccaluva, L., Azzouni-Sekkal, A., Benhallou, A., Bianchini, G., Ellam, R.M. (2007) Intracratonic asthenosphere upwelling and lithosphere rejuvenation beneath the Hoggar swell (Algeria): Evidence from HIMU metasomatised lherzolite mantle xenoliths. *Earth Planet. Sci. Lett.*, 260, 482-494.

Beccaluva, L., Bianchini, G., Ellam, R.M., Marzoli, M., Oun, K.M., Siena, F., Stuart, F.M. (2008) The role of HIMU metasomatic components in the North African lithospheric mantle: petrological evidence from the Gharyan lherzolite xenoliths, NW Libya. In:

Coltorti, M. and Grégoire, M. (Eds.) Metasomatism in oceanic and continental lithospheric mantle. *Geol. Soc. London, Spec. Public.,* 293, 253–277.

Beier, C., Stracke, A., Haase, K.M. (2007) The peculiar geochemical signatures of São Miguel lavas: metasomatised or recycled mantle sources? *Earth Planet. Sci. Lett.*, 259,186-199.

Bell, K., Simonetti, A. (1996) Carbonatite magmatism and plume activity: implications from the Nd, Pb and Sr isotope systematics of Oldoinyo Lengai. *J. Petrol.*, 137, 1321-1339.

Bell, K., Simonetti, A. (2010) Source of parental melts to carbonatites - critical isotopic constraints. *Mineral. Petrol.*, 98, 77-89.

Bell, K., Tilton, G.R. (2001) Nd, Pb and Sr isotopic compositions of East African Carbonatites: evidence for mantle mixing and plume inhomogeneity. *J. Petrol.*, 42, 1927–1945.

Begg, G., Griffin, W.L., Natapov, L.M., O'Reilly, S.Y., Grand, S., O'Neill, C.J., Poudjom Djomani, Y., Deen, T., Hronsky, J., Bowden, P. (2009) The lithospheric architecture of Africa: seismic tomography, mantle petrology and tectonic evolution. *Geosphere,* 5, 23–50. doi:10.1130/GES00179.1.

Bernard-Griffiths, J., Cantagrel, J.M., Alves, C.A.M., Mendes, E., Serralheiro, A., Macedo, J. (1975) Données radiométriques potassium-argon sur quelques formations magmatiques des îles de l'archipel du Cap Vert. *C. R. Acad. Sci.*, 280, 2429–2432.

Best, M.G., Christiansen, E.H. (2001) *Igneous Petrology*. Blackwell Science, Malden, Massachussets, 458 pp.

Bianchini, G., Beccaluva, L., Bonadiman, C., Nowell, G., Pearson, D.G., Siena, F., Wilson, M. (2010) Mantle metasomatism by melts of HIMU piclogite components: new insights from Fe-lherzolite xenoliths (Calatrava Volcanic District, central Spain). In: Coltorti, M., Downes, H., Grégoire, M. and O'Reilly, S.Y. (Eds.) Petrological evolution of the European lithospheric mantle. *Geol. Soc. London, Spec. Public.*, 337, 107-124.

Bianco, T.A., Ito, G., van Huen, J., Ballmer, M.D., Mahoney, J.J. (2008) Geochemical variation at the Hawaiian hot spot caused by upper mantle Dynamics and melting of a heterogeneous plume. *Geochem. Geophys. Geosyst.*, 9, doi: 10.1029/2008GC002111.

Blichert-Toft, J., Albarède, F. (1997) The Lu-Hf isotope geochemistry of chondrites and the evolution of the mantle-crust system. *Earth Planet. Sci. Lett.*, 148, 243-258.

Blichert-Toft, J., White, W.M. (2001) Hf isotope geochemistry of the Galapagos Islands. *Geochem. Geophys. Geosyst.*, 2, doi: 10.1029/2000GC000138.

Blichert-Toft, J., Chauvel, C., Albare`de, F., (1997) Separation of Hf and Lu for high precision isotope analysis of rock samples by magnetic sector-multiple collector ICP-MS. *Contrib. Mineral. Petrol.*, 127, 248 – 260.

Blichert-Toft, J., Frey, F., Albarède, F. (1999) Hf isotope evidence for pelagic sediments in the source of Hawaiian basalts. *Science*, 285, 879-882.

Blundy, J., Dalton, J. (2000) Experimental comparison of trace element partitioning between clinopyroxene and melt in carbonate and silicate systems, and implications for mantle metasomatism. *Contrib. Mineral. Petrol.*, 139, 356-371.

Blundy, J.D., Robinson, J.A.C., Wood, B.J. (1998) Heavy REE are compatible in clinopyroxene on the spinel lherzolite solidus. *Earth Planet. Sci. Lett.*, 160, 493-504.

Bonadiman, C., Beccaluva, L., Coltorti, M., Siena, F. (2005) Kimberlite-like metasomatism and "garnet signature" in spinel-peridotite xenoliths from Sal, Cape Verde archipelago: relics of a subcontinental mantle domain within the Atlantic Ocean lithosphere? *J. Petrol.*, 46, 2465-2493.

Bonadiman, C., Coltorti, M., Beccaluva, L., Siena, F. (2010) Mantle metasomatism vs. host magma interaction at Sal Island (Cape Verde archipelago). *Geophys. Res. Abstr.*, 12, 14830.

Bouvier, A., Vervoort, J.D., Patchett, P. J. (2008) The Lu–Hf and Sm–Nd isotopic composition of CHUR: constraints from unequilibrated chondrites and implications for the bulk composition of terrestrial planets. *Earth Planet. Sci. Lett.*, 273, 48–57.

Brandenburg, J.P., van Keken, P.E. (2007) Deep storage of oceanic crust in a vigorously convecting mantle. *J. Geophys. Res.*, 112, B06403, doi: 10.1029/2006JB004813.

Brandl, P., Regelous, M., Beier, C., Haase, K. (2013) High mantle temperatures following rifting caused by continental insulation. *Nat. Geosci.*, 6, 391–394.

Brandon, A. D., Graham, D. W., Waight, T., Gautason, B. (2007) ^{186}Os and ^{187}Os enrichments and high $^{3}He/^{4}He$ sources in the Earth's mantle: Evidence from Icelandic picrites. *Geochim. Cosmochim. Acta*, 71, 4570–4591.

Brey, G., Green, D.H. (1975) The role of CO_2 in the genesis of olivine melilitite. *Contrib. Mineral. Petrol.,* 49, 93–103.

Brey, G., Green, D.H. (1977) Systematic study of liquidus phase relations in olivine melilitite+H_2O+CO_2 at high pressures and petrogenesis of an olivine melilitite magma. *Contrib. Mineral. Petrol.*, 61, 141-162.

Brod, J.A., Gaspar, J.C., Araújo, D.P., GibsonN, S.A., Thompson, R.N., Junqueira-Brod, T.C. (2001) Phlogopite and tetra-ferriphlogopite from Brazilian carbonatite complexes: petrogenetic constraints and implications for mineral-chemistry systematics. *J. Asian Earth Sci.*, 19, 265-296.

Brum da Silveira, A., Madeira, J., Serralheiro, A., (1997) A estrutura da ilha do Fogo, Cabo Verde. In: Réffega, A. (Eds.) A Erupção Vulcânica de 1995 na Ilha do Fogo, Cabo Verde. IICT, Lisboa, 63-78.

Bryan, W.B., Frey, F.A., Thompson, G. (1977) Oldest Atlantic Seafloor - Mesozoic basalts from Western North Atlantic margin and Eastern North America. *Contrib. Mineral. Petrol.*, 64, 223-242.

Burke, K., Steinberger, B., Torsvik, T., Smethurst, M. (2008) Plume generation zones at the margins of the Large Low Shear Velocity Provinces on the core-mantle boundary. *Earth Planet. Sci. Lett.*, 265, 49-60.

Burov, E.B., Guillou-Frottier, L. (2005) The plume head-continental lithosphere interaction using a tectonically realistic formulation for the lithosphere. *Geophy. J. Int.*, 161, 469-490.

Calmant, S., Francheteau, J., Cazenave, A. (1990) Elastic layer thickening with age of the oceanic lithosphere. *Geophys. J.*, 100, 59-67.

Campbell, I.H. (2007) Testing the plume theory. *Chem. Geol.*, 241, 153-176.

Cannat, M., Chatin, F., Whitechurch, H., Ceuleneer, G. (1997) Gabbroic rocks trapped in the upper mantle at the Mid-Atlantic Ridge. In: Karson, J.A., Cannat, M., Miller, D.J., Elton, D. (Eds.). *Proc. ODP, Sci. Res.*, 153, 243-264.

Carmichael, L.S., Nicholls, J., Smith, A.L. (1970) Silica activity in igneous rocks. *Am. Mineral.*, 55, 246-263.

Carmody, L. (2012) Geochemical characteristics of carbonatite-related volcanism and sub-volcanic metasomatism at Oldoinyo Lengai, Tanzania. PhD thesis, University College of London, 338 pp.

Carreira, P., Marques, J., Pina, A., Mota Gomes, A., Fernades, P., Santos, F.M. (2009) Groundwater assessment at Santiago Island (Cabo Verde): a multidisciplinary approach to a recurring source of water supply. *Water Resour. Manag.*, 24, 1139-1159.

Cas, R.A.F., Wright, J.V. (1987) Volcanic successions. Chapman and Hall, London, 544p.

Cazenave, A., Dominh, K., Rabinowicz, M., Ceuleneer, G. (1988) Geoid and depth anomalies over ocean swells and troughs: evidence of an increasing trend of the geoid to depth ratio with age of plate. *J. Geophys. Res.*, 93, 8064-8077.

Chaffey, D. J., Cliff, R.A., Wilson, B.M. (1989) Characterization of the St. Helena magma source, In: Saunders, A.D. and Norry, M.J. (Eds.), Magmatism in Ocean Basins. *Geol. Soc. Spec. Publ. London*, 42, 257–276.

Chase, C.G. (1981) Oceanic island Pb - 2-stage histories and mantle evolution. *Earth Planet. Sci. Lett.*, 52, 277–284.

Chauvel, C., Hofmann, A.W., Vidal, P. (1992) HIMU-EM: The French Polynesian connection. *Earth Planet. Sci. Lett.*, 110, 99–119.

Chauvel, C., Lewin, E., Carpentier, M., Arndt, N., Marini, J.-C. (2008) Role of recycled oceanic basalt and sediment in generating the Hf–Nd mantle array. *Nat. Geosci.*, 1, 64–67.

Chen, J.H., Wasserburg, G.J. (1983) The least radiogenic Pb in iron meteorites. *14th Lunar Planet Sci. Conf.*, 103–104.

Chevalier, A. (1935) Plantes nouvelles de 1'Archipel des Iles du Cap Vert. *Bulletin du Muséum National d'Histoire Naturelle*, 7, 137-144.

Christensen, B., Holm, P., Jambon, A., Wilson, J. (2001) Helium, argon and lead isotopic composition of volcanics from Santo Antão and Fogo, Cape Verde Islands. *Chem. Geol.*, 178, 127–142.

Church, A.A., Jones, A.P. (1995) Silicate - Carbonate Immiscibility at Oldoinyo Lengai. *J. Petrol.*, 36, 869-889.

Clague, D.A., Frey, F.A. (1982) Petrology and trace element geochemistry of the Honolulu volcanics, Oahu: Implications for the oceanic mantle below Hawaii. *J. Petrol.*, 23, 447-504.

Class, C., Goldstein, S.L. (1994) Ocean island basalts and lithospheric melting: constraints from the source mineralogy. *Mineral. Mag.*, 58A, 175-176.

Class, C., Goldstein, S.L. (1997) Plume-lithosphere interactions in the ocean basins: constraints from the source mineralogy. *Earth Planet. Sci. Lett.*, 150, 245-260.

Class, C., le Roex, A.P. (2008) Ce anomalies in Gough Island lavas - Trace element characteristics of a recycled sediment component. *Earth Planet. Sci. Lett.*, 265, 475-486.

Class, C., Goldstein, S. L., Altherr, R., Bachelery, P. (1998) The process of plume lithosphere interactions in the ocean basins—the case of Grande Comore. *J. Petrol.* 39, 881-903.

Collerson, K.D., Kamber, B.S. (1999) Evolution of the continents and the atmosphere inferred from Th–U–Nb systematics of the depleted mantle. *Science*, 283, 1519–1522.

Collerson, K., Williams, Q., Ewart, A., Murphy, D. (2010) Origin of HIMU and EM-1 domains sampled by ocean island basalts, kimberlites and carbonatites: the role of CO_2-fluxed lower mantle in thermochemical upwelling. *Phys. Earth Planet. Int.*, 181, 112-131.

Coltorti, M., Beccaluva, L., Bonadiman, C., Salvini, L., Siena, F. (2000) Glasses in mantle xenoliths as geochemical indicators of metasomatic agents. *Earth Planet. Sci. Lett*,. 183, 303-320.

Coltorti, M., Bonadiman, C., O'Reilly, S., Griffin, W., Pearson, N. (2009) Disrupted subcontinental mantle in an ocean basin: Sal Island, Cape Verde Archipelago. *Geophys. Res. Abstr.*, Vol. 11, 9447.

Coltorti, M., Bonadiman, C., O'Reilly, S.Y., Griffin, W.L., Pearson, N.J. (2010) Buoyant ancient continental mantle embedded in oceanic lithosphere (Sal Island, Cape Verde Archipelago). *Lithos*, 120, 223-233.

Comin-Chiaramonti, P., Gomes, C., Castorina, F., Censi, P., Antonini, P., Furtado, S., Ruberti, E., Scheibe, F. (2002) Geochemistry and geodynamic implications of the Anitápolis and Lages alkaline-carbonatite complexes, Santa Catarina State, Brazil. *Rev. Bras. Geo.*, 32, 43-58.

Condie, K.C. (2001) Mantle plumes and their record in Earth's history. Cambridge University Press, 303 pp.

Condie, K.C. (2005) Earth as an Evolving Planetary System. Elsevier Academic Press, 574pp.

Conrad, C., Wu, B., Smith, E., Bianco, T., Tibbetts, A. (2010) Shear-driven upwelling induced by lateral viscosity variations and asthenospheric shear: A mechanism for intraplate volcanism. *Phys. Earth Planet. Int.*, 178, 162-175.

Courtillot, V., Davaille, A., Besse, J., Stock, J. (2003) Three distinct types of hotspots in the Earth's mantle. *Earth Planet. Sci. Lett.*, 205, 295-308.

Courtney, R., White, R. (1986) Anomalous heat flow and geoid across the Cape Verde Rise: Evidence for dynamic support from a thermal plume in the mantle. *Geophys. J. Roy. Astr. Soc.*, 87, 815-868.

Cox, K.G., Bell, J.D., Pankhurst, R.J. (1979) The interpretation of igneous rocks. George Allen and Unwin Ltd. London, 450 pp.

Crevola, G. (1995) Cenozoic volcanism in Western Senegal and its relationship to the opening of the Central Atlantic Ocean – Comment. *Tectonophysics*, 246, 201-204.

Crough, S.T. (1982) Geoid height anomalies over the Cape Verde rise. *Mar. Geophys. Res.*, 5, 263-271.

Cserepes, L., Christensen, U.R., Ribe, N.M. (2000) Geoid height versus topography for a plume model of the Hawaiian swell. *Earth Planet. Sci. Lett.*, 178, 29-38.

Dalpe, C., Baker, D.R. (1994) Partition coefficients for rare-earth elements between calcic amphibole and Ti-rich basanitic glass at 1.5 GPa, 1100 degrees C. *Mineral. Mag.*, 58, 207-208.

Dalton, J.A., Wood, B.J. (1993) The compositions of primary carbonate melts and their evolution through wallrock reaction in the mantle. *Earth Planet. Sci. Lett.*, 119, 511-525.

Darwin, C. R. (1844) Geological observations on the volcanic islands visited during the voyage of H.M.S. Beagle, together with some brief notices of the geology of Australia and the Cape of Good Hope. Being the second part of the geology of the voyage of the Beagle, under the command of Capt. Fitzroy, R.N. during the years 1832 to 1836. London: Smith Elder and Co. (http://darwin-online.org.uk/).

Dasgupta, R., Hirschmann, M.M. (2010) The deep carbon cycle and melting in the Earth's interior. *Earth Planet. Sci. Lett.*, 298, 1-13.

Dasgupta, R., Hirschmann, Withers, A. (2004) Deep global cycling of carbon constrained by the solidus of anhydrous, carbonated eclogite under upper mantle conditions. *Earth Planet. Sci. Lett.*, 227, 73-85.

Dasgupta, R., Hirschmann, M.M., Stalker, K. (2006) Immiscible transition from carbonate-rich to silicate-rich melts in the 3GPa melting interval of eclogite+CO_2 and genesis of silica undersaturated ocean island lavas. *J. Petrol.*, 47, 647-671.

Dasgupta, R., Hirschmann, M., Smith, N. (2007) Partial melting experiments of peridotite + CO_2 at 3 GPa and genesis of alkalic ocean island basalts. *J. Petrol.*, 48, 2093-2124.

Dasgupta, R., Hirschmann, M.M., McDonough, W.F, Spiegelman, M., Withers, A. (2009) Trace element partitioning between garnet lherzolite and carbonatite at 6.6 and 8.6 GPa with applications to the geochemistry of the mantle and of mantle-derived melts. *Chem. Geol.*, 262, 57-77.

Dasgupta, R., Jackson, M., Lee, C.-T. (2010) Major element chemistry of ocean island basalts – conditions of mantle melting and heterogeneity of mantle source. *Earth Planet. Sci. Lett.*, 289, 377-392.

Dash, B.P., Ball, M.M., King, G.A., Butler, I.W., Rona, P.A. (1976) Geophysical investigation of the Cape Verde archipelago. *J. Geophy. Res.*, 81, 5249-5259.

Davaille, A. (1999) Simultaneous generation of hotspots and superswells by convection in a heterogeneous planetary mantle. *Nature*, 402, 756-760.

Davaille, A., Sturzmann, E., Silveira, G., Besse, J., Courtillot, V. (2005) Convective patterns under the Indo-Atlantic « box ». *Earth Planet. Sci. Lett.*, 239, 233-252.

David, K., Schiano, P., Allègre, C.J. (2000) Assessment of the Zr/Hf fractionation in oceanic basalts and continental materials during petrogenetic processes. *Earth Planet. Sci. Lett.*, 178, 285-301.

Davies, G., Norry, D., Gerlach, D., Cliff, R. (1989) A combined chemical and Pb-Sr-Nd isotope study of the Azores and Cape Verde hot-spots: the geodynamic implications. In: Saunders, A.D. and Norry, M.J. (Eds.) Magmatism in the Ocean Basins. *Geol. Soc. London, Spec. Public.*, 42, 231-255.

Davies, G. R., Stolz, A.J., Mahotkin, I.L., Nowell, G.M., Pearson, D.G. (2006) Trace element and Sr-Pb-Nd-Hf isotope evidence for ancient, fluid-dominated enrichment of the source of Aldan shield lamproites. *J. Petrol.*, 47, 1119-1146.

Davis, E.E., Lister, C.R. (1974) Fundamentals of ridge crest topography. *Earth Planet. Sci. Lett.*, 21, 405-413.

Dawson, L.B. (1984) Contrasting types of upper mantle metasomatism? Kornprobst, J. (Ed.) In: *Kimberlites II. The mantle and crust-mantle relationships*. Amsterdam and New York, Elsevier Science Publisher, pp. 289-294.

Day, J.M.D., Pearson, D.G., Macpherson, C.G., Lowry, D., Carracedo, J.-C. (2009) Pyroxenite-rich mantle formed by recycled oceanic lithosphere: Oxygen-osmium isotope evidence from Canary Island lavas. *Geology*, 37, 555-558.

de Ignacio, C., Muñoz, M., Sagredo, J., Fernandez-Santin, S., Johansson, A. (2006) Isotope geochemistry and FOZO mantle component of the alkaline–carbonatitic association of Fuerteventura, Canary Islands, Spain. *Chem. Geol.*, 232, 99–113.

De Paepe, P., Klerkx, J., Hertogen, J., Plinke, P. (1974) Oceanic tholeiites on the Cape Verde Islands: Petrochemical and geochemical evidence. *Earth Planet. Sci. Lett.*, 22, 347–354.

DeLaughter, J.E., Stein, C.A., Stein, S. (2005) Hotspots: a view from the swells. In: Foulger, G.R., Natland, G.R., Presnall, D.C., Anderson, D.L. (Eds.) Plates, Plumes, and Paradigms. *Geol. Soc. Am. Special Paper*, 388, 257-278.

Delpech, G., Grégoire, M., O'Reilly, S., Cottin, S.Y., Moine, B., Michon, G., Giret, A. (2004) Feldspar from carbonate-rich silicate metasomatism in the shallow oceanic mantle under Kerguelen Islands (South Indian Ocean). *Lithos*, 75, 209-237.

DePaolo, D., Wasserburg, G. (1976) Nd isotopic variations and petrogenetic models. *Geophys. Res. Lett.*, 3, 249-252.

Deschamps, F., Kaminski, E., Tachkley, P. (2011) A deep mantle origin for the primitive signature of ocean island basalt. *Nat. Geosci.*, 7, 879-882.

Detrick, R.S., Crough, S.T. (1978) Island subsidence, hotspots and lithospheric thinning. *J. Geophys. Res.*, 83, 1236-1244.

Dick, H., Lin, J., Schouten, H. (2003) An ultraslow-spreading class of ocean ridge. *Nature*, 426, 405-412.

Dickin, A.P. (2005) Radiogenic Isotope Geology. Cambridge University Press, 508 pp.

Dobson, D.P., Jones, A. P., Rabe, R., Sekine, T., Kurita, K., Taniguchi,T., Kondo, T., Kato, T., Shimomura, O., Urakawa, S. (1996) In-situ measurement of viscosity and density of carbonate melts at high pressure. *Earth Planet. Sci. Lett.*, 143, 207–215.

Dosso, L., Hanan, B.B., Bougault, H., Schilling, J.G., Joron, J.L. (1991) Sr-Nd-Pb geochemical morphologybetween 10 and 17 N on the Mid-Atlantic Ridge: A new MORB isotope signature. *Earth Planet. Sci. Lett.*, 106, 29–43.

Dosso, L., Bougault, H., Langmuir, C., Bollinger, C., Bonnier, O., Etoubleau, J. (1999) The age and distribution of mantle heterogeneity along the Mid-Atlantic Ridge (31-41º N). *Earth Planet. Sci. Lett.*, 170, 269-286.

Doucelance, R., Escrig, S., Moreira, M., Gariépy, C., Kurz, M.D. (2003) Pb-Sr-He isotope and trace element geochemistry of the Cape Verde Archipelago. *Geochim. Cosmochim. Acta*, 67, 3717-3733.

Doucelance, R., Hammouda, T., Moreira, M., Martins, J.C. (2010) Geochemical constraints on depth of origin of oceanic carbonatites: the Cape Verde case. *Geochim. Cosmochim. Acta*, 74, 7261-7282.

Duprat, H., Friis, J., Holm, P., Grandvuinet, T., Sørensen, R. (2007) The volcanic and geochemical development of São Nicolau, Cape Verde Islands: Constraints from field and $^{40}Ar/^{39}Ar$ evidence. *J. Volcanol. Geotherm. Res.*, 162, 1-19.

Dupuy, C., Liotard, J., Dostal, J. (1992) Zr/Hf fractionation in intraplate basaltic rocks: carbonate metasomatism in the mantle source. *Geochim. Cosmochim. Acta*, 56, 2417–2423.

Dyhr, C.T., Holm, P.M., (2010) A volcanological and geochemical investigation of Boa Vista, Cape Verde Islands; $^{40}Ar/^{39}Ar$ geochronology and field constraints. *J. Volcanol. Geotherm. Res.*, 189, 19-32.

Dziewonski, A.M., Lekic, V., Romanowicz, B. (2010) Mantle anchor structure: an argument for bottom up tectonics. *Earth Planet. Sci. Lett.*, 299, 69-79.

Eisele, J., Sharma, M., Galer, S.J.G., Blichert-Toft, J., Devey, C.W., Hofmann, A.W. (2002) The role of sediment recycling in EM-1 inferred from Os, Pb, Hf, Nd, Sr isotope and trace element systematics of the Pitcairn hotspot. *Earth Planet. Sci. Lett.*, 196, 197-212.

Ellam, R.M., (1992) Lithospheric thickness as a control on basalt geochemistry. *Geology*, 20, 153-156.

Ellam, R.H., Stuart, F. M. (2000) The sub-lithospheric source of North Atlantic basalts: evidence for, and significance of, a common end-member. *J. Petrol.*, 41, 919-932.

Elliott, T., Blichert-Toft, J., Heumann, A., Koetsier, G., Forjaz, V. (2007) The origin of enriched mantle beneath Sao Miguel, Azores. *Geochim. Cosmochim. Acta*, 71, 219-240.

Emmermann, R., Puchelt, H. (1979) Major and Trace Element Chemistry of Basalts from Holes 417D and 418A, Deep Sea Drilling Project Legs 51-53. In: Donnelly, T., Francheteau, J., Bryan, W., Robinson, P., Flower, M., Salisbury, M., (Eds.) *Initial Reports of the Deep Sea Drilling Project*, 51-53. Washington, D.C., U.S. Gov. Printing Office.

Escrig, S., Doucelance, R., Moreira, M., Allègre, C.J. (2005) Os isotope systematics in Fogo Island: evidence for lower continental crust fragments under the Cape Verde Southern islands. *Chem Geol.*, 219, 93-113.

Elkins-Tanton, L., Grove, T. (2003) Evidence for deep melting of hydrous, metasomatized mantle: Pliocene high potassium magmas from the Sierra Nevadas. *J. Geophys. Res.*, 108, 2350, doi: 10.1029/2002JB002168.

Farley, K.A., Natland, J.H., Craig, H. (1992) Binary mixing of enriched and undegassed (primitive?) mantle components (He, Sr, Nd, Pb) in Samoan lavas. *Earth Planet. Sci. Lett.*, 111, 183–199.

Farnetani, C.G., Hofmann, A.W. (2009) Dynamics and internal structure of a lower mantle plume conduit. *Earth Planet. Sci. Lett.*, 282, 314–322.

Farnetani, C.G., Samuel, H. (2003) Lagrangian structures and stirring in the Earth's mantle. *Earth Planet. Sci. Lett.*, 206, 335-348.

Farnetani, C.G., Samuel, H. (2005) Beyond the thermal plume paradigm. *Geophys. Res. Lett.*, 32, 10.1029/2005GL022360.

Farnetani, C.G., Legras, B., Tackley, P. (2002) Mixing and deformations in mantle plumes. *Earth Planet. Sci. Lett.*, 196, 1-15.

Faure, G., Mensing, T.M. (2005) Isotopes: Principles and Applications. John Wiley & Sons, New Jersey, 928 pp.

Fedorov, A., Dekens, P., McCarthy, M., Ravelo, A., deMenocal., P., Barreiro, M., Pacanowski, R., Philander, S. (2006) The Pliocene Paradox (mechanisms for a permanent El Niño). *Science*, 312, 1485-1489.

Foley, S.F., Jackson, S.E., Fryer, B.J., Greenough, J.D., Jenner, G.A. (1996) Trace element partition coefficients for clinopyroxene and phlogopite in an alkaline lamprophyre from Newfoundland by LAM---ICP-MS. *Geochim. Cosmochim. Acta*, 60, 629-638.

Foley, S.F., Yaxley, G.M., Rosenthal, A., Buhre, S., Kiseeva, E.S., Rapp, R.P., Jacob. D.E. (2009) The composition of near-solidus melts of peridotite in the presence of CO_2 and H_2O between 40 and 60 kbar. *Lithos*, 112, 274-283.

Forte, A.M., Quere, S., Moucha, R., Simmons, N.A., Grand, S.P., Mitrovica, J.X., Rowley, D.B. (2010) Joint seismic-geodynamic-mineral physical modelling of African geodynamics: a reconciliation of deep-mantle convection with surface geophysical constraints. *Earth Planet. Sci. Lett.*, 295, 329–341.

Fourcade, E., Azéma, J., Wever, P., Busnardo, R. (1990) Contribution à la datation de la croûte océanique de l'Atlantique central: Age valanginien inférieur des basaltes océaniques et âge néocomien des calcaires Maiolica de Maio (Iles du Cap Vert). *Mar. Geol.*, 95, 31–44.

Francis, D., Ludden, J. (1995) The signature of amphibole in mafic alkaline lavas, a study in the Northern Canadian Cordillera. *J. Petrol.*, 36, 1171-1191.

Frey, F.A., Green, D.H., Roy, S.D. (1978) Integrated models of basalt petrogenesis: a study of quartz tholeiites to olivine melilitites from South Eastern Australia utilizing geochemical and experimental petrological data. *J. Petrol.*, 19, 463-513.

Frost, D., Rost, S., Selby, N., Stuart, G. (2013) Detection of a tall ridge at the core–mantle boundary from scattered PKP energy. *Geophys. J. Int.*, 195, 558-574.

Fukao, Y., Widiyantoro, S., Obayashi, M. (2001) Stagnant slabs in the upper and lower mantle transition region. *Rev. Geophys.*, 39, 291–323.

Fukao, Y., Obayashi, M., Nakakuki,T., Deep Slab Project Group (2009) Stagnant slab: a review. *Annu. Rev. Earth Planet. Sci.*, 37, 19-46.

Gaffney, A.M., Nelson, B.K., Blichert-Toft, J. (2004) Geochemical constraints on the role of oceanic lithosphere in intra-volcano heterogeneity at West Maui, Hawaii. *J. Petrol.*, 45, 1663–1687.

Gaina, C., Torsvik, T., van Hinsbergen, D., Medvedev, S., Werner, S., Labails, C. (2013) The African Plate: A history of oceanic crust accretion and subduction since the Jurassic. *Tectonophysics*, 604, 4-25.

Gale, A., Dalton, C., Langmuir, C., Su, Y., Schilling, J-G., (2013) The mean composition of ocean ridge basalts. *Geochem. Geophys. Geosyst.*, 14, doi: 10.1029/2012GC004334.

Galer, S.J.G., O'Nions, R.K. (1985) Residence time of thorium, uranium and lead in the mantle with implications for mantle convection. *Nature*, 316, 778-782.

Galer, S.J.G., Abouchami, W. (1998) Practical application of lead triple spiking for correction of instrumental mass discrimination. *Mineral. Mag.*, 62A, 491–492.

Garcia, M.O. (1996) Petrography and olivine and glass chemistry of lavas from the Hawaii scientific drilling project. *J. Geophy. Res.*, B101, 11701-11713.

Gasparik, T., Litvin, Y.A. (2002) Experimental investigation of the effect of metasomatism by carbonatic melt on the composition and structure of the deep mantle. *Lithos*, 60, 129–143.

Gasperini, D., Blichert-Toft, J., Bosch, D., Del Moro, A., Macera, P., Telouk, P., Albarède, F. (2000) Evidence from Sardinian basalt geochemistry for recycling of plume heads into the Earth's mantle. *Nature*, 408, 701–704.

Geldmacher, J., Hoernle, K., Klügel, A., van den Bogaard, P., Bindeman, I. (2008) Geochemistry of a new enriched mantle type locality in the Northern hemisphere: implications for the origin of the EM-1 source. *Earth Planet. Sci. Lett.*, 265, 167–182.

Geldmacher, J., Hanan, B.B., Hoernle, K., Blichert-Toft, J. (2009) Hafnium isotopic variations in East Atlantic intraplate volcanism. *Geophy. Res. Abstr.*, 11, 2528.

George, R.M., Rogers, N.W. (2002) Plume dynamics beneath the African plate inferred from the geochemistry of the Tertiary basalts of Southern Ethiopia. *Contrib. Mineral. Petrol.*, 144, 286-304.

Gerbode, C, Dasgupta, R. (2010) Carbonate-fluxed melting of MORB-like pyroxenite at 2.9 GPa and Genesis of HIMU ocean island basalts. *J. Petrol.*, 51, 2067-2088.

Gerlach, D., Cliff, R., Davies, G., Norry, M., Hodgson, N. (1988) Magma sources of the Cape Verde archipelago: Isotopic and trace element constraints. *Geochim. Cosmochim. Acta*, 52, 2979-2992.

Girnis, A.V., Bulatov, V.K., Lahaye, Y., Brey, G.P. (2006) Partitioning of trace element between carbonate-silicate melts and mantle minerals: experimental and petrological consequences. *Petrology*, 14, 524-547.

Golonka, J., Bocharova, N. (2000) Hot spot activity and the break-up of Pangea. *Paleogeo. Paleoclim. Paleoecol.*, 161, 49-69.

Gonçalves, R., Mota Gomes, A., Lobo de Pina, A., Almeida, E., Santos, F.M. (2006) Hydrogeophysical investigation in Santiago Island (Republic of Cape Verde) using transient (TDEM method). 5ª Conferencia Luso- Espanhola de Geodesia e Geofísica.

Goto, Y., McPhie, J. (2004) Morphology and propagation styles of Miocene submarine basanite lavas at Stanley, northwestern Tasmania, Australia. *J. Volcanol. Geotherm. Res.*, 130, 307-328.

Green, T.H. (1995) Significance of Nb/Ta as an indicator of geochemical processes in the crust-mantle system. *Chem. Geol.*, 120, 347-359.

Green, T.H., Pearson, N.J. (1987) An experimental study of Nb and Ta partitioning between Ti-rich minerals and silicate liquids at high pressure and temperature. *Geochim. Cosmochim. Acta*, 51, 55-62.

Green, T.H., Blundy, J.D., Adam, J., Yaxley, G.M. (2000) SIMS determination of trace element partition coefficients between garnet, clinopyroxene and hydrous basaltic liquids at 2-7.5 GPa and 1080-1200ºC. *Lithos*, 53, 165-187.

Green, D.H., Ringwood, A.E (1970) Mineralogy of peridotitic compositions under upper mantle conditions. *Phys. Earth Planet. Int.*, 3, 359-371.

Green, D.H., Hibberson, W.O., Kovács, I., Rosenthal, A., (2010) Water and its influence on the lithosphere–asthenosphere boundary. *Nature*, 467, 448–451.

Greenough, J. D. (1988) Minor phases in the Earth's mantle: evidence from trace- and minor-element patterns in primitive alkaline magmas. *Chem. Geol.*, 69, 177–192.

Greenough, J., Dostal, J., Mallory-Greenough, L. (2005) Igneous Rock Associations 5. Oceanic Island Volcanism II: Mantle Processes. *Geosc. Canada*, 32 (2).

Grégoire, M., Mione, B.N., O'Reilly, S.Y., Cottin, J.Y., Giret, A. (2000) Element residence and partitioning in mantle xenoliths metasomatized by high alkaline silicate and carbonate-rich melts (Kerguelen Island, Indian Ocean). *J. Petrol.*, 41, 477-509.

Grevemeyer, I. (1999) Isostatic anomalies over mid-plate swells in the Central North Atlantic. *Geodynamics*, 28, 41-50.

Grevemeyer, I., The Shipboard Scientific Party (2004) Meteor report, Equatorial and South Atlantic, Part 3, Cruise no. M62, Leg 3, CHARISMA—Cape Verde Hotspot: A Seismic

Refraction study of ISostasy and MAgmatic underplating. 2004. Cruise report (unpublished), IFM-GEOMAR.

Grevemeyer, I., Helffrich, G., Faria, B., Booth-Rea, G., Schnabel, M., Weinrebe, W. (2010) Seismic activity at Cadamosto seamount near Fogo Island, Cape Verdes - formation of a new ocean island? *Geophys. J. Int.*, 180, 252-258.

Grousset, F., Quétel, C., Thomas, B., Buat-Ménard,P. (1994) Transient Pb isotopic signatures in the Western European atmosphere. *Environ. Sci. Technol.*, 28, 1605-1608.

Gudfinnsson, G., Presnall, D. (2005) Continuous gradation among primary carbonatitic, kimberlitic, melilititic, basaltic, picritic, and komatiitic melts in equilibrium with garnet lherzolite at 3-8 GPa. *J. Petrol.*, 446, 1645-1659.

Guest, J., Spudis, P., Greeley, R., Taylor, G., Baloga, S. (1995) Emplacement of xenolith nodules in the Kaupulehu lava flow, Hualalai volcano, Hawaii. *Bull. Volcanol.*, 57, 179-184.

Gurenko, A., Sobolev, A., Hoernle, K., Hauff, F., Schmincke, H-H. (2009) Enriched, HIMU-type peridotite and depleted recycled pyroxenite in the Canary plume: a mixed-up mantle. *Earth Planet. Sci. Lett.*, 277, 514-524.

Gurnis, M., Davies, G.F. (1986) Mixing in numerical models of mantle convection incorporating plate kinematics. *J. Geophys. Res.*, 91, 6375-6395.

Gutierrez, M., Casillas, R., Fernandez, C., Balogh, K., Ahijado, A., Castillo, C., Colmenero, J. R., Garcia-Navarro, E. (2006) The submarine volcanic succession of the basal complex of Fuerteventura, Canary Islands: A model of submarine growth and emergence of tectonic volcanic islands. *Geol. Soc. Am. Bull.*, 118, 785-804.

Hall, R., Spakman, W. (2002) Subducted slabs beneath the eastern Indonesia-Tonga region: insights from tomography. *Earth Planet. Sci. Lett.*, 201, 321-336.

Halliday, A.N., Lee, D.-C., Tommasini, S., Davies, G.R., Paslick, C.R., Fitton, J.G., James, D.E. (1995) Incompatible trace elements in OIB and Morb and source enrichment in the sub-oceanic mantle. *Earth Planet. Sci. Lett.*, 133, 379-395.

Hamblin, W.K., Christiansen, E.H. (1998) Earth's dynamic system. Prentice Hall Inc., Tokyo, 740 pp.

Hammouda, T., Laporte, D. (2000) Ultrafast mantle impregnation by carbonatite melts. *Geology*, 28, 283-285.

Hanan, B.B., Graham, D.W. (1996) Lead and helium isotope evidence from oceanic basalts for a common deep source of mantle plumes. *Science,* 272, 991-995.

Hanano, D. (2008) Geochemistry of post-shield lavas from Kea- and Loa-trend Hawaiian volcanoes: constraints on the origin and distribution of heterogeneities in the Hawaiian mantle plume. Master thesis. University of British Columbia, 149 pp.

Hansen, D.M., Redfern, J., Federici, F., di Biase, D., Bertozzi, G. (2008) Miocene igneouc activity in the Northern Subbasin, offshore Senegal, NW Africa. *Mar. Petrol. Geol.*, 25, 1-15.

Hanyu, T., Tatsumi, Y., Senda, R., Miyazaki, T., Chang, Q., Hirahara, Y., Takahashi, T., Kawabata, H., Suzuki, K.,. Kimura, J.-I, Nakai, S. (2011) Geochemical characteristics and origin of the HIMU reservoir: A possible mantle plume source in the lower mantle. *Geochem. Geophys. Geosyst.*, 12, doi:10.1029/2010GC003252.

Hardenbol, J., Thierry, J., Farley, M., Jaquin, T., deGraciansky, P., Vail, P. (1998) Mesozoic and Cenozoic sequence chronostratigraphic framework of European basins. In: deGraciansky, P., Hardenbol, J., Vail, P. (Eds.). Mesozoic and Cenozoic Sequence Statigraphy of European Basins, 60. SEPM Special Publications, 60 p.

Harlow, G., Davies, R. (2004) Status report on stability of K-rich phases at mantle conditions. *Lithos*, 77, 647-653.

Harmer, R.E. (1999) The petrogenetic association of carbonatite and alkaline magmatism: constraints from the Spitskop Complex, South Africa. *J. Petrol.*, 40, 525-548.

Harmer, R.E., Gittins, J. (1998) The case of primary, mantle derived carbonatite magma. *J. Petrol.*, 39, 1895-1903.

Harris, R.N., McNutt, M. (2007) Heat flow on hotspot swells: evidence for fluid flow. *J. Geophy. Res.*, 112, B03407, doi:10.1029/2008JB004299.

Hart, S.R. (1984) A large-scale isotope anomaly in the Southern Hemisphere mantle. *Nature*, 309, 753-757.

Hart, S.R. (1988) Heterogeneous mantle domains: signatures, genesis and mixing chronologies. *Earth Planet. Sci. Lett.*, 90, 273-296.

Hart, S.R., Gaetani, G.A. (2006) Mantle Pb paradox: the sulfide solution. *Contrib. Mineral. Petrol.*, 152, 295-308.

Hart, S.R., Hauri, E.H., Oschmann, L.A., Whitehead, J.A. (1992) Mantle Plumes and Entrainment: Isotopic Evidence. *Science*, 256, 517-520.

Harte, B., Hunter, R.H., Kinny, P.D. (1993) Melt geometry, movement and crystallization in relations to mantle dykes, veins and metasomatism. *Philos. Trans. R. Soc. London A,* 34, 1–21.

Hashizume, K., Chaussidon, M., Marty, B., Terada, K., (2004) Protosolar carbon isotopic composition: implications for the origin of meteoritic organics. *Astrophys. J.*, 600, 480-484.

Haase, K.M. (1996) The relationship between the age of the lithosphere and the composition of oceanic magmas: Constraints on partial melting, mantle sources and the thermal structure of the plates. *Earth Planet. Sci. Lett.*, 144, 75-92.

Hassler, D.R. (1999) Plume-lithosphere interaction: geochemical evidence from upper mantle and lower crustal xenoliths from the Kerguelen Islands. Doctoral Dissertation. MIT/ WHOI joint program, 368 pp.

Hauri, E. (2000) Mantle components and mantle reservoirs: bridging the disconnect. *2000 Goldschmidt Conference (Oxford, UK), J. Conf. Abst.,* 5, 495.

Hauri, E.H., Whitehead, J.A., Hart, S.R. (1994) Fluid dynamic and geochemical aspects of entrainment in mantle plumes. *J. Geophys. Res.*, 99, 24275-24300.

Haxby, W., Weissel, J. (1986) Evidence For Small-Scale Mantle Convection From Seasat Altimeter Data. *J. Geophys. Res.*, 91, 3507-3520.

Hayes, D.E., Rabinowitz, P.D. (1975) Mesozoic magnetic lineations and the magnetic quiet zone off Northwest Africa. *Earth Planet. Sci. Lett.*, 75, 105-115.

Haywood, A., Valdês, P. (2004) Modelling Pliocene warmth: contribution of atmosphere, oceans and cryosphere. *Earth Planet. Sci. Lett.*, 218, 363-377.

Helffrich, G. (2000) Topography of the transition zone seismic discontinuities. *Rev. Geophys.*, 38, 141-158.

Helffrich, G., Wood, B.J. (2001) The Earth's mantle. *Nature*, 412, 501-507.

Helffrich, G., Faria, B., Fonseca, J.F.B.D., Lodge, A., Kaneshima, S., (2010) Transition zone structure under a stationary hot spot: Cape Verde. *Earth Planet. Sci. Lett.*, 289,156–161.

Hem, J.D. (1992) Study and interpretation of the chemical characteristics of natural water. U.S. Geological Survey Water Supply Paper 2254, 263 p.

Herzberg, C., Asimow, P. (2008) Petrology of some oceanic island basalts: PRIMELT2.XLS software for primary magma calculation. *Geochem. Geophys. Geosyst.*, 9, doi : 10.1029/2008GC002057.

Herzberg, C., Asimow, P.D., Arndt, N., Niu, Y., Lesher, C.M., Fitton, J.G., Cheadle, M.J., Saunders, A.D. (2007) Temperatures in ambient mantle and plumes: constraints from basalts, picrites, and komatiites. *Geochem. Geophys. Geosyst.*, 8, 10.1029/2006GC001390.

Hill, M.N. (1957) Recent geophysical exploration of the ocean floor. *Phys. Chem. Earth*, 2, 129-163.

Hirose, K., Takafuji, N., Sata, N., Ohishi, Y. (2005) Phase transition and density of subducted MORB crust in the lower mantle. *Earth Planet. Sci. Lett.*, 237, 239– 251.

Hirschmann, M.M., Stolper, E.M. (1996) A possible role for garnet pyroxenite in the origin of the "garnet signature" in MORB. *Contrib. Mineral. Petrol.*, 124, 185-208.

Hirschmann, M.M., Dasgupta, R. (2009) The H/C ratios of Earth's near-surface and deep reservoirs, and consequences for deep Earth volatile cycles. *Chem. Geol.*, 262, 4-16.

Hirschmann, M.M., Kogiso, T., Baker, M.B., Stolper, E.M. (2003) Alkalic magmas generated by partial melting of garnet pyroxenite. *Geology*, 31, 481-484.

Hoernle, K., Tilton, G., Schmincke, H.-U. (1991) Sr-Nd-Pb isotopic evolution of Gran Canaria: evidence for shallow enriched mantle beneath the Canary Islands. *Earth Planet. Sci. Lett.*, 106, 44-63.

Hoernle, K., Tilton, G., Le Bas, M.J., Duggen, S., Garbe-Schönberg, C.D. (2002) Geochemistry of oceanic carbonatites compared with continental carbonatites: mantle recycling of oceanic crustal carbonate. *Contrib. Mineral. Petrol.*, 142, 520-542.

Hofmann, A.W. (1997) Mantle geochemistry: the message from oceanic volcanism. *Nature*, 385, 219-229.

Hofmann, A.W. (2003) Sampling mantle heterogeneity trough oceanic basalts: isotopes and trace elements. In: Carlson, R. (Ed.) Treatise on geochemistry, vol. 2 - The mantle and core. Elsevier-Pergamon, Oxford, pp. 61 – 101.

Hofmann, A.W., White, W.M. (1982) Mantle plumes from ancient oceanic crust. *Earth Planet. Sci. Lett.*, 57, 421–436.

Hofmann, A.W., Jochum, K.P., Seufert, M., White, W.M. (1986) Nb and Pb in oceanic basalts: new constraints on mantle evolution. *Earth Planet. Sci. Lett.*, 79, 33-45.

Hofmann, A.W., Sobolev, A.V., Abouchami, W., Galer, S.J.G., Jochum, K.P. (2003) Scales of mantle heterogeneity and melting. *Geochim. Cosmochim. Acta*, 67, A153.

Holm, P.M., Wilson, J.R., Christensen, B.P., Hansen, L., Hansen, S.L., Hein, K.M., Mortensen, A.K., Pedersen, R., Plesner, S., Runge, M.K. (2006) Sampling the Cape Verde mantle plume: evolution of melt compositions on Santo Antão, Cape Verde Islands. *J. Petrol.*, 47, 145-189.

Holm, P.M., Grandvuinet, T., Friis, J., Wilson, J.R., Barker, A.K., Plesner, S. (2008) An ^{40}Ar-^{39}Ar study of the Cape Verde hot spot: Temporal evolution in a semistationary plate environment. *J. Geophys. Res.*, 113, B08201.

Holmes, A. (1946) An estimate of the age of the earth. *Nature*, 157, 680-684.

Houtermans, F.G. (1946). Die Isotopenhaufigkeiten im Naturalichen blei und das alter des Urans. *Naturwissenschaften*, 33, 185-186.

Houtz, R., and Ewing, J. (1976) Upper crustal structure as a function of plate age. *J. Geophy. Res.*, 81, 2490-2498.

Huang, S., Frey, F.A. (2005) Recycled oceanic crust in the Hawaiian plume: evidence from temporal geochemical variations within the Koolau Shield. *Contrib. Mineral. Petrol.*, 149, 556–575.

Huang, S., Frey, F., Blichert-Toft, J., Fodor, V., Bauer, G., Xu, G. (2005) Enriched components in the Hawaiian plume: Evidence from Kahoolawe Volcano, Hawaii. *Geochem. Geophys. Geosyst.*, 6, doi:10.1029/2005GC001012.

Humler, E., Langmuir, C., Daux, V. (1999) Depth versus age; new perspectives from the chemical compositions of ancient crust. *Earth Planet. Sci. Lett.*, 173, 7-23.

Humphreys, E., Niu, Y. (2009) On the composition of ocean island basalts (OIB): the effects of lithospheric thickness variation and mantle metasomatism. *Lithos*, 112, 118-136.

Humphris, S.E. (1976) The hydrothermal alteration of oceanic basalts by seawater. PhD thesis. Woods Hole Oceanographic Institute/M.I.T. 248 p.

Ionov, D.A., Dupuy, C., O'Reilly, S.Y., Kopylova, M.G., Genshaft, Y.S. (1993) Carbonated peridotite xenoliths from Spitsbergen: implications for trace element signature of mantle carbonate metasomatism. *Earth Planet. Sci. Lett.*, 119, 283–297.

Ionov, D.A., Griffin, W.L., O'Reilly, S.Y. (1997) Volatile-bearing minerals and lithophilic trace elements in the upper mantle. *Chem. Geol.*, 141, 153– 184.

Irvine, T.N., Baragar, W.R.A., (1971) A Guide to the Chemical Classification of the Common Volcanic Rocks. *Can. J. Earth Sci.*, 8, 523-548.

Ishikawa, A., Kurirani, T., Makishima, A., Nakamura, E. (2007) Ancient recycled crust beneath the Ontong Java Plateau; isotopic evidence from the garnet clinopyroxenite xenoliths. Malaita Solomon Islands. *Earth Planet. Sci. Lett.*, 259, 134-148.

Isshiki, M., Irifune, T., Hirose, K., Ono, S., Ohishi, Y., Watanuki, T., Nishiborl, E., Takata, M., Sakata, M. (2004) Stability of magnesite and its high-pressure from the lowermost mantle. *Nature*, 427, 60–63.

Jackson, M.G., Kurz, M.D., Hart, S., Workman, R.K. (2007) New Samoan lavas from Ofu Island reveal a hemispherically heterogeneous high $^{3}He/^{4}He$ mantle. *Earth Planet. Sci. Lett.*, 264, 360-374.

Jackson, M.G., Kurz, M.D., Hart, S.R. (2009) Helium and neon isotopes in phenocrysts from Samoan lavas: Evidence for heterogeneity in the terrestrial high $^{3}He/^{4}He$ mantle. *Earth Planet. Sci. Lett.*, 287, 519-528.

Jaffey, A.H., Flynn, K.F., Glendenin, L.E., Bentley, W.C., Essling, A.M. (1971) Precision measurements of half-lives and specific activities of ^{235}U and ^{238}U. *Phys. Rev.*, C4, 1889-1906.

Jafri, S.H., Charan, S.N. (1992) Quench textures in pillow basalt from the Andaman– Nicobar Islands, Bay of Bengal, India. *Proc. Indian Acad. Sci. (Earth and Planetary Sciences)*, 101, 99–107.

Jahn, B., Bernard-Griffiths, J., Charlot, R., Cornichet, J. & Vidal, F. (1980) Nd and Sr isotopic compositions and REE abundances of Cretaceous MORB (Holes 417D and 418A, Legs 51, 52, and 53). *Earth Planet. Sci. Lett.*, 48, 171–184.

Janney, P., Castillo, P. (2001) Geochemistry of the oldest Atlantic oceanic crust suggests mantle plume involvement in the early history of the central Atlantic Ocean. *Earth Planet. Sci. Lett.*, 192, 291-302.

Janney, P.E., Le Roex, A.P., Carlson, R.W. (2005) Hafnium isotope and trace element constraints on the nature of mantle heterogeneity beneath the Central Southwest Indian Ridge (13ºE to 47ºE). *J. Petrol.*, 46, 2427-2464.

Jarvis, G.T., Lowman, J.P. (2007) Survival times of subducted slab remnants in numerical models of mantle flow. *Earth Planet. Sci. Lett.*, 260, 23-36.

Johnson, K.T. (1998) Experimental determination of partition coefficients for rare earth and high-field-strength elements between clinopyroxene, garnet, and basaltic melt at high pressures. *Contrib. Mineral. Petrol.*, 133, 60-68.

Johnson, K.T., Dick, H.J., Shimizu, N. (1990) Melting in the oceanic upper mantle: an ion microprobe study of diopsides in abyssal peridotites. *J. Geophy. Res.*, 95, 2661–2678.

Jørgensen, J.Ø., Holm, P.M. (2002) Temporal variation and carbonatite contamination in primitive ocean island volcanics from São Vicente, Cape Verde Islands. *Chem. Geol.*, 192, 249-267.

Jung, S., Hoernes, S. (2000) The major- and trace-element and isotopic (Sr, Nd, O) geochemistry of Cenozoic alkaline rift-type volcanic rocks from the Rhön area (central Germany): petrology, mantle source characteristics and implications for asthenosphere-lithosphere interactions. *J. Volcanol. Geotherm. Res.*, 99, 27-53.

Kalt, A., Hegner, E., Satir, M. (1997) Nd, Sr and Pb isotopic evidence for diverse lithospheric mantle sources of East African Rift carbonatites. *Tectonophysics*, 278, 31–45.

Kamber, B.S., Collerson, K.D. (2000) Role of 'hidden' deeply subducted slabs in mantle depletion. *Chem. Geol.*, 166, 241–254.

Kauahikaua, J.; Cashman, K.; Clague, D.; Champion, D.; Hagstrum, J.(2002) Emplacement of the most recent lava flows on Hualalai Volcano, Hawai'i. *Bull. Volcanol.*, 64, 229-253.

Kawakatsu, H., Kumar, P., Takei, Y., Shinohara, M., Kanazawa, T., Arakai, E., Suyehiro K. (2009) Seismic evidence for sharp lithosphere-asthenosphere boundaries of oceanic plates. *Science*, 324, 499-502.

Kelemen, P.B., Dick, H.J. (1995) Focused melt flow and localized deformation in the upper mantle: Juxtaposition of replacive dunite and ductile shear zones in the Josephine peridotite, SW Oregon. *J. Geophys. Res.*, 100, 423-438.

Kelley, K.A., Plank, T., Ludden, J., Staudigel, H. (2003) Composition of altered oceanic crust at ODP Sites 801 and 1149. *Geochem. Geophys. Geosyst.*, 4, 8910. doi:10.1029/2002GC000435.

Kellogg, L.H., Hager, B.H., van der Hilst, R.D. (1999) Compositional stratification in the deep mantle. *Science*, 283, 1881-1884.

Kellogg, J.B., Jacobsen, S.B., O'Connell, R.J. (2002) Modeling the distribution of isotopic ratios in geochemical reservoirs. *Earth Planet. Sci. Lett.*, 204, 183-202.

Kendall J., Silver P. (1998) Investigating causes of D″ anistropy. *Geodyn. Ser.*, 28, 97-118.

Kennett, J.P. (1982) Marine Geology. Prentice-Hall, Englewood Cliffs, New Jersey

Keshav, S., Bizimis, M., Gudfinnsson, G., Sen, G., Fei, Y. (2006) Response to the comment by M. Lustrino on "High-pressure melting experiments on garnet pyroxenite and the alkalic-tholeiitic transition in ocean-island basalts" by Keshav et al. Earth Planet. Sci. Lett., 223, 365-379 (2004). *Earth Planet. Sci. Lett.*, 241, 997-999.

King. S. (2007) Hotspots and edge-driven convection. *Geology*, 65, 223-226.

King, S., Ritsema (2000) African hotspot volcanism: small-scale convection in the upper mantle beneath cratons. *Science*, 290, 1137–1140.

King, S., Anderson, D. (1998) Edge-driven convection. *Earth Planet. Sci. Lett.*, 160, 289-296.

Klemme, S., van der Laan, S.R., Foley, S.F., Günther, D. (1995) Experimentally determined trace and minor element partitioning between clinopyroxene and carbonatite melt under upper mantle conditions. *Earth Planet. Sci. Lett.*, 133, 439-448.

Klemme, S., Blundy, J.D., Wood, B.J. (2002) Experimental constraints on major and trace element partitioning during partial melting of eclogite. *Geochim. Cosmochim. Acta*, 66, 3109-3123.

Klemme, S., Prowatke, S., Hametner, K., Günther, D. (2005) The partitioning of trace elements between rutile and silicate melts: implications for subduction zones. *Geochim. Cosmochim. Acta*, 69, 2361–2371.

Klemme, S., Gunther, D., Hametner, K., Prowatke, S., Zack, T. (2006) The partitioning of trace elements between ilmenite, ulvospinel, armalcolite and silicate melts with implications for the early differentiation of the moon. *Chem. Geol.*, 234, 251–263.

Kogarko, L.N. (1993) Geochemical characteristics of oceanic carbonatites from the Cape Verde Islands. *S. Afr. J. Geol.*, 96, 119-125.

Kogarko, L.N.; Ryabukhin, V.A.; Volynets, M.P. (1992) Cape Verde Island carbonatite geochemistry. *Geochem. Int.*, 29, 62-74.

Kogarko, L., Kurat, G., Ntaflos, T. (2001) Carbonate metasomatism of the oceanic mantle beneath Fernando de Noronha Island, Brazil. *Contrib. Mineral. Petrol.*, 140, 577-587.

Kogiso, T., Hirose, K., Takahashi, E. (1998) Melting experiments on homogeneous mixtures of peridotite and basalt: application to the genesis of ocean island basalts. *Earth Planet. Sci. Lett.*, 162, 45-61.

Kogiso, T., Hirschmann, M. M., Frost, D. J. (2003) High-pressure partial melting of garnet pyroxenite: possible mafic lithologies in the source of ocean island basalts. *Earth Planet Sci. Lett.*, 216, 603-617.

Kogiso, T., Hirschmann, M.M., Pertermann, M. (2004) High pressure partial melting of mafic lithologies in the mantle. *J. Petrol.*, 45, 2407-2422.

Kokfelt, T.F., Holm, P.M., Hawkesworth, C.J., Peate, D.W. (1998) A lithospheric mantle source for the Cape Verde Island magmatism: Trace element and isotopic evidence from the island of Fogo. *Mineral. Mag.*, 62A, 801–802.

Korenaga, J. (2009) A method to estimate the composition of the bulk silicate Earth in the presence of a hidden geochemical reservoir. *Geochim. Cosmochim. Acta*, 73, 6952-6964.

Kurszlaukis, S., Lorenz, V. (1997) Volcanological features of low-viscosity melt: carbonatitic Gross Brukkaros Volcanic Field, Namibia. *Bull. Volcanol.*, 58, 421-431.

Labails, C., Olivet, J.L., Aslanian, D., Roest, W.R. (2010) An alternative early opening scenario for the Central Atlantic Ocean. *Earth Planet Sci. Lett.*, 297, 355–368.

Labrosse, S., Hernlund, J.W., Coltice, N. (2007) A crystallizing dense magma ocean at the base of the Earth's mantle. *Nature*, 450, 866–869.

Langmuir, C.H., Klein, E.M., Plank, T. (1992) Petrology systematics of mid-ocean ridge basalts: constraints on melt generation beneath ocean ridges. In: Phipps Morgan, J., Blackman, D. K. and Sinton, J. M. (Eds) Mantle Flow and Melt Generation at Mid-Ocean Ridges. Geophysical Monograph, American Geophyisical Union 71,183–280.

Lancelot, Y., Seibold, E., Cepek, P., Dean, W., Eremeeev, V., Gardener, J. et al. (1978) Site 368: Cape Verde rise. In: Lancelot, Y., Seibold, E., Cepek, P., Dean, W., Eremeeev, V., Gardener, J. et al. (Eds) Initial Reports of the Deep Sea Drilling Project 41. Washington D.C., U.S. Government Printing Office.

Laske, G., Phipps Morgan, J., Orcutt, J. (2007) The Hawaiian SWELL pilot experiment – evidence for lithosphere rejuvenation from ocean bottom surface wave data. In: Foulger, G.R., Jurdy, D.M. (Eds.). Plates, Plumes, and Planetary Processes. *Geol. Soc. Am. Special Paper*, 430, pp. 257-278.

LaTourrette, T.Z., Hervig, R.L., Holloway, J.R. (1995) Trace element partitioning between amphibole, phlogopite, and basanite melt. *Earth Planet. Sci. Lett.*, 135, 13-30.

Lay, T., Williams, Q., Garnero, E. (1998) The core-mantle boundary layer and deep Earth dynamics. *Nature*, 392, 461-468.

Lay, T., Hernlund, J., Buffett, B. A. (2008) Core-mantle boundary heat flow. *Nat. Geosci.*, 1, 25-32.

Le Bas, M. (1962) The role of aluminum in igneous clinopyroxenes with relation to their parentage. *Am. J. Sci.*, 260, 267-288.

Le Bas, M. (1981) Carbonatite magmas. *Mineral. Mag.*, 44, 133-140.

Le Bas, M. (1989) Nephelinitic and basanitic rocks. *J. Petrol.*, 30, 1299-1312.

Le Bas, M. (2008) Fenites associated with carbonatites. *Can. Min.*, 46, 915-932.

Le Bas, M., Streckeisen, A. (1991) The IUGS systematics of igneous rocks. *J. Geol. Soc. London*, 148, 825-833.

Le Bas, M., Le Maitre, R.W., Streckeisen, A.L., Zanettin, B. (1986) A chemical classification of volcanic rocks based on the Total Alkali-Silica diagram. *J. Petrol.*, 27, 745-750.

Le Bas, T.P.; Masson, D.G.; Wynn, R.B.; Grevemeyer, L. (2005) Catastrophic landslides around the Cape Verde Islands. Abstracts of the International Workshop on Oeean Island Volcanism, Sal, Cape Verde: 49.

Le Maitre, R.W., Streickeisen, A., Zanettin, B., Le Bas, M.J., Bonin, B., Bateman, P., Bellieni, G., Dudek, A., Efremova, S., Keller, J., Lamey, J., Sabine, P.A., Schmid, R., Sørensen, H., Woolley, A.R. (2002) Igneous Rocks, a classification and glossary of terms, 2nd Edition. Cambridge University Press, 236 p.

Le Roux, V., Lee, C.-T., Turner, S.J. (2010) Zn/Fe systematics in mafic and ultramafic systems: implications for detecting major element heterogeneities in the Earth's mantle. *Geochim. Cosmochim. Acta*, 74, 2779-2796.

Leake, B.E., Woolley, A.R., Arps, C.E.S., Birch, W.D., Gilbert, M.C., Grice, J.D., Hawthorne, F.C., Kato, A., Kisch, H.J., Krivovichev, V.G., Linthout, K., Laird, J., Mandarino, J.A., Maresch, W.V., Nickel, E.H., Rock, N.M.S., Schumacher, J.C., Smith, D.C., Stephenson, N.C.N., Ungaretti, L., Whittaker, E.J.W., Youzhi, G. (1997) Nomenclature of amphiboles: Report of the Subcommittee on Amphiboles of the International Mineralogical Association, Commission on New Minerals and Mineral Names. *Am. Mineral.*, 82, 1019–1037.

Lee, C.-T., Luffi, P., Höink, T., Dasgupta, R., Hernlund, J. (2010) Upside-down differentiation and generation of a "primordial" lower mantle. *Nature*, 463, 930-935.

Lee, W.-J., Wyllie, P.J., (1994) Experimental data bearing on liquid immiscibility, crystal fractionation, and the origin of calciocarbonatites. *Int. Geol. Rev.*, 36, 797–819.

Lee, W.-J., Wyllie, P.J., (1998) Processes of crustal carbonatite formation by liquid immiscibility and differentiation, elucidated by model systems. *J. Petrol.*, 39, 2005–2013.

Leterrier, J., Maury, R.C., Thonon, P., Girard, D., Marchal, M., (1982) Clinopyroxene composition as a method of identification of the magmatic affinities of paleo-volcanic series. *Earth Planet Sci. Lett.*, 59, 139-154.

Li, C., Ripley, E.M. (2010) The relative effects of composition and temperature on olivine-liquid Ni partitioning: statistical deconvolution and implications for petrologic modeling. *Chem. Geol.*, 275, 99-104.

Li, X., Götze, H-J. (2001) Ellipsoid, geoid, gravity, geodesy, and geophysics. *Geophysics*, 66, 1660-1668.

Lo, P.G., Dia, A., Kampunzu, A.B. (1992) Cenozoic volcanism in Western Senegal and its relationship to the opening of the Central Atlantic Ocean. *Tectonophysics*, 209, 281-291.

Lodge, A., Helffrich, G. (2006) Depleted swell root beneath the Cape Verde Islands. *Geology*, 34, 449-452.

Lopes, V., Meyer, J. (1993) Watershed management program on Santiago Island, Cape Verde. *Environ. Manage.*, 17, 51-57.

Lundstrom, C.C., Hoernle, K., Gill, J. (2003) U-series disequilibria in volcanic rocks from the Canary Islands: plume versus lithospheric melting. *Geochim. Cosmochim. Acta*, 67, 4153–4177.

Lynner, C., Long, M. (2014) Lowermost mantle anisotropy and deformation along the boundary of the African LLSVP. *Geophys. Res. Lett.*, 41, 3447–3454,

Lyubetskaya, T., Korenaga, J. (2007a) Chemical composition of Earth's primitive mantle and its variance: 1. Methods and results. *J. Geophys. Res.*, 112, B03211. doi:10.1029/2005JB004223.

Lyubetskaya, T., Korenaga, J. (2007b) Chemical composition of Earth's primitive mantle and its variance: 2. Implications for global geodynamics. *J. Geophys. Res.*, 112, B03212. doi:10.1029/2005JB004224.

Macdonald, G.A., Katsura, T. (1964) Chemical composition of Hawaiian lavas. *J. Petrol.*, 5, 82-133.

Machado, F. (1967) Geologia das Ilhas de Cabo Verde. Agrupamento Científico de Geologia da Universidade de Lisboa da Junta de Investigação do Ultramar, 1-25.

Madeira, J., Brum da Silveira, A. (2005) Geomorphic and structural analysis of the Fogo island volcano (Cape Verde). Abstracts of the International Workshop on Ocean Island Volcanism, Sal, Cape Verde: 49.

Madeira, J., Munhá, J., Tassinari, C., Mata, J., Brum, A., Martins, S. (2005) K/Ar ages of carbonatites from the Island of Fogo (Cape Verde). VIII Congresso Ibérico de Geoquímica e XIV Semana de Geoquímica (Portugal).

Madeira, J., Brum da Silveira, A., Mata, J., Mourão, C., Martins, S., (2008) The role of mass movements on the geomorphologic evolution of ocean islands: examples from Fogo and Brava in the Cape Verde archipelago. *Comun. Geol.*, 95, 99–112.

Madeira, J., Mata, J., Mourão, C., Brum da Silveira, A., Martins, S., Ramalho, R., Hoffmann, D.L. (2010) Volcano-stratigraphic and structural evolution of Brava Island (Cape Verde) based on $^{40}Ar/^{39}Ar$, U–Th and field constraints. *J. Volcanol. Geotherm. Res.*, 196, 219-235.

Madureira, P., Mata, J., Mattielli, N., Queiroz, G., Silva, P. (2011) Mantle source heterogeneity, magma generation and magmatic evolution at Terceira Island (Azores archipelago): Constraints from elemental and isotopic (Sr, Nd, Hf, and Pb) data. *Lithos*, 126, 402-418.

Mannaerts, C.M., Gabriels, D. (2000) Rainfall erosivity in Cape Verde. *Soil & Tillage Research*, 55, 207-212.

Marks, K.M., Sandwell, D.T. (1991) Analysis of geoid height versus topography for oceanic plateaus and swells using nonbiased linear regression. *J. Geophys. Res.*, 96, 8045-8055.

Martins, S. (2003) Petrologia e geoquímica das lavas da ilha de Santiago (Cabo Verde). Departamento de Geologia (Faculdade de Ciências da Universidade de Lisboa). Masters dissertation, 233 pp.

Martins, S., Mata, J., Munhá, J. (2003) Chemical evidence for complex and variable mantle residual paragenesis in the Santiago Island (Cape Verde). *Memórias e Notícias (Universidade de Coimbra)*, 2, 19-37.

Martins, S., Mata, J., Munhá, J., Mattielli, N. (2007) Elemental and isotopic constraints on the nature of mantle metasomatism at Santiago Island (Cape Verde). European Geosciences Meeting (Vienna, Austria). *Geophys. Res. Abstr.*, 9, 10296.

Martins, S., Mata, J., Munhá, J., Mendes, M.H., Maerschalk, C., Caldeira, R., Mattielli, N. (2010) Chemical and mineralogical evidence of the occurrence of mantle metasomatism by carbonate-rich melts in an oceanic environment (Santiago Island, Cape Verde). *Mineral. Petrol.*, 99, 43-65.

Masson, D.G., Le Bas, T.P., Grevemeyer, L.; Weinrebe,W. (2008) Flank collapse and large-scale landsliding in the Cape Verde Islands, off West Africa. *Geochem. Geophys. Geosyst.*, 9, doi:10.1029/2008GCOOI983.

Mata, J. (1996) Petrologia e Geoquímica das lavas da Ilha da Madeira: implicações para os modelos de evolução do manto. PhD thesis (Lisbon University), 471 pp.

Mata, J. (1998) Earth mantle geochemical evolution: a diachronic fractionation model for U/Pb and Th/U ratios. Goldschmidt Conference (Toulouse, France). *Mineral. Mag.*, 62A, 965-966.

Mata, J., Kerrich, R. (2003) Lead paradoxes as a result of the secular evolution of crustal recycling processes. American Geophysical Union-2003 Fall Meeting, S. Francisco (USA).

Mata, J., Kerrich, R., Macrae, N.D., Wu, T-W. (1998) Elemental and isotopic (Sr, Nd, and Pb) characteristics of Madeira Island basalts: evidence for a composite HIMU - EMI plume fertilizing lithosphere. *Can. J. Earth Sci.*, 35, 980-997.

Mata, J., Munhá, J., Kerrich, R. (1999) Evidências para a ocorrência de metassomatismo carbonatitico na fonte mantélica da Ilha da Madeira. Anais do V Congresso Geoquímico dos Países de Língua Portuguesa (Porto Seguro, Brasil), 550-551.

Mata, J., Kerrich, R., Gonçalves, M.A. (2007) Earth's mantle Th/U and U/Pb evolution in the Archean. 2007 Goldschmidt Conference (Cologne). *Geochim. Cosmochim. Acta*, 71 (15S), A635.

Mata, J., Moreira, M., Doucelance, R., Ader, M., and Silva, L. C. (2010) Noble gas and carbon isotopic signatures of Cape Verde oceanic carbonatites: Implications for carbon provenance. *Earth Planet. Sci. Lett.,* 291, 70–83.

Mata, J., Martins, S., Mourão, C., Munhá, J. (2010) The lithosphere influence on the composition of plume magmas at the Cape Verde archipelago. American Geophysical Union 2010 Meeting of Americas (Iguaçú, Brasil).

Matias, L., Cruz, J., Pena, J.A., Martins, I., Senos, M.L., (1997) A sismicidade registada na ilha do Fogo durante os primeiros dias de actividade do vulcão na erupção de Abril de 1995. In: Réffega, A. (Eds.), A Erupção Vulcânica de 1995 na Ilha do Fogo, Cabo Verde. IICT, Lisboa, 13-32.

Mattielli, N., Weis, D., Scoates, J.S., Shimizu, N., Mennessier, J.-P., Grégoire, M., Cottin, J.-Y., Giret, A. (1999) Evolution of heterogeneous lithospheric mantle in a plume environment beneath the Kerguelen Archipelago. *J. Petrol.*, 40, 1721-1744.

Mattielli, N., Weis, D., Blichert-Toft, J., Albarède, F. (2002) Hf isotope evidence for Miocene change in the Kerguelen mantle plume composition. *J. Petrol.*, 43, 1327-1339.

Matveev, S., O'Neill, H.St.C., Ballhaus, C., Taylor, W.R., Green, D.H. (2001) Effect of silica activity for low-aSiO_2 mantle metasomatism. *J. Petrol.*, 42, 721-729.

Matyska, C., Yuen, D.A. (2008) Lower mantle material properties and convection models of multiscale plumes. in Foulger, G.R., and Jurdy, D.M., (Eds.) Plates, plumes, and planetary processes. *Geol. Soc. Am. Special Paper*, 430, pp. 137–163

McBirney, A. (2007) Igneous Petrology, 3rd Edition. Jones & Bartlett Publishers, 550 p.

McDade, P., Blundy, J.D., Wood, B.J. (2003) Trace element partitioning on the Tinaquillo lherzolite solidus at 1.5 GPa. *Phys. Earth Planet. Inter.*, 139, 129-147.

McDonough, W.F., Sun, S.-S. (1995) The composition of the Earth. *Chem. Geol.*, 120, 223-253.

McKenzie, D., Bickle, M. (1988) The volume and composition of melt generated by extension of the lithosphere. *J. Petrol.*, 29, 625-697.

McKenzie, D., O'Nions, R.K. (1991) Partial melt distributions from inversion of rare earth element concentrations. *J. Petrol.*, 32, 1021-1091.

McKenzie, D., Jackson, J., Priestley, K. (2005) Thermal structure of oceanic and continental lithosphere. *Earth Planet. Sci. Lett.*, 233, 337–349.

McNamara, A., Garnero, E., Rost, S. (2010) Tracking deep mantle reservoirs with ultra-low velocity zones. *Earth Planet. Sci. Lett.*, 299, 1-9.

McNutt, M.K. (1988) Thermal and mechanical properties of the Cape Verde Rise. J. *Geophys. Res.*, 93, 2784-2794.

McPherson, E., Thirlwall, M.F., Parkinson, I.J., Menzies, M.A., Bodinier, J.L., Woodland, A., Bussod, G. (1996) Geochemistry of metasomatism adjacent to amphibole-bearing veins in the Lherz peridotite massif. *Chem. Geol.*, 134, 135-157.

Meco, J., Scaillet, S., Guillou, H., Lomoschitz, A., Carracedo, J., Ballester, J., Betancort, J-F., Cilleros, A. (2007) Evidence for long-term uplift on the Canary Islands from emergent Mio-Pliocene littoral deposits. *Global Planet. Change*, 57, 222-234.

Meibom, A., Anderson, D. (2003) The statistical upper mantle assemblage. *Earth Planet. Sci. Lett.*, 217, 123-139.

Mendes, M.H. (1995) Petrologia e geoquímica dos xenólitos peridotíticos da ilha de Santiago, arquipélago de Cabo Verde. Thesis, IICT, Portugal, pp. 186.

Mendes, M.H., Silva, L.C. (2001) Xenólitos crustais nas ilhas de Cabo Verde: características petrográficas e química mineral. VI Congresso de Geoquímica dos Países de Língua Portuguesa, XII Semana da Geoquímica, 153-156.

Meschede, M. (1986) A method of discriminating between different types of mid-ocean ridge basalts and continental tholeiites with the Nb-Zr-Y diagram. *Chem. Geol.*, 56, 207–218.

Meurer, W.P., Sturm, M.A., Klein, E.M., Karson, J.A. (2001) Basalt compositions from the Mid-Atlantic Ridge at the SMARK area (22°30′N to 22°50′N)—implications for parental liquid variability at isotopically homogeneous spreading centers. *Earth Planet. Sci. Lett.*, 186, 451–469

Middlemost, E.A.K. (1975) The basalt clan. *Earth-Sci. Rev.*, 11, 337-364.

Middlemost, E.A.K. (1989) Iron oxidation ratios, norms and the classification of volcanic rocks. *Chem. Geol.*, 77, 19-26.

Miller, K., Kominz, M., Browning, J., Wright, J., Mountain, G., Katz, M., Sugarman, P., Cramer, B., Christie-Blick, N., Pekar, S. (2005) The Phanerozoic record of global sea-level change. *Science*, 310, 1293-1298.

Millet, M.A., Doucelance, R., Schiano, P., David, K., Bosq, C. (2008) Mantle plume heterogeneity versus shallow-level interactions: A case study, the São Nicolau Island, Cape Verde archipelago *J. Volcanol. Geotherm. Res.*, 176, 265-276.

Mirnejad, H., Bell, K. (2006) Origin and source evolution of the Leucite Hills lamproites: evidence from Sr-Nd-Pb-O isotopic compositions. *J. Petrol.*, 47, 2463-2489.

Mitchell, J.G., Le Bas, M.J., Zielonka, J., Furnes, H. (1983) On dating the magmatism of Maio, Cape Verde Islands. *Earth Planet. Sci. Lett.*, 64, 61-76.

Mitchell-Thomé, R.C. (1976) Geology of Midlle Atlantic Islands. Gebrüder Borntraeger (Berlin), 382 pp.

Moine, B.N., Grégoire, M., O'Reilly, S.Y., Sheppard, S.M.F., Cottin, J.Y. (2001) High field strength element fractionation in the upper mantle: evidence from amphibole-rich composite mantle xenoliths from the Kerguelen Islands (Indian Ocean). *J. Petrol.*, 42, 2145-2167.

Moine B.N., Grégoire, M., O'Reilly, S.Y., Delpech, G., Sheppard, S., Lorand, J.P., Renac, C., Giret, A., Cottin, J.Y. (2004) Carbonatite melt in oceanic upper mantle beneath the Kerguelen Archipelago. *Lithos*, 75, 239-252.

Monnereau, M., Cazenave, A. (1988) Variation of the apparent compensation depth of hotspot swells with age of plate. *Earth Planet. Sci. Lett.*, 91, 179-197.

Montelli, R., Nolet, G., Dahlen, F., Masters, G., Engdahl, E., Hung, S-H. (2004) Finite-frequency tomography reveals a variety of plumes in the mantle. *Science*, 303, 338-343.

Montelli, R., Nolet, G., Dahlen, F.A., Masters, G. (2006) A catalogue of deep mantle plumes: new results from finite-frequency tomography. *Geochem. Geophys. Geosyst.*, 7, doi:10.1029/2006GC001248.

Moreira, M., Kunz, J., Allègre, C. (1998) Rare gas systematics in popping rock: isotopic and elemental compositions in the upper mantle. *Science*, 279, 1178–1181.

Morgan, W.J. (1971) Convection plumes in the lower mantle. *Nature*, 230, 42-43.

Mortensen, A.K., Wilson, J.R., Holm, P. (2009) The Cão Grande phonolitic fall deposit on Snato Antão, Cape Verde Islands. *J. Volcanol. Geotherm. Res.*, 179, 120-132.

Mourão, C., Mata, J., Moreira, M., Doucelance, R., Madeira, J. (2007) Further Helium isotopic evidence for a lower mantle contribution to the Cape Verde plume. 2007 Goldschmidt Conference (Cologne). *Geochim. Cosmochim. Acta*, 71 (15S), A691.

Mourão, C., Mata, J., Doucelance, R., Madeira, J., Brum da Silveira, A., Silva, L.C., Moreira, M. (2010) Quaternary extrusive calciocarbonatite volcanism on Brava Island (Cape Verde): a nephelinite–carbonatite immiscibility product. *J. Afr. Earth Sci.*, 56, 59–74.

Mourão, C., Moreira, M., Mata, J., Raquin, A., Madeira, J. (2012a) Primary and secondary processes constraining the noble gas isotopic signatures of carbonatites and silicate rocks from Brava Island: evidence for a lower mantle origin of the Cape Verde plume. *Contrib. Mineral. Petrol.*, 163, 995–1009.

Mourão, C., Mata, J., Doucelance, R., Madeira, J., Millet, M-A., Moreira, M. (2012b) Geochemical temporal evolution of Brava Island magmatism: constraints on the variability of Cape Verde mantle sources and on the carbonatite-silicate magma link. *Chem. Geol.*, 334, 44-61.

Müller, R.D., Sdrolias, M., Gaina, C., Roest, W.R. (2008) Age, spreading rates and spreading symmetry of the world's ocean crust. *Geochem. Geophys. Geosyst.*, 9, doi:10.1029/2007GC001743.

Munhá, J., Mata, J., Martins, S., Tassinari, C., Madeira, J. (2006) Physical-chemical conditions during crystallization of Fogo Holocene lavas (Cape Verde): implications for the morphological evolution of oceanic islands. European Geosciences Meeting (Vienna, Austria). *Geophys. Res. Abs.*, 8, 09043.

Münker, C., Pfänder, J.A., Weyer, S., Büchl, A., Kleine, T., Mezger, K. (2003) Evolution of planetary cores and the Earth–Moon system from Nb/Ta systematics. *Science*, 301, 84–87.

Nakamura, K., Kato, Y., Tamaki, K., Teruaki, I. (2007) Geochemistry of hydrothermally altered basaltic rocks from the Southwest Indian Ridge near the Rodriguez Triple Junction. *Mar Geol.*, 239, 125–141.

Nelson, D.R., Chivas, A.R., Chappell, B.W., MuCulloch, M.T. (1988) Geochemical and isotopic systematics in carbonatites and implications for the evolution of ocean-island sources. *Geochim. Cosmochim. Acta*, 52, 1-17.

Neumann, H., Mead, J., Vitaliano, C.J. (1954) Trace element variations during fractional crystallization as calculated from the distribution law. *Geochim. Cosmochim Acta*, 6, 90-99.

Neuman, E.-R., Sorensen,V. B., Simonsen, S. L, Johnson, K. (2000) Gabbroic xenoliths from La Palma, Tenerife and Lanzarote, Canary Islands: evidence for reactions between mafic alkaline Canary Islands melts and old oceanic crust. *J. Volcanol. Geotherm. Res.*, 103, 313-342.

Neumann, E.-R., Vannucci, R.,Tiepolo, M. (2005) N-MORB crust beneath Fuerteventura in the easternmost part of the Canary Islands: evidence from gabbroic xenoliths. *Contrib. Mineral. Petrol.*, 150, 156- 173.

Ni, S., Tan, E., Gurnis, M., Helmberger, D. (2002) Sharp sides to the African superplume. Science, 296, 1850-1852.

Niu, Y. (2009) Some basic concepts and problems on the petrogenesis of intra-plate ocean island basalts. *Chinese Sci. Bull.*, 54, 4148-4160.

Niu, Y., Hékinian, R. (1997) Basaltic liquids and harzburgitic residues in the Garrett Transform: A case study at fast-spreading ridges. *Earth Planet Sci. Lett.*, 146, 243-258

Niu, Y., O'Hara, M.J. (2003) Origin of ocean island basalts; a new perspective from petrology, geochemistry, and mineral physics considerations. *J. Geophys. Res.*, 108, doi: 10.1029/2002JB002048.

Niu, Y., O'Hara, M.J. (2004) Mantle plumes are not from ancient oceanic crust. In: Hekinian, R., Stoffers, P., Cheminée, J.-L. (Eds.) Oceanic Hotspots, Intraplate Submarine Magmatism and Tectonism. Springer-Verlag, New York, pp. 239–252.

Niu Y., O'Hara, M J. (2007) Varying Ni in OIB olivines-product of process not source. *Geochim. Cosmochim. Acta*, 71, A721-A721.

Niu, Y., O'Hara, M.J. (2008) Global correlations of ocean ridge basalt chemistry with axial depth: A new perspective. *J. Petrol.*, 49, 633-664.

Niu, Y., Wilson, M., Humphreys, E., O'Hara, M. (2011) The Origin of Intra-plate Ocean Island Basalts (OIB): the Lid Effect and its Geodynamic Implications. *J. Petrol.*, 52, 1443-1468.

Niu, Y.L., Wilson, M., Humphreys, E.R., O'Hara, M.J. (2012) A trace element perspective on the source of ocean island basalts (OIB) and fate of subducted ocean crust (SOC) and mantle lithosphere (SML). *Episodes*, 35, 310-317.

Nobre Silva, I.G., Weis, D., Barling, J., Scoates, J. (2009) Leaching systematics and matrix elimination for the determination of high-precision Pb isotope compositions of ocean island basalts. *Geochem. Geophys. Geosyst.*, 10, doi:10.1029/2009GC002537.

O'Connor, J., Stoffers, P., van der Bogaard, P., McWilliams, M. (1999) First seamount age evidence for significantly slower African plate motion since 19 to 30 Ma. *Earth Planet. Sci. Lett.*, 171, 575-589.

O'Hara, M.J., Richardson, S.W., Wilson, G. (1971) Garnet-peridotite stability and occurrence in crust and mantle. *Contrib. Mineral. Petrol.*, 32, 48-68.

O'Nions, R.K., Oxburgh, E.R. (1983) Heat and helium budget in the Earth. *Nature*, 306, 429-431.

O'Nions, R.K., Frank, M., von Blanckenburg, F., Ling, H.-F. (1998) Secular variation of Nd and Pb isotopes in ferromanganese crusts. *Earth Planet. Sci. Lett.*, 155, 15-28.

O'Reilly, S.Y., Griffin, W.L. (2012) Mantle Metasomatism. In: Harlov, D., Austrheim, H. (Eds.) Metasomatism and the Chemical Transformation of Rock: The Role of Fluids in Terrestrial and Extraterrestrial Processes (Lecture Notes in Earth System Sciences). Springer-Verlag, Berlin, pp. 471-533.

O'Reilly, S.Y., Griffin, W.L., Ryan, C.G. (1991) Residence of trace elements in metasomatized spinel lherzolite xenoliths: a proton-ion microprobe study. *Contrib. Mineral. Petrol.*, 109, 98-113.

O'Reilly, S.Y., Zhang, M., Griffin, W.L., Begg, G., Hronsky, J. (2009) Ultradeep continental roots and their oceanic remnants: a solution to the geochemical "mantle reservoir" problem? *Lithos*, 112, 1043-1054.

Odling, N.W.A. (1994) An experimental simulation of upper mantle metasomatism. *Am. Mineral.*, 79, 148-153.

Oyarzun, R., Doblas, M., López-Ruiz, J., Cebriá, J.M. (1997) Opening of the central Atlantic and asymmetric mantle upwelling phenomena: implications for long-lived magmatism in western North Africa and Europe. *Geology*, 25, 727-730.

Palme, H., O'Neill, H.St.C. (2003) Cosmochemical estimates of mantle compositions. In: Carlson, R. (Ed.) The mantle and core. Treatise on Geochemistry, 2, pp. 1-38.

Panina, L.I., Motorina, I.V. (2008) Liquid immiscibility in deep-seated magmas and the generation of carbonatite melts. *Geochem. Internal.*, 46, 448–464.

Parson, B., Sclater, J.G. (1977) An analysis of the variation of ocean floor bathymetry and heat flow with age. *J. Geophys. Res.*, 82, 803-827.

Patriat, M., Labails, C. (2006). Linking the Canary and Cape Verde hot-spots, Northwest Africa. *Mar. Geophys. Res.*, 27, 201-215.

Patterson, C. (1956) Age of meteorites and the Earth. *Geochim. Cosmochim. Acta*, 10, 230–237.

Pearson, D.G., Canil, D., Shirey, S.B. (2003) Mantle samples included in volcanic rocks: xenoliths and diamonds. In: Carlson, R. (Ed.) The mantle and core. Treatise on Geochemistry, 2, pp. 171-275.

Perinelli, C., Orlando, A., Conte, A.M., Armienti, P., Borrini, D., Faccini, B., Misiti, V. (2008) Metasomatism induced by alkaline magma in the upper mantle of northern Victoria Land (Antarctica): an experimental approach. In: Coltorti,M., Grégoire, M. (Eds). Metasomatism in Oceanic and Continental Lithospheric Mantle. *Geol. Soc. Spec. Publ.,* 293, 279-302.

Pertermann, M., Hirschmann, M.M., Hametner, K., Günther, D., Schmidt, M.W. (2004) Experimental determination of trace element partitioning between garnet and silica-rich liquid during anhydrous partial melting of MORB-like eclogite. *Geochem. Geophys. Geosyst.*, 5, doi:10.1029/2003GC000638.

Pfänder, J., Münker, C., Stracke, A., Mezger, K. (2007) Nb/Ta and Zr/Hf in ocean island basalts – implications for crust-mantle differentiation and the fate of Niobium. *Earth Planet. Sci. Lett.*, 254, 158-172.

Philpotts, J.A. (1970) Redox estimation from a calculation of Eu^{2+} and Eu^{3+} concentration in natural phases. *Earth Planet. Sci. Lett.*, 9, 257-268.

Pilet, S., Hernandez, J., Villemant, B. (2002) Evidence for high silicic melt circulation and metasomatic events in the mantle beneath alkaline provinces: the Na-Fe-augitic green-core pyroxenes in the Tertiary alkali basalts of the Cantal massif (French Massif Central). *Min. Petrol.*, 76, 39-62.

Pilet, S., Hernandez, J., Sylvester, P., Poujol, M. (2005) The metasomatic alternative for oceanic basalt chemical heterogeneity. *Earth Planet. Sci. Lett.*, 236, 148-166.

Pilet, S., Baker, M., Stolper, E. (2008) Metasomatized lithosphere and the origin of alkaline lavas. *Science*, 320, 916-919.

Pim, J. (2006) Crustal structure, lithospheric flexure and the origin of the Cape Verde Rise. MESci. thesis (unpublished). University of Oxford, 95 pp.

Pim, J., Peirce, C., Watts, A.B., Grevemeyer, I., Krabbenhoeft, A. (2008) Crustal structure and the origin of the Cape Verde Rise. *Earth Planet. Sci. Lett.*, 272, 422-428.

Plesner, S., Holm, P.M., Wilson, J.R. (2002) ^{40}Ar-^{39}Ar geochronology of Santo Antao, Cape Verde Islands. *J. Volcanol. Geotherm. Res.*, 120, 103-121.

Plimer, I. (2003) The Past is the Key to the Present: Greenhouse and Icehouse over Time. *Institute of Public Affairs Review*, 9–13.

Pollitz, F. (1991) Two-stage model of African absolute motion during the last 30 million years. *Tectonophysics*, 194, 91-106.

Prelević, D., Stracke, A., Foley, S.F., Romer, R.L., Conticelli, S. (2010) Hf isotope compositions of Mediterranean lamproites: Mixing of melts from asthenosphere and crustally contaminated mantle lithosphere. *Lithos*, 119, 297-312.

Presnall, D.C., Gudfinnsson, G.H., Walter, M.J. (2002) Generation of mid-ocean ridge basalts at pressures from 1 to 7 GPa. *Geochim. Cosmochim. Acta*, 66, 2073-2090.

Prytulak, J., Elliott, T. (2007) TiO_2 enrichment in ocean island basalts. *Earth Planet Sci Lett.*, 263, 388-403.

Putirka, K. (2005) Mantle potential temperatures at Hawaii, Iceland, and the mid-ocean ridge system, as inferred from olivine phenocrysts: Evidence for thermally driven mantle plumes. *Geochem. Geophys. Geosys.*, 6, doi:10.1029/2005GC000915.

Putirka, K. (2008) Excess temperatures at ocean islands: Implications for mantle layering and convection. *Geology*, 36, 283-286.

Putirka, K.D., Ryerson, F. (2008) Olivine compositions from the Hawaii Scientific Drilling Project, Phase 2: evidence for a peridotite mantle source region. *American Geophysical Union, Fall Meeting*, V13D-2145.

Putirka, K.D., Perfit, M., Ryerson, F.J., Jackson, M.G. (2007) Ambient and excess mantle temperatures, olivine thermometry, and active vs. passive upwelling. *Chem. Geol.*, 241, 177–206.

Rabinowicz, M., Ricard, Y., Grégoire, M. (2002) Compaction in a mantle with a very small melt concentration: implications for the generation of carbonatitic and carbonate-bearing high alkaline mafic melt impregnations. *Earth Planet. Sci. Lett.*, 203, 205-220.

Raitt, R.W. (1963) The crustal rocks, in Hill, M.N., ed., The Sea, Volume 3: New York, Wiley Interscience, 85-102.

Ramalho, R. (2012) The evolution of ocean island volcanoes in a stationary plate environment and its implications concerning hotspot dynamics. *Geophys. Res. Abs.*, 14, 4084.

Ramalho, R., Helffrich, G., Cosca, M., Vance, D., Hoffmann, D., Schmidt, D.N. (2010a) Episodic swell growth inferred from variable uplift of the Cape Verde hotspot islands. *Nat. Geosci.,* 3, 774-777.

Ramalho, R., Helffrich, G., Cosca, M., Vance, D., Hoffmann, D., Schmidt, D.N. (2010b) Vertical movements of ocean island volcanoes: insights from a stationary plate environment. *Mar. Geol.*, 275, 84-95.

Ramalho, R., Helffrich, G., Schmidt, D.N., Vance, D. (2010c) Tracers of uplift and subsidence in the Cape Verde archipelago. *J. Geol. Soc. London*, 167, 1-19.

Raymo, M., Grant, B., Horowitz, M., Rau, G. (1996) Mid-Pliocene warmth: stronger greenhouse and strong conveyor. *Mar. Micropalentol.*, 27, 313-326.

Rehkämper, M., Hofmann, A.W. (1997) Recycled ocean crust and sediment in Indian Ocean MORB. *Earth Planet. Sci. Lett.*, 147, 93-106.

Rice, S., Langmuir, C.H., Bender, J.F., Hanson, G.N.,. Bence, A.E, Taylor, S. (1980) Basalts from Deep Sea Drilling Project holes 417A and 417D, fractionated melts of a light rare-earth depleted source. Initial Reports of the Deep Sea Drilling Project Vol. 51, 52, 53 (Part 2) Publisher: Texas A & M University, Ocean Drilling Program, College Station, TX, United States.

Rickli, J., Frank, M., Halliday, A. (2009) The hafnium–neodymium isotopic composition of Atlantic seawater. *Earth Planet. Sci. Lett.*, 280, 118-127.

Rieder, M., Cavazzini, G., D'Yakonov, Y.S., Frank-Kamenetskii, V.A., Gottardi, G., Guggenheim, S., Koval, P.V., Muller, G., Neiva, A.M.R., Radoslovich, E.W., Robert, J.-L., Sassi, F.P., Takeda, H.,Weiss, Z., Wones, D.R., 1998. Nomenclature of micas. *Can. Mineral.*, 36, 41-48.

Roeder, P.L., Emslie, R.F. (1970) Olivine-liquid equilibrium. *Contrib. Mineral. Petrol.*, 29, 275-289.

Rollinson, H. (1993) Using Geochemical Data: Evaluation, Presentation, Interpretation. Longman, 352 pp.

Rosatelli, G., Wall, F., Stoppa, F. (2007) Calcio-carbonatite melts and metasomatism in the mantle beneath Mt. Vulture (Southern Italy). *Lithos*, 99, 229-248.

Rosenbaum, J.M. (1993) Mantle phlogopite: a significant lead repository) *Chem. Geol.*, 106, 475-483.

Roy, S., Négrel, P. (2001) A Pb isotope and trace element study of rainwater from the Massif Central (France). *Sci Total Environ.*, 277, 225-239.

Rudnick, R., Gao, S. (2003) Composition of the continental crust. In: Rudnick R (Ed.) *The Crust - Treatise on Geochemistry*, 3, pp 1–64.

Rudnick, R.L., McDonough, W.F., Chappell, B.W. (1993) Carbonatite metasomatism in the Northern Tanzanian mantle: petrographic and geochemical characteristics. *Earth Planet. Sci. Lett.*, 114, 463-475.

Ryabchikov, J.D., Ntaflos, T., Kurat, G., Kogarko, L.N. (1995) Glass-bearing xenoliths from Cape Verde: Evidence for a hot rising mantle jet. *Mineral. Petrol.*, 55, 217-237.

Salminen, R. (chief ed.) (2005) Geochemical Atlas of Europe. Part 1 - Background Information, Methodology and Maps. Geological Survey of Finland, Otamedia Oy, Espoo, 525 pp.

Salters, V.J., Hart, S.R. (1991) The mantle source of ocean ridges, island arcs: the Hf-isotope connection. *Earth Planet. Sci. Lett.*, 104, 364-380.

Salters, V.J., White, W.M. (1998) Hf isotope constraints on mantle evolution. *Chem. Geol.*, 145, 447-460.

Salters, V.J., Sachi-Kocher, A. (2010) An ancient metasomatic source for the Walvis Ridge basalts. *Chem. Geol.*, 273, 151-167.

Salters, V.J., Longhi, J.E., Bizimis, M. (2002) Near solidus trace element partitioning at pressures up to 3.4 GPa. *Geochem. Geophys. Geosyst.*, 3, doi:10.1029/2001GC000173..

Sandwell, D.T., MacKenzie, K.R. (1989) Geoid height versus topography for oceanic plateau and swells. *J. Geophys. Res.*, 94, 7403-7418.

Sandwell, D.T., Smith, W.H. (1997) Marine gravity anomaly from Geosat and ERS 1 satellite altimetry. *J. Geophys. Res.*, 102, 10039-10054.

Scheidegger, A. E. (2002) Morphometric analysis and its relation to tectonics in Macaronesia. *Geomorphology*, 46, 95-115.

Schiano, P., Clocchiatti, R. (1994) Worldwide occurrence of silica-rich melts in sub-continental and sub-oceanic mantle minerals. *Nature*, 368, 621–624.

Schiano, P., Eiler, J., Hutcheon, I.D., Stolper, E.M. (2000) Primitive CaO rich, silica-undersaturated melts in island arcs: Evidence for the involvement of clinopyroxene-rich lithologies in the petrogenesis of arc magmas. *Geochem. Geophys. Geosyst.*, 3, doi:10.1029/1999GC000032.

Schlager, W. (2005) Secular oscillations in the stratigraphic record – an acute debate. *Facies*, 51, 12-16.

Schubert, G., Turcotte, D.L., Olson, P. (2001) Mantle convection in the Earth and Planets. Cambridge University Press, 913 pp.

Schweitzer, E.L., Papike, J.J., Bence, A.E. (1979) Statistical analysis of clinopyroxenes from deep-sea basalts. *Am. Mineral.*, 64, 501-13.

Seifert, K.E., Chang, C.-W., Brunotte, D.A. (1997) Evidence from Ocean Drilling Program Leg 149 mafic igneous rocks for oceanic crust in the Iberia Abyssal Plain ocean-continent transition zone. *J. Geophys. Res.*, 102, 7915-7928

Serralheiro, A. (1976) A geologia da Ilha de Santiago (Cabo Verde). Tese de Doutoramento, Bol. Mus. Lab. Min. Geol. Fac. Ciênc. Univ. Lisboa, 14 (2), 218 p.

Shahnas, M.H., Pysklywec, R. (2004) Anomalous topography in the western Atlantic caused by edge-driven convection. *Geophys. Res. Lett.*, 31, L18611.

Shaw, D.M. (1970) Trace element fractionation during anatexis. *Geochim. Cosmochim. Acta*, 34, 237-243.

Shaw, D.M. (2006) Trace Elements in Magmas. A Theoretical Treatment. Cambridge University Press. 243 pp.

Shaw, C. (1999) Dissolution of orthopyroxene in basanitic magma between 0.4 and 2 GPa: further implications for the origin of Si-rich alkaline glass inclusions in mantle xenoliths. *Contrib. Mineral. Petrol.*, 135, 114–132.

Shaw, C. (2009) Textural development of amphibole during breakdown reactions in a synthetic peridotite. *Lithos*, 110, 215-228.

Shaw, C., Heidelbach, F., Dingwell, D. (2006) The origin of reaction textures in mantle peridotite xenoliths from Sal Island, Cape Verde: the case for "metasomatism" by the host lava. *Contrib. Mineral. Petrol.*, 151, 681-697.

Shervais, J.W. (1982) Ti–V plots and the petrogenesis of modern ophiolitic lavas. *Earth Planet. Sci. Lett.*, 59, 101–118.

Shirey, S.B., Bender, J.F., Langmuir, C.H. (1987) Three-component isotopic heterogeneity near the oceanographer transform, Mid-Atlantic Ridge. *Nature*, 325, 217–223.

Silva, L.C., Le Bas, M.J., Robertson, A.H. (1981) An oceanic carbonatite volcano on Santiago, Cape Verde Islands. *Nature*, 294, 644-645.

Silva, L.C. (1979) Considerações geológicas e estudos preliminares sobre inclusões primárias, fluidas e sólidas, em apatites de rochas carbonatíticas e ijolíticas da Ilha de Santiago, República de Cabo Verde. *Comunicações dos Serviços Geológicos de Portugal*, Tomo LXIV, 261-268.

Silver, P., Russo, R., Lithgow-Bertelloni, C. (1998) Coupling of South American and African plate motion and plate deformation. *Science*, 279, 60-63.

Sims, K.W., DePaolo, D.J. (1997) Inferences about mantle magma sources from incompatible element concentration ratios in oceanic basalts. *Geochim. Cosmochim. Acta*, 61, 765–784.

Sinton, J.M., Smaglik, S.M., Mahoney, J.J., Macdonald, K.C. (1991) Magmatic processes at superfast spreading mid-ocean ridges. *J. Geophys. Res.*, 96, 6133-6155.

Skolotnev, S., Turko, N., Sokolov, S., Peyve, A., Tsukanov, N., Kolodyazhnyi, S., Chamov, N., Baramykov, Y., Ponomarev, A., Efimov, V., Eskin, A., Petrova, V., Golovina, L., Lavrushin, V., Letyagina, E., Shevchenko, E., Krivosheya, K., Zotov, L. (2007) New data on the

geological structure of the junction of the Cape Verde Rise, Cape Verde Abyssal Basin, and the Bathymetrists Seamounts (Central Atlantic Ocean). *Dokl. Earth Sci.*, 416, 1037-1041.

Skolotnev, S., Kolodyazhnyi, S., Tsukanov, N., Chamov, N., Sokolov, S. (2009) Neotectonic morphostructures in the junction zone of the Cape Verde rise and Cape Verde abyssal plain, Central Atlantic. *Geotectonics*, 43, 51-66.

Sleep, N.H. (1990) Hotspots and mantle plumes: some phenomenology. *J. Geophy. Res.*, 95, 6715-6736.

Sobolev, A.V., Hofmann, A.W., Sobolev, S V., Nikogosian, I.K. (2005) An olivine-free mantle source of Hawaiian shield basalts. *Nature*, 434, 590-597.

Sobolev, A.V., Hofmann, A.W., Kuzmin, D.V., Yaxley, G.M., Arndt, N.T., Chung, S.-L.,Danyushevsky, L.V., Elliott, T., Frey, F.A., Garcia, M.O., Gurenko, A.A., Kamenetsky, V.S., Kerr, A.C., Krivolutskaya, N.A., Matvienkov, V.V., Nikogosian, I.K., Rocholl, A.,Sigurdsson, I.A., Sushchevskaya, N.M., Teklay, M. (2007) The amount of recycled crust in sources of mantle-derived melts. *Science*, 316, 412–417.

Späth, A., Le Roex, A.P., Opiyo-Akech, N. (2001) Plume-lithosphere interaction and the origin of continental rift-related alkaline volcanism. The Chyulu Hills Volcanic Province, Southern Kenya. *J. Petrol.*, 42, 765-787.

Stacey, J.S., Kramers, J.D. (1975) Approximation of terrestrial lead isotope evolution by a two-stage model. *Earth Planet. Sci. Lett.*, 26, 207-221.

Staudigel, H., Plank, T., White, W., Schmincke. H.-U (1996) Geochemical fluxes during seafloor alteration of the basaltic upper oceanic crust: DSDP Sites 417–418 (Overview). Pp. 19–38 in Subduction Top to Bottom. G.E. Bebout, D.W. Scholl, S.H. Kirby, J.P. Platt, eds, American Geophysical Union Monograph Series 96, Washington, DC.

Steiger, R.H., Jäger, E. (1977) Subcomission on geochronology: Convention on the use of decay constants in Geo- and Cosmochronology. *Earth Planet Sci. Lett.*, 36, 359-362.

Stein, C.A., Stein, S. (1992) A model for the global variation in oceanic depth and heat flow with lithospheric age. *Nature*, 359, 123-129.

Stein, C.A., Stein, S. (1993) Constraints on Pacific mid-plate swells from global depth-age and heat flow-age models. In: AGU (Eds.) *The Mesozoic Pacific: geology, tectonics, and volcanism*. Geophysical Monograph, 77, pp. 53-76.

Stein, C.A., Von Herzen, R. (2007) Potential effects of hydrothermal circulation and magmatism on heat flow at hotspot swells. In: Foulger, G.R., and Jurdy, D.M. (Eds.) Plates, plumes, and planetary processes. *Geol. Soc. Am. Special Paper,* 430, p. 261–274

Steiner, C., Hobson, A., Favre, P., Stampfli, G., Hernandez, J. (1998) Mesozoic sequence of Fuerteventura (Canary Islands): Witness of Early Jurassic sea-floor spreading in the central Atlantic. *GSA Bulletin*, 110, 1304–1317.

Stillman, C.J., Fuster, J.M., Bennell-Baker, M.J., Munoz, M., Smewing, J.D., Sagredo, J. (1975) Basal complex of Fuerteventura (Canary Islands) is an oceanic intrusive complex with rift-system affinities. *Nature*, 257, 469–470.

Stillman, C.J., Furnes, H., Le Bas, M.J., Robertson, A.H., Zielonka, J. (1982) The geological history of Maio, Cape Verde islands. *J. Geol. Soc.*, 139, 347–361.

Stracke, A. (2010) Mantle heterogeneity: what is the message from geochemistry? European Geosciences Meeting (Vienna, Austria). *Geophys. Res. Abstr.*, 12, 10980.

Stracke, A. (2012) Earth's heterogeneous mantle: A product of convection-driven interaction between crust and mantle. *Chem. Geol.*, 274-299, 2012.

Stracke, A., Salters, V.J., Sims, K. (1999) Assessing the presence of garnet-pyroxenite in the mantle source of basalts through combined hafnium-neodymium-thorium isotope systematics. *Geochem. Geophys. Geosyst.*, 1, doi: 10.1029/1999GC000013.

Stracke, A., Bizimis, M., Salters, V.J.M. (2003) Recycling oceanic crust: Quantitative constraints. *Geochem. Geophys. Geosyst.*, 4, doi: 8010.1029/2001GC000223.

Stracke, A., Hofmann, A.W., Hart, S.R. (2005) FOZO, HIMU, and the rest of the mantle zoo. *Geochem. Geophys. Geosyst.*, 6, doi:10.1029/2004GC000824.

Stüwe, K. (2007) Geodynamics of the lithosphere – an introduction. 2nd Edition. Springer. 493 pp.

Su, B., Zhang, H., Sakyi, P., Ying, J., Tang, Y., Yang, Y., Qin, K., Xiao, Y., Zhao, X. (2010) Compositionally stratified lithosphere and carbonatite metasomatism recorded in mantle xenoliths from the Western Qinling (Central China). *Lithos*, 116, 111-128.

Sun, S.S., Hanson, G.H. (1975) Origin of Ross Island basanitoids and limitations upon the heterogeneity of mantle sources for alkali basalts and nephelinites. *Contrib. Mineral. Petrol.*, 52, 77-106.

Sun, S.S., McDonough W.F. (1989) Chemical and isotopic systematics of oceanic basalts: implications for mantle compositions and processes. In: Saunders, A.D., Norry, M.J. (Eds.) Magmatism in the Ocean Basins. *Geol. Soc. Spec. Publ.*, 42: 313-345.

Sun, W., Hu, Y., Kamenetsky, V.S., Eggins, S., Chen, M., Arculus, R. (2008) Constancy of Nb/U in the mantle revisited. *Geochim. Cosmochim. Acta*, 72, 3542-3549.

Tackley, P.J. (2008) Layer cake or plum pudding? *Nat. Geosci,*, 1, 157-158.

Tackley, P.J. (2011) Living dead slabs in 3-D: The dynamics of compositionally-stratified slabs entering a "slab graveyard" above the core-mantle boundary. *Phys. Earth Planet. In.*, 188, 150–162.

Tatsumi, Y. (2000) Continental crust formation by crustal delamination in subduction zones and complementary accumulation of the enriched mantle I component in the mantle. *Geochem. Geophys. Geosyst.*, 1, doi:10.1029/2000GC000094.

Thibault, Y., Edgar, A.D., Lloyd, F.E. (1992) Experimental investigation of melts from a carbonated phlogopite lherzolite: implications for metasomatism in the continental lithospheric mantle. *Am. Mineral.*, 77, 784–794.

Thirlwall, M.F. (1995) Generation of the Pb isotopic characteristics of the Iceland plume. *J. Geol. Soc. London*, 152, 991–996.

Thirlwall, M.F. (1997) Pb isotopic and elemental evidence for OIB derivation from young HIMU mantle. *Chem. Geol.*, 139, 51–74.

Thompson, R.N. (1984) Dispatches from the basalt front.1-Experiments. *Proc. Geol. Ass.*, 95, 249-262.

Tiepolo, M.; Vannucci, R.; Oberti, R.; Foley, S.; Bottazzi, P.; Zanetti, A. (2000) Nb and Ta incorporation and fractionation in titanian pargasite and kaersutite: crystal-chemical constraints and implications for natural systems. *Earth Planet. Sci. Lett.*, 176, 185-201.

Tiepolo, M.; Bottazzi, P.; Foley, S.; Oberti, R.; Vannucci, R.; Zanetti, A. (2001) Fractionation of Nb and Ta from Zr and Hf at mantle depth: the role of titanian pargasite and kaersutite. *J. Petrol.*, 42(1), 221-232.

Tilton, G.R., Bryce, J.G., Mateen, A. (1998) Pb-Sr-Nd Isotope data from 30 and 300 Ma Collision Zone Carbonatites in Northwest Pakistan. *Mineral. Mag.*, 62A, 1521-1522.

Tolstikhin, I.N., Kramers, J.D., Hofmann, A.W. (2006) A chemical Earth model with whole mantle convection: the importance of a core-mantle boundary layer (D") and its early formation. *Chem. Geol.*, 226, 79-99.

Tolstikhin, I.N., Hofmann, A.W. (2005) Early crust on top of the Earth's core. Phys. *Earth Planet. Int.*, 148, 109–130.

Torres, P.C. (1998) Geologia e petrogénese das formações vulcânicas da ilha do Sal, Arquipélago de Cabo Verde. Dissertação apresentada ao Instituto de Investigação Científica e Tropical para prestação de provas de acesso à categoria de Investigador auxiliar, 212 p.

Torres, P.C., Madeira, J., Silva, L.C., Brum da Silveira, A., Serralheiro, A., Mota Gomes, A. (1997a) Carta geológica das erupções históricas da Ilha do Fogo: revisão e actualização. In: Réffega, A. (Eds.) A Erupção Vulcânica de 1995 na Ilha do Fogo, Cabo Verde. IICT, Lisboa, pp. 119-132.

Torres, P.C., Silva, L.C., Mendes, M.H., Serralheiro, A., Madeira, J., Brum da Silveira, A., Mota Gomes, A. (1997b) Cronologia da erupção vulcânica de 1995 na Ilha do Fogo, Cabo Verde. In: Réffega, A. (Eds.) A Erupção Vulcânica de 1995 na Ilha do Fogo, Cabo Verde. IICT, Lisboa, pp. 133-144.

Torres, P., Silva, L.C., Serralheiro, A., Tassinari, C., Munhá, J. (2002) Enquadramento geocronológico pelo método K-Ar das principais sequências vulcano-estratigráficas da Ilha do Sal –Cabo Verde. *Garcia Orta*, Ser. Geol., 18, 9-13.

Torres, P., Silva, L.C., Munhá, J., Caldeira, R., Mata, J., Tassinari, C. (2010) Petrology and Geochemistry of lavas from Sal Island: Implications for the variability of the Cape Verde magmatism. *Comunicações Geológicas*, 97, 35-62.

Torsvik, T.H., Smethurst, M.A., Burke, K., Steinberger, B. (2006) Large igneous provinces generated from the margins of the large low-velocity provinces in the deep mantle. *Geophys. J. Intern.*, 167, 1447–1460.

Trindade, M.J.F. (2002) Contribuição para o estudo petrológico e geoquímico do vulcanismo "recente" da ilha de S. Vicente (Cabo Verde). Master's thesis, Lisbon University, 229 p.

Trønnes, R. (2010) Structure, mineralogy and dynamics of the lowermost mantle. *Mineral. Petrol.*, 99, 243-261.

Turcotte, D.L., Schubert, G. (2002) Geodynamics 2nd Edition. Cambridge University Press, 456 pp.

Urchulutegui, J.F. (2007) Development of numerical methods to determine the lithospheric structure combining geopotencial, lithostatic and heat transport equations. Application to the Gibraltar arc system. PhD thesis, Barcelona. 240 pp.

van der Hilst, R. (2004) Changing Views on Earth's Deep Mantle. *Science*, 306, 817-818.

van der Hilst, R., Kárason, H. (1999) Compositional heterogeneities in the bottom 1000 km of Earth's mantle: Towards a hybrid convection model. *Science*, 283, 1885–1888.

van der Hilst, R.,Widiyantoro, S., Engdahl, E.R. (1997) Evidence for deep mantle circulation from global tomography. *Nature*, 386, 578–584.

van Keken, P.E., Kiefer, B., Peacock, S.M. (2002) High-resolution models of subduction zones: Implications for mineral dehydration reactions and the transport of water into the deep mantle. *Geochem. Geophys. Geosyst.*, 3,doi:10.1029/2001GC000256.

van Westrenen, W., Blundy, J.D., Wood, B.J. (2001) High field strength element/rare earth element fractionation during partial melting in the presence of garnet: Implications for identification of mantle heterogeneities. *Geochem. Geophys. Geosyst.*, 2, doi:10.1029/2000GC000133.

Veizer, J. (1989) Strontium isotopes in seawater through time. *An. Rev. Earth Planet. Sci.*, 17, 141-167.

Verma, S.P., Torres-Alvarado, I.S., Sotelo-Rodríguez, Z.T. (2002) SINCLAS: Standard Igneous Norm and Volcanic Rock Classification System. *Comp. Geosciences*, 28, 711-715.

Vermeesch, P. (2006) Tectonic discrimination diagrams revisited. *Geochem. Geophys. Geosyst.*, 7, doi: 10.1029/2005GC001092

Vervoort, J., Patchett, P., Blichert-Toft, J., Albarède, F. (1999) Relationships between Lu-Hf and Sm-Nd isotopic systems in the global sedimentary system. *Earth Planet. Sci. Lett.*, 168, 79-99.

Vervoort, J.D., Patchett, P.J., Albarede, F., Blichert-Toft, J., Rudnick, R.L., Downes, H. (2000) Hf-Nd isotopic evolution of the lower crust. *Earth Planet. Sci. Lett.*, 181, 115–129.

Vidal, P. (1992) Mantle: More HIMU in the future? *Geochim. Cosmochim. Acta*, 56, 4295–4299.

Veizer, J. (1989) Strontium isotopes in seawater trough time. *Annu. Rev. Earth Planet. Sci.*, 17, 141-167.

Vinnik, L., Silveira, G., Kiselev, S., Farra, V., Weber, M., Stutzmann, E. (2012) Cape Verde hotspot from the upper crust to the top of the lower mantle. *Earth Planet. Sci. Lett.*, 319-320, 259-268.

von Blanckenburg, F., O'Nions, R.K., Hein, J.R. (1996) Distribution and sources of pre-anthropogenic lead isotopes in deep ocean water from Fe-Mn crusts. *Geochim. Cosmochim, Acta*, 60, 4957-4963.

Von Herzen, R.P. (2004) Geothermal evidence for continuing hydrothermal circulation in older (>60 M.y.) ocean crust. In: Davis, E.E., Elderfield, E. H. (Eds.) *Hydrogeology of the oceanic lithosphere*. Cambridge University Press, Cambridge, pp. 414-447.

Wallace, M.E., Green, D.H. (1991) The effect of bulk rock composition on the stability of amphibole in the upper mantle: implications for solidus positions and mantle metasomatism. *Mineral. Petrol.*, 44, 1-19.

Wallenstein, N., Gaspar, J., Guest, J., Duncan, A. (1997) Estilos eruptivos observados durante a etupção vulcânica de 1995 na ilha do Fogo, Cabo Verde. In: Réffega, A. (Eds.) A Erupção Vulcânica de 1995 na Ilha do Fogo, Cabo Verde. IICT, Lisboa, pp. 145-152.

Walter, M. (1998) Melting of garnet peridotite and the origin of komatiite and depeleted lithosphere. *J. Petrol.*, 39, 29-60.

Wang, C., Gaetani, G.A. (2007) Producing Ni-rich olivine phenocrysts by mixing partial melts of eclogite and peridotite: an alternative to an olivine-free source for Hawaiian shield basalts. *American Geophysical Union, Fall Meeting*, U14A-07.

Wang, C., Gaetani, G.A. (2008) Partitioning of Ni between olivine and siliceous eclogite partial melt: experimental constraints on the mantle source of Hawaiian basalts. *Contrib. Mineral. Petrol.*, 156, 661–678.

Wasserburg, G.J., DePaolo, D.J. (1979) Models of Earth structure inferred from neodymium and strontium isotopic abundances. *Proc. Natl. Acad. Sci. USA*, 76, 3594-3598.

Watson, S., McKenzie, D. (1991) Melt generation by plumes: A study of Hawaiian volcanism. *J. Petrol.*, 32, 501-537.

Watts, A.B., Zhong, S. (2000) Observations of flexure and the rheology of oceanic lithosphere. *Geophys. J. Int.*, 142, 855-875.

Weaver, B.L. (1990) Geochemistry of highly-undersaturated ocean island basalt suites from the South Atlantic Ocean: Fernando de Noronha and Trindade islands. *Contrib. Mineral. Petrol.*, 105, 502-515.

Weaver, B.L. (1991) The origin of ocean island end-member compositions: trace element and isotopic constraints. *Earth Planet. Sci. Lett.*, 104, 381–397.

Weis, D., Frey, F. A. (1991) Isotope geochemistry of the Ninetyeast Ridge basement basalts: Sr, Nd, and Pb evidence for involvement of the Kerguelen hot spot. In.: Weissel, J., Peirce, J. Taylor E., Alt, J. et al (Eds.) *Proc. Ocean Drilling Program, Scientific Results*, 121, pp. 591-610.

Weis, D., Frey, F.A. (1996) Role of the Kerguelen plume in generating the eastern Indian Ocean seafloor. *J. Geophys. Res.*, 101, 13841–13849.

Weis, D., Kieffer, B., Maerschalk, C., Pretoriu,s W., Barling, J. (2005) High-precision Pb-Sr-Nd-Hf isotopic characterization of USGS BHVO-1 and BHVO-2 reference materials. *Geochem. Geophys. Geosyst.*, 6, doi: 10.1029/2004GC000852.

Weis, D., Kieffer, B., Maerschalk, C., Barling, J., de Jong, J., Williams, G., Hanano, D., Pretorius, W., Mattielli, N., Scoates, J., Goolaerts, A., Friedman, R., Mahoney, J. (2006) High-precision isotopic characterization of USGS reference materials by TIMS and MC-ICP-MS. *Geochem Geophys Geosyst.,* 7, doi:10.1029/2006GC001283

West, H. B., M. O. Garcia, D. C. Gerlach, Romano, L. (1992) Geochemistry of tholeiites from Lanai, Hawaii. *Contrib. Mineral. Petrol.*, 112, 520–542.

White, W. (1985) The sources of ocean basalts: radiogenic isotopic evidence. *Geology*, 13, 115–118.

White, W. (2007) Are “constant” trace element ratios in oceanic basalts really constant? *Geochim. Cosmochim. Acta*, 71, 15 - Supplement1, A1106.

White, W. (2013) Geochemistry. Wiley-Blackwell, 668 pp.

White, R.S., McKenzie, D.P., O'Nions, (1992) Oceanic crustal thickness from seismic measurements and rare earth element inversions. *J. Geophys. Res.,* 97, 19683-19715.

Willbold, M. (2005) Multi-element isotope dilution (ID) sector field ICP-MS: a novel technique that leads to new perspectives on the trace element systematics of ocean island basalts. PhD Dissertation. LMU München, Faculty of Geosciences, 116 pp.

Willbold, M., Stracke, A. (2006) Trace element composition of mantle end-members: Implications for recycling of oceanic and upper and lower continental crust. *Geochem Geophys Geosyst.*, 7, doi:10.1029/2005GC001005.

Willbold, M., Stracke, A. (2010) Formation of enriched mantle components by recycling of upper and lower continental crust. *Chem. Geol.*, 276, 188-197.

Williams, C., Hill, I., Young, R., White, R.S. (1990). Fracture zones across the Cape Verde Rise, NE Atlantic. *J. Geol. Soc. London*, 147, 851-857.

Williams, H.M., Turner, S.P., Pearce, J.A., Kelley, S.P., Harris, N. (2004) Nature of the source regions for post-collisional, potassic magmatism in southern and northern Tibet from geochemical variations and inverse trace element modeling. *J. Petrol.*, 45, 555-607.

Wilson, D. (2011) Crustal structure of the Cape Verde Swell: insights into the flexural response of the lithosphere to loading. PhD thesis, Durham University, 259 pp.

Wilson, D., Peirce1, C., Watts, A., Grevemeyer, I. (2013) Uplift at lithospheric swells-II: is the Cape Verde mid-plate swell supported by a lithosphere of varying mechanical strength? *Geophys. J. Int.*, 193, 798-819.

Wilson, M., Rosenbaum, J.M., Dunworth, E.A. (1995) Melilitites: partial melts of the thermal boundary layer? *Contrib. Mineral. Petrol.*, 119, 181-195.

Wipf, M., Glasmacher, U.A., Stockli, D., Emmerich, A., Bechstädt, T., Baur, H. (2009) Reconstruction of the differentiated long-term exhumation history of Fuerteventura, Canary Islands, Spain, through fission-track and (U-Th–Sm)/He data. *Int. J. Earth Sci.*, 99, 675-686.

Winchester, J.A., Floyd, P.A. (1976) Geochemical magma type discrimination; application to altered and metamorphosed basic igneous rocks. *Earth Planet. Sci. Lett.*, 28, 459-460.

Winchester, J.A., Floyd, P.A. (1977) Geochemical discrimination of different magma series and their differentiation products using immobile elements. *Chem. Geol.*, 20, 325-343.

Winter, J.D. (2001) An Introduction to Igneous and Metmorphic Petrology. Prentice Hall, 697 p.

Wittig, N., Pearson, D.G., Downes, H., Baker, J.A. (2009) The U, Th and Pb elemental and isotope compositions of mantle clinopyroxenes and their grain boundary contamination derived from leaching and digestion experiments. *Geochim. Cosmochim. Acta*, 73, 469-488.

Wittig, N., Pearson, D.G., Duggen, S., Baker, J.A., Hoernle, K. (2010) Tracing the metasomatic and magmatic evolution of continental mantle roots with Sr, Nd, Hf and Pb isotopes: a case study of Middle Atlas (Morocco) peridotite xenoliths. *Geochim. Cosmochim. Acta*, 74, 1417-1435.

Woodhead, J.D. (1996) Extreme HIMU in an oceanic setting: the geochemistry of Mangaia Island (Polynesia), and temporal evolution of the Cook-Austral hotspot. *J. Volcanol. Geotherm. Res.*, 72, 1–19.

Woolley, A.R., Kjarsgaard, B.A. (2008) Carbonatite occurrences of the world: map and database. Geological Survey of Canada, Open File 5796.

Woolley, A.R., Bergman, S.C., Edgar, A.D., Le Bas, M.J., Mitchell, R.H., Rock, N.M.S., Smith, B.H.S. (1996) Classification of lamprophyres, lamproites, kimberlites, and the kalsilitic, melilitic, and leucitic rocks. *Can. Mineral.*, 34, 175-186.

Workman, R.K., Hart, S.R. (2005) Major and trace element composition of the depleted MORB mantle (DMM). *Earth Planet. Sci. Lett.*, 231, 53–72.

Workman, R. K., Hart, S. R., Jackson, M., Regelous, M., Farley, K. A., Blusztajn, J., Kurz, M., Staudigel, H. (2004) Recycled metasomatized lithosphere as the origin of the Enriched Mantle II (EM2) end-member: Evidence from the Samoan Volcanic Chain. *Geochem. Geophys. Geosyst.*, 5, doi:10.1029/2003GC000623.

Yasuda, A., Fujii, T., Kurita, K. (1994) Melting phase relations of an anhydrous mid-ocean ridge basalt from 3 to 20 GPa: implications for the behavior of subducted oceanic crust in the mantle. *J. Geophys. Res.*, 99, 9401–9414.

Yaxley, G.M., Green, D.H. (1996) Experimental reconstruction of sodic dolomitic carbonatite melts from metasomatised lithosphere. *Contrib. Mineral. Petrol.*, 124, 359-369.

Yaxley, G.M., Kamenetsky, V. (1999) In situ origin for glass in mantle xenoliths from southeastern: insights from trace element compositions of glasses and metasomatic phases. *Earth Planet. Sci. Lett.*, 172, 97–109.

Yaxley, G.M., Crawford, A.J., Green, D.H. (1991) Evidence for carbonatite metasomatism in spinel peridotite xenoliths from western Victoria, Australia. *Earth Planet. Sci. Lett.*, 107, 305-317.

Yaxley, G.M., Green, D., Kamenetsky, V. (1998) Carbonatite metasomatism in the southeastern Australian lithosphere. *J. Petrol.*, 39, 1917-1930.

Yeats, R.S.; Forbes, W.C.; Heath, G.R.; Scheidegger, K.F. (1973) Petrology and geochemistry of DSDP Leg 16 basalts, eastern equatorial Pacific: In Van Andel, T.H., Heath, G.R., et al. (Eds.) Initial Reports of the Deep Sea Drilling Project, Volume 16, Washington (U.S. Government Printing Office), 617-640.

Yoder, H.S., Tilley, C.E. (1962) Origin of basaltic magmas: An experimental study of natural and synthetic rock systems. *J. Petrol.*, 3, 342-532.

Yokoyama, T., Aka, F.T., Kusakabe, M, Nakamura, E. (2007) Plume–lithosphere interaction beneath Mt. Cameroon volcano, West Africa: Constraints from ^{238}U–^{230}Th–^{226}Ra and Sr–Nd–Pb isotope systematics. *Geochim. Cosmochim. Acta*, 71, 1835–1854.

Young, R., Hill, A. (1993) An estimate of the effective elastic thickness of the Cape Verde Rise. *J. Geophys. Res.*, 91, 4854-4867.

Zack, T., Brumm, R. (1998) Ilmenite/liquid partition coefficients of 26 trace elements determined through ilmenite/clinopyroxene partitioning in garnet pyroxenites. Extended Abstract of the 7th International Kimberlite Conference, 986-988.

Zazo, C., Goy, J., Dabrio, C., Soler, V., Hillaire-Marcel, Cl., Ghaleb, B., González-Delgado, J., Bardají, T., Cabero, A. (2007) Quaternary marine terraces on Sal Island (Cape Verde archipelago). *Quaternary Sci. Rev.*, 27, 876-893.

Zindler, A., Hart, S.R. (1986) Chemical geodynamics. *Annu. Rev. Earth Planet. Sci.*, 14, 493–571.

Zindler, A., Jagoutz, E., Goldstein, S. (1982) Nd, Sr and Pb isotopic systematics in a three-component mantle: A new perspective. *Nature*, 298, 519-523.

Zeng. G., Chen, L-H., Xu, X-S., Jiang, S-Y., Hofmann, A.W. (2010) Carbonated mantle sources for Cenozoic intra-plate alkaline basalts in Shandong. North China. *Chem. Geol.*, 273, 35-45.

Zhong, S., Watts, A. (2002) Constraints on the dynamics of mantle plumes from uplift of Hawaiian islands. *Earth Planet. Sci. Lett.*, 203, 105-116.

Zhao, D. (2007) Seismic images under 60 hotspots: search for mantle plumes. *Gondwana Res.*, 12, 335-355.

Zou, H.B. (2007) Quantitative Geochemistry. Imperial College Press, London, 304 pp.

Internet Material

GEOROC, Geochemistry of Rocks of the Oceans and continents (2006) Max Planck Institute für Chemie. Available from: http://georoc.mpch-mainz.gwdg.de/georoc/Entry.html.

GERM, Geochemical Earth Reference Model. Available from: http://earthref.org/GERM

King, S. (2004) Understanding the edge-driven convection hypothesis. Available from: http://www.mantleplumes.org/EDGE.html.

PETDB, Petrological database of the ocean floor (2007). Available from: http://www.petdb.org.

APPENDIX I

SAMPLING STRATEGY

I - Sampling strategy

One of the main objectives of the present study is to investigate the mantle source signature portrayed by Santiago magmas. In order to accomplish this, rocks considered to be representative of magmas which, after generation by mantle melting did not suffered significant amounts of fractionation, are preferred. All the rocks collected are mafic, and rocks like phonolites and trachytes were avoided considering the effects of fractionation on the primordial magma signature.

A particular outcropping of ancient pillow lavas of MORB affinity was also sampled as well as a set of gabbroic xenoliths, present in the pillow lavas of the main eruptive formation.

I.1 - Alkaline lavas

A total of 70 alkaline lava were collected from the entire volcanic sequence of Santiago Island (Cape Verde archipelago), in order to obtain a representative sample set of all the volcanostratigraphic units and as much of the magmatic temporal evolution as possible (see Fig. A1).

The samples were collected in two separate field trips to Santiago Island during September 1999 and October 2006, on the basis of the geologic maps (11 sheets; scale 1:25000) elaborated by Serralheiro (1976). On the latter, specific locations were targeted on the main eruptive formation (Pico da Antónia) due to the identification of a possible geochemical distinction within the formation, between subaerial and submarine events, identified in a preliminary study of the data (Martins, 2003). Whenever possible fresh samples were collected from the interior of exposed rocks to avoid the effects of alteration processes.

Later in the laboratory, 56 lava samples were selected on the basis of their petrographic characteristics and freshness, for bulk geochemical analyses.

I.2 - MORB lavas

Santiago

The oldest unit identified in Santiago comprises Mesozoic oceanic crust that outcrop in the Angra area (see Fig. I.2). From the outcrop composed of yellowish altered pillow lavas, 12 samples

were collected. Even tough the alteration is widespread and ubiquitous in all the outcrop, only the core of the pillow lavas were sampled in order to avoid the most extreme alteration degree.

Maio

In the neighbouring Island of Maio, 3 samples were collected from the Batalha Formation by Professor João Mata on a field campaign (2009) of the project CV-Plume. These samples were used in Chapter 6 in association with pillow lavas of MORB-affinity of Santiago Island to check for similarities or distinctiveness.

I.3 - Gabbroic Xenoliths

In the Angra bay, Santiago Island (see Fig. I.2), 11 gabbroic xenoliths were collected from the Lower Pico da Antónia outcropping pillow lavas. The gabbroic xenoliths are centimetric with medium to coarse granularity and are easily found and identified in the field.

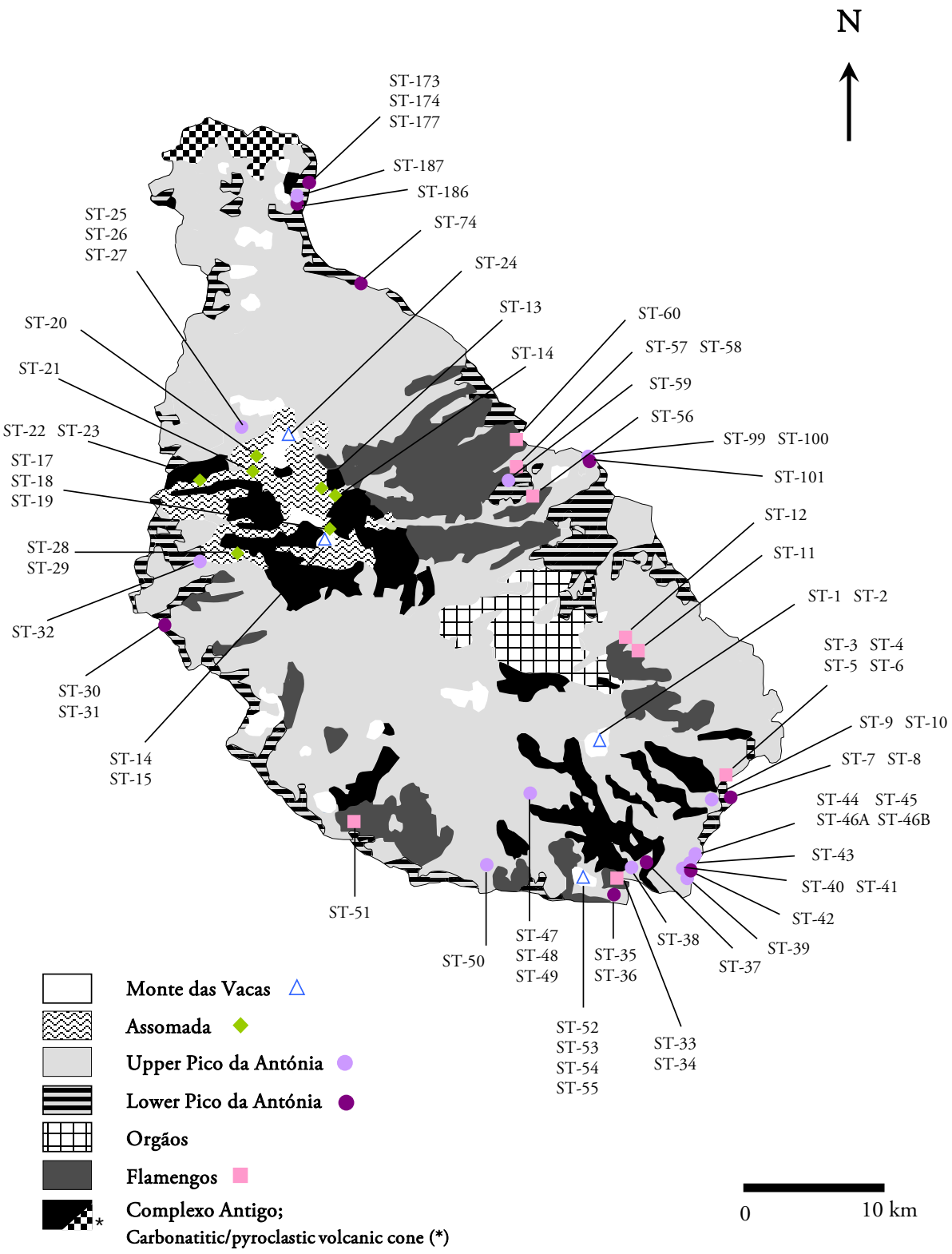

Figure I.1 - Simplified Santiago geological map (adapted from Serralheiro, 1976; Alves et al., 1979; Silva et al., 1981).

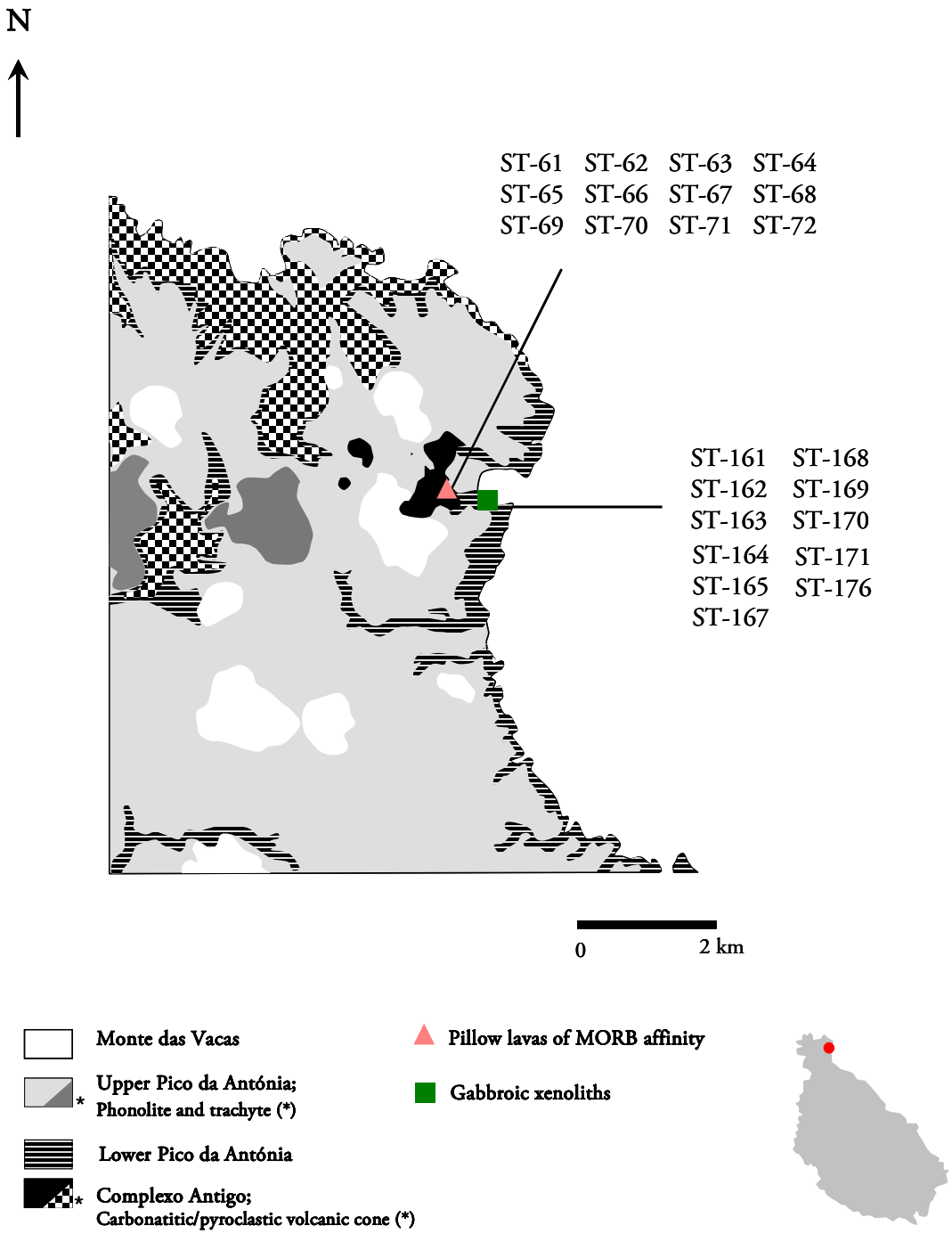

Figure I.2 - Simplified Santiago geological map of the Angra area (adapted from Serralheiro, 1976; Alves et al., 1979; Silva et al., 1981).

APPENDIX II

METHODOLOGY AND ANALYTICAL PROCEDURES

II – Methodology and analytical procedures

II.1. Rock crushing/powdering

Samples were processed at the Departamento de Geologia, Faculdade de Ciências da Universidade de Lisboa.

The raw lava samples were reduced in size to fragments of approximately 5 cm with a hydraulic press, being removed all visible signs of alteration. The material was further reduced in size by a jaw crusher to fragments of < 2.5 cm. Approximately 150 g of the crushed chips were then powdered to < 80 μm in an agate ring and puck mill. This powdered rock material was used for major, trace and isotopic determinations.

A rock fragment of approximately 30 x 25 x 18 mm was sawed from each sample for the preparation of thin sections and polished thin sections. The thin sections were observed in the microscope enabling the petrographic description of the samples, while the polished thin sections were used in the EMPA.

II.2. Whole rock major and trace element analyses

Geochemical analyses of the samples were carried out at Activation Laboratories, Ltd (Ancaster, Ontario, Canada) being selected the geochemical analytical package 4Lithoresearch (lithium metaborate/tetraborate fusion - ICP and ICP/MS).

In order to determine the elemental composition, the samples are subjected to a series of chemical procedures prior to analytical measurement. The samples are mixed with a flux of lithium metaborate and lithium tetraborate and fused in an induction furnace. The molten melt is poured into a solution of 5% nitric acid containing an internal standard, and mixed continuously until completely dissolved (~30 min).

Major oxides and selected trace elements (Ba, Sc, Sr, V, Y and Zr) were analysed by ICP-OES using a Thermo Jarrell-Ash ENVIRO II ICP or a Varian Vista 735 ICP. Trace elements were analysed by ICP-MS using one of the following equipments: Perkin Elmer SCIEX ELAN 6000,

6100 or 9000 ICP-MS. Duplicates are fused and analyzed every 15 samples. Instrument is recalibrated every 40 samples.

Several certified reference materials from USGS and CCRMP[1] were run to check for accuracy. In Table II.1 selected standards are reported for each of the sample groups, analysed in different batches. The errors associated with the accuracy is, mostly ≤ 1% for major-element contents (SiO_2, Al_2O_3, Fe_2O_3, MnO, MgO, Na_2O, K_2O and CaO) and between 3 and 6 % for rare earth elements (REE). For other elements commonly considered to be incompatible in oceanic context (Rb, Ba, Nb, Ta, Zr, Hf) the error associated is, on average, 7%.

More detailed information regarding chemical or analytical procedures can be found in www.actlabs.com.

[1] USGS stands for United States Geological Survey and CCRMP for Canadian Certificate Reference Material Project.

Table II.1. - Certified and measured values of internationally reference materials for each of the sample groups (DNC: Dolerite; BIR: Iceland basalt; W-2a: Diabase from USGS and SY3: Syenite from CCRMP).

	Alkaline lavas I				Alkaline lavas II				
Standard	DNC-1		SY3		BIR-1		DNC-1		D. limit
	Meas.	Cert.	Meas.	Cert.	Meas.	Cert.	Meas.	Cert.	
Major elements (wt.%)									
SiO_2	46.98	*47.04*	59.74	*59.62*	49.00	47.80	44.81	*47.04*	0.01
TiO_2	0.470	*0.48*	0.137	*0.15*	0.99	0.96	0.47	*0.48*	0.001
Al_2O_3	18.43	*18.30*	11.71	*11.75*	16.02	15.40	17.66	*18.30*	0.01
$Fe_2O_3^T$	9.92	*9.93*	6.47	*6.49*	11.66	11.30	9.54	*9.93*	0.01
MnO	0.145	*0.15*	0.326	*0.32*	0.18	0.17	0.14	*0.15*	0.001
MgO	10.15	*10.05*	2.62	*2.67*	9.91	9.68	9.81	*10.05*	0.01
CaO	11.19	*11.27*	8.23	*8.26*	13.67	13.20	10.84	*11.27*	0.01
Na_2O	1.87	*1.87*	4.10	*4.12*	1.81	1.75	1.83	*1.87*	0.01
K_2O	0.23	*0.23*	4.25	*4.23*	0.06	0.03	0.34	*0.23*	0.01
P_2O_5	0.07	0.09	0.54	*0.54*	0.02	0.05	0.07	0.09	0.01
Trace elements (ppm)									
Sc	32	31	8	6.8	44	44	30	31	1
V	152	*148*	51	50	346	313	153	*148*	5
Cr	284	*285*	-40	11	390	382	280	*285*	20
Co	57	*54.7*	7	8.8	51	51.4	55	*54.7*	1
Ni	244	*247*	-	-	170	166	250	*247*	20
Cu	85	*96*	-	-	150	126	110	*96*	10
Zn	46	*66*	-	-	90	71	60	*66*	30
Ga	15	15	25	*27.0*	16	16	14	15	1
Ge	1.2	1.3	3	1.4	1.4	1.5	1.3	1.3	0.5
Rb	4	4.5	211	*206*	< 1	0.25	4	4.5	1
Sr	149	*145*	323	*302*	113	108	138	*145*	2
Y	18.2	*18*	720	*718*	16.2	16	17.8	*18*	0.5
Zr	37	*41*	353	320	14	16	37	*41*	1
Nb	2.1	3	160	148	0.7	0.6	1.8	3	0.2
Cs	0.2	0.34	2.8	2.5	< 0.1	0.005	0.2	0.34	0.1
Ba	108	*114*	445	450	11	7	103	*114*	3
La	3.85	*3.8*	1 340	*1 340*	0.73	0.62	3.99	*3.8*	0.05
Ce	8.89	10.6	2 210	*2 230*	2.1	1.95	8.59	10.6	0.05
Pr	1.10	1.3	222	*223*	0.41	0.38	1.17	1.3	0.01
Nd	5.01	*4.9*	675	670	2.37	2.5	4.86	*4.9*	0.05
Sm	1.41	*1.38*	110	109	1.16	1.1	1.51	*1.38*	0.01
Eu	0.567	*0.59*	17.1	*17*	0.592	0.54	0.66	*0.59*	0.005
Gd	1.85	2	105	*105*	2.02	1.85	2.17	2	0.01
Tb	0.45	*0.41*	18.0	18	0.43	0.36	0.45	*0.41*	0.01
Dy	2.87	2.7	119	118	2.78	2.5	2.94	2.7	0.01
Ho	0.65	0.62	29.5	*29.50*	0.57	0.57	0.61	0.62	0.01
Er	2.12	*2*	68.4	*68*	1.78	1.7	1.99	*2*	0.01
Tm	0.320	0.3	11.7	11.60	0.29	0.26	0.333	0.3	0.005
Yb	2.13	*2.01*	62.2	62.0	1.75	1.65	2	*2.01*	0.01
Lu	0.333	*0.32*	7.93	7.90	0.255	0.26	0.298	*0.32*	0.002
Hf	1.1	*1.01*	11.7	9.70	0.6	0.6	1.1	*1.01*	0.1
Ta	0.08	*0.098*	28.6	30	0.02	0.04	0.08	*0.098*	0.01
Pb	5	6.3	-	-	< 5	3	6	6.3	5
Th	0.27	0.2	1 000	1 003	< 0.05	0.03	0.25	0.2	0.05
U	0.05	0.10	649	650	< 0.01	0.01	0.05	0.10	0.01

Italic data are recommended values; underlined data are informative values; remaining data are proposed values. "Meas." stands for measured," Cert." for certified and "D. limit" for detection limit.

Continuation Table II.1.

	Gabbroic xenoliths				Santiago MORB				
Standard	BIR-1a		DNC-1		DNC-1		SY3		D. limit
	Meas.	Cert.	Meas.	Cert.	Meas.	Cert.	Meas.	Cert.	
Major elements (wt.%)									
SiO_2	48.35	47.80	47.28	*47.04*	47.33	47.04	57.17	59.63	0.01
TiO_2	0.97	0.96	0.49	*0.48*	0.48	0.48	0.135	0.15	0.001
Al_2O_3	15.51	15.40	18.67	*18.30*	18.51	18.03	11.2	11.75	0.01
$Fe_2O_3^T$	11.29	11.30	10.07	*9.93*	9.93	9.93	6.29	6.49	0.01
MnO	0.17	0.17	0.15	*0.15*	0.15	0.15	0.32	0.32	0.001
MgO	9.42	9.68	10.40	*10.05*	10.11	10.05	2.54	2.67	0.01
CaO	13.34	13.20	11.35	*11.27*	11.28	11.27	8.09	8.26	0.01
Na_2O	1.78	1.75	1.92	*1.87*	1.84	1.87	4.15	4.12	0.01
K_2O	< 0.01	0.03	0.19	*0.23*	0.24	0.23	4.25	4.23	0.01
P_2O_5	0.03	0.05	0.08	0.09	0.1	0.08	0.52	0.54	0.01
Trace elements (ppm)									
Sc	42	44	32	31	-	-	-	-	1
V	331	313	157	*148*	136	148	45	50	5
Cr	380	382	290	*285*	-	-	-	-	20
Co	49	51.4	57	*54.7*	-	-	-	-	1
Ni	150	166	270	*247*	-	-	-	-	20
Cu	110	126	100	*96*	-	-	-	-	10
Zn	90	71	80	*66*	-	-	-	-	30
Ga	14	16	14	15	14	15	35	*27*	1
Ge	1	1.5	1	1.3	1.3	1.3	3.2	1.4	0.5
Rb	< 1	0.25	4	4.5	3	4.5	206		1
Sr	108	108	143	*145*	144	145	301	302	2
Y	15	16	18	*18*	19	18	719	718	0.5
Zr	17	16	39	*41*	39	41	316	320	1
Nb	< 0.2	0.6	2	3	0.8	3	149	148	0.2
Cs	< 0.1	0.005	< 0.1	0.34	0.2	0.34	2.7	2.5	0.1
Ba	8	7	107	*114*	113	114	456	450	3
La	0.6	0.62	3.5	*3.8*	3.76	*3.8*	1341	*1340*	0.05
Ce	1.8	1.95	7.8	10.6	8	10.6	2231	*2230*	0.05
Pr	0.37	0.38	1.11	1.3	1.04	1.3	223	*223*	0.01
Nd	2.2	2.5	4.8	*4.9*	4.87	*4.9*	672	670	0.05
Sm	1	1.1	1.4	*1.38*	1.43	*1.38*	110	109	0.01
Eu	0.49	0.54	0.59	*0.59*	0.624	*0.59*	17.15	*17*	0.005
Gd	1.7	1.85	2	2	1.99	*2*	105	*105*	0.01
Tb	0.4	0.36	0.4	*0.41*	0.39	*0.41*	18.1	18	0.01
Dy	2.6	2.5	2.9	2.7	2.7	*2.7*	118	118	0.01
Ho	0.6	0.57	0.6	0.62	0.62	*0.62*	29.5	*29.5*	0.01
Er	1.7	1.7	2.1	*2*	2	*5*	68	68	0.01
Tm	0.3	0.26	0.32	0.3	0.315	0.33	11.62	*11.6*	0.005
Yb	1.6	1.65	2	*2.01*	2	*2.01*	62.2	62	0.01
Lu	0.25	0.26	0.3	*0.32*	0.321	*0.32*	7.918	7.9	0.002
Hf	0.6	0.6	1.1	*1.01*	1.1	*1.01*	12	9.7	0.1
Ta	< 0.01	0.04	< 0.01	*0.098*	0.1	*0.098*	24	*30*	0.01
Pb	< 5	3	11	6.3	-	-	-	-	1
Th	< 0.05	0.03	0.2	0.2	0.27	0.2	1003	*1003*	0.05
U	< 0.01	0.01	< 0.01	0.10	0.05	0.1	650	*650*	0.01

Italic data are recommended values; underlined data are informative values; remaining data are proposed values. "Meas." stands for measured," Cert." for certified and "D. limit" for detection limit.

Continuation Table II.1.

Standard	Maio MORB W-2a		D. limit
	Meas.	Cert.	
Major elements (wt.%)			
SiO_2	52.43	52.4	0.01
TiO_2	1.067	1.06	0.001
Al_2O_3	15.22	15.4	0.01
$Fe_2O_3^T$	10.69	10.7	0.01
MnO	0.166	0.163	0.001
MgO	6.28	6.37	0.01
CaO	10.65	10.9	0.01
Na_2O	2.18	2.14	0.01
K_2O	0.63	0.626	0.01
P_2O_5	0.13	0.13	0.01
Trace elements (ppm)			
Sc	35	36	1
V	248	262	5
Cr	80	92	20
Co	41	43	1
Ni	-	-	20
Cu	-	-	10
Zn	-	-	30
Ga	16	17	1
Ge	-	-	0.5
Rb	-	-	1
Sr	194	190	2
Y	22	24	0.5
Zr	91	94	1
Nb	-	-	0.2
Cs	1	0.99	0.1
Ba	172	182	3
La			0.05
Ce	24.5	23	0.05
Pr	-	-	0.01
Nd	12.8	13	0.05
Sm	3.23	3.3	0.01
Eu	1.02	1	0.005
Gd	-	-	0.01
Tb	0.63	0.63	0.01
Dy	-	-	0.01
Ho	0.74	0.76	0.01
Er	-	-	0.01
Tm	-	-	0.005
Yb	2.02	2.1	0.01
Lu	0.33	0.33	0.002
Hf	2.4	2.6	0.1
Ta	0.52	0.5	0.01
Pb	-	-	5
Th	2.33	2.4	0.05
U	0.55	0.53	0.01

Italic data are recommended values; underlined data are informative values; remaining data are proposed values. "Meas." stands for measured," Cert." for certified and "D. limit" for detection limit.

II.3. Mineral major element chemistry

Mineral analyses were performed on carbon-coated polished thin sections using a JEOL SUPERPROBE, model JXA-8200, in wavelength dispersive mode at the Centro de Geologia da Universidade de Lisboa. Minerals were analysed with an acceleration voltage of 15 kV and a current of 25 nA, using a beam 5 μm wide. The work was supervised by Dr. Pedro Rodrigues.

The performed analyses in each mineral phase were calibrated using the composition of reference material (see Table II.2.).

Table II.2. - Reference material used in the calibration of each element in the analysed minerals.

Element	Olivine	Plagioclase	Pyroxene	Amphibole	Mica	Sulphide
Si	Almandine	Plagioclase	Almandine	Almandine	Almandine	-
Ti	Kaersutite	Rutile	Kaersutite	Kaersutite	Kaersutite	-
Mg	Almandine	Almandine	Diopside	Diopside	Almandine	-
Mn	Bustamite	-	Bustamite	Bustamite	Bustamite	Bustamite
Fe	Almandine	Almandine	Almandine	Almandine	Almandine	Pyrite
Ca	Almandine	Plagioclase	Almandine	Almandine	Almandine	-
Al	Almandine	Plagioclase	Chlorite	Chlorite	Almandine	-
Cr	Chromium ox.	-	Chromium ox.	Chromium ox.	-	-
Na	Tugtupite	Plagioclase	Albite	Albite	Albite	-
K	Sanidine	Sanidine	Biotite	Biotite	Sanidine	-
Ni	Nickel sil.	-	-	-	-	Pentlandite
Ba	-	Benitoite	-	-	Benitoite	-
Sr	-	Celestite	-	-	-	-
Zn	-	-	Willemite	-	-	Sphalerite
F	-	-	-	-	-	-
Cs	-	-	-	-	-	-
Cl	-	-	-	-	Tugtupite	-
Rb	-	-	-	-	-	-
Sb	-	-	-	-	-	Stibnite
As	-	-	-	-	-	Gallium ars.
Sn	-	-	-	-	-	Cassiterite
S	-	-	-	-	-	Sphalerite
Cu	-	-	-	-	-	Cuprite
Au	-	-	-	-	-	Au b 1
Co	-	-	-	-	-	Skutterudi
Ag	-	-	-	-	-	Ag b 1
Pb	-	-	-	-	-	Galena

II.4. Isotopic analyses

II.4.1. Sr-Nd-Hf-Pb isotopic analyses at ULB (Brussels, Belgium)

The isotopic analyses of Pb, Nd and Hf were performed at the Department of Earth and Environmental Sciences of the Université Libre de Bruxelles (Belgium) on the Nu instrument Multi-Collector Inductively Coupled Mass Spectrometer (MC-ICP-MS), under the supervision of Professor Nadine Mattielli. Standards were systematically run between every two samples to monitor the machine performance. To assess the accuracy of the chemistry and the reproducibility of the isotopic measurements, several duplicates and replicates were performed (see Appendix III). Sr analyses were determined on the Finnigan Triton Thermo-Ionization Mass Spectrometer (TIMS) at the Pacific Centre for Isotopic and Geochemical Research at the University of British Columbia.

The chemical procedure that preceded the isotopic determination by MC-ICP-MS was performed by Claude Maerschalk.

During a two months internship at Université Libre de Bruxelles (Belgium) (February to March, 2006) at the investigation unit "Isotopes, Petrology and Environment" I acquire experience in the area of treatment and chemical preparation of geological samples for subsequent Sr, Nd, Hf e Pb isotopic analyses as well as working with the Nu Plasma MC-ICP-MS, under the supervision of Professor Nadine Mattielli and Claude Maerschalk. I performed all the chemical treatment on a set of 3 sample duplicates and run the samples in the mass spectrometer for Nd isotopic ratios determination.

II.4.1.1. Leaching and chemical separation

The isotopic analyses and chemical preparation of 18 samples were performed in the clean laboratories of the Department of Earth and Environmental Sciences of the "Université Libre de Bruxelles" (Belgium). To remove secondary phases and any potential contamination, a leaching procedure was applied to rock powder samples (about 250 mg), with repeated additions of 6N sub-boiled HCl (5 or 6 times) followed by 30-minutes ultrasonic baths until a clear solution was

obtained. Samples were then rinsed twice with milli-Q water and treated with ultrasound for 30 minutes (see Weis and Frey, 1996).

The sample dissolution was performed in 15 ml screw-top closed Savillex® beakers with a mixture of 10 ml sub-boiled HF (48%) and 1.0 ml of HNO_3 (14 N) acids, on a hot plate for 48 hours at 130 ºC. After evaporation, the samples were re-dissolved in 6N sub-boiled HCl for another 24 hours at 130 ºC.

All samples were first processed by Pb columns loaded with AG1-X8 100-200 mesh Biorad resin, from which resulted the recovery of the Pb fraction and other fraction containing Sr, REE and Hf (see Weis et al., 2005). The Sr was isolated using a column loaded 18.5 ml of Dowex AG50W-X8 100-200 mesh cation exchange resin. From this procedure results an Hf cut, a REE cut and a pure Sr fraction. The Nd is recovered loading the REE cut on to a column with HDEHP-coated Teflon. Hafnium was separated following the two column procedure described in Blichert-Toft et al. (1997), involving anion and cation exchange columns (Mattielli et al., 2002; Weis et al., 2005).

Measurements of the total procedural Pb, Nd, Sr and Hf blanks gave 10 pg, 28pg, 400 pg and 23pg, respectively.

II.4.1.2. Mass spectrometry analyses

MC-ICP-MS

The isotopic compositions of Pb, Nd and Hf were determined on a Nu plasma multi-collector inductively coupled mass spectrometer (MC-ICP-MS) at the Department of Earth and Environmental Sciences of the "Université Libre de Bruxelles".

At the beginning of every analytical session, collected analyte (Pb, Nd or Hf) elution fractions were re-dissolved in 100 µl of concentrated HNO_3, evaporated and finally dissolved in 1.5 ml of HNO_3 0.05 N.

Tl was added to each Pb sample and standard to control instrumental mass fractionation. Solutions were prepared to obtain a Pb/Tl rate of ≈ 4 and a signal of 100 mV in the axial collector (^{204}Pb) as well as to reach the Pb and Tl concentrations of the reference material (200 ppb of Pb

and 50 ppb of Tl). All Pb measurements were automatically corrected according to the Tl mass fractionation and then by using the standard bracketing method with the recommended values of Galer and Abouchami (1998) and Abouchami et al. (2000). Due to the fact that the amount of Pb was low in some samples, some analyzes were made in dry plasma mode (Nu-instruments DSN-100 desolvator).

Standards were systematically run between every two samples to monitor the instrumental mass bias during the analyses session, resulting in $^{143}Nd/^{144}Nd=0.511935 \pm 20$ (2σ, n=57) for the Rennes Nd standard, $^{176}Hf/^{177}Hf=0.282143 \pm 19$ (2σ, n=30) for the JMC 475 Hf standard and $^{206}Pb/^{204}Pb=19.937 \pm 0.001$, $^{207}Pb/^{204}Pb= 15.492 \pm 0.001$, $^{208}Pb/^{204}Pb=36.702 \pm 0.004$ (2σ, n=13) for the NBS981 standard. The Nd and Hf isotopic measurements were internally normalised to $^{179}Hf/^{177}Hf=0.7325$ and $^{146}Nd/^{144}Nd=0.7219$, respectively.

TIMS

The Sr isotopic ratios were analysed on the Finnigan Triton Thermo-Ionization Mass Spectrometer (TIMS) at the Pacific Centre for Isotopic and Geochemical Research at the University of British Columbia (Canada). The NBS 987 Sr standard was run after every ten samples, and gave a mean value of $^{87}Sr/^{86}Sr=0.710244 \pm 7$ (2σ) for six measurements. The raw data were corrected for mass fractionation using $^{86}Sr/^{88}Sr=0.1194$.

II.4.1.3. Precision and accuracy

The quality of chemical preparation procedures and reproducibility of isotopic measurements can be assessed by duplicate analyses of three samples, which are better than 66 ppm, 64 ppm and 25 ppm for $^{143}Nd/^{144}Nd$, $^{176}Hf/^{177}Hf$ and $^{87}Sr/^{86}Sr$, respectively and 12 replicates which are better than 30 ppm, 53 ppm and 4 ppm for $^{143}Nd/^{144}Nd$, $^{176}Hf/^{177}Hf$ and $^{87}Sr/^{86}Sr$, respectively (see Appendix III.2.1.1).

II.4.2. Sr-Nd isotopic analyses at Laboratório de Geologia Isotópica (Aveiro, Portugal)

Sr and Nd isotopic compositions were determined for nine whole-rock samples, six from Santiago MORB and three from Maio MORB at Laboratório de Geologia Isotópica da Universidade de Aveiro, Portugal. Chemical procedures and analytic determinations were done by Sara Ribeiro, the laboratory technician under the supervision of Professor Maria do Rosário.

II.4.2.1. Leaching and chemical separation

Due to their submarine nature and petrographically evident alteration paragenesis, the basaltic samples were subjected to a leaching procedure similar to the one used by Millet et al. (2008), but using 1N acetic acid. The efficiency and necessity of the leaching procedure was confirmed by analyzing the same sample (S17), leached (0.702917±18, 2SD) and unleached (0.703292±14, 2SD). After the leaching process the samples (200 g) were dissolved with 2 mL HF acid (22N) and 1mL HNO_3 (1N) at 200ºC, for three days.

After evaporation the solid residues were dissolved with HCL (2.5N) and purified using conventional ion chromatography techniques. Sr and REE elements were separated using an ion exchange column with AG8 50 W Bio-Rad cation exchange resin and the purification of Nd (from other lanthanide elements) was achieved using columns with Ln resin from ELChrom Tecnologies.

II.4.2.2. Mass spectrometry analyses

$^{87}Sr/^{86}Sr$ and $^{143}Nd/^{144}Nd$ isotopic ratios were carried out in a Multi-Collector Thermal Ionization Mass Spectrometer (TIMS) VG Sector 54. The Sr and Nd residues were dissolved with H_3PO_4 acid and deposited in Ta filaments for mass spectrometry.

Sr and Nd isotopic ratios were corrected for mass fractionation relative to $^{88}Sr/^{86}Sr = 0.1194$ and $^{146}Nd/^{144}Nd = 0.7219$. The SRM-987 standard gave an average of $^{87}Sr/^{86}Sr = 0.710247(16)$ (N = 12; conf. lim = 95 %) and $^{143}Nd/^{144}Nd = 0.5121026(77)$ (N = 11; conf. lim = 95 %) for the JNdi-1 standard, when Santiago MORB samples were analysed and $^{87}Sr/^{86}Sr = 0.710250$ (19) (N = 10; conf. lim = 95 %) and $^{143}Nd/^{144}Nd = 0.5121034$ (46) (N = 10; conf. lim = 95 %) when Maio MORB samples were processed.

APPENDIX III

ANALYTICAL RESULTS

III– Analytical results

III.1. Whole rock

Major element data were recalculated anhydrous to 100%, using the SINCLAS (Standard Igneous Norm and Volcanic Rock Classification System) software which also calculates the Fe_2O_3/FeO ratio by the method of Middlemost (1989) (Verma et al., 2002). These compositions are used in all diagrams involving major elements. Mg# stands for magnesium number, the ratio of magnensium to iron in a rock (see Chapter 4). The following abbreviations are used in the tables: BSN – Basanite, TEP – Tephrite, MNP – Melanephelinite, PIC – Picrite, B – Basalt, TB – Trachybasalt, G – Gabbro.

III.1.1. Santiago Alkaline lavas

III.1.1.1. Monte das Vacas Formation

Sample	ST-1	ST-2	ST-16	ST-24	ST-52	ST-54
Rock type	BSN	TEP	BSN	BSN	BSN	BSN
Major elements (wt.%)						
SiO_2	43.70	44.38	43.39	43.47	43.36	43.53
TiO_2	3.63	3.73	3.69	4.05	3.90	3.93
Al_2O_3	14.18	14.41	15.43	14.17	14.53	14.72
$Fe_2O_3^T$	14.80	15.23	13.14	15.82	15.15	15.04
MnO	0.22	0.24	0.19	0.22	0.23	0.22
MgO	4.95	5.09	6.25	5.59	5.14	5.03
CaO	8.81	8.81	9.77	8.94	9.07	8.95
Na_2O	3.81	4.46	2.89	3.85	4.15	3.87
K_2O	2.88	3.01	2.52	2.80	2.86	2.85
P_2O_5	0.88	0.77	0.64	0.74	1.19	0.92
LOI	1.46	0.71	1.60	0.04	0.39	0.07
Total	99.32	99.41	99.50	99.69	99.19	98.99
Fe_2O_3 recalc.	3.25	3.27	2.07	3.42	3.27	3.27
FeO recalc.	10.85	10.91	10.35	11.39	10.91	10.89
Trace elements (ppm)						
Sc	14	14	20	16	15	14
V	210	225	288	247	220	233
Cr	-20	-20	78	-20	-20	-20
Co	29	32	37	35	33	20
Ni	1	2	29	8	5	4
Cu	7	6	23	13	10	9
Ga	22	23	19	23	24	19
Ge	1.3	1.7	1.4	1.4	1.1	0.6
Rb	71	70	50	68	71	73
Sr	1 600	1 250	1 200	1 210	1 180	1 310
Y	31.0	31.1	25.6	30.3	31.0	34.1
Zr	321	160	130	200	337	177
Nb	85.0	76.5	64.5	77.6	91.1	78.7
Cs	1.0	0.9	0.8	1.0	0.8	0.8
Ba	1 020	1 030	1 040	975	1 030	1 040
La	56.5	61.4	44.7	57.4	57.6	65.8
Ce	115	127	95.3	118	121	136
Pr	13.2	14.6	11.1	13.6	13.8	15.8
Nd	53.1	60.0	45.5	56.0	56.7	65.7
Sm	9.80	11.0	8.92	10.5	11.0	12.1
Eu	3.30	3.63	3.07	3.54	3.65	4.15
Gd	7.50	8.32	6.80	8.98	8.27	9.49
Tb	1.15	1.28	1.09	1.23	1.24	1.40
Dy	5.99	6.48	5.63	6.39	6.52	7.21
Ho	1.04	1.14	0.98	1.10	1.11	1.24
Er	2.73	2.97	2.51	2.88	2.81	3.20
Tm	0.33	0.36	0.30	0.34	0.33	0.38
Yb	1.81	1.93	1.64	1.83	1.77	2.01
Lu	0.24	0.26	0.21	0.24	0.22	0.24
Hf	8.26	3.62	3.25	4.29	8.39	8.63
Ta	6.37	6.94	5.84	6.32	6.43	7.29
Pb	9	-5	3.7*	4.6*	10	8
Th	6.69	5.17	3.61	5.06	5.76	6.15
U	1.57	1.78	1.28	1.46	1.39	1.59
Mg#	45.69	45.68	52.65	47.06	46.05	45.69

III.1.1.2. Assomada Formation

Sample	ST-13	ST-14	ST-18	ST-19	ST-20	ST-21	ST-22	ST-23
Rock type	BSN	BSN	MNP	BSN	BSN	PIC	BSN	MNP
Major elements (wt.%)								
SiO_2	43.42	43.37	36.49	42.32	42.85	40.66	43.70	42.21
TiO_2	3.69	3.78	3.43	3.18	3.24	3.41	3.95	3.57
Al_2O_3	15.07	15.29	10.24	13.34	13.56	10.10	14.02	13.89
$Fe_2O_3^T$	13.52	13.37	12.93	13.02	12.88	13.24	15.51	13.08
MnO	0.18	0.19	0.25	0.18	0.18	0.18	0.22	0.18
MgO	6.65	6.12	12.12	9.93	9.77	15.13	5.64	8.48
CaO	9.92	9.70	15.76	10.22	10.35	11.98	9.00	11.06
Na_2O	4.14	4.15	3.43	2.71	2.91	2.21	3.70	2.93
K_2O	0.78	0.91	1.45	1.56	1.81	0.46	2.65	2.22
P_2O_5	0.61	0.62	1.26	0.55	0.60	0.38	0.73	0.61
LOI	1.02	1.70	1.62	3.13	0.81	1.54	0.16	0.91
Total	99.00	99.20	98.97	100.14	98.96	99.28	98.96	99.14
Fe_2O_3 recalc.	2.13	2.12	2.05	2.07	2.02	1.63	3.37	2.05
FeO recalc.	10.65	10.58	10.24	10.35	10.12	10.87	11.23	10.27
Trace elements (ppm)								
Sc	22	21	21	22	22	30	16	23
V	298	305	302	306	294	272	249	348
Cr	109	67	483	155	346	961	-20	268
Co	6	41	35	15	49	44	38	14
Ni	36	26	251	134	203	328	10	131
Cu	24	22	47	30	46	64	11	57
Zn	67	70	108	110	101	86	118	101
Ga	6	23	15	9	21	15	24	8
Ge	-0.5	1.4	0.8	0.5	1.3	0.8	1.4	0.6
Rb	42	58	30	46	48	41	58	45
Sr	1 060	1 220	2 270	1 000	902	633	1 250	962
Y	21.4	26.8	40.8	24.5	22.0	18.6	31.2	23.3
Zr	167	158	264	179	239	183	213	193
Nb	29.5	80.9	143	38.9	60.5	50.3	79.4	26.1
Cs	0.5	0.8	0.4	0.6	0.5	0.4	0.7	0.4
Ba	938	1 120	952	799	801	546	972	842
La	38.7	51.0	131	59.3	40.8	28.9	61.1	42.6
Ce	80.5	108	264	121	89.6	64.0	126	91.7
Pr	9.39	12.8	29.3	13.2	10.5	7.81	14.6	11.0
Nd	39.1	53.5	111	52.6	43.6	34.1	59.8	46.2
Sm	7.57	10.3	18.1	9.24	7.97	6.90	11.2	8.61
Eu	2.63	3.51	5.66	2.97	2.60	2.28	3.79	2.86
Gd	6.06	7.73	13.0	6.95	5.82	5.30	8.42	6.75
Tb	0.96	1.18	1.75	1.04	0.90	0.81	1.29	1.00
Dy	4.98	6.10	9.18	5.37	4.71	4.09	6.85	5.27
Ho	0.85	1.07	1.54	0.91	0.79	0.69	1.18	0.89
Er	2.16	2.60	3.74	2.27	1.96	1.67	2.99	2.26
Tm	0.253	0.299	0.414	0.259	0.232	0.191	0.364	0.268
Yb	1.39	1.58	2.14	1.46	1.23	1.04	1.98	1.37
Lu	0.178	0.211	0.241	0.156	0.150	0.115	0.263	0.159
Hf	5.5	7.1	7.1	7.0	6.4	6.1	4.8	6.7
Ta	4.70	5.92	11.2	5.08	4.70	4.87	6.81	4.95
Pb	6	-5	5.9*	5	5	1.6*	10	3.2*
Th	4.08	5.43	11.6	5.14	3.85	2.56	5.12	3.85
U	0.97	1.26	5.65	1.09	0.90	0.62	1.57	1.03
Mg#	53.48	51.69	68.66	64.06	63.94	71.98	47.77	60.25

Sample	ST-28	ST-29
Rock type	TEP	TEP
Major elements (wt.%)		
SiO_2	46.47	43.73
TiO_2	3.25	4.05
Al_2O_3	15.90	14.53
$Fe_2O_3^T$	13.23	14.93
MnO	0.24	0.21
MgO	3.78	5.34
CaO	8.77	9.08
Na_2O	3.54	4.06
K_2O	2.90	2.73
P_2O_5	1.38	0.75
LOI	0.09	0.13
Total	99.36	99.28
Fe_2O_3 recalc.	2.86	3.23
FeO recalc.	9.53	10.77
Trace elements (ppm)		
Sc	11	17
V	130	202
Cr	-20	-20
Co	16	24
Ni	4	4
Cu	-1	4
Zn	131	105
Ga	22	20
Ge	1.1	1.1
Rb	61	59
Sr	1 430	1 210
Y	36.0	30.0
Zr	333	198
Nb	84.3	68.0
Cs	0.3	0.6
Ba	1 200	909
La	70.3	51.5
Ce	147	110
Pr	16.8	12.9
Nd	70.6	54.5
Sm	13.3	10.6
Eu	4.46	3.55
Gd	10.3	8.54
Tb	1.51	1.27
Dy	7.89	6.42
Ho	1.37	1.08
Er	3.44	2.76
Tm	0.400	0.325
Yb	2.17	1.74
Lu	0.266	0.213
Hf	8.3	6.8
Ta	6.05	5.14
Pb	5	6
Th	6.32	4.30
U	1.54	1.08
Mg#	41.82	47.36

III.1.1.3. Upper Pico da Antónia Formation

Sample	ST-9	ST-10	ST-26	ST-27	ST-32	ST-38	ST-39	ST-40
Rock type	BSN	MNP	NP	MNP	MNP	B	TEP	BSN
Major elements (wt.%)								
SiO_2	43.76	40.88	41.45	41.27	42.71	44.15	43.64	42.63
TiO_2	3.03	3.08	3.25	2.90	3.75	2.45	3.25	3.13
Al_2O_3	12.90	12.46	15.68	10.06	14.17	12.82	14.70	13.00
Fe_2O_3T	12.83	12.15	10.79	12.61	11.56	11.89	12.08	13.33
MnO	0.17	0.17	0.25	0.18	0.17	0.17	0.17	0.19
MgO	10.68	10.82	4.85	14.80	7.23	10.15	6.13	10.16
CaO	11.79	12.49	10.95	12.55	12.71	12.80	13.26	12.19
Na_2O	2.24	2.01	5.24	2.65	3.70	2.74	3.02	2.73
K_2O	1.29	0.87	2.60	0.53	1.84	1.05	1.62	0.73
P_2O_5	0.45	0.71	1.18	0.67	0.49	0.52	0.60	0.56
LOI	1.13	3.52	2.69	1.90	0.79	1.20	0.80	2.04
Total	100.27	99.16	98.92	100.12	99.11	99.94	99.27	100.69
Fe_2O_3 recalc.	2.00	1.96	2.40	1.98	1.81	1.86	1.89	2.09
FeO recalc.	9.98	9.79	8.02	9.90	9.06	9.28	9.45	10.42
Trace elements (ppm)								
Sc	27	27	10	27	24	25	26	29
V	260	270	235	276	294	231	278	288
Cr	515	521	-20	793	185	492	101	523
Co	12	50	25	41	43	38	40	56
Ni	144	152	17	387	78	241	68	210
Cu	40	50	43	50	58	60	69	60
Zn	64	71	126	90	86	91	98	96
Ga	6	20	27	15	21	16	23	20
Ge	0.5	1.4	1.0	0.6	1.2	0.7	1.2	1.2
Rb	19	24	70	20	42	20	36	16
Sr	613	910	2 310	1 030	1 260	864	852	749
Y	20.0	24.6	48.0	24.3	26.0	22.6	25.1	23.1
Zr	165	256	541	189	200	151	247	250
Nb	23.3	68.4	164	62.3	63.1	58.8	69.5	61.3
Cs	0.2	0.7	1.2	0.5	0.8	0.2	0.3	0.5
Ba	467	677	1 100	709	1 170	810	774	1 150
La	27.4	42.7	141	60.1	58.0	45.3	43.4	37.2
Ce	59.3	90.1	271	121	118	93.1	91.1	78.7
Pr	7.19	10.4	29.3	13.3	13.4	10.3	10.6	9.25
Nd	30.2	44.2	111	53.2	54.8	42.6	44.3	39.2
Sm	6.21	8.66	18.4	9.41	10.0	7.81	8.56	7.85
Eu	2.18	2.93	5.77	3.05	3.28	2.67	2.93	2.61
Gd	5.12	6.83	13.9	7.01	7.78	6.29	6.92	6.25
Tb	0.81	1.06	1.92	1.06	1.11	0.91	1.06	0.97
Dy	4.46	5.48	9.91	5.30	5.61	4.74	5.39	4.97
Ho	0.76	0.94	1.71	0.87	0.95	0.81	0.90	0.86
Er	1.94	2.35	4.21	2.17	2.25	2.01	2.33	2.18
Tm	0.228	0.276	0.514	0.243	0.256	0.239	0.270	0.256
Yb	1.26	1.45	2.67	1.28	1.34	1.26	1.41	1.36
Lu	0.164	0.189	0.312	0.137	0.148	0.154	0.171	0.180
Hf	5.1	6.7	10.6	5.6	4.5	4.6	6.4	6.6
Ta	3.69	5.07	11.4	4.40	6.05	3.96	4.95	4.67
Pb	6	-5	11	4*	-5	5	6	2.1*
Th	2.80	4.25	13.3	5.20	4.09	4.07	4.05	3.44
U	0.52	0.92	4.75	1.44	1.29	0.93	0.68	0.60
Mg#	66.05	67.55	53.07	73.29	59.38	66.62	54.26	64.05

Sample	ST-41	ST-43	ST-44	ST-45	ST-46B	ST-48	ST-50	ST-59
Rock type	TEP	MNP	MNP	MNP	MNP	MNP	BSN	BSN
Major elements (wt.%)								
SiO_2	43.37	43.41	40.72	39.65	39.79	38.96	44.21	41.68
TiO_2	3.21	3.23	3.35	3.35	3.29	3.06	2.64	3.39
Al2O3	14.74	14.72	11.32	11.36	11.40	9.68	12.91	12.75
$Fe_2O_3^T$	11.82	11.97	12.53	12.37	12.21	11.71	12.22	12.66
MnO	0.17	0.17	0.18	0.18	0.17	0.18	0.17	0.18
MgO	6.18	6.04	13.15	13.35	13.35	15.64	10.51	8.46
CaO	13.45	13.74	12.16	11.95	12.09	13.81	11.96	11.28
Na_2O	2.50	2.77	2.95	2.23	2.49	2.84	2.85	3.93
K_2O	1.51	1.59	0.61	0.68	0.69	0.75	1.27	0.53
P_2O_5	0.53	0.75	0.55	0.60	0.64	0.92	0.55	0.92
LOI	1.24	1.46	1.85	3.34	3.20	1.90	0.09	3.35
Total	98.72	99.84	99.37	99.05	99.33	99.45	99.38	99.13
Fe_2O_3 recalc.	1.87	1.88	1.98	1.99	1.96	1.85	1.90	2.04
FeO recalc.	9.34	9.38	9.91	9.97	9.79	9.25	9.48	10.19
Trace elements (ppm)								
Sc	24	26	27	28	28	28	25	22
V	272	268	281	334	273	268	247	290
Cr	106	97	627	598	615	854	490	358
Co	39	35	37	27	54	61	24	20
Ni	70	67	283	259	271	390	227	161
Cu	72	66	45	56	47	63	57	44
Zn	99	91	85	84	83	83	90	114
Ga	21	21	16	12	19	17	11	16
Ge	1.3	1.1	0.5	0.7	1.1	1.1	0.5	-0.5
Rb	31	32	10	17	17	27	23	38
Sr	836	861	906	789	925	1 150	870	1 370
Y	25.3	23.6	23.4	22.1	23.5	26.2	23.3	30.4
Zr	152	234	151	202	278	259	144	206
Nb	53.2	63.2	61.4	39.6	69.6	78.5	37.1	85.1
Cs	0.3	0.3	0.7	0.4	0.5	0.4	0.3	1.0
Ba	758	864	822	684	772	947	657	930
La	42.2	38.9	45.0	41.7	46.1	74.0	46.3	85.5
Ce	92.0	82.9	93.9	88.4	98.3	149	96.6	173
Pr	10.5	9.65	10.8	10.3	11.4	16.8	10.9	19.3
Nd	43.9	40.1	44.8	42.3	46.8	65.9	43.1	74.0
Sm	8.61	7.92	8.55	8.06	8.72	11.6	8.01	12.3
Eu	2.89	2.64	2.77	2.62	2.81	3.62	2.66	3.91
Gd	6.77	6.26	6.37	5.98	6.70	8.48	6.30	9.00
Tb	1.04	0.95	1.00	0.92	0.98	1.20	0.93	1.22
Dy	5.50	5.03	5.02	4.71	5.05	5.90	4.75	6.38
Ho	0.93	0.85	0.82	0.78	0.86	0.94	0.82	1.04
Er	2.37	2.18	2.11	1.97	2.18	2.29	2.11	2.64
Tm	0.283	0.260	0.240	0.232	0.246	0.249	0.229	0.287
Yb	1.51	1.37	1.29	1.24	1.35	1.26	1.25	1.46
Lu	0.178	0.173	0.151	0.141	0.166	0.115	0.152	0.158
Hf	3.5	5.7	6.0	5.1	6.7	6.5	3.4	8.8
Ta	4.64	4.57	4.86	4.69	5.15	5.25	3.85	6.73
Pb	-5	-5	2.8*	-5	-5	3.8*	2.7	5.5
Th	3.13	3.63	3.94	3.43	4.48	7.49	3.23	7.72
U	0.73	0.75	0.87	0.84	0.96	1.81	1.06	2.06
Mg#	55.00	54.12	71.04	71.61	71.88	75.74	66.78	60.97

Sample	ST-99	ST-187
Rock type	BSN	MNP
Major elements (wt.%)		
SiO_2	42.54	40.75
TiO_2	3.46	4.09
Al_2O_3	11.65	10.68
$Fe_2O_3^T$	12.70	13.67
MnO	0.17	0.18
MgO	11.70	12.11
CaO	11.28	11.92
Na_2O	2.60	2.94
K_2O	0.98	0.62
P_2O_5	0.44	0.70
LOI	1.76	2.71
Total	99.28	100.38
Fe_2O_3 recalc.	2.01	2.16
FeO recalc.	10.04	10.80
Trace elements (ppm)		
Sc	27	27
V	304	364
Cr	560	620
Co	62	60
Ni	252	238
Cu	51	50
Zn	90	88
Ga	21	20
Ge	1.3	1.4
Rb	15	45
Sr	719	812
Y	21.1	24.9
Zr	274	313
Nb	78.3	77.9
Cs	0.4	0.7
Ba	562	701
La	30.9	55.4
Ce	61	112
Pr	8.4	12.9
Nd	31.8	47.6
Sm	7.4	10.2
Eu	2.53	3.35
Gd	6.83	8.90
Tb	0.91	1.15
Dy	4.48	5.67
Ho	0.76	0.93
Er	1.93	2.36
Tm	0.247	0.301
Yb	1.42	1.64
Lu	0.177	0.205
Hf	6.9	8.3
Ta	5.42	4.42
Pb	6	< 5
Th	3.15	4.75
U	0.67	1.16
Mg#	68.29	67.43

III.1.1.4. Lower Pico da Antónia Formation

Sample	ST-37	ST-42	ST-8	ST-30	ST-36	ST-74	ST-101	ST-173
Rock type	MNP	MNP	MNP	MNP	B	MNP	MNP	MNP
Major elements (wt.%)								
SiO_2	41.39	41.31	41.03	42.34	43.63	40.21	42.38	40.84
TiO_2	3.26	3.27	3.72	3.46	3.04	3.46	3.38	3.37
Al_2O_3	11.32	11.37	13.10	12.68	13.21	11.34	11.14	10.80
$Fe_2O_3^T$	12.35	12.21	12.51	12.74	11.35	12.70	12.27	13.96
MnO	0.17	0.17	0.21	0.18	0.17	0.17	0.18	0.18
MgO	13.33	13.26	8.21	9.34	9.60	11.93	12.86	14.73
CaO	12.02	11.85	12.38	12.93	12.25	11.41	12.27	11.02
Na_2O	1.87	2.05	2.28	2.37	2.74	1.86	1.64	2.12
K_2O	1.76	2.01	1.67	1.78	1.02	2.07	1.41	1.58
P_2O_5	0.46	0.44	0.87	0.53	0.41	0.86	0.46	0.67
LOI	1.76	1.24	3.33	0.99	2.09	2.78	2.04	1.70
Total	99.69	99.19	99.31	99.33	99.51	98.79	100.04	100.97
Fe_2O_3 recalc.	1.94	1.92	2.01	2.00	1.80	2.04	1.93	2.17
FeO recalc.	9.72	9.61	10.05	9.99	8.97	10.20	9.65	10.85
Trace elements (ppm)								
Sc	29	28	25	28	25	23	31	24
V	294	275	321	292	265	276	314	295
Cr	762	775	238	469	544	501	890	690
Co	39	21	46	28	47	57	65	67
Ni	323	320	81	148	176	267	264	351
Cu	60	62	41	65	89	42	72	57
Zn	80	84	84	86	92	102	75	95
Ga	14	9	21	15	19	21	20	19
Ge	0.6	-0.5	1.6	-0.5	1.1	1.2	1.4	1.3
Rb	38	42	40	35	23	54	38	34
Sr	682	681	1 470	834	771	1 100	579	945
Y	19.6	19.1	37.6	22.9	22.7	25.7	22.2	24.9
Zr	186	195	186	161	235	311	264	263
Nb	48.9	48.1	94.0	58.8	52.7	84.3	74.1	78.8
Cs	0.4	0.6	0.5	0.4	0.3	0.6	0.4	0.4
Ba	624	657	870	629	501	887	461	643
La	35.9	35.9	120	41.0	40.2	61.5	35.2	48.7
Ce	75.5	75.6	228	87.6	83.6	129	70	94
Pr	8.67	8.84	24.9	10.2	9.41	14.5	9.5	12.4
Nd	35.6	36.4	98.0	42.0	38.0	57.9	36.4	46.8
Sm	7.00	6.99	16.1	8.21	7.45	10.5	8.1	9.8
Eu	2.36	2.30	4.89	2.76	2.47	3.44	2.69	3.16
Gd	5.49	5.62	11.1	6.59	5.87	7.79	7.21	8.66
Tb	0.80	0.82	1.58	0.96	0.91	1.09	1.01	1.15
Dy	4.22	4.19	8.21	4.90	4.74	5.58	5.01	5.57
Ho	0.71	0.71	1.33	0.83	0.84	0.92	0.84	0.92
Er	1.75	1.83	3.26	2.07	2.18	2.22	2.08	2.39
Tm	0.205	0.204	0.392	0.236	0.251	0.232	0.266	0.309
Yb	1.06	1.11	2.08	1.23	1.39	1.21	1.52	1.75
Lu	0.137	0.128	0.232	0.145	0.165	0.130	0.193	0.213
Hf	5.2	5.9	3.5	6.4	5.7	7.4	6.5	6.3
Ta	4.58	4.67	8.30	5.06	3.76	5.92	4.99	4.82
Pb	2.3	2.7	-5	2.7	8	4.1	< 5	6
Th	3.41	3.71	6.34	3.52	3.87	6.46	3.83	4.32
U	0.89	0.90	3.69	0.91	0.93	1.67	1.13	1.13
Mg#	71.62	71.74	60.54	63.15	66.41	68.71	71.01	71.15

Sample	ST-174	ST-177	ST-186
Rock type	MNP	MNP	MNP
Major elements (wt.%)			
SiO_2	39.76	40.09	41.47
TiO_2	3.32	3.31	3.57
Al_2O_3	10.44	10.42	11.45
$Fe_2O_3^T$	13.37	13.76	13.73
MnO	0.17	0.17	0.19
MgO	14.22	14.03	11.07
CaO	11.43	10.63	11.38
Na_2O	2.16	2.13	2.67
K_2O	1.57	1.55	2.23
P_2O_5	0.72	0.65	0.93
LOI	2.24	1.73	0.18
Total	99.41	98.47	98.51
Fe_2O_3 recalc.	2.12	2.20	2.15
FeO recalc.	10.62	10.98	10.74
Trace elements (ppm)			
Sc	26	25	25
V	297	293	312
Cr	780	720	510
Co	72	67	66
Ni	362	352	197
Cu	62	63	74
Zn	86	89	103
Ga	22	21	26
Ge	1.3	1.2	1.5
Rb	39	36	56
Sr	937	893	1 109
Y	26.6	24.9	32.7
Zr	276	264	342
Nb	83.3	79.7	106.0
Cs	0.5	0.4	0.7
Ba	609	618	760
La	51.5	47.8	72.1
Ce	98	92	135
Pr	13.3	12.6	18.3
Nd	49.6	45.9	66.2
Sm	10.7	9.7	13.4
Eu	3.43	3.24	4.34
Gd	9.50	8.87	11.80
Tb	1.24	1.17	1.53
Dy	5.93	5.47	7.33
Ho	0.98	0.91	1.19
Er	2.49	2.31	3.03
Tm	0.324	0.307	0.391
Yb	1.88	1.73	2.15
Lu	0.221	0.214	0.253
Hf	6.5	6.2	8.5
Ta	5.02	4.79	6.61
Pb	5	5	10
Th	4.54	4.32	6.95
U	1.23	1.16	1.92
Mg#	71.32	70.44	65.33

III.1.1.5. Flamengos Formation

Sample	ST-4	ST-5	ST-6	ST-11	ST-12	ST-34	ST-51	ST-56
Rock type	MNP	MNP	B	MNP	PIC	MNP	MNP	BSN
Major elements (wt.%)								
SiO_2	41.08	40.98	42.90	42.15	42.83	40.81	41.12	42.19
TiO_2	4.14	4.18	3.10	3.44	2.64	3.33	3.65	3.62
Al_2O_3	12.13	12.18	12.19	12.07	10.35	11.18	13.55	15.64
$Fe_2O_3^T$	12.09	12.06	10.95	12.71	11.94	12.33	12.32	12.27
MnO	0.18	0.18	0.17	0.18	0.16	0.18	0.20	0.19
MgO	9.80	9.33	10.43	9.87	15.05	13.31	6.91	5.53
CaO	11.77	11.87	12.20	12.89	11.84	12.51	13.35	11.43
Na_2O	2.29	2.09	2.04	2.85	1.41	2.45	2.85	2.54
K_2O	1.78	1.99	1.62	0.78	1.41	1.74	1.67	1.80
P_2O_5	0.57	0.61	0.44	0.53	0.34	0.57	0.90	0.91
LOI	3.47	3.90	3.22	1.85	1.03	0.93	2.66	3.09
Total	99.30	99.36	99.26	99.32	99.01	99.34	99.18	99.22
Fe_2O_3 recalc.	1.95	1.95	1.76	2.01	1.47	1.93	1.97	1.97
FeO recalc.	9.73	9.74	8.78	10.06	9.77	9.66	9.84	9.84
Trace elements (ppm)								
Sc	22	23	26	28	28	27	23	16
V	305	320	271	303	244	281	320	322
Cr	546	528	637	518	1 040	759	173	54
Co	47	49	48	30	44	55	46	32
Ni	161	155	186	136	316	284	98	50
Cu	50	51	64	60	63	57	48	35
Zn	75	75	62	72	59	79	92	81
Ga	19	21	18	16	13	19	23	22
Ge	1.3	1.4	1.4	0.7	0.7	1.1	1.2	1.1
Rb	42	51	44	33	42	40	60	55
Sr	1 030	1 040	853	957	643	853	1 370	1 330
Y	27.2	28.2	23.2	27.9	17.8	21.3	35.1	35.8
Zr	248	276	211	183	129	276	344	270
Nb	77.6	88.7	58.1	52.2	34.9	73.3	100	85.1
Cs	0.6	0.6	0.5	0.8	0.3	0.5	0.7	1.1
Ba	810	893	708	653	458	682	1 280	944
La	56.2	58.7	42.4	47.7	21.9	43.1	86.7	89.8
Ce	113	118	84.9	96.7	47.9	91.1	178	184
Pr	13.0	13.7	9.83	11.4	5.96	10.4	20.0	20.4
Nd	54.1	57.5	40.0	48.0	26.5	44.0	79.2	79.8
Sm	10.1	10.5	7.71	9.28	5.77	8.37	14.1	13.8
Eu	3.26	3.40	2.59	3.05	1.92	2.74	4.43	4.42
Gd	8.21	7.94	6.22	7.37	4.71	6.41	10.6	9.91
Tb	1.15	1.20	0.96	1.19	0.76	0.95	1.49	1.47
Dy	5.87	6.20	5.14	6.18	3.79	4.72	7.60	7.39
Ho	0.97	1.04	0.89	1.07	0.67	0.80	1.26	1.26
Er	2.49	2.54	2.25	2.81	1.70	1.96	3.12	3.14
Tm	0.292	0.309	0.279	0.333	0.197	0.215	0.362	0.372
Yb	1.53	1.62	1.51	1.75	1.04	1.13	1.87	1.97
Lu	0.186	0.194	0.206	0.225	0.133	0.125	0.204	0.239
Hf	5.1	6.9	4.9	6.3	4.7	6.9	8.6	5.4
Ta	6.88	7.30	4.52	4.54	2.98	5.49	7.00	7.54
Pb	5	3.4*	-5	-5	1.7*	2.7*	-5	5
Th	5.18	5.80	4.43	5.14	2.33	4.11	7.51	6.60
U	1.46	1.65	1.71	1.31	0.57	0.98	2.35	2.29
Mg#	65.46	64.39	69.01	64.48	73.92	71.62	56.73	51.31

Sample	ST-57	ST-58	ST-60
Rock type	TEP	MNP	BSN
Major elements (wt.%)			
SiO_2	41.43	41.90	43.16
TiO_2	4.90	4.99	3.37
Al_2O_3	12.78	12.92	12.94
$Fe_2O_3^T$	12.26	12.33	11.92
MnO	0.15	0.16	0.18
MgO	7.10	7.30	9.63
CaO	13.18	13.09	11.74
Na_2O	2.09	1.67	2.15
K_2O	1.06	2.68	1.77
P_2O_5	0.48	0.47	0.50
LOI	3.93	1.87	1.66
Total	99.36	99.38	99.02
Fe_2O_3 recalc.	1.98	1.95	1.89
FeO recalc.	9.91	9.75	9.43
Trace elements (ppm)			
Sc	31	32	27
V	368	397	285
Cr	180	184	759
Co	44	46	31
Ni	110	104	172
Cu	93	87	56
Zn	82	75	82
Ga	22	22	14
Ge	1.1	1.3	0.7
Rb	36	72	43
Sr	591	676	752
Y	22.4	23.1	22.6
Zr	282	292	221
Nb	60.9	61.5	54.9
Cs	3.2	0.6	0.4
Ba	575	784	711
La	35.3	35.5	46.7
Ce	76.5	78.6	96.2
Pr	9.20	9.58	10.7
Nd	39.3	40.6	43.3
Sm	7.89	8.21	8.04
Eu	2.61	2.73	2.55
Gd	6.09	6.57	5.95
Tb	0.95	0.99	0.91
Dy	4.85	5.03	4.87
Ho	0.80	0.86	0.84
Er	2.05	2.20	2.13
Tm	0.234	0.252	0.260
Yb	1.25	1.34	1.41
Lu	0.146	0.154	0.182
Hf	8.2	8.9	5.8
Ta	5.20	5.46	5.19
Pb	-5	-5	-5
Th	3.52	3.67	4.13
U	0.76	0.81	1.06
Mg#	57.51	58.05	65.38

III.1.2. Santiago MORB lavas

Sample	ST-61	ST-62	ST-63	ST-64	ST-65	ST-66	ST-67	ST-68
Rock type	B	B	B	B	B	B	B	B
Major elements (wt.%)								
SiO_2	47.19	45.16	46.27	43.37	46.78	45.53	46.73	45.74
TiO_2	0.825	0.84	0.845	0.81	0.83	0.805	0.84	0.83
Al_2O_3	15.18	15.45	15.35	14.48	15.25	14.97	15.56	15.1
$Fe_2O_3^T$	10.14	9.01	9.7	8.91	9.03	9.65	9.63	9.03
MnO	0.18	0.12	0.16	0.17	0.17	0.15	0.14	0.17
MgO	7.49	5.05	6.49	6.16	7.19	6.91	6.74	6.95
CaO	12.39	12.27	12.67	14.3	12.14	12.2	12.81	13.58
Na_2O	2.89	3.43	3.37	3.4	2.95	3.41	3.3	2.92
K_2O	0.76	0.5	0.47	0.47	0.83	0.85	0.6	0.39
P_2O_5	0.08	0.09	0.09	0.09	0.07	0.07	0.08	0.09
LOI	3.26	7.15	4.5	7.73	3.32	5.06	4.43	4.65
Total	100.39	99.06	99.92	99.89	98.55	99.61	100.87	99.45
Fe_2O_3 recalc.	1.606	1.507	1.564	1.487	1.458	1.57	1.536	1.464
FeO recalc.	8.033	7.537	7.82	7.434	7.289	7.851	7.68	7.323
Trace elements (ppm)								
Sc	39.5	39.8	38.7	37.7	38.8	38.2	37.7	38.8
V	264	261	262	272	253	266	259	254
Cr	393	396	377	400	390	380	377	382
Co	44.8	39.8	43.1	38.9	44.5	43.7	43.1	42.2
Ni	99	92	95	98	98	96	95	96
Cu	101	99	102	98	99	99	97	98
Zn	82	79	78	76	84	81	82	80
Ga	15	18	16	15	14	15	15	15
Ge	1.2	1.2	1.2	1.1	1	1	1	0.9
Rb	17	7	8	7	20	17	13	4
Sr	78	153	96	105	81	116	90	87
Y	29	24	24	33	24	35	24	23
Zr	58	55	52	52	48	61	53	50
Nb	1.1	0.7	nd	2.5	0.9	2.3	nd	nd
Cs	-0.1	-0.1	0.3	0.1	0.5	0.3	0.3	-0.1
Ba	32	693	332	99	30	70	41	18
La	1.02	0.95	0.96	1	0.85	0.9	1.05	0.86
Ce	3.3	3.1	3.4	3.4	3	3.4	3.4	3
Pr	0.66	0.62	0.67	0.67	0.59	0.66	0.67	0.62
Nd	4.67	4	4.43	4.48	4.01	4.7	4.78	4.22
Sm	2.16	1.8	1.96	1.92	1.82	2.2	1.98	1.81
Eu	0.958	0.75	0.82	0.891	0.798	0.984	0.832	0.794
Gd	3.45	2.76	3.05	3.41	2.85	3.68	3.04	3.02
Tb	0.63	0.54	0.56	0.68	0.53	0.74	0.56	0.56
Dy	4.3	3.57	3.75	4.65	3.67	4.94	3.84	3.6
Ho	0.93	0.79	0.84	1.05	0.83	1.06	0.84	0.8
Er	2.95	2.53	2.55	3.39	2.56	3.37	2.62	2.58
Tm	0.453	0.385	0.395	0.522	0.406	0.512	0.418	0.404
Yb	2.85	2.48	2.44	3.14	2.54	3.09	2.49	2.41
Lu	0.432	0.391	0.383	0.487	0.403	0.487	0.408	0.365
Hf	1.4	1.5	1.4	1.5	1.3	1.4	1.4	1.4
Ta	-0.1	-0.1	-0.1	-0.1	-0.1	-0.1	-0.1	-0.1
Pb	9	10	7	8	12	10	9	9
Th	7.97	2.5	2.19	4.47	4.04	7.63	3.8	1.64
U	0.15	0.1	0.21	0.14	0.11	0.18	0.19	0.14
Mg#	63.33	56.71	61.00	61.77	65.05	62.60	62.07	64.27

Sample	ST-69	ST-70	ST-71	ST-72
Rock type	B	B	B	B
Major elements (wt.%)				
SiO_2	46.47	45.52	45.85	45.37
TiO_2	0.865	0.83	0.81	0.84
Al_2O_3	15.45	14.91	14.97	15.3
$Fe_2O_3^T$	8.81	9.8	9.93	9.89
MnO	0.15	0.16	0.17	0.16
MgO	6.49	6.77	6.82	6.78
CaO	12.6	12.49	12.58	12.45
Na_2O	3.55	3.14	3.12	3.03
K_2O	0.64	0.49	0.38	0.58
P_2O_5	0.09	0.08	0.08	0.09
LOI	4.96	4.34	4.69	4.42
Total	100.07	98.52	99.4	98.89
Fe_2O_3 recalc.	1.424	1.601	1.613	1.611
FeO recalc.	7.119	8.005	8.067	8.053
Trace elements (ppm)				
Sc	40.2	39.8	38.4	40.2
V	277	257	256	266
Cr	406	393	387	396
Co	39.6	43.5	43.6	45.5
Ni	92	93	97	101
Cu	102	102	100	101
Zn	80	80	80	81
Ga	15	14	15	15
Ge	1.1	1	1.1	1
Rb	10	10	7	13
Sr	104	92	90	76
Y	25	24	25	24
Zr	57	51	47	60
Nb	1.1	0.7	1.1	0.8
Cs	0.2	0.1	0.1	0.2
Ba	55	27	21	8
La	0.8	0.84	0.72	0.76
Ce	3.5	3.2	3	3.1
Pr	0.68	0.63	0.61	0.62
Nd	4.58	4.43	4.16	4.39
Sm	1.95	1.93	1.77	1.85
Eu	0.844	0.807	0.761	0.777
Gd	3.14	3.07	2.95	2.96
Tb	0.58	0.56	0.56	0.55
Dy	3.99	3.74	3.81	3.81
Ho	0.88	0.83	0.85	0.82
Er	2.76	2.55	2.71	2.58
Tm	0.438	0.404	0.418	0.411
Yb	2.73	2.46	2.55	2.47
Lu	0.421	0.373	0.407	0.391
Hf	1.5	1.3	1.4	1.5
Ta	-0.1	-0.1	-0.1	-0.1
Pb	10	8	8	8
Th	3.8	3.68	1.35	3.84
U	0.16	0.12	nd	0.11
Mg#	63.26	61.76	61.62	61.58

III.1.3. Maio MORB lavas

Sample	CVP-79	CVP-80	CVP-83
Rock type	TB	TB	TB
Major elements (wt.%)			
SiO_2	47.97	47.99	43.40
TiO_2	1.50	1.49	1.52
Al_2O_3	14.75	14.49	14.15
$Fe_2O_3^T$	11.56	11.86	11.62
MnO	0.124	0.142	0.193
MgO	7.09	6.43	6.08
CaO	9.39	10.37	9.3
Na_2O	3.05	3.18	4.18
K_2O	2.13	1.68	1.34
P_2O_5	0.13	0.13	0.13
LOI	1.95	2.29	7.07
Total	99.65	100	98.97
Fe_2O_3 recalc.	2.539	2.604	2.714
FeO recalc.	8.463	8.679	9.048
Trace elements (ppm)			
Sc	45	44	45
V	390	389	368
Cr	270	270	260
Co	40	35	34
Ni	nd	nd	nd
Cu	nd	nd	nd
Zn	nd	nd	nd
Ga	nd	nd	nd
Ge	nd	nd	nd
Rb	32	26	26
Sr	279	238	604
Y	37.3	35.3	35.7
Zr	86	83	87
Nb	1.6	1.4	1.6
Cs	0.3	0.2	0.2
Ba	90	88	183
La	2.51	2.43	4.16
Ce	8.94	8.12	10.2
Pr	1.48	1.39	1.68
Nd	8.61	8.19	9.22
Sm	3.3	3.17	3.42
Eu	1.19	1.12	1.16
Gd	4.91	4.64	4.73
Tb	0.92	0.91	0.92
Dy	5.92	5.83	5.86
Ho	1.28	1.24	1.25
Er	3.65	3.73	3.82
Tm	0.575	0.556	0.596
Yb	4.01	3.74	3.99
Lu	0.628	0.597	0.623
Hf	2.3	2.2	2.4
Ta	0.08	0.08	0.07
Pb	nd	nd	nd
Th	0.13	0.11	0.15
U	0.04	0.21	0.12
Mg#	60.677	57.698	56.83

III.1.4. Santiago Gabbroic Xenoliths

Sample	ST-164	ST-167	ST-168	ST-169
Rock type	G	G	G	G
Major elements (wt.%)				
SiO_2	41.32	45.08	48.04	48.41
TiO_2	0.089	0.167	0.189	0.202
Al_2O_3	23.55	25.62	19.79	17.52
$Fe_2O_3^T$	5.82	6.15	5.62	5.74
MnO	0.099	0.059	0.076	0.097
MgO	7.02	3.75	6.53	9.78
CaO	15.62	16.31	15.16	14.51
Na_2O	1.63	1.68	1.7	1.61
K_2O	0.02	0.04	0.22	0.17
P_2O_5	0.02	0.17	0.14	0.03
LOI	3.82	1.8	0.99	0.67
Total	99.01	100.8	98.47	98.72
Fe_2O_3 recalc.	0.73	0.95	0.88	0.90
FeO recalc.	4.87	4.76	4.42	4.49
Trace elements (ppm)				
Sc	10	22	33	38
V	46	143	133	132
Cr	320	1070	480	400
Co	38	16	23	35
Ni	280	150	90	130
Cu	60	90	50	70
Zn	< 30	50	< 30	< 30
Ga	12	17	13	11
Ge	0.7	0.8	1.2	1.3
Rb	< 1	1	3	3
Sr	237	132	122	117
Y	2.1	4.6	5.6	5.7
Zr	12	45	17	13
Nb	0.9	10.1	4.4	2.1
Cs	< 0.1	< 0.1	< 0.1	< 0.1
Ba	112	17	59	42
La	0.31	2.13	1.8	0.51
Ce	0.73	2.64	3.44	1.1
Pr	0.11	0.43	0.46	0.2
Nd	0.54	1.61	2.1	1.28
Sm	0.17	0.41	0.6	0.51
Eu	0.218	0.285	0.343	0.334
Gd	0.27	0.56	0.79	0.78
Tb	0.05	0.12	0.15	0.16
Dy	0.38	0.81	1.02	1.06
Ho	0.08	0.17	0.22	0.23
Er	0.24	0.5	0.66	0.68
Tm	0.035	0.071	0.096	0.098
Yb	0.22	0.44	0.59	0.6
Lu	0.033	0.062	0.094	0.088
Hf	0.3	0.3	0.4	0.4
Ta	< 0.01	0.01	0.21	0.12
Pb	< 5	< 5	< 5	< 5
Th	< 0.05	0.08	0.12	0.05
U	0.11	0.24	0.14	0.16
Mg#	73.06	58.77	73.09	79.93

III.2. Isotopic data

III.2.1. Santiago Alkaline lavas[1]

Formation	Sample	$^{143}Nd/^{144}Nd$	$^{176}Hf/^{177}Hf$	$^{87}Sr/^{86}Sr$	$^{206}Pb/^{204}Pb$	$^{207}Pb/^{204}Pb$	$^{208}Pb/^{204}Pb$
Monte das Vacas	ST-16	0.5126871 (15)	0.282933 (11)	0.703623 (07)	19.075 (3)	15.574 (1)	38.921 (3)
	ST-16 rep				19.085 (1)	15.574 (1)	38.929 (2)
	ST-24	0.5126318 (12)	0.282892 (12)	0.703767 (08)	19.014 (1)	15.567 (1)	38.905 (3)
	ST-24 rep		0.282875 (14)		19.011 (1)	15.565 (1)	38.897 (2)
	ST-24 rep1		0.282884 (09)				
	ST-24 dupl	0.5126601 (10)	0.282895 (06)	0.703775 (06)			
	ST-24 dupl1	0.5126109 (15)	0.282876 (10)	0.703743 (70)			
Assomada	ST-18	0.5128025 (13)	0.282929 (09)	0.703424 (09)	19.745 (1)	15.600 (1)	39.415 (03)
	ST-18 dupl				19.778 (1)	15.604 (1)	39.451 (2)
	ST-18 rep	0.5127739 (12)					
	ST-18 rep1	0.5127682 (11)					
	ST-21	0.5127735 (12)	0.282960 (08)	0.703422 (06)	19.135 (1)	15.574 (1)	38.985 (2)
	ST-23	0.5126138 (11)	0.282879 (10)	0.703822 (07)	18.999 (1)	15.561 (1)	38.885 (2)
	ST-23 rep		0.282886 (07)				
Upper Pico da Antónia	ST-27	0.5126966 (13)	0.282902 (09)	0.703611 (07)	19.165 (1)	15.573 (1)	39.050 (2)
	ST-40	0.5127498 (10)	0.282949 (09)	0.703527 (07)	19.161 (1)	15.575 (1)	38.978 (2)
	ST-44	0.5127288 (12)	0.282934 (12)	0.703529 (08)	19.247 (1)	15.579 (1)	39.059 (2)
	ST-48	0.5127921 (13)	0.282941 (14)	0.703362 (08)	19.606 (1)	15.605 (1)	39.449 (2)
	ST-48 rep	0.5127547 (18)	0.282950 (14)				
	ST-50	0.5127897 (19)	0.282956 (05)	0.703365 (08)	19.299 (1)	15.580 (1)	39.053 (2)
	ST-50 rep	0.5127898 (25)					
	ST-50 dupl	0.5127813 (14)	0.282952 (08)	0.703370 (07)			
	ST-50 dupl1	0.5127659 (27)	0.282946 (08)	0.703356 (07)			
	ST-59	0.5126343 (11)	0.282842 (12)	0.703907 (08)	18.930 (2)	15.547 (1)	38.911 (3)
	ST-59 rep		0.282853 (09)				
	ST-59 rep1		0.282851 (05)				
Lower Pico da Antónia	ST-37	0.5127027 (14)	0.282957 (09)	0.703549 (07)	19.113 (2)	15.584 (2)	38.957 (5)
	ST-42	0.5127215 (12)	0.282945 (10)	0.703538 (10)	19.087 (2)	15.588 (2)	38.935 (4)
	ST-42 rep			0.703538 (09)			
	ST-30	0.5127359 (13)	0.282926 (09)	0.703547 (07)	19.258 (1)	15.586 (1)	39.050 (2)
	ST-30 rep		0.282954 (09)				
	ST-30 dupl	0.5127383 (11)	0.282943 (08)	0.703541 (07)			
	ST-30 dupl1	0.5127128 (15)	0.282945 (08)	0.703542 (06)			
	ST-74	0.5126717 (20)	0.282897 (20)	0.703521 (08)	19.186 (2)	15.588 (1)	39.132 (3)
	ST-74 rep	0.5126864 (12)	0.282939 (15)	0.703561 (07)			
	ST-74 rep1		0.282903 (07)				
Flamengos	ST-5	0.5128686 (10)	0.282976 (08)	0.703177 (08)	19.475 (2)	15.603 (1)	39.492 (2)
	ST-5 dupl				19.459 (2)	15.602 (1)	39.468 (3)
	ST-5 rep		0.282963 (09)				
	ST-12	0.5127722 (11)	0.282975 (17)	0.703400 (09)	19.109 (1)	15.571 (1)	
	ST-12 dupl				19.102 (1)	15.570 (1)	39.014 (2)
	ST-12rep		0.282965 (08)				
	ST-34	0.5127057 (11)	0.282937 (09)	0.703523 (13)	19.171 (2)	15.579 (1)	39.002 (3)
	ST-34rep			0.703534 (09)			

[1] Rep. stands for replicate analyses and Dupl. for duplicate analyses. The number in parenthesis refers to the uncertainties on the last two significant digits (expressed in 2σ).

III.2.1.1 - Santiago Alkaline lavas - duplicate and replicate analyses

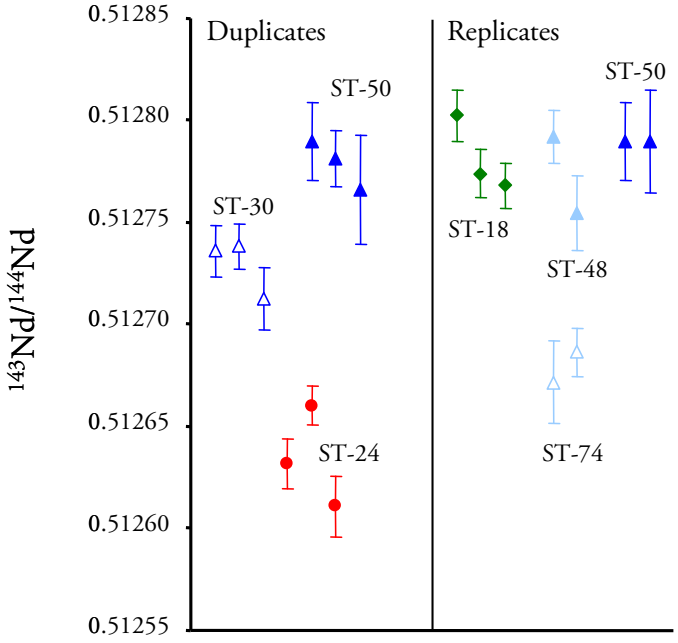

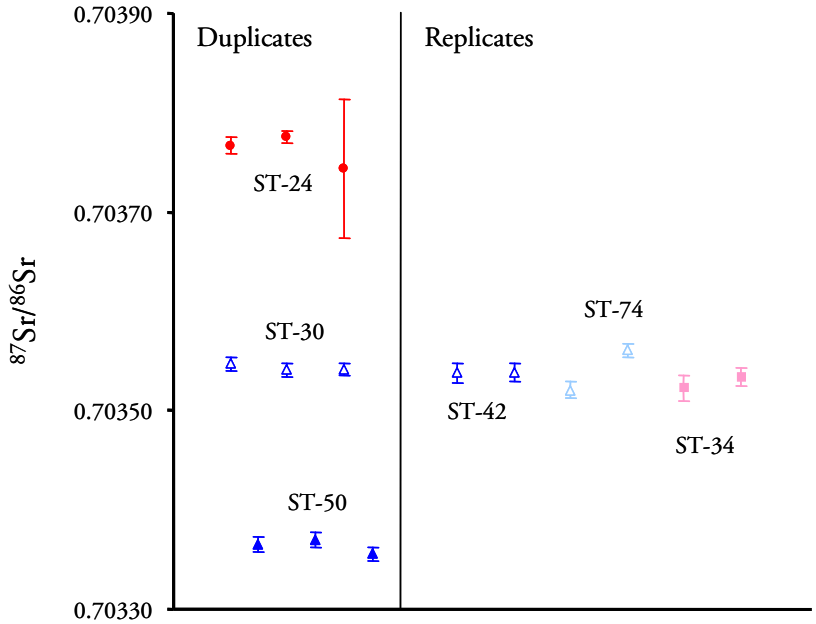

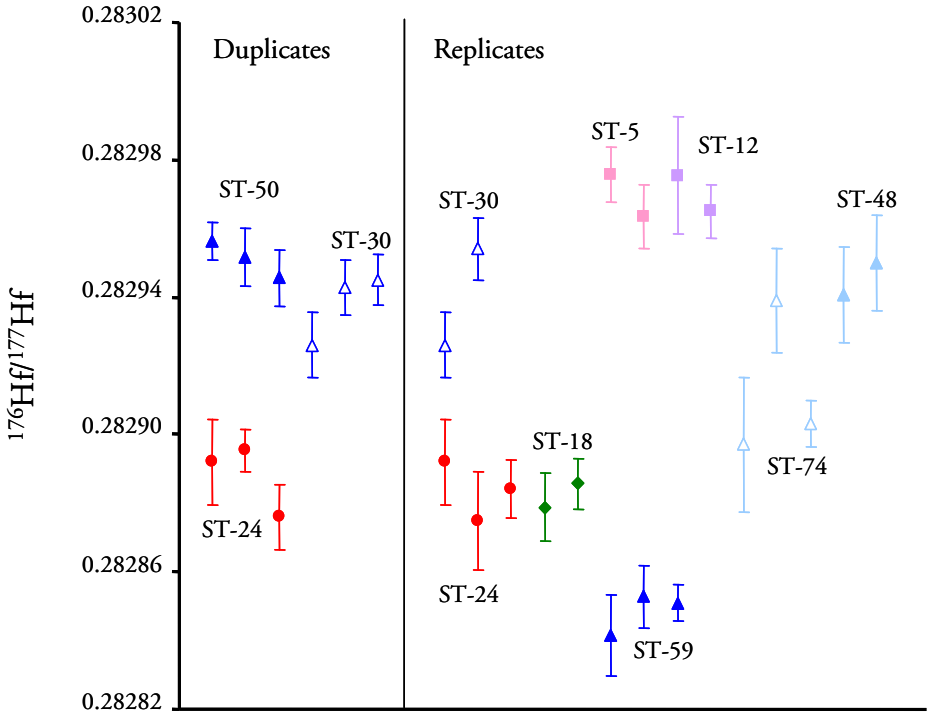
0.28302
0.28298
0.28294
0.28290
0.28286
0.28282
176Hf/177Hf
Duplicates
Replicates
ST-50
ST-30
ST-24
ST-30
ST-5
ST-12
ST-48
ST-18
ST-74
ST-24
ST-59

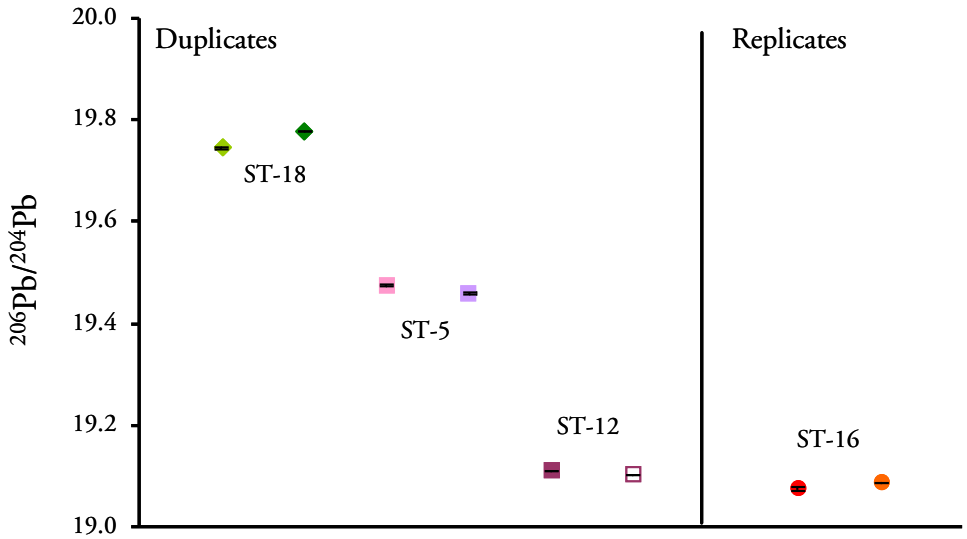
20.0
19.8
19.6
19.4
19.2
19.0
206Pb/204Pb
Duplicates
Replicates
ST-18
ST-5
ST-12
ST-16

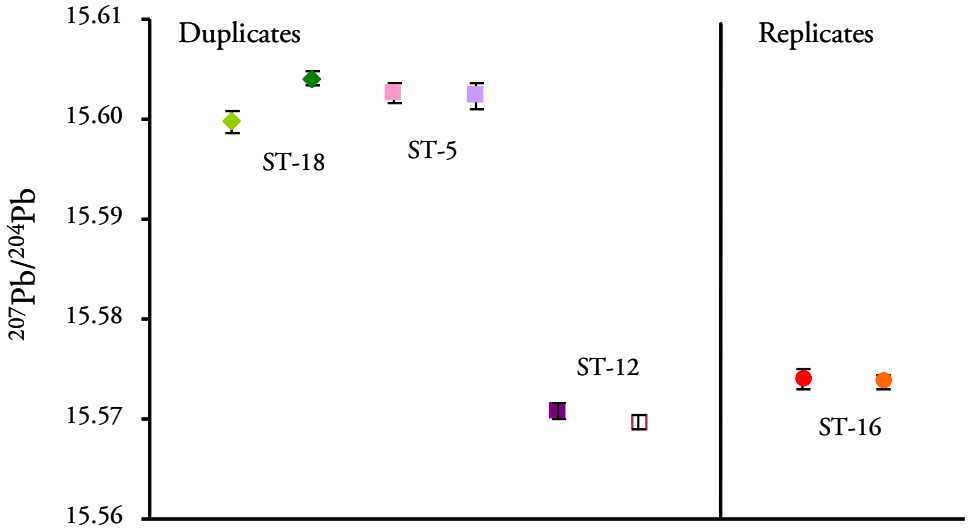
15.61
15.60
15.59
15.58
15.57
15.56
207Pb/204Pb
Duplicates
Replicates
ST-18
ST-5
ST-12
ST-16

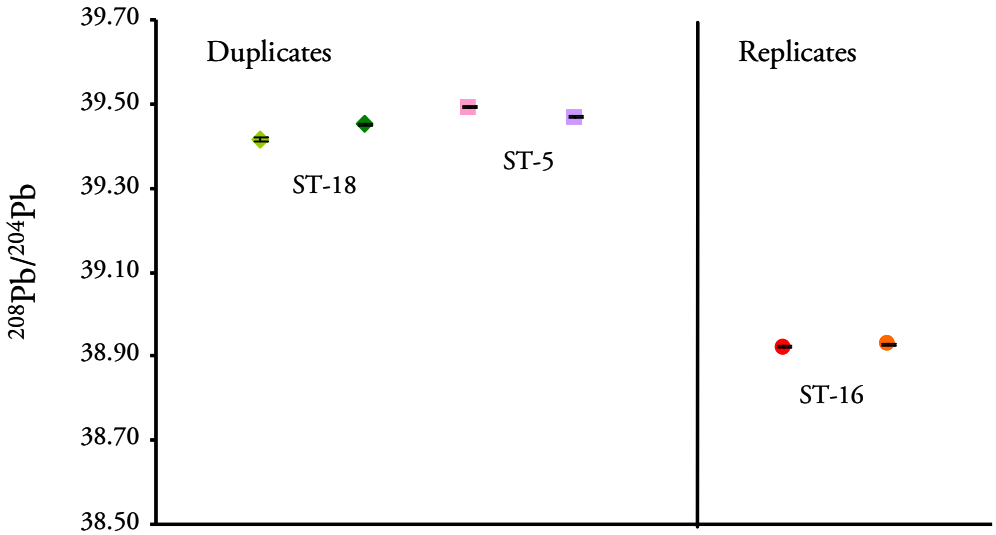
39.70
39.50
39.30
39.10
38.90
38.70
38.50
208Pb/204Pb
Duplicates
Replicates
ST-18
ST-5
ST-16

III.2.2. Santiago MORB lavas

Sample	$^{143}Nd/^{144}Nd$	$^{87}Sr/^{86}Sr$
ST-61	0.513139 (18)	0.703121 (30)
ST-65	0.513136 (22)	0.702865 (24)
ST-66	0.513143 (15)	0.703119 (25)
ST-67	0.513160 (17)	0.702908 (24)
ST-71	0.513191 (20)	0.703035 (18)
ST-72	0.513139 (14)	0.702776 (20)

III.2.3. Maio MORB lavas

Sample	$^{143}Nd/^{144}Nd$	$^{87}Sr/^{86}Sr$
CVP-79	0.513104 (16)	0.703497 (18)
CVP-80	0.513107 (10)	0.703554 (21)
CVP-83	0.513086 (16)	0.703534 (20)

III.3. EMPA data

III.3.1. Santiago MORB lavas

III.3.1.1. Pyroxene

Sample	ST-61	ST-61	ST-61	ST-61	ST-61	ST-61	ST-61	ST-61	ST-61	ST-61
Reference	1	2	3	4	5	6	7	8	9	10
Zone	M	M	M	M	M	M	M	M	M	M
SiO_2	48.42	47.09	47.45	47.22	48.36	47.91	48.45	47.91	47.72	47.27
TiO_2	0.80	1.41	1.35	1.29	1.14	0.93	0.86	0.90	1.31	1.25
Al_2O_3	5.88	6.18	5.77	5.80	5.01	5.93	5.05	5.41	6.42	5.86
Fe_2O_3	3.62	4.05	5.32	4.56	4.45	4.45	4.85	4.48	3.18	5.51
FeO	6.18	5.68	6.26	5.84	6.52	4.55	5.72	5.61	5.32	4.43
MnO	0.25	0.19	0.16	0.18	0.19	0.18	0.23	0.20	0.12	0.16
MgO	14.20	13.74	13.18	13.63	13.86	14.52	13.95	14.57	14.17	14.31
CaO	20.02	20.27	18.75	19.71	18.64	20.35	19.89	19.57	20.56	19.24
K_2O	0.00	0.00	0.06	0.01	0.02	0.01	0.01	0.00	0.00	0.03
Na_2O	0.26	0.26	0.83	0.44	0.76	0.29	0.51	0.27	0.26	0.60
ZnO	0.01	0.03	0.01	0.01	0.00	0.06	0.00	0.00	0.00	0.00
Cr_2O_3	0.26	0.32	0.28	0.28	0.23	0.21	0.26	0.29	0.20	0.29
Total	99.89	99.23	99.42	98.96	99.17	99.39	99.78	99.20	99.26	98.96
Number of cation base d on 6 oxygens atoms normalized for 4 cations										
Si	1.804	1.771	1.786	1.782	1.818	1.788	1.811	1.797	1.783	1.775
Al^{IV}	0.196	0.229	0.214	0.218	0.182	0.212	0.189	0.203	0.217	0.225
$Fe^{3+\ IV}$	0.000	0.000	0.000	0.000	0.000	0.000	0.000	0.000	0.000	0.000
Al^{VI}	0.062	0.045	0.042	0.039	0.040	0.050	0.034	0.036	0.066	0.035
$Fe^{3+\ VI}$	0.101	0.114	0.151	0.129	0.126	0.125	0.136	0.126	0.089	0.156
Ti	0.022	0.040	0.038	0.037	0.032	0.026	0.024	0.025	0.037	0.035
Cr	0.008	0.009	0.008	0.008	0.007	0.006	0.008	0.009	0.006	0.009
Zn	0.000	0.001	0.000	0.000	0.000	0.002	0.000	0.000	0.000	0.000
Mg	0.789	0.770	0.739	0.767	0.777	0.808	0.777	0.815	0.789	0.801
Fe^{2+}	0.981	0.949	0.937	0.951	0.982	0.933	0.956	0.979	0.956	0.905
Mn	0.008	0.006	0.005	0.006	0.006	0.006	0.007	0.006	0.004	0.005
Ca	0.799	0.817	0.756	0.797	0.751	0.814	0.797	0.787	0.823	0.774
K	0.000	0.000	0.003	0.000	0.001	0.001	0.001	0.000	0.000	0.002
Na	0.019	0.019	0.060	0.032	0.055	0.021	0.037	0.019	0.019	0.044
%Enstatite	41.74	40.84	40.01	40.73	41.66	42.65	40.99	42.66	42.16	42.71
%Ferrosillite	15.97	15.86	19.10	16.96	18.08	14.38	17.00	16.17	13.87	16.00
%Wollastonite	42.29	43.30	40.89	42.31	40.27	42.96	42.01	41.18	43.97	41.29
%Jadeite	----------	----------	----------	----------	----------	----------	----------	----------	----------	----------
%Aegirine	----------	----------	----------	----------	----------	----------	----------	----------	----------	----------
%Quad	----------	----------	----------	----------	----------	----------	----------	----------	----------	----------
Classification according to Morimoto et al. (1988)										
Group	Quad	Quad	Quad	Quad	Quad	Quad	Quad	Quad	Quad	Quad
Classification	augite	augite	augite	augite	augite	augite	augite	augite	augite	augite

Sample	ST-61	ST-65	ST-65	ST-65	ST-65	ST-65	ST-65	ST-65	ST-65	ST-65
Reference	11	1	2	3	5	6	7	8	9	10
Zone	M	M	M	M	M	M	M	M	M	M
SiO_2	46.23	50.41	50.87	51.40	49.53	50.07	49.29	50.66	49.79	51.72
TiO_2	2.88	0.61	0.59	0.61	0.82	0.72	1.01	0.74	1.07	0.67
Al_2O_3	5.07	4.59	2.62	3.31	5.39	4.85	5.53	4.54	5.60	2.92
Fe_2O_3	10.81	2.771	3.099	1.90	3.17	2.74	2.43	2.00	4.78	2.46
FeO	4.08	4.549	7.045	8.18	5.09	4.72	5.04	5.55	4.31	5.83
MnO	0.13	0.12	0.22	0.24	0.14	0.16	0.13	0.15	0.12	0.14
MgO	14.17	16.00	16.39	16.75	15.09	15.35	15.46	16.34	14.79	16.56
CaO	16.38	20.74	18.59	17.59	19.58	21.27	20.26	19.90	18.51	19.92
K_2O	0.50	0.01	0.01	0.01	0.06	0.01	0.01	0.00	0.06	0.04
Na_2O	1.27	0.20	0.22	0.24	0.54	0.21	0.25	0.20	1.25	0.27
ZnO	0.00	0.10	0.04	0.04	0.07	0.04	0.00	0.00	0.03	0.06
Cr_2O_3	0.19	0.32	0.24	0.44	0.42	0.30	0.45	0.33	0.57	0.08
Total	101.71	100.42	99.91	100.71	99.90	100.42	99.87	100.40	100.88	100.68
Number of ions on the base of 6 oxygens. normalized for 4 cations										
Si	1.713	1.849	1.888	1.888	1.830	1.841	1.820	1.856	1.822	1.894
Al^{IV}	0.221	0.151	0.112	0.112	0.170	0.159	0.180	0.144	0.178	0.106
$Fe^{3+\ IV}$	0.066	0.000	0.000	0.000	0.000	0.000	0.000	0.000	0.000	0.000
Al^{VI}	0.000	0.047	0.002	0.031	0.065	0.051	0.061	0.052	0.063	0.020
$Fe^{3+\ VI}$	0.236	0.076	0.087	0.053	0.088	0.076	0.068	0.055	0.131	0.068
Ti	0.080	0.017	0.016	0.017	0.023	0.020	0.028	0.020	0.029	0.018
Cr	0.006	0.009	0.007	0.013	0.012	0.009	0.013	0.010	0.017	0.002
Zn	0.000	0.003	0.001	0.001	0.002	0.001	0.000	0.000	0.001	0.002
Mg	0.783	0.875	0.907	0.917	0.831	0.841	0.851	0.893	0.806	0.904
Fe^{2+}	0.805	0.140	0.219	0.251	0.157	0.145	0.156	0.170	0.132	0.179
Mn	0.004	0.004	0.007	0.007	0.004	0.005	0.004	0.005	0.004	0.004
Ca	0.650	0.815	0.739	0.692	0.775	0.838	0.801	0.781	0.725	0.781
K	0.024	0.000	0.000	0.001	0.003	0.000	0.000	0.000	0.003	0.002
Na	0.091	0.015	0.016	0.017	0.039	0.015	0.018	0.014	0.089	0.019
%Enstatite	41.98	45.81	46.31	47.74	44.78	44.16	45.27	46.89	44.83	46.68
%Ferrosillite	23.16	11.51	15.94	16.21	13.46	11.86	12.10	12.07	14.85	12.95
%Wollastonite	34.87	42.68	37.75	36.04	41.76	43.98	42.63	41.04	40.32	40.36
%Jadeite	----------	----------	----------	----------	----------	----------	----------	----------	----------	----------
%Aegirine	----------	----------	----------	----------	----------	----------	----------	----------	----------	----------
%Quad	----------	----------	----------	----------	----------	----------	----------	----------	----------	----------
Classification according to Morimoto et al. (1988)										
Group	Quad	Quad	Quad	Quad	Quad	Quad	Quad	Quad	Quad	Quad
Classification	augite	augite	augite	augite	augite	augite	augite	augite	augite	augite

Sample	ST-65	ST-65	ST-65	ST-65	ST-66	ST-66	ST-66	ST-66	ST-66	ST-66
Reference	11	12	13	14	1	2	3	4	5	1A
Zone	M	M	M	M	M	M	M	M	M	M
SiO_2	50.41	51.06	50.28	49.72	48.44	49.15	49.37	50.02	47.83	53.43
TiO_2	0.65	0.59	0.75	0.89	1.49	1.31	0.97	0.93	1.07	0.41
Al_2O_3	4.30	4.37	4.32	5.35	5.76	5.92	2.94	3.52	5.73	0.30
Fe_2O_3	3.52	2.34	3.35	2.74	1.07	0.00	0.75	0.00	7.82	28.65
FeO	4.51	5.20	4.43	4.76	9.07	9.04	17.59	15.30	3.72	0.00
MnO	0.16	0.14	0.13	0.18	0.15	0.14	0.38	0.32	0.20	0.00
MgO	16.27	16.35	16.21	15.72	12.73	13.25	11.28	12.77	11.99	2.01
CaO	20.30	20.36	20.31	20.57	19.19	19.99	16.23	15.49	17.74	2.31
K_2O	0.02	0.00	0.00	0.00	0.03	0.00	0.00	0.04	0.30	0.00
Na_2O	0.24	0.21	0.28	0.19	0.56	0.26	0.21	0.43	1.99	12.92
ZnO	0.04	0.04	0.02	0.03	0.09	0.01	0.06	0.00	0.01	0.06
Cr_2O_3	0.27	0.30	0.26	0.41	0.31	0.26	0.04	0.04	0.36	0.04
Total	100.68	100.95	100.35	100.56	98.89	99.32	99.81	98.85	98.75	100.13
Number of ions on the base of 6 oxygens. normalized for 4 cations										
Si	1.846	1.861	1.846	1.823	1.831	1.843	1.902	1.915	1.806	2.011
Al^{IV}	0.154	0.139	0.154	0.177	0.169	0.157	0.098	0.085	0.194	0.000
$Fe^{3+\ IV}$	0.000	0.000	0.000	0.000	0.000	0.000	0.000	0.000	0.000	0.000
Al^{VI}	0.032	0.049	0.033	0.054	0.087	0.105	0.035	0.074	0.061	0.013
$Fe^{3+\ VI}$	0.097	0.064	0.093	0.076	0.030	0.000	0.022	0.000	0.222	0.876
Ti	0.018	0.016	0.021	0.024	0.042	0.037	0.028	0.027	0.030	0.012
Cr	0.008	0.009	0.007	0.012	0.009	0.008	0.001	0.001	0.011	0.001
Zn	0.001	0.001	0.001	0.001	0.002	0.000	0.002	0.000	0.000	0.002
Mg	0.888	0.888	0.887	0.859	0.717	0.741	0.648	0.729	0.675	0.113
Fe^{2+}	0.138	0.158	0.136	0.146	0.287	0.283	0.567	0.490	0.118	0.000
Mn	0.005	0.004	0.004	0.006	0.005	0.004	0.012	0.010	0.006	0.000
Ca	0.796	0.795	0.799	0.808	0.777	0.803	0.670	0.635	0.718	0.093
K	0.001	0.000	0.000	0.000	0.001	0.000	0.000	0.002	0.014	0.000
Na	0.017	0.015	0.020	0.014	0.041	0.019	0.016	0.032	0.145	0.943
%Enstatite	46.14	46.51	46.25	45.35	39.49	40.45	33.77	39.08	38.82	----------
%Ferrosillite	12.48	11.87	12.12	12.00	17.73	15.71	31.32	26.84	19.91	----------
%Wollastonite	41.38	41.62	41.63	42.66	42.78	43.84	34.92	34.08	41.28	----------
%Jadeite	----------	----------	----------	----------	----------	----------	----------	----------	----------	1.35
%Aegirine	----------	----------	----------	----------	----------	----------	----------	----------	----------	88.79
%Quad	----------	----------	----------	----------	----------	----------	----------	----------	----------	9.86
Classification according to Morimoto et al. (1988)										
Group	Quad	Quad	Quad	Quad	Quad	Quad	Quad	Quad	Quad	Na
Classification	augite	augite	augite	augite	augite	augite	augite	augite	augite	aegirine

Sample	ST-66	ST-66	ST-66	ST-66	ST-67	ST-67	ST-67	ST-67	ST-67	ST-67
Reference	2A	5A	19M	20M	1	3	4	5	6	7
Zone	M	M	M	M	M	M	M	M	M	M
SiO_2	52.75	52.57	51.63	53.01	49.08	49.11	48.76	48.35	49.30	48.33
TiO_2	0.87	1.17	1.10	0.69	0.87	1.08	1.03	1.24	1.05	1.18
Al_2O_3	0.28	0.25	0.20	0.39	7.52	4.07	4.88	6.38	5.41	5.67
Fe_2O_3	27.98	27.52	30.69	28.77	0.63	3.62	3.13	3.28	3.01	3.80
FeO	0.00	0.00	0.00	0.00	6.92	8.02	6.10	5.01	4.91	4.65
MnO	0.00	0.00	0.05	0.04	0.13	0.22	0.17	0.17	0.14	0.18
MgO	2.13	2.09	0.42	1.68	14.20	14.22	14.34	14.52	14.76	15.28
CaO	1.74	1.66	0.48	1.70	20.31	19.16	20.61	20.96	21.39	19.94
K_2O	0.01	0.00	0.00	0.01	0.00	0.00	0.00	0.00	0.00	0.00
Na_2O	13.26	13.62	14.59	13.68	0.23	0.33	0.22	0.22	0.23	0.24
ZnO	0.09	0.05	0.00	0.00	0.00	0.04	0.00	0.01	0.05	0.11
Cr_2O_3	0.00	0.05	0.01	0.00	0.25	0.34	0.25	0.28	0.16	0.32
Total	99.09	98.99	99.18	99.96	100.13	100.19	99.47	100.42	100.41	99.71
Number of ions on the base of 6 oxygens. normalized for 4 cations										
Si	1.998	1.987	1.962	1.991	1.809	1.836	1.824	1.785	1.818	1.794
Al^{IV}	0.002	0.011	0.009	0.009	0.191	0.164	0.176	0.215	0.182	0.206
$Fe^{3+\ IV}$	0.000	0.002	0.029	0.000	0.000	0.000	0.000	0.000	0.000	0.000
Al^{VI}	0.011	0.000	0.000	0.008	0.135	0.015	0.039	0.063	0.053	0.042
$Fe^{3+\ VI}$	0.863	0.847	0.935	0.884	0.017	0.102	0.088	0.091	0.083	0.106
Ti	0.025	0.033	0.031	0.020	0.024	0.030	0.029	0.034	0.029	0.033
Cr	0.000	0.002	0.000	0.000	0.007	0.010	0.007	0.008	0.005	0.009
Zn	0.002	0.001	0.000	0.000	0.000	0.001	0.000	0.000	0.001	0.003
Mg	0.120	0.118	0.024	0.094	0.780	0.793	0.800	0.799	0.811	0.846
Fe^{2+}	0.000	0.000	0.000	0.000	0.213	0.251	0.191	0.155	0.152	0.144
Mn	0.000	0.000	0.002	0.001	0.004	0.007	0.005	0.005	0.004	0.006
Ca	0.070	0.067	0.020	0.068	0.802	0.767	0.826	0.829	0.845	0.793
K	0.000	0.000	0.000	0.000	0.000	0.000	0.000	0.000	0.000	0.000
Na	0.974	0.998	1.075	0.996	0.017	0.024	0.016	0.015	0.017	0.018
%Enstatite	----------	----------	----------	----------	42.94	41.29	41.87	42.52	42.80	44.62
%Ferrosillite	----------	----------	----------	----------	12.92	18.74	14.89	13.36	12.63	13.52
%Wollastonite	----------	----------	----------	----------	44.14	39.97	43.24	44.12	44.57	41.86
%Jadeite	1.10	0.00	0.00	0.82	----------	----------	----------	----------	----------	----------
%Aegirine	90.00	91.52	98.01	91.65	----------	----------	----------	----------	----------	----------
%Quad	8.90	8.48	1.99	7.53	----------	----------	----------	----------	----------	----------
Classification according to Morimoto et al. (1988)										
Group	Na	Na	Na	Na	Quad	Quad	Quad	Quad	Quad	Quad
Classification	aegirine	aegirine	aegirine	aegirine	augite	augite	augite	augite	augite	augite

Sample	ST-67	ST-67	ST-67	ST-67	ST-67	ST-67	ST-69	ST-69	ST-70	ST-70
Reference	8	9	10	11	12	13	1V	2V	1	2
Zone	M	M	M	M	M	M	V	V	M	M
SiO_2	48.43	48.86	49.09	49.62	48.25	48.65	53.09	53.44	51.10	51.20
TiO_2	1.00	1.00	0.73	0.68	1.11	0.97	1.31	0.81	0.79	0.70
Al_2O_3	6.12	6.21	4.92	3.13	5.85	4.82	0.08	0.35	3.47	3.26
Fe_2O_3	3.84	3.54	4.97	4.29	3.90	3.51	31.00	29.34	0.00	0.00
FeO	4.49	4.47	1.95	10.48	4.50	5.05	0.00	0.00	9.92	12.20
MnO	0.13	0.12	0.12	0.33	0.13	0.18	0.01	0.00	0.14	0.26
MgO	15.02	15.33	16.58	14.51	14.86	14.87	0.61	1.56	13.70	14.40
CaO	20.47	20.39	20.22	17.29	20.04	20.43	0.38	0.91	19.73	16.87
K_2O	0.01	0.00	0.08	0.00	0.00	0.00	0.00	0.01	0.00	0.00
Na_2O	0.24	0.28	0.34	0.24	0.41	0.23	14.21	13.84	0.22	0.23
ZnO	0.05	0.01	0.01	0.02	0.00	0.07	0.00	0.00	0.03	0.00
Cr_2O_3	0.29	0.26	0.44	0.00	0.35	0.15	0.12	0.18	0.30	0.23
Total	100.08	100.47	99.44	100.59	99.39	98.92	100.81	100.44	99.40	99.35
Number of ions on the base of 6 oxygens. normalized for 4 cations										
Si	1.790	1.795	1.811	1.860	1.796	1.823	1.995	2.001	1.920	1.929
Al^{IV}	0.210	0.205	0.189	0.138	0.204	0.177	0.003	0.000	0.080	0.071
$Fe^{3+\ IV}$	0.000	0.000	0.000	0.002	0.000	0.000	0.002	0.000	0.000	0.000
Al^{VI}	0.057	0.064	0.025	0.000	0.052	0.036	0.000	0.016	0.074	0.073
$Fe^{3+\ VI}$	0.107	0.098	0.138	0.119	0.109	0.099	0.951	0.897	0.000	0.000
Ti	0.028	0.028	0.020	0.019	0.031	0.027	0.037	0.023	0.022	0.020
Cr	0.008	0.007	0.013	0.000	0.010	0.004	0.004	0.005	0.009	0.007
Zn	0.001	0.000	0.000	0.001	0.000	0.002	0.000	0.000	0.001	0.000
Mg	0.828	0.839	0.912	0.811	0.824	0.831	0.034	0.087	0.768	0.808
Fe^{2+}	0.139	0.137	0.060	0.329	0.140	0.158	0.000	0.000	0.312	0.384
Mn	0.004	0.004	0.004	0.010	0.004	0.006	0.000	0.000	0.005	0.008
Ca	0.811	0.803	0.800	0.694	0.799	0.820	0.015	0.036	0.795	0.681
K	0.000	0.000	0.004	0.000	0.000	0.000	0.000	0.001	0.000	0.000
Na	0.017	0.020	0.024	0.017	0.029	0.017	1.035	1.005	0.016	0.017
%Enstatite	43.85	44.63	47.67	41.26	43.91	43.41	----------	----------	40.87	42.97
%Ferrosillite	13.22	12.71	10.54	23.41	13.50	13.74	----------	----------	16.83	20.86
%Wollastonite	42.93	42.67	41.78	35.33	42.58	42.85	----------	----------	42.30	36.17
%Jadeite	----------	----------	----------	----------	----------	----------	0.00	1.60	----------	----------
%Aegirine	----------	----------	----------	----------	----------	----------	97.67	92.62	----------	----------
%Quad	----------	----------	----------	----------	----------	----------	2.33	5.78	----------	----------
Classification according to Morimoto et al. (1988)										
Group	Quad	Quad	Quad	Quad	Quad	Quad	Na	Na	Quad	Quad
Classification	augite	augite	augite	augite	augite	augite	aegirine	aegirine	augite	augite

Sample	ST-70	ST-70	ST-70	ST-70
Reference	15	16	17	18
Zone	M	M	M	M
SiO_2	50.86	49.51	50.43	50.99
TiO_2	0.79	0.94	0.73	0.70
Al_2O_3	4.35	5.93	5.43	3.57
Fe_2O_3	0.00	0.00	0.00	0.00
FeO	8.76	7.24	7.54	9.89
MnO	0.15	0.10	0.13	0.21
MgO	14.57	14.52	14.80	14.85
CaO	18.75	19.48	19.69	18.13
K_2O	0.01	0.00	0.00	0.01
Na_2O	0.33	0.22	0.24	0.29
ZnO	0.00	0.05	0.05	0.06
Cr_2O_3	0.19	0.48	0.25	0.21
Total	98.75	98.47	99.28	98.90
Number of ions on the base of 6 oxygens. normalized for 4 cations				
Si	1.908	1.856	1.873	1.914
Al^{IV}	0.092	0.144	0.127	0.086
$Fe^{3+\ IV}$	0.000	0.000	0.000	0.000
Al^{VI}	0.100	0.118	0.111	0.072
$Fe^{3+\ VI}$	0.000	0.000	0.000	0.000
Ti	0.022	0.026	0.020	0.020
Cr	0.006	0.014	0.007	0.006
Zn	0.000	0.001	0.001	0.002
Mg	0.815	0.811	0.819	0.831
Fe^{2+}	0.275	0.227	0.234	0.310
Mn	0.005	0.003	0.004	0.007
Ca	0.753	0.782	0.784	0.729
K	0.000	0.000	0.000	0.000
Na	0.024	0.016	0.017	0.021
%Enstatite	44.10	44.49	44.51	44.28
%Ferrosillite	15.12	12.62	12.93	16.88
%Wollastonite	40.78	42.89	42.56	38.84
%Jadeite	----------	----------	----------	----------
%Aegirine	----------	----------	----------	----------
%Quad	----------	----------	----------	----------
Classification according to Morimoto et al. (1988)				
Group	Quad	Quad	Quad	Quad
Classification	augite	augite	augite	augite

III.3.1.2. Plagioclase

Sample	ST-61	ST-61	ST-61	ST-61	ST-61	ST-61	ST-61	ST-61	ST-61	ST-61
Reference	1	2	4	5	7	8	1LA1	2LA1	3LA1	4LA1
Zone	MC	MR	MR	MC	MR	M	L. Ph.	L. Ph.	L. Ph.	L. Ph.
SiO_2	50.46	51.57	51.72	47.76	50.99	49.41	49.83	50.26	50.21	50.26
TiO_2	0.03	0.04	0.06	0.02	0.06	0.01	0.02	0.05	0.00	0.04
Al_2O_3	29.63	28.98	28.77	31.77	29.00	30.33	30.60	30.25	30.40	30.65
$Fe_2O_3^T$	0.57	0.76	0.70	0.39	0.69	0.51	0.50	0.47	0.44	0.41
MgO	0.33	0.44	0.42	0.21	0.41	0.32	0.28	0.30	0.31	0.32
CaO	15.22	14.44	14.71	16.89	14.59	15.66	16.23	15.75	15.86	16.12
Na_2O	2.52	2.99	2.78	1.58	3.03	2.26	1.90	2.14	2.16	1.92
K_2O	0.01	0.01	0.01	0.01	0.02	0.02	0.01	0.02	0.00	0.01
BaO	0.00	0.00	0.00	0.07	0.00	0.04	0.00	0.03	0.04	0.04
SrO	0.00	0.00	0.00	0.00	0.00	0.00	0.00	0.00	0.00	0.00
Total	98.77	99.23	99.17	98.69	98.78	98.55	99.36	99.25	99.42	99.77
Number of cations calculated based on 32 oxygen atoms										
Si	9.321	9.467	9.497	8.880	9.416	9.166	9.165	9.243	9.223	9.198
Ti	0.004	0.005	0.009	0.003	0.008	0.002	0.003	0.007	0.000	0.005
Al	6.451	6.269	6.225	6.961	6.310	6.632	6.632	6.556	6.580	6.611
Fe^{3+}	0.079	0.105	0.096	0.054	0.096	0.071	0.069	0.064	0.061	0.057
Mg	0.091	0.121	0.116	0.057	0.111	0.087	0.076	0.081	0.084	0.088
Ca	3.011	2.839	2.894	3.365	2.886	3.113	3.197	3.103	3.121	3.161
Na	0.902	1.064	0.990	0.570	1.084	0.811	0.678	0.762	0.769	0.681
K	0.002	0.003	0.002	0.002	0.004	0.004	0.002	0.004	0.001	0.002
Ba	0.000	0.000	0.000	0.005	0.000	0.003	0.000	0.002	0.003	0.003
Sr	0.000	0.000	0.000	0.000	0.000	0.000	0.000	0.000	0.000	0.000
Final terms										
An	76.91	72.68	74.47	85.48	72.62	79.26	82.47	80.19	80.21	82.23
Ab	23.04	27.24	25.47	14.48	27.28	20.65	17.48	19.70	19.77	17.72
Or	0.05	0.08	0.05	0.04	0.10	0.09	0.05	0.11	0.02	0.05

Sample	ST-61	ST-61	ST-61	ST-61	ST-61	ST-61	ST-61	ST-61	ST-61	ST-61
Reference	5LA1	6LA1	7LA1	8LA1	9LA1	10LA1	11LA1	12LA1	13LA1	14LA1
Zone	L. Ph.	L. Ph.	L. Ph.	L. Ph.	L. Ph.	L. Ph.	L. Ph.	L. Ph.	L. Ph.	L. Ph.
SiO_2	50.42	49.95	49.65	51.38	51.90	51.78	49.26	49.06	49.06	49.69
TiO_2	0.03	0.03	0.00	0.02	0.05	0.05	0.00	0.02	0.00	0.02
Al_2O_3	29.85	31.02	30.85	29.64	29.14	29.38	31.65	31.54	31.44	30.94
$Fe_2O_3^T$	0.58	0.42	0.43	0.48	0.60	0.46	0.43	0.46	0.41	0.41
MgO	0.65	0.27	0.29	0.31	0.49	0.33	0.25	0.26	0.26	0.27
CaO	15.23	16.49	16.34	15.28	14.57	14.96	17.21	16.96	16.83	16.49
Na_2O	2.36	1.80	1.88	2.39	2.76	2.66	1.46	1.57	1.53	1.79
K_2O	0.26	0.01	0.00	0.01	0.09	0.01	0.01	0.01	0.01	0.00
BaO	0.06	0.05	0.02	0.02	0.01	0.00	0.02	0.01	0.00	0.05
SrO	0.00	0.00	0.00	0.00	0.00	0.00	0.00	0.00	0.00	0.00
Total	99.43	100.03	99.46	99.51	99.60	99.64	100.29	99.88	99.54	99.65
Number of cations calculated based on 32 oxygen atoms										
Si	9.270	9.128	9.126	9.402	9.483	9.458	8.998	8.996	9.019	9.119
Ti	0.003	0.004	0.000	0.002	0.007	0.006	0.000	0.003	0.000	0.002
Al	6.467	6.681	6.683	6.391	6.275	6.323	6.812	6.815	6.811	6.691
Fe^{3+}	0.081	0.058	0.060	0.065	0.083	0.064	0.059	0.063	0.057	0.056
Mg	0.178	0.075	0.078	0.084	0.133	0.091	0.068	0.071	0.072	0.075
Ca	2.999	3.229	3.218	2.995	2.852	2.927	3.369	3.333	3.315	3.241
Na	0.840	0.636	0.670	0.849	0.977	0.943	0.517	0.557	0.544	0.635
K	0.062	0.002	0.000	0.001	0.021	0.003	0.002	0.002	0.002	0.000
Ba	0.004	0.003	0.001	0.002	0.001	0.000	0.001	0.000	0.000	0.004
Sr	0.000	0.000	0.000	0.000	0.000	0.000	0.000	0.000	0.000	0.000
Final terms										
An	76.89	83.49	82.76	77.89	74.09	75.58	86.64	85.63	85.86	83.60
Ab	21.53	16.45	17.23	22.08	25.37	24.34	13.31	14.31	14.10	16.39
Or	1.59	0.06	0.01	0.03	0.54	0.08	0.05	0.05	0.04	0.01

Sample	ST-61	ST-61	ST-61	ST-61	ST-61	ST-61	ST-61	ST-61	ST-61	ST-61
Reference	15LA1	16LA1	17LA1	18LA1	19LA1	20LA1	1LA2	2LA2	3LA2	4LA2
Zone	L. Ph.	L. Ph.	L. Ph.	L. Ph.	L. Ph.	L. Ph.	L. Ph.	L. Ph.	L. Ph.	L. Ph.
SiO_2	50.48	50.55	50.64	49.33	52.06	50.95	50.99	50.61	50.50	49.47
TiO_2	0.03	0.01	0.00	0.04	0.02	0.03	0.01	0.02	0.04	0.00
Al_2O_3	30.34	30.37	30.27	31.14	28.57	29.89	29.34	30.01	30.15	30.47
$Fe_2O_3^T$	0.47	0.41	0.48	0.41	0.64	0.47	0.62	0.44	0.49	0.44
MgO	0.32	0.31	0.31	0.27	0.71	0.31	0.41	0.32	0.30	0.30
CaO	16.10	15.83	15.62	16.75	13.99	15.45	15.29	15.64	15.64	16.01
Na_2O	2.18	2.14	2.34	1.69	2.94	2.31	2.57	2.33	2.33	2.16
K_2O	0.01	0.01	0.02	0.00	0.31	0.00	0.01	0.02	0.01	0.01
BaO	0.00	0.02	0.01	0.00	0.00	0.00	0.01	0.03	0.00	0.01
SrO	0.00	0.00	0.00	0.00	0.00	0.00	0.00	0.00	0.00	0.00
Total	99.92	99.65	99.69	99.61	99.22	99.40	99.24	99.43	99.45	98.88
Number of cations calculated based on 32 oxygen atoms										
Si	9.230	9.256	9.269	9.062	9.549	9.341	9.375	9.290	9.267	9.150
Ti	0.004	0.001	0.000	0.005	0.002	0.004	0.001	0.003	0.005	0.000
Al	6.537	6.552	6.530	6.741	6.175	6.457	6.357	6.493	6.521	6.641
Fe^{3+}	0.065	0.056	0.067	0.056	0.089	0.065	0.085	0.061	0.068	0.062
Mg	0.088	0.086	0.085	0.073	0.194	0.083	0.111	0.088	0.082	0.083
Ca	3.153	3.105	3.064	3.296	2.750	3.035	3.011	3.076	3.075	3.173
Na	0.771	0.760	0.829	0.601	1.044	0.820	0.916	0.829	0.828	0.773
K	0.002	0.002	0.005	0.000	0.072	0.000	0.003	0.005	0.003	0.003
Ba	0.000	0.001	0.001	0.000	0.000	0.000	0.001	0.002	0.000	0.001
Sr	0.000	0.000	0.000	0.000	0.000	0.000	0.000	0.000	0.000	0.000
Final terms										
An	80.32	80.28	78.60	84.58	71.14	78.73	76.62	78.66	78.73	80.36
Ab	19.64	19.66	21.28	15.42	27.01	21.27	23.30	21.21	21.21	19.57
Or	0.04	0.06	0.12	0.00	1.85	0.00	0.08	0.14	0.07	0.07

Sample	ST-61	ST-61	ST-61	ST-61	ST-61	ST-61	ST-61	ST-61	ST-61	ST-61
Reference	5LA2	6LA2	7LA2	8LA2	9LA2	10LA2	11LA2	12LA2	13LA2	14LA2
Zone	L. Ph.	L. Ph.	L. Ph.	L. Ph.	L. Ph.	L. Ph.	L. Ph.	L. Ph.	L. Ph.	L. Ph.
SiO_2	50.13	49.92	49.59	49.06	50.21	50.98	51.55	50.88	51.73	50.52
TiO_2	0.03	0.02	0.04	0.02	0.01	0.00	0.03	0.00	0.03	0.03
Al_2O_3	30.40	30.44	30.49	31.11	30.31	29.66	29.07	29.90	29.31	30.20
$Fe_2O_3^T$	0.42	0.45	0.42	0.43	0.43	0.44	0.43	0.37	0.45	0.39
MgO	0.29	0.30	0.30	0.25	0.30	0.35	0.38	0.32	0.35	0.31
CaO	16.01	16.24	16.11	16.69	15.96	15.38	14.96	15.43	15.04	15.85
Na_2O	2.06	1.99	2.12	1.66	2.14	2.72	2.76	2.53	2.68	2.16
K_2O	0.02	0.01	0.01	0.01	0.01	0.02	0.02	0.02	0.01	0.01
BaO	0.00	0.00	0.03	0.00	0.00	0.00	0.04	0.01	0.00	0.02
SrO	0.00	0.00	0.00	0.00	0.00	0.00	0.00	0.00	0.00	0.00
Total	99.35	99.38	99.11	99.22	99.36	99.56	99.23	99.46	99.60	99.49
Number of cations calculated based on 32 oxygen atoms										
Si	9.214	9.182	9.152	9.049	9.228	9.346	9.464	9.330	9.456	9.266
Ti	0.004	0.003	0.006	0.002	0.001	0.000	0.004	0.000	0.005	0.003
Al	6.585	6.598	6.631	6.762	6.564	6.409	6.289	6.461	6.313	6.528
Fe^{3+}	0.058	0.062	0.059	0.060	0.059	0.061	0.059	0.051	0.061	0.054
Mg	0.079	0.083	0.083	0.070	0.082	0.096	0.103	0.088	0.096	0.086
Ca	3.152	3.200	3.186	3.297	3.142	3.021	2.943	3.032	2.946	3.115
Na	0.734	0.710	0.758	0.595	0.763	0.968	0.982	0.899	0.951	0.768
K	0.004	0.003	0.002	0.001	0.003	0.005	0.005	0.005	0.002	0.002
Ba	0.000	0.000	0.002	0.000	0.000	0.000	0.003	0.001	0.000	0.002
Sr	0.000	0.000	0.000	0.000	0.000	0.000	0.000	0.000	0.000	0.000
Final terms										
An	81.02	81.78	80.74	84.68	80.41	75.63	74.89	77.02	75.57	80.19
Ab	18.87	18.15	19.21	15.28	19.52	24.23	24.98	22.85	24.39	19.76
Or	0.11	0.07	0.05	0.04	0.07	0.13	0.13	0.12	0.04	0.04

Sample	ST-61	ST-61	ST-61	ST-61	ST-61	ST-61	ST-61	ST-61	ST-61	ST-61
Reference	15LA2	16LA2	17LA2	18LA2	19LA2	20LA2	1LB1	2LB1	3LB1	4LB1
Zone	L. Ph.	L. Ph.	L. Ph.	L. Ph.	L. Ph.	L. Ph.	L. Ph.	L. Ph.	L. Ph.	L. Ph.
SiO_2	50.13	48.95	50.04	50.79	50.40	50.22	50.14	48.59	48.64	48.71
TiO_2	0.00	0.00	0.00	0.03	0.00	0.04	0.01	0.02	0.02	0.04
Al_2O_3	30.27	30.96	30.57	30.07	30.13	30.20	30.36	31.25	31.84	31.64
$Fe_2O_3^T$	0.46	0.40	0.42	0.42	0.42	0.47	0.47	0.56	0.38	0.40
MgO	0.29	0.27	0.29	0.32	0.31	0.30	0.31	0.43	0.21	0.20
CaO	15.83	16.82	16.23	15.81	15.91	15.88	15.89	16.96	17.18	17.02
Na_2O	2.21	1.74	2.02	2.26	2.23	2.25	2.26	1.58	1.37	1.54
K_2O	0.01	0.01	0.00	0.01	0.00	0.00	0.00	0.06	0.01	0.01
BaO	0.01	0.00	0.00	0.00	0.00	0.03	0.00	0.01	0.00	0.00
SrO	0.00	0.00	0.00	0.00	0.00	0.00	0.00	0.00	0.00	0.00
Total	99.20	99.15	99.57	99.70	99.40	99.39	99.44	99.45	99.65	99.55
Number of cations calculated based on 32 oxygen atoms										
Si	9.229	9.045	9.183	9.294	9.257	9.233	9.212	8.963	8.941	8.964
Ti	0.000	0.000	0.000	0.005	0.000	0.005	0.001	0.002	0.003	0.005
Al	6.567	6.741	6.612	6.484	6.523	6.543	6.575	6.795	6.898	6.863
Fe^{3+}	0.064	0.055	0.058	0.058	0.058	0.065	0.065	0.077	0.052	0.055
Mg	0.079	0.074	0.080	0.088	0.086	0.083	0.086	0.119	0.058	0.054
Ca	3.122	3.329	3.191	3.099	3.131	3.127	3.127	3.351	3.383	3.356
Na	0.788	0.625	0.719	0.803	0.795	0.800	0.806	0.565	0.487	0.548
K	0.003	0.001	0.000	0.001	0.000	0.001	0.000	0.014	0.002	0.002
Ba	0.000	0.000	0.000	0.000	0.000	0.002	0.000	0.001	0.000	0.000
Sr	0.000	0.000	0.000	0.000	0.000	0.000	0.000	0.000	0.000	0.000
Final terms										
An	79.78	84.17	81.60	79.39	79.75	79.60	79.50	85.26	87.37	85.92
Ab	20.14	15.79	18.40	20.58	20.25	20.37	20.50	14.39	12.58	14.04
Or	0.08	0.04	0.01	0.03	0.01	0.02	0.00	0.35	0.05	0.04

Sample	ST-61	ST-61	ST-61	ST-61	ST-61	ST-61	ST-61	ST-61	ST-61	ST-61
Reference	5LB1	6LB1	7LB1	8LB1	9LB1	10LB1	11LB1	12LB1	13LB1	14LB1
Zone	L. Ph.	L. Ph.	L. Ph.	L. Ph.	L. Ph.	L. Ph.	L. Ph.	L. Ph.	L. Ph.	L. Ph.
SiO_2	48.49	48.72	48.80	48.80	48.42	48.54	48.67	48.89	48.68	48.36
TiO_2	0.01	0.04	0.01	0.02	0.00	0.02	0.02	0.02	0.00	0.03
Al_2O_3	31.45	31.48	31.55	31.49	31.82	31.79	31.58	31.51	31.61	31.56
$Fe_2O_3^T$	0.42	0.43	0.41	0.43	0.42	0.41	0.41	0.40	0.44	0.45
MgO	0.21	0.24	0.20	0.26	0.20	0.19	0.22	0.21	0.20	0.22
CaO	17.22	16.95	16.99	17.04	17.24	17.29	16.78	16.98	16.99	17.13
Na_2O	1.52	1.64	1.62	1.59	1.41	1.42	1.61	1.56	1.65	1.58
K_2O	0.01	0.00	0.01	0.01	0.02	0.01	0.01	0.01	0.01	0.01
BaO	0.06	0.00	0.03	0.00	0.02	0.00	0.02	0.01	0.00	0.00
SrO	0.00	0.00	0.00	0.00	0.00	0.00	0.00	0.00	0.00	0.00
Total	99.38	99.51	99.61	99.63	99.55	99.67	99.32	99.58	99.56	99.34
Number of cations calculated based on 32 oxygen atoms										
Si	8.952	8.973	8.978	8.976	8.919	8.930	8.975	8.992	8.961	8.931
Ti	0.001	0.006	0.001	0.003	0.000	0.003	0.002	0.002	0.000	0.004
Al	6.843	6.832	6.841	6.827	6.908	6.891	6.863	6.831	6.858	6.868
Fe^{3+}	0.058	0.060	0.056	0.059	0.059	0.057	0.057	0.055	0.061	0.063
Mg	0.057	0.066	0.053	0.070	0.054	0.052	0.059	0.057	0.055	0.061
Ca	3.406	3.345	3.350	3.357	3.403	3.406	3.316	3.346	3.350	3.388
Na	0.544	0.586	0.579	0.566	0.502	0.506	0.575	0.557	0.588	0.566
K	0.001	0.001	0.003	0.003	0.004	0.003	0.002	0.003	0.001	0.002
Ba	0.004	0.000	0.002	0.000	0.001	0.000	0.002	0.001	0.000	0.000
Sr	0.000	0.000	0.000	0.000	0.000	0.000	0.000	0.000	0.000	0.000
Final terms										
An	86.19	85.07	85.20	85.50	87.06	87.01	85.18	85.66	85.04	85.64
Ab	13.78	14.91	14.72	14.41	12.85	12.92	14.76	14.26	14.92	14.30
Or	0.03	0.02	0.08	0.08	0.10	0.07	0.06	0.08	0.04	0.06

Sample	ST-61	ST-61	ST-61	ST-61	ST-61	ST-61	ST-61	ST-61	ST-61	ST-61
Reference	15LB1	16LB1	17LB1	18LB1	19LB1	20LB1	1LB2	2LB2	3LB2	4LB2
Zone	L. Ph.	L. Ph.	L. Ph.	L. Ph.	L. Ph.	L. Ph.	L. Ph.	L. Ph.	L. Ph.	L. Ph.
SiO_2	48.46	48.01	48.81	48.96	49.43	50.94	50.44	49.84	49.14	49.19
TiO_2	0.00	0.01	0.01	0.01	0.04	0.07	0.01	0.04	0.00	0.02
Al_2O_3	31.84	31.96	31.67	31.55	30.89	30.08	30.40	30.29	30.77	31.02
$Fe_2O_3^T$	0.42	0.42	0.38	0.42	0.40	0.51	0.50	0.51	0.44	0.42
MgO	0.21	0.23	0.20	0.21	0.27	0.32	0.30	0.43	0.31	0.27
CaO	17.20	17.32	17.14	17.05	16.38	15.82	16.19	15.74	16.22	16.53
Na_2O	1.42	1.43	1.49	1.53	1.94	2.33	2.10	2.29	2.11	1.89
K_2O	0.01	0.01	0.01	0.00	0.00	0.01	0.02	0.12	0.00	0.01
BaO	0.00	0.01	0.01	0.05	0.04	0.02	0.00	0.01	0.00	0.08
SrO	0.00	0.00	0.00	0.00	0.00	0.00	0.00	0.00	0.00	0.00
Total	99.55	99.39	99.72	99.76	99.40	100.10	99.97	99.26	98.99	99.42
Number of cations calculated based on 32 oxygen atoms										
Si	8.923	8.866	8.968	8.991	9.099	9.292	9.221	9.184	9.087	9.063
Ti	0.000	0.001	0.002	0.001	0.006	0.009	0.002	0.006	0.000	0.003
Al	6.908	6.955	6.857	6.828	6.701	6.467	6.550	6.577	6.706	6.734
Fe^{3+}	0.058	0.059	0.053	0.058	0.056	0.070	0.069	0.070	0.061	0.059
Mg	0.056	0.063	0.055	0.057	0.075	0.087	0.082	0.118	0.086	0.073
Ca	3.392	3.426	3.373	3.355	3.231	3.092	3.170	3.107	3.213	3.263
Na	0.508	0.511	0.530	0.544	0.693	0.824	0.744	0.819	0.755	0.673
K	0.002	0.003	0.003	0.000	0.000	0.003	0.004	0.028	0.001	0.001
Ba	0.000	0.001	0.001	0.003	0.003	0.001	0.000	0.001	0.000	0.006
Sr	0.000	0.000	0.000	0.000	0.000	0.000	0.000	0.000	0.000	0.000
Final terms										
An	86.94	86.96	86.37	86.04	82.33	78.91	80.90	78.59	80.96	82.87
Ab	13.02	12.98	13.56	13.95	17.67	21.03	18.98	20.71	19.01	17.10
Or	0.04	0.07	0.07	0.01	0.00	0.07	0.11	0.70	0.02	0.03

Sample	ST-61	ST-61	ST-61	ST-61	ST-61	ST-61	ST-61	ST-61	ST-61	ST-61
Reference	5LB2	6LB2	7LB2	8LB2	9LB2	10LB2	11LB2	12LB2	13LB2	14LB2
Zone	L. Ph.	L. Ph.	L. Ph.	L. Ph.	L. Ph.	L. Ph.	L. Ph.	L. Ph.	L. Ph.	L. Ph.
SiO_2	48.11	49.19	48.26	48.43	48.65	48.43	48.24	48.26	48.57	48.51
TiO_2	0.02	0.01	0.01	0.01	0.04	0.03	0.03	0.00	0.03	0.02
Al_2O_3	31.71	31.38	31.61	31.47	31.53	31.55	31.62	31.71	31.45	31.24
$Fe_2O_3^T$	0.37	0.36	0.34	0.36	0.38	0.38	0.42	0.40	0.39	0.74
MgO	0.24	0.21	0.19	0.20	0.23	0.20	0.20	0.22	0.21	0.68
CaO	17.19	17.07	17.15	17.11	17.08	17.03	17.38	17.33	17.07	16.38
Na_2O	1.42	1.62	1.50	1.57	1.59	1.56	1.44	1.43	1.57	1.62
K_2O	0.02	0.01	0.01	0.01	0.01	0.00	0.02	0.02	0.01	0.24
BaO	0.01	0.06	0.02	0.02	0.00	0.00	0.00	0.00	0.00	0.02
SrO	0.00	0.00	0.00	0.00	0.00	0.00	0.00	0.00	0.00	0.00
Total	99.08	99.91	99.09	99.18	99.51	99.18	99.35	99.38	99.28	99.45
Number of cations calculated based on 32 oxygen atoms										
Si	8.904	9.022	8.931	8.954	8.961	8.950	8.912	8.909	8.967	8.951
Ti	0.003	0.002	0.002	0.002	0.006	0.003	0.005	0.000	0.004	0.003
Al	6.918	6.783	6.893	6.856	6.845	6.871	6.884	6.900	6.842	6.793
Fe^{3+}	0.051	0.050	0.047	0.050	0.053	0.053	0.059	0.056	0.054	0.103
Mg	0.065	0.058	0.052	0.056	0.063	0.054	0.056	0.061	0.058	0.188
Ca	3.409	3.353	3.400	3.389	3.370	3.372	3.439	3.428	3.376	3.239
Na	0.509	0.575	0.539	0.563	0.566	0.559	0.514	0.513	0.561	0.580
K	0.004	0.002	0.002	0.002	0.003	0.001	0.004	0.004	0.002	0.056
Ba	0.000	0.005	0.002	0.001	0.000	0.000	0.000	0.000	0.000	0.002
Sr	0.000	0.000	0.000	0.000	0.000	0.000	0.000	0.000	0.000	0.000
Final terms										
An	86.91	85.33	86.28	85.72	85.55	85.76	86.91	86.89	85.71	83.57
Ab	12.98	14.62	13.68	14.23	14.38	14.22	12.99	13.01	14.25	14.97
Or	0.11	0.05	0.04	0.04	0.08	0.02	0.10	0.10	0.04	1.46

Sample	ST-61	ST-61	ST-61	ST-61	ST-61	ST-61	ST-65	ST-65	ST-65	ST-65
Reference	15LB2	16LB2	17LB2	18LB2	19LB2	20LB2	1	2	3	4
Zone	L. Ph.	L. Ph.	L. Ph.	L. Ph.	L. Ph.	L. Ph.	M	M	M	M
SiO_2	47.90	47.85	48.68	48.38	49.03	52.16	51.55	51.01	52.37	53.15
TiO_2	0.02	0.02	0.00	0.03	0.00	0.05	0.00	0.00	0.05	0.05
Al_2O_3	31.90	31.81	31.53	31.54	31.47	28.50	29.68	29.81	29.18	28.35
$Fe_2O_3^T$	0.39	0.32	0.38	0.37	0.39	0.68	0.57	0.60	0.75	0.86
MgO	0.20	0.22	0.22	0.21	0.29	0.48	0.35	0.37	0.40	0.43
CaO	17.28	17.26	17.20	17.10	15.08	14.10	15.54	15.26	14.72	14.09
Na_2O	1.39	1.41	1.49	1.48	1.74	3.23	2.39	2.55	2.93	3.25
K_2O	0.01	0.02	0.00	0.01	0.82	0.08	0.00	0.02	0.01	0.01
BaO	0.01	0.00	0.00	0.02	0.00	0.02	0.03	0.00	0.00	0.03
SrO	0.00	0.00	0.00	0.00	0.00	0.00	0.00	0.00	0.00	0.00
Total	99.09	98.91	99.49	99.14	98.82	99.30	100.10	99.61	100.40	100.22
Number of cations calculated based on 32 oxygen atoms										
Si	8.869	8.876	8.967	8.946	9.073	9.563	9.389	9.341	9.497	9.644
Ti	0.003	0.003	0.000	0.004	0.000	0.007	0.000	0.000	0.007	0.007
Al	6.960	6.952	6.845	6.874	6.863	6.157	6.370	6.432	6.237	6.062
Fe^{3+}	0.055	0.045	0.052	0.052	0.054	0.094	0.078	0.083	0.102	0.118
Mg	0.055	0.061	0.060	0.058	0.079	0.130	0.095	0.100	0.107	0.117
Ca	3.428	3.430	3.395	3.387	2.989	2.770	3.031	2.993	2.860	2.738
Na	0.498	0.505	0.531	0.532	0.624	1.147	0.844	0.904	1.031	1.143
K	0.003	0.006	0.000	0.002	0.194	0.020	0.000	0.004	0.003	0.002
Ba	0.001	0.000	0.000	0.001	0.000	0.001	0.002	0.000	0.000	0.002
Sr	0.000	0.000	0.000	0.000	0.000	0.000	0.000	0.000	0.000	0.000
Final terms										
An	87.26	87.04	86.48	86.37	78.50	70.36	78.22	76.72	73.45	70.51
Ab	12.66	12.82	13.52	13.57	16.39	29.14	21.78	23.18	26.46	29.44
Or	0.07	0.14	0.00	0.06	5.11	0.50	0.00	0.10	0.08	0.05

Sample	ST-65	ST-65	ST-65	ST-65	ST-65	ST-65	ST-65	ST-65	ST-65	ST-65
Reference	5	7	8	1LA	2LA	3LA	4LA	5LA	6LA	7LA
Zone	M	M	M	L. Ph.	L. Ph.	L. Ph.	L. Ph.	L. Ph.	L. Ph.	L. Ph.
SiO_2	51.60	51.16	52.27	55.72	52.17	50.39	49.70	49.14	50.55	51.42
TiO_2	0.02	0.00	0.02	0.07	0.01	0.02	0.02	0.00	0.00	0.00
Al_2O_3	29.65	29.66	29.05	27.27	29.64	30.66	31.42	31.54	30.87	30.08
$Fe_2O_3^T$	0.56	0.59	0.72	1.01	0.61	0.48	0.43	0.50	0.44	0.45
MgO	0.41	0.36	0.35	0.17	0.34	0.30	0.27	0.26	0.30	0.35
CaO	14.98	15.23	14.82	12.24	15.13	16.17	16.78	15.95	16.14	15.45
Na_2O	2.66	2.60	2.76	4.33	2.70	2.15	1.78	1.65	2.04	2.49
K_2O	0.02	0.01	0.01	0.03	0.01	0.00	0.02	0.65	0.01	0.01
BaO	0.02	0.00	0.03	0.02	0.08	0.00	0.02	0.00	0.04	0.00
SrO	0.00	0.00	0.00	0.00	0.00	0.00	0.00	0.00	0.00	0.00
Total	99.91	99.61	100.04	100.86	100.70	100.16	100.43	99.68	100.39	100.25
Number of cations calculated based on 32 oxygen atoms										
Si	9.408	9.366	9.512	9.990	9.442	9.193	9.059	9.033	9.195	9.349
Ti	0.002	0.001	0.003	0.010	0.002	0.003	0.002	0.000	0.000	0.000
Al	6.370	6.399	6.230	5.762	6.321	6.593	6.748	6.832	6.619	6.444
Fe^{3+}	0.077	0.082	0.099	0.137	0.084	0.065	0.060	0.069	0.061	0.062
Mg	0.110	0.097	0.096	0.044	0.090	0.081	0.074	0.072	0.081	0.094
Ca	2.927	2.987	2.889	2.351	2.934	3.160	3.275	3.140	3.146	3.010
Na	0.939	0.923	0.974	1.504	0.948	0.761	0.630	0.587	0.718	0.877
K	0.004	0.001	0.003	0.008	0.003	0.001	0.004	0.152	0.002	0.002
Ba	0.001	0.000	0.002	0.001	0.006	0.000	0.001	0.000	0.003	0.000
Sr	0.000	0.000	0.000	0.000	0.000	0.000	0.000	0.000	0.000	0.000
Final terms										
An	75.62	76.37	74.73	60.86	75.53	80.57	83.78	80.96	81.37	77.40
Ab	24.28	23.60	25.19	38.93	24.40	19.41	16.12	15.13	18.58	22.56
Or	0.10	0.03	0.08	0.20	0.07	0.02	0.10	3.91	0.05	0.04

Sample	ST-65	ST-65	ST-65	ST-65	ST-65	ST-65	ST-65	ST-65	ST-65	ST-65
Reference	8LA	9LA	10LA	11LA	12LA	13LA	14LA	15LA	16LA	17LA
Zone	L. Ph.	L. Ph.	L. Ph.	L. Ph.	L. Ph.	L. Ph.	L. Ph.	L. Ph.	L. Ph.	L. Ph.
SiO_2	51.93	50.48	49.67	51.66	51.34	52.17	51.75	50.73	51.80	49.82
TiO_2	0.00	0.04	0.04	0.02	0.04	0.06	0.04	0.03	0.02	0.04
Al_2O_3	29.64	30.79	31.53	30.12	30.24	29.62	30.16	30.34	29.72	30.98
$Fe_2O_3^T$	0.44	0.41	0.39	0.42	0.48	0.53	0.39	0.41	0.46	0.51
MgO	0.33	0.29	0.27	0.33	0.30	0.39	0.30	0.29	0.33	0.40
CaO	14.89	16.03	16.86	15.72	15.41	15.17	15.62	15.76	14.99	16.77
Na_2O	2.67	2.09	1.64	2.30	2.44	2.57	2.34	2.33	2.66	1.73
K_2O	0.02	0.01	0.00	0.00	0.02	0.00	0.00	0.00	0.01	0.07
BaO	0.00	0.00	0.00	0.01	0.00	0.02	0.00	0.01	0.01	0.04
SrO	0.00	0.00	0.00	0.00	0.00	0.00	0.00	0.00	0.00	0.00
Total	99.92	100.14	100.40	100.58	100.27	100.55	100.59	99.90	99.98	100.36
Number of cations calculated based on 32 oxygen atoms										
Si	9.453	9.202	9.051	9.359	9.331	9.445	9.369	9.267	9.428	9.092
Ti	0.000	0.006	0.005	0.003	0.006	0.009	0.005	0.004	0.002	0.005
Al	6.359	6.614	6.771	6.431	6.477	6.321	6.435	6.531	6.375	6.664
Fe^{3+}	0.060	0.056	0.053	0.057	0.065	0.073	0.053	0.057	0.062	0.070
Mg	0.088	0.077	0.072	0.090	0.081	0.106	0.080	0.078	0.088	0.107
Ca	2.903	3.131	3.290	3.051	3.001	2.943	3.029	3.085	2.924	3.279
Na	0.943	0.737	0.579	0.807	0.858	0.902	0.821	0.824	0.937	0.614
K	0.006	0.003	0.001	0.000	0.005	0.000	0.001	0.000	0.003	0.017
Ba	0.000	0.000	0.000	0.000	0.000	0.002	0.000	0.001	0.000	0.003
Sr	0.000	0.000	0.000	0.000	0.000	0.000	0.000	0.000	0.000	0.000
Final terms										
An	75.38	80.89	85.01	79.08	77.67	76.53	78.66	78.92	75.66	83.88
Ab	24.47	19.05	14.97	20.92	22.20	23.47	21.32	21.08	24.26	15.69
Or	0.14	0.07	0.02	0.00	0.13	0.00	0.02	0.00	0.08	0.42

Sample	ST-65	ST-65	ST-65	ST-65	ST-65	ST-65	ST-65	ST-65	ST-65	ST-65
Reference	18LA	19LA	20LA	21LA	22LA	23LA	24LA	1LB	2LB	3LB
Zone	L. Ph.	L. Ph.	L. Ph.	L. Ph.	L. Ph.	L. Ph.	L. Ph.	L. Ph.	L. Ph.	L. Ph.
SiO_2	49.68	51.04	50.51	51.06	52.02	51.75	53.87	52.29	51.80	51.68
TiO_2	0.02	0.02	0.06	0.01	0.00	0.04	0.05	0.02	0.03	0.04
Al_2O_3	31.30	30.44	30.69	30.22	29.70	29.39	28.01	29.12	29.55	29.90
$Fe_2O_3^T$	0.40	0.45	0.46	0.46	0.53	0.59	0.90	0.76	0.59	0.53
MgO	0.27	0.31	0.31	0.32	0.38	0.36	0.31	0.37	0.45	0.33
CaO	16.80	15.83	15.94	15.81	13.74	15.09	13.56	14.72	14.86	15.29
Na_2O	1.69	2.24	2.14	2.26	3.53	2.70	3.63	2.95	2.81	2.59
K_2O	0.01	0.01	0.00	0.02	0.07	0.03	0.05	0.01	0.04	0.02
BaO	0.00	0.01	0.02	0.04	0.00	0.00	0.00	0.00	0.00	0.02
SrO	0.00	0.00	0.00	0.00	0.00	0.00	0.00	0.00	0.00	0.00
Total	100.17	100.34	100.13	100.19	99.97	99.94	100.37	100.23	100.14	100.40
Number of cations calculated based on 32 oxygen atoms										
Si	9.073	9.279	9.210	9.300	9.464	9.436	9.746	9.501	9.424	9.381
Ti	0.002	0.002	0.008	0.001	0.000	0.005	0.007	0.002	0.004	0.005
Al	6.737	6.522	6.595	6.487	6.368	6.314	5.972	6.235	6.335	6.397
Fe^{3+}	0.056	0.061	0.064	0.063	0.072	0.081	0.122	0.104	0.081	0.073
Mg	0.074	0.083	0.083	0.086	0.104	0.098	0.083	0.099	0.122	0.090
Ca	3.287	3.083	3.114	3.085	2.678	2.948	2.629	2.865	2.897	2.973
Na	0.597	0.789	0.757	0.796	1.245	0.955	1.272	1.040	0.990	0.913
K	0.002	0.003	0.001	0.004	0.016	0.006	0.012	0.002	0.010	0.004
Ba	0.000	0.001	0.001	0.003	0.000	0.000	0.000	0.000	0.000	0.001
Sr	0.000	0.000	0.000	0.000	0.000	0.000	0.000	0.000	0.000	0.000
Final terms										
An	84.60	79.56	80.43	79.41	76.00	75.40	67.19	73.34	74.34	76.43
Ab	15.36	20.36	19.55	20.50	31.61	24.44	32.50	26.61	25.42	23.46
Or	0.04	0.07	0.02	0.10	0.41	0.15	0.31	0.05	0.24	0.11

Sample	ST-65	ST-65	ST-65	ST-65	ST-65	ST-65	ST-65	ST-65	ST-65	ST-65
Reference	4LB	5LB	6LB	7LB	8LB	9LB	10LB	11LB	12LB	13LB
Zone	L. Ph.	L. Ph.	L. Ph.	L. Ph.	L. Ph.	L. Ph.	L. Ph.	L. Ph.	L. Ph.	L. Ph.
SiO_2	50.61	49.40	50.83	48.48	50.92	51.17	50.37	51.55	50.69	51.78
TiO_2	0.04	0.02	0.04	0.02	0.05	0.02	0.02	0.04	0.01	0.03
Al_2O_3	30.60	30.99	30.74	31.95	30.18	30.59	30.58	29.94	30.49	30.01
$Fe_2O_3^T$	0.49	0.54	0.35	0.42	0.43	0.44	0.56	0.44	0.45	0.48
MgO	0.31	0.52	0.25	0.23	0.33	0.30	0.42	0.29	0.31	0.34
CaO	15.85	15.91	15.83	17.08	15.38	15.77	15.69	15.48	15.76	15.23
Na_2O	2.19	2.17	2.16	1.52	2.44	2.14	2.23	2.33	2.31	2.56
K_2O	0.01	0.01	0.02	0.01	0.02	0.01	0.06	0.02	0.02	0.03
BaO	0.00	0.05	0.00	0.00	0.00	0.00	0.02	0.00	0.06	0.00
SrO	0.00	0.00	0.00	0.00	0.00	0.00	0.00	0.00	0.00	0.00
Total	100.11	99.61	100.22	99.70	99.75	100.44	99.96	100.09	100.09	100.46
Number of cations calculated based on 32 oxygen atoms										
Si	9.228	9.077	9.247	8.913	9.305	9.285	9.205	9.380	9.247	9.386
Ti	0.006	0.003	0.006	0.002	0.007	0.002	0.003	0.005	0.002	0.005
Al	6.575	6.710	6.591	6.922	6.501	6.542	6.585	6.421	6.555	6.412
Fe^{3+}	0.068	0.075	0.048	0.058	0.060	0.060	0.077	0.060	0.061	0.065
Mg	0.085	0.141	0.067	0.063	0.090	0.081	0.114	0.078	0.083	0.093
Ca	3.096	3.131	3.085	3.365	3.011	3.065	3.073	3.018	3.081	2.958
Na	0.772	0.773	0.763	0.540	0.865	0.753	0.791	0.822	0.817	0.899
K	0.003	0.003	0.003	0.003	0.004	0.002	0.015	0.005	0.004	0.006
Ba	0.000	0.004	0.000	0.000	0.000	0.000	0.001	0.000	0.004	0.000
Sr	0.000	0.000	0.000	0.000	0.000	0.000	0.000	0.000	0.000	0.000
Final terms										
An	79.98	80.15	80.09	86.10	77.62	80.22	79.21	78.50	78.96	76.56
Ab	19.95	19.79	19.81	13.83	22.29	19.72	20.40	21.38	20.94	23.28
Or	0.07	0.07	0.09	0.07	0.10	0.06	0.38	0.13	0.10	0.16

Sample	ST-65	ST-65	ST-65	ST-65	ST-65	ST-65	ST-65	ST-65	ST-65	ST-65
Reference	14LB	15LB	16LB	17LB	18LB	19LB	20LB	21LB	22LB	23LB
Zone	L. Ph.	L. Ph.	L. Ph.	L. Ph.	L. Ph.	L. Ph.	L. Ph.	L. Ph.	L. Ph.	L. Ph.
SiO_2	51.60	51.26	51.56	51.48	49.89	51.24	51.85	49.40	49.47	50.57
TiO_2	0.00	0.01	0.02	0.00	0.04	0.04	0.02	0.04	0.03	0.02
Al_2O_3	29.93	30.06	29.97	30.10	31.03	28.75	30.37	31.54	31.51	30.85
$Fe_2O_3^T$	0.46	0.41	0.44	0.44	0.44	0.49	0.45	0.43	0.45	0.47
MgO	0.30	0.30	0.29	0.31	0.28	0.31	0.33	0.25	0.25	0.29
CaO	15.31	15.32	15.24	15.18	16.12	15.45	15.70	16.71	16.63	15.95
Na_2O	2.44	2.48	2.44	2.46	2.04	2.15	2.31	1.64	1.70	2.11
K_2O	0.01	0.01	0.00	0.01	0.02	0.03	0.03	0.01	0.01	0.01
BaO	0.00	0.04	0.01	0.00	0.00	0.04	0.06	0.00	0.00	0.02
SrO	0.00	0.00	0.00	0.00	0.00	0.00	0.00	0.00	0.00	0.00
Total	100.05	99.89	99.97	99.97	99.85	98.50	101.12	100.00	100.04	100.29
Number of cations calculated based on 32 oxygen atoms										
Si	9.390	9.350	9.387	9.372	9.131	9.475	9.347	9.035	9.044	9.204
Ti	0.000	0.002	0.002	0.000	0.006	0.006	0.003	0.005	0.004	0.003
Al	6.419	6.463	6.431	6.457	6.692	6.266	6.451	6.798	6.790	6.616
Fe^{3+}	0.063	0.056	0.061	0.061	0.060	0.068	0.061	0.059	0.062	0.065
Mg	0.082	0.082	0.079	0.083	0.075	0.085	0.088	0.068	0.067	0.079
Ca	2.984	2.993	2.972	2.960	3.160	3.060	3.032	3.275	3.257	3.111
Na	0.860	0.878	0.861	0.869	0.725	0.772	0.807	0.583	0.603	0.745
K	0.001	0.003	0.001	0.003	0.004	0.006	0.006	0.001	0.002	0.003
Ba	0.000	0.003	0.000	0.000	0.000	0.003	0.005	0.000	0.000	0.001
Sr	0.000	0.000	0.000	0.000	0.000	0.000	0.000	0.000	0.000	0.000
Final terms										
An	77.60	77.26	77.51	77.23	81.25	79.72	78.86	84.86	84.34	80.62
Ab	22.37	22.68	22.46	22.68	18.65	20.11	20.98	15.11	15.61	19.30
Or	0.04	0.07	0.02	0.08	0.11	0.17	0.17	0.04	0.05	0.08

Sample	ST-65	ST-66	ST-66	ST-66	ST-66	ST-66	ST-66	ST-66	ST-66	ST-66
Reference	24LB	1	2	3	4	5	7	8	9	10
Zone	L. Ph.	M	M	Ph	Ph	Ph	Ph	Ph	Ph	Ph
SiO_2	51.08	50.69	51.72	50.35	51.26	50.59	49.42	48.73	48.15	50.39
TiO_2	0.01	0.01	0.01	0.01	0.02	0.02	0.00	0.00	0.00	0.06
Al_2O_3	30.21	29.98	29.34	30.30	29.66	30.02	30.97	31.32	31.99	30.63
$Fe_2O_3^T$	0.57	0.71	0.86	0.58	0.72	0.69	0.53	0.57	0.48	0.48
MgO	0.35	0.43	0.40	0.33	0.39	0.38	0.28	0.31	0.24	0.30
CaO	15.27	14.46	14.14	14.93	14.44	14.67	15.64	15.74	16.49	15.19
Na_2O	2.54	2.81	3.09	2.63	2.82	2.76	2.29	2.11	1.68	2.39
K_2O	0.03	0.10	0.02	0.01	0.02	0.02	0.01	0.03	0.01	0.01
BaO	0.03	0.03	0.00	0.00	0.00	0.00	0.00	0.04	0.00	0.01
SrO	0.00	0.00	0.00	0.00	0.00	0.00	0.00	0.00	0.00	0.00
Total	100.08	99.23	99.59	99.12	99.34	99.15	99.14	98.85	99.03	99.45
Number of cations calculated based on 32 oxygen atoms										
Si	9.309	9.315	9.454	9.262	9.395	9.302	9.111	9.020	8.904	9.236
Ti	0.002	0.001	0.002	0.001	0.003	0.003	0.000	0.001	0.000	0.008
Al	6.488	6.493	6.320	6.568	6.406	6.505	6.727	6.832	6.972	6.615
Fe^{3+}	0.078	0.098	0.118	0.080	0.099	0.096	0.074	0.080	0.067	0.066
Mg	0.094	0.118	0.110	0.089	0.107	0.104	0.078	0.084	0.065	0.082
Ca	2.982	2.847	2.769	2.942	2.835	2.889	3.090	3.122	3.267	2.982
Na	0.896	1.002	1.096	0.937	1.002	0.983	0.819	0.757	0.600	0.849
K	0.007	0.024	0.006	0.002	0.004	0.005	0.002	0.006	0.002	0.002
Ba	0.002	0.002	0.000	0.000	0.000	0.000	0.000	0.003	0.000	0.001
Sr	0.000	0.000	0.000	0.000	0.000	0.000	0.000	0.000	0.000	0.000
Final terms										
An	76.76	73.51	71.54	75.80	73.81	74.51	79.02	80.35	84.44	77.81
Ab	23.07	25.86	28.31	24.14	26.08	25.36	20.94	19.48	15.52	22.15
Or	0.17	0.63	0.14	0.06	0.12	0.13	0.04	0.16	0.04	0.04

Sample	ST-66	ST-66	ST-66	ST-66	ST-66	ST-66	ST-66	ST-66	ST-66	ST-66
Reference	11	12	13	14	15	16	17	18	22	23
Zone	Ph	M	M	Ph	Ph	Ph	Ph	M	M	M
SiO_2	48.46	50.08	50.63	50.19	49.33	48.40	51.74	50.22	49.89	50.63
TiO_2	0.01	0.04	0.00	0.02	0.03	0.02	0.02	0.02	0.02	0.01
Al_2O_3	31.86	30.60	29.61	30.57	31.11	31.29	28.83	30.00	30.12	29.98
$Fe_2O_3^T$	0.46	0.47	0.60	0.51	0.48	0.46	0.78	0.59	0.61	0.66
MgO	0.26	0.32	0.37	0.31	0.31	0.26	0.47	0.35	0.32	0.35
CaO	16.26	14.93	14.32	15.16	15.71	16.05	13.82	14.72	14.93	14.73
Na_2O	1.80	2.63	2.85	2.44	2.23	1.91	3.17	2.63	2.55	2.68
K_2O	0.03	0.12	0.35	0.01	0.02	0.10	0.02	0.01	0.02	0.00
BaO	0.03	0.03	0.00	0.00	0.00	0.02	0.03	0.03	0.06	0.01
SrO	0.00	0.00	0.00	0.00	0.00	0.00	0.00	0.00	0.00	0.00
Total	99.16	99.21	98.74	99.21	99.22	98.52	98.87	98.57	98.52	99.06
Number of cations calculated based on 32 oxygen atoms										
Si	8.945	9.214	9.356	9.225	9.088	8.995	9.518	9.288	9.244	9.316
Ti	0.001	0.005	0.000	0.003	0.004	0.003	0.002	0.003	0.003	0.002
Al	6.930	6.633	6.449	6.622	6.754	6.854	6.251	6.539	6.575	6.500
Fe^{3+}	0.065	0.065	0.083	0.071	0.067	0.065	0.108	0.082	0.085	0.092
Mg	0.071	0.087	0.103	0.084	0.085	0.072	0.128	0.096	0.088	0.095
Ca	3.217	2.942	2.835	2.985	3.100	3.196	2.724	2.917	2.964	2.903
Na	0.645	0.937	1.021	0.870	0.797	0.689	1.129	0.941	0.916	0.957
K	0.006	0.028	0.083	0.003	0.004	0.024	0.004	0.003	0.004	0.001
Ba	0.002	0.002	0.000	0.000	0.000	0.001	0.002	0.002	0.004	0.001
Sr	0.000	0.000	0.000	0.000	0.000	0.000	0.000	0.000	0.000	0.000
Final terms										
An	83.17	75.30	71.97	77.38	79.46	81.76	70.62	75.55	76.32	75.19
Ab	16.68	23.99	25.93	22.55	20.44	17.62	29.29	24.37	23.58	24.79
Or	0.15	0.71	2.09	0.07	0.09	0.62	0.09	0.08	0.10	0.02

Sample	ST-67	ST-67	ST-67	ST-67	ST-67	ST-67	ST-67	ST-67	ST-67	ST-67
Reference	1	2	3	4	5	6	7	8	9	10
Zone	M	M	M	M	M	M	M	M	M	M
SiO_2	49.72	51.39	48.85	50.65	52.75	51.03	51.10	50.75	51.45	51.58
TiO_2	0.01	0.04	0.04	0.05	0.03	0.00	0.02	0.01	0.02	0.06
Al_2O_3	31.05	30.02	31.29	30.02	28.26	29.92	29.75	30.02	29.45	29.41
$Fe_2O_3^T$	0.51	0.55	0.36	0.56	0.97	0.60	0.53	0.48	0.59	0.77
MgO	0.28	0.55	0.23	0.33	0.40	0.35	0.35	0.32	0.34	0.37
CaO	15.75	15.02	16.99	15.62	13.49	15.40	15.07	15.28	15.08	15.14
Na_2O	1.82	2.40	1.62	2.32	3.40	2.45	2.44	2.32	2.49	2.68
K_2O	0.36	0.12	0.01	0.01	0.04	0.00	0.15	0.04	0.02	0.01
BaO	0.00	0.01	0.00	0.02	0.00	0.00	0.00	0.02	0.03	0.00
SrO	0.00	0.00	0.00	0.00	0.00	0.00	0.00	0.00	0.00	0.00
Total	99.50	100.09	99.38	99.57	99.33	99.75	99.40	99.23	99.47	100.02
Number of cations calculated based on 32 oxygen atoms										
Si	9.134	9.352	9.005	9.286	9.648	9.330	9.369	9.320	9.421	9.405
Ti	0.002	0.005	0.005	0.006	0.004	0.000	0.003	0.001	0.002	0.008
Al	6.722	6.439	6.798	6.485	6.091	6.447	6.428	6.497	6.355	6.320
Fe^{3+}	0.070	0.076	0.049	0.078	0.133	0.082	0.073	0.067	0.082	0.106
Mg	0.076	0.149	0.064	0.090	0.109	0.095	0.095	0.089	0.092	0.101
Ca	3.100	2.929	3.355	3.067	2.644	3.016	2.960	3.006	2.959	2.958
Na	0.646	0.847	0.580	0.825	1.205	0.868	0.866	0.824	0.885	0.947
K	0.084	0.027	0.002	0.003	0.010	0.001	0.034	0.010	0.004	0.001
Ba	0.000	0.001	0.000	0.001	0.000	0.000	0.000	0.001	0.002	0.000
Sr	0.000	0.000	0.000	0.000	0.000	0.000	0.000	0.000	0.000	0.000
Final terms										
An	80.93	77.03	85.23	78.74	68.52	77.63	76.68	78.28	76.89	75.72
Ab	16.87	22.27	14.73	21.19	31.22	22.34	22.44	21.46	23.01	24.25
Or	2.20	0.70	0.04	0.08	0.27	0.02	0.88	0.26	0.10	0.03

Sample	ST-67	ST-67	ST-67	ST-67	ST-67	ST-67	ST-67	ST-67	ST-67	ST-67
Reference	11	1LA	2LA	3LA	4LA	5LA	6LA	7LA	8LA	9LA
Zone	M	L. Ph.	L. Ph.	L. Ph.	L. Ph.	L. Ph.	L. Ph.	L. Ph.	L. Ph.	L. Ph.
SiO_2	50.92	52.67	49.32	47.68	47.82	47.83	49.58	51.55	47.73	48.25
TiO_2	0.04	0.03	0.01	0.03	0.03	0.00	0.00	0.01	0.00	0.00
Al_2O_3	30.46	29.32	31.16	32.27	32.28	32.22	31.01	29.59	32.42	32.17
$Fe_2O_3^T$	0.53	0.81	0.49	0.40	0.43	0.42	0.38	0.75	0.43	0.44
MgO	0.33	0.55	0.26	0.18	0.23	0.17	0.15	0.67	0.18	0.17
CaO	15.85	14.30	16.47	17.70	16.01	17.54	16.05	11.98	17.55	17.32
Na_2O	2.27	2.91	1.94	1.20	1.32	1.30	2.44	2.80	1.28	1.40
K_2O	0.01	0.19	0.03	0.01	0.64	0.01	0.02	1.47	0.03	0.01
BaO	0.00	0.02	0.00	0.01	0.04	0.03	0.01	0.00	0.05	0.00
SrO	0.00	0.00	0.00	0.00	0.00	0.00	0.00	0.00	0.00	0.00
Total	100.41	100.81	99.67	99.46	98.80	99.52	99.63	98.81	99.67	99.75
Number of cations calculated based on 32 oxygen atoms										
Si	9.257	9.510	9.059	8.805	8.875	8.826	9.107	9.494	8.798	8.871
Ti	0.005	0.004	0.001	0.004	0.005	0.000	0.000	0.001	0.000	0.000
Al	6.526	6.239	6.746	7.022	7.060	7.007	6.714	6.422	7.044	6.972
Fe^{3+}	0.073	0.111	0.067	0.055	0.060	0.058	0.052	0.105	0.060	0.061
Mg	0.089	0.149	0.072	0.049	0.063	0.047	0.041	0.184	0.049	0.047
Ca	3.088	2.766	3.241	3.501	3.182	3.468	3.159	2.364	3.466	3.412
Na	0.801	1.020	0.691	0.428	0.473	0.464	0.869	0.999	0.456	0.498
K	0.003	0.044	0.006	0.002	0.152	0.003	0.004	0.345	0.006	0.001
Ba	0.000	0.001	0.000	0.000	0.003	0.002	0.001	0.000	0.004	0.000
Sr	0.000	0.000	0.000	0.000	0.000	0.000	0.000	0.000	0.000	0.000
Final terms										
An	79.35	72.23	82.30	89.07	83.57	88.14	78.35	63.75	88.23	87.22
Ab	20.59	26.63	17.55	10.89	12.43	11.79	21.55	26.94	11.62	12.74
Or	0.07	1.14	0.15	0.04	4.00	0.07	0.10	9.32	0.15	0.04

Sample	ST-67	ST-67	ST-67	ST-67	ST-67	ST-67	ST-67	ST-67	ST-67	ST-67
Reference	10LA	11LA	12LA	13LA	14LA	15LA	16LA	17LA	18LA	19LA
Zone	L. Ph.	L. Ph.	L. Ph.	L. Ph.	L. Ph.	L. Ph.	L. Ph.	L. Ph.	L. Ph.	L. Ph.
SiO_2	48.65	53.77	48.61	48.64	48.09	48.75	47.75	48.40	48.06	49.80
TiO_2	0.00	0.00	0.00	0.00	0.00	0.02	0.01	0.00	0.01	0.00
Al_2O_3	31.80	28.66	31.66	31.76	32.05	31.89	32.12	32.03	32.06	31.13
$Fe_2O_3^T$	0.58	0.74	0.44	0.47	0.47	0.47	0.46	0.41	0.42	0.41
MgO	0.37	0.66	0.18	0.19	0.19	0.18	0.18	0.16	0.17	0.23
CaO	16.76	9.42	17.34	17.39	17.43	16.15	17.21	17.41	17.31	16.58
Na_2O	1.60	4.16	1.39	1.48	1.36	1.68	1.42	1.31	1.43	1.85
K_2O	0.10	2.01	0.01	0.01	0.02	0.35	0.06	0.00	0.01	0.02
BaO	0.02	0.00	0.00	0.02	0.00	0.06	0.00	0.00	0.00	0.02
SrO	0.00	0.00	0.00	0.00	0.00	0.00	0.00	0.00	0.00	0.00
Total	99.88	99.42	99.62	99.95	99.62	99.54	99.21	99.72	99.46	100.05
Number of cations calculated based on 32 oxygen atoms										
Si	8.931	9.809	8.946	8.929	8.861	8.973	8.836	8.898	8.866	9.106
Ti	0.000	0.000	0.000	0.000	0.001	0.002	0.002	0.000	0.001	0.000
Al	6.881	6.160	6.866	6.872	6.960	6.916	7.003	6.941	6.969	6.707
Fe^{3+}	0.080	0.102	0.061	0.064	0.066	0.065	0.065	0.056	0.058	0.057
Mg	0.102	0.179	0.049	0.051	0.051	0.050	0.050	0.045	0.046	0.063
Ca	3.296	1.841	3.418	3.420	3.441	3.184	3.411	3.429	3.422	3.248
Na	0.569	1.469	0.496	0.525	0.487	0.599	0.511	0.467	0.510	0.657
K	0.024	0.467	0.003	0.003	0.004	0.083	0.013	0.000	0.002	0.005
Ba	0.001	0.000	0.000	0.002	0.000	0.004	0.000	0.000	0.000	0.001
Sr	0.000	0.000	0.000	0.000	0.000	0.000	0.000	0.000	0.000	0.000
Final terms										
An	84.74	48.74	87.26	86.63	87.51	82.36	86.68	88.00	86.99	83.07
Ab	14.63	38.89	12.66	13.30	12.39	15.51	12.98	11.99	12.96	16.81
Or	0.63	12.37	0.08	0.08	0.10	2.14	0.34	0.01	0.05	0.13

Sample	ST-67	ST-67	ST-67	ST-67	ST-67	ST-67	ST-67	ST-67	ST-67	ST-67
Reference	20LA	1LB	2LB	3LB	4LB	5LB	6LB	7LB	8LB	9LB
Zone	L. Ph.	L. Ph.	L. Ph.	L. Ph.	L. Ph.	L. Ph.	L. Ph.	L. Ph.	L. Ph.	L. Ph.
SiO_2	50.10	51.78	49.66	47.74	48.53	48.29	48.22	51.86	49.46	48.00
TiO_2	0.00	0.04	0.04	0.01	0.01	0.02	0.05	0.00	0.02	0.02
Al_2O_3	30.52	29.15	31.21	32.03	31.81	31.86	32.05	27.99	30.20	31.98
$Fe_2O_3^T$	0.52	0.71	0.45	0.36	0.45	0.40	0.39	0.39	0.43	0.44
MgO	0.31	0.50	0.27	0.21	0.17	0.19	0.17	0.23	0.20	0.18
CaO	16.00	14.60	13.54	17.35	17.08	17.41	17.50	14.75	16.32	17.23
Na_2O	2.20	2.84	2.67	1.43	1.40	1.41	1.39	3.20	1.97	1.46
K_2O	0.04	0.12	0.94	0.05	0.07	0.00	0.00	0.07	0.03	0.02
BaO	0.00	0.02	0.00	0.03	0.00	0.00	0.00	0.04	0.00	0.00
SrO	0.00	0.00	0.00	0.00	0.00	0.00	0.00	0.00	0.00	0.00
Total	99.68	99.76	98.77	99.20	99.51	99.57	99.78	98.53	98.62	99.32
Number of cations calculated based on 32 oxygen atoms										
Si	9.188	9.459	9.178	8.838	8.937	8.898	8.869	9.596	9.174	8.869
Ti	0.000	0.005	0.005	0.002	0.001	0.002	0.007	0.000	0.002	0.002
Al	6.597	6.276	6.797	6.988	6.904	6.918	6.948	6.103	6.601	6.962
Fe^{3+}	0.071	0.098	0.062	0.050	0.062	0.055	0.055	0.055	0.059	0.062
Mg	0.083	0.137	0.075	0.058	0.046	0.052	0.047	0.062	0.056	0.050
Ca	3.143	2.856	2.681	3.442	3.371	3.437	3.449	2.924	3.242	3.409
Na	0.783	1.007	0.957	0.511	0.501	0.503	0.495	1.146	0.709	0.523
K	0.009	0.027	0.221	0.011	0.016	0.000	0.000	0.017	0.007	0.005
Ba	0.000	0.001	0.000	0.002	0.000	0.000	0.000	0.003	0.000	0.000
Sr	0.000	0.000	0.000	0.000	0.000	0.000	0.000	0.000	0.000	0.000
Final terms										
An	79.88	73.42	69.46	86.82	86.71	87.24	87.45	71.53	81.91	86.59
Ab	19.90	25.88	24.80	12.90	12.88	12.76	12.55	28.04	17.91	13.29
Or	0.22	0.69	5.73	0.27	0.42	0.00	0.00	0.43	0.18	0.12

Sample	ST-67	ST-67	ST-67	ST-67	ST-67	ST-67	ST-67	ST-67	ST-67	ST-67
Reference	10LB	11LB	12LB	13LB	14LB	15LB	16LB	17LB	18LB	19LB
Zone	L. Ph.	L. Ph.	L. Ph.	L. Ph.	L. Ph.	L. Ph.	L. Ph.	L. Ph.	L. Ph.	L. Ph.
SiO_2	48.72	48.12	47.96	47.88	48.33	50.20	48.33	47.50	48.62	48.53
TiO_2	0.00	0.00	0.00	0.03	0.05	0.02	0.01	0.00	0.00	0.02
Al_2O_3	32.02	32.06	32.25	32.20	32.02	31.89	31.24	32.31	31.76	31.53
$Fe_2O_3^T$	0.48	0.42	0.38	0.38	0.40	0.55	0.58	0.38	0.55	0.40
MgO	0.26	0.16	0.19	0.18	0.21	0.47	0.43	0.19	0.42	0.24
CaO	14.53	17.37	17.50	17.30	16.14	11.42	16.55	17.57	15.07	16.99
Na_2O	1.31	1.34	1.33	1.41	1.41	1.54	1.82	1.27	1.65	1.67
K_2O	1.47	0.02	0.01	0.06	0.67	2.33	0.15	0.00	0.87	0.01
BaO	0.00	0.06	0.03	0.00	0.00	0.04	0.00	0.00	0.00	0.01
SrO	0.00	0.00	0.00	0.00	0.00	0.00	0.00	0.00	0.00	0.00
Total	98.78	99.54	99.65	99.44	99.23	98.43	99.10	99.22	98.93	99.41
Number of cations calculated based on 32 oxygen atoms										
Si	9.025	8.872	8.836	8.838	8.930	9.268	8.951	8.792	8.997	8.952
Ti	0.000	0.001	0.000	0.004	0.006	0.002	0.002	0.000	0.000	0.003
Al	6.990	6.965	7.002	7.005	6.972	6.938	6.818	7.048	6.928	6.855
Fe^{3+}	0.066	0.058	0.053	0.052	0.056	0.076	0.080	0.053	0.076	0.055
Mg	0.073	0.044	0.051	0.050	0.059	0.129	0.120	0.053	0.114	0.066
Ca	2.883	3.431	3.454	3.420	3.195	2.259	3.285	3.484	2.987	3.357
Na	0.469	0.477	0.476	0.506	0.503	0.550	0.652	0.455	0.593	0.598
K	0.347	0.006	0.002	0.013	0.157	0.548	0.034	0.001	0.206	0.003
Ba	0.000	0.004	0.002	0.000	0.000	0.003	0.000	0.000	0.000	0.001
Sr	0.000	0.000	0.000	0.000	0.000	0.000	0.000	0.000	0.000	0.000
Final terms										
An	77.92	87.66	87.84	86.82	82.88	67.29	82.72	88.42	78.89	84.83
Ab	12.69	12.19	12.12	12.84	13.05	16.38	16.41	11.56	15.67	15.10
Or	9.39	0.14	0.05	0.34	4.07	16.33	0.87	0.02	5.43	0.07

Sample	ST-67	ST-67	ST-67	ST-67	ST-67	ST-67	ST-67	ST-67	ST-67	ST-67
Reference	20LB	1LC	2LC	3LC	4LC	5LC	6LC	7LC	8LC	9LC
Zone	L. Ph.	L. Ph.	L. Ph.	L. Ph.	L. Ph.	L. Ph.	L. Ph.	L. Ph.	L. Ph.	L. Ph.
SiO_2	51.44	52.70	51.04	51.58	50.84	51.15	50.94	51.01	50.33	51.41
TiO_2	0.01	0.02	0.00	0.04	0.05	0.05	0.00	0.05	0.02	0.04
Al_2O_3	29.89	28.92	29.99	30.12	30.34	30.08	30.63	30.68	30.42	30.05
$Fe_2O_3^T$	0.64	0.77	0.62	0.47	0.44	0.44	0.46	0.43	0.49	0.44
MgO	0.32	0.37	0.62	0.32	0.28	0.31	0.32	0.32	0.30	0.32
CaO	15.25	14.67	15.55	15.51	15.58	15.50	14.83	16.29	16.05	15.66
Na_2O	2.63	2.96	2.30	2.55	2.46	2.50	2.13	2.14	2.25	2.32
K_2O	0.01	0.02	0.06	0.01	0.02	0.02	0.67	0.02	0.02	0.04
BaO	0.00	0.03	0.00	0.00	0.00	0.00	0.05	0.01	0.00	0.04
SrO	0.00	0.00	0.00	0.00	0.00	0.00	0.00	0.00	0.00	0.00
Total	100.18	100.46	100.17	100.60	100.00	100.04	100.03	100.95	99.87	100.31
Number of cations calculated based on 32 oxygen atoms										
Si	9.363	9.550	9.299	9.348	9.276	9.324	9.292	9.231	9.211	9.345
Ti	0.002	0.003	0.000	0.006	0.007	0.007	0.000	0.007	0.003	0.005
Al	6.410	6.176	6.440	6.433	6.524	6.462	6.585	6.543	6.561	6.438
Fe^{3+}	0.087	0.105	0.084	0.064	0.060	0.060	0.063	0.058	0.067	0.061
Mg	0.085	0.100	0.168	0.086	0.075	0.085	0.088	0.087	0.082	0.088
Ca	2.973	2.849	3.036	3.012	3.046	3.027	2.897	3.158	3.147	3.049
Na	0.928	1.041	0.812	0.895	0.870	0.882	0.755	0.749	0.797	0.817
K	0.003	0.005	0.013	0.002	0.005	0.003	0.157	0.004	0.004	0.008
Ba	0.000	0.002	0.000	0.000	0.000	0.000	0.004	0.001	0.000	0.003
Sr	0.000	0.000	0.000	0.000	0.000	0.000	0.000	0.000	0.000	0.000
Final terms										
An	76.15	73.15	78.64	77.05	77.68	77.36	76.07	80.74	79.70	78.70
Ab	23.77	26.74	21.03	22.90	22.19	22.55	19.81	19.15	20.19	21.08
Or	0.08	0.12	0.34	0.05	0.12	0.09	4.11	0.11	0.11	0.22

Sample	ST-67	ST-67	ST-67	ST-67	ST-67	ST-67	ST-67	ST-67	ST-67	ST-67
Reference	10LC	11LC	12LC	13LC	14LC	15LC	1LD	2LD	3LD	4LD
Zone	L. Ph.	L. Ph.	L. Ph.	L. Ph.	L. Ph.	L. Ph.	L. Ph.	L. Ph.	L. Ph.	L. Ph.
SiO_2	51.64	51.61	51.67	52.28	51.30	52.56	52.54	51.25	50.50	50.94
TiO_2	0.01	0.01	0.02	0.01	0.02	0.04	0.01	0.04	0.03	0.03
Al_2O_3	30.10	29.48	30.19	28.95	30.11	28.69	29.05	29.64	30.04	30.17
$Fe_2O_3^T$	0.49	0.80	0.44	0.61	0.50	0.83	0.65	0.52	0.58	0.45
MgO	0.33	0.67	0.29	0.53	0.37	0.42	0.52	0.36	0.48	0.33
CaO	15.59	15.29	15.46	14.56	15.68	14.54	14.15	15.36	16.15	15.65
Na_2O	2.50	2.44	2.42	3.02	2.37	3.10	3.11	2.56	2.05	2.34
K_2O	0.01	0.11	0.07	0.06	0.00	0.04	0.10	0.00	0.04	0.02
BaO	0.00	0.00	0.00	0.05	0.00	0.03	0.04	0.03	0.01	0.01
SrO	0.00	0.00	0.00	0.00	0.00	0.00	0.00	0.00	0.00	0.00
Total	100.68	100.42	100.55	100.07	100.37	100.23	100.16	99.75	99.88	99.94
Number of cations calculated based on 32 oxygen atoms										
Si	9.353	9.380	9.362	9.515	9.323	9.553	9.542	9.370	9.244	9.299
Ti	0.001	0.002	0.002	0.002	0.003	0.005	0.001	0.005	0.004	0.004
Al	6.424	6.313	6.447	6.210	6.449	6.144	6.217	6.387	6.479	6.490
Fe^{3+}	0.067	0.109	0.060	0.084	0.069	0.113	0.089	0.071	0.080	0.062
Mg	0.088	0.182	0.077	0.144	0.101	0.113	0.140	0.097	0.130	0.090
Ca	3.025	2.978	3.002	2.839	3.052	2.832	2.753	3.009	3.167	3.059
Na	0.879	0.859	0.849	1.065	0.836	1.093	1.094	0.907	0.727	0.828
K	0.003	0.025	0.016	0.015	0.000	0.009	0.022	0.000	0.010	0.004
Ba	0.000	0.000	0.000	0.003	0.000	0.002	0.003	0.002	0.000	0.001
Sr	0.000	0.000	0.000	0.000	0.000	0.000	0.000	0.000	0.000	0.000
Final terms										
An	77.43	77.10	77.63	72.44	78.49	71.99	71.15	76.83	81.12	78.60
Ab	22.49	22.24	21.96	27.18	21.51	27.78	28.28	23.17	18.62	21.28
Or	0.08	0.65	0.41	0.38	0.01	0.23	0.57	0.00	0.25	0.11

Sample	ST-67	ST-67	ST-67	ST-67	ST-67	ST-67	ST-67	ST-67	ST-67	ST-67
Reference	5LD	6LD	7LD	8LD	9LD	10LD	1LE	2LE	3LE	4LE
Zone	L. Ph.	L. Ph.	L. Ph.	L. Ph.	L. Ph.	L. Ph.	L. Ph.	L. Ph.	L. Ph.	L. Ph.
SiO_2	50.72	51.22	51.38	51.51	51.69	52.25	49.47	50.38	50.73	49.76
TiO_2	0.03	0.01	0.03	0.04	0.07	0.03	0.05	0.01	0.04	0.02
Al_2O_3	30.52	30.63	30.17	30.51	29.72	29.48	29.86	29.53	29.76	30.23
$Fe_2O_3^T$	0.45	0.46	0.42	0.50	0.56	0.61	0.71	0.42	0.47	0.48
MgO	0.31	0.28	0.29	0.32	0.35	0.37	0.49	0.32	0.30	0.30
CaO	15.95	16.03	15.68	15.53	15.31	15.03	15.49	15.06	15.25	15.70
Na_2O	2.29	2.20	2.30	2.49	2.56	2.75	2.32	2.67	2.42	2.24
K_2O	0.01	0.01	0.01	0.02	0.03	0.00	0.08	0.01	0.01	0.01
BaO	0.00	0.05	0.00	0.00	0.00	0.02	0.01	0.00	0.00	0.00
SrO	0.00	0.00	0.00	0.00	0.00	0.00	0.00	0.00	0.00	0.00
Total	100.27	100.89	100.28	100.91	100.29	100.55	98.47	98.40	98.96	98.73
Number of cations calculated based on 32 oxygen atoms										
Si	9.236	9.267	9.338	9.306	9.394	9.464	9.191	9.338	9.342	9.206
Ti	0.004	0.001	0.004	0.006	0.010	0.005	0.007	0.002	0.005	0.003
Al	6.551	6.531	6.463	6.497	6.365	6.292	6.539	6.450	6.458	6.590
Fe^{3+}	0.062	0.063	0.058	0.068	0.077	0.084	0.099	0.059	0.065	0.067
Mg	0.083	0.075	0.078	0.086	0.095	0.099	0.136	0.088	0.081	0.082
Ca	3.112	3.107	3.053	3.005	2.980	2.917	3.083	2.991	3.009	3.112
Na	0.808	0.773	0.810	0.871	0.901	0.964	0.836	0.958	0.862	0.802
K	0.002	0.003	0.003	0.005	0.008	0.001	0.019	0.001	0.002	0.002
Ba	0.000	0.004	0.000	0.000	0.000	0.002	0.001	0.000	0.000	0.000
Sr	0.000	0.000	0.000	0.000	0.000	0.000	0.000	0.000	0.000	0.000
Final terms										
An	79.34	80.02	78.96	77.43	76.64	75.14	78.30	75.72	77.70	79.46
Ab	20.61	19.90	20.95	22.44	23.16	24.83	21.22	24.25	22.26	20.48
Or	0.05	0.08	0.08	0.13	0.20	0.02	0.48	0.03	0.04	0.06

Sample	ST-67	ST-67	ST-67	ST-67	ST-67	ST-67	ST-67	ST-67	ST-67	ST-67
Reference	5LE	6LE	7LE	8LE	9LE	10LE	11LE	12LE	13LE	14LE
Zone	L. Ph.	L. Ph.	L. Ph.	L. Ph.	L. Ph.	L. Ph.	L. Ph.	L. Ph.	L. Ph.	L. Ph.
SiO_2	50.43	50.69	48.05	55.49	50.12	48.22	50.11	49.64	49.39	50.68
TiO_2	0.05	0.04	0.02	0.02	0.05	0.01	0.01	0.02	0.00	0.03
Al_2O_3	29.59	29.81	31.65	26.85	30.00	30.82	29.99	30.02	30.20	29.89
$Fe_2O_3^T$	0.45	0.50	0.41	0.37	0.45	0.40	0.44	0.49	0.45	0.45
MgO	0.33	0.31	0.22	0.25	0.29	0.20	0.30	0.30	0.31	0.31
CaO	15.16	15.29	16.97	11.21	14.74	16.28	15.75	15.76	15.84	15.27
Na_2O	2.57	2.47	1.52	5.02	2.72	2.00	2.22	2.28	2.24	2.52
K_2O	0.01	0.00	0.02	0.08	0.09	0.02	0.01	0.00	0.01	0.01
BaO	0.00	0.00	0.01	0.00	0.07	0.00	0.00	0.00	0.06	0.00
SrO	0.00	0.00	0.00	0.00	0.00	0.00	0.00	0.00	0.00	0.00
Total	98.60	99.11	98.87	99.29	98.53	97.96	98.83	98.51	98.48	99.16
Number of cations calculated based on 32 oxygen atoms										
Si	9.329	9.326	8.912	10.078	9.282	9.019	9.257	9.210	9.174	9.320
Ti	0.007	0.005	0.002	0.003	0.007	0.001	0.002	0.003	0.000	0.003
Al	6.450	6.464	6.918	5.747	6.547	6.793	6.529	6.563	6.609	6.478
Fe^{3+}	0.063	0.069	0.057	0.050	0.063	0.057	0.062	0.068	0.062	0.063
Mg	0.090	0.085	0.061	0.069	0.079	0.055	0.083	0.084	0.087	0.086
Ca	3.004	3.014	3.372	2.181	2.924	3.263	3.117	3.132	3.151	3.008
Na	0.922	0.880	0.548	1.769	0.976	0.726	0.794	0.819	0.805	0.897
K	0.003	0.000	0.004	0.018	0.022	0.006	0.001	0.001	0.001	0.001
Ba	0.000	0.000	0.001	0.000	0.005	0.000	0.000	0.000	0.004	0.000
Sr	0.000	0.000	0.000	0.000	0.000	0.000	0.000	0.000	0.000	0.000
Final terms										
An	76.46	77.40	85.94	54.97	74.55	81.68	79.67	79.25	79.63	76.99
Ab	23.46	22.60	13.96	44.59	24.89	18.18	20.30	20.73	20.34	22.97
Or	0.08	0.00	0.11	0.44	0.57	0.14	0.03	0.02	0.03	0.04

Sample	ST-67	ST-67	ST-67	ST-67	ST-67	ST-67	ST-67	ST-67	ST-67	ST-67
Reference	15LE	16LE	17LE	18LE	19LE	20LE	1LF	2LF	3LF	4LF
Zone	L. Ph.	L. Ph.	L. Ph.	L. Ph.	L. Ph.	L. Ph.	L. Ph.	L. Ph.	L. Ph.	L. Ph.
SiO_2	50.48	48.32	49.13	51.36	51.77	52.31	48.68	50.90	50.81	50.99
TiO_2	0.02	0.01	0.03	0.05	0.03	0.04	0.00	0.02	0.00	0.02
Al_2O_3	29.73	31.32	30.63	29.09	28.69	28.32	31.45	29.62	29.82	29.76
$Fe_2O_3^T$	0.44	0.40	0.44	0.64	0.64	0.64	0.45	0.47	0.46	0.45
MgO	0.31	0.25	0.29	0.35	0.35	0.39	0.27	0.34	0.30	0.34
CaO	15.15	16.77	16.06	14.56	14.57	13.98	16.40	15.14	15.45	15.25
Na_2O	2.38	1.72	1.98	2.91	3.03	3.31	1.58	2.56	2.33	2.56
K_2O	0.01	0.01	0.03	0.01	0.03	0.01	0.23	0.01	0.01	0.02
BaO	0.00	0.00	0.00	0.00	0.02	0.00	0.06	0.00	0.00	0.00
SrO	0.00	0.00	0.00	0.00	0.00	0.00	0.00	0.00	0.00	0.00
Total	98.51	98.81	98.58	98.95	99.12	99.01	99.11	99.06	99.18	99.38
Number of cations calculated based on 32 oxygen atoms										
Si	9.335	8.964	9.113	9.452	9.514	9.607	8.998	9.364	9.338	9.352
Ti	0.003	0.001	0.005	0.007	0.005	0.006	0.000	0.002	0.000	0.003
Al	6.480	6.848	6.695	6.309	6.215	6.130	6.851	6.423	6.459	6.434
Fe^{3+}	0.061	0.056	0.062	0.088	0.088	0.088	0.062	0.065	0.064	0.062
Mg	0.085	0.070	0.080	0.095	0.097	0.106	0.073	0.092	0.081	0.093
Ca	3.001	3.333	3.191	2.871	2.868	2.751	3.247	2.984	3.042	2.996
Na	0.852	0.620	0.711	1.037	1.078	1.178	0.567	0.915	0.831	0.910
K	0.001	0.001	0.007	0.001	0.008	0.003	0.053	0.003	0.002	0.004
Ba	0.000	0.000	0.000	0.000	0.001	0.000	0.005	0.000	0.000	0.000
Sr	0.000	0.000	0.000	0.000	0.000	0.000	0.000	0.000	0.000	0.000
Final terms										
An	77.87	84.29	81.64	73.43	72.54	69.97	83.95	76.48	78.52	76.64
Ab	22.10	15.68	18.18	26.53	27.27	29.96	14.67	23.44	21.44	23.27
Or	0.03	0.04	0.18	0.04	0.19	0.07	1.38	0.08	0.04	0.09

Sample	ST-67	ST-67	ST-67	ST-67	ST-67	ST-67	ST-69	ST-69	ST-69	ST-69
Reference	5LF	6LF	7LF	8LF	9LF	10LF	1	2	3	4
Zone	L. Ph.	L. Ph.	L. Ph.	L. Ph.	L. Ph.	L. Ph.	M	M	M	M
SiO_2	50.89	51.18	48.86	50.85	50.54	50.89	52.80	52.17	53.05	52.86
TiO_2	0.03	0.04	0.04	0.02	0.01	0.02	0.06	0.04	0.05	0.03
Al_2O_3	30.23	28.33	31.28	30.12	30.11	29.90	27.70	28.30	27.89	27.48
$Fe_2O_3^T$	0.41	0.48	0.46	0.46	0.45	0.57	1.02	0.90	0.82	1.12
MgO	0.27	0.46	0.24	0.31	0.29	0.32	0.82	0.57	0.52	0.75
CaO	15.50	14.28	16.91	15.62	15.56	15.42	13.20	14.81	13.61	13.90
Na_2O	2.23	3.00	1.58	2.26	2.27	2.34	3.33	2.79	3.39	3.24
K_2O	0.01	0.37	0.00	0.01	0.00	0.01	0.35	0.02	0.04	0.04
BaO	0.01	0.00	0.00	0.00	0.06	0.00	0.00	0.00	0.00	0.03
SrO	0.00	0.00	0.00	0.00	0.00	0.00	0.00	0.00	0.00	0.00
Total	99.58	98.15	99.35	99.63	99.30	99.47	99.28	99.58	99.36	99.44
Number of cations calculated based on 32 oxygen atoms										
Si	9.310	9.511	9.007	9.305	9.286	9.328	9.676	9.548	9.698	9.678
Ti	0.005	0.006	0.005	0.002	0.002	0.003	0.009	0.005	0.007	0.004
Al	6.517	6.205	6.797	6.496	6.520	6.458	5.981	6.103	6.008	5.929
Fe^{3+}	0.057	0.068	0.063	0.063	0.063	0.078	0.141	0.124	0.113	0.154
Mg	0.073	0.127	0.065	0.083	0.078	0.089	0.223	0.154	0.141	0.204
Ca	3.038	2.844	3.339	3.062	3.063	3.027	2.591	2.904	2.664	2.725
Na	0.790	1.081	0.563	0.802	0.810	0.831	1.184	0.989	1.201	1.150
K	0.002	0.088	0.000	0.002	0.000	0.003	0.082	0.004	0.009	0.009
Ba	0.001	0.000	0.000	0.000	0.005	0.000	0.000	0.000	0.000	0.002
Sr	0.000	0.000	0.000	0.000	0.000	0.000	0.000	0.000	0.000	0.000
Final terms										
An	79.32	70.87	85.57	79.20	79.09	78.40	67.17	74.52	68.76	70.16
Ab	20.63	26.94	14.43	20.75	20.91	21.52	30.70	25.37	31.01	29.62
Or	0.05	2.19	0.00	0.05	0.00	0.08	2.13	0.11	0.23	0.22

Sample	ST-69	ST-69	ST-69	ST-69	ST-69	ST-69	ST-69	ST-69	ST-69	ST-69
Reference	6	7	8	9	10	12	13	14	15	16
Zone	M	M	Ph	Ph	M	M	Ph	Ph	M	M
SiO_2	53.65	53.16	51.20	51.09	52.54	52.86	51.39	52.26	51.61	53.14
TiO_2	0.33	0.05	0.00	0.03	0.08	0.04	0.02	0.04	0.12	0.06
Al_2O_3	26.24	27.74	29.78	28.61	27.86	27.82	29.32	28.98	27.31	27.66
$Fe_2O_3^T$	2.19	0.90	0.46	0.97	1.01	0.90	0.62	0.71	2.07	1.08
MgO	0.80	0.56	0.34	0.75	0.54	0.54	0.43	0.74	1.58	0.63
CaO	11.88	13.73	15.26	14.85	14.33	13.96	14.16	13.67	13.76	13.60
Na_2O	4.24	3.34	2.56	2.70	3.13	3.30	2.65	3.24	3.16	3.37
K_2O	0.17	0.02	0.01	0.05	0.01	0.02	0.39	0.15	0.17	0.05
BaO	0.02	0.02	0.00	0.00	0.00	0.00	0.01	0.01	0.04	0.00
SrO	0.00	0.00	0.00	0.00	0.00	0.00	0.00	0.00	0.00	0.00
Total	99.52	99.51	99.60	99.03	99.49	99.42	98.99	99.80	99.83	99.58
Number of cations calculated based on 32 oxygen atoms										
Si	9.821	9.707	9.368	9.421	9.619	9.669	9.452	9.524	9.475	9.702
Ti	0.046	0.007	0.001	0.004	0.011	0.005	0.003	0.006	0.017	0.008
Al	5.662	5.969	6.420	6.216	6.012	5.997	6.356	6.223	5.909	5.950
Fe^{3+}	0.301	0.124	0.063	0.134	0.139	0.125	0.086	0.098	0.286	0.148
Mg	0.219	0.152	0.092	0.205	0.147	0.146	0.117	0.202	0.433	0.170
Ca	2.330	2.686	2.991	2.933	2.810	2.735	2.790	2.669	2.707	2.660
Na	1.504	1.182	0.907	0.964	1.111	1.170	0.944	1.144	1.123	1.192
K	0.040	0.003	0.002	0.011	0.003	0.004	0.092	0.034	0.040	0.011
Ba	0.001	0.001	0.000	0.000	0.000	0.000	0.000	0.001	0.003	0.000
Sr	0.000	0.000	0.000	0.000	0.000	0.000	0.000	0.000	0.000	0.000
Final terms										
An	60.15	69.37	76.70	75.06	71.60	69.97	72.92	69.38	69.94	68.85
Ab	38.82	30.54	23.26	24.67	28.31	29.92	24.66	29.73	29.02	30.86
Or	1.03	0.09	0.04	0.27	0.08	0.11	2.42	0.89	1.03	0.28

Sample	ST-69	ST-69	ST-69	ST-69	ST-70	ST-70	ST-70	ST-70	ST-70	ST-70
Reference	17	18	19	20	1	2	3	4	6	8
Zone	Ph	Ph	Ph	Ph	Ph	Ph	M	M	M	M
SiO_2	49.75	50.27	50.33	51.10	49.87	50.57	50.98	51.38	50.65	50.74
TiO_2	0.03	0.00	0.03	0.03	0.01	0.00	0.07	0.03	0.00	0.00
Al_2O_3	30.37	30.16	30.19	29.27	30.43	29.78	29.68	29.09	29.63	29.54
$Fe_2O_3^T$	0.46	0.46	0.48	0.61	0.57	0.65	0.82	0.79	0.65	0.67
MgO	0.29	0.31	0.32	0.40	0.35	0.34	0.43	0.44	0.39	0.41
CaO	16.06	15.62	15.61	14.95	15.02	14.71	14.20	13.54	14.24	14.33
Na_2O	2.11	2.27	2.30	2.68	2.46	2.76	2.96	3.40	3.07	2.77
K_2O	0.03	0.02	0.01	0.02	0.01	0.00	0.03	0.06	0.03	0.01
BaO	0.00	0.00	0.02	0.00	0.00	0.00	0.00	0.01	0.00	0.01
SrO	0.00	0.00	0.00	0.00	0.00	0.00	0.00	0.00	0.00	0.00
Total	99.08	99.11	99.29	99.07	98.71	98.82	99.15	98.73	98.66	98.48
Number of cations calculated based on 32 oxygen atoms										
Si	9.180	9.256	9.252	9.403	9.215	9.329	9.366	9.471	9.355	9.379
Ti	0.004	0.000	0.005	0.004	0.002	0.000	0.009	0.004	0.000	0.001
Al	6.603	6.546	6.541	6.348	6.625	6.474	6.426	6.319	6.450	6.435
Fe^{3+}	0.063	0.063	0.066	0.085	0.079	0.090	0.113	0.109	0.090	0.094
Mg	0.079	0.085	0.089	0.110	0.095	0.095	0.116	0.121	0.108	0.113
Ca	3.175	3.082	3.075	2.946	2.973	2.907	2.794	2.673	2.819	2.838
Na	0.754	0.812	0.821	0.956	0.882	0.987	1.055	1.214	1.099	0.991
K	0.006	0.004	0.003	0.004	0.001	0.001	0.007	0.015	0.007	0.002
Ba	0.000	0.000	0.001	0.000	0.000	0.000	0.000	0.001	0.000	0.001
Sr	0.000	0.000	0.000	0.000	0.000	0.000	0.000	0.000	0.000	0.000
Final terms										
An	80.69	79.07	78.87	75.41	77.10	74.65	72.46	68.50	71.81	74.08
Ab	19.15	20.83	21.05	24.48	22.86	25.33	27.35	31.12	28.00	25.88
Or	0.16	0.11	0.08	0.11	0.04	0.02	0.19	0.38	0.19	0.04

Sample	ST-70	ST-70	ST-70	ST-70	ST-70	ST-70	ST-70	ST-70	ST-70	ST-70
Reference	9	10	11	12	13	14	16	17	19	20
Zone	M	M	PhC	PhR	M	Ph	Ph	Ph	M	M
SiO_2	50.87	50.37	50.11	55.37	51.02	50.28	50.40	49.04	50.20	50.99
TiO_2	0.00	0.00	0.05	0.08	0.01	0.00	0.00	0.01	0.03	0.03
Al_2O_3	29.54	29.99	30.33	26.45	29.59	30.04	30.83	31.19	30.40	29.72
$Fe_2O_3^T$	0.71	0.73	0.56	1.42	0.70	0.63	0.80	0.54	0.67	0.69
MgO	0.42	0.37	0.37	0.13	0.38	0.39	0.55	0.27	0.34	0.35
CaO	14.25	14.46	14.87	10.70	14.12	14.58	15.28	15.67	14.58	14.30
Na_2O	3.04	2.85	2.67	5.10	2.92	2.62	2.75	2.02	2.67	3.04
K_2O	0.04	0.02	0.01	0.05	0.02	0.02	0.04	0.04	0.03	0.26
BaO	0.00	0.04	0.00	0.06	0.00	0.00	0.00	0.01	0.00	0.00
SrO	0.00	0.00	0.00	0.00	0.00	0.00	0.00	0.00	0.00	0.00
Total	98.88	98.83	98.97	99.37	98.75	98.56	100.65	98.78	98.91	99.36
Number of cations calculated based on 32 oxygen atoms										
Si	9.376	9.294	9.236	10.074	9.400	9.294	9.159	9.070	9.249	9.362
Ti	0.000	0.000	0.007	0.011	0.001	0.000	0.000	0.001	0.004	0.004
Al	6.416	6.522	6.587	5.671	6.425	6.543	6.603	6.799	6.602	6.431
Fe^{3+}	0.099	0.101	0.077	0.195	0.097	0.088	0.110	0.075	0.092	0.095
Mg	0.116	0.101	0.102	0.035	0.104	0.106	0.148	0.074	0.093	0.096
Ca	2.814	2.859	2.936	2.086	2.786	2.888	2.976	3.104	2.878	2.813
Na	1.085	1.021	0.954	1.799	1.044	0.938	0.968	0.725	0.955	1.081
K	0.008	0.005	0.003	0.011	0.004	0.005	0.010	0.008	0.006	0.060
Ba	0.000	0.003	0.000	0.004	0.000	0.000	0.000	0.001	0.000	0.000
Sr	0.000	0.000	0.000	0.000	0.000	0.000	0.000	0.000	0.000	0.000
Final terms										
An	72.01	73.59	75.42	53.54	72.66	75.38	75.26	80.89	74.97	71.14
Ab	27.77	26.28	24.51	46.18	27.23	24.49	24.49	18.88	24.87	27.35
Or	0.22	0.13	0.07	0.28	0.12	0.13	0.26	0.22	0.16	1.52

Sample	ST-70	ST-70	ST-70	ST-70	ST-70	ST-70	ST-70	ST-70	ST-70	ST-70
Reference	21	22	23	24	25	26	27	28	29	31
Zone	M	Ph	Ph	Ph	Ph	M	M	M	M	M
SiO_2	50.55	48.93	46.85	47.73	47.28	50.89	51.05	50.79	50.82	49.46
TiO_2	0.02	0.00	0.03	0.00	0.00	0.02	0.01	0.00	0.03	0.01
Al_2O_3	29.81	31.22	32.76	32.52	32.45	29.74	29.30	29.59	29.55	30.62
$Fe_2O_3^T$	0.75	0.53	0.40	0.40	0.43	0.62	0.81	0.73	0.74	0.58
MgO	0.39	0.29	0.19	0.20	0.19	0.38	0.47	0.40	0.40	0.34
CaO	14.61	15.73	16.83	16.71	16.68	14.81	14.16	14.42	14.43	15.34
Na_2O	2.83	2.12	1.34	1.33	1.43	2.59	2.97	2.87	2.84	2.46
K_2O	0.01	0.02	0.02	0.01	0.02	0.01	0.02	0.04	0.00	0.00
BaO	0.00	0.02	0.00	0.00	0.03	0.00	0.01	0.00	0.01	0.03
SrO	0.00	0.00	0.00	0.00	0.00	0.00	0.00	0.00	0.00	0.00
Total	98.96	98.85	98.42	98.90	98.51	99.05	98.78	98.85	98.82	98.83
Number of cations calculated based on 32 oxygen atoms										
Si	9.316	9.050	8.729	8.835	8.797	9.358	9.411	9.363	9.369	9.146
Ti	0.002	0.000	0.004	0.000	0.000	0.003	0.002	0.000	0.004	0.002
Al	6.474	6.806	7.195	7.092	7.116	6.445	6.366	6.430	6.421	6.673
Fe^{3+}	0.103	0.073	0.057	0.056	0.060	0.086	0.113	0.101	0.103	0.080
Mg	0.108	0.080	0.052	0.054	0.054	0.104	0.128	0.111	0.110	0.093
Ca	2.884	3.117	3.360	3.314	3.325	2.917	2.796	2.849	2.849	3.039
Na	1.011	0.759	0.484	0.478	0.514	0.922	1.060	1.026	1.016	0.881
K	0.001	0.004	0.004	0.003	0.005	0.002	0.004	0.010	0.000	0.001
Ba	0.000	0.002	0.000	0.000	0.002	0.000	0.000	0.000	0.001	0.002
Sr	0.000	0.000	0.000	0.000	0.000	0.000	0.000	0.000	0.000	0.000
Final terms										
An	74.02	80.33	87.32	87.33	86.50	75.94	72.44	73.33	73.72	77.52
Ab	25.94	19.56	12.58	12.60	13.38	24.00	27.46	26.40	26.28	22.46
Or	0.04	0.11	0.11	0.07	0.12	0.06	0.10	0.27	0.00	0.02

III.3.1.3. Amphibole

Sample	ST-65	ST-65	ST-69	ST-69
Reference	1	2	1	2
Zone	Min. R.	Min. R.	Min. R.	Min. R.
SiO_2	54.10	52.87	55.27	54.32
TiO_2	2.69	2.76	0.19	0.19
Al_2O_3	0.68	1.32	0.26	0.25
Cr_2O_3	0.30	0.28	0.14	0.10
Fe_2O_3	7.45	0.56	9.38	11.75
FeO	12.22	16.70	5.51	3.24
MnO	0.04	0.00	0.04	0.01
MgO	10.78	11.26	14.98	15.33
CaO	0.18	3.09	0.26	0.28
Na_2O	8.64	7.98	9.51	9.09
K_2O	0.81	0.80	0.74	0.74
Total	97.89	97.62	96.27	95.29
Number of cations calculated based on 23 oxygen atoms				
Si	7.894	7.820	7.997	7.912
Al^{IV}	0.106	0.180	0.003	0.042
T	8.0	8.0	8.0	8.0
Al^{VI}	0.010	0.050	0.041	0.000
Ti	0.295	0.307	0.021	0.021
Cr	0.035	0.033	0.016	0.011
Fe^{3+}	0.819	0.062	1.021	1.288
Fe^{2+}	1.491	2.065	0.667	0.395
Mn	0.005	0.000	0.005	0.001
Mg	2.346	2.483	3.230	3.330
Sum C	5.0	5.0	5.0	5.0
Ca	0.028	0.490	0.040	0.044
Na	1.972	1.510	1.960	1.956
Sum B	2.0	2.0	2.0	2.0
Na	0.473	0.779	0.707	0.612
K	0.152	0.152	0.137	0.137
Sum A	0.6	0.9	0.8	0.7
Classification according to Mogessie et al. (2004)				
	Mg-arfved.	Mg-arfved.	Mg-arfved.	Mg-arfved.

Min. R. : Mineral Rim

III.3.1.4. Mica

Sample	ST-65	ST-65	ST-65
Reference	1	2	3
Zone	M	Min. R.	Min. R.
SiO_2	39.38	41.50	43.92
TiO_2	1.21	1.52	0.91
Al_2O_3	8.71	10.61	10.05
FeO	13.16	12.81	10.24
MnO	0.05	0.01	0.05
MgO	21.90	20.66	21.99
CaO	0.28	0.25	0.30
Na_2O	1.15	0.37	0.16
K_2O	7.03	8.58	8.11
BaO	0.13	0.015	0.03
Cl	0.00	0.00	0.01
Total	93.02	96.34	95.77
Number of cations calculated based on 22 oxygen atoms			
Si	5.949	6.019	6.274
Al^{IV}	1.551	1.814	1.692
Fe^{3+}	0.500	0.000	0.000
Sum T	8.000	7.833	7.966
Al^{VI}	0.000	0.000	0.000
Ti	0.137	0.166	0.097
Cr	0.000	0.000	0.000
Fe^{2+}	1.162	1.554	1.223
Mn	0.006	0.001	0.006
Mg	4.933	4.467	4.683
Sum C	6.238	6.189	6.009
Ba	0.008	0.001	0.001
Ca	0.047	0.039	0.046
Na	0.337	0.105	0.043
K	1.355	1.589	1.477
Sum B	1.739	1.733	1.567
F	0.000	0.000	0.000
Cl	0.000	0.000	0.003
OH	4.000	4.000	3.997
Total	4.000	4.000	4.000
Classification according to Rieder et al. (1998)			
	Phlogopite	Phlogopite	Phlogopite

III.3.2. Santiago Gabbroic Xenoliths

III.3.2.1. Pyroxene

Sample	ST-161A	ST-161A	ST-161A	ST-161A	ST-161B	ST-161B	ST-161B	ST-161B	ST-161B	ST-161B
Reference	2	4	6	7	1	2	3	4	5	6
SiO_2	52.88	55.29	56.40	55.80	53.56	53.12	53.37	52.39	52.96	53.32
TiO_2	0.04	0.10	0.26	0.26	0.40	0.38	0.28	0.49	0.48	0.43
Al_2O_3	1.14	1.30	1.18	1.17	2.07	2.31	2.62	3.16	2.64	2.12
Fe_2O_3	2.53	0.00	0.00	0.00	0.28	1.00	0.73	1.19	0.67	0.91
FeO	3.34	5.59	13.52	13.64	5.89	5.02	5.87	5.38	5.71	4.51
MnO	0.09	0.10	0.20	0.19	0.12	0.13	0.16	0.12	0.07	0.10
MgO	17.27	18.06	28.56	28.61	16.66	16.70	18.17	16.25	16.40	16.07
CaO	22.20	19.79	0.63	0.71	21.37	21.53	18.92	20.93	21.29	22.98
K_2O	0.05	0.01	0.00	0.02	0.00	0.00	0.02	0.00	0.00	0.00
Na_2O	0.10	0.50	0.04	0.02	0.28	0.29	0.29	0.39	0.32	0.31
ZnO	0.00	0.00	0.00	0.00	0.00	0.00	0.00	0.00	0.00	0.00
Cr_2O_3	0.01	0.00	0.04	0.00	0.38	0.39	0.46	0.42	0.38	0.27
Total	99.64	100.75	100.83	100.41	100.97	100.77	100.81	100.59	100.86	100.93
Number of ions on the base of 6 oxygens normalized for 4 cations										
Si	1.944	1.996	2.000	1.986	1.946	1.931	1.931	1.910	1.927	1.937
Al^{IV}	0.049	0.004	0.000	0.014	0.054	0.069	0.069	0.090	0.073	0.063
$Fe^{3+\ IV}$	0.007	0.000	0.000	0.000	0.000	0.000	0.000	0.000	0.000	0.000
Al^{VI}	0.000	0.052	0.049	0.035	0.034	0.030	0.042	0.046	0.040	0.028
$Fe^{3+\ VI}$	0.063	0.000	0.000	0.000	0.008	0.027	0.020	0.033	0.018	0.025
Ti	0.001	0.003	0.007	0.007	0.011	0.010	0.008	0.013	0.013	0.012
Cr	0.000	0.000	0.001	0.000	0.011	0.011	0.013	0.012	0.011	0.008
Zn	0.000	0.000	0.000	0.000	0.000	0.000	0.000	0.000	0.000	0.000
Mg	0.946	0.972	1.510	1.518	0.902	0.905	0.980	0.883	0.889	0.870
Fe^{2+}	0.103	0.169	0.401	0.406	0.179	0.153	0.178	0.164	0.174	0.137
Mn	0.003	0.003	0.006	0.006	0.004	0.004	0.005	0.004	0.002	0.003
Ca	0.874	0.766	0.024	0.027	0.832	0.839	0.733	0.818	0.830	0.895
K	0.002	0.001	0.000	0.001	0.000	0.000	0.001	0.000	0.000	0.000
Na	0.007	0.035	0.002	0.001	0.020	0.021	0.021	0.027	0.022	0.022
%Enstatite	47.41	50.91	77.80	77.59	46.89	46.94	51.16	46.46	46.48	45.10
%Ferrosillite	8.79	9.00	20.97	21.04	9.89	9.55	10.56	10.54	10.15	8.54
%Wollastonite	43.80	40.09	1.23	1.37	43.22	43.51	38.28	43.00	43.37	46.36
%Jadeite	----------	----------	----------	----------	----------	----------	----------	----------	----------	----------
%Aegirine	----------	----------	----------	----------	----------	----------	----------	----------	----------	----------
%Quad	----------	----------	----------	----------	----------	----------	----------	----------	----------	----------
Classification according to Morimoto et al. (1988)										
Group	Quad	Quad	Quad	Quad	Quad	Quad	Quad	Quad	Quad	Quad
Classification	augite	augite	enstatite	enstatite	augite	augite	augite	augite	augite	diopside

Sample	ST-161B	ST-161B	ST-162	ST-162	ST-162	ST-162	ST-162	ST-162	ST-162	ST-162
Reference	7	8	1	2	3	4	5	8	9	10
SiO_2	52.17	52.35	52.63	52.45	52.92	53.12	53.11	53.17	51.45	52.82
TiO_2	0.43	0.42	0.47	0.38	0.38	0.41	0.33	0.39	0.41	0.48
Al_2O_3	3.34	3.44	2.49	2.68	1.86	2.00	1.97	1.94	3.54	2.49
Fe_2O_3	1.24	0.90	0.09	0.27	0.36	1.01	0.57	0.04	1.02	0.78
FeO	5.58	5.09	5.41	6.17	4.82	4.35	4.74	5.66	4.91	6.28
MnO	0.13	0.12	0.14	0.09	0.06	0.07	0.14	0.12	0.12	0.10
MgO	16.75	16.56	15.27	16.43	15.37	15.78	16.47	15.51	15.17	16.90
CaO	20.16	21.03	22.65	20.24	23.27	23.23	21.96	22.68	21.90	20.05
K_2O	0.01	0.00	0.00	0.00	0.00	0.01	0.02	0.00	0.00	0.00
Na_2O	0.29	0.28	0.34	0.34	0.33	0.33	0.30	0.31	0.38	0.30
ZnO	0.00	0.00	0.00	0.00	0.00	0.00	0.00	0.00	0.00	0.00
Cr_2O_3	0.75	0.54	0.25	0.23	0.29	0.29	0.23	0.21	0.40	0.30
Total	100.72	100.65	99.73	99.26	99.62	100.51	99.77	100.02	99.20	100.42
Number of ions on the base of 6 oxygens normalized for 4 cations										
Si	1.899	1.905	1.940	1.936	1.952	1.940	1.948	1.955	1.905	1.929
Al^{IV}	0.101	0.095	0.060	0.064	0.048	0.060	0.052	0.045	0.095	0.071
$Fe^{3+\ IV}$	0.000	0.000	0.000	0.000	0.000	0.000	0.000	0.000	0.000	0.000
Al^{VI}	0.043	0.052	0.048	0.053	0.033	0.026	0.033	0.039	0.059	0.036
$Fe^{3+\ VI}$	0.034	0.025	0.002	0.008	0.010	0.028	0.016	0.001	0.028	0.021
Ti	0.012	0.012	0.013	0.011	0.011	0.011	0.009	0.011	0.012	0.013
Cr	0.022	0.015	0.007	0.007	0.008	0.008	0.007	0.006	0.012	0.009
Zn	0.000	0.000	0.000	0.000	0.000	0.000	0.000	0.000	0.000	0.000
Mg	0.909	0.898	0.839	0.904	0.845	0.859	0.901	0.850	0.837	0.920
Fe^{2+}	0.170	0.155	0.167	0.191	0.149	0.133	0.145	0.174	0.152	0.192
Mn	0.004	0.004	0.004	0.003	0.002	0.002	0.004	0.004	0.004	0.003
Ca	0.786	0.820	0.895	0.800	0.920	0.909	0.863	0.893	0.869	0.785
K	0.000	0.000	0.000	0.000	0.000	0.001	0.001	0.000	0.000	0.000
Na	0.021	0.020	0.024	0.024	0.024	0.023	0.021	0.022	0.027	0.021
%Enstatite	47.75	47.24	44.00	47.45	43.89	44.49	46.69	44.22	44.30	47.89
%Ferrosillite	10.93	9.64	9.09	10.55	8.33	8.43	8.57	9.29	9.75	11.26
%Wollastonite	41.31	43.12	46.91	42.00	47.77	47.08	44.74	46.48	45.96	40.85
%Jadeite	----------	----------	----------	----------	----------	----------	----------	----------	----------	----------
%Aegirine	----------	----------	----------	----------	----------	----------	----------	----------	----------	----------
%Quad	----------	----------	----------	----------	----------	----------	----------	----------	----------	----------
Classification according to Morimoto et al. (1988)										
Group	Quad	Quad	Quad	Quad	Quad	Quad	Quad	Quad	Quad	Quad
Classification	augite	augite	diopside	augite	diopside	diopside	augite	diopside	diopside	augite

Sample	ST-162	ST-162	ST-162	ST-162	ST-162	ST-162	ST-162	ST-162	ST-163	ST-163
Reference	11	12	13	14	15	16	17	18	1	1A
SiO_2	52.37	52.67	52.59	52.92	53.10	52.02	52.81	52.54	49.65	49.73
TiO_2	0.58	0.47	0.41	0.35	0.46	0.38	0.42	0.45	0.62	0.60
Al_2O_3	3.21	2.19	2.30	2.02	2.27	2.89	2.18	2.39	2.10	2.10
Fe_2O_3	0.06	0.00	0.90	0.46	0.56	1.35	0.44	0.56	4.38	3.29
FeO	6.77	6.20	5.45	5.16	5.79	5.72	5.35	5.23	6.02	8.15
MnO	0.12	0.09	0.11	0.06	0.04	0.13	0.10	0.12	0.17	0.15
MgO	16.63	16.10	16.17	15.55	16.54	16.35	15.37	15.47	13.91	13.72
CaO	19.07	20.92	21.30	22.68	21.16	20.28	22.76	22.57	21.66	20.41
K_2O	0.00	0.00	0.01	0.00	0.00	0.00	0.00	0.00	0.01	0.01
Na_2O	0.47	0.34	0.34	0.34	0.32	0.34	0.33	0.30	0.25	0.23
ZnO	0.00	0.00	0.00	0.00	0.00	0.00	0.00	0.00	0.00	0.00
Cr_2O_3	0.42	0.29	0.31	0.32	0.26	0.55	0.34	0.31	0.04	0.02
Total	99.70	99.27	99.80	99.81	100.44	99.88	100.06	99.88	98.80	98.41
Number of ions on the base of 6 oxygens normalized for 4 cations										
Si	1.924	1.948	1.934	1.948	1.938	1.912	1.942	1.934	1.882	1.897
Al^{IV}	0.076	0.052	0.066	0.052	0.062	0.088	0.058	0.066	0.094	0.094
$Fe^{3+\ IV}$	0.000	0.000	0.000	0.000	0.000	0.000	0.000	0.000	0.024	0.009
Al^{VI}	0.063	0.044	0.034	0.035	0.036	0.037	0.036	0.038	0.000	0.000
$Fe^{3+\ VI}$	0.002	0.000	0.025	0.013	0.016	0.037	0.012	0.016	0.101	0.086
Ti	0.016	0.013	0.011	0.010	0.013	0.011	0.012	0.012	0.018	0.017
Cr	0.012	0.008	0.009	0.009	0.007	0.016	0.010	0.009	0.001	0.001
Zn	0.000	0.000	0.000	0.000	0.000	0.000	0.000	0.000	0.000	0.000
Mg	0.911	0.888	0.887	0.853	0.900	0.896	0.842	0.849	0.786	0.780
Fe^{2+}	0.208	0.192	0.168	0.159	0.177	0.176	0.165	0.161	0.191	0.260
Mn	0.004	0.003	0.003	0.002	0.001	0.004	0.003	0.004	0.005	0.005
Ca	0.751	0.829	0.839	0.895	0.828	0.799	0.897	0.890	0.880	0.834
K	0.000	0.000	0.000	0.000	0.000	0.000	0.000	0.000	0.000	0.000
Na	0.033	0.024	0.024	0.024	0.023	0.024	0.024	0.022	0.018	0.017
%Enstatite	48.58	46.44	46.13	44.41	46.85	46.85	43.90	44.23	39.56	39.53
%Ferrosillite	11.39	10.18	10.19	9.03	10.07	11.37	9.38	9.40	16.17	18.20
%Wollastonite	40.03	43.38	43.68	46.56	43.08	41.78	46.73	46.38	44.27	42.27
%Jadeite	----------	----------	----------	----------	----------	----------	----------	----------	----------	----------
%Aegirine	----------	----------	----------	----------	----------	----------	----------	----------	----------	----------
%Quad	----------	----------	----------	----------	----------	----------	----------	----------	----------	----------
Classification according to Morimoto et al. (1988)										
Group	Quad	Quad	Quad	Quad	Quad	Quad	Quad	Quad	Quad	Quad
Classification	augite	augite	augite	diopside	augite	augite	diopside	diopside	augite	augite

Sample	ST-163	ST-163	ST-163	ST-163	ST-163	ST-163	ST-163	ST-163	ST-163	ST-163
Reference	1B	2	3	4	5	6	7	8	9	10
SiO_2	52.39	52.06	52.06	51.43	51.80	51.81	52.14	51.60	51.32	51.61
TiO_2	0.63	0.72	0.71	0.72	0.66	0.77	0.59	0.73	0.62	0.74
Al_2O_3	2.20	2.35	2.38	2.32	2.09	2.39	1.87	2.37	2.03	2.12
Fe_2O_3	0.22	0.48	0.18	1.36	1.38	1.10	1.06	1.48	1.15	1.20
FeO	9.78	9.42	10.18	10.69	11.14	9.73	8.99	9.33	13.72	8.66
MnO	0.19	0.21	0.16	0.19	0.23	0.20	0.20	0.18	0.24	0.20
MgO	13.77	13.83	13.52	14.26	14.90	13.88	14.11	14.00	15.35	13.36
CaO	21.40	21.30	21.08	19.27	18.34	20.94	21.24	20.83	15.31	22.08
K_2O	0.00	0.01	0.01	0.01	0.00	0.00	0.02	0.00	0.00	0.00
Na_2O	0.27	0.28	0.30	0.24	0.24	0.25	0.27	0.26	0.22	0.30
ZnO	0.00	0.00	0.00	0.00	0.00	0.00	0.00	0.00	0.00	0.00
Cr_2O_3	0.01	0.01	0.01	0.01	0.00	0.04	0.05	0.05	0.02	0.02
Total	100.88	100.66	100.59	100.49	100.77	101.10	100.55	100.82	99.97	100.32
Number of ions on the base of 6 oxygens normalized for 4 cations										
Si	1.941	1.932	1.936	1.919	1.925	1.919	1.937	1.916	1.929	1.926
Al^{IV}	0.059	0.068	0.064	0.081	0.075	0.081	0.063	0.084	0.071	0.074
$Fe^{3+\ IV}$	0.000	0.000	0.000	0.000	0.000	0.000	0.000	0.000	0.000	0.000
Al^{VI}	0.037	0.035	0.041	0.020	0.017	0.024	0.019	0.020	0.019	0.020
$Fe^{3+\ VI}$	0.006	0.013	0.005	0.038	0.038	0.031	0.030	0.041	0.033	0.034
Ti	0.017	0.020	0.020	0.020	0.018	0.021	0.016	0.020	0.018	0.021
Cr	0.000	0.000	0.000	0.000	0.000	0.001	0.001	0.001	0.000	0.001
Zn	0.000	0.000	0.000	0.000	0.000	0.000	0.000	0.000	0.000	0.000
Mg	0.761	0.765	0.750	0.793	0.826	0.767	0.782	0.775	0.860	0.743
Fe^{2+}	0.303	0.292	0.317	0.334	0.346	0.301	0.279	0.290	0.431	0.270
Mn	0.006	0.007	0.005	0.006	0.007	0.006	0.006	0.006	0.008	0.006
Ca	0.850	0.847	0.840	0.770	0.730	0.831	0.845	0.828	0.616	0.883
K	0.000	0.000	0.001	0.000	0.000	0.000	0.001	0.000	0.000	0.000
Na	0.019	0.020	0.022	0.018	0.017	0.018	0.019	0.019	0.016	0.022
%Enstatite	39.50	39.76	39.12	40.86	42.39	39.59	40.24	39.93	44.15	38.38
%Ferrosillite	16.38	16.23	17.05	19.45	20.12	17.48	16.24	17.36	24.21	16.03
%Wollastonite	44.12	44.01	43.82	39.69	37.50	42.93	43.52	42.70	31.64	45.59
%Jadeite	----------	----------	----------	----------	----------	----------	----------	----------	----------	----------
%Aegirine	----------	----------	----------	----------	----------	----------	----------	----------	----------	----------
%Quad	----------	----------	----------	----------	----------	----------	----------	----------	----------	----------
Classification according to Morimoto et al. (1988)										
Group	Quad	Quad	Quad	Quad	Quad	Quad	Quad	Quad	Quad	Quad
Classification	augite	augite	augite	augite	augite	augite	augite	augite	augite	diopside

Sample	ST-163	ST-163	ST-163	ST-163	ST-163	ST-163	ST-163	ST-163	ST-163	ST-163
Reference	11	13	14	15	16	17	18	19	20	21
SiO_2	51.59	52.02	51.73	51.91	51.35	52.99	51.88	51.80	51.55	51.52
TiO_2	0.69	0.72	0.68	0.69	0.85	0.32	0.76	0.64	0.69	0.80
Al_2O_3	2.19	2.20	2.15	2.14	2.06	1.01	2.32	2.03	2.26	2.33
Fe_2O_3	0.93	0.56	0.75	0.93	1.03	0.10	0.79	0.70	0.80	0.90
FeO	10.09	9.21	9.41	8.92	11.22	23.58	8.80	11.27	9.21	10.49
MnO	0.20	0.21	0.15	0.11	0.17	0.27	0.14	0.24	0.15	0.27
MgO	13.91	13.24	13.62	13.65	14.42	21.50	13.39	14.64	13.82	14.04
CaO	20.22	22.25	21.32	22.01	18.55	1.13	22.11	18.62	21.04	19.81
K_2O	0.00	0.00	0.00	0.00	0.01	0.00	0.01	0.01	0.00	0.00
Na_2O	0.28	0.29	0.29	0.24	0.28	0.01	0.34	0.22	0.28	0.25
ZnO	0.00	0.00	0.00	0.00	0.00	0.00	0.00	0.00	0.00	0.00
Cr_2O_3	0.01	0.03	0.00	0.00	0.01	0.00	0.07	0.04	0.01	0.00
Total	100.11	100.72	100.08	100.61	99.95	100.89	100.61	100.21	99.82	100.40
Number of ions on the base of 6 oxygens normalized for 4 cations										
Si	1.929	1.934	1.933	1.930	1.926	1.968	1.928	1.935	1.929	1.923
Al^{IV}	0.071	0.066	0.067	0.070	0.074	0.032	0.072	0.065	0.071	0.077
$Fe^{3+\ IV}$	0.000	0.000	0.000	0.000	0.000	0.000	0.000	0.000	0.000	0.000
Al^{VI}	0.026	0.030	0.028	0.024	0.017	0.012	0.030	0.024	0.029	0.025
$Fe^{3+\ VI}$	0.026	0.016	0.021	0.026	0.029	0.003	0.022	0.020	0.023	0.025
Ti	0.019	0.020	0.019	0.019	0.024	0.009	0.021	0.018	0.020	0.022
Cr	0.000	0.001	0.000	0.000	0.000	0.000	0.002	0.001	0.000	0.000
Zn	0.000	0.000	0.000	0.000	0.000	0.000	0.000	0.000	0.000	0.000
Mg	0.775	0.734	0.759	0.757	0.806	1.190	0.742	0.815	0.771	0.781
Fe^{2+}	0.316	0.286	0.294	0.277	0.352	0.732	0.273	0.352	0.288	0.327
Mn	0.006	0.007	0.005	0.003	0.005	0.008	0.005	0.008	0.005	0.009
Ca	0.810	0.886	0.854	0.876	0.746	0.045	0.880	0.745	0.844	0.792
K	0.000	0.000	0.000	0.000	0.000	0.000	0.000	0.000	0.000	0.000
Na	0.021	0.021	0.021	0.018	0.020	0.001	0.024	0.016	0.020	0.018
%Enstatite	40.10	38.04	39.26	39.01	41.60	60.15	38.59	42.03	39.94	40.37
%Ferrosillite	17.99	16.00	16.55	15.81	19.94	37.58	15.61	19.55	16.35	18.68
%Wollastonite	41.91	45.95	44.19	45.19	38.46	2.27	45.79	38.42	43.71	40.94
%Jadeite	----------	----------	----------	----------	----------	----------	----------	----------	----------	----------
%Aegirine	----------	----------	----------	----------	----------	----------	----------	----------	----------	----------
%Quad	----------	----------	----------	----------	----------	----------	----------	----------	----------	----------
Classification according to Morimoto et al. (1988)										
Group	Quad	Quad	Quad	Quad	Quad	Quad	Quad	Quad	Quad	Quad
Classification	augite	diopside	augite	diopside	augite	enstatite	diopside	augite	augite	augite

Sample	ST-163	ST-163	ST-164	ST-164	ST-164	ST-164	ST-164	ST-164	ST-164	ST-164
Reference	22	23	1	2	3	5	6	7	8	9
SiO_2	51.16	51.33	49.84	51.88	51.21	51.70	51.44	52.60	52.19	52.10
TiO_2	0.81	0.90	0.72	0.60	0.61	0.52	0.64	0.47	0.62	0.61
Al_2O_3	2.14	2.26	3.02	2.97	2.87	2.69	2.51	1.99	3.35	2.73
Fe_2O_3	1.81	1.56	4.38	2.49	2.59	3.13	4.01	2.39	1.46	2.21
FeO	11.53	10.29	3.44	3.02	2.61	2.94	4.02	2.58	4.31	3.25
MnO	0.17	0.18	0.16	0.10	0.12	0.13	0.16	0.10	0.13	0.15
MgO	14.78	14.01	15.76	16.49	15.81	16.93	17.70	16.42	16.57	15.88
CaO	17.77	20.02	20.97	22.11	22.69	21.42	19.45	23.40	21.13	22.98
K_2O	0.02	0.00	0.00	0.02	0.02	0.00	0.00	0.01	0.00	0.00
Na_2O	0.22	0.24	0.36	0.36	0.37	0.35	0.31	0.29	0.41	0.36
ZnO	0.00	0.00	0.00	0.00	0.00	0.00	0.00	0.00	0.00	0.00
Cr_2O_3	0.04	0.00	0.90	0.41	0.46	0.39	0.63	0.22	0.55	0.43
Total	100.45	100.77	99.55	100.45	99.36	100.20	100.87	100.47	100.73	100.71
Number of ions on the base of 6 oxygens normalized for 4 cations										
Si	1.913	1.912	1.852	1.893	1.892	1.891	1.875	1.919	1.898	1.901
Al^{IV}	0.087	0.088	0.132	0.107	0.108	0.109	0.108	0.081	0.102	0.099
$Fe^{3+\ IV}$	0.000	0.000	0.015	0.000	0.000	0.000	0.017	0.000	0.000	0.000
Al^{VI}	0.007	0.011	0.000	0.020	0.017	0.007	0.000	0.004	0.042	0.018
$Fe^{3+\ VI}$	0.051	0.044	0.107	0.068	0.072	0.086	0.093	0.066	0.040	0.061
Ti	0.023	0.025	0.020	0.017	0.017	0.014	0.017	0.013	0.017	0.017
Cr	0.001	0.000	0.026	0.012	0.013	0.011	0.018	0.006	0.016	0.012
Zn	0.000	0.000	0.000	0.000	0.000	0.000	0.000	0.000	0.000	0.000
Mg	0.824	0.778	0.873	0.897	0.871	0.923	0.962	0.893	0.898	0.864
Fe^{2+}	0.361	0.320	0.107	0.092	0.081	0.090	0.123	0.079	0.131	0.099
Mn	0.005	0.006	0.005	0.003	0.004	0.004	0.005	0.003	0.004	0.005
Ca	0.712	0.799	0.835	0.864	0.898	0.839	0.760	0.915	0.823	0.899
K	0.001	0.000	0.000	0.001	0.001	0.000	0.000	0.001	0.000	0.000
Na	0.016	0.017	0.026	0.026	0.027	0.025	0.022	0.021	0.029	0.026
%Enstatite	42.20	39.96	44.94	46.61	45.23	47.52	49.10	45.69	47.37	44.83
%Ferrosillite	21.35	18.99	12.07	8.49	8.13	9.27	12.11	7.53	9.23	8.54
%Wollastonite	36.45	41.04	42.99	44.91	46.64	43.21	38.79	46.78	43.41	46.63
%Jadeite	----------	----------	----------	----------	----------	----------	----------	----------	----------	----------
%Aegirine	----------	----------	----------	----------	----------	----------	----------	----------	----------	----------
%Quad	----------	----------	----------	----------	----------	----------	----------	----------	----------	----------
Classification according to Morimoto et al. (1988)										
Group	Quad	Quad	Quad	Quad	Quad	Quad	Quad	Quad	Quad	Quad
Classification	augite	augite	augite	augite	diopside	augite	augite	diopside	augite	diopside

Sample	ST-164	ST-164	ST-164	ST-164	ST-164	ST-164	ST-164	ST-164	ST-164	ST-164
Reference	10	11	12	13	14	15	16	18	19	20
SiO_2	51.97	51.59	51.79	52.10	52.31	51.28	52.38	51.89	51.55	51.64
TiO_2	0.60	0.63	0.64	0.59	0.53	0.71	0.53	0.53	0.68	0.61
Al_2O_3	2.74	2.77	2.78	2.56	2.68	2.82	2.25	2.75	2.70	2.69
Fe_2O_3	2.09	2.80	1.07	2.15	2.53	2.64	2.23	3.40	2.50	4.24
FeO	2.96	2.56	4.07	2.81	3.45	2.71	3.10	4.68	2.74	3.06
MnO	0.08	0.08	0.07	0.12	0.14	0.17	0.14	0.14	0.14	0.16
MgO	15.76	15.81	15.04	15.97	16.64	15.71	16.03	18.42	15.77	17.60
CaO	23.35	23.27	23.40	23.28	21.98	23.25	23.31	18.30	23.10	20.52
K_2O	0.01	0.00	0.00	0.00	0.02	0.01	0.01	0.00	0.00	0.00
Na_2O	0.35	0.35	0.34	0.35	0.33	0.27	0.31	0.31	0.36	0.30
ZnO	0.00	0.00	0.00	0.00	0.00	0.00	0.00	0.00	0.00	0.00
Cr_2O_3	0.39	0.44	0.43	0.41	0.43	0.42	0.26	0.67	0.45	0.60
Total	100.28	100.32	99.64	100.34	101.04	99.98	100.53	101.09	99.99	101.44
Number of ions on the base of 6 oxygens normalized for 4 cations										
Si	1.903	1.890	1.913	1.905	1.900	1.886	1.914	1.882	1.894	1.870
Al^{IV}	0.097	0.110	0.087	0.095	0.100	0.114	0.086	0.118	0.106	0.115
$Fe^{3+\ IV}$	0.000	0.000	0.000	0.000	0.000	0.000	0.000	0.001	0.000	0.015
Al^{VI}	0.021	0.010	0.034	0.016	0.014	0.009	0.011	0.000	0.011	0.000
$Fe^{3+\ VI}$	0.058	0.077	0.030	0.059	0.069	0.073	0.061	0.092	0.069	0.101
Ti	0.017	0.017	0.018	0.016	0.014	0.020	0.014	0.014	0.019	0.017
Cr	0.011	0.013	0.013	0.012	0.012	0.012	0.008	0.019	0.013	0.017
Zn	0.000	0.000	0.000	0.000	0.000	0.000	0.000	0.000	0.000	0.000
Mg	0.860	0.864	0.828	0.870	0.901	0.862	0.873	0.996	0.864	0.950
Fe^{2+}	0.091	0.079	0.126	0.086	0.105	0.084	0.095	0.142	0.084	0.093
Mn	0.002	0.003	0.002	0.004	0.004	0.005	0.004	0.004	0.004	0.005
Ca	0.916	0.914	0.926	0.912	0.855	0.916	0.912	0.711	0.909	0.796
K	0.000	0.000	0.000	0.000	0.001	0.001	0.000	0.000	0.000	0.000
Na	0.025	0.025	0.024	0.025	0.023	0.019	0.022	0.022	0.026	0.021
%Enstatite	44.65	44.62	43.32	45.06	46.57	44.41	44.87	51.17	44.73	48.49
%Ferrosillite	7.82	8.18	8.25	7.71	9.22	8.35	8.23	12.29	8.17	10.89
%Wollastonite	47.53	47.20	48.43	47.22	44.21	47.23	46.89	36.54	47.10	40.62
%Jadeite	----------	----------	----------	----------	----------	----------	----------	----------	----------	----------
%Aegirine	----------	----------	----------	----------	----------	----------	----------	----------	----------	----------
%Quad	----------	----------	----------	----------	----------	----------	----------	----------	----------	----------
Classification according to Morimoto et al. (1988)										
Group	Quad	Quad	Quad	Quad	Quad	Quad	Quad	Quad	Quad	Quad
Classification	diopside	diopside	diopside	diopside	augite	diopside	diopside	augite	diopside	augite

Sample	ST-164	ST-165	ST-165	ST-165	ST-165	ST-165	ST-165	ST-165	ST-165	ST-165
Reference	21	1	2	3	4	5	6	7	8	9
SiO_2	52.15	55.25	52.58	52.76	52.14	51.64	51.06	51.50	52.92	52.45
TiO_2	0.65	0.14	0.39	0.41	0.39	0.37	0.40	0.36	0.41	0.46
Al_2O_3	2.97	1.45	2.42	2.43	3.23	3.83	3.52	3.87	2.45	2.81
Fe_2O_3	2.29	1.33	1.32	2.07	2.07	1.85	2.11	1.72	1.60	2.11
FeO	3.10	10.96	3.52	3.21	3.70	3.06	2.83	3.56	3.51	2.63
MnO	0.14	0.18	0.07	0.08	0.09	0.12	0.10	0.08	0.07	0.02
MgO	15.77	30.26	16.47	16.76	16.70	15.59	15.96	16.74	16.56	16.22
CaO	23.29	0.86	22.51	22.64	21.65	23.00	22.12	20.95	22.78	23.29
K_2O	0.02	0.00	0.01	0.00	0.02	0.01	0.00	0.00	0.00	0.01
Na_2O	0.37	0.00	0.30	0.28	0.29	0.35	0.36	0.34	0.29	0.37
ZnO	0.00	0.00	0.00	0.00	0.00	0.00	0.00	0.00	0.00	0.00
Cr_2O_3	0.46	0.37	0.56	0.51	0.70	0.80	1.03	1.03	0.55	0.56
Total	101.20	100.80	100.16	101.15	100.98	100.61	99.49	100.14	101.15	100.92
Number of ions on the base of 6 oxygens normalized for 4 cations										
Si	1.894	1.944	1.922	1.911	1.893	1.883	1.881	1.881	1.917	1.904
Al^{IV}	0.106	0.056	0.078	0.089	0.107	0.117	0.119	0.119	0.083	0.096
$Fe^{3+\ IV}$	0.000	0.000	0.000	0.000	0.000	0.000	0.000	0.000	0.000	0.000
Al^{VI}	0.021	0.004	0.026	0.015	0.031	0.048	0.034	0.047	0.022	0.024
$Fe^{3+\ VI}$	0.063	0.035	0.036	0.056	0.057	0.051	0.058	0.047	0.044	0.058
Ti	0.018	0.004	0.011	0.011	0.011	0.010	0.011	0.010	0.011	0.012
Cr	0.013	0.010	0.016	0.015	0.020	0.023	0.030	0.030	0.016	0.016
Zn	0.000	0.000	0.000	0.000	0.000	0.000	0.000	0.000	0.000	0.000
Mg	0.854	1.587	0.897	0.905	0.904	0.847	0.877	0.911	0.894	0.878
Fe^{2+}	0.094	0.322	0.108	0.097	0.112	0.093	0.087	0.109	0.106	0.080
Mn	0.004	0.005	0.002	0.002	0.003	0.004	0.003	0.002	0.002	0.001
Ca	0.906	0.033	0.882	0.878	0.842	0.899	0.873	0.820	0.884	0.906
K	0.001	0.000	0.001	0.000	0.001	0.000	0.000	0.000	0.000	0.000
Na	0.026	0.000	0.021	0.019	0.020	0.025	0.026	0.024	0.021	0.026
%Enstatite	44.44	80.05	46.61	46.66	47.14	44.74	46.17	48.24	46.33	45.68
%Ferrosillite	8.38	18.31	7.59	8.05	8.95	7.82	7.83	8.39	7.89	7.19
%Wollastonite	47.17	1.64	45.79	45.29	43.91	47.45	46.00	43.38	45.79	47.14
%Jadeite	----------	----------	----------	----------	----------	----------	----------	----------	----------	----------
%Aegirine	----------	----------	----------	----------	----------	----------	----------	----------	----------	----------
%Quad	----------	----------	----------	----------	----------	----------	----------	----------	----------	----------
Classification according to Morimoto et al. (1988)										
Group	Quad	Quad	Quad	Quad	Quad	Quad	Quad	Quad	Quad	Quad
Classification	diopside	enstatite	diopside	diopside	augite	diopside	diopside	augite	diopside	diopside

Sample	ST-167	ST-167	ST-167	ST-167	ST-167	ST-167	ST-167	ST-167	ST-167	ST-167
Reference	1	2	3	4	5	6	7	8	9	10
SiO_2	51.25	49.21	50.48	51.08	52.04	51.27	51.65	51.32	51.52	51.53
TiO_2	0.57	0.51	0.53	0.62	0.43	0.42	0.52	0.51	0.56	0.60
Al_2O_3	3.19	3.07	3.24	3.34	3.22	3.16	2.50	2.84	2.83	2.87
Fe_2O_3	3.10	8.01	4.66	3.22	3.12	4.39	2.79	3.52	3.15	2.80
FeO	1.80	1.22	0.82	1.80	3.09	1.54	2.44	2.11	3.00	2.31
MnO	0.09	0.18	0.12	0.09	0.13	0.13	0.16	0.13	0.17	0.07
MgO	16.23	18.98	17.08	15.88	18.44	17.75	16.60	17.73	17.58	16.79
CaO	22.90	17.70	21.68	23.10	19.34	20.71	22.32	20.63	20.34	22.06
K_2O	0.00	0.00	0.00	0.02	0.00	0.00	0.00	0.00	0.01	0.01
Na_2O	0.34	0.30	0.35	0.38	0.36	0.37	0.31	0.33	0.32	0.33
ZnO	0.06	0.03	0.03	0.00	0.07	0.11	0.02	0.03	0.01	0.04
Cr_2O_3	0.89	1.46	0.77	0.87	0.66	0.71	0.60	0.61	0.92	0.62
Total	100.42	100.67	99.77	100.40	100.91	100.57	99.89	99.75	100.41	100.01
Number of ions on the base of 6 oxygens normalized for 4 cations										
Si	1.872	1.799	1.852	1.868	1.881	1.864	1.895	1.879	1.879	1.886
Al^{IV}	0.128	0.132	0.140	0.132	0.119	0.135	0.105	0.121	0.121	0.114
$Fe^{3+\ IV}$	0.000	0.069	0.007	0.000	0.000	0.001	0.000	0.000	0.000	0.000
Al^{VI}	0.009	0.000	0.000	0.012	0.018	0.000	0.003	0.002	0.001	0.010
$Fe^{3+\ VI}$	0.085	0.152	0.121	0.089	0.085	0.119	0.077	0.097	0.086	0.077
Ti	0.016	0.014	0.015	0.017	0.012	0.012	0.014	0.014	0.015	0.016
Cr	0.026	0.042	0.022	0.025	0.019	0.021	0.017	0.018	0.027	0.018
Zn	0.002	0.001	0.001	0.000	0.002	0.003	0.000	0.001	0.000	0.001
Mg	0.884	1.034	0.934	0.866	0.993	0.962	0.908	0.968	0.956	0.916
Fe^{2+}	0.055	0.037	0.025	0.055	0.093	0.047	0.075	0.065	0.092	0.071
Mn	0.003	0.006	0.004	0.003	0.004	0.004	0.005	0.004	0.005	0.002
Ca	0.896	0.693	0.852	0.905	0.749	0.807	0.878	0.809	0.795	0.865
K	0.000	0.000	0.000	0.001	0.000	0.000	0.000	0.000	0.000	0.000
Na	0.024	0.021	0.025	0.027	0.026	0.026	0.022	0.023	0.023	0.023
%Enstatite	45.95	51.95	48.05	45.15	51.61	49.60	46.74	49.82	49.43	47.42
%Ferrosillite	7.45	13.22	8.10	7.64	9.47	8.81	8.08	8.51	9.47	7.78
%Wollastonite	46.59	34.83	43.84	47.21	38.91	41.59	45.18	41.67	41.10	44.80
%Jadeite	----------	----------	----------	----------	----------	----------	----------	----------	----------	----------
%Aegirine	----------	----------	----------	----------	----------	----------	----------	----------	----------	----------
%Quad	----------	----------	----------	----------	----------	----------	----------	----------	----------	----------
Classification according to Morimoto et al. (1988)										
Group	Quad	Quad	Quad	Quad	Quad	Quad	Quad	Quad	Quad	Quad
Classification	diopside	augite	augite	diopside	augite	augite	diopside	augite	augite	augite

Sample	ST-167	ST-167	ST-167	ST-167	ST-167	ST-167	ST-167	ST-167	ST-167	ST-167
Reference	11	12	13	14	15	16	17	18	19	20
SiO_2	50.29	51.07	51.06	51.56	50.55	51.58	51.35	50.72	50.77	50.86
TiO_2	0.66	0.63	0.54	0.48	0.52	0.60	0.49	0.59	0.49	0.49
Al_2O_3	2.91	3.07	2.98	3.09	3.11	2.73	3.12	2.82	3.21	3.30
Fe_2O_3	4.66	3.23	3.85	4.14	5.17	2.96	3.50	4.53	3.42	4.30
FeO	1.35	1.65	1.45	2.46	1.97	1.67	1.93	0.24	1.39	2.92
MnO	0.12	0.16	0.08	0.14	0.14	0.09	0.12	0.09	0.15	0.14
MgO	16.02	16.34	16.88	19.19	18.62	16.34	17.69	16.78	16.37	19.13
CaO	22.52	22.56	21.98	18.66	18.93	23.16	20.91	22.71	22.59	17.76
K_2O	0.01	0.00	0.01	0.01	0.00	0.00	0.00	0.00	0.00	0.00
Na_2O	0.38	0.38	0.37	0.29	0.29	0.34	0.31	0.39	0.31	0.27
ZnO	0.04	0.03	0.00	0.04	0.03	0.08	0.04	0.02	0.04	0.08
Cr_2O_3	1.01	0.71	0.62	0.71	0.84	0.66	0.70	0.68	0.85	0.90
Total	99.97	99.82	99.82	100.75	100.16	100.21	100.17	99.56	99.59	100.14
Number of ions on the base of 6 oxygens normalized for 4 cations										
Si	1.853	1.875	1.872	1.865	1.846	1.887	1.872	1.864	1.868	1.854
Al^{IV}	0.126	0.125	0.128	0.132	0.134	0.113	0.128	0.122	0.132	0.142
$Fe^{3+\ IV}$	0.020	0.000	0.000	0.004	0.020	0.000	0.000	0.014	0.000	0.005
Al^{VI}	0.000	0.008	0.001	0.000	0.000	0.004	0.006	0.000	0.007	0.000
$Fe^{3+\ VI}$	0.109	0.089	0.106	0.109	0.122	0.081	0.096	0.111	0.095	0.113
Ti	0.018	0.017	0.015	0.013	0.014	0.016	0.013	0.016	0.014	0.013
Cr	0.029	0.020	0.018	0.020	0.024	0.019	0.020	0.020	0.025	0.026
Zn	0.001	0.001	0.000	0.001	0.001	0.002	0.001	0.000	0.001	0.002
Mg	0.880	0.894	0.922	1.034	1.014	0.891	0.962	0.919	0.898	1.040
Fe^{2+}	0.042	0.051	0.045	0.074	0.060	0.051	0.059	0.008	0.043	0.089
Mn	0.004	0.005	0.003	0.004	0.004	0.003	0.004	0.003	0.005	0.004
Ca	0.889	0.887	0.863	0.723	0.740	0.908	0.817	0.894	0.891	0.693
K	0.001	0.000	0.001	0.000	0.000	0.000	0.000	0.000	0.000	0.000
Na	0.027	0.027	0.027	0.020	0.020	0.024	0.022	0.028	0.022	0.019
%Enstatite	45.28	46.42	47.57	53.08	51.69	46.07	49.64	47.16	46.50	53.47
%Ferrosillite	8.98	7.52	7.91	9.82	10.54	7.00	8.18	6.96	7.36	10.87
%Wollastonite	45.74	46.06	44.52	37.10	37.76	46.94	42.18	45.88	46.13	35.66
%Jadeite	----------	----------	----------	----------	----------	----------	----------	----------	----------	----------
%Aegirine	----------	----------	----------	----------	----------	----------	----------	----------	----------	----------
%Quad	----------	----------	----------	----------	----------	----------	----------	----------	----------	----------
Classification according to Morimoto et al. (1988)										
Group	Quad	Quad	Quad	Quad	Quad	Quad	Quad	Quad	Quad	Quad
Classification	diopside	diopside	augite	augite	augite	diopside	augite	diopside	diopside	augite

Sample	ST-167	ST-167	ST-167	ST-167	ST-167	ST-167	ST-167	ST-167	ST-167	ST-167
Reference	21	22	23	24	25	26	27	28	29	30
SiO_2	50.58	51.23	51.84	50.74	50.86	51.61	50.58	42.32	44.40	42.40
TiO_2	0.55	0.56	0.54	0.49	0.47	0.47	0.61	3.85	3.52	4.11
Al_2O_3	3.06	3.10	2.95	2.88	3.09	3.26	2.95	10.19	9.17	10.74
Fe_2O_3	4.42	3.35	3.55	4.23	3.66	3.99	4.12	7.31	5.44	5.16
FeO	0.49	2.07	2.69	0.91	1.33	2.56	0.77	0.52	2.23	2.51
MnO	0.10	0.15	0.09	0.11	0.10	0.16	0.08	0.06	0.04	0.06
MgO	16.43	17.69	19.47	16.56	16.38	18.88	16.50	12.25	12.71	11.64
CaO	23.11	20.55	18.36	22.67	22.48	18.83	22.66	23.01	22.85	22.78
K_2O	0.01	0.00	0.02	0.00	0.01	0.01	0.00	0.00	0.00	0.00
Na_2O	0.32	0.35	0.30	0.32	0.37	0.33	0.37	0.47	0.43	0.41
ZnO	0.00	0.04	0.02	0.05	0.06	0.06	0.02	0.01	0.05	0.00
Cr_2O_3	0.63	0.76	0.74	0.71	0.63	0.71	0.75	0.00	0.02	0.04
Total	99.70	99.84	100.58	99.66	99.44	100.88	99.40	99.98	100.86	99.84
Number of ions on the base of 6 oxygens normalized for 4 cations										
Si	1.860	1.873	1.874	1.867	1.874	1.865	1.864	1.582	1.642	1.589
Al^{IV}	0.133	0.127	0.126	0.125	0.126	0.135	0.128	0.418	0.358	0.411
$Fe^{3+\ IV}$	0.008	0.000	0.000	0.009	0.000	0.000	0.007	0.000	0.000	0.000
Al^{VI}	0.000	0.007	0.000	0.000	0.008	0.004	0.000	0.030	0.041	0.063
$Fe^{3+\ VI}$	0.115	0.092	0.097	0.109	0.101	0.108	0.107	0.206	0.151	0.146
Ti	0.015	0.015	0.015	0.014	0.013	0.013	0.017	0.108	0.098	0.116
Cr	0.018	0.022	0.021	0.021	0.018	0.020	0.022	0.000	0.001	0.001
Zn	0.000	0.001	0.000	0.001	0.002	0.002	0.001	0.000	0.001	0.000
Mg	0.900	0.965	1.050	0.908	0.899	1.017	0.907	0.682	0.701	0.650
Fe^{2+}	0.015	0.063	0.081	0.028	0.041	0.077	0.024	0.016	0.069	0.079
Mn	0.003	0.005	0.003	0.003	0.003	0.005	0.002	0.002	0.001	0.002
Ca	0.910	0.805	0.711	0.894	0.887	0.729	0.895	0.921	0.905	0.915
K	0.000	0.000	0.001	0.000	0.001	0.001	0.000	0.000	0.000	0.000
Na	0.023	0.025	0.021	0.023	0.027	0.023	0.026	0.034	0.031	0.029
%Enstatite	46.13	49.99	54.07	46.56	46.55	52.51	46.68	37.35	38.35	36.31
%Ferrosillite	7.21	8.29	9.30	7.62	7.52	9.85	7.23	12.23	12.12	12.63
%Wollastonite	46.65	41.73	36.63	45.82	45.93	37.64	46.09	50.42	49.53	51.07
%Jadeite	----------	----------	----------	----------	----------	----------	----------	----------	----------	----------
%Aegirine	----------	----------	----------	----------	----------	----------	----------	----------	----------	----------
%Quad	----------	----------	----------	----------	----------	----------	----------	----------	----------	----------
Classification according to Morimoto et al. (1988)										
Group	Quad	Quad	Quad	Quad	Quad	Quad	Quad	Quad	Quad	Quad
Classification	diopside	augite	augite	diopside	diopside	augite	diopside	wollast.	diopside	wollast.

Sample	ST-167	ST-167	ST-167	ST-167	ST-167	ST-167	ST-167	ST-167	ST-168	ST-168
Reference	31	32	33	34	35	36	37	38	1	2
SiO_2	43.12	41.77	51.54	50.74	51.03	51.09	50.30	51.04	51.55	51.16
TiO_2	4.14	4.34	0.57	0.41	0.52	0.46	0.57	0.62	0.31	0.68
Al_2O_3	10.57	10.71	2.96	3.25	3.28	2.90	3.08	3.02	1.51	2.76
Fe_2O_3	5.94	6.20	2.76	4.50	3.40	3.89	5.23	4.04	3.31	2.98
FeO	1.54	1.59	2.31	1.87	1.46	1.46	0.00	1.35	2.47	3.70
MnO	0.09	0.07	0.15	0.13	0.13	0.13	0.13	0.13	0.06	0.10
MgO	12.35	11.84	16.59	18.11	16.11	17.48	16.90	16.68	15.69	15.86
CaO	23.16	22.83	22.26	19.61	22.91	21.16	22.60	22.47	23.42	21.94
K_2O	0.00	0.00	0.01	0.00	0.00	0.00	0.01	0.01	0.01	0.00
Na_2O	0.41	0.39	0.32	0.35	0.40	0.35	0.33	0.34	0.30	0.34
ZnO	0.06	0.01	0.09	0.00	0.00	0.00	0.03	0.02	0.00	0.00
Cr_2O_3	0.00	0.02	0.75	0.87	0.80	0.68	0.64	0.76	0.12	0.13
Total	101.38	99.77	100.30	99.84	100.03	99.60	99.81	100.47	98.75	99.65
Number of ions on the base of 6 oxygens normalized for 4 cations										
Si	1.588	1.567	1.883	1.857	1.870	1.874	1.846	1.864	1.921	1.890
Al^{IV}	0.412	0.433	0.117	0.140	0.130	0.126	0.133	0.130	0.066	0.110
$Fe^{3+\ IV}$	0.000	0.000	0.000	0.003	0.000	0.001	0.021	0.006	0.013	0.000
Al^{VI}	0.047	0.041	0.011	0.000	0.012	0.000	0.000	0.000	0.000	0.010
$Fe^{3+\ VI}$	0.165	0.175	0.076	0.121	0.094	0.107	0.126	0.105	0.080	0.083
Ti	0.115	0.123	0.016	0.011	0.014	0.013	0.016	0.017	0.009	0.019
Cr	0.000	0.001	0.022	0.025	0.023	0.020	0.019	0.022	0.003	0.004
Zn	0.002	0.000	0.002	0.000	0.000	0.000	0.001	0.001	0.000	0.000
Mg	0.678	0.662	0.904	0.988	0.880	0.956	0.924	0.908	0.872	0.873
Fe^{2+}	0.047	0.050	0.071	0.057	0.045	0.045	0.000	0.041	0.077	0.114
Mn	0.003	0.002	0.005	0.004	0.004	0.004	0.004	0.004	0.002	0.003
Ca	0.914	0.918	0.871	0.769	0.900	0.831	0.889	0.879	0.935	0.869
K	0.000	0.000	0.000	0.000	0.000	0.000	0.000	0.000	0.000	0.000
Na	0.029	0.029	0.023	0.025	0.028	0.025	0.023	0.024	0.022	0.025
%Enstatite	37.53	36.64	46.91	50.87	45.79	49.17	47.08	46.74	44.06	44.97
%Ferrosillite	11.89	12.57	7.85	9.54	7.41	8.05	7.65	8.03	8.68	10.32
%Wollastonite	50.58	50.79	45.23	39.60	46.80	42.78	45.27	45.24	47.26	44.72
%Jadeite	----------	----------	----------	----------	----------	----------	----------	----------	----------	----------
%Aegirine	----------	----------	----------	----------	----------	----------	----------	----------	----------	----------
%Quad	----------	----------	----------	----------	----------	----------	----------	----------	----------	----------
Classification according to Morimoto et al. (1988)										
Group	Quad	Quad	Quad	Quad	Quad	Quad	Quad	Quad	Quad	Quad
Classification	wollast.	wollast.	diopside	augite	diopside	augite	diopside	diopside	diopside	augite

Sample	ST-168	ST-168	ST-168	ST-168	ST-168	ST-168	ST-168	ST-168	ST-168	ST-168
Reference	3	4	5	6	7	8	9	10	11	12
SiO_2	51.90	51.86	51.77	51.57	52.93	52.25	52.39	52.37	53.00	53.05
TiO_2	0.50	0.34	0.37	0.62	0.43	0.51	0.43	0.41	0.41	0.39
Al_2O_3	2.30	1.88	1.96	2.67	2.39	2.44	2.49	2.68	2.28	1.92
Fe_2O_3	2.80	3.30	2.82	2.32	2.18	1.65	2.44	2.06	2.20	2.08
FeO	6.08	3.03	3.54	3.78	8.08	5.16	5.37	4.79	7.12	3.90
MnO	0.15	0.12	0.15	0.14	0.18	0.13	0.14	0.10	0.14	0.14
MgO	18.84	15.81	15.84	15.25	20.46	16.54	17.28	16.55	20.24	16.07
CaO	16.71	22.95	22.53	23.04	14.01	20.86	19.72	21.25	15.18	23.11
K_2O	0.02	0.02	0.00	0.00	0.01	0.01	0.00	0.00	0.00	0.01
Na_2O	0.27	0.33	0.31	0.34	0.21	0.30	0.31	0.30	0.21	0.32
ZnO	0.00	0.00	0.00	0.00	0.00	0.00	0.00	0.00	0.00	0.00
Cr_2O_3	0.12	0.14	0.11	0.21	0.15	0.14	0.13	0.16	0.14	0.13
Total	99.70	99.77	99.40	99.94	101.02	99.99	100.71	100.67	100.91	101.10
Number of ions on the base of 6 oxygens normalized for 4 cations										
Si	1.906	1.914	1.917	1.902	1.913	1.919	1.910	1.911	1.916	1.929
Al^{IV}	0.094	0.082	0.083	0.098	0.087	0.081	0.090	0.089	0.084	0.071
$Fe^{3+\ IV}$	0.000	0.004	0.000	0.000	0.000	0.000	0.000	0.000	0.000	0.000
Al^{VI}	0.005	0.000	0.003	0.018	0.015	0.025	0.017	0.026	0.013	0.011
$Fe^{3+\ VI}$	0.077	0.087	0.079	0.064	0.059	0.046	0.067	0.056	0.060	0.057
Ti	0.014	0.009	0.010	0.017	0.012	0.014	0.012	0.011	0.011	0.011
Cr	0.004	0.004	0.003	0.006	0.004	0.004	0.004	0.005	0.004	0.004
Zn	0.000	0.000	0.000	0.000	0.000	0.000	0.000	0.000	0.000	0.000
Mg	1.031	0.870	0.874	0.839	1.102	0.906	0.939	0.900	1.091	0.871
Fe^{2+}	0.187	0.094	0.110	0.116	0.244	0.159	0.164	0.146	0.215	0.119
Mn	0.005	0.004	0.005	0.004	0.005	0.004	0.004	0.003	0.004	0.004
Ca	0.657	0.908	0.894	0.910	0.543	0.821	0.770	0.831	0.588	0.900
K	0.001	0.001	0.000	0.000	0.000	0.000	0.000	0.000	0.000	0.000
Na	0.019	0.024	0.022	0.025	0.015	0.022	0.022	0.021	0.014	0.022
%Enstatite	52.69	44.23	44.57	43.35	56.42	46.80	48.30	46.49	55.71	44.65
%Ferrosillite	13.72	9.61	9.85	9.58	15.81	10.77	12.09	10.61	14.26	9.22
%Wollastonite	33.59	46.16	45.58	47.07	27.77	42.43	39.61	42.90	30.03	46.13
%Jadeite	----------	----------	----------	----------	----------	----------	----------	----------	----------	----------
%Aegirine	----------	----------	----------	----------	----------	----------	----------	----------	----------	----------
%Quad	----------	----------	----------	----------	----------	----------	----------	----------	----------	----------
Classification according to Morimoto et al. (1988)										
Group	Quad	Quad	Quad	Quad	Quad	Quad	Quad	Quad	Quad	Quad
Classification	augite	diopside	diopside	diopside	augite	augite	augite	augite	augite	diopside

Sample	ST-168	ST-168	ST-168	ST-168	ST-168	ST-168	ST-168	ST-168	ST-168	ST-168
Reference	13	14	15	16	17	18	19	20	21	22
SiO_2	52.69	52.31	52.65	52.73	52.63	52.26	52.81	52.55	52.43	52.73
TiO_2	0.47	0.51	0.34	0.45	0.38	0.39	0.36	0.49	0.40	0.34
Al_2O_3	2.38	2.62	2.69	2.16	2.06	2.90	2.01	2.35	2.52	2.11
Fe_2O_3	2.20	2.10	2.38	2.31	2.45	2.77	2.49	1.41	2.18	2.24
FeO	5.06	5.45	5.67	3.76	3.86	3.80	6.52	4.63	5.23	3.30
MnO	0.11	0.10	0.16	0.14	0.12	0.14	0.10	0.06	0.13	0.14
MgO	17.58	17.73	18.23	16.03	16.10	16.36	19.62	15.83	17.25	16.06
CaO	19.98	19.14	18.45	22.93	22.76	21.87	16.26	22.46	19.84	23.38
K_2O	0.01	0.00	0.02	0.00	0.00	0.00	0.00	0.02	0.01	0.00
Na_2O	0.28	0.29	0.27	0.34	0.31	0.37	0.22	0.33	0.33	0.31
ZnO	0.00	0.00	0.00	0.00	0.00	0.00	0.00	0.00	0.00	0.00
Cr_2O_3	0.12	0.14	0.18	0.16	0.21	0.23	0.09	0.17	0.21	0.19
Total	100.87	100.38	101.04	101.01	100.87	101.09	100.49	100.31	100.50	100.79
Number of ions on the base of 6 oxygens normalized for 4 cations										
Si	1.915	1.909	1.908	1.920	1.920	1.899	1.920	1.926	1.914	1.923
Al^{IV}	0.085	0.091	0.092	0.080	0.080	0.101	0.080	0.074	0.086	0.077
$Fe^{3+\ IV}$	0.000	0.000	0.000	0.000	0.000	0.000	0.000	0.000	0.000	0.000
Al^{VI}	0.016	0.022	0.023	0.012	0.008	0.023	0.006	0.028	0.022	0.013
$Fe^{3+\ VI}$	0.060	0.058	0.065	0.063	0.067	0.076	0.068	0.039	0.060	0.062
Ti	0.013	0.014	0.009	0.012	0.010	0.011	0.010	0.013	0.011	0.009
Cr	0.003	0.004	0.005	0.005	0.006	0.007	0.003	0.005	0.006	0.006
Zn	0.000	0.000	0.000	0.000	0.000	0.000	0.000	0.000	0.000	0.000
Mg	0.953	0.964	0.985	0.870	0.875	0.886	1.063	0.865	0.939	0.873
Fe^{2+}	0.154	0.166	0.172	0.115	0.118	0.116	0.198	0.142	0.160	0.098
Mn	0.003	0.003	0.005	0.004	0.004	0.004	0.003	0.002	0.004	0.004
Ca	0.778	0.748	0.716	0.894	0.890	0.851	0.633	0.882	0.776	0.913
K	0.001	0.000	0.001	0.000	0.000	0.000	0.000	0.001	0.000	0.000
Na	0.019	0.021	0.019	0.024	0.022	0.026	0.016	0.024	0.023	0.022
%Enstatite	48.91	49.71	50.70	44.69	44.81	45.83	54.09	44.81	48.44	44.77
%Ferrosillite	11.15	11.71	12.43	9.36	9.65	10.13	13.70	9.48	11.52	8.39
%Wollastonite	39.94	38.58	36.87	45.95	45.54	44.04	32.21	45.71	40.04	46.84
%Jadeite	----------	----------	----------	----------	----------	----------	----------	----------	----------	----------
%Aegirine	----------	----------	----------	----------	----------	----------	----------	----------	----------	----------
%Quad	----------	----------	----------	----------	----------	----------	----------	----------	----------	----------
Classification according to Morimoto et al. (1988)										
Group	Quad	Quad	Quad	Quad	Quad	Quad	Quad	Quad	Quad	Quad
Classification	augite	augite	augite	diopside	diopside	augite	augite	diopside	augite	diopside

Sample	ST-168	ST-168	ST-168	ST-168	ST-168	ST-168	ST-168	ST-168	ST-168	ST-168
Reference	23	24	25	26	27	28	L1_1	L1_2	L1_3	L1_4
SiO_2	53.63	52.97	54.13	52.96	52.50	52.76	52.22	51.27	51.23	51.41
TiO_2	0.14	0.38	0.09	0.52	0.35	0.34	0.45	0.57	0.54	0.65
Al_2O_3	1.23	1.94	0.62	2.37	2.50	1.91	2.57	2.70	2.73	2.77
Fe_2O_3	1.92	2.54	2.23	2.16	3.23	2.60	3.60	3.58	4.08	3.28
FeO	3.19	3.33	2.49	5.57	4.33	3.72	4.72	2.63	3.10	2.98
MnO	0.09	0.14	0.10	0.16	0.06	0.09	0.13	0.15	0.19	0.17
MgO	16.33	16.02	16.62	17.88	16.97	16.22	19.09	15.97	17.15	16.09
CaO	24.13	23.53	24.77	19.36	20.97	22.81	17.61	22.49	20.51	22.31
K_2O	0.00	0.02	0.01	0.00	0.00	0.00	0.00	0.00	0.00	0.00
Na_2O	0.21	0.31	0.18	0.30	0.34	0.32	0.29	0.37	0.35	0.36
ZnO	0.00	0.00	0.00	0.00	0.00	0.00	0.05	0.02	0.01	0.00
Cr_2O_3	0.18	0.18	0.06	0.15	0.20	0.17	0.10	0.22	0.16	0.10
Total	101.04	101.36	101.31	101.42	101.45	100.92	100.83	99.98	100.04	100.10
Number of ions on the base of 6 oxygens normalized for 4 cations										
Si	1.948	1.922	1.960	1.914	1.902	1.923	1.893	1.886	1.880	1.888
Al^{IV}	0.052	0.078	0.027	0.086	0.098	0.077	0.107	0.114	0.118	0.112
$Fe^{3+\ IV}$	0.000	0.000	0.014	0.000	0.000	0.000	0.000	0.000	0.002	0.000
Al^{VI}	0.001	0.005	0.000	0.015	0.009	0.005	0.002	0.003	0.000	0.008
$Fe^{3+\ VI}$	0.052	0.069	0.047	0.059	0.088	0.071	0.098	0.099	0.110	0.091
Ti	0.004	0.010	0.003	0.014	0.010	0.009	0.012	0.016	0.015	0.018
Cr	0.005	0.005	0.002	0.004	0.006	0.005	0.003	0.006	0.005	0.003
Zn	0.000	0.000	0.000	0.000	0.000	0.000	0.001	0.001	0.000	0.000
Mg	0.884	0.867	0.897	0.964	0.917	0.881	1.032	0.876	0.938	0.881
Fe^{2+}	0.097	0.101	0.075	0.168	0.131	0.113	0.143	0.081	0.095	0.091
Mn	0.003	0.004	0.003	0.005	0.002	0.003	0.004	0.005	0.006	0.005
Ca	0.939	0.915	0.961	0.750	0.814	0.891	0.684	0.887	0.806	0.878
K	0.000	0.001	0.000	0.000	0.000	0.000	0.000	0.000	0.000	0.000
Na	0.015	0.022	0.013	0.021	0.024	0.022	0.021	0.027	0.025	0.026
%Enstatite	44.76	44.31	44.91	49.53	46.97	44.98	52.61	44.98	47.91	45.26
%Ferrosillite	7.70	8.93	6.96	11.92	11.32	9.56	12.52	9.49	10.92	9.62
%Wollastonite	47.54	46.77	48.12	38.54	41.71	45.46	34.87	45.53	41.18	45.12
%Jadeite	----------	----------	----------	----------	----------	----------	----------	----------	----------	----------
%Aegirine	----------	----------	----------	----------	----------	----------	----------	----------	----------	----------
%Quad	----------	----------	----------	----------	----------	----------	----------	----------	----------	----------
Classification according to Morimoto et al. (1988)										
Group	Quad	Quad	Quad	Quad	Quad	Quad	Quad	Quad	Quad	Quad
Classification	diopside	diopside	diopside	augite	augite	diopside	augite	diopside	augite	diopside

Sample	ST-168	ST-168	ST-168	ST-168	ST-168	ST-168	ST-168	ST-168	ST-168	ST-168
Reference	L1_5	L1_6	L1_7	L1_8	L1_9	L1_10	L1_11	L1_12	L1_13	L1_14
SiO_2	51.29	51.26	52.26	52.68	52.28	51.67	51.64	54.42	53.73	53.65
TiO_2	0.51	0.63	0.50	0.38	0.57	0.54	0.55	0.15	0.16	0.13
Al_2O_3	2.66	2.71	2.41	2.07	2.49	2.67	2.64	1.09	1.11	0.96
Fe_2O_3	3.69	3.69	4.36	2.60	2.67	3.88	3.78	3.06	4.72	4.89
FeO	3.39	3.65	5.59	6.44	5.25	3.89	3.66	12.30	10.92	10.72
MnO	0.21	0.21	0.20	0.18	0.22	0.19	0.17	0.32	0.33	0.30
MgO	17.53	17.38	21.18	20.20	18.41	18.18	17.66	28.94	29.25	29.41
CaO	19.63	19.76	14.13	15.31	18.21	18.86	19.69	0.72	0.74	0.59
K_2O	0.01	0.00	0.00	0.00	0.00	0.00	0.01	0.01	0.01	0.00
Na_2O	0.38	0.36	0.26	0.23	0.30	0.35	0.36	0.00	0.00	0.01
ZnO	0.02	0.01	0.09	0.02	0.00	0.03	0.03	0.02	0.03	0.00
Cr_2O_3	0.19	0.16	0.26	0.16	0.23	0.15	0.18	0.10	0.05	0.08
Total	99.49	99.82	101.23	100.26	100.62	100.40	100.35	101.14	101.05	100.74
Number of ions on the base of 6 oxygens normalized for 4 cations										
Si	1.888	1.884	1.882	1.916	1.902	1.885	1.887	1.931	1.909	1.910
Al^{IV}	0.112	0.116	0.102	0.084	0.098	0.115	0.113	0.046	0.046	0.040
$Fe^{3+\ IV}$	0.000	0.000	0.016	0.000	0.000	0.000	0.000	0.023	0.045	0.049
Al^{VI}	0.003	0.001	0.000	0.004	0.009	0.000	0.000	0.000	0.000	0.000
$Fe^{3+\ VI}$	0.102	0.102	0.102	0.071	0.073	0.106	0.104	0.059	0.081	0.082
Ti	0.014	0.017	0.014	0.010	0.016	0.015	0.015	0.004	0.004	0.004
Cr	0.006	0.005	0.007	0.005	0.006	0.004	0.005	0.003	0.001	0.002
Zn	0.000	0.000	0.002	0.000	0.000	0.001	0.001	0.001	0.001	0.000
Mg	0.962	0.952	1.137	1.095	0.998	0.988	0.962	1.531	1.549	1.561
Fe^{2+}	0.104	0.112	0.168	0.196	0.160	0.119	0.112	0.365	0.324	0.319
Mn	0.007	0.007	0.006	0.006	0.007	0.006	0.005	0.009	0.010	0.009
Ca	0.774	0.778	0.545	0.596	0.710	0.737	0.771	0.028	0.028	0.022
K	0.001	0.000	0.000	0.000	0.000	0.000	0.000	0.000	0.000	0.000
Na	0.027	0.026	0.018	0.016	0.021	0.024	0.026	0.000	0.000	0.001
%Enstatite	49.36	48.81	57.57	55.76	51.25	50.52	49.24	76.00	76.02	76.42
%Ferrosillite	10.93	11.31	14.83	13.88	12.30	11.80	11.30	22.63	22.60	22.48
%Wollastonite	39.72	39.89	27.60	30.36	36.45	37.68	39.46	1.37	1.38	1.10
%Jadeite	----------	----------	----------	----------	----------	----------	----------	----------	----------	----------
%Aegirine	----------	----------	----------	----------	----------	----------	----------	----------	----------	----------
%Quad	----------	----------	----------	----------	----------	----------	----------	----------	----------	----------
Classification according to Morimoto et al. (1988)										
Group	Quad	Quad	Quad	Quad	Quad	Quad	Quad	Quad	Quad	Quad
Classification	augite	augite	augite	augite	augite	augite	augite	enstatite	enstatite	enstatite

Sample	ST-168	ST-168	ST-168	ST-168	ST-168	ST-168	ST-168	ST-168	ST-168	ST-168
Reference	L1_15	L1_16	L1_17	L1_18	L1_19	L1_20	L1_21	L1_22	L1_23	L1_24
SiO_2	51.65	53.12	51.98	51.35	51.27	51.23	51.40	51.22	51.13	50.32
TiO_2	0.41	0.28	0.37	0.71	0.56	0.63	0.66	0.54	0.55	0.68
Al_2O_3	1.91	1.96	2.03	2.41	2.46	2.77	2.73	2.53	2.60	2.96
Fe_2O_3	3.98	2.13	3.14	2.92	4.04	3.90	3.48	4.33	4.12	4.28
FeO	1.86	7.02	2.91	3.31	3.80	3.76	3.77	4.48	4.25	2.06
MnO	0.11	0.21	0.16	0.16	0.20	0.15	0.18	0.16	0.19	0.17
MgO	16.44	21.34	16.24	16.35	18.22	17.68	17.40	19.49	18.37	15.88
CaO	22.97	13.70	22.52	21.70	18.60	19.30	19.89	16.44	18.02	22.17
K_2O	0.00	0.02	0.02	0.00	0.00	0.00	0.00	0.00	0.00	0.01
Na_2O	0.31	0.19	0.34	0.35	0.32	0.36	0.34	0.28	0.29	0.39
ZnO	0.02	0.03	0.00	0.00	0.00	0.01	0.03	0.01	0.01	0.01
Cr_2O_3	0.15	0.09	0.19	0.22	0.14	0.17	0.10	0.13	0.07	0.05
Total	99.79	100.08	99.91	99.47	99.63	99.96	100.00	99.61	99.59	98.97
Number of ions on the base of 6 oxygens normalized for 4 cations										
Si	1.901	1.927	1.912	1.897	1.885	1.879	1.885	1.878	1.881	1.870
Al^{IV}	0.083	0.073	0.088	0.103	0.107	0.120	0.115	0.109	0.113	0.129
$Fe^{3+\ IV}$	0.016	0.000	0.000	0.000	0.009	0.001	0.000	0.012	0.006	0.001
Al^{VI}	0.000	0.011	0.000	0.002	0.000	0.000	0.003	0.000	0.000	0.000
$Fe^{3+\ VI}$	0.094	0.058	0.087	0.081	0.103	0.106	0.096	0.107	0.108	0.119
Ti	0.011	0.008	0.010	0.020	0.015	0.017	0.018	0.015	0.015	0.019
Cr	0.004	0.003	0.006	0.006	0.004	0.005	0.003	0.004	0.002	0.001
Zn	0.000	0.001	0.000	0.000	0.000	0.000	0.001	0.000	0.000	0.000
Mg	0.902	1.154	0.891	0.900	0.999	0.967	0.951	1.066	1.007	0.880
Fe^{2+}	0.057	0.213	0.090	0.102	0.117	0.115	0.116	0.137	0.131	0.064
Mn	0.003	0.006	0.005	0.005	0.006	0.005	0.006	0.005	0.006	0.005
Ca	0.906	0.532	0.887	0.859	0.733	0.759	0.782	0.646	0.710	0.883
K	0.000	0.001	0.001	0.000	0.000	0.000	0.000	0.000	0.000	0.001
Na	0.022	0.013	0.024	0.025	0.023	0.025	0.024	0.020	0.021	0.028
%Enstatite	45.59	58.76	45.45	46.23	50.79	49.51	48.78	53.99	51.18	45.08
%Ferrosillite	8.64	14.13	9.27	9.67	11.95	11.65	11.14	13.27	12.73	9.69
%Wollastonite	45.78	27.11	45.28	44.09	37.26	38.84	40.08	32.74	36.09	45.23
%Jadeite	----------	----------	----------	----------	----------	----------	----------	----------	----------	----------
%Aegirine	----------	----------	----------	----------	----------	----------	----------	----------	----------	----------
%Quad	----------	----------	----------	----------	----------	----------	----------	----------	----------	----------
Classification according to Morimoto et al. (1988)										
Group	Quad	Quad	Quad	Quad	Quad	Quad	Quad	Quad	Quad	Quad
Classification	diopside	augite	diopside	augite	augite	augite	augite	augite	augite	diopside

Sample	ST-168	ST-168	ST-168	ST-168	ST-168	ST-168	ST-168	ST-168	ST-168	ST-168
Reference	L2_1	L2_2	L2_3	L2_4	L2_5	L2_6	L2_7	L2_8	L2_9	L2_10
SiO_2	51.96	51.69	51.43	51.61	52.00	51.54	51.80	51.57	51.83	52.20
TiO_2	0.34	0.50	0.46	0.42	0.44	0.33	0.35	0.43	0.44	0.38
Al_2O_3	1.86	2.72	2.83	2.68	2.62	2.44	2.83	2.87	2.83	2.19
Fe_2O_3	3.26	4.03	3.31	3.92	2.98	2.24	2.99	2.71	2.94	3.22
FeO	2.77	3.30	3.06	3.25	4.56	6.76	4.08	4.10	4.35	2.87
MnO	0.16	0.14	0.14	0.18	0.15	0.16	0.15	0.10	0.22	0.17
MgO	16.53	17.91	16.60	17.51	18.19	19.77	17.24	17.07	17.66	16.55
CaO	22.33	19.49	21.29	20.03	18.78	14.53	20.09	20.21	19.25	22.26
K_2O	0.00	0.00	0.00	0.00	0.01	0.01	0.00	0.00	0.00	0.00
Na_2O	0.30	0.40	0.40	0.39	0.29	0.24	0.34	0.32	0.36	0.36
ZnO	0.03	0.08	0.00	0.00	0.00	0.02	0.00	0.04	0.02	0.02
Cr_2O_3	0.15	0.14	0.13	0.16	0.17	0.17	0.12	0.25	0.21	0.23
Total	99.37	99.98	99.31	99.75	99.88	97.99	99.68	99.39	99.81	100.12
Number of ions on the base of 6 oxygens normalized for 4 cations										
Si	1.914	1.885	1.893	1.888	1.899	1.912	1.898	1.896	1.896	1.908
Al^{IV}	0.081	0.115	0.107	0.112	0.101	0.088	0.102	0.104	0.104	0.092
$Fe^{3+\ IV}$	0.006	0.000	0.000	0.000	0.000	0.000	0.000	0.000	0.000	0.000
Al^{VI}	0.000	0.002	0.015	0.004	0.012	0.019	0.020	0.021	0.018	0.002
$Fe^{3+\ VI}$	0.085	0.110	0.092	0.108	0.082	0.062	0.082	0.075	0.081	0.089
Ti	0.009	0.014	0.013	0.012	0.012	0.009	0.010	0.012	0.012	0.010
Cr	0.004	0.004	0.004	0.005	0.005	0.005	0.004	0.007	0.006	0.007
Zn	0.001	0.002	0.000	0.000	0.000	0.001	0.000	0.001	0.001	0.001
Mg	0.908	0.974	0.910	0.955	0.990	1.094	0.942	0.936	0.963	0.902
Fe^{2+}	0.085	0.101	0.094	0.099	0.139	0.210	0.125	0.126	0.133	0.088
Mn	0.005	0.004	0.004	0.005	0.005	0.005	0.005	0.003	0.007	0.005
Ca	0.881	0.761	0.839	0.785	0.735	0.578	0.789	0.796	0.754	0.871
K	0.000	0.000	0.000	0.000	0.000	0.000	0.000	0.000	0.000	0.000
Na	0.022	0.028	0.028	0.028	0.021	0.017	0.024	0.023	0.025	0.026
%Enstatite	46.09	49.92	46.92	48.90	50.76	56.12	48.49	48.34	49.70	46.13
%Ferrosillite	9.18	11.04	9.81	10.89	11.56	14.23	10.90	10.54	11.38	9.28
%Wollastonite	44.73	39.03	43.27	40.21	37.68	29.65	40.60	41.12	38.92	44.59
%Jadeite	----------	----------	----------	----------	----------	----------	----------	----------	----------	----------
%Aegirine	----------	----------	----------	----------	----------	----------	----------	----------	----------	----------
%Quad	----------	----------	----------	----------	----------	----------	----------	----------	----------	----------
Classification according to Morimoto et al. (1988)										
Group	Quad	Quad	Quad	Quad	Quad	Quad	Quad	Quad	Quad	Quad
Classification	augite	augite	augite	augite	augite	augite	augite	augite	augite	augite

Sample	ST-168	ST-168	ST-168	ST-168	ST-168	ST-168	ST-168	ST-168	ST-168	ST-168
Reference	L2_11	L2_12	L2_13	L2_14	L2_15	L2_16	L2_17	L2_18	L2_19	L2_20
SiO_2	51.98	51.57	50.55	53.40	52.11	51.86	50.82	50.31	51.50	51.70
TiO_2	0.31	0.36	0.38	0.13	0.38	0.39	0.31	0.49	0.50	0.52
Al_2O_3	1.78	2.08	2.16	1.27	2.69	2.74	2.47	2.89	2.77	2.85
Fe_2O_3	3.75	3.92	4.11	5.59	2.82	2.53	3.22	4.52	3.44	2.81
FeO	1.71	2.04	2.23	9.48	4.58	3.68	5.40	2.28	3.09	3.37
MnO	0.11	0.14	0.14	0.34	0.15	0.17	0.20	0.16	0.14	0.14
MgO	16.57	16.44	16.03	29.75	17.99	16.76	18.98	16.89	17.11	16.46
CaO	23.10	22.49	21.99	0.75	19.03	21.14	15.80	20.52	20.80	21.56
K_2O	0.00	0.00	0.00	0.00	0.00	0.00	0.00	0.03	0.00	0.00
Na_2O	0.32	0.36	0.36	0.03	0.31	0.33	0.29	0.36	0.35	0.39
ZnO	0.02	0.03	0.01	0.00	0.04	0.03	0.00	0.00	0.02	0.00
Cr_2O_3	0.19	0.16	0.21	0.14	0.16	0.14	0.18	0.10	0.18	0.23
Total	99.44	99.19	97.76	100.31	99.98	99.51	97.36	98.10	99.57	99.76
Number of ions on the base of 6 oxygens normalized for 4 cations										
Si	1.910	1.901	1.893	1.895	1.902	1.905	1.899	1.872	1.889	1.896
Al^{IV}	0.077	0.090	0.095	0.053	0.098	0.095	0.101	0.127	0.111	0.104
$Fe^{3+\ IV}$	0.013	0.009	0.011	0.052	0.000	0.000	0.000	0.002	0.000	0.000
Al^{VI}	0.000	0.000	0.000	0.000	0.018	0.023	0.008	0.000	0.009	0.019
$Fe^{3+\ VI}$	0.090	0.100	0.105	0.097	0.077	0.070	0.091	0.125	0.095	0.078
Ti	0.009	0.010	0.011	0.003	0.010	0.011	0.009	0.014	0.014	0.014
Cr	0.005	0.005	0.006	0.004	0.005	0.004	0.005	0.003	0.005	0.007
Zn	0.001	0.001	0.000	0.000	0.001	0.001	0.000	0.000	0.001	0.000
Mg	0.908	0.903	0.895	1.574	0.978	0.918	1.058	0.937	0.935	0.899
Fe^{2+}	0.053	0.063	0.070	0.281	0.140	0.113	0.169	0.071	0.095	0.103
Mn	0.003	0.004	0.005	0.010	0.005	0.005	0.006	0.005	0.004	0.004
Ca	0.909	0.888	0.883	0.028	0.744	0.832	0.633	0.818	0.817	0.847
K	0.000	0.000	0.000	0.000	0.000	0.000	0.000	0.001	0.000	0.000
Na	0.022	0.025	0.026	0.002	0.022	0.023	0.021	0.026	0.025	0.028
%Enstatite	45.92	45.91	45.48	77.04	50.32	47.36	54.07	47.86	48.05	46.56
%Ferrosillite	8.07	8.94	9.67	21.57	11.42	9.72	13.59	10.34	9.98	9.59
%Wollastonite	46.01	45.14	44.85	1.39	38.26	42.92	32.34	41.79	41.98	43.85
%Jadeite	----------	----------	----------	----------	----------	----------	----------	----------	----------	----------
%Aegirine	----------	----------	----------	----------	----------	----------	----------	----------	----------	----------
%Quad	----------	----------	----------	----------	----------	----------	----------	----------	----------	----------
Classification according to Morimoto et al. (1988)										
Group	Quad	Quad	Quad	Quad	Quad	Quad	Quad	Quad	Quad	Quad
Classification	diopside	diopside	diopside	enstatite	augite	augite	augite	augite	augite	augite

Sample	ST-168	ST-168	ST-168	ST-168	ST-168	ST-168	ST-168	ST-168	ST-168	ST-168
Reference	L3_1	L3_2	L3_3	L3_4	L3_5	L3_6	L3_7	L3_8	L3_9	L3_10
SiO_2	51.59	51.01	51.17	50.12	51.50	51.40	52.64	51.53	51.47	52.22
TiO_2	0.49	0.48	0.49	0.75	0.46	0.46	0.38	0.39	0.38	0.33
Al_2O_3	2.60	2.41	2.73	3.05	2.92	2.73	2.10	2.22	2.13	1.70
Fe_2O_3	3.24	3.65	3.77	6.13	3.56	3.05	4.46	3.45	3.60	3.14
FeO	3.28	2.87	2.87	2.44	2.70	3.49	5.45	2.59	2.40	2.25
MnO	0.15	0.20	0.18	0.19	0.18	0.16	0.18	0.16	0.12	0.18
MgO	16.79	16.07	16.82	17.98	16.33	16.54	22.22	16.29	16.27	16.57
CaO	21.39	21.69	21.08	19.09	21.86	21.26	12.82	22.36	22.54	22.84
K_2O	0.00	0.02	0.00	0.01	0.00	0.01	0.01	0.00	0.00	0.01
Na_2O	0.29	0.40	0.34	0.30	0.42	0.31	0.34	0.33	0.32	0.32
ZnO	0.00	0.00	0.00	0.05	0.04	0.04	0.03	0.02	0.01	0.01
Cr_2O_3	0.20	0.13	0.17	0.13	0.17	0.23	0.22	0.19	0.15	0.10
Total	99.70	98.55	99.25	99.62	99.79	99.37	100.39	99.19	99.02	99.35
Number of ions on the base of 6 oxygens normalized for 4 cations										
Si	1.893	1.896	1.885	1.838	1.888	1.894	1.894	1.902	1.902	1.921
Al^{IV}	0.107	0.104	0.115	0.132	0.112	0.106	0.089	0.097	0.093	0.074
$Fe^{3+\ IV}$	0.000	0.000	0.000	0.030	0.000	0.000	0.017	0.002	0.005	0.006
Al^{VI}	0.006	0.002	0.003	0.000	0.014	0.012	0.000	0.000	0.000	0.000
$Fe^{3+\ VI}$	0.089	0.102	0.105	0.139	0.098	0.084	0.104	0.094	0.095	0.081
Ti	0.014	0.013	0.014	0.021	0.013	0.013	0.010	0.011	0.011	0.009
Cr	0.006	0.004	0.005	0.004	0.005	0.007	0.006	0.006	0.004	0.003
Zn	0.000	0.000	0.000	0.001	0.001	0.001	0.001	0.000	0.000	0.000
Mg	0.918	0.891	0.923	0.983	0.892	0.909	1.192	0.896	0.896	0.909
Fe^{2+}	0.101	0.089	0.089	0.075	0.083	0.108	0.164	0.080	0.074	0.069
Mn	0.005	0.006	0.006	0.006	0.005	0.005	0.005	0.005	0.004	0.006
Ca	0.841	0.864	0.832	0.750	0.858	0.839	0.494	0.884	0.893	0.900
K	0.000	0.001	0.000	0.000	0.000	0.001	0.000	0.000	0.000	0.000
Na	0.021	0.029	0.024	0.021	0.030	0.022	0.024	0.024	0.023	0.023
%Enstatite	47.00	45.63	47.27	49.58	46.06	46.72	60.31	45.70	45.57	46.12
%Ferrosillite	9.97	10.11	10.17	12.60	9.63	10.13	14.68	9.21	9.05	8.20
%Wollastonite	43.03	44.26	42.57	37.82	44.31	43.16	25.00	45.09	45.38	45.68
%Jadeite	----------	----------	----------	----------	----------	----------	----------	----------	----------	----------
%Aegirine	----------	----------	----------	----------	----------	----------	----------	----------	----------	----------
%Quad	----------	----------	----------	----------	----------	----------	----------	----------	----------	----------
Classification according to Morimoto et al. (1988)										
Group	Quad	Quad	Quad	Quad	Quad	Quad	Quad	Quad	Quad	Quad
Classification	augite	augite	augite	augite	augite	augite	augite	diopside	diopside	diopside

Sample	ST-168	ST-168	ST-168	ST-168	ST-168	ST-168	ST-168	ST-168	ST-168	ST-168
Reference	L3_11	L3_12	L3_13	L3_14	L3_15	L3_16	L3_17	L3_18	L3_19	L3_20
SiO_2	50.22	50.88	50.97	50.96	51.14	52.01	51.45	51.74	51.25	51.83
TiO_2	0.40	0.40	0.36	0.35	0.36	0.32	0.35	0.37	0.37	0.32
Al_2O_3	3.00	3.06	2.91	2.90	2.98	2.80	2.81	2.87	2.81	2.78
Fe_2O_3	4.60	3.71	4.42	4.91	3.54	2.55	4.02	3.43	3.71	3.33
FeO	4.28	2.70	2.74	2.51	3.27	5.06	3.83	3.79	3.59	4.13
MnO	0.15	0.19	0.16	0.19	0.17	0.16	0.15	0.15	0.16	0.14
MgO	17.27	16.57	17.62	18.08	17.23	18.62	18.88	17.95	18.03	18.65
CaO	18.37	21.31	19.92	19.35	20.27	17.80	17.68	19.38	19.06	18.32
K_2O	0.02	0.00	0.00	0.01	0.00	0.00	0.01	0.01	0.00	0.00
Na_2O	0.34	0.30	0.30	0.33	0.28	0.27	0.31	0.29	0.27	0.27
ZnO	0.00	0.07	0.05	0.00	0.04	0.01	0.06	0.05	0.03	0.05
Cr_2O_3	0.21	0.29	0.32	0.23	0.28	0.26	0.24	0.24	0.21	0.25
Total	98.40	99.11	99.33	99.30	99.20	99.61	99.41	99.92	99.12	99.72
Number of ions on the base of 6 oxygens normalized for 4 cations										
Si	1.868	1.877	1.872	1.868	1.882	1.902	1.882	1.888	1.884	1.892
Al^{IV}	0.132	0.123	0.126	0.125	0.118	0.098	0.118	0.112	0.116	0.108
$Fe^{3+\ IV}$	0.000	0.000	0.002	0.006	0.000	0.000	0.000	0.000	0.000	0.000
Al^{VI}	0.000	0.010	0.000	0.000	0.011	0.022	0.003	0.012	0.006	0.011
$Fe^{3+\ VI}$	0.129	0.103	0.120	0.129	0.098	0.070	0.111	0.094	0.103	0.092
Ti	0.011	0.011	0.010	0.010	0.010	0.009	0.010	0.010	0.010	0.009
Cr	0.006	0.009	0.009	0.007	0.008	0.008	0.007	0.007	0.006	0.007
Zn	0.000	0.002	0.001	0.000	0.001	0.000	0.002	0.001	0.001	0.001
Mg	0.958	0.912	0.965	0.989	0.946	1.015	1.030	0.977	0.989	1.014
Fe^{2+}	0.133	0.083	0.084	0.077	0.101	0.155	0.117	0.116	0.110	0.126
Mn	0.005	0.006	0.005	0.006	0.005	0.005	0.005	0.005	0.005	0.004
Ca	0.732	0.842	0.784	0.760	0.800	0.697	0.693	0.758	0.751	0.716
K	0.001	0.000	0.000	0.000	0.000	0.000	0.000	0.000	0.000	0.000
Na	0.025	0.022	0.022	0.023	0.020	0.019	0.022	0.021	0.019	0.019
%Enstatite	48.94	46.84	49.22	50.26	48.52	52.25	52.66	50.11	50.50	51.95
%Ferrosillite	13.64	9.88	10.77	11.09	10.45	11.84	11.90	11.01	11.14	11.36
%Wollastonite	37.42	43.28	40.00	38.65	41.03	35.91	35.43	38.89	38.35	36.68
%Jadeite	----------	----------	----------	----------	----------	----------	----------	----------	----------	----------
%Aegirine	----------	----------	----------	----------	----------	----------	----------	----------	----------	----------
%Quad	----------	----------	----------	----------	----------	----------	----------	----------	----------	----------
Classification according to Morimoto et al. (1988)										
Group	Quad	Quad	Quad	Quad	Quad	Quad	Quad	Quad	Quad	Quad
Classification	augite	augite	augite	augite	augite	augite	augite	augite	augite	augite

Sample	ST-169	ST-169	ST-169	ST-169	ST-169	ST-169	ST-169	ST-169	ST-169	ST-169
Reference	1	2	3	4	5	6	7	8	9	10
SiO_2	52.80	52.93	52.87	52.52	52.91	52.92	52.93	52.94	52.67	53.07
TiO_2	0.45	0.46	0.50	0.45	0.49	0.48	0.51	0.51	0.49	0.48
Al_2O_3	2.38	2.45	2.28	2.32	2.26	2.30	2.29	2.35	2.38	2.38
Fe_2O_3	2.08	0.97	0.41	0.85	1.30	0.04	0.62	0.74	1.34	0.43
FeO	4.44	5.05	5.55	5.21	4.58	5.93	5.46	5.31	4.40	5.62
MnO	0.13	0.13	0.13	0.12	0.11	0.16	0.14	0.06	0.14	0.10
MgO	15.82	15.79	15.52	15.67	15.81	16.05	15.56	15.67	15.78	15.71
CaO	22.48	22.42	22.26	22.10	22.71	21.48	22.25	22.57	22.61	22.16
K_2O	0.02	0.01	0.01	0.01	0.01	0.01	0.02	0.02	0.00	0.01
Na_2O	0.41	0.35	0.39	0.34	0.37	0.32	0.40	0.32	0.38	0.38
ZnO	0.00	0.00	0.00	0.00	0.00	0.00	0.00	0.00	0.00	0.00
Cr_2O_3	0.14	0.14	0.23	0.19	0.16	0.15	0.15	0.14	0.14	0.14
Total	101.16	100.69	100.14	99.77	100.71	99.83	100.32	100.62	100.34	100.46
Number of ions on the base of 6 oxygens normalized for 4 cations										
Si	1.921	1.932	1.942	1.935	1.931	1.946	1.940	1.935	1.928	1.941
Al^{IV}	0.079	0.068	0.058	0.065	0.069	0.054	0.060	0.065	0.072	0.059
$Fe^{3+\ IV}$	0.000	0.000	0.000	0.000	0.000	0.000	0.000	0.000	0.000	0.000
Al^{VI}	0.023	0.037	0.041	0.036	0.028	0.045	0.039	0.036	0.031	0.044
$Fe^{3+\ VI}$	0.057	0.027	0.011	0.024	0.036	0.001	0.017	0.020	0.037	0.012
Ti	0.012	0.013	0.014	0.012	0.013	0.013	0.014	0.014	0.014	0.013
Cr	0.004	0.004	0.007	0.006	0.005	0.004	0.004	0.004	0.004	0.004
Zn	0.000	0.000	0.000	0.000	0.000	0.000	0.000	0.000	0.000	0.000
Mg	0.858	0.859	0.850	0.861	0.860	0.880	0.850	0.854	0.861	0.857
Fe^{2+}	0.135	0.154	0.170	0.161	0.140	0.182	0.167	0.162	0.135	0.172
Mn	0.004	0.004	0.004	0.004	0.003	0.005	0.004	0.002	0.004	0.003
Ca	0.876	0.877	0.876	0.872	0.888	0.846	0.874	0.884	0.887	0.868
K	0.001	0.000	0.000	0.001	0.001	0.000	0.001	0.001	0.000	0.000
Na	0.029	0.025	0.027	0.024	0.026	0.022	0.028	0.023	0.027	0.027
%Enstatite	44.45	44.74	44.47	44.82	44.64	45.95	44.46	44.41	44.76	44.81
%Ferrosillite	10.15	9.62	9.70	9.77	9.27	9.85	9.87	9.60	9.14	9.77
%Wollastonite	45.40	45.64	45.82	45.41	46.09	44.20	45.68	45.99	46.09	45.42
%Jadeite	----------	----------	----------	----------	----------	----------	----------	----------	----------	----------
%Aegirine	----------	----------	----------	----------	----------	----------	----------	----------	----------	----------
%Quad	----------	----------	----------	----------	----------	----------	----------	----------	----------	----------
Classification according to Morimoto et al. (1988)										
Group	Quad	Quad	Quad	Quad	Quad	Quad	Quad	Quad	Quad	Quad
Classification	diopside	diopside	diopside	diopside	diopside	augite	diopside	diopside	diopside	diopside

Sample	ST-169	ST-169	ST-169	ST-169	ST-169	ST-169	ST-173	ST-173	ST-173	ST-173
Reference	11	12	13	14	15	16	1	2	3	4
SiO_2	53.02	53.25	52.81	53.02	52.75	55.18	45.89	52.31	51.94	51.72
TiO_2	0.48	0.49	0.52	0.50	0.55	0.23	2.36	0.62	0.41	0.77
Al_2O_3	2.29	2.38	2.32	2.31	2.50	1.28	6.68	2.47	2.71	2.69
Fe_2O_3	0.42	0.00	0.00	1.17	1.26	1.68	5.84	2.36	2.53	2.51
FeO	5.71	6.57	6.26	4.89	5.80	12.36	1.60	3.53	3.64	3.07
MnO	0.06	0.07	0.09	0.09	0.14	0.21	0.08	0.16	0.15	0.16
MgO	16.01	15.85	16.11	15.52	17.01	29.47	13.37	16.40	16.58	16.10
CaO	21.80	20.89	20.91	22.96	20.09	0.82	23.31	22.46	21.82	22.95
K_2O	0.00	0.00	0.01	0.01	0.00	0.00	0.01	0.00	0.00	0.01
Na_2O	0.35	0.32	0.34	0.38	0.34	0.01	0.33	0.28	0.24	0.25
ZnO	0.00	0.00	0.00	0.00	0.00	0.00	0.06	0.08	0.06	0.04
Cr_2O_3	0.21	0.21	0.21	0.22	0.16	0.10	0.07	0.18	0.23	0.30
Total	100.35	100.02	99.57	101.06	100.59	101.34	99.02	100.61	100.06	100.31
Number of ions on the base of 6 oxygens normalized for 4 cations										
Si	1.941	1.958	1.947	1.931	1.924	1.944	1.716	1.905	1.901	1.891
Al^{IV}	0.059	0.042	0.053	0.069	0.076	0.053	0.284	0.095	0.099	0.109
$Fe^{3+\ IV}$	0.000	0.000	0.000	0.000	0.000	0.003	0.000	0.000	0.000	0.000
Al^{VI}	0.039	0.061	0.048	0.030	0.031	0.000	0.010	0.011	0.018	0.007
$Fe^{3+\ VI}$	0.012	0.000	0.000	0.032	0.034	0.042	0.164	0.065	0.070	0.069
Ti	0.013	0.014	0.014	0.014	0.015	0.006	0.066	0.017	0.011	0.021
Cr	0.006	0.006	0.006	0.006	0.005	0.003	0.002	0.005	0.007	0.009
Zn	0.000	0.000	0.000	0.000	0.000	0.000	0.002	0.002	0.002	0.001
Mg	0.873	0.869	0.885	0.843	0.925	1.548	0.745	0.891	0.905	0.878
Fe^{2+}	0.175	0.202	0.193	0.149	0.177	0.364	0.050	0.107	0.111	0.094
Mn	0.002	0.002	0.003	0.003	0.004	0.006	0.002	0.005	0.005	0.005
Ca	0.855	0.823	0.826	0.896	0.785	0.031	0.934	0.876	0.855	0.899
K	0.000	0.000	0.000	0.001	0.000	0.000	0.001	0.000	0.000	0.000
Na	0.025	0.023	0.024	0.027	0.024	0.000	0.024	0.020	0.017	0.018
%Enstatite	45.57	45.83	46.42	43.83	48.03	77.64	39.30	45.81	46.49	45.14
%Ferrosillite	9.82	10.76	10.27	9.57	11.20	20.80	11.44	9.11	9.55	8.63
%Wollastonite	44.61	43.41	43.31	46.60	40.77	1.56	49.26	45.08	43.96	46.23
%Jadeite	----------	----------	----------	----------	----------	----------	----------	----------	----------	----------
%Aegirine	----------	----------	----------	----------	----------	----------	----------	----------	----------	----------
%Quad	----------	----------	----------	----------	----------	----------	----------	----------	----------	----------
Classification according to Morimoto et al. (1988)										
Group	Quad	Quad	Quad	Quad	Quad	Quad	Quad	Quad	Quad	Quad
Classification	augite	augite	augite	diopside	augite	enstatite	diopside	diopside	augite	diopside

Sample	ST-173	ST-173	ST-173	ST-173	ST-173	ST-173	ST-173	ST-173	ST-173	ST-173
Reference	5	6	7	8	9	10	11	12	13	14
SiO_2	51.41	52.25	52.29	42.77	51.36	52.60	46.46	45.60	52.14	51.93
TiO_2	0.44	0.38	0.53	4.02	0.64	0.59	2.71	3.52	0.41	0.41
Al_2O_3	2.83	2.67	2.65	8.67	2.70	2.54	5.86	7.51	2.69	2.78
Fe_2O_3	3.50	2.72	2.00	5.77	3.07	1.81	5.52	3.98	2.18	3.28
FeO	2.45	3.78	3.85	3.27	2.99	4.43	1.43	3.46	4.74	3.36
MnO	0.19	0.15	0.10	0.06	0.16	0.11	0.04	0.05	0.14	0.16
MgO	16.39	17.47	16.35	11.44	16.15	16.82	14.23	12.81	17.41	17.21
CaO	22.26	20.77	22.26	22.84	22.27	21.57	23.21	23.26	19.97	20.95
K_2O	0.00	0.00	0.00	0.01	0.00	0.00	0.00	0.00	0.00	0.00
Na_2O	0.31	0.24	0.30	0.38	0.33	0.27	0.29	0.33	0.26	0.28
ZnO	0.09	0.02	0.01	0.00	0.00	0.06	0.09	0.02	0.01	0.12
Cr_2O_3	0.27	0.22	0.23	0.00	0.38	0.30	0.13	0.19	0.33	0.36
Total	99.77	100.39	100.36	98.65	99.74	100.90	99.41	100.32	100.05	100.51
Number of ions on the base of 6 oxygens normalized for 4 cations										
Si	1.886	1.901	1.908	1.623	1.887	1.910	1.727	1.691	1.905	1.889
Al^{IV}	0.114	0.099	0.092	0.377	0.113	0.090	0.257	0.309	0.095	0.111
$Fe^{3+\ IV}$	0.000	0.000	0.000	0.000	0.000	0.000	0.016	0.000	0.000	0.000
Al^{VI}	0.008	0.015	0.022	0.011	0.004	0.019	0.000	0.020	0.021	0.008
$Fe^{3+\ VI}$	0.097	0.074	0.055	0.165	0.085	0.050	0.138	0.111	0.060	0.090
Ti	0.012	0.010	0.015	0.115	0.018	0.016	0.076	0.098	0.011	0.011
Cr	0.008	0.006	0.007	0.000	0.011	0.009	0.004	0.005	0.010	0.010
Zn	0.002	0.001	0.000	0.000	0.000	0.002	0.002	0.000	0.000	0.003
Mg	0.896	0.947	0.889	0.647	0.885	0.910	0.788	0.708	0.949	0.933
Fe^{2+}	0.075	0.115	0.118	0.104	0.092	0.134	0.044	0.107	0.145	0.102
Mn	0.006	0.005	0.003	0.002	0.005	0.003	0.001	0.002	0.004	0.005
Ca	0.875	0.810	0.870	0.929	0.877	0.839	0.925	0.924	0.782	0.817
K	0.000	0.000	0.000	0.000	0.000	0.000	0.000	0.000	0.000	0.000
Na	0.022	0.017	0.021	0.028	0.023	0.019	0.021	0.023	0.018	0.020
%Enstatite	45.99	48.55	45.95	35.05	45.53	47.00	41.21	38.23	48.92	47.94
%Ferrosillite	9.12	9.94	9.07	14.65	9.35	9.67	10.46	11.88	10.77	10.11
%Wollastonite	44.89	41.50	44.98	50.30	45.12	43.32	48.33	49.89	40.31	41.94
%Jadeite	----------	----------	----------	----------	----------	----------	----------	----------	----------	----------
%Aegirine	----------	----------	----------	----------	----------	----------	----------	----------	----------	----------
%Quad	----------	----------	----------	----------	----------	----------	----------	----------	----------	----------
Classification according to Morimoto et al. (1988)										
Group	Quad	Quad	Quad	Quad	Quad	Quad	Quad	Quad	Quad	Quad
Classification	augite	augite	augite	wollast.	diopside	augite	diopside	diopside	augite	augite

Sample	ST-173	ST-173	ST-173	ST-173	ST-173	ST-173	ST-173	ST-173	ST-173	ST-173
Reference	15	16	17	18	19	20	21	22	23	24
SiO_2	52.33	51.88	42.82	51.88	46.39	45.83	43.82	47.08	45.69	48.67
TiO_2	0.37	0.48	4.26	0.53	3.38	3.13	3.90	3.02	3.46	0.92
Al_2O_3	2.99	2.78	9.37	2.60	6.72	6.04	8.87	5.80	6.52	4.10
Fe_2O_3	1.83	2.75	5.67	2.82	4.32	4.50	5.31	3.84	4.68	7.48
FeO	4.75	3.84	3.24	2.90	2.73	3.64	3.07	3.64	3.63	7.53
MnO	0.15	0.15	0.02	0.10	0.06	0.11	0.09	0.12	0.07	0.46
MgO	17.38	16.93	11.52	16.07	13.44	13.17	12.04	13.61	13.10	8.51
CaO	19.78	21.14	22.91	22.85	23.29	22.56	22.82	23.09	22.89	20.70
K_2O	0.00	0.00	0.00	0.00	0.01	0.01	0.01	0.00	0.00	0.00
Na_2O	0.35	0.26	0.40	0.34	0.41	0.31	0.43	0.30	0.29	1.99
ZnO	0.04	0.00	0.02	0.00	0.00	0.04	0.00	0.04	0.03	0.12
Cr_2O_3	0.41	0.37	0.08	0.43	0.14	0.04	0.00	0.03	0.02	0.00
Total	100.19	100.31	99.75	100.23	100.45	98.92	99.83	100.17	99.90	99.72
Number of ions on the base of 6 oxygens normalized for 4 cations										
Si	1.907	1.893	1.606	1.897	1.713	1.725	1.637	1.746	1.704	1.848
Al^{IV}	0.093	0.107	0.394	0.103	0.287	0.268	0.363	0.253	0.287	0.152
$Fe^{3+\ IV}$	0.000	0.000	0.000	0.000	0.000	0.008	0.000	0.001	0.009	0.000
Al^{VI}	0.036	0.013	0.020	0.009	0.005	0.000	0.027	0.000	0.000	0.032
$Fe^{3+\ VI}$	0.050	0.075	0.160	0.077	0.120	0.120	0.149	0.106	0.122	0.214
Ti	0.010	0.013	0.120	0.015	0.094	0.089	0.109	0.084	0.097	0.026
Cr	0.012	0.011	0.002	0.012	0.004	0.001	0.000	0.001	0.000	0.000
Zn	0.001	0.000	0.001	0.000	0.000	0.001	0.000	0.001	0.001	0.003
Mg	0.944	0.921	0.644	0.876	0.740	0.739	0.670	0.752	0.728	0.482
Fe^{2+}	0.145	0.117	0.102	0.089	0.084	0.115	0.096	0.113	0.113	0.239
Mn	0.005	0.005	0.001	0.003	0.002	0.003	0.003	0.004	0.002	0.015
Ca	0.773	0.827	0.921	0.895	0.921	0.910	0.913	0.917	0.915	0.842
K	0.000	0.000	0.000	0.000	0.000	0.000	0.001	0.000	0.000	0.000
Na	0.025	0.019	0.029	0.024	0.029	0.023	0.031	0.021	0.021	0.147
%Enstatite	49.28	47.35	35.25	45.15	39.62	39.02	36.59	39.72	38.54	26.88
%Ferrosillite	10.41	10.14	14.37	8.71	11.03	12.95	13.54	11.82	13.05	26.11
%Wollastonite	40.31	42.51	50.39	46.13	49.34	48.03	49.86	48.45	48.41	47.00
%Jadeite	----------	----------	----------	----------	----------	----------	----------	----------	----------	----------
%Aegirine	----------	----------	----------	----------	----------	----------	----------	----------	----------	----------
%Quad	----------	----------	----------	----------	----------	----------	----------	----------	----------	----------
Classification according to Morimoto et al. (1988)										
Group	Quad	Quad	Quad	Quad	Quad	Quad	Quad	Quad	Quad	Quad
Classification	augite	augite	wollast.	diopside	diopside	diopside	diopside	diopside	diopside	diopside

Sample	ST-173	ST-173	ST-173	ST-173	ST-173	ST-173	ST-173	ST-173	ST-173	ST-173
Reference	25	26	27	28	29	30	31	32	33	34
SiO_2	48.96	49.24	47.60	54.94	55.30	40.00	39.17	55.65	55.55	51.93
TiO_2	0.88	0.93	1.33	0.23	0.21	0.00	0.00	0.24	0.23	0.57
Al_2O_3	4.11	3.95	6.13	1.34	1.44	0.01	0.00	1.13	1.41	2.57
Fe_2O_3	7.35	7.08	8.07	3.94	2.02	21.83	21.64	2.09	2.13	3.18
FeO	7.73	7.35	7.04	9.14	10.62	0.00	0.00	10.86	10.87	3.20
MnO	0.46	0.47	0.45	0.27	0.24	0.25	0.24	0.28	0.24	0.15
MgO	8.51	9.05	8.44	31.21	30.76	43.08	43.42	30.68	30.60	17.42
CaO	20.81	20.97	20.76	0.61	0.48	0.00	0.00	0.68	0.59	21.08
K_2O	0.00	0.00	0.01	0.01	0.00	0.01	0.00	0.01	0.00	0.00
Na_2O	2.00	1.90	1.92	0.01	0.00	0.00	0.00	0.00	0.02	0.26
ZnO	0.08	0.06	0.05	0.00	0.00	0.08	0.02	0.04	0.12	0.00
Cr_2O_3	0.02	0.00	0.02	0.09	0.11	0.00	0.00	0.08	0.11	0.22
Total	100.16	100.31	101.01	101.38	100.99	103.06	102.33	101.52	101.64	100.27
Number of ions on the base of 6 oxygens normalized for 4 cations										
Si	1.852	1.855	1.783	1.914	1.937	1.323	1.301	1.942	1.937	1.892
Al^{IV}	0.148	0.145	0.217	0.055	0.059	0.000	0.000	0.046	0.058	0.108
$Fe^{3+\ IV}$	0.000	0.000	0.000	0.031	0.004	0.612	0.612	0.011	0.006	0.000
Al^{VI}	0.035	0.030	0.054	0.000	0.000	0.000	0.000	0.000	0.000	0.002
$Fe^{3+\ VI}$	0.209	0.201	0.228	0.072	0.049	0.000	0.000	0.044	0.050	0.087
Ti	0.025	0.026	0.037	0.006	0.006	0.000	0.000	0.006	0.006	0.016
Cr	0.001	0.000	0.001	0.002	0.003	0.000	0.000	0.002	0.003	0.006
Zn	0.002	0.002	0.001	0.000	0.000	0.002	0.001	0.001	0.003	0.000
Mg	0.480	0.508	0.471	1.621	1.606	2.124	2.150	1.596	1.590	0.946
Fe^{2+}	0.244	0.232	0.220	0.266	0.311	0.000	0.000	0.317	0.317	0.098
Mn	0.015	0.015	0.014	0.008	0.007	0.007	0.007	0.008	0.007	0.004
Ca	0.843	0.847	0.833	0.023	0.018	0.000	0.000	0.025	0.022	0.823
K	0.000	0.000	0.000	0.000	0.000	0.000	0.000	0.000	0.000	0.000
Na	0.146	0.139	0.140	0.001	0.000	0.000	0.000	0.000	0.001	0.018
%Enstatite	26.78	28.20	26.68	80.20	80.47	77.43	77.65	79.73	79.83	48.31
%Ferrosillite	26.15	24.83	26.16	18.68	18.62	22.57	22.35	19.00	19.07	9.67
%Wollastonite	47.07	46.97	47.16	1.12	0.91	0.00	0.00	1.27	1.11	42.02
%Jadeite	----------	----------	----------	----------	----------	----------	----------	----------	----------	----------
%Aegirine	----------	----------	----------	----------	----------	----------	----------	----------	----------	----------
%Quad	----------	----------	----------	----------	----------	----------	----------	----------	----------	----------
Classification according to Morimoto et al. (1988)										
Group	Quad	Quad	Quad	Quad	Quad	Quad	Quad	Quad	Quad	Quad
Classification	diopside	diopside	diopside	enstatite	enstatite	enstatite	enstatite	enstatite	enstatite	augite

Sample	ST-173	ST-173	ST-173	ST-173	ST-173	ST-173	ST-173	ST-173	ST-173	ST-173
Reference	35	36	37	38	39	40	41	42	43	44
SiO_2	52.47	53.08	51.99	52.61	46.12	45.14	53.33	52.32	52.13	51.33
TiO_2	0.53	0.54	0.48	0.47	3.15	3.57	0.60	0.57	0.54	0.56
Al_2O_3	2.35	2.42	2.51	2.83	6.19	6.91	2.20	2.41	2.66	2.90
Fe_2O_3	2.39	1.44	3.53	1.71	5.11	4.64	0.74	2.16	2.25	3.55
FeO	4.04	4.78	4.25	4.86	2.94	3.53	5.15	5.28	4.25	5.57
MnO	0.18	0.12	0.18	0.13	0.11	0.09	0.16	0.15	0.15	0.16
MgO	17.72	17.40	19.43	17.55	13.39	12.74	16.89	18.00	16.97	16.25
CaO	20.44	21.02	17.56	20.20	22.94	22.79	21.58	19.04	20.97	22.55
K_2O	0.00	0.00	0.00	0.00	0.00	0.00	0.00	0.00	0.00	0.01
Na_2O	0.25	0.22	0.22	0.25	0.35	0.36	0.25	0.25	0.27	0.32
ZnO	0.08	0.11	0.00	0.05	0.05	0.00	0.09	0.01	0.06	0.02
Cr_2O_3	0.26	0.20	0.17	0.36	0.03	0.07	0.16	0.30	0.29	0.46
Total	100.46	101.17	99.96	100.82	99.87	99.36	101.08	100.27	100.29	100.12
Number of ions on the base of 6 oxygens normalized for 4 cations										
Si	1.907	1.919	1.890	1.907	1.717	1.693	1.933	1.908	1.903	1.878
Al^{IV}	0.093	0.081	0.108	0.093	0.272	0.306	0.067	0.092	0.097	0.122
$Fe^{3+\ IV}$	0.000	0.000	0.002	0.000	0.012	0.001	0.000	0.000	0.000	0.000
Al^{VI}	0.008	0.022	0.000	0.028	0.000	0.000	0.027	0.011	0.017	0.003
$Fe^{3+\ VI}$	0.065	0.039	0.094	0.047	0.132	0.130	0.020	0.059	0.062	0.098
Ti	0.015	0.015	0.013	0.013	0.088	0.101	0.016	0.016	0.015	0.015
Cr	0.007	0.006	0.005	0.010	0.001	0.002	0.005	0.009	0.008	0.013
Zn	0.002	0.003	0.000	0.001	0.001	0.000	0.002	0.000	0.002	0.000
Mg	0.961	0.938	1.053	0.948	0.743	0.712	0.913	0.978	0.923	0.886
Fe^{2+}	0.123	0.144	0.129	0.147	0.092	0.111	0.156	0.161	0.130	0.073
Mn	0.005	0.004	0.005	0.004	0.004	0.003	0.005	0.005	0.004	0.005
Ca	0.796	0.814	0.684	0.784	0.915	0.916	0.838	0.744	0.820	0.884
K	0.000	0.000	0.000	0.000	0.000	0.000	0.000	0.000	0.000	0.000
Na	0.017	0.016	0.015	0.017	0.025	0.026	0.017	0.018	0.019	0.022
%Enstatite	49.25	48.35	53.50	49.12	39.19	38.04	47.24	50.26	47.61	45.55
%Ferrosillite	9.93	9.66	11.75	10.25	12.57	13.05	9.38	11.55	10.10	9.01
%Wollastonite	40.82	41.98	34.75	40.63	48.24	48.91	43.38	38.20	42.29	45.44
%Jadeite	----------	----------	----------	----------	----------	----------	----------	----------	----------	----------
%Aegirine	----------	----------	----------	----------	----------	----------	----------	----------	----------	----------
%Quad	----------	----------	----------	----------	----------	----------	----------	----------	----------	----------
Classification according to Morimoto et al. (1988)										
Group	Quad	Quad	Quad	Quad	Quad	Quad	Quad	Quad	Quad	Quad
Classification	augite	augite	augite	augite	diopside	diopside	augite	augite	augite	diopside

Sample	ST-176	ST-176	ST-176	ST-176	ST-176	ST-176	ST-176	ST-176	ST-176	ST-176
Reference	1	2	3	4	5	6	7	9	10	12
SiO_2	54.86	54.61	51.62	51.57	52.15	52.35	52.24	52.39	52.20	52.01
TiO_2	0.24	0.31	0.82	0.57	0.79	0.61	0.59	0.77	0.65	0.83
Al_2O_3	1.32	1.55	3.08	2.93	2.94	3.60	2.73	2.89	2.86	3.07
Fe_2O_3	0.00	0.00	0.86	2.37	1.03	0.00	0.81	0.27	0.60	0.42
FeO	14.00	14.46	5.06	6.38	4.98	8.04	7.52	5.95	7.03	6.00
MnO	0.24	0.26	0.18	0.17	0.17	0.12	0.11	0.06	0.15	0.13
MgO	27.48	28.03	14.98	16.09	15.54	16.25	16.88	15.28	17.41	15.09
CaO	1.13	0.59	22.57	19.88	22.54	18.63	18.63	22.49	18.28	21.99
K_2O	0.01	0.00	0.00	0.01	0.01	0.02	0.00	0.00	0.01	0.00
Na_2O	0.01	0.00	0.35	0.31	0.28	0.45	0.30	0.27	0.29	0.36
ZnO	0.00	0.00	0.00	0.00	0.00	0.00	0.00	0.00	0.00	0.00
Cr_2O_3	0.15	0.17	0.38	0.74	0.31	0.45	0.46	0.40	0.47	0.42
Total	99.46	99.99	99.89	101.03	100.74	100.51	100.26	100.77	99.93	100.32
Number of ions on the base of 6 oxygens normalized for 4 cations										
Si	1.980	1.958	1.905	1.889	1.907	1.916	1.918	1.917	1.916	1.912
Al^{IV}	0.020	0.042	0.095	0.111	0.093	0.084	0.082	0.083	0.084	0.088
$Fe^{3+\ IV}$	0.000	0.000	0.000	0.000	0.000	0.000	0.000	0.000	0.000	0.000
Al^{VI}	0.036	0.024	0.039	0.016	0.033	0.071	0.036	0.042	0.039	0.045
$Fe^{3+\ VI}$	0.000	0.000	0.024	0.065	0.028	0.000	0.022	0.007	0.017	0.012
Ti	0.007	0.008	0.023	0.016	0.022	0.017	0.016	0.021	0.018	0.023
Cr	0.004	0.005	0.011	0.021	0.009	0.013	0.013	0.012	0.014	0.012
Zn	0.000	0.000	0.000	0.000	0.000	0.000	0.000	0.000	0.000	0.000
Mg	1.478	1.499	0.824	0.879	0.847	0.887	0.924	0.834	0.953	0.827
Fe^{2+}	0.423	0.434	0.156	0.195	0.152	0.246	0.231	0.182	0.216	0.186
Mn	0.007	0.008	0.006	0.005	0.005	0.004	0.004	0.002	0.005	0.004
Ca	0.044	0.023	0.892	0.780	0.883	0.730	0.733	0.882	0.719	0.866
K	0.000	0.000	0.000	0.000	0.001	0.001	0.000	0.000	0.000	0.000
Na	0.001	0.000	0.025	0.022	0.020	0.032	0.021	0.019	0.021	0.026
%Enstatite	75.73	76.36	43.32	45.65	44.22	47.49	48.27	43.73	49.91	43.65
%Ferrosillite	22.02	22.49	9.76	13.81	9.70	13.38	13.43	10.03	12.42	10.66
%Wollastonite	2.25	1.15	46.92	40.54	46.08	39.13	38.30	46.24	37.67	45.70
%Jadeite	----------	----------	----------	----------	----------	----------	----------	----------	----------	----------
%Aegirine	----------	----------	----------	----------	----------	----------	----------	----------	----------	----------
%Quad	----------	----------	----------	----------	----------	----------	----------	----------	----------	----------
Classification according to Morimoto et al. (1988)										
Group	Quad	Quad	Quad	Quad	Quad	Quad	Quad	Quad	Quad	Quad
Classification	enstatite	enstatite	diopside	augite	diopside	augite	augite	diopside	augite	diopside

Sample	ST-176	ST-176	ST-176	ST-176	ST-176	ST-176	ST-176	ST-176
Reference	13	14	15	16	17	18	19	20
SiO_2	55.28	52.21	54.95	54.80	52.54	51.07	54.65	52.11
TiO_2	0.21	0.80	0.63	0.17	0.70	0.79	0.17	0.67
Al_2O_3	1.46	2.90	1.36	1.77	2.79	3.05	2.09	3.20
Fe_2O_3	0.00	0.08	0.00	0.00	0.96	2.74	0.00	0.36
FeO	14.27	6.40	15.00	13.58	7.35	5.12	15.70	6.68
MnO	0.23	0.12	0.23	0.09	0.12	0.10	0.18	0.05
MgO	27.32	16.03	26.91	26.72	18.21	15.12	25.82	16.24
CaO	1.25	20.81	1.18	3.08	17.33	21.99	1.72	20.06
K_2O	0.01	0.00	0.00	0.01	0.02	0.01	0.01	0.02
Na_2O	0.01	0.30	0.03	0.03	0.27	0.30	0.02	0.32
ZnO	0.00	0.00	0.00	0.00	0.00	0.00	0.00	0.00
Cr_2O_3	0.19	0.39	0.17	0.18	0.29	0.66	0.27	0.39
Total	100.25	100.05	100.44	100.42	100.58	100.94	100.62	100.09
Number of ions on the base of 6 oxygens normalized for 4 cations								
Si	1.982	1.919	1.974	1.961	1.914	1.876	1.968	1.914
Al^{IV}	0.018	0.081	0.026	0.039	0.086	0.124	0.032	0.086
$Fe^{3+\ IV}$	0.000	0.000	0.000	0.000	0.000	0.000	0.000	0.000
Al^{VI}	0.044	0.045	0.032	0.036	0.034	0.008	0.056	0.052
$Fe^{3+\ VI}$	0.000	0.002	0.000	0.000	0.026	0.076	0.000	0.010
Ti	0.006	0.022	0.017	0.004	0.019	0.022	0.005	0.018
Cr	0.005	0.011	0.005	0.005	0.008	0.019	0.008	0.011
Zn	0.000	0.000	0.000	0.000	0.000	0.000	0.000	0.000
Mg	1.460	0.878	1.441	1.425	0.989	0.828	1.386	0.889
Fe^{2+}	0.428	0.197	0.451	0.406	0.224	0.157	0.473	0.205
Mn	0.007	0.004	0.007	0.003	0.004	0.003	0.005	0.002
Ca	0.048	0.819	0.045	0.118	0.676	0.866	0.066	0.789
K	0.001	0.000	0.000	0.001	0.001	0.000	0.001	0.001
Na	0.001	0.021	0.002	0.002	0.019	0.022	0.001	0.023
%Enstatite	75.15	46.22	74.14	73.01	51.54	42.90	71.80	46.92
%Ferrosillite	22.38	10.66	23.54	20.95	13.22	12.23	24.77	11.43
%Wollastonite	2.47	43.12	2.33	6.05	35.24	44.86	3.43	41.65
%Jadeite	----------	----------	----------	----------	----------	----------	----------	----------
%Aegirine	----------	----------	----------	----------	----------	----------	----------	----------
%Quad	----------	----------	----------	----------	----------	----------	----------	----------
Classification according to Morimoto et al. (1988)								
Group	Quad	Quad	Quad	Quad	Quad	Quad	Quad	Quad
Classification	enstatite	augite	enstatite	pigeonite	augite	augite	enstatite	augite

III.3.2.2. Plagioclase

Sample	ST-161A	ST-161A	ST-161A	ST-161A	ST-161A	ST-161A	ST-161A	ST-161A	ST-161A	ST-161A
Reference	1	2	3	4	5	6	7	8	9	10
SiO_2	49.75	50.07	50.27	50.37	49.65	49.87	48.76	49.34	50.12	49.89
TiO_2	0.00	0.00	0.00	0.00	0.00	0.00	0.00	0.00	0.00	0.00
Al_2O_3	32.45	31.83	32.44	32.01	32.47	32.65	32.87	32.96	32.36	31.58
$Fe_2O_3^T$	0.23	0.24	0.16	0.29	0.21	0.21	0.21	0.19	0.20	0.36
MgO	0.00	0.00	0.00	0.00	0.00	0.00	0.00	0.00	0.00	0.00
CaO	14.69	14.79	14.13	14.46	14.53	14.64	15.25	14.79	14.34	14.58
Na_2O	2.45	2.50	2.75	2.56	2.35	2.47	2.17	2.24	2.55	2.41
K_2O	0.02	0.02	0.04	0.02	0.01	0.03	0.03	0.03	0.01	0.01
BaO	0.00	0.00	0.00	0.00	0.00	0.00	0.00	0.00	0.00	0.00
SrO	0.00	0.00	0.00	0.00	0.00	0.00	0.00	0.00	0.00	0.00
Total	99.59	99.45	99.79	99.70	99.22	99.87	99.29	99.53	99.59	98.82
Number of cations calculated based on 32 oxygen atoms										
Si	9.084	9.158	9.145	9.177	9.089	9.078	8.951	9.012	9.138	9.177
Ti	0.000	0.000	0.000	0.000	0.000	0.000	0.000	0.000	0.000	0.000
Al	6.983	6.861	6.956	6.874	7.006	7.003	7.111	7.096	6.952	6.845
Fe^{3+}	0.031	0.033	0.023	0.039	0.029	0.029	0.030	0.026	0.028	0.050
Mg	0.000	0.000	0.000	0.000	0.000	0.000	0.000	0.000	0.000	0.000
Ca	2.874	2.899	2.753	2.822	2.849	2.855	2.998	2.894	2.801	2.873
Na	0.866	0.886	0.969	0.905	0.834	0.873	0.772	0.792	0.903	0.858
K	0.006	0.005	0.009	0.004	0.003	0.007	0.007	0.006	0.003	0.003
Ba	0.000	0.000	0.000	0.000	0.000	0.000	0.000	0.000	0.000	0.000
Sr	0.000	0.000	0.000	0.000	0.000	0.000	0.000	0.000	0.000	0.000
Final terms										
An	76.72	76.49	73.80	75.63	77.29	76.45	79.38	78.40	75.56	76.95
Ab	23.13	23.38	25.96	24.26	22.62	23.38	20.44	21.44	24.36	22.97
Or	0.15	0.13	0.24	0.12	0.09	0.17	0.18	0.16	0.08	0.08

Sample	ST-161A	ST-161A	ST-161A	ST-161A	ST-161A	ST-161B	ST-161B	ST-161B	ST-161B	ST-161B
Reference	11	12	13	14	15	1	2	3	4	5
SiO_2	49.61	49.69	49.34	49.76	48.53	50.84	50.77	50.18	49.69	49.55
TiO_2	0.00	0.00	0.00	0.00	0.00	0.00	0.00	0.00	0.00	0.00
Al_2O_3	32.15	31.97	32.16	31.74	32.22	31.86	31.93	32.67	32.75	33.12
$Fe_2O_3^T$	0.36	0.27	0.32	0.26	0.34	0.19	0.23	0.25	0.21	0.20
MgO	0.00	0.00	0.00	0.00	0.00	0.00	0.00	0.00	0.00	0.00
CaO	14.96	14.85	15.16	14.86	15.87	13.99	14.05	14.58	14.92	15.24
Na_2O	2.28	2.41	2.21	2.35	1.87	2.89	2.77	2.47	2.28	2.21
K_2O	0.01	0.00	0.02	0.01	0.01	0.00	0.01	0.01	0.00	0.01
BaO	0.00	0.00	0.00	0.00	0.00	0.00	0.00	0.00	0.00	0.00
SrO	0.00	0.00	0.00	0.00	0.00	0.00	0.00	0.00	0.00	0.00
Total	99.38	99.19	99.20	98.98	98.84	99.77	99.75	100.16	99.85	100.32
Number of cations calculated based on 32 oxygen atoms										
Si	9.087	9.114	9.059	9.144	8.965	9.243	9.232	9.102	9.049	8.992
Ti	0.000	0.000	0.000	0.000	0.000	0.000	0.000	0.000	0.000	0.000
Al	6.939	6.912	6.959	6.875	7.015	6.827	6.843	6.984	7.030	7.083
Fe^{3+}	0.050	0.038	0.044	0.036	0.047	0.026	0.031	0.034	0.029	0.027
Mg	0.000	0.000	0.000	0.000	0.000	0.000	0.000	0.000	0.000	0.000
Ca	2.936	2.918	2.982	2.925	3.140	2.725	2.737	2.833	2.911	2.963
Na	0.809	0.857	0.785	0.838	0.670	1.017	0.977	0.869	0.806	0.776
K	0.003	0.001	0.004	0.002	0.002	0.000	0.001	0.001	0.000	0.002
Ba	0.000	0.000	0.000	0.000	0.000	0.000	0.000	0.000	0.000	0.000
Sr	0.000	0.000	0.000	0.000	0.000	0.000	0.000	0.000	0.000	0.000
Final terms										
An	78.33	77.28	79.07	77.70	82.38	72.82	73.68	76.50	78.31	79.20
Ab	21.59	22.70	20.81	22.25	17.58	27.18	26.28	23.46	21.69	20.74
Or	0.07	0.02	0.12	0.04	0.04	0.00	0.04	0.04	0.00	0.06

Sample	ST-161B	ST-161B	ST-161B	ST-161B	ST-161B	ST-161B	ST-161B	ST-162	ST-162	ST-162
Reference	6	7	8	9	10	11	12	1	2	3
SiO_2	49.36	49.24	49.17	49.64	48.82	49.52	49.72	49.20	49.70	48.16
TiO_2	0.00	0.00	0.00	0.00	0.00	0.00	0.00	0.00	0.00	0.00
Al_2O_3	32.74	32.77	32.45	32.71	33.20	32.71	32.63	31.85	31.29	32.78
$Fe_2O_3^T$	0.26	0.22	0.21	0.13	0.20	0.15	0.15	0.20	0.30	0.18
MgO	0.00	0.00	0.00	0.00	0.00	0.00	0.00	0.00	0.00	0.00
CaO	14.87	15.30	15.18	14.90	15.38	15.05	14.73	15.70	14.62	15.96
Na_2O	2.32	2.22	2.22	2.29	1.93	2.28	2.28	1.92	2.52	1.93
K_2O	0.00	0.01	0.00	0.00	0.00	0.00	0.00	0.03	0.02	0.03
BaO	0.00	0.00	0.00	0.00	0.00	0.00	0.00	0.00	0.00	0.00
SrO	0.00	0.00	0.00	0.00	0.00	0.00	0.00	0.00	0.00	0.00
Total	99.56	99.76	99.22	99.67	99.53	99.72	99.51	98.89	98.46	99.04
Number of cations calculated based on 32 oxygen atoms										
Si	9.021	8.994	9.024	9.055	8.932	9.036	9.077	9.068	9.184	8.884
Ti	0.000	0.000	0.000	0.000	0.000	0.000	0.000	0.000	0.000	0.000
Al	7.053	7.053	7.020	7.031	7.158	7.034	7.021	6.917	6.814	7.127
Fe^{3+}	0.036	0.031	0.029	0.018	0.028	0.021	0.021	0.028	0.041	0.025
Mg	0.000	0.000	0.000	0.000	0.000	0.000	0.000	0.000	0.000	0.000
Ca	2.912	2.994	2.984	2.911	3.014	2.942	2.880	3.101	2.895	3.154
Na	0.823	0.785	0.790	0.810	0.686	0.807	0.807	0.685	0.904	0.690
K	0.000	0.002	0.000	0.000	0.000	0.000	0.000	0.007	0.005	0.008
Ba	0.000	0.000	0.000	0.000	0.000	0.000	0.000	0.000	0.000	0.000
Sr	0.000	0.000	0.000	0.000	0.000	0.000	0.000	0.000	0.000	0.000
Final terms										
An	77.96	79.17	79.07	78.24	81.46	78.46	78.11	81.77	76.10	81.89
Ab	22.04	20.77	20.93	21.76	18.53	21.53	21.89	18.06	23.76	17.91
Or	0.00	0.06	0.00	0.00	0.01	0.01	0.00	0.17	0.14	0.20

Sample	ST-162	ST-162	ST-162	ST-162	ST-162	ST-162	ST-162	ST-162	ST-162	ST-162
Reference	4	5	6	7	8	9	10	11	12	13
SiO_2	49.41	49.31	49.44	48.98	49.48	49.41	49.37	49.39	49.49	48.58
TiO_2	0.00	0.00	0.00	0.00	0.00	0.00	0.00	0.00	0.00	0.00
Al_2O_3	32.45	33.09	33.04	32.88	32.55	32.68	32.59	32.67	32.62	32.46
$Fe_2O_3^T$	0.22	0.21	0.31	0.24	0.24	0.11	0.28	0.24	0.11	0.14
MgO	0.00	0.00	0.00	0.00	0.00	0.00	0.00	0.00	0.00	0.00
CaO	15.13	15.23	15.46	15.45	15.25	15.42	15.20	15.53	15.20	15.23
Na_2O	2.28	2.24	2.16	2.08	2.23	2.31	2.33	2.24	2.33	2.03
K_2O	0.03	0.01	0.02	0.02	0.01	0.02	0.02	0.00	0.03	0.02
BaO	0.00	0.00	0.00	0.00	0.00	0.00	0.00	0.00	0.00	0.00
SrO	0.00	0.00	0.00	0.00	0.00	0.00	0.00	0.00	0.00	0.00
Total	99.52	100.08	100.43	99.65	99.76	99.95	99.79	100.06	99.78	98.46
Number of cations calculated based on 32 oxygen atoms										
Si	9.042	8.973	8.974	8.959	9.033	9.010	9.017	9.000	9.033	8.986
Ti	0.000	0.000	0.000	0.000	0.000	0.000	0.000	0.000	0.000	0.000
Al	6.998	7.097	7.067	7.089	7.004	7.023	7.013	7.017	7.016	7.077
Fe^{3+}	0.030	0.028	0.042	0.033	0.033	0.015	0.039	0.032	0.015	0.019
Mg	0.000	0.000	0.000	0.000	0.000	0.000	0.000	0.000	0.000	0.000
Ca	2.965	2.970	3.007	3.028	2.983	3.012	2.974	3.032	2.972	3.017
Na	0.810	0.789	0.760	0.738	0.789	0.817	0.826	0.790	0.826	0.728
K	0.006	0.002	0.003	0.005	0.002	0.003	0.004	0.000	0.006	0.004
Ba	0.000	0.000	0.000	0.000	0.000	0.000	0.000	0.000	0.000	0.000
Sr	0.000	0.000	0.000	0.000	0.000	0.000	0.000	0.000	0.000	0.000
Final terms										
An	78.42	78.96	79.76	80.30	79.05	78.59	78.17	79.34	78.13	80.48
Ab	21.42	20.99	20.15	19.57	20.90	21.32	21.71	20.66	21.71	19.41
Or	0.16	0.05	0.09	0.12	0.05	0.09	0.12	0.00	0.16	0.11

Sample	ST-162	ST-162	ST-162	ST-162	ST-162	ST-162	ST-162	ST-162	ST-162	ST-162
Reference	14	15	16	17	18	19	20	21	22	23
SiO_2	49.10	49.48	49.69	49.62	50.06	49.83	48.82	48.45	48.97	48.96
TiO_2	0.00	0.00	0.00	0.00	0.00	0.00	0.00	0.00	0.00	0.00
Al_2O_3	32.21	32.50	32.09	33.17	32.30	32.75	32.83	32.90	33.09	33.63
$Fe_2O_3^T$	0.23	0.28	0.27	0.20	0.22	0.22	0.19	0.17	0.21	0.30
MgO	0.00	0.00	0.00	0.00	0.00	0.00	0.00	0.00	0.00	0.00
CaO	15.22	14.74	14.36	15.08	14.33	14.94	15.26	15.24	15.11	15.41
Na_2O	2.23	2.18	2.40	1.99	2.41	2.29	2.31	1.92	2.15	1.95
K_2O	0.02	0.01	0.05	0.02	0.02	0.03	0.00	0.03	0.01	0.01
BaO	0.00	0.00	0.00	0.00	0.00	0.00	0.00	0.00	0.00	0.00
SrO	0.00	0.00	0.00	0.00	0.00	0.00	0.00	0.00	0.00	0.00
Total	99.01	99.19	98.85	100.09	99.34	100.04	99.42	98.71	99.55	100.26
Number of cations calculated based on 32 oxygen atoms										
Si	9.035	9.066	9.131	9.012	9.145	9.059	8.953	8.939	8.957	8.896
Ti	0.000	0.000	0.000	0.000	0.000	0.000	0.000	0.000	0.000	0.000
Al	6.986	7.019	6.948	7.099	6.953	7.016	7.096	7.152	7.132	7.201
Fe^{3+}	0.032	0.039	0.038	0.027	0.030	0.029	0.026	0.023	0.029	0.041
Mg	0.000	0.000	0.000	0.000	0.000	0.000	0.000	0.000	0.000	0.000
Ca	3.000	2.893	2.827	2.935	2.805	2.909	2.999	3.012	2.961	2.999
Na	0.796	0.775	0.853	0.701	0.855	0.806	0.820	0.688	0.763	0.687
K	0.005	0.003	0.011	0.004	0.004	0.006	0.001	0.008	0.003	0.003
Ba	0.000	0.000	0.000	0.000	0.000	0.000	0.000	0.000	0.000	0.000
Sr	0.000	0.000	0.000	0.000	0.000	0.000	0.000	0.000	0.000	0.000
Final terms										
An	78.93	78.80	76.58	80.62	76.56	78.18	78.51	81.23	79.45	81.31
Ab	20.94	21.11	23.11	19.27	23.33	21.65	21.46	18.55	20.46	18.61
Or	0.14	0.09	0.31	0.11	0.11	0.16	0.02	0.22	0.09	0.08

Sample	ST-163	ST-163	ST-163	ST-163	ST-163	ST-163	ST-163	ST-163	ST-163	ST-163
Reference	1	2	3	4	5	6	7	8	9	10
SiO_2	53.13	53.28	51.25	53.24	52.99	53.21	52.72	52.53	52.58	52.81
TiO_2	0.00	0.00	0.00	0.00	0.00	0.00	0.00	0.00	0.00	0.00
Al_2O_3	30.11	30.16	31.19	30.22	29.77	30.09	30.23	30.65	30.47	30.67
$Fe_2O_3^T$	0.20	0.27	0.35	0.25	0.28	0.16	0.28	0.22	0.23	0.20
MgO	0.00	0.00	0.00	0.00	0.00	0.00	0.00	0.00	0.00	0.00
CaO	11.99	12.22	13.67	12.38	12.26	12.28	12.50	12.78	12.74	12.95
Na_2O	3.92	3.83	3.14	3.83	3.81	3.86	3.72	3.71	3.65	3.71
K_2O	0.04	0.02	0.02	0.02	0.04	0.04	0.05	0.01	0.01	0.01
BaO	0.00	0.00	0.00	0.00	0.00	0.00	0.00	0.00	0.00	0.00
SrO	0.00	0.00	0.00	0.00	0.00	0.00	0.00	0.00	0.00	0.00
Total	99.39	99.78	99.61	99.94	99.13	99.63	99.49	99.90	99.68	100.35
Number of cations calculated based on 32 oxygen atoms										
Si	9.638	9.633	9.333	9.616	9.647	9.635	9.573	9.509	9.534	9.519
Ti	0.000	0.000	0.000	0.000	0.000	0.000	0.000	0.000	0.000	0.000
Al	6.438	6.426	6.694	6.433	6.387	6.422	6.470	6.538	6.511	6.514
Fe^{3+}	0.027	0.037	0.048	0.034	0.038	0.022	0.039	0.031	0.031	0.027
Mg	0.000	0.000	0.000	0.000	0.000	0.000	0.000	0.000	0.000	0.000
Ca	2.331	2.366	2.666	2.396	2.392	2.382	2.431	2.479	2.475	2.500
Na	1.380	1.342	1.107	1.341	1.344	1.356	1.308	1.301	1.283	1.297
K	0.009	0.005	0.006	0.003	0.008	0.008	0.011	0.002	0.003	0.002
Ba	0.000	0.000	0.000	0.000	0.000	0.000	0.000	0.000	0.000	0.000
Sr	0.000	0.000	0.000	0.000	0.000	0.000	0.000	0.000	0.000	0.000
Final terms										
An	62.65	63.73	70.56	64.05	63.88	63.59	64.84	65.55	65.81	65.81
Ab	37.09	36.14	29.29	35.86	35.89	36.19	34.88	34.39	34.11	34.13
Or	0.26	0.13	0.15	0.09	0.22	0.22	0.28	0.06	0.07	0.05

Sample	ST-163	ST-163	ST-163	ST-163	ST-164	ST-164	ST-164	ST-164	ST-164	ST-164
Reference	11	12	14	15	25	26	27	28	29	30
SiO_2	53.97	53.96	53.63	53.55	49.32	48.99	48.61	50.14	48.84	47.26
TiO_2	0.00	0.00	0.00	0.00	0.00	0.00	0.00	0.00	0.00	0.00
Al_2O_3	29.24	30.09	30.04	29.76	32.50	32.87	33.04	31.85	32.71	34.36
$Fe_2O_3^T$	0.39	0.26	0.25	0.31	0.38	0.40	0.34	0.39	0.34	0.32
MgO	0.00	0.00	0.00	0.00	0.00	0.00	0.00	0.00	0.00	0.00
CaO	11.86	12.32	12.19	12.05	15.09	15.45	15.56	14.43	15.42	16.64
Na_2O	3.98	3.95	3.98	3.95	2.30	1.97	1.97	2.55	2.10	1.23
K_2O	0.02	0.02	0.01	0.01	0.02	0.03	0.03	0.03	0.03	0.01
BaO	0.00	0.00	0.00	0.00	0.00	0.00	0.00	0.00	0.00	0.00
SrO	0.00	0.00	0.00	0.00	0.00	0.00	0.00	0.00	0.00	0.00
Total	99.47	100.59	100.10	99.62	99.61	99.70	99.54	99.38	99.43	99.82
Number of cations calculated based on 32 oxygen atoms										
Si	9.776	9.677	9.664	9.693	9.022	8.958	8.908	9.171	8.959	8.660
Ti	0.000	0.000	0.000	0.000	0.000	0.000	0.000	0.000	0.000	0.000
Al	6.243	6.359	6.380	6.347	7.007	7.083	7.137	6.864	7.071	7.420
Fe^{3+}	0.053	0.036	0.033	0.042	0.052	0.054	0.047	0.054	0.047	0.044
Mg	0.000	0.000	0.000	0.000	0.000	0.000	0.000	0.000	0.000	0.000
Ca	2.302	2.367	2.354	2.337	2.958	3.026	3.055	2.826	3.030	3.266
Na	1.398	1.372	1.390	1.385	0.815	0.698	0.700	0.902	0.745	0.436
K	0.005	0.004	0.003	0.003	0.005	0.006	0.006	0.007	0.006	0.003
Ba	0.000	0.000	0.000	0.000	0.000	0.000	0.000	0.000	0.000	0.000
Sr	0.000	0.000	0.000	0.000	0.000	0.000	0.000	0.000	0.000	0.000
Final terms										
An	62.13	63.24	62.81	62.73	78.29	81.12	81.24	75.67	80.14	88.17
Ab	37.74	36.66	37.10	37.18	21.58	18.71	18.60	24.16	19.71	11.76
Or	0.13	0.10	0.09	0.09	0.12	0.17	0.16	0.17	0.15	0.08

Sample	ST-164	ST-164	ST-164	ST-164	ST-164	ST-164	ST-164	ST-164	ST-164	ST-165
Reference	31	32	33	34	35	36	37	38	39	1
SiO_2	48.02	48.86	46.16	49.78	49.06	48.65	47.87	47.71	49.35	46.65
TiO_2	0.00	0.00	0.00	0.00	0.00	0.00	0.00	0.00	0.00	0.00
Al_2O_3	33.07	32.68	34.18	32.10	32.34	32.58	33.23	33.31	32.29	34.29
$Fe_2O_3^T$	0.31	0.33	0.33	0.31	0.37	0.31	0.41	0.25	0.30	0.14
MgO	0.00	0.00	0.00	0.00	0.00	0.00	0.00	0.00	0.00	0.00
CaO	15.72	14.78	17.09	14.80	15.17	15.28	16.20	16.40	15.14	17.09
Na_2O	1.86	2.04	1.15	2.46	2.13	2.12	1.64	1.66	2.27	1.15
K_2O	0.01	0.02	0.00	0.02	0.03	0.01	0.03	0.02	0.02	0.07
BaO	0.00	0.00	0.00	0.00	0.00	0.00	0.00	0.00	0.00	0.00
SrO	0.00	0.00	0.00	0.00	0.00	0.00	0.00	0.00	0.00	0.00
Total	98.98	98.71	98.91	99.47	99.09	98.94	99.38	99.35	99.35	99.39
Number of cations calculated based on 32 oxygen atoms										
Si	8.857	9.003	8.561	9.108	9.021	8.964	8.808	8.785	9.048	8.602
Ti	0.000	0.000	0.000	0.000	0.000	0.000	0.000	0.000	0.000	0.000
Al	7.188	7.096	7.470	6.921	7.007	7.075	7.206	7.229	6.976	7.451
Fe^{3+}	0.044	0.046	0.047	0.043	0.052	0.043	0.057	0.035	0.041	0.020
Mg	0.000	0.000	0.000	0.000	0.000	0.000	0.000	0.000	0.000	0.000
Ca	3.106	2.916	3.395	2.900	2.987	3.016	3.194	3.235	2.973	3.376
Na	0.665	0.728	0.412	0.872	0.758	0.756	0.586	0.594	0.806	0.413
K	0.001	0.004	0.000	0.005	0.006	0.003	0.007	0.004	0.004	0.015
Ba	0.000	0.000	0.000	0.000	0.000	0.000	0.000	0.000	0.000	0.000
Sr	0.000	0.000	0.000	0.000	0.000	0.000	0.000	0.000	0.000	0.000
Final terms										
An	82.34	79.92	89.16	76.78	79.63	79.90	84.36	84.39	78.59	88.75
Ab	17.63	19.96	10.83	23.08	20.21	20.02	15.47	15.50	21.31	10.85
Or	0.03	0.12	0.01	0.14	0.16	0.08	0.17	0.11	0.11	0.40

Sample	ST-165	ST-165	ST-165	ST-165	ST-165	ST-165	ST-165	ST-165	ST-165	ST-165
Reference	2	3	4	12	13	14	15	16	17	18
SiO_2	48.47	48.89	48.04	46.25	48.09	47.58	48.45	46.97	48.50	48.57
TiO_2	0.00	0.00	0.00	0.00	0.00	0.00	0.00	0.00	0.00	0.00
Al_2O_3	33.21	32.72	33.31	33.98	33.51	33.51	32.91	34.05	33.33	33.29
$Fe_2O_3^T$	0.14	0.26	0.14	0.13	0.15	0.10	0.33	0.17	0.27	0.29
MgO	0.00	0.00	0.00	0.00	0.00	0.00	0.00	0.00	0.00	0.00
CaO	15.69	15.29	15.93	16.95	16.12	16.19	15.23	16.46	15.92	15.51
Na_2O	1.86	2.27	1.79	1.19	1.71	1.69	1.79	1.44	1.75	1.87
K_2O	0.01	0.00	0.02	0.03	0.02	0.02	0.04	0.00	0.01	0.02
BaO	0.00	0.00	0.00	0.00	0.00	0.00	0.00	0.00	0.00	0.00
SrO	0.00	0.00	0.00	0.00	0.00	0.00	0.00	0.00	0.00	0.00
Total	99.37	99.43	99.22	98.53	99.59	99.09	98.75	99.09	99.79	99.54
Number of cations calculated based on 32 oxygen atoms										
Si	8.893	8.965	8.838	8.602	8.818	8.776	8.934	8.670	8.869	8.894
Ti	0.000	0.000	0.000	0.000	0.000	0.000	0.000	0.000	0.000	0.000
Al	7.180	7.072	7.222	7.448	7.242	7.283	7.151	7.407	7.183	7.185
Fe^{3+}	0.019	0.036	0.020	0.019	0.021	0.014	0.046	0.023	0.037	0.040
Mg	0.000	0.000	0.000	0.000	0.000	0.000	0.000	0.000	0.000	0.000
Ca	3.084	3.005	3.139	3.378	3.166	3.199	3.009	3.256	3.119	3.043
Na	0.660	0.806	0.639	0.429	0.608	0.603	0.641	0.516	0.621	0.662
K	0.002	0.001	0.005	0.007	0.004	0.005	0.010	0.001	0.003	0.005
Ba	0.000	0.000	0.000	0.000	0.000	0.000	0.000	0.000	0.000	0.000
Sr	0.000	0.000	0.000	0.000	0.000	0.000	0.000	0.000	0.000	0.000
Final terms										
An	82.33	78.83	82.98	88.58	83.81	84.03	82.21	86.29	83.31	82.02
Ab	17.62	21.15	16.89	11.24	16.09	15.85	17.52	13.69	16.60	17.86
Or	0.06	0.02	0.13	0.17	0.10	0.12	0.27	0.02	0.09	0.13

Sample	ST-165	ST-167	ST-167	ST-167	ST-167	ST-167	ST-167	ST-167	ST-167	ST-167
Reference	19	1	2	3	4	5	6	7	8	9
SiO_2	47.94	49.67	49.59	50.10	50.33	49.42	50.29	51.07	50.32	50.62
TiO_2	0.00	0.00	0.01	0.12	0.02	0.05	0.03	0.01	0.02	0.03
Al_2O_3	33.29	31.78	31.46	31.16	31.11	31.56	31.14	30.89	31.10	31.32
$Fe_2O_3^T$	0.18	0.25	0.27	0.31	0.26	0.24	0.27	0.23	0.26	0.23
MgO	0.00	0.02	0.03	0.02	0.03	0.04	0.03	0.01	0.00	0.04
CaO	15.93	16.29	16.38	15.69	15.88	16.26	15.82	15.49	15.67	15.99
Na_2O	1.76	2.02	2.03	2.40	2.28	2.07	2.24	2.48	2.41	2.21
K_2O	0.00	0.04	0.04	0.03	0.04	0.06	0.04	0.05	0.04	0.06
BaO	0.00	0.02	0.00	0.00	0.01	0.01	0.00	0.00	0.02	0.03
SrO	0.00	0.00	0.00	0.00	0.00	0.00	0.00	0.00	0.00	0.00
Total	99.11	100.07	99.81	99.84	99.96	99.71	99.86	100.23	99.83	100.55
Number of cations calculated based on 32 oxygen atoms										
Si	8.832	9.069	9.083	9.161	9.189	9.062	9.187	9.283	9.197	9.188
Ti	0.000	0.000	0.002	0.017	0.002	0.007	0.004	0.001	0.002	0.004
Al	7.227	6.838	6.791	6.715	6.694	6.820	6.704	6.616	6.699	6.700
Fe^{3+}	0.025	0.034	0.038	0.043	0.036	0.034	0.037	0.032	0.036	0.031
Mg	0.000	0.004	0.007	0.006	0.009	0.011	0.007	0.003	0.000	0.011
Ca	3.144	3.186	3.215	3.073	3.105	3.195	3.095	3.016	3.068	3.110
Na	0.629	0.713	0.719	0.850	0.805	0.736	0.795	0.873	0.854	0.779
K	0.001	0.009	0.010	0.007	0.010	0.013	0.009	0.012	0.008	0.015
Ba	0.000	0.001	0.000	0.000	0.001	0.001	0.000	0.000	0.001	0.002
Sr	0.000	0.000	0.000	0.000	0.000	0.000	0.000	0.000	0.000	0.000
Final terms										
An	83.32	81.51	81.51	78.19	79.21	81.01	79.38	77.31	78.07	79.66
Ab	16.66	18.25	18.24	21.64	20.54	18.67	20.38	22.38	21.72	19.96
Or	0.02	0.24	0.25	0.17	0.24	0.33	0.23	0.31	0.21	0.38

Sample	ST-167	ST-167	ST-167	ST-167	ST-167	ST-167	ST-167	ST-167	ST-167	ST-167
Reference	10	11	12	13	14	15	16	17	18	19
SiO_2	50.26	50.06	49.93	49.90	49.56	50.25	50.68	52.82	53.95	44.97
TiO_2	0.10	0.04	0.01	0.03	0.01	0.00	0.00	0.29	0.21	1.27
Al_2O_3	31.00	30.97	31.66	31.26	31.86	31.27	31.20	28.97	28.27	26.16
$Fe_2O_3^T$	0.32	0.26	0.28	0.26	0.29	0.38	0.26	0.71	0.71	5.76
MgO	0.03	0.05	0.08	0.01	0.02	0.41	0.03	0.13	0.09	2.04
CaO	15.49	15.61	16.46	15.87	16.33	16.05	15.81	13.07	12.19	17.65
Na_2O	2.47	2.42	1.88	2.37	2.05	2.28	2.36	3.22	3.73	2.87
K_2O	0.01	0.03	0.06	0.02	0.02	0.03	0.01	0.46	0.58	0.44
BaO	0.00	0.00	0.01	0.00	0.02	0.04	0.00	0.18	0.16	0.14
SrO	0.00	0.00	0.00	0.00	0.00	0.00	0.00	0.00	0.00	0.00
Total	99.67	99.44	100.37	99.71	100.15	100.72	100.34	99.85	99.88	101.30
Number of cations calculated based on 32 oxygen atoms										
Si	9.198	9.187	9.090	9.140	9.046	9.123	9.210	9.616	9.797	8.482
Ti	0.013	0.005	0.001	0.004	0.001	0.000	0.000	0.039	0.029	0.180
Al	6.685	6.698	6.793	6.747	6.854	6.691	6.682	6.216	6.049	5.815
Fe^{3+}	0.044	0.036	0.039	0.035	0.040	0.052	0.036	0.097	0.096	0.817
Mg	0.007	0.013	0.022	0.003	0.006	0.112	0.008	0.035	0.025	0.574
Ca	3.036	3.069	3.210	3.113	3.193	3.121	3.078	2.550	2.370	3.566
Na	0.876	0.860	0.665	0.842	0.724	0.803	0.830	1.138	1.313	1.048
K	0.002	0.007	0.013	0.004	0.006	0.006	0.003	0.107	0.135	0.106
Ba	0.000	0.000	0.001	0.000	0.001	0.003	0.000	0.013	0.012	0.010
Sr	0.000	0.000	0.000	0.000	0.000	0.000	0.000	0.000	0.000	0.000
Final terms										
An	77.58	77.99	82.57	78.65	81.41	79.41	78.71	67.20	62.08	75.55
Ab	22.38	21.85	17.10	21.26	18.45	20.43	21.22	29.98	34.39	22.19
Or	0.04	0.17	0.33	0.09	0.14	0.16	0.07	2.82	3.53	2.25

Sample	ST-167	ST-167	ST-167	ST-167	ST-167	ST-167	ST-168	ST-168	ST-168	ST-168
Reference	20	21	22	23	24	25	10	13	14	15
SiO_2	50.00	49.87	49.96	49.41	48.50	49.92	48.66	49.40	49.04	49.68
TiO_2	0.02	0.01	0.00	0.01	0.02	0.05	0.00	0.00	0.00	0.00
Al_2O_3	31.12	31.07	31.26	31.54	31.51	30.76	32.82	32.18	32.28	32.21
$Fe_2O_3^T$	0.28	0.30	0.33	0.31	0.26	0.58	0.26	0.24	0.19	0.15
MgO	0.00	0.03	0.02	0.04	0.02	0.42	0.00	0.00	0.00	0.00
CaO	15.66	16.35	15.91	16.13	16.01	15.80	15.39	14.77	15.00	14.77
Na_2O	2.36	1.85	2.29	2.14	1.94	2.41	2.15	2.40	2.32	2.47
K_2O	0.04	0.09	0.03	0.06	0.02	0.02	0.02	0.01	0.00	0.01
BaO	0.00	0.00	0.00	0.00	0.01	0.00	0.00	0.00	0.00	0.00
SrO	0.00	0.00	0.00	0.00	0.00	0.00	0.00	0.00	0.00	0.00
Total	99.46	99.57	99.80	99.63	98.28	99.95	99.29	98.99	98.83	99.30
Number of cations calculated based on 32 oxygen atoms										
Si	9.173	9.149	9.143	9.067	9.018	9.136	8.938	9.079	9.035	9.100
Ti	0.002	0.002	0.000	0.001	0.002	0.007	0.000	0.000	0.000	0.000
Al	6.727	6.717	6.742	6.821	6.905	6.634	7.105	6.970	7.010	6.953
Fe^{3+}	0.038	0.041	0.045	0.042	0.037	0.080	0.035	0.033	0.027	0.021
Mg	0.000	0.009	0.007	0.012	0.004	0.116	0.000	0.000	0.000	0.000
Ca	3.077	3.214	3.119	3.170	3.189	3.098	3.028	2.909	2.960	2.899
Na	0.838	0.658	0.813	0.761	0.700	0.857	0.764	0.854	0.829	0.879
K	0.008	0.022	0.006	0.013	0.006	0.004	0.004	0.003	0.000	0.003
Ba	0.000	0.000	0.000	0.000	0.001	0.000	0.000	0.000	0.000	0.000
Sr	0.000	0.000	0.000	0.000	0.000	0.000	0.000	0.000	0.000	0.000
Final terms										
An	78.44	82.54	79.21	80.38	81.87	78.27	79.76	77.25	78.11	76.69
Ab	21.35	16.90	20.64	19.29	17.98	21.64	20.12	22.67	21.89	23.24
Or	0.21	0.56	0.15	0.33	0.15	0.09	0.12	0.07	0.00	0.07

Sample	ST-168	ST-168	ST-168	ST-168	ST-168	ST-168	ST-168	ST-169	ST-169	ST-169
Reference	16	29	30	31	32	40	41	20	21	22
SiO_2	48.68	49.14	49.19	49.35	48.66	49.83	49.40	50.11	49.81	50.23
TiO_2	0.00	0.00	0.00	0.00	0.00	0.00	0.00	0.00	0.00	0.00
Al_2O_3	32.45	32.26	32.75	32.15	33.12	31.86	32.42	31.79	31.77	31.52
$Fe_2O_3^T$	0.17	0.28	0.27	0.27	0.18	0.21	0.27	0.28	0.31	0.32
MgO	0.00	0.00	0.00	0.00	0.00	0.00	0.00	0.00	0.00	0.00
CaO	15.27	14.96	15.29	14.78	15.62	14.36	14.56	14.70	14.47	14.37
Na_2O	2.23	2.27	2.26	2.29	1.97	2.51	2.30	2.78	2.84	2.59
K_2O	0.02	0.00	0.01	0.00	0.01	0.02	0.00	0.01	0.02	0.02
BaO	0.00	0.00	0.00	0.00	0.00	0.00	0.00	0.00	0.00	0.00
SrO	0.00	0.00	0.00	0.00	0.00	0.00	0.00	0.00	0.00	0.00
Total	98.82	98.92	99.77	98.84	99.56	98.78	98.95	99.67	99.22	99.04
Number of cations calculated based on 32 oxygen atoms										
Si	8.981	9.045	8.987	9.082	8.912	9.162	9.073	9.154	9.139	9.214
Ti	0.000	0.000	0.000	0.000	0.000	0.000	0.000	0.000	0.000	0.000
Al	7.056	6.997	7.051	6.972	7.149	6.903	7.016	6.844	6.871	6.813
Fe^{3+}	0.024	0.039	0.038	0.037	0.025	0.029	0.038	0.038	0.043	0.044
Mg	0.000	0.000	0.000	0.000	0.000	0.000	0.000	0.000	0.000	0.000
Ca	3.019	2.949	2.993	2.914	3.065	2.829	2.865	2.876	2.844	2.824
Na	0.796	0.811	0.802	0.818	0.699	0.893	0.818	0.985	1.010	0.921
K	0.004	0.000	0.001	0.000	0.002	0.004	0.000	0.001	0.005	0.004
Ba	0.000	0.000	0.000	0.000	0.000	0.000	0.000	0.000	0.000	0.000
Sr	0.000	0.000	0.000	0.000	0.000	0.000	0.000	0.000	0.000	0.000
Final terms										
An	79.05	78.43	78.84	78.07	81.38	75.92	77.79	74.46	73.69	75.33
Ab	20.84	21.57	21.12	21.93	18.57	23.96	22.21	25.50	26.17	24.57
Or	0.12	0.01	0.04	0.00	0.04	0.12	0.00	0.04	0.13	0.10

Sample	ST-169	ST-169	ST-169	ST-169	ST-169	ST-169	ST-169	ST-169	ST-169	ST-169
Reference	23	24	25	26	27	28	29	32	33	34
SiO_2	50.27	50.16	50.56	50.45	50.77	50.48	50.21	49.40	50.49	50.63
TiO_2	0.00	0.00	0.00	0.00	0.00	0.00	0.00	0.00	0.00	0.00
Al_2O_3	31.76	31.50	31.75	31.86	31.77	32.03	32.64	32.92	32.01	31.97
$Fe_2O_3^T$	0.33	0.44	0.39	0.38	0.32	0.33	0.27	0.28	0.30	0.25
MgO	0.00	0.00	0.00	0.00	0.00	0.00	0.00	0.00	0.00	0.00
CaO	13.96	14.01	13.86	13.99	13.91	13.86	14.74	15.24	14.42	14.06
Na_2O	2.47	2.51	2.69	2.56	2.68	2.55	2.38	2.17	2.68	2.80
K_2O	0.02	0.02	0.01	0.02	0.01	0.01	0.11	0.03	0.04	0.02
BaO	0.00	0.00	0.00	0.00	0.00	0.00	0.00	0.00	0.00	0.00
SrO	0.00	0.00	0.00	0.00	0.00	0.00	0.00	0.00	0.00	0.00
Total	98.80	98.64	99.26	99.25	99.46	99.26	100.35	100.04	99.92	99.74
Number of cations calculated based on 32 oxygen atoms										
Si	9.223	9.227	9.238	9.219	9.253	9.216	9.099	8.994	9.182	9.213
Ti	0.000	0.000	0.000	0.000	0.000	0.000	0.000	0.000	0.000	0.000
Al	6.867	6.829	6.836	6.861	6.824	6.891	6.970	7.064	6.859	6.855
Fe^{3+}	0.045	0.061	0.053	0.052	0.044	0.045	0.036	0.038	0.041	0.035
Mg	0.000	0.000	0.000	0.000	0.000	0.000	0.000	0.000	0.000	0.000
Ca	2.744	2.761	2.714	2.739	2.717	2.711	2.862	2.972	2.808	2.742
Na	0.879	0.894	0.951	0.906	0.947	0.903	0.838	0.766	0.943	0.987
K	0.004	0.005	0.002	0.004	0.002	0.003	0.026	0.007	0.008	0.006
Ba	0.000	0.000	0.000	0.000	0.000	0.000	0.000	0.000	0.000	0.000
Sr	0.000	0.000	0.000	0.000	0.000	0.000	0.000	0.000	0.000	0.000
Final terms										
An	75.66	75.43	74.01	75.05	74.11	74.97	76.82	79.36	74.69	73.41
Ab	24.23	24.44	25.94	24.83	25.84	24.95	22.48	20.44	25.09	26.44
Or	0.11	0.13	0.05	0.11	0.04	0.08	0.71	0.20	0.22	0.15

Sample	ST-173	ST-173	ST-173	ST-173	ST-173	ST-173	ST-173	ST-173	ST-173	ST-176
Reference	1	2	3	4	5	6	7	8	9	24
SiO_2	49.75	50.03	50.18	49.46	49.06	50.08	50.36	49.45	49.92	50.45
TiO_2	0.04	0.04	0.03	0.03	0.01	0.03	0.03	0.02	0.01	0.00
Al_2O_3	30.66	30.82	30.83	30.74	30.98	30.84	30.62	31.27	30.83	32.02
$Fe_2O_3^T$	0.18	0.16	0.24	0.28	0.27	0.20	0.26	0.18	0.18	0.19
MgO	0.02	0.04	0.05	0.00	0.12	0.01	0.04	0.01	0.04	0.00
CaO	15.53	15.44	15.61	15.74	15.92	15.48	15.51	15.92	15.56	15.02
Na_2O	2.47	2.51	2.26	2.35	2.17	2.41	2.45	2.21	2.48	2.71
K_2O	0.01	0.00	0.22	0.02	0.01	0.02	0.02	0.02	0.02	0.02
BaO	0.00	0.00	0.00	0.00	0.02	0.00	0.00	0.04	0.00	0.00
SrO	0.00	0.00	0.00	0.00	0.00	0.00	0.00	0.00	0.00	0.00
Total	98.65	99.04	99.41	98.62	98.55	99.06	99.30	99.11	99.03	100.41
Number of cations calculated based on 32 oxygen atoms										
Si	9.201	9.211	9.213	9.160	9.098	9.216	9.247	9.113	9.197	9.150
Ti	0.005	0.006	0.004	0.004	0.001	0.004	0.004	0.003	0.002	0.000
Al	6.682	6.686	6.670	6.710	6.771	6.688	6.627	6.791	6.693	6.842
Fe^{3+}	0.025	0.023	0.034	0.039	0.038	0.028	0.036	0.025	0.025	0.026
Mg	0.004	0.011	0.013	0.001	0.033	0.003	0.012	0.004	0.010	0.000
Ca	3.078	3.045	3.070	3.122	3.163	3.051	3.052	3.143	3.070	2.918
Na	0.887	0.896	0.804	0.845	0.780	0.859	0.874	0.788	0.886	0.954
K	0.002	0.001	0.052	0.006	0.003	0.004	0.005	0.004	0.004	0.004
Ba	0.000	0.000	0.000	0.000	0.001	0.000	0.000	0.003	0.000	0.000
Sr	0.000	0.000	0.000	0.000	0.000	0.000	0.000	0.000	0.000	0.000
Final terms										
An	77.59	77.25	78.19	78.60	80.15	77.96	77.64	79.88	77.52	75.28
Ab	22.36	22.73	20.47	21.26	19.77	21.94	22.23	20.02	22.36	24.61
Or	0.05	0.02	1.34	0.14	0.08	0.10	0.13	0.10	0.11	0.11

Sample	ST-176	ST-176	ST-176	ST-176	ST-176	ST-176	ST-176	ST-176	ST-176	ST-176
Reference	25	26	27	28	29	30	31	32	33	34
SiO_2	50.10	48.93	49.83	49.24	49.14	49.99	49.59	50.07	49.25	48.99
TiO_2	0.00	0.00	0.00	0.00	0.00	0.00	0.00	0.00	0.00	0.00
Al_2O_3	32.68	32.87	33.05	33.06	32.26	32.64	32.14	32.04	33.25	32.65
$Fe_2O_3^T$	0.24	0.36	0.19	0.32	0.33	0.29	0.42	0.25	0.37	0.36
MgO	0.00	0.00	0.00	0.00	0.00	0.00	0.00	0.00	0.00	0.00
CaO	14.99	15.53	15.33	15.93	15.07	14.88	14.89	14.63	15.31	15.23
Na_2O	2.32	2.20	2.19	1.98	2.39	2.38	2.48	2.46	2.07	2.09
K_2O	0.02	0.02	0.01	0.01	0.01	0.03	0.01	0.02	0.01	0.01
BaO	0.00	0.00	0.00	0.00	0.00	0.00	0.00	0.00	0.00	0.00
SrO	0.00	0.00	0.00	0.00	0.00	0.00	0.00	0.00	0.00	0.00
Total	100.35	99.90	100.59	100.53	99.19	100.20	99.53	99.46	100.25	99.33
Number of cations calculated based on 32 oxygen atoms										
Si	9.080	8.940	9.016	8.939	9.029	9.076	9.077	9.149	8.949	8.986
Ti	0.000	0.000	0.000	0.000	0.000	0.000	0.000	0.000	0.000	0.000
Al	6.981	7.077	7.047	7.073	6.986	6.983	6.933	6.900	7.121	7.057
Fe^{3+}	0.033	0.049	0.026	0.043	0.045	0.039	0.058	0.034	0.051	0.050
Mg	0.000	0.000	0.000	0.000	0.000	0.000	0.000	0.000	0.000	0.000
Ca	2.911	3.040	2.972	3.098	2.967	2.893	2.919	2.863	2.980	2.993
Na	0.816	0.779	0.767	0.697	0.850	0.839	0.879	0.870	0.729	0.744
K	0.003	0.004	0.003	0.001	0.003	0.006	0.003	0.004	0.001	0.002
Ba	0.000	0.000	0.000	0.000	0.000	0.000	0.000	0.000	0.000	0.000
Sr	0.000	0.000	0.000	0.000	0.000	0.000	0.000	0.000	0.000	0.000
Final terms										
An	78.04	79.52	79.42	81.61	77.68	77.41	76.80	76.60	80.32	80.04
Ab	21.87	20.37	20.50	18.36	22.24	22.44	23.12	23.29	19.65	19.89
Or	0.09	0.11	0.08	0.04	0.08	0.15	0.08	0.11	0.04	0.06

Sample	ST-176	ST-176
Reference	35	36
SiO_2	50.08	49.75
TiO_2	0.00	0.00
Al_2O_3	31.79	32.88
$Fe_2O_3^T$	0.30	0.28
MgO	0.00	0.00
CaO	14.60	15.13
Na_2O	2.51	2.31
K_2O	0.01	0.01
BaO	0.00	0.00
SrO	0.00	0.00
Total	99.29	100.36
Number of cations calculated based on 32 oxygen atoms		
Si	9.169	9.026
Ti	0.000	0.000
Al	6.859	7.029
Fe^{3+}	0.042	0.039
Mg	0.000	0.000
Ca	2.863	2.941
Na	0.889	0.812
K	0.003	0.002
Ba	0.000	0.000
Sr	0.000	0.000
Final terms		
An	76.24	78.31
Ab	23.68	21.64
Or	0.09	0.05

APPENDIX IV

CIPW NORM

IV - CIPW norm

The CIPW norm was developed by four petrologists Cross, Iddings, Pirsson and Washington (CIPW). The norm is a way of converting the chemical composition of an igneous rock to an ideal mineral composition, which calculates mineral composition as if the magma were anhydrous (water is simply treated as a separate phase) and at low pressure.

The CIPW norm was calculated using the SINCLAS (Standard Igneous Norm and Volcanic Rock Classification System) software (see Verma et al., 2002).

The following abbreviations are used in the tables: BSN – Basanite, TEP – Tephrite, MNP – Melanephelinite, PIC – Picrite, B – Basalt, TB – Trachybasalt, G – Gabbro.

IV.1. Santiago Alkaline lavas

IV.1.1. Monte das Vacas Formation

Sample	ST-1	ST-2	ST-16	ST-24	ST-52	ST-54
Rock type	BSN	TEP	BSN	BSN	BSN	BSN
Orthoclase	17.60	17.98	15.39	16.82	17.18	17.21
Albite	12.12	9.18	9.67	9.49	10.23	10.95
Anorthite	13.53	10.52	22.40	13.32	12.78	14.69
Leucite	0.00	0.00	0.00	0.00	0.00	0.00
Nepheline	11.49	15.70	8.45	12.80	13.79	12.19
Diopside	21.21	23.56	19.10	22.07	20.62	20.20
Olivine	10.09	9.36	13.21	11.00	10.31	10.22
Magnetite	4.72	4.75	3.00	4.95	4.75	4.74
Ilmenite	7.12	7.15	7.24	7.81	7.53	7.62
Apatite	2.11	1.80	1.53	1.74	2.80	2.18
Dicalcium silicate	0.00	0.00	0.00	0.00	0.00	0.00

IV.1.2. Assomada Formation

Sample	ST-13	ST-14	ST-18	ST-19	ST-20	ST-21	ST-22
Rock type	BSN	BSN	MNP	BSN	BSN	PIC	BSN
Orthoclase	4.76	5.58	0.00	9.62	11.02	2.81	16.00
Albite	18.04	18.71	0.00	8.32	6.82	0.55	11.56
Anorthite	20.90	21.18	8.58	20.46	19.16	16.86	14.12
Leucite	0.00	0.00	6.98	0.00	0.00	0.00	0.00
Nepheline	9.83	9.60	16.34	8.45	10.05	10.19	11.06
Diopside	21.10	20.11	16.65	23.17	24.01	33.76	21.87
Olivine	13.60	12.81	25.26	19.36	18.23	25.86	11.12
Magnetite	3.09	3.07	2.97	3.00	2.93	2.36	4.88
Ilmenite	7.24	7.46	6.76	6.30	6.34	6.70	7.66
Apatite	1.46	1.49	3.03	1.33	1.43	0.91	1.73
Dicalcium silicate	0.00	0.00	13.42	0.00	0.00	0.00	0.00

Sample Rock type	ST-23 MNP	ST-28 TEP	ST-29 TEP
Orthoclase	13.51	17.42	16.42
Albite	1.64	22.62	10.19
Anorthite	18.73	19.24	13.60
Leucite	0.00	0.00	0.00
Nepheline	12.94	4.24	13.42
Diopside	27.29	13.11	22.39
Olivine	14.48	9.73	9.70
Magnetite	2.98	4.14	4.68
Ilmenite	6.97	6.26	7.82
Apatite	1.46	3.25	1.77
Dicalcium silicate	0.00	0.00	0.00

IV.1.3. Upper Pico da Antónia Formation

Sample Rock type	ST-9 BSN	ST-10 MNP	ST-26 NP	ST-27 MNP	ST-32 MNP	ST-38 B	ST-39 TEP
Orthoclase	7.78	5.44	14.76	3.23	10.71	6.35	9.82
Albite	7.93	4.98	0.00	0.36	0.00	6.85	5.09
Anorthite	21.76	23.68	12.14	14.40	17.08	20.04	22.34
Leucite	0.00	0.00	1.06	0.00	0.36	0.00	0.00
Nepheline	6.18	7.04	25.18	12.31	17.42	9.14	11.45
Diopside	28.16	29.70	29.89	36.16	35.94	33.48	33.61
Olivine	18.38	18.39	4.15	23.41	7.39	15.46	7.19
Magnetite	2.89	2.84	3.49	2.87	2.63	2.69	2.74
Ilmenite	5.87	6.19	6.47	5.67	7.31	4.76	6.33
Apatite	1.06	1.74	2.87	1.60	1.17	1.23	1.43
Dicalcium silicate	0.00	0.00	0.00	0.00	0.00	0.00	0.00

Sample Rock type	ST-40 BSN	ST-41 TEP	ST-43 MNP	ST-44 MNP	ST-45 MNP	ST-46B MNP	ST-48 MNP
Orthoclase	4.42	9.25	9.65	3.74	4.24	4.21	0.00
Albite	7.87	6.11	4.79	0.73	0.89	0.00	0.00
Anorthite	21.60	25.43	23.66	16.43	20.05	18.82	11.86
Leucite	0.00	0.00	0.00	0.00	0.00	0.06	3.60
Nepheline	8.57	8.57	10.45	13.62	10.32	12.00	13.48
Diopside	29.65	32.76	33.76	33.96	30.77	31.90	27.15
Olivine	17.44	7.58	6.90	20.73	22.66	22.04	27.17
Magnetite	3.02	2.71	2.72	2.87	2.89	2.84	2.68
Ilmenite	6.09	6.33	6.29	6.59	6.72	6.58	6.03
Apatite	1.33	1.27	1.78	1.32	1.47	1.56	2.21
Dicalcium silicate	0.00	0.00	0.00	0.00	0.00	0.00	5.82

Sample Rock type	ST-50 BSN	ST-59 BSN	ST-99 BSN	ST-187 MNP
Orthoclase	7.64	3.31	6.00	3.79
Albite	7.30	12.41	7.95	4.40
Anorthite	19.02	16.45	17.86	14.63
Leucite	0.00	0.00	0.00	0.00
Nepheline	9.34	12.30	8.05	11.58
Diopside	30.43	29.41	29.87	33.66
Olivine	17.13	14.12	19.49	19.07
Magnetite	2.75	2.96	2.91	3.13
Ilmenite	5.10	6.79	6.81	8.06
Apatite	1.30	2.25	1.06	1.68
Dicalcium silicate	0.00	0.00	0.00	0.00

IV.1.4. Lower Pico da Antónia Formation

Sample Rock type	ST-37 MNP	ST-42 MNP	ST-8 MNP	ST-30 MNP	ST-36 B	ST-74 MNP	ST-101 MNP
Orthoclase	3.33	0.52	10.40	9.95	6.25	8.18	8.59
Albite	0.00	0.00	3.46	0.00	9.00	0.00	2.40
Anorthite	17.85	16.40	21.68	19.23	21.49	17.36	19.46
Leucite	5.81	9.21	0.00	0.68	0.00	3.69	0.00
Nepheline	8.85	9.70	9.14	11.17	8.15	8.98	6.46
Diopside	32.50	33.06	29.98	34.88	31.19	29.19	32.22
Olivine	21.35	20.88	12.86	13.19	14.34	20.63	20.35
Magnetite	2.82	2.79	2.91	2.90	2.60	2.96	2.80
Ilmenite	6.40	6.41	7.45	6.75	5.99	6.92	6.63
Apatite	1.10	1.05	2.12	1.26	0.99	2.10	1.10
Dicalcium silicate	0.00	0.00	0.00	0.00	0.00	0.00	0.00

Sample Rock type	ST-173 MNP	ST-174 MNP	ST-177 MNP	ST-186 MNP
Orthoclase	4.34	0.00	7.14	9.22
Albite	0.00	0.00	0.00	0.00
Anorthite	15.59	14.74	14.95	12.99
Leucite	4.06	7.58	1.92	3.37
Nepheline	9.91	10.31	10.22	12.55
Diopside	28.62	31.16	28.72	31.19
Olivine	26.23	24.66	25.73	18.41
Magnetite	3.15	3.08	3.18	3.11
Ilmenite	6.53	6.57	6.57	6.95
Apatite	1.58	1.74	1.58	2.21
Dicalcium silicate	0.00	0.16	0.00	0.00

IV.1.5. Flamengos Formation

Sample Rock type	ST-4 MNP	ST-5 MNP	ST-6 B	ST-11 MNP	ST-12 PIC	ST-34 MNP	ST-51 MNP
Orthoclase	11.10	12.45	10.06	4.78	8.60	0.00	10.34
Albite	2.04	1.45	4.87	5.19	1.10	0.00	0.32
Anorthite	18.52	19.03	20.31	18.50	18.31	14.76	20.16
Leucite	0.00	0.00	0.00	0.00	0.00	8.28	0.00
Nepheline	9.97	9.36	7.19	10.75	6.07	11.53	13.51
Diopside	31.44	31.43	32.34	35.70	32.03	31.76	35.01
Olivine	14.43	13.56	15.42	14.11	25.77	21.32	8.36
Magnetite	2.82	2.82	2.55	2.92	2.12	2.80	2.85
Ilmenite	8.29	8.40	6.18	6.78	5.18	6.49	7.27
Apatite	1.39	1.50	1.07	1.27	0.81	1.36	2.19
Dicalcium silicate	0.00	0.00	0.00	0.00	0.00	1.70	0.00

Sample Rock type	ST-56 BSN	ST-57 TEP	ST-58 MNP	ST-60 BSN
Orthoclase	11.19	6.64	11.65	10.86
Albite	10.85	8.48	0.00	6.25
Anorthite	27.30	23.69	20.57	21.20
Leucite	0.00	0.00	3.74	0.00
Nepheline	6.36	5.56	7.94	6.84
Diopside	21.36	34.11	35.13	28.88
Olivine	10.63	7.63	7.21	15.38
Magnetite	2.85	2.87	2.83	2.74
Ilmenite	7.24	9.85	9.82	6.65
Apatite	2.22	1.18	1.13	1.20
Dicalcium silicate	0.00	0.00	0.00	0.00

IV.2. Santiago MORB lavas

Sample	ST-61	ST-62	ST-63	ST-64	ST-65	ST-66	ST-67
Rock type	B	B	B	B	B	B	B
Orthoclase	4.66	3.24	2.94	3.04	5.19	5.36	3.71
Albite	17.71	19.69	17.59	6.62	18.44	13.99	16.57
Anorthite	27.22	27.74	26.82	25.01	27.44	24.57	27.06
Nepheline	4.17	6.58	6.81	13.47	4.32	9.10	6.84
Diopside	29.43	31.56	31.90	42.45	29.14	32.25	31.73
Olivine	12.66	7.03	9.77	5.36	11.52	10.65	10.00
Magnetite	2.33	2.19	2.27	2.16	2.11	2.28	2.23
Ilmenite	1.63	1.75	1.70	1.68	1.67	1.63	1.67
Apatite	0.19	0.23	0.22	0.23	0.17	0.17	0.20

Sample	ST-68	ST-69	ST-70
Rock type	B	B	B
Orthoclase	2.45	4.01	3.10
Albite	15.04	16.92	17.05
Anorthite	28.65	25.78	26.93
Nepheline	6.09	8.08	6.18
Diopside	34.49	32.46	31.76
Olivine	9.26	8.72	10.77
Magnetite	2.12	2.06	2.32
Ilmenite	1.68	1.74	1.69
Apatite	0.22	0.22	0.20

IV.3. Maio MORB lavas

Sample	CVP-79	CVP-80	CVP-83
Rock type	TB	TB	TB
Orthoclase	13.01	10.25	8.71
Albite	20.66	21.36	16.21
Anorthite	20.94	20.97	17.46
Nepheline	3.25	3.48	12.28
Diopside	21.43	25.58	26.45
Olivine	13.78	11.34	11.47
Magnetite	3.68	3.78	3.94
Ilmenite	2.94	2.92	3.17
Apatite	0.31	0.31	0.33

IV.4. Santiago Gabbroic Xenoliths

Sample	ST-164	ST-167	ST-168	ST-169
Rock type	G	G	G	G
Orthoclase	0.00	0.24	1.34	1.03
Albite	0.00	10.08	14.83	13.96
Anorthite	60.08	63.19	47.14	41.07
Leucite	0.10	0.00	0.00	0.00
Nepheline	7.89	2.36	0.00	0.00
Diopside	16.93	14.66	23.76	25.97
Hypersthene	0.00	0.00	6.84	6.85
Olivine	13.51	7.37	4.10	9.36
Magnetite	1.06	1.38	1.28	1.30
Ilmenite	0.18	0.32	0.37	0.39
Apatite	0.05	0.40	0.33	0.07
Dicalcium silicate	0.21	0.00	0.00	0.00

APPENDIX V

QUANTITATIVE MODELLING

V - Quantitative modelling

V.1. Partial melting

V.1.1. Batch partial melting

The generation of melt from distinct mantle paragenesis under different partition coefficients and/or percentage of melting can be modelled in order to evaluate the importance of each of these factors to the genesis of the studied OIB and MORB. Santiago's lavas heterogeneity on K, Gd, Yb and HFSE were tested for the presence of garnet and amphibole as residual mantle minerals (section 4.4.3.2) and for the ability of some of these residual minerals to fractionate HFSE (section 4.2.4.2).

The modelled regime used was the modal batch melting of Shaw (1970), where the minerals contribute to the melt in proportion to their concentration in the rock (equation V.1):

$$C_L = \frac{C_0}{D_0 + F \cdot (1 - D_0)} \qquad \text{(V.1)}$$

C_L= weight concentration of a trace element in the liquid;

C_0=weight concentration of a trace element in the original unmelted solid;

F=weight fraction of melt produced;

D_0=Bulk distribution coefficient of the original solids

$D = \sum x^i \cdot K^i$

x^i = normative weight fraction of mineral *i* in the source

K^i =mineral-melt partition coefficient

However modal melting is unlikely to occur due to preferential melting of some minerals in the source and so non-modal batch melting (Shaw, 1970) was also used. In this melting regime

minerals melt in different proportions than those in which they occur in the source ($D_0 \neq P$) (equation V.2):

$$C_L = \frac{C_0}{D_0 + F \cdot (1 - P)} \qquad \text{(V.2)}$$

C_L= weight concentration of a trace element in the liquid

C_0=weight concentration of a trace element in the original unmelted solid

D_0=Bulk distribution coefficient of the original solids

F=weight fraction of melt produced

P=Bulk distribution coefficient of minerals which make up a melt

$$P = \sum p^i \cdot K^i$$

p^i =normative weight fraction contribution of mineral *i* to the melt

K^i =mineral-melt partition coefficient

V.1.2. Aggregated fractional melting

As opposed to batch partial melting in fractional partial melting, the melt leaves the system as soon as it is formed, and so the instantaneous fractional melts will become very depleted in highly incompatible elements as melting proceeds. In section 6.3.1.9. aggregation fractional melting (equation V.3) was chosen to model the generation of Santiago outcropping MORB lavas. In this type of melting process the melt increments are collected together in a common reservoir prior to eruption, the numerical results being very similar to those of batch melting process.

$$\frac{\overline{C}_L}{C_0} = \frac{1}{F} \cdot \left[1 - (1 - F)^{1/D_0}\right] \qquad \text{(V.3)}$$

$\overline{C}_L$ = averaged weight concentration of a trace element in a mixed melt;

the other terms used in equation (V.3) are the same as equation (V.1).

V.2. Fractional crystallization

By analyzing major and trace element behaviour along a liquid line of descent it is possible to infer the crystallizing mineral assemblage. In fractional crystallization it is assumed that the crystals remain in equilibrium which each melt increment being described by the Rayleigh law,

$$C_L = C_0 \cdot F^{(D-1)} \qquad \text{(V.4)}$$

where,

C_L= Concentration of an element in residual liquid

C_0= Initial concentration of an element

F= Fraction of residual liquid

D=partition coefficient for an element

Each of the Santiago formations were analyzed separately since they present differences that imply distinct magma sources and so different crystallization paths. However the Assomada e Monte das Vacas formations were the most studied for crystallization processes since they present the most evolved rocks (section 4.4.2.).

V.3. Mixing

In order to identify possible association of systems with distinct geochemical properties (mantle end-members, distinct mantle lithotypes) bulk mixing processes were modelled in Santiago lavas. The observed variation in Nb/Ta and Zr/Hf ratios as well as heterogeneities in $^{207}Pb/^{204}Pb$ vs. $^{206}Pb/^{204}Pb$, $^{143}Nd/^{144}Nd$ vs. $^{87}Sr/^{86}Sr$ and $^{143}Nd/^{144}Nd$ vs. $^{206}Pb/^{204}Pb$ isotopic ratios were modelled as two component mixing (binary mixing) (Langmuir, 1978; Albarède, 1996; Zou, 2007) (sections 4.2.4.2 and 4.5.5, respectively).

If it's considered that mass fraction f_a of end-member **a** and f_b of end-member **b**, is such that $f_a+f_b=1$, then an element Z to have mass balance must be characterized by:

$$[Z]_{mix} = f_b \cdot [Z]_b + (1 - f_b) \cdot [Z]_a \qquad \text{(V.5)}$$

$[Z]_{mix}$ = concentration of element Z in the mixture

$[Z]_b$ = concentration of element Z in component b

$[Z]_a$ = concentration of element Z in component a

f_b = mass proportion of component b

$(1-f_b)$ = mass proportion of component a

If a ratio of two elements (a/b) in a two component mixture is considered, then:

$$y_{mix} = \left(\frac{a}{b}\right)_{mix} = \frac{a_1 \cdot f_1 + a_2 \cdot (1 - f_1)}{b_1 \cdot f_1 + b_2 \cdot (1 - f_1)} \qquad \text{(V.6)}$$

When two components are considered with two distinct element ratios (a/b) and (c/d), then:

$$\text{Component 1 : } y_1 = \left(\frac{a_1}{b_1}\right) \qquad \text{Component 2: } y_2 = \left(\frac{a_2}{b_2}\right)$$

$$y_{mix} = \frac{b_1 \cdot y_1 \cdot f_1 + b_2 \cdot y_2 \cdot (1 - f_1)}{b_1 \cdot f_1 + b_2 \cdot (1 - f_1)} \qquad \text{(V.7)}$$

$$\text{Component 1 : } x_1 = \left(\frac{c_1}{d_1}\right) \qquad \text{Component 2: } x_2 = \left(\frac{c_2}{d_2}\right)$$

$$x_{mix} = \frac{d_1 \cdot x_1 \cdot f_1 + d_2 \cdot x_2 \cdot (1 - f_1)}{d_1 \cdot f_1 + d_2 \cdot (1 - f_1)} \qquad \text{(V.8)}$$

The mixing curve obtained is an hyperbola, with **r** (equation G) representing the extent of the curvature of the hyperbolic curve (Fig. A5.1):

$$r = \frac{b_1 \cdot d_2}{b_2 \cdot d_1} = \frac{b_1/d_1}{b_2/d_2} \qquad \text{(V.9)}$$

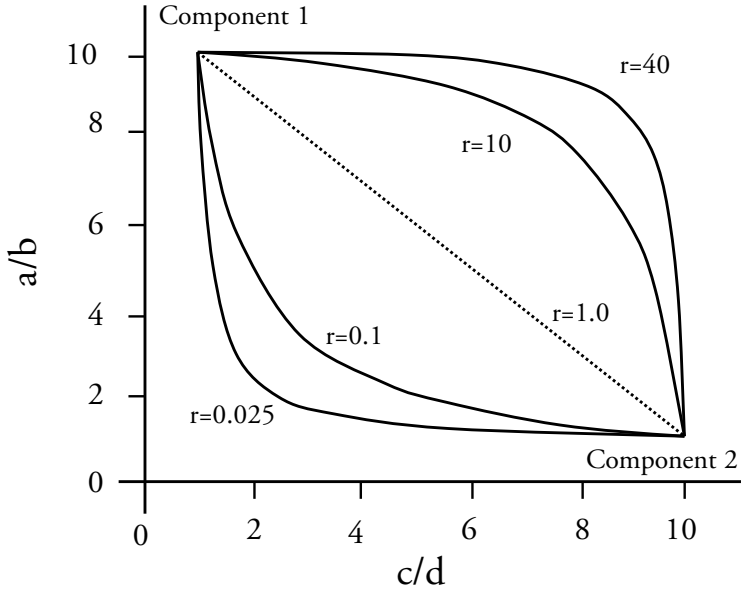

Figure V.1 – Two component mixing curves with different r (adapted from Zou, 2007).

When r=1, the mixing curve is a straight line as in the case of two component mixing in $^{207}Pb/^{204}Pb$ vs. $^{206}Pb/^{204}Pb$ plot, since the denominator is the same in both ratios (section 4.5.5).

When r≠1, the sense of the hyperbola curvature is dependent on the relative concentration of **b** and **d** in the distinct components, as in the case of Nb/Ta vs. Zr/Hf, $^{143}Nd/^{144}Nd$ vs. $^{87}Sr/^{86}Sr$ and $^{143}Nd/^{144}Nd$ vs. $^{206}Pb/^{204}Pb$ plots. The mixing calculations of the Sr-Nd-Hf systems were accomplished using the excel spreadsheet "Binary Mixing" developed by Professor José Munhá, which is based on the above described methodology.

V.4. Inverse modelling

The inverse modelling approach proposed by Class and Goldstein (1994) is thoroughly explained in section 4.4.3.3. In this appendix only particular explanations are presented in order to complement the description already presented.

In Table V.1 the slopes, intercepts and r^2 values for the regressions against La, (that allows the calculation of the concentration for all the element in the highest and lowest degree of melting) as well as the enrichment ratios, are presented for the Assomada, Upper and Lower Pico da Antónia and Flamengos formations.

Particularities in partition coefficients set used

Potassium was not used in the modelling of the Assomada and Upper Pico da Antónia because the set of experimentally determined partition coefficients of Dasgupta et al. (2009) did not include this element.

The data supports the presence of pargasitic amphibole in order to explain the Nb/Ta ratios and the compatibility of Ti within the Assomada and Upper Pico da Antónia formations. The partition coefficients of Nb, Ta and Ti for pargasitic amphibole are from Tiepolo et al. (2000), because, as pointed out by Class and Goldstein (1997), the values of partition coefficients for Nb, Ta and Ti determined experimentally, are significantly lower compared to those determined in amphibole/clinopyroxene in xenoliths.

Regarding the hydrous K mineral in the Flamengos formations, a small amount of phlogopite was added to better fit the enrichment factor of Rb and Ba. The partition coefficients used for amphibole, were of Tiepolo et al. (2000) for the Lower Pico da Antónia and those of Tourette et al. (1995) for Flamengos formation. The choice of a particular partition coefficient for amphibole was done according with the better fit in Nb, Ta and Ti enrichment factors.

Table V.1. - Regression parameters of the elements selected against La and enrichment ratios for Assomada, Upper Pico da Antónia, Lower Pico da Antónia and Flamengos formations.

Formation	Element	Slope	Intercept	r^2	CFL	CFH	E
Assomada	Rb	-0.150	50.96	0.69	31.36	46.64	0.67
	Ba	3.036	576.82	0.68	974.50	664.55	1.47
	Th	0.088	0.09	1.00	11.55	2.62	4.41
	Ta	0.067	2.12	0.94	10.86	4.05	2.68
	Nb	0.946	11.67	0.84	135.63	39.02	3.48
	La	1.000	0.00	1.00	131.00	28.90	4.53
	Ce	1.942	8.08	0.99	262.52	64.21	4.09
	Nd	0.752	11.41	0.99	109.90	33.14	3.32
	Zr	0.640	174.37	0.48	258.16	192.85	1.34
	Hf	0.009	6.02	0.70	7.24	6.29	1.15
	Sm	0.111	3.34	0.99	17.84	6.54	2.73
	Eu	0.034	1.20	0.99	5.59	2.17	2.58
	Ti	7.474	20105.00	0.20	21084.09	20321.00	1.04
	Y	0.213	12.60	0.99	40.53	18.76	2.16
	Yb	0.010	0.79	0.99	2.15	1.09	1.97
	Lu	0.001	0.09	0.97	0.25	0.12	1.98
Upper Pico da Antónia	Rb	0.205	9.62	0.31	24.76	15.23	1.63
	Ba	6.001	479.56	0.17	923.61	643.98	1.43
	Th	0.095	-0.15	0.87	6.88	2.45	2.81
	Ta	0.011	4.16	0.05	4.94	4.45	1.11
	Nb	0.592	31.32	0.19	75.15	47.55	1.58
	La	1.000	0.00	1.00	74.00	27.40	2.70
	Ce	1.957	5.27	0.99	150.06	58.88	2.55
	Nd	0.744	10.42	0.97	65.46	30.80	2.13
	Zr	0.345	195.18	0.01	220.74	204.64	1.08
	Hf	0.002	5.66	0.01	5.81	5.71	1.02
	Sm	0.099	3.92	0.90	11.23	6.63	1.69
	Eu	0.027	1.57	0.89	3.53	2.30	1.54
	Ti	-34.137	20587.00	0.04	18060.86	19651.65	0.92
	Y	0.116	17.86	0.77	26.45	21.04	1.26
	Yb	-0.002	1.40	0.10	1.26	1.35	0.94
	Lu	-0.001	0.21	0.59	0.12	0.18	0.66

Continuation Table V.1.

Formation	Element	Slope	Intercept	r^2	CFL[1]	CFH[1]	E[1]
Lower Pico da Antónia	Rb	0.564	13.143	0.51	53.84	33.01	1.63
	Ba	7.342	290.240	0.54	819.56	548.66	1.49
	Th	0.095	0.095	0.92	6.92	3.43	2.02
	Ta	0.054	2.429	0.71	6.34	4.34	1.46
	Nb	1.335	9.295	0.76	105.52	56.27	1.88
	La	1.000	0.000	1.00	72.10	35.20	2.05
	Ce	1.787	9.591	0.96	138.44	72.50	1.91
	Nd	0.841	5.797	0.99	66.44	35.40	1.88
	Zr	3.519	91.845	0.80	345.59	215.73	1.60
	Hf	0.070	3.154	0.80	8.17	5.60	1.46
	Sm	0.159	1.718	0.90	13.17	7.31	1.80
	Eu	0.050	0.678	0.91	4.26	2.43	1.76
	Ti	52.720	18160.0	0.54	21961.11	20015.74	1.10
	Y	0.302	9.880	0.87	31.64	20.50	1.54
	Yb	0.019	0.652	0.40	1.99	1.30	1.52
	Lu	0.002	0.097	0.25	0.23	0.16	1.41
Flamengos	Rb	0.131	35.796	0.09	43.50	38.67	1.12
	Ba	10.983	198.970	0.93	843.67	439.50	1.92
	Th	0.091	0.313	0.93	5.62	2.29	2.45
	Ta	0.112	0.288	0.85	6.85	2.74	2.50
	Nb	1.283	4.925	0.72	80.23	33.02	2.43
	La	1.000	0.000	1.00	58.70	21.90	2.68
	Ce	1.896	7.183	0.99	118.45	48.69	2.43
	Nd	0.822	7.986	0.97	56.24	25.99	2.16
	Zr	3.456	64.133	0.61	267.02	139.83	1.91
	Hf	0.037	4.270	0.26	6.43	5.08	1.27
	Sm	0.127	2.869	0.94	10.31	5.65	1.83
	Eu	0.039	1.018	0.91	3.33	1.88	1.77
	Ti	278.250	9256.700	0.90	25589.98	15350.38	1.67
	Y	0.291	10.862	0.80	27.95	17.24	1.62
	Yb	0.017	0.649	0.61	1.63	1.02	1.61
	Lu	0.002	0.089	0.41	0.20	0.13	1.54

[1] C_{FL}: concentration of the element at the lowest degree of melting; C_{FH}: concentration of the element at the highest degree of melting; E: enrichment factor (C_{FL}/C_{FH}).

Table V.2. - Partition coefficients set used in the trace element inverse modelling for mineral-silicate melt.

Mineral	Olivine	Orthopyroxene	Clinopyroxene	Amphibole	Phlogopite	Garnet	Ilmenite
Data source	1	1	1, 2	1, 3, 4/5	1, 4, 6, 7	2	8
Rb	0.0003	0.0002	0.0004	0.22	4.7588	0.0002	
Ba	0.000005	0.000006	0.00018	0.278	3.9139	7E-12	
Th	0.000007	0.00002	0.0021	0.0039	0.0014	0.0021	0.0011
Ta	0.00005	0.0025	0.022	0.074 / 0.35	0.1069	0.0025	1.8075
Nb	0.00005	0.0013	0.0067	0.05 / 0.46	0.0853	0.00054	1.2325
La	0.0002	0.0008	0.057	0.039	0.0004	0.0014	
Ce	0.00007	0.0016	0.12	0.067	0.0007	0.0029	0.00255
Nd	0.0003	0.0056	0.33	0.142	0.0019	0.03	
Zr	0.001	0.032	0.18	0.124	0.0151	0.12	0.7025
Hf	0.0029	0.06	0.31	0.331	0.0053	0.07	0.9625
Sm	0.01	0.015	0.58	0.188	0.0045	0.18	0.0051
Eu	0.0005	0.03	0.77	0.351	0.0095	0.33	
Ti	0.015	0.086	0.4	0.717 / 2.77	2.8671	0.6	
Y	0.0082	0.095	1.1	0.333	0.036	3.9	0.0207
Yb	0.024	0.22	1.2	0.349	0.033	6.5	
Lu	0.024	0.22	0.98	0.246	0.0395	6.7	0.1178

Data sources of partition coefficients: (1) Halliday et al. (1995); (2) Green et al. (2000); (3) Dalpe and Baker (1994); (4) LaTourette et al. (1995); (5) Tiepolo et al. (2006); (6) Gregoire et al. (2000); (7) Foley et al. (1996) and (8) Klemme et al. (2006).

Table V.3. - Partition coefficients set used in the trace element inverse modelling for mineral-silicate melt and mineral-carbonatitic melt.

Mineral	Olivine	Orthopyroxene	Clinopyroxene	Amphibole	Phlogopite	Garnet	Ilmenite
Data source	9	9	9	1, 3, 4	1, 4, 6, 7	9	8
Rb	0	0	0.003	0.22	4.7588	0.013	
Ba	1E-9	0.00001	0.008	0.278	3.9139	0.0007	
Th	1E-9	0.00001	0.002	0.0039	0.0014	0.017	0.0011
Ta	0	0.0029	0.002	0.074	0.1069	0.041	1.8075
Nb	0	0.0029	0.001	0.05	0.0853	0.06	1.2325
La	0.000007	0.001	0.006	0.039	0.0004	0.006	
Ce	0.00001	0.003	0.012	0.067	0.0007	0.015	0.00255
Nd	0.00007	0.009	0.033	0.142	0.0019	0.006	
Zr	0.036	0.17	0.024	0.124	0.0151	1.06	0.7025
Hf	0.036	0.17	0.063	0.331	0.0053	1.41	0.9625
Sm	0.0007	0.02	0.053	0.188	0.0045	0.053	0.0051
Eu	0.00095	0.03	0.07	0.351	0.0095	0.17	
Ti	0.015	0.13	0.14	0.717	2.8671	1.21	
Y	0.023	0.18	0.13	0.333	0.036	1.34	0.0207
Yb	0.023	0.1	0.16	0.349	0.033	3.5	
Lu	0.03	0.52	0.17	0.246	0.0395	4.6	0.1178

Data sources of partition coefficients: (1) Halliday et al. (1995); (3) Dalpe and Baker (1994); (4) LaTourette et al. (1995); (6) Gregoire et al. (2000); (7) Foley et al. (1996); (8) Klemme et al. (2006) and (9) Dasgupta et al. (2009).

V.5. Isotopic data calculations

V.5.1. Isotopic data parameters

εNd

$$\varepsilon_{Nd} = \left[\frac{\left({}^{143}Nd/{}^{144}Nd \right)_m}{I^0_{CHUR}} - 1 \right] \cdot 10^4 \qquad \text{(V.10)}$$

where

$\left({}^{143}Nd/{}^{144}Nd \right)_m$ = ^{143}Nd/^{144}Nd measured in the sample

I^0_{CHUR} = 0.512638 (Chondritic uniform reservoir value; DePaolo and Wasserburg, 1976)

εHf

$$\varepsilon_{Hf} = \left[\frac{\left({}^{176}Hf/{}^{177}Hf \right)_m}{I^0_{CHUR}} - 1 \right] \cdot 10^4 \qquad \text{(V.11)}$$

$\left({}^{176}Hf/{}^{177}Hf \right)_m$ = ^{176}Hf/^{177}Hf measured in the sample

I^0_{CHUR} = 0.282772 (Chondritic uniform reservoir value; Blichert-Toft and Albaréde, 1997)

NHRL (Northern Hemisphere Reference Line)

$$\left({}^{207}Pb/{}^{204}Pb \right) = 0.1084 \cdot \left({}^{206}Pb/{}^{204}Pb \right) + 13.491 \qquad \text{(V.12)}$$

$$\left({}^{208}Pb/{}^{204}Pb \right) = 1.209 \cdot \left({}^{206}Pb/{}^{204}Pb \right) + 15.627 \qquad \text{(V.13)}$$

Δ7/4 and Δ8/4 values

Delta values were calculated according to Hart (1984) and represent the offset to the NHRL

$$\Delta 7/4 = \left[\left(^{207}Pb/^{204}Pb\right)_m - \left(^{207}Pb/^{204}Pb\right)_{NHRL}\right]\cdot 100 \qquad (V.14)$$

$$\Delta 8/4 = \left[\left(^{208}Pb/^{204}Pb\right)_m - \left(^{207}Pb/^{204}Pb\right)_{NHRL}\right]\cdot 100 \qquad (V.15)$$

where

subscript m and NHRL stands for measured and NHRL $^{207}Pb/^{204}Pb$ and $^{208}Pb/^{204}Pb$ ratios.

$^{208}Pb^*/^{206}Pb^*$

$$^{208}Pb^*/^{206}Pb^* = \left[\left(^{208}Pb/^{204}Pb\right)_m - \left(^{208}Pb/^{204}Pb\right)_{CD}\right]/\left[\left(^{207}Pb/^{204}Pb\right)_m - \left(^{207}Pb/^{204}Pb\right)_{CD}\right] \qquad (V.16)$$

subscript m and CD referring to the measured and Canyon Diablo data ($^{206}Pb/^{204}Pb$=9.3066; $^{208}Pb/^{204}Pb$=29.475; Chen and Wasserburg, 1983). See Allègre et al. (1986)

V.5.2. Parent-isotope ratios determination

Considering the equations that describe the ^{238}U ,^{235}U and ^{232}Th decay to ^{206}Pb, ^{207}Pb and ^{208}Pb , respectively, and divided by ^{204}Pb the only non-radiogenic isotope, in order to obtain isotope ratios instead of absolute nuclide abundances (Dickin, 2005):

$$\left(\frac{^{206}Pb}{^{204}Pb}\right) = \left(\frac{^{206}Pb}{^{204}Pb}\right)_{ini} + \frac{^{238}U}{^{204}Pb}\times\left(e^{\lambda_{238}\times T} - e^{\lambda_{238}\times t}\right) \qquad (V.17)$$

$$\left(\frac{^{207}Pb}{^{204}Pb}\right) = \left(\frac{^{207}Pb}{^{204}Pb}\right)_{ini} + \frac{^{235}U}{^{204}Pb}\times\left(e^{\lambda_{235}\times T} - e^{\lambda_{235}\times t}\right) \qquad (V.18)$$

$$\left(\frac{^{208}Pb}{^{204}Pb}\right)=\left(\frac{^{208}Pb}{^{204}Pb}\right)_{ini}+\frac{^{232}Th}{^{204}Pb}\times\left(e^{\lambda_{232}\times T}-e^{\lambda_{232}\times t}\right) \qquad (V.19)$$

where,

$\left(\frac{^{206}Pb}{^{204}Pb}\right)$, $\left(\frac{^{207}Pb}{^{204}Pb}\right)$, $\left(\frac{^{208}Pb}{^{204}Pb}\right)$ = measured isotopic ratios at time t

$\left(\frac{^{206}Pb}{^{204}Pb}\right)_{ini}$, $\left(\frac{^{207}Pb}{^{204}Pb}\right)_{ini}$, $\left(\frac{^{208}Pb}{^{204}Pb}\right)_{ini}$ = measured isotopic ratios at the initial time T and where T<t

$\left(\frac{^{238}U}{^{204}Pb}\right)$, $\left(\frac{^{235}U}{^{204}Pb}\right)$, $\left(\frac{^{232}Th}{^{204}Pb}\right)$ = U/Pb and Th/Pb parent ratios

λ = decay constant of respective element (see Table V.4)

it becomes clear that, if the U/Pb and Th/Pb parent ratios ($^{238}U/^{204}Pb$, $^{238}U/^{204}Pb$, $^{232}Th/^{204}Pb$) are known then the initial $^{206}Pb/^{204}Pb$ and $^{207}Pb/^{204}Pb$ ratios at a specific time T relative to the present time (t=0), can be determined.

Table V.4. - Parameters of Pb isotopic system

	Parent	Daughter	Ratio	λ	$t_{1/2}$
U-Pb	^{238}U	^{206}Pb	$^{206}Pb/^{204}Pb$	1.551 x10^{-10} a^{-1}	4.47 Ga
U-Pb	^{235}U	^{207}Pb	$^{207}Pb/^{204}Pb$	9.849 x10^{-10} a^{-1}	0.707 Ga
Th-Pb	^{232}Th	^{208}Pb	$^{208}Pb/^{204}Pb$	4.948 x10^{-11} a^{-1}	14 Ga

λ=decay constant from Steiger and Jager, 1977; $t^{1/2}$=half-life, the time for half the parent nuclides to decay to daughter nuclides (Jaffey et al., 1971).

Since the parent-isotope ratios were not determined analytically a more simplistic approach using element concentration and isotopic ratios was used:

$$\frac{^{238}U}{^{204}Pb} = \frac{U \cdot \left(\frac{P^{238U}}{A^{U}} \right)}{Pb \cdot \left(\frac{P^{204Pb}}{A^{Pb}} \right)} = \mu \qquad \text{(V.20)}$$

$$\frac{^{235}U}{^{204}Pb} = \frac{U \cdot \left(\frac{P^{235U}}{A^{U}} \right)}{Pb \cdot \left(\frac{P^{204Pb}}{A^{Pb}} \right)} = \gamma \qquad \text{(V.21)}$$

$$\frac{^{232}Th}{^{204}Pb} = \frac{Th \cdot \left(\frac{P^{232Th}}{A^{Th}} \right)}{Pb \cdot \left(\frac{P^{204Pb}}{A^{Pb}} \right)} = \omega \qquad \text{(V.22)}$$

where,

U, Pb, Th = measured trace element concentration

A^{Pb}, A^{U}, A^{Th} = atomic weight of Pb, U and Th in the sample, respectively

P^{238U}, P^{235U}, P^{232Th}=atomic proportion of ^{238}U, ^{235}U and ^{232}Th, respectively

Atomic weight of Pb, U and Th are determined as follows:

$$A^{Pb} = P^{204Pb} \cdot A^{204Pb} + P^{206Pb} \cdot A^{206Pb} + P^{207Pb} \cdot A^{207Pb} + P^{208Pb} \cdot A^{208Pb} \quad (V.23)$$

$$A^{U} = P^{238U} \cdot A^{238U} + P^{235U} \cdot A^{235U} \quad (V.24)$$

$$A^{Th} = P^{232Th} \cdot A^{232Th} \quad (V.25)$$

Where $A^{\#\#}$ denotes standard atomic mass for each of the isotopes (Table V.5)

Table V.5. – Atomic mass from Pb, U and Th isotopes

Isotope	Mass (DeLaeter, 2003)
^{204}Pb	203.973029
^{206}Pb	205.974449
^{207}Pb	206.975881
^{208}Pb	207.976636
^{235}U	235.043923
^{238}U	238.050783
^{232}Th	232.038050

The atomic proportion of Pb isotopes in equations (V.20, V.21, V.22) are calculated as follows:

$$P^{204Pb} = \frac{1}{1 + (^{206}Pb/^{204}Pb)_m + (^{207}Pb/^{204}Pb)_m + (^{208}Pb/^{204}Pb)_m} \quad (V.26)$$

$$P^{206Pb} = \frac{\left(^{206}Pb/^{204}Pb\right)_m}{1 + (^{206}Pb/^{204}Pb)_m + (^{207}Pb/^{204}Pb)_m + (^{208}Pb/^{204}Pb)_m} \quad (V.27)$$

$$P^{207Pb} = \frac{\left(^{207}Pb/^{204}Pb\right)_m}{1+(^{206}Pb/^{204}Pb)_m+(^{207}Pb/^{204}Pb)_m+(^{208}Pb/^{204}Pb)_m} \quad \text{(V.28)}$$

$$P^{208Pb} = \frac{\left(^{208}Pb/^{204}Pb\right)_m}{1+(^{206}Pb/^{204}Pb)_m+(^{207}Pb/^{204}Pb)_m+(^{208}Pb/^{204}Pb)_m} \quad \text{(V.29)}$$

$(^{20\#}Pb/^{204}Pb)_m$ = measured Pb isotopic ratios in the sample

The percentages of U isotopes are constant throughout the solar system with ^{238}U and ^{235}U values of 0.99279954 and 0.00720046, respectively (137.88/138.88 and 1/138.88, respectively). The percentage of ^{232}Th is 1 because it is the only radiogenic Th isotope.

V.5.3. Pb mantle evolution: two stage model

To infer the isotopic character of Santiago source two-stage Pb evolution model, introduced by Stacey and Kramers (1975), was modelled (see also, Chase 1981). This model assumes Pb isotopic evolution by two closed systems with distinct μ values (μ_1 and μ_2), an Earth age of 4.55 Ga and its primordial composition assumed to be represented by Canyon Diablo troilite (see Table V.6).

Table V.6. - Isotopic ratios of primeval Pb (Canyon Diablo troilite)

	Chen and Wassenburg (1983)
$^{206}Pb/^{204}Pb$	9.3066
$^{207}Pb/^{204}Pb$	10.293
$^{208}Pb/^{204}Pb$	29.475

The first stage (from 4.55 to 1.5/1.6 Ga) evolved from Pb primeval values, assumed as the Canyon Diablo troilite values with a μ_1 of 8.1. The second stage represents the evolution, after subduction of the altered oceanic crust between 1.5/1.6 Ga ago and the present day. The μ_2 is significantly higher because during subduction, hydrothermal processes are responsible for the addition of U and Pb loss. The Pb removed by hydrothermal fluids is re-deposited as sulphide minerals that will dissolved during dehydration of the plate during subduction, making the descending slab with a high U/Pb ratio. In Santiago Island the μ_2 was modelled to be about 15, which is consistent with values obtained by Barker et al. (2010).